THE UNIVERSITY of ADELAIDE

Development of Eco-Friendly and High Performance Construction Materials and Technologies

Aliakbar Gholampour

Thesis submitted in fulfilment of the requirements for the degree of Doctor of Philosophy

The University of Adelaide
Faculty of Engineering, Computer and Mathematical Sciences
School of Civil, Environmental and Mining Engineering

Table of Contents

Abstract

Because of global environmental concerns for concrete and waste materials and increased awareness of non-renewable natural resources, there is an urgent need to find ways to develop eco-friendly concretes. This is reflected in the large number of recent studies undertaken toward this end. However, the existing studies lack some of main parameters and points, such as the influence of the quality of recycled aggregates, influence of the full replacement of dry constituents with waste-based alternatives, influence of high performance graphene nanomaterials, and influence of the lateral confinement at the material level on the properties of concretes. This thesis contains a series of journal papers focused on the development of eco-friendly and high performance construction materials. In this research the behaviour of different types of concretes and mortars, including recycled aggregate concrete (RAC), geopolymer mortar, waste-based concrete and mortar, and graphene-based cement mortar, is studied. In addition, this thesis presents the behaviour of geopolymer concrete and steel fibre-reinforced concrete (SFRC) under active confinement and high-strength concrete (HSC) under shape memory alloy (SMA) confinement.

The experimental study on time-dependent and long-term mechanical properties of RACs shows that high-strength RACs, prepared with full replacement of natural aggregates with recycled concrete aggregates having a high parent concrete strength (110 MPa), exhibit the properties similar to or better than those of companion natural aggregate concretes. Using gene expression programming (GEP) technique, new empirical models are developed to accurately predict mechanical properties of RACs. In addition, analytical studies on RACs reveal that multivariate adaptive regression splines (MARS), M5 model tree (M5Tree), and least squares support vector regression (LSSVR) models provide close predictions of mechanical properties of RACs by accurately capturing influences of key parameters.

The experimental study on waste-based concrete reveals that concretes containing ground granulated blast furnace slag (GGBS) at up to 90% cement replacement exhibit nearly similar mechanical properties to the conventional concrete after 28

days of curing age. The experimental studies on geopolymer and waste-based mortars show that mortars with full replacement of sand with lead smelter slag (LSS) and glass sand (GS) and up to 80% replacement of cement with GGBS exhibit nearly similar mechanical properties to the conventional mortar.

The study on the influence of graphene oxide (GO) dosage on physiochemical and mechanical properties of cement mortars shows considerable dosage dependence with the optimum dosage of 0.1% GO (by weight of cement) that increases 28-day tensile and compressive strength of the composite by 37.5% and 77.7%, respectively. The study on the influence of oxygen functional groups of graphene on the properties of cement mortars reveals that an addition of 0.1% reduced GO (rGO) prepared by 15 min reduction and 0.2% (wt%) hydrazine results in a maximum enhancement of 45.0% and 83.7% in the 28-day tensile and compressive strengths compared to the plain cement mortar, respectively.

The experimental study on the behaviour of ambient- and oven-cured geopolymer concretes under active confinement reveals that oven-cured geopolymers exhibit a less ductile behaviour and lateral dilation than their ambient-cured counterparts. The experimental study on the compressive behaviour of SMA-confined HSCs shows that confinement of HSC by 9.5% prestrained SMA spirals leads to 23.6% higher peak axial stress and 346% higher corresponding axial strain than that of unconfined HSC. The experimental study on the compressive behaviour of actively confined SFRC reveals that an increase in the steel fibre volume fraction leads to an increase in ductility of SFRCs. A finite element (FE) model is also developed to accurately predict the compressive behaviour of fibre-reinforced polymer (FRP)-confined SFRCs.

The promising findings of this research point to the possibility of the development of eco-friendly and high performance composite members for structural applications in the construction industry.

Statement of Originality

I, Aliakbar Gholampour, hereby declare that this work contains no material which has been accepted for the award of any other degree or diploma in any university or other tertiary institution in my name and, to the best of my knowledge and belief, contains no material previously published or written by another person, except where due reference has been made in the text. In addition, I certify that no part of this work will, in the future, be used in a submission in my name, for any other degree or diploma in any university or other tertiary institution without the prior approval of the University of Adelaide and, where applicable, any partner institution responsible for the joint-award of this degree.

I give consent to this copy of my thesis when deposited in the University Library, being made available for loan and photocopying, subject to the provisions of the Copyright Act 1968.

The author acknowledges that copyright of published works contained within this thesis resides with the copyright holder(s) of those works.

I also give permission for the digital version of my thesis being made available on the web, via the University's digital research repository, the Library Catalogue, the Australian Digital Thesis Program (ADTP) and also through web search engines, unless permission has been granted by the University to restrict access for a period of time.

Signed: …….…… Date: …….

Acknowledgements

I would like to acknowledge the support of my supervisors Professor Togay Ozbakkaloglu, Associate Professor Ching-Tai Ng, and Dr. Terry Bennett. Without their supervision and support this thesis would not be possible. I am particularly grateful to Professor Togay Ozbakkaloglu for not only his unreserved guidance but also the encouragement and emotional supports during my candidature. I am also grateful to Associate Professor Ching-Tai Ng for his motivation during the last year of my candidature.

I would also like to acknowledge all academics and technical staffs who helped me technically with this thesis in their field of expertise. I would specifically appreciate the support of Professor Dusan Losic, Professor Ozgur Kisi, Dr. Thomas Vincent, Dr. Amir Hossein Gandomi, Dr. Meisam Valizadeh Kiamahalleh, Dr. Diana Tran, and Dr. Iman Mansouri for their technical support during my PhD candidature.

I would like to sincerely thank my dearest wife, Hadis, for her unwavering support and motivation. Words are unable to express my deepest appreciation and love to her. Without her unconditional love, this work would hardly be completed.

Finally, I would like to thank the University of Adelaide for offering me the precious opportunity to seek the light in the deep ocean of science.

List of Tables

List of Figures

List of Publications

Citations: GoogleScholar = 346; Scopus = 269

H-index: GoogleScholar = 12; Scopus = 10

Accepted/Published

Journal Papers

JP1. **Gholampour A**, Pour AF, Hassanli R, Ozbakkaloglu T. Behavior of actively confined rubberized concrete under cyclic axial compression. *Journal of Structural Engineering*, *ASCE*. 2019, accepted (IF = 2.021; Q1).

JP2. Pour AF, **Gholampour A**, Zheng J, Ozbakkaloglu T. Behavior of FRP-confined high-strength concrete under eccentric compression: tests on concrete-filled FRP tube columns. *Composite Structures*, *Elsevier*. 2019;220:261-72 (IF = 4.451; Q1).

JP3. *__Gholampour A__, Ho VD, Ozbakkaloglu T. Ambient-cured geopolymer mortars prepared with waste-based sands: mechanical and durability-related properties and microstructure. *Composites Part B*, *Elsevier*. 2019;160:519-34 (IF = 4.920; Q1).

JP4. *__Gholampour A__, Ozbakkaloglu T. Fiber-reinforced concrete containing ultra high-strength micro steel fibers under active confinement. *Construction and Building Materials*, *Elsevier*. 2018;187:299-306 (IF = 4.039; Q1).

JP5. *__Gholampour A__, Mansouri I, Kisi O, Ozbakkaloglu T. Evaluation of mechanical properties of concretes containing coarse recycled concrete aggregates using multivariate adaptive regression splines (MARS), M5 model tree (M5Tree), and least squares support vector regression (LSSVR) models. *Neural Computing and Applications*, *Springer*. 2018;10.1007/s00521-018-3630-y (IF = 4.213; Q1).

JP6. *__Gholampour A__, Ozbakkaloglu T. Understanding the compressive behavior of shape memory alloy (SMA)-confined normal- and high-strength concrete. *Composite Structures*, *Elsevier*. 2018;202:943-53 (IF = 4.451; Q1).

JP7. *__Gholampour A__, Ozbakkaloglu T. Behavior of steel fiber-reinforced concrete-filled FRP tube columns: experimental results and a finite element model. *Composite Structures, Elsevier*. 2018;194:252-62 (IF = 4.451; Q1).

JP8. Pour AF, **Gholampour A**, Ozbakkaloglu T. Influence of the measurement method on the axial strain of FRP-confined concrete. *Composite Structures*, *Elsevier*. 2018;188:415-24 (IF = 4.451; Q1).

JP9. *__Gholampour A__, Ozbakkaloglu T. Time-dependent and long-term mechanical properties of concretes incorporating different grades of coarse recycled concrete aggregates. *Engineering Structures*. *Elsevier*, 2014;157:224-34 (IF = 3.060; Q1).

JP10. Xie T, **Gholampour A**, Ozbakkaloglu T. Toward the development of

* Papers considered in the main body of the thesis.

sustainable concretes with recycled concrete aggregates: a comprehensive review of studies on mechanical properties. *Journal of Materials in Civil Engineering*. *ASCE*. 2017;10.1061/(ASCE)MT.1943-5533.0002304 (IF = 1.644; Q1).

JP11. Ozbakkaloglu T, **Gholampour A**, Xie T. Mechanical and durability properties of recycled aggregate concrete: effect of recycled aggregate properties and content. *Journal of Materials in Civil Engineering*, *ASCE*. 2017;30(2):04017275 (IF = 1.644; Q1).

JP12. *__Gholampour A__, Valizadeh Kiamahalleh M, Tran DNH, Ozbakkaloglu T, Losic D. From graphene oxide to reduced graphene oxide: impact on the physiochemical and mechanical properties of graphene-cement composites. *ACS Applied Materials & Interfaces*. 2017;10.1021/acsami.7b16736 (IF = 8.097; Q1).

JP13. *__Gholampour A__, Valizadeh Kiamahalleh M, Tran DNH, Ozbakkaloglu T, Losic D. Revealing the dependence of the physiochemical and mechanical properties of cement composites on graphene oxide concentration. *RSC Advances*.2017;7(87):55148-56 (IF = 2.936; Q1).

JP14. *__Gholampour A__, Ozbakkaloglu T. Performance of sustainable concretes containing very high volume class-F fly ash and ground granulated blast furnace slag. *Journal of Cleaner Production*, *Elsevier*. 2017;162:1407-17 (IF = 6.352; Q1).

JP15. Gholampour A, Ozbakkaloglu T, Hassanli R. Behavior of rubberized concrete under active confinement. *Construction and Building Materials*, *Elsevier*. 2017;138:372-82 (IF = 4.039; Q1).

JP16. Ozbakkaloglu T, Gu L, **Gholampour A.** Short-term mechanical properties of concrete containing recycled polypropylene coarse aggregates under ambient and elevated temperature. *Journal of Materials in Civil Engineering*, *ASCE*. 2017;29(10):04017191 (IF = 1.644; Q1).

JP17. *__Gholampour A__, Gandomi AH, Ozbakkaloglu T. New formulations for mechanical properties of recycled aggregate concrete using gene expression programming. *Construction and Building Materials*, *Elsevier*. 2017;130:122-45 (IF = 4.039; Q1).

JP18. Keshtegar B, Sadeghian P, **Gholampour A**, Ozbakkaloglu T. Nonlinear modeling of ultimate strength and strain of FRP-confined concrete using chaos control method. *Composite Structures*, *Elsevier*. 2017;163:423-31 (IF = 4.451; Q1).

JP19. Ozbakkaloglu T, Fang C, **Gholampour A.** Influence of FRP anchor configuration on the behavior of FRP plates externally bonded on concrete members. *Engineering Structures*, *Elsevier*. 2017;133:133-50 (IF = 3.060; Q1).

JP20. Keshtegar B, Ozbakkaloglu T, **Gholampour A.** Modeling the behavior of FRP-confined concrete using dynamic harmony search algorithm. *Engineering with Computers*, *Springer*. 2016;10.1007/s00366-016-0481-y (IF = 1.951; Q1).

JP21. Mansouri I, **Gholampour A**, Kisi O, Ozbakkaloglu T. Evaluation of peak and residual conditions of actively confined concrete using neuro-fuzzy and neural computing techniques. *Neural Computing and Applications*, *Springer*. 2016;10.1007/s00521-016-2492-4 (IF = 4.213; Q1).

JP22. Lim J, Ozbakkaloglu T, **Gholampour A**, Bennett T, Sadeghi R. Finite-element modeling of actively confined normal-strength and high-strength concrete under uniaxial, biaxial, and triaxial compression. *Journal of Structural Engineering*, *ASCE*. 2016;10.1061/(ASCE)ST.1943-541X.0001589 (IF =

2.021; Q1).

JP23. Ozbakkaloglu T, **Gholampour A**, Lim J. Damage-plasticity model for FRP-confined normal-strength and high-strength concrete. *Journal of Composites for Construction*, *ASCE*. 2016;10.1061/(ASCE)CC.1943-5614.0000712 (IF = 2.648; Q1).

Magazine Papers

M1. Gholampour A, Ozbakkaloglu T, Hassanli R. Rubberized concrete under confinement. *Concrete in Australia*, *Concrete Institute of Australia*. 2017;43(2):49-53.

M2. Ozbakkaloglu T, **Gholampour A**, Fang C. FRP plates bonded on concrete with different FRP anchor configurations. *FRP Composite*, *International Institute for FRP in Construction*. 2017;14(2):21-3.

Conference Papers

C1. Gholampour A, Pour AF, Hassanli R, Ozbakkaloglu T. Cyclic behavior of actively confined rubberized concrete under axial compression. *25th Australasian Conference on Mechanics of Structures and Materials, ACMSM25*, December 2018.

C2. Gholampour A, Valizadeh Kiamahalleh M, Tran DNH, Ozbakkaloglu T, Losic D. Mechanical properties of cement mortar composites containing graphene oxide. *25th Australasian Conference on Mechanics of Structures and Materials, ACMSM25*, December 2018.

C3. Gholampour A, Ozbakkaloglu T. Confinement of normal- and high-strength concrete by shape memory alloy (SMA) spirals. *5th Annual International Conference on Materials Science and Environmental Engineering*, *MSEE*, Published in IOP: Materials Science and Engineering, 2017;301:012056.

C4. Pour AF, **Gholampour A**, Zheng J, Ozbakkaloglu T. Behaviour of square FRP-confined high-strength concrete columns under eccentric compression. *5th Annual International Conference on Materials Science and Environmental Engineering*, *MSEE*, Published in IOP: Materials Science and Engineering, 2017;301:012058.

C5. Gholampour A, Ozbakkaloglu T. Finite element modeling of FRP-confined concrete using extended damage-plasticity approach. *International Conference on Materials, Alloys and Experimental Mechanics*, *ICMAEM*, Published in IOP: Materials Science and Engineering, 2017;225:012147.

C6. Gholampour A, Valizadeh Kiamahalleh M, Tran DNH, Ozbakkaloglu T, Losic D. Physiochemical and mechanical properties of graphene oxide (GO)-cement mortar composite. *20th International Conference on Composite Structures*, *ICCS20*, Paris, France, 2017.

C7. Gholampour A, Ozbakkaloglu T. Shape memory alloy (SMA)-confined normal- and high-strength concrete. *20th International Conference on Composite Structures*, *ICCS20*, Paris, France, 2017.

C8. Gholampour A, Keshtegar B, Ozbakkaloglu T. Reliability analysis of FRP-

confined concrete test databases. *6th Asia-Pacific Conference on FRP in Structures*, *APFIS*, Singapore, 2017.

C9. Pour AF, Ozbakkaloglu T, **Gholampour A**, Zheng J. FRP-confined high-strength concrete under eccentric compression. *6th Asia-Pacific Conference on FRP in Structures*, *APFIS*, Singapore, 2017.

C10. Gholampour A, Ozbakkaloglu T, Hassanli R. Use of fine rubber particles as fine concrete aggregates in actively confined concrete. *3rd International Conference on Mechanical Structures and Smart Materials*, *ICMSSM*, Published in Key Engineering Materials, 2017;729:122-7.

C11. Gholampour A, Ozbakkaloglu T. Extended constitutive model for FRP-confined concrete in circular sections. *International Conference on Advanced Material Research and Application*, *AMRA*, Published in Advanced Materials Research, 2017;1142:349-54.

C12. Gholampour A, Ozbakkaloglu T. Finite element analysis of constitutive behavior of FRP-confined steel fiber reinforced concrete. *International Conference on Material Science and Engineering Technology*, *ICMSET*, Published in Key Engineering Materials, 2017.

Submitted

Journal Papers

JS1. *__Gholampour A__, Ozbakkaloglu T, Etemadi E, Vincent T. Mechanical properties and microstructure of waste-based mortars containing fly ash, ground granulated blast furnace slag, glass powder, and lead smelter slag. *Construction and Building Materials*, *Elsevier*. submitted on 14/01/2019 (IF = 4.920; Q1).

JS2. *__Gholampour A__, Ozbakkaloglu T, Ng CT. Ambient- and oven-cured geopolymer concretes under active confinement. *Construction and Building Materials*, *Elsevier*. submitted on 26/11/2018 (IF = 4.920; Q1).

JS3. Gholampour A, Ozbakkaloglu T. A comprehensive review of natural fiber composites: properties, modification and processing techniques, characterization, applications. *Progress in Materials Science*, *Elsevier*, submitted on 6/5/2017 (IF = 33.190; Q1).

Introduction and General Overview

The production of ordinary Portland cement (OPC), a core component of concrete, releases a significant amount of greenhouse gases (essentially CO_2) into the atmosphere. Therefore, in an effort to reduce CO_2 emissions associated with the concrete industry it is crucial to identify alternative materials that can replace OPC to produce an eco-friendly concrete. Meanwhile, the high demand for natural aggregates as fine and coarse aggregates in the construction industry has led to their over-exploitation, resulting in harmful environmental issues, such as depletion of non-renewable natural aggregates and negative effects on the ecosystem. Therefore, finding an alternative material to natural aggregates has also become imperative.

Recently, the use of industrial by-products, such as fly ash (FA), ground granulated blast furnace slag (GGBS), and glass powder (GP), and waste-based materials, such as glass sand (GS), lead smelter slag (LSS), and recycled concrete aggregates obtained from construction and demolition (C&D) waste, in concrete has received significant attention to develop eco-friendly construction materials with the aim of enabling the use of abundant wastes, reducing the extraction of non-renewable natural resources, and reducing the CO_2 emissions associated with concrete and cement production. Furthermore, graphene nanomaterial, which is obtained from oxidation of waste graphite with unique planar structure, outstanding high surface area, chemical, mechanical, and thermodynamic properties, has offered new opportunities to improve mechanical properties of cement mortars. However, the use of waste materials in concrete and mortar comes with its own challenges which have to be overcome before they can be used in the construction industry.

With the aim of development of high performance concretes for seismically active zones, high-strength concrete (HSC) has become a promising alternative in the construction of new high performance concretes owing to its superior structural properties over normal-strength concrete (NSC). However, because of the inherent brittleness of conventional HSC, its application has been somewhat limited especially in constructions undertaken in seismically active zones. It is now well

known that significant improvements in the ductility and compressive strength of concrete can be achieved by its lateral confinement. In order to understand the mechanical behaviour of HSCs under lateral confinement, the study of the actively confined HSC is of vital importance to simulate the behaviour of concrete under constant confining pressure (e.g. steel-confined concrete) and varying confining pressure (e.g. fibre-reinforced polymer (FRP)-confined concrete).

With the aim of development of eco-friendly and high performance construction materials and technologies, this research studies the behaviour of three different types of concretes and mortars in Chapters 1 and 2, including recycled aggregate concrete (RAC) containing recycled concrete aggregates obtained from C&D waste, geopolymer mortar containing FA, GGBS, LSS, and GS, and waste-based concrete and mortar containing FA, GGBS, GP, and LSS, to investigate the possibility of the development of new structural grade concretes using full or near full replacement of cement and natural aggregates with waste-based materials. Then, the physiochemical and mechanical behaviours of graphene-based cement mortar composite containing graphene oxide (GO) and reduced graphene oxide (rGO) are studied in Chapter 3 to investigate the possibility of the development of the new generation of high performance cement mortar composite with the use of waste graphite. Subsequently, with the aim of development of high performance concrete, the mechanical behaviour of geopolymer concrete containing FA and GGBS, and steel fibre-reinforced concrete (SFRC) containing ultra high performance micro steel fibres under active confinement is studied in Chapter 4. The mechanical behaviour of HSC under shape memory alloy (SMA) confinement is also studied in this chapter to investigate the possibility of the use of SMA spirals as a novel confinement technique to develop high performance composite structural members.

The major research results and contributions in this thesis are presented in 12 journal papers in four chapters.

In **Chapter 1**, a study on the time-dependent and long-term mechanical properties of high-strength RACs manufactured with coarse recycled aggregates of different parent concrete strength is first presented. The findings of this study show that

structural members prepared with high-quality recycled concrete aggregates can be designed to exhibit similar long-term deflections/shortening behaviour under sustained loading compared to conventional concrete members. New models are also developed using gene expression programming (GEP) technique to predict the compressive strength, elastic modulus, flexural strength, and splitting tensile strength of RACs. Finally, an investigation into the capability of three most efficient artificial intelligence models, including multivariate adaptive regression splines (MARS), M5 model tree (M5Tree), and least squares support vector regression (LSSVR), for the prediction of mechanical properties of RACs is presented. The findings of these two studies point to the possibility of the application of these techniques and developed models in the pre-design and modelling of structures manufactured with RACs.

In **Chapter 2**, the results of an experimental study on the properties of concretes containing very high percentages of FA, GGBS, and their combinations as cement replacement are first presented. This study points to the great potential of the development of waste-based concrete with up to 90% cement replacement exhibiting similar or even better properties compared to those of conventional concrete. The mechanical and durability-related properties of geopolymer and waste-based mortars with full replacement of cement and natural river sand with waste-based materials are also studied in this chapter. The results of these studies show that it is possible to develop new structural grade mortars using full or near full replacement of cement with waste-based materials, e.g. FA, GGBS, and GP, and full replacement of natural sand with waste-based sands, e.g. GS and LSS.

In **Chapter 3**, a comprehensive study is initially presented to evaluate the influence of GO dosage on the physiochemical and mechanical properties of cement mortar composites. The results of this study show that inclusion of the optimal GO dosage (i.e. 0.1%) in the cement mortar composite results in 37.5% and 77.7% increase in the 28-day tensile and compressive strengths of the composite compared to those of plain composite, respectively. The influence of oxygen functional groups of graphene and defectiveness of graphene structures on the axial tension and compression properties of graphene-based cement mortar composites is also investigated in this chapter. This study reveals that the use of rGO with 0.1% dosage

with the optimal reduction condition (i.e. 15 min reduction by 0.2% hydrazine) leads to 45.0% and 83.7% increase in the 28-day tensile and compressive strengths of rGO-cement mortar composites compared to those of the plain cement mortar composite. The results of these two studies point to the possibility of the development of high performance cement mortar composite by the use of graphene nanoparticles with a low dosage of 0.1% by weight of cement.

In **Chapter 4**, after the development of different eco-friendly construction materials in chapters 1-3, the influence of lateral confinement on the axial compressive behaviour (ductility and compressive strength) of different types of concretes is studied to develop high performance concrete column members. Firstly, the axial compressive behaviour of actively confined geopolymer concretes is investigated. The findings of this study reveal the possibility of the use of geopolymer concretes in new laterally confined structural columns designed to undergo large deformations for resilience against extreme events such as earthquakes. The axial compressive behaviour of HSC confined by SMA spiral is then investigated. The results of this study point to the possibility of the use of SMA spirals as a novel confinement technique to develop high performance composite structural members and as an efficient prestressing technique to strengthen and retrofit existing concrete members. In this chapter, the compressive behaviour of SFRC containing ultra high-strength micro steel fibres under active confining pressure is also investigated. The promising findings of this study point that ultra high-strength micro steel fibres can be used in concretes for the development of high performance composite structural members in applications where the concrete will be subjected to lateral confinement. Following this, a finite element model for the compressive behaviour of FRP-confined SFRC is presented. The developed concrete damage-plasticity model presented in this study is able to provide improved accuracy over the best performing existing models of FRP-confined plain concrete in predicting the behaviour of FRP-confined SFRC.

Finally, conclusions are summarized and recommendations are provided for further research toward the development of eco-friendly and high performance concretes.

Chapter 1

Recycled aggregate concrete

Publications:

Gholampour A, Ozbakkaloglu T. Time-dependent and long-term mechanical properties of concretes incorporating different grades of coarse recycled concrete aggregates. *Engineering Structures*. 2017;157:224-34. ***Citations: 14***

Gholampour A, Gandomi AH, Ozbakkaloglu T. New formulations for mechanical properties of recycled aggregate concrete using gene expression programming. *Construction and Building Materials.* 2017;130:122-45. ***Citations: 32***

Gholampour A, Mansouri I, Kisi O, Ozbakkaloglu T. Evaluation of mechanical properties of concretes containing coarse recycled concrete aggregates using multivariate adaptive regression splines (MARS), M5 model tree (M5Tree), and least squares support vector regression (LSSVR) models. *Neural Computing and Applications*. 2018;10.1007/s00521-018-3630-y. ***Citations: 6***

Statement of Authorship

Title of Paper	Time-dependent and long-term mechanical properties of concretes incorporating different grades of coarse recycled concrete aggregates
Publication Status	☑ Published ☐ Accepted for Publication ☐ Submitted for Publication ☐ Unpublished and Unsubmitted work written in manuscript style
Publication Details	Gholampour A, Ozbakkaloglu T. Time-dependent and long-term mechanical properties of concretes incorporating different grades of coarse recycled concrete aggregates. *Engineering Structures*. 2017;157:224-34.

Principal Author

Name of Principal Author (Candidate)	Aliakbar Gholampour		
Contribution to the Paper	Literature review, analysis of test results, and preparation of the manuscript.		
Overall percentage (%)	80%		
Certification:	This paper reports on original research I conducted during the period of my Higher Degree by Research candidature and is not subject to any obligations or contractual agreements with a third party that would constrain its inclusion in this thesis. I am the primary author of this paper.		
Signature		Date	31/01/2019

Co-Author Contributions

By signing the Statement of Authorship, each author certifies that:

i. the candidate's stated contribution to the publication is accurate (as detailed above);

ii. permission is granted for the candidate in include the publication in the thesis; and

iii. the sum of all co-author contributions is equal to 100% less the candidate's stated contribution.

Name of Co-Author	Togay Ozbakkaloglu		
Contribution to the Paper	Research supervision and review of manuscript.		
Signature		Date	31/01/2019

Name of Co-Author			
Contribution to the Paper			
Signature		Date	

Please cut and paste additional co-author panels here as required.

Time-Dependent and Long-Term Mechanical Properties of Concretes Incorporating Different Grades of Coarse Recycled Concrete Aggregates

ABSTRACT

It is now accepted that replacement of natural aggregates in concrete with recycled concrete aggregates obtained from construction and demolition waste is a promising technology to conserve natural resources and reduce the environmental impact of concrete. This paper presents a study on long-term properties of concretes manufactured with recycled aggregates of different parent concrete strengths. A total of six batches of recycled aggregate concretes (RACs) were manufactured. Tests were undertaken to establish the long-term compressive strength, elastic modulus, splitting tensile strength, workability, drying shrinkage, and creep of each batch. Scanning electron microscopy (SEM) and energy-dispersive X-ray spectroscopy (EDX) characterizations were performed to explain the mechanisms behind the observed time-dependent and mechanical properties of RACs. Test parameters comprised the replacement ratio and parent concrete strength of the recycled aggregates used in the preparation of the new concrete mixes. The results indicate that the parent concrete strength of the recycled aggregates significantly affects the time-dependent and long-term mechanical properties of RACs. It is shown that concrete mixes containing lower strength recycled concrete aggregates develop lower mechanical properties and higher shrinkage strain and creep deformation compared to mixes prepared with higher strength recycled concrete aggregates. Normal-strength RAC mixes containing higher strength recycled concrete aggregates develop slightly lower splitting tensile strength at all curing ages but similar compressive strength and elastic modulus in longer term (i.e. over 90 days) compared to that of the control mix. It is also shown that high-strength RACs, prepared with full replacement of natural aggregates with recycled concrete aggregates having a higher parent concrete strength, exhibit time-dependent and long-term mechanical properties that are similar to or better than those of companion natural aggregate concretes.

KEYWORDS: Recycled aggregate concrete (RAC); High-strength concrete (HSC); Recycled concrete aggregate; Mechanical properties; Long-term; Shrinkage; Creep.

INTRODUCTION

In recent decades, the increased use of concrete has resulted in excessive consumption of natural aggregates [1, 2], which constitute approximately 70% of the total volume in a concrete mix [3]. The use of construction and demolition (C&D) wastes, which are conventionally disposed of in landfills at a significant cost, in concrete has recently received significant attention, as this technology enables conservation of non-renewable natural resources while also significantly reducing the environmental impact of both concrete and C&D waste [4, 5]. Within this context, recycled concrete aggregate, which is obtained from demolished concrete structures, has been considered as an alternative material to natural aggregate in the production of structural concretes. Although recycled aggregate concrete (RAC), which is produced from partial or full substitution of natural aggregates by recycled concrete aggregates, has significant economic and environmental benefits [6–8], its use has so far been limited in construction industry because of the concerns regarding the inferior quality of recycled aggregate compared to that of natural aggregate [9].

Over the past three decades, a large number of studies have been conducted to understand the performance of RAC containing coarse recycled aggregates [10]. The review of the existing literature on RACs show that most of the existing studies were concerned with the short-term behaviour and only a limited number of studies have been reported to date on the long-term behaviour of RACs [11–22]. It has been shown that the strength of the parent concrete (the concrete from which recycled aggregates are derived) affects the long-term behaviour of RACs [18, 21]. Therefore, understanding the mechanisms behind the effect of the parent concrete strength on the long-term behaviour of RACs is of significant interest. Moreover, although the popularity of high-strength concretes in the construction industry has been on a steady incline [23–25], only one study (i.e. [18]) has been reported to date on the time-dependent and long-term mechanical properties of high-strength RACs

with different parent concrete strengths, which focused on RAC mixes containing fly ash. Therefore, there are currently no studies on the long-term behaviour of conventional high-strength RACs prepared with recycled aggregates having different parent concrete strengths. Moreover, the creep behaviour, a highly important time-dependent property, of high-strength RACs and microstructure of RAC mixes with different parent concrete strengths have not yet been investigated. Therefore, it is clear that additional studies are required to better understand the effect of the parent concrete strength on the time-dependent and long-term mechanical properties of high-strength RACs and mechanisms behind the observed test results.

This paper presents an experimental study conducted to address the research gaps outlined above by investigating the variation of physical, mechanical, and time-dependent properties of normal- and high-strength RACs with the parent concrete strength of coarse recycled aggregates. The paper initially provides a summary of the experimental program, including material properties, specimen properties, and testing procedures, which is followed by the results of the experimental program. A detailed discussion together with microstructural analysis of different mixes using scanning electron micrographs (SEM) and energy-dispersive X-ray spectroscopy (EDX) at 28 days curing is subsequently presented to explain the mechanisms behind the test results.

TEST PROGRAM

Materials

Natural and recycled concrete aggregates

The natural aggregates (crushed basalt) were sourced from McLaren Vale Quarry in Fleurieu Peninsula in South Australia. The natural sand having a 2-mm maximum nominal size was obtained from Price Pit in Yorke Peninsula and used as the fine aggregate in all concrete mixes. Three different recycled concrete aggregates with parent concrete strength of 20, 40, and 110 MPa were used to study the influence of lower and higher parent concrete strength recycled aggregates on the properties of RACs. In the production of the recycled aggregates, three different concrete mixes

with three target 28-day strengths of 20, 40, and 110 MPa were prepared in the Materials Laboratory of the University of Adelaide using the same crushed basalt as the coarse aggregate. Once the parent concretes attained their 28-day strengths, they were crushed using a jaw crusher, such that the particle size distribution of the resulting aggregates would be similar to that of the natural coarse aggregates (refer to Fig. 1.1). The crushed recycled aggregates were subsequently added to the RAC mixes when they were approximately 56 days old.

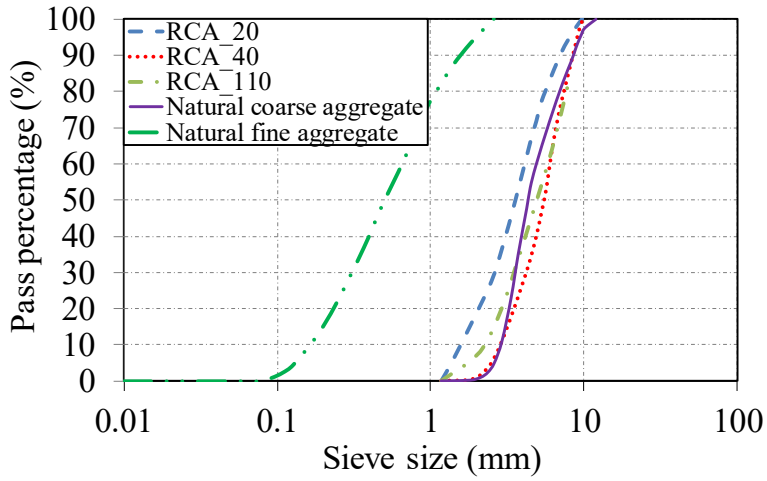

Figure 1.1. Sieving test results of coarse and fine aggregates: Particle Size Distribution (PSD)

The physical properties of natural and recycled aggregates are shown in Table 1.1. The attached mortar content, which is a measure of the percentage (by weight) of attached mortar in the recycled coarse aggregates, was determined as described in Ref. [26].

Table 1.1. Properties of coarse and fine aggregates

Aggregate type	Maximum size (mm)	Specific Gravity (OD)	Water absorption (%)	Fineness modulus	Attached mortar content (%)
NCA	9.5	2.60	2.0	5.4	–
RCA_20	10.0	2.16	6.8	5.1	53
RCA_40	10.0	2.24	5.9	5.9	48
RCA_110	10.0	2.36	5.0	5.7	42
Sand	2.0	2.60	0.4	2.3	–

OD: oven dry
NCA: natural coarse aggregate
RCA_20: Recycled coarse aggregate with 28-day parent concrete strength of 20 MPa
RCA_40: Recycled coarse aggregate with 28-day parent concrete strength of 40 MPa
RCA_110: Recycled coarse aggregate with 28-day parent concrete strength of 110 MPa

Cement and pozzolanic admixture

The chemical composition of the ordinary Portland cement and silica fume used in this study are shown in Table 1.2. The Blaine fineness of the ordinary Portland cement and silica fume was 330 and 18000 m^2/kg, respectively.

Table 1.2. Chemical composition of cementitious materials

Compounds	Ordinary Portland cement (%)	Silica fume (%)
SiO_2	21.4	92.5
ZrO_2+HfO_2	–	5.50
Al_2O_3	5.55	0.35
Fe_2O_3	3.46	0.40
P_2O_5	–	0.30
CaO	64	0.03
MgO	1.86	–
SO_3	1.42	0.90
K_2O	0.54	0.02
Na_2O	0.26	0.02

Test specimens

Six unique batches of concrete were prepared, which included: two control batches of natural aggregate concrete and four batches of RAC. The control mixes were designed as normal- and high-strength concrete (NSC and HSC) mixes with a 28-day compressive strength of 40 and 80 MPa, respectively. A series of tests including: the workability, compressive strength, modulus of elasticity, splitting tensile strength, drying shrinkage, and creep was undertaken on each batch to evaluate the properties of fresh and hardened concrete. Two types of specimens were manufactured for testing, including: prisms and cylinders. The compressive strength and modulus of elasticity of the concretes were established by the compression tests using cylinder specimens with a 100 mm diameter and 200 mm height. The splitting tensile strength tests were conducted on the same size cylinder specimens. 75 × 75 × 285 mm prism specimens were used to monitor the drying shrinkages of the concrete. The creep tests were performed on 100 × 200 mm cylinders. The test parameters included: replacement ratio of natural aggregates with recycled coarse aggregate (*RCA%*) and parent concrete strength of recycled aggregates. In each test, three nominally identical specimens were used for each unique specimen configuration.

Mix design, specimen preparation, and designation

Table 1.3 shows the mix proportions of different concrete batches used in this study. Normal- and high-strength RAC mixes were prepared with 50% and 100% *RCA%* (as the volume replacement of natural aggregates), respectively. The aggregates were washed to remove the impurities and subsequently oven dried for 24 hours at 105˚C. The sand and coarse aggregates were added to the mixes in the oven-dry condition, and the effective water-to-cement ratio (effective *w/b*) was kept constant among different mixes in each series. In Table 1.3, the terms 'water-total' and 'water-effective' refer to the total water added to each mix and the water available to react with the binder, respectively. The effective water was determined by subtracting the saturation water that was absorbed by coarse and fine aggregates from the total water. A polycarboxylic ether polymer-based superplasticizer and silica fume were used in HSC mixes.

Table 1.3. Mix proportions of concrete

Concrete mix	NSC			HSC		
	NC-REF	NC-40	NC-110	HC-REF	HC-20	HC-110
Cement (kg/m^3)	350	350	350	437	437	437
Silica Fume (kg/m^3)	0	0	0	38	38	38
Sand (kg/m^3)	720	720	720	730	730	730
Natural Aggregate (kg/m^3)	1080	540	540	1095	0	0
Recycled Aggregate (kg/m^3)	0	465	480	0	910	973
Water-Effective (kg/m^3)	175	175	175	128	128	128
Water-Total (kg/m^3)	199	216	213	153	193	180
Superplasticizer (kg/m^3)	0	0	0	10	10	10
Effective *w/b* *	0.50	0.50	0.50	0.27	0.27	0.27
Slump (mm)	130	115	115	170	140	150
Fresh Density (kg/m^3)	2385	2351	2364	2455	2356	2407
Hardened Density (kg/m^3)	2359	2330	2345	2432	2341	2381

* Including the water coming from the superplasticizer (i.e. 70% water by weight)

RAC mixes were prepared by two stage mixing approach (TSMA) [27], in which the coarse and fine aggregates were initially dry-mixed for three minutes and the water that saturated the fine and coarse aggregates together with one-half of the effective water was then added to the mix and the mixing continued for an additional three minutes. The binder was subsequently added to the mix and the mixing continued for two more minutes to finish the first stage. In the next stage, the second

half of the effective water was added together with the superplasticizer (if used) and wet mixing continued for five minutes. To ensure proper placement of concrete, 15 seconds of external vibration was applied during the pouring of all concrete mixes. Once the specimens were demolded, they were cured in the fog room until test day at a constant temperature of 23±2°C according to ASTM C192/C192M-07 [28].

The concrete series in Table 1.3 were labelled as follows: the letters NC and HC were used for the normal- and high-strength RAC mixes, respectively. The label of the RAC mixes included the parent concrete strength in MPa, whereas the control mixes contained the letter REF in their designation. For instance, NC-110 is a normal-strength RAC mix with a *RCA%* of 50% that contained recycled coarse aggregates with 110 MPa parent concrete strength.

Testing

The mechanical properties were measured up to 180 days of curing age to study the long-term behaviour of RAC mixes. The shrinkage and creep strains were measured up to 450 days of curing age to study the time-dependent properties of the mixes. The experimental methods used in determining these properties are summarized in Table 1.4. The workability of fresh concrete was evaluated by a slump test, which was performed in accordance with ASTM C143/C143M-12 [29]. The fresh and hardened densities of concrete were obtained in accordance with ASTM C138/C138M-16 [30] and ASTM C642-13 [31], respectively. The mechanical properties, including the compressive strength (ASTM C39/C39M-16b [32]), elastic modulus (ASTM C469/C469M-14 [33]), and splitting tensile strength (ASTM C496/C496M-04 [34]) of concrete were determined using a universal testing machine. Prior to the compression tests, all cylinder specimens were ground by a surface-grinding machine to ensure uniform distribution of the applied load at the specimen ends. The shrinkage and creep tests were carried out in accordance with ASTM standards C596-07 [35] and C512/C512M-15 [36], respectively. In the creep tests the specimens were subjected to a stress level that corresponded to 20% of their 28-day compressive strength.

Table 1.4. Experimental methods used to determine various fresh and hardened concrete properties

Target properties	Method
Fresh concrete	
Slump test	ASTM C143/C143M-12 [29]
Fresh density	ASTM C138/C138M-16 [30]
Hardened concrete	
Hardened density	ASTM C642-13 [31]
Compressive strength	ASTM C39/C39M-16b [32]
Modulus of elasticity	ASTM C469/C469M-14 [33]
Splitting tensile strength	ASTM C496/C496M-04 [34]
Shrinkage	ASTM C596-07 [35]
Creep	ASTM C512/C512M-15 [36]

The crack formations and interfacial transition zones (ITZ) in the mixes were evaluated by scanning electron microscopy (SEM) analysis, which was conducted by High Resolution Field Emission Scanning Electron Microscope (FEI Quanta 450) on the polished fresh cut surface of the specimens. For composition analysis of the mixes, energy dispersive X-ray (EDX) spectroscopy was conducted using TEAM EDS with SDD Detector to determine the constituent elements of the concrete mixes.

TEST RESULTS AND EXPERIMENTAL OBSERVATIONS

Workability of fresh concrete

As can be seen from the results of the slump test shown in Table 1.3, RAC mixes had similar but slightly lower slumps than those of the companion control mixes. It can also be seen in the table that HSC mix with 110 MPa recycled aggregates developed a slightly higher slump compared to that of the companion mix with 20 MPa recycled aggregates.

Density of hardened concrete

The results in Table 1.3 show that, as expected, HSC mixes obtained a slightly higher hardened density (at 28 days of curing) than NSC mixes, and the density of RAC mixes were lower than that of the companion control mixes. The results also

show that, in both NC and HC series, mixes with a higher parent concrete strength exhibited a slightly higher hardened density, which is attributed to the higher specific gravity of the higher grade aggregates.

Mechanical properties of hardened concrete

Compressive strength

Figure 1.2 shows the compressive strength of each concrete batch at curing ages of 7, 28, 56, 90, and 180 days. As can be seen in Fig. 1.2, in both NC and HC series, the strength of mixes containing lower strength recycled concrete aggregates was lower than those of control mixes at all curing ages. In NC series, the observed reduction tended to decrease with time from 12.3% at 7 days to 3.6% at 180 days. On the other hand, this reduction was less significant in HC series (i.e. from 20.0% at 7 days to 18.0% at 180 days). It can also be seen in the figure that the strength of mixes prepared using higher strength recycled concrete aggregates was higher than those mixes with lower strength recycled concrete aggregates. This finding is consistent with the previous studies [18, 21] and the difference was particularly significant in HC series. Notably, HC-110 series develop consistently higher compressive strengths than those of the control mix, with the difference becoming more pronounced after the curing age of 90 days. As discussed in detail in the section of SEM Analysis, this is attributed to the further hydration of the old cement mortar in HC-110 mix, which resulted in improved bond between the recycled concrete aggregate and the new paste.

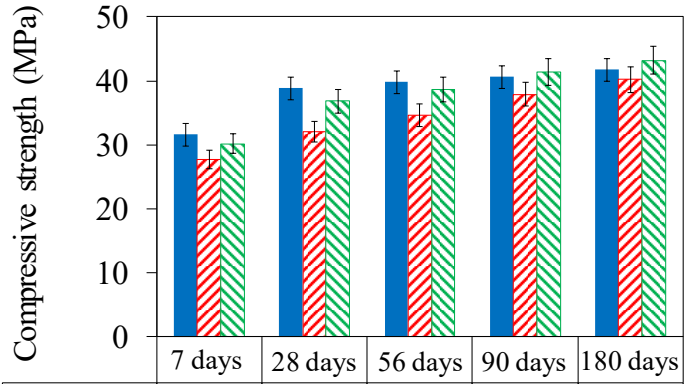

	7 days	28 days	56 days	90 days	180 days
NC-REF	31.6	38.8	39.8	40.6	41.7
NC-40	27.7	32.0	34.6	37.9	40.2
NC-110	30.2	36.8	38.6	41.4	43.2

(a)

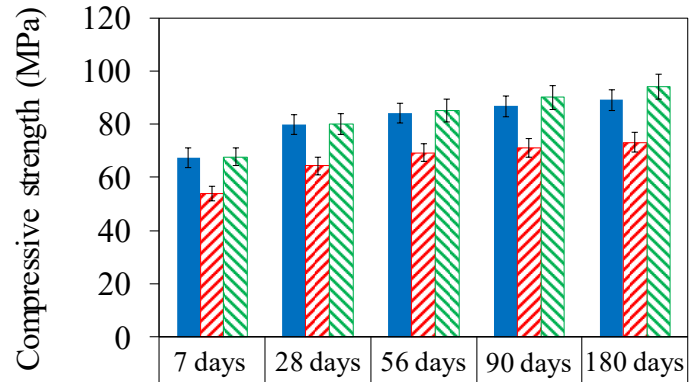

	7 days	28 days	56 days	90 days	180 days
HC-REF	67.4	79.8	84.1	86.7	89.1
HC-20	53.9	64.3	69.3	71.0	73.1
HC-110	67.7	80.1	85.2	90.0	94.1

(b)

Figure 1.2. Variation of compressive strength of concrete with time: (a) NSC group (with 50% *RCA%*); (b) HSC group (with 100% *RCA%*)

As can be seen in Fig. 1.2(a), NC-110 series develop slightly lower compressive strengths at 7 (4.4%), 28 (5.1%), and 56 (3.0%) days but slightly higher at 90 (2%) and 128 (3.6%) days compared to the control mix. Comparison of Figs. 1.2(a) and 2(b) reveals that the strength increase resulting from the increase in the parent concrete strength of recycled aggregates was more significant in HSC mixes than they were in NSC mixes. This phenomenon can be attributed to different failure mechanisms of normal- and high-strength RAC mixes, which is explained later in the section of SEM Analysis.

Modulus of elasticity

Figure 1.3 shows the elastic modulus of specimens at curing ages of 28, 56, 90, and 180 days. As can be seen in the figure, NC-110 and HC-110 series exhibited very similar elastic moduli at all curing ages compared to those of the companion control mixes, and their relative elastic modulus increased with respect to the companion control mixes with time. It can also be seen in Fig. 1.3 that, in both NC and HC series, the elastic modulus of mixes containing lower strength recycled concrete aggregates was lower than those of the control mixes at all curing ages. The observed reduction in the elastic modulus of the mixes containing lower strength recycled concrete aggregates did not change significantly by the curing age, and it was approximately 12% and 20% in the case of NC and HC series, respectively. The lower elastic modulus of mixes containing lower strength recycled concrete

aggregates is attributed to the porous nature and lower stiffness of the mortar attached on the surface of lower strength recycled aggregates [18, 21]. It can also be seen in Fig. 1.3 that the increase in elastic modulus resulting from the increase in the parent concrete strength of recycled aggregates was more significant in HC series than they were in NC series. This can be attributed to the higher replacement ratio level in HC series and the larger difference between the strength of parent concrete in HC series than those in NC series.

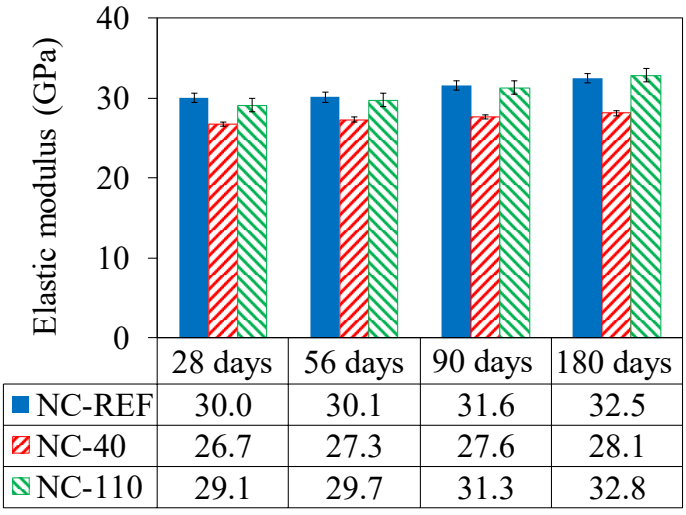

	28 days	56 days	90 days	180 days
NC-REF	30.0	30.1	31.6	32.5
NC-40	26.7	27.3	27.6	28.1
NC-110	29.1	29.7	31.3	32.8

(a)

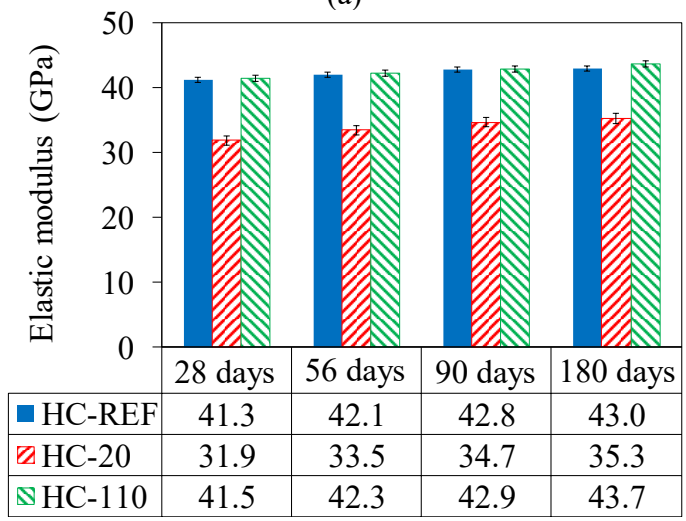

	28 days	56 days	90 days	180 days
HC-REF	41.3	42.1	42.8	43.0
HC-20	31.9	33.5	34.7	35.3
HC-110	41.5	42.3	42.9	43.7

(b)

Figure 1.3. Variation of modulus of elasticity of concrete with time: (a) NSC group (with 50% *RCA%*); (b) HSC group (with 100% *RCA%*)

Splitting tensile strength

Figure 1.4 shows the variation of the splitting tensile strength of NC and HC series mixes with time. As can be seen in the figure, HC-110 series developed similar

splitting tensile strengths to those of the companion control mix at all curing ages. It can also be seen in Fig. 1.4 that the remaining mixes containing recycled aggregates develop lower splitting tensile strength compared to those of the companion control mixes. The splitting tensile strength of NC-110 series mix was only slightly lower than that of the companion control mix at all curing ages (by 6% at 28 days and 2% at 180 days), and its relative strength increased with respect to the control mix with curing age. The reduction seen in the splitting tensile strength of the remaining two mixes did not change significantly with curing age and it was approximately 10% and 24% in NC-40 and HC-20 series mixes, respectively.

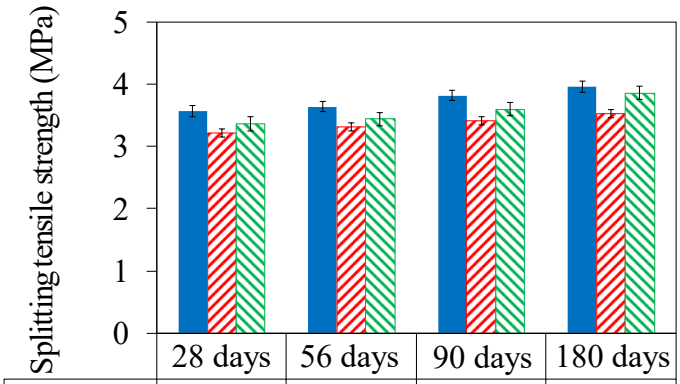

	28 days	56 days	90 days	180 days
NC-REF	3.57	3.64	3.82	3.96
NC-40	3.22	3.32	3.41	3.52
NC-110	3.36	3.44	3.60	3.86

(a)

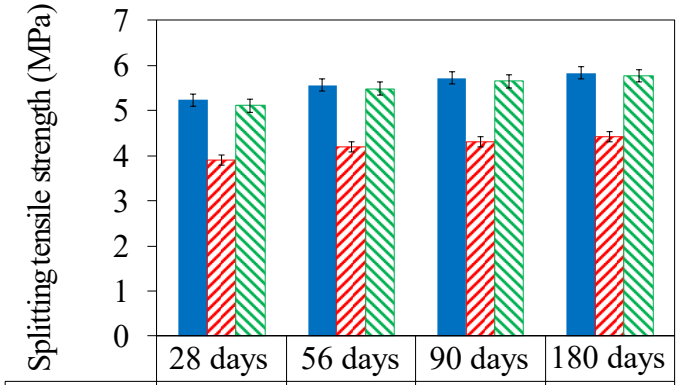

	28 days	56 days	90 days	180 days
HC-REF	5.23	5.56	5.72	5.83
HC-20	3.90	4.20	4.31	4.42
HC-110	5.11	5.48	5.65	5.77

(b)

Figure 1.4. Variation of splitting tensile strength of concrete with time: (a) NSC group (with 50% *RCA%*); (b) HSC group (with 100% *RCA%*)

Comparisons between experimental results and predictions of design code expressions

Table 1.5 presents the expressions recommended by the existing design codes and standards for the prediction of the elastic modulus (E_c) and splitting tensile strength (f_{st}) of conventional concrete based on its mean or characteristic compressive strength (f_{cm} or f'_c). In order to evaluate the applicability of these expressions to RACs, they were used to predict E_c and f_{st} of the specimens of the present study at the curing age of 28 days.

Table 1.5. Summary of conventional concrete mechanical property models given in current design codes

Model	Elastic modulus (E_c) (GPa)	Splitting tensile strength (f_{st}) (MPa)
AS 3600-09 [37]	$4.3 \times 10^{-5}(\rho_h)^{1.5}\sqrt{f_{cm}}$ * when $f_{cm} \leq 40$ MPa $\left(2.4(\rho_h)^{1.5}\sqrt{f_{cm}} + 12\right) \times 10^{-5}$ when $40 < f_{cm} \leq 100$ MPa	$0.4\sqrt{f'_c}$
ACI 318-11 [38]	$4.73\sqrt{f'_c}$	$0.53\sqrt{f'_c}$
CSA A23.3-04 [39]	$4.5\sqrt{f'_c}$	–
Eurocode 2-04 [40]	$22(f_{cm}/10)^{0.3}$	$0.3(f'_c)^{2/3}$
JSCE-07 [41]	$4.7\sqrt{f'_c}$	$0.44\sqrt{f'_c}$
JCI-08 [42]	$6.3{f'_c}^{0.45}$	$0.13(f'_c)^{0.85}$
NZS 3101:2006 [43]	$3.32(\sqrt{f'_c}) + 6.9$	$0.44\sqrt{f'_c}$

f'_c, f_{cm}, and f_{st} are in MPa, E_c is in GPa, and ρ_h is the hardened density of concrete in kg/m^3
* f_{cm} and f'_c are the mean and characteristic compressive strength, respectively ($f'_c = f_{cm} - 8$ MPa as per Eurocode 2)

Figures 1.5(a) and 1.5(b) show the comparison of experimental results of 28-day E_c and f_{st} with predictions of code expressions, respectively. As can be seen in Fig. 1.5(a), the experimental results of E_c are in general agreement with the code expressions predictions. A closer look into the results reveals that EC-04 expression consistently overpredicts E_c of mixes, except for mixes HC-REF and HC-110. It can also be seen in Fig. 1.5(a) that ACI-11, CSA-04, JSCE-07, and NZS-06 underpredict E_c, except for mix HC-20 that developed an E_c that was lower than that predicted by any of the existing models. As can be seen in Fig. 1.5(a), JCI-08 expression provides the closest predictions of E_c for the NSC mixes, whereas EC-04 expression gives the closest predictions of E_c for the HSC mixes. It can be seen in Fig. 1.5(b) that all the code expressions underpredict f_{st} of the normal-strength mixes of the current study.

As can be seen in the figure, EC-04 and JCI-08 provide reasonably close predictions of the experimental results of f_{st} for the high-strength mixes, whereas the remaining code expressions tend to underpredict these results.

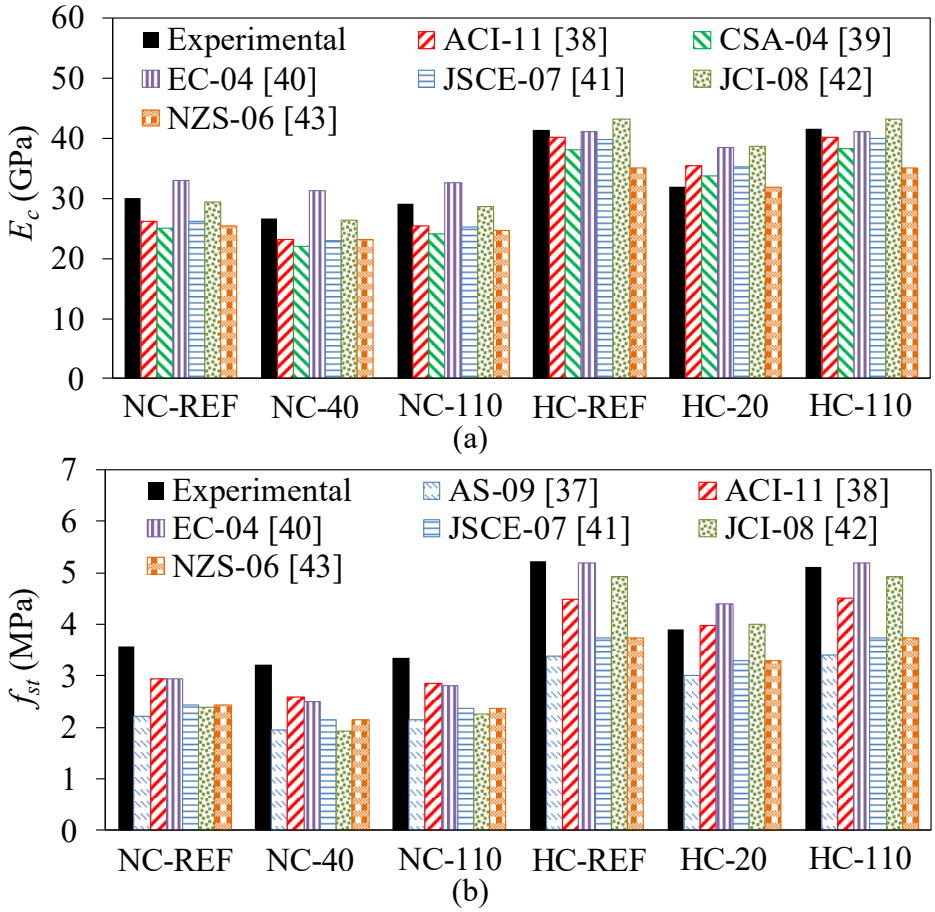

Figure 1.5. Comparisons of experimental values and design code predictions for (a) elastic modulus and (b) splitting tensile strength of RACs

Time-dependent properties

Drying shrinkage

Figure 1.6 shows the shrinkage of the different concrete mixes. As can be seen in the figure, the drying shrinkage of the RACs containing higher strength recycled aggregates was slightly higher than that of the companion control mixes. The difference was around 7% and 10% in the case of NC and HC series, respectively, and it did not change significantly with curing age. It can also be seen in Fig. 1.6 that at a given curing age HC series mixes exhibited lower drying shrinkage than NC series mixes. This phenomenon can be explained by the presence of a larger amount of residual water in the structure of NC series mixes after hydration whose evaporation resulted in higher shrinkage strains [18, 44, 45].

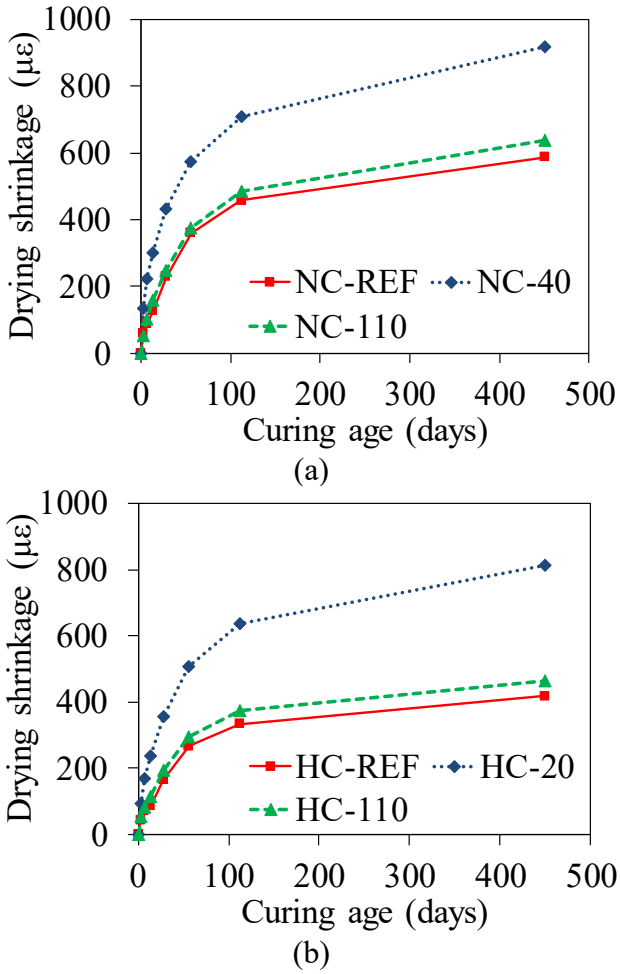

Figure 1.6. Variation of drying shrinkage of concrete with time: (a) NSC group (with 50% *RCA%*); (b) HSC group (with 100% *RCA%*)

It is evident from Fig. 1.6 that, in both NC and HC series, the parent concrete strength of recycled aggregates had a pronounced influence on the drying shrinkage, with the concretes containing lower strength recycled aggregates exhibiting a significantly higher shrinkage strain at a given curing age. This finding is consistent with previous research [18] and can be explained by the higher water absorption, caused by the higher attached old mortar content, and lower elastic modulus of the lower strength recycled aggregates compared to those of higher strength recycled aggregates [18, 46].

Creep

Figure 1.7 shows the variation of creep coefficient (defined by the ratio of the ultimate creep strain to the elastic strain) of different concrete mixes with curing age. This coefficient is of great importance for estimating deflections in concrete

structures under sustained loading [13]. As can be seen in Fig. 1.7, HC series mixes exhibited a higher creep coefficient at a given curing age compared to that of NC series mixes, except for HC-110 series mix, which exhibited nearly identical creep coefficient to NC-110 series mix. The observation on the higher creep coefficient of higher strength mixes is consistent with previous research on conventional concrete [47]. It can also be seen in Fig. 1.7 that at a given curing age the creep coefficient of both NC and HC series RAC mixes containing higher strength recycled aggregates was similar to and slightly lower than that of companion control mixes. On the other hand, in both NC and HC series, the creep coefficient of mixes containing lower strength recycled aggregates was significantly higher than that of companion control mixes at all curing ages.

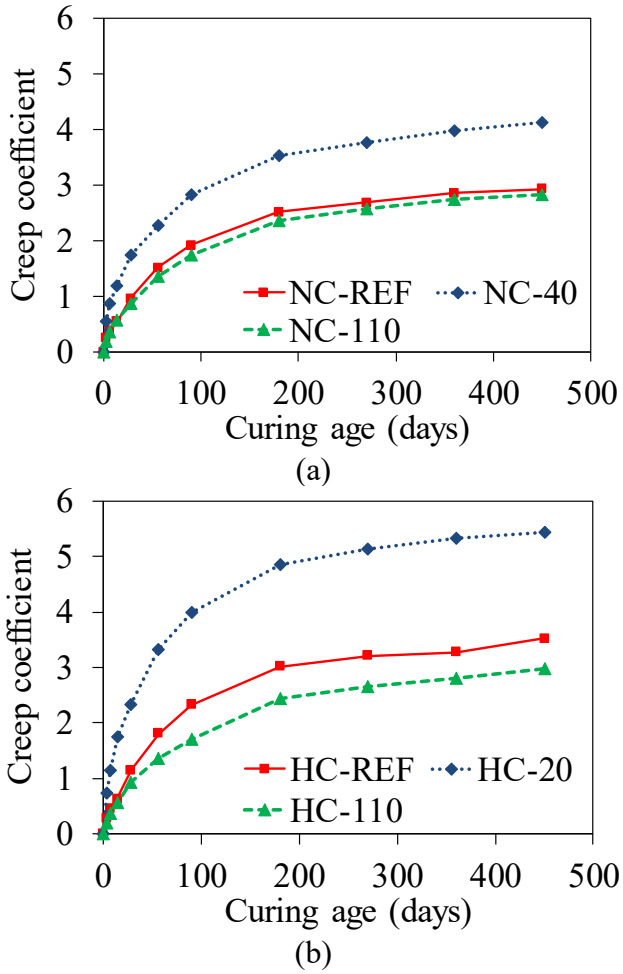

Figure 1.7. Variation of creep coefficient of concrete with time: (a) NSC group (with 50% *RCA%*); (b) HSC group (with 100% *RCA%*)

Figure 1.8 shows the variation of the specific creep (defined by creep strain per unit of applied stress) of different concrete mixes with time. This parameter is often used

to compare the creep strain of concretes having different compressive strengths [13]. It can be seen in Fig. 1.8 that HC-REF and HC-110 series mixes exhibited a slightly lower specific creep at a given curing age compared to that of companion NC series mixes. The observation on the lower specific creep of HC series is consistent with previous research on the conventional NSC and HSC [48]. It can also be seen in the figure that RAC mixes developed a higher specific creep compared to that of control mixes at a given curing age, except for HC-110 series mix, which exhibited nearly identical specific creep to the companion control mix. As can be seen in Fig. 1.8, in both NC and HC series, the specific creep of mixes containing lower strength recycled aggregates was significantly higher than that of companion mixes containing higher strength recycled aggregates at all curing ages, which is consistent with the previous research on the creep behaviour of normal strength RAC [49].

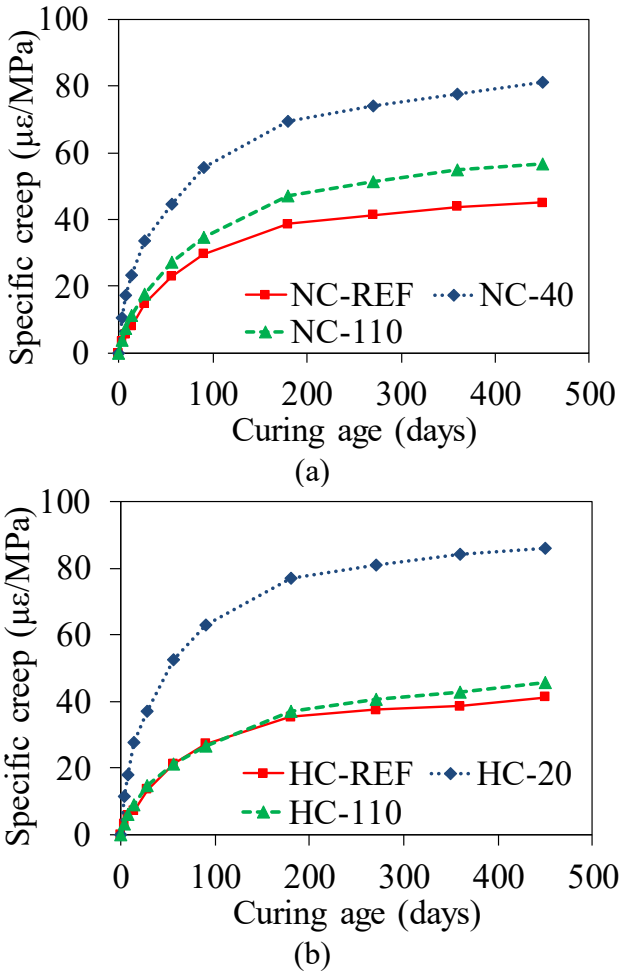

Figure 1.8. Variation of specific creep of concrete with time: (a) NSC group (with 50% *RCA%*); (b) HSC group (with 100% *RCA%*)

The lower creep deformation of mixes containing higher strength recycled aggregates can be attributed to the higher stiffness of the higher strength recycled aggregates compared to that of lower strength recycled aggregates [13, 17, 49] and improved bond at the ITZ between new and old cement paste in mixes with higher strength recycled aggregates, which is discussed further in the section of SEM Analysis. Lower creep coefficient and specific creep of mixes with higher strength recycled aggregates indicate that long-term deflections and/or shortening the structural members manufactured with these mixes would exhibit lower under sustained loading, which is desirable from structural point of view.

Microstructural analysis of hardened concrete

SEM analysis

Figures 1.9(a)–1.9(c) show the SEM images at the polished fresh cut surface of NC-REF, NC-40, and NC-110 series mixes, respectively, after the completion of 28-day compression tests. The additional ITZ of RACs between the aggregate and attached old mortar (i.e. old ITZ) is visible in these figures. As ITZ is often the weak-link in concrete, it is known that the presence of an additional ITZ in RAC can result in a lower strength concrete [50]. Furthermore, because of the porous nature of the old mortar attached to the surface of recycled concrete aggregates, the ITZ between the old and new mortar (new ITZ) often has a relatively low strength and it forms another weak-link in the concrete, which in turn results in a lower strength [51]. As can be seen in Fig. 1.9, in both NC-40 and NC-110 normal-strength RAC series, the failure of concrete started in the new ITZ, suggesting that the new ITZ of these mixes was weaker than their old ITZ. Because NC-110 series had higher strength recycled concrete aggregates, this mix developed slightly higher mechanical properties compared to that of NC-40 series; however, as discussed previously, the difference between the mechanical properties of these mixes were relatively small and the SEM images explain why more significant increases were not observed.

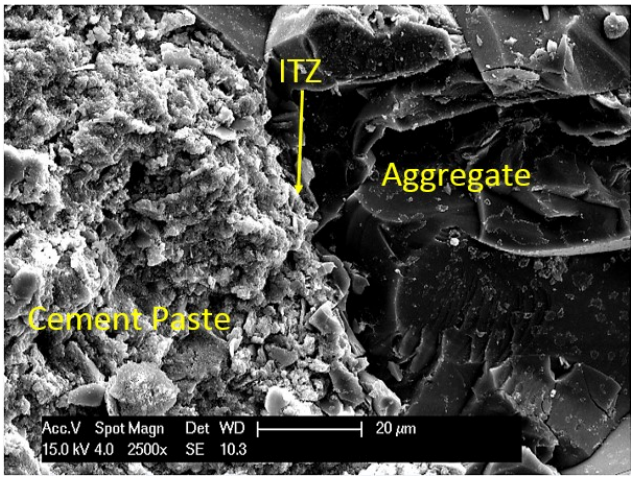

(a)

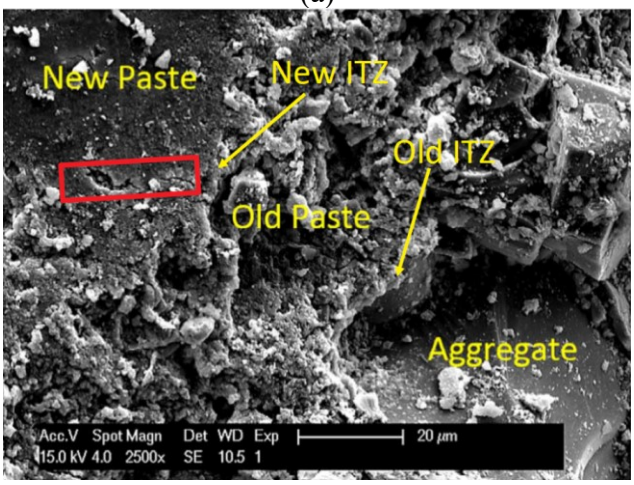

(b)

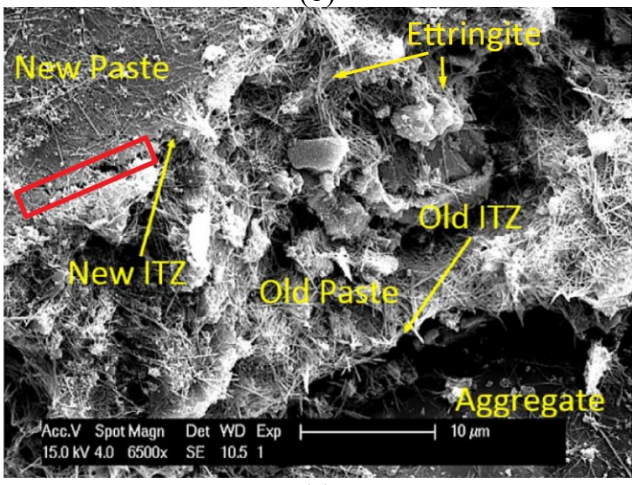

(c)

Figure 1.9. SEM micrographs of the surface of (a) NC-REF, (b) NC-40, and c) NC-110 mix. Red boxes highlight the micro-cracks on the surface

Figures 1.10(a)–1.10(c) illustrate the SEM images of HC-REF, HC-20, and HC-110 series mixes at 28 days curing age, respectively. As can be seen in the figures, unlike to the NC series, the failure of HC series RACs started in the old ITZ, suggesting

that the new ITZ was stronger than the old ITZ in these mixes. This is as expected for HC-20 series given the significantly higher strength of the new concrete mix compared to that of the old concrete. However, the reason behind it is not as clear for HC-110 series mixes and becomes apparent only after the EDX analysis, which showed that the old ITZ in HC series had higher amount of hydration products than the new ITZ (explained further in the section of EDX Analysis). As discussed in the section of Compressive Strength, the effect of recycled aggregate parent concrete strength was more significant on the mechanical properties of HC series than on those of NC series. SEM images shown in Fig. 1.10 explains the sensitivity of the properties of HC series mixes to the quality of recycled concrete aggregates.

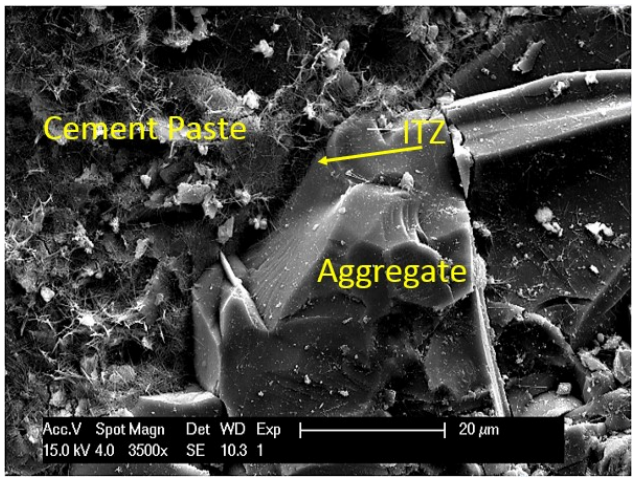

(a)

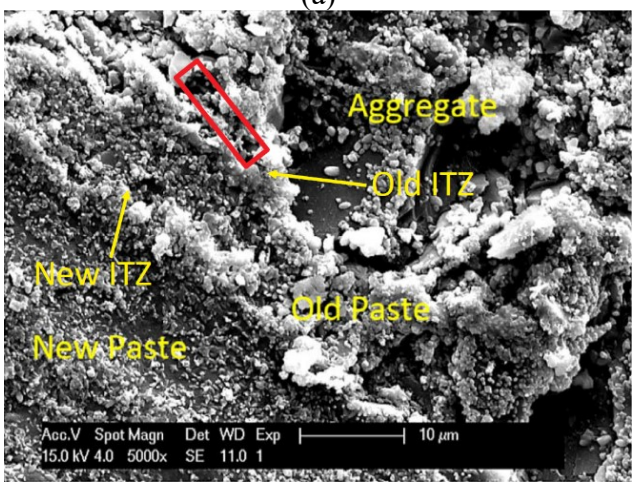

(b)

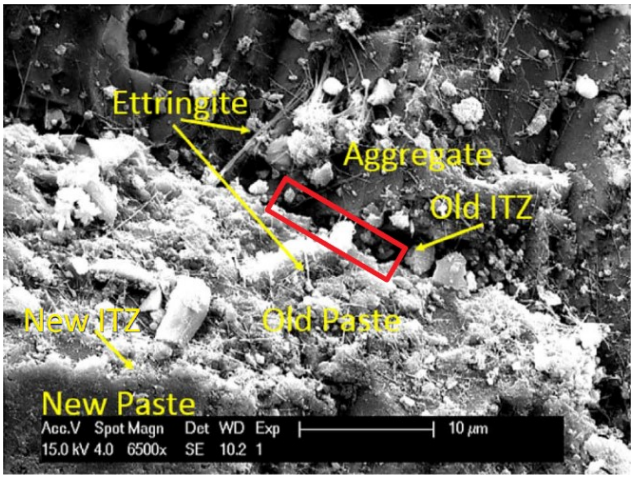

(c)

Figure 1.10. SEM micrographs of the surface of (a) HC-REF, (b) HC-20, and (c) HC-110 mix. Red boxes highlight the micro-cracks on the surface

High amount of silicon and aluminum in the old cement paste of higher strength recycled concrete aggregates (as shown in the section of EDX Analysis) resulted in further hydration of sulphate ion (SO_4) over the aluminate phase within the recycled concrete aggregates. Consequently, as can be seen in Figs. 1.9 and 1.10, ettringite crystals (calcium sulfoaluminate), which appeared in needle form as another hydration product, were observed in higher strength recycled concrete aggregates, which resulted in the development of a stronger bond between the old cement paste and aggregate [52, 53]. As the failure of the HC series started in the old ITZ, it is likely that this strengthened bond contributed further to the significant difference between the mechanical properties of HC-20 and HC-110 series mixes.

EDX analysis

Figure 1.11 shows the EDX elemental analysis results at the polished fresh cut surface of normal-strength RAC mixes at 28 days curing age. It can be seen in the figure that the combined weight of silicon, aluminum, calcium, and oxygen (i.e. SiO_2, Al_2O_3, and CaO) was higher in the old ITZ than in the new ITZ in both NC-40 and NC-110 series. This indicates that old ITZ had higher amount of hydration products of calcium silicate hydrate (C–S–H) than the new ITZ, which suggests a relatively stronger old ITZ and explains the initiation of micro-crack formations in the new ITZ. As can be seen in Fig. 1.11, both the new and old ITZ of NC-110 series exhibited higher combined amount of silicon, aluminum, calcium, and oxygen than

those of NC-40 series leading to the higher amount of C–S–H in NC-110 series and contributing to their higher strength.

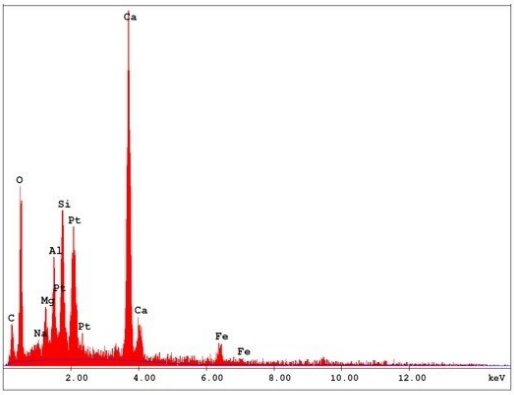

Element	Series	Weight %	Atomic %
Carbon	K series	9.61	18.69
Oxygen	K series	27.93	40.77
Sodium	K series	1.24	1.26
Magnesium	K series	3.12	3.00
Aluminum	K series	5.26	4.56
Silicon	K series	8.99	7.47
Calcium	K series	35.99	20.97

(a)

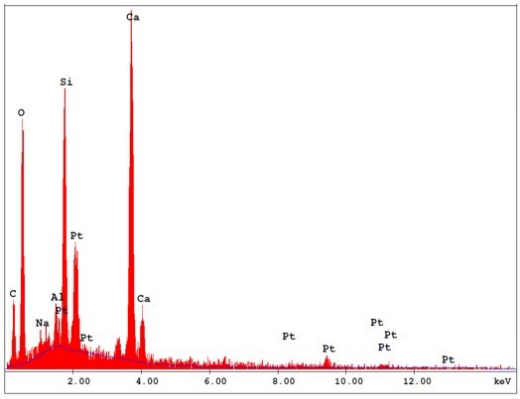

Element	Series	Weight %	Atomic %
Carbon	K series	13.08	22.70
Oxygen	K series	33.55	47.61
Sodium	K series	1.20	1.09
Aluminum	K series	1.58	1.22
Silicon	K series	11.92	8.84
Calcium	K series	35.67	18.54

(b)

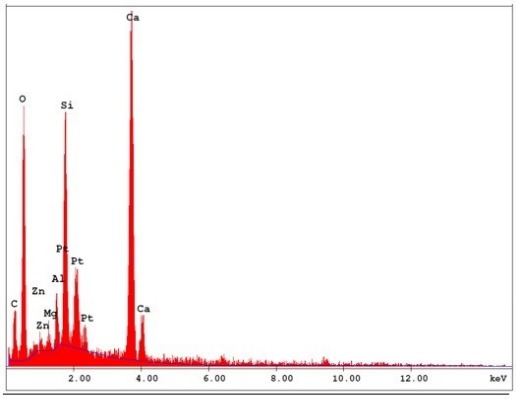

Element	Series	Weight %	Atomic %
Carbon	K series	10.72	19.16
Oxygen	K series	37.00	49.64
Zinc	L series	1.58	0.52
Magnesium	K series	1.80	1.58
Aluminum	K series	1.02	0.81
Silicon	K series	11.47	8.77
Calcium	K series	30.93	19.51

(c)

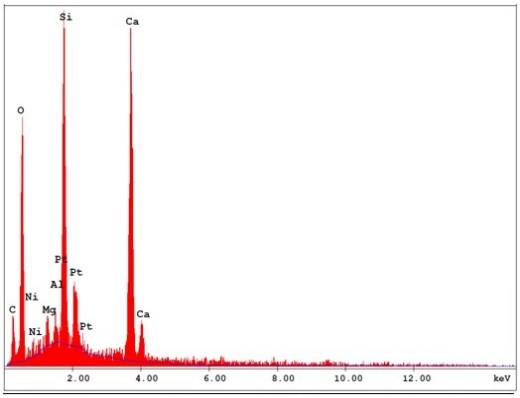

Element	Series	Weight %	Atomic %
Carbon	K series	10.93	19.52
Oxygen	K series	35.85	48.05
Nickel	L series	2.34	0.85
Magnesium	K series	0.39	0.35
Aluminum	K series	2.26	1.79
Silicon	K series	15.93	12.16
Calcium	K series	32.30	17.28

(d)

Figure 1.11. EDX composition analysis of normal-strength RAC: (a) NC-40, new ITZ; (b) NC-40, old ITZ; (c) NC-110, new ITZ; (d) NC-110, old ITZ

Figure 1.12 shows the EDX elemental analysis results of high-strength RAC mixes at 28 days curing age. As can be seen in the figure, the weight percentage of SiO_2, Al_2O_3, and CaO was higher in the new ITZ than in the old ITZ in HC-20 and HC-110 series mixes. This indicates that new ITZ had higher C–S–H than the old ITZ. This confirms the weaker old ITZ and initiation of micro-crack formation in this zone and explains why the failure of HC-110 series mix was still in the old ITZ although the parent concrete strength of these aggregates was higher (i.e. 110 MPa) than the strength of the new concrete (i.e. 80 MPa). However, it should be noted that the difference between the combined amount of silicon, aluminum, calcium, and oxygen in the old and new ITZ was very small in the case of HC-110 series. It can also be seen in the figure that, at the old ITZ, HC-110 series exhibited higher amount of SiO_2, Al_2O_3, and CaO compared to that of HC-20 series, resulting in higher amount of C–S–H in HC-110 series mix.

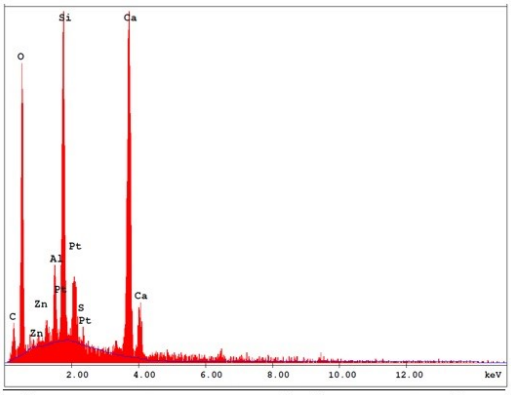

Element	Series	Weight %	Atomic %
Carbon	K series	7.29	13.29
Oxygen	K series	38.78	53.07
Zinc	L series	0.98	0.33
Aluminum	K series	3.18	2.58
Silicon	K series	14.95	11.66
Sulfur	K series	0.37	0.25
Calcium	K series	34.45	18.82

(a)

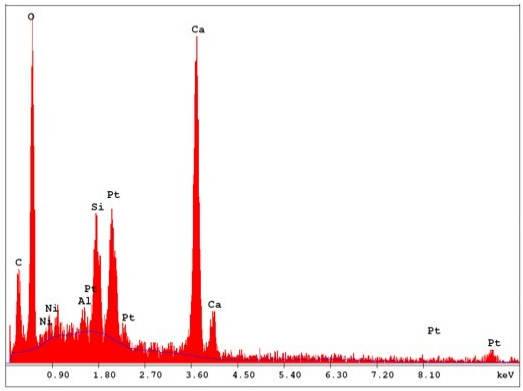

Element	Series	Weight %	Atomic %
Carbon	K series	13.27	22.39
Oxygen	K series	34.45	43.62
Nickel	L series	4.30	1.49
Aluminum	K series	0.67	0.50
Silicon	K series	5.75	4.15
Calcium	K series	32.56	16.46

(b)

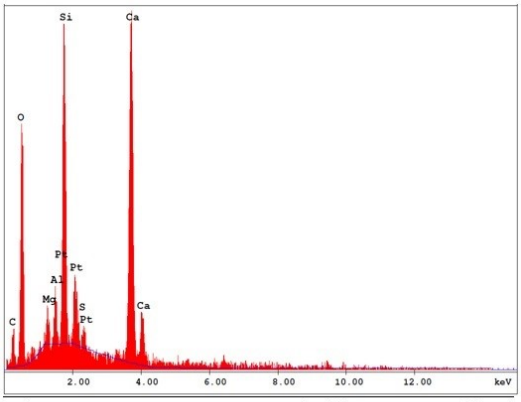

Element	Series	Weight %	Atomic %
Carbon	K series	7.88	14.46
Oxygen	K series	36.47	50.21
Magnesium	K series	1.63	1.48
Aluminum	K series	2.13	1.74
Silicon	K series	14.7	11.53
Sulfur	K series	1.04	0.71
Calcium	K series	35.14	19.86

(c)

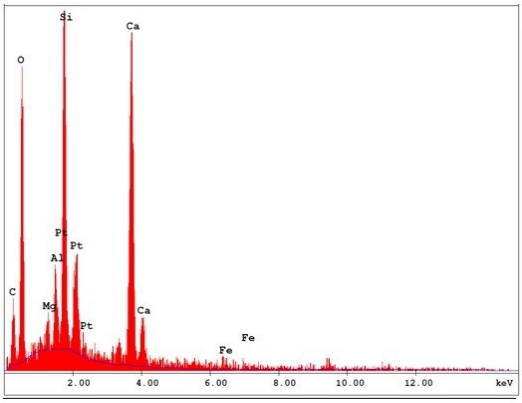

Element	Series	Weight %	Atomic %
Carbon	K series	12.65	22.16
Oxygen	K series	35.04	46.09
Magnesium	K series	1.21	1.04
Aluminum	K series	3.18	2.48
Silicon	K series	15.34	11.49
Calcium	K series	31.98	15.74

(d)

Figure 1.12. EDX composition analysis of high-strength RAC: (a) HC-20, new ITZ; (b) HC-20, old ITZ; (c) HC-110, new ITZ; (d) HC-110, old ITZ

CONCLUSIONS

The first experimental study on the time-dependent and long-term mechanical properties of high-strength RACs manufactured with coarse recycled aggregates of different parent concrete strength has been presented. On the basis of the experimental results and discussions the following conclusions can be drawn:

1- The compressive strength of high-strength RACs containing high-strength recycled concrete aggregates of 110-MPa strength is slightly higher than that of the high-strength conventional concrete that is prepared with the same effective *w/b*. The elastic modulus and splitting tensile strength of these high-strength RACs are similar to those of companion natural aggregate concrete at all curing ages.

2- The elastic modulus of normal-strength RACs containing high-strength (i.e. 110 MPa) recycled concrete aggregates is similar to that of the normal-strength natural aggregate concrete that is prepared with the same effective *w/b*. The compressive strength of these normal-strength RACs is slightly higher at longer

curing ages and their splitting tensile strength is slightly lower than the companion conventional concrete at all curing ages.

3- RACs containing low-strength (i.e. 40 MPa) recycled concrete aggregates develop significantly higher shrinkage strain than the conventional concrete at all curing ages, whereas RACs containing high-strength (i.e. 110 MPa) recycled concrete aggregates exhibit only slightly higher shrinkage strain than the conventional concrete.
4- RACs containing high-strength recycled concrete aggregates exhibit similar creep deformations, as defined by creep coefficient and specific creep, to those of the conventional concrete. On the other hand, RACs containing low-strength recycled concrete aggregates develop significantly higher creep deformations (~60%) than RACs containing high-strength recycled concrete aggregates.
5- The SEM analysis of RACs showed that, unlike in normal-strength RACs where the failure initiates in the new ITZ, in high-strength RACs the cracks initiate in the old ITZ between the old paste and aggregate. For this reason, properties of high-strength RACs are highly sensitive to the quality of recycled concrete aggregates.
6- The EDX analysis of RACs indicated that, unlike in normal-strength RACs that contain a higher amount of C–S–H hydration products in their old ITZ than their new ITZ, higher amounts of C–S–H exist in the new ITZ of high-strength RACs.

The experimental results of this study indicate that properly designed mixes with high-quality recycled concrete aggregates can develop time-dependent and long-term mechanical properties similar to or better than those of natural aggregate concretes. These findings, especially those on the creep behaviour, are very promising as they indicate that structural members prepared by such high-quality recycled concrete aggregates can be designed to exhibit similar long-term deflections/shortening behaviour under sustained loading compared to conventional concrete members.

ACKNOWLEDGEMENTS

The authors gratefully acknowledge the financial support from the National Natural Science Foundation of China through Grant No. 51650110495 and the University of Adelaide through a Research Excellence Grant awarded to the second author.

REFERENCES

[1] Torgal FP, Ding Y, Miraldo S, Abdollahnejad Z, Labrincha JS. Are geopolymers more suitable than portland cement to produce high volume recycled aggregates HPC. *Construction and Building Materials*. 2012;36:1048-52.

[2] Gholampour A, Ozbakkaloglu T. Performance of sustainable concretes containing very high volume class-F fly ash and ground granulated blast furnace slag. *Journal of Cleaner Production*. 2017;162:1407-17.

[3] Torgal FP, Jalali S. *Construction and Demolition (C&D) Wastes, In: Eco-efficient Construction and Building Materials*, Springer London, 2011, 51-73.

[4] Kou SC, Poon CS, Wan HW. Properties of concrete prepared with low-grade recycled aggregates. *Construction and Building Materials*. 2012;36:881-9.

[5] Silva RV, de Brito J, Dhir RK. Comparative analysis of existing prediction models on the creep behaviour of recycled aggregate concrete. *Engineering Structures*. 2015;100:31-42.

[6] Wang Y, Chen J, Geng Y. Testing and analysis of axially loaded normal-strength recycled aggregate concrete filled steel tubular stub columns. *Engineering Structures*. 2015;86:192-212.

[7] Ignjatovic IS, Marinkovic SB, Tosic N. Shear behavior of recycled aggregate concrete beams with and without shear reinforcement. *Engineering Structures.* 2017;141:386-401.

[8] Gholampour A, Gandomi AH, Ozbakkaloglu T. New formulations for mechanical properties of recycled aggregate concrete using gene expression programming. *Construction and Building Materials*. 2017;130:122-45.

[9] Topcu IB. Physical and mechanical properties of concretes produced with waste concrete. *Cement and Concrete Research*. 1997;27(12):1817-23.

[10] Xie, T, Gholampour A, Ozbakkaloglu T. Toward the development of sustainable concretes with recycled concrete aggregates: a comprehensive review of studies on mechanical properties. *Journal of Materials in Civil Engineering*. 2017;30(9):04018211.

[11] Corinaldesi V, Moriconi G. Influence of mineral additions on the performance of 100% recycled aggregate concrete. *Construction and Building Materials*. 2009;23:2869-76.

[12] Domingo-Cabo A, Lázaro C, López-Gayarre F, Serrano-López MA, Serna P, Castaño-Tabares JO. Creep and shrinkage of recycled aggregate concrete. *Construction and Building Materials*. 2009;23(7):2545-53.

[13] Domingo A, Lázaro C, Gayarre FL, Serrano MA, Lopez-Colina C. Long term deformations by creep and shrinkage in recycled aggregate concrete. *Materials and Structures*. 2010;43:1147-60.

[14] Kou SC, Poon CS, Etxeberria M. Influence of recycled aggregates on long term mechanical properties and pore size distribution of concrete. *Cement and Concrete Composites*. 2011;33:286-91

[15] Kou SC, Poon CS. Enhancing the durability properties of concrete prepared with coarse recycled aggregate. *Construction and Building Materials*. 2012;35:69-76.

[16] Manzi S, Mazzotti C, Bignozzi MC. Short and long-term behavior of structural concrete with recycled concrete aggregate. *Cement and Concrete Composites*. 2013;37:312-8.

[17] Xiao JZ, Li L, Tam VW. The state of the art regarding the long-term properties of recycled aggregate concrete. *Structural Concrete*. 2014;15(1):3-12.

[18] Kou SC, Poon CS. Effect of the quality of parent concrete on the properties of high performance recycled aggregate concrete. *Construction and Building Materials*. 2015;77:501-8.

[19] Tam VW, Kotrayothar D, Xiao J. Long-term deformation behaviour of recycled aggregate concrete. *Construction and Building Materials*. 2015;100:262-72.

[20] de Brito J, Ferreira J, Pacheco J, Soares D, Guerreiro M. Structural, material, mechanical and durability properties and behaviour of recycled aggregates concrete. *Journal of Building Engineering*. 2015;6:1-16.

[21] Dodds W, Goodier C, Christodoulou C, Austin S, Dunne D. Durability performance of sustainable structural concrete: effect of coarse crushed concrete aggregate on microstructure and water ingress. *Construction and Building Materials*. 2017;145;183-95.

[22] Pedro D, de Brito J, Evangelista L. Evaluation of high-performance concrete with recycled aggregates: use of densified silica fume as cement replacement. *Construction and Building Materials*. 2017;147:803-14.

[23] Limbachiya MC, Leelawat T, Dhir RK. Use of recycled concrete aggregate in high-strength concrete. *Materials and Structures*. 2000;33(9):574-80.

[24] Ozbakkaloglu T, Gholampour A, Lim JC. Damage-plasticity model for FRP-confined normal-strength and high-strength concrete. *Journal of Composites for Construction*. 2016;20(6):04016053.

[25] Ozbakkaloglu T, Gholampour A, Xie T. Mechanical and durability properties of recycled aggregate concrete: effect of recycled aggregate properties and content on the behaviour. *Journal of Materials in Civil Engineering*. 2017;30(2):04017275.

[26] Abbas A, Fathifazl G, Isgor OB, Razaqpur AG, Rournier B, Foo S. Proposed method for determining the residual mortar content of recycled concrete aggregates. *Journal of ASTM International*. 2008;5(1):1-12.

[27] Tam VW, Tam CM. Assessment of durability of recycled aggregate concrete produced by two-stage mixing approach. *Journal of Materials Science*. 2007;42(10):3592-602.

[28] ASTM C192/C192M-07. *Standard Practice for Making and Curing Concrete Test Specimens in the Laboratory*, West Conshohocken, PA, USA, ASTM International, 2007.

[29] ASTM C143/C143M-12. *Standard Test Method for Slump of Hydraulic-Cement Concrete*, West Conshohocken, ASTM International, 2012.

[30] ASTM C138/C138M-16. *Standard Test Method for Density (Unit Weight), Yield, and Air Content (Gravimetric) of Concrete*, West Conshohocken, PA, USA, ASTM International, 2016.

[31] ASTM C642-13. *Standard Test Method for Density, Absorption, and Voids in Hardened Concrete*, West Conshohocken, ASTM International, 2013.

[32] ASTM C39/C39M-16b. *Standard Test Method for Compressive Strength of Cylindrical Concrete Specimens*, West Conshohocken, PA, USA, ASTM International, 2016.

[33] ASTM C469/C469M-14. *Standard Test Method for Static Modulus of Elasticity and Poisson's Ratio of Concrete in Compression*, West Conshohocken, PA, ASTM International, 2014.

[34] ASTM C496/C496M-04. *Standard Test Method for Splitting Tensile Strength of Cylindrical Concrete Specimens*, West Conshohocken, PA, ASTM International, 2004.

[35] ASTM C596-07. *Standard Test Method for Drying Shrinkage of Mortar Containing Hydraulic Cement*, West Conshohocken, PA, ASTM International, 2007.

[36] ASTM C512/C512M-15. *Standard Test Method for Creep of Concrete in Compression*, West Conshohocken, PA, ASTM International, 2015.

[37] AS3600-09. *Australian Standard for Concrete Structures*, S. A, North Sydney, 2009.

[38] ACI 318-11. *Building Code Requirements for Structural Concrete and Commentary, PCA notes on ACI 318-11: with design applications*, Farmington Hills, Mich: ACI International, 2011.

[39] CSA. A23.3-04. *Design of concrete structures*, Canadian Standard Association, 2004.

[40] Eurocode 2-04. *Design of Concrete Structures: Part 1-1: General Rules and Rules for Buildings*. British Standards Institution. 2004.

[41] JSCE-07. *Standard specification for concrete structure*. JSCE No. 15, Tokyo, Japan, 2007.

[42] JCI-08. *Guidelines for Control of Cracking of Mass Concrete*, Japan Concrete Institute, 2008.

[43] NZS 3101:2006. *Concrete structures standard. The design of concrete structures*, Wellington, New Zealand, 2006.

[44] Kovler K, Zhutovsky S. Overview and future trends of shrinkage research. *Materials and Structures*. 2006;39(9):827-47.

[45] Gilbert RI. Shrinkage, cracking and deflection-the serviceability of concrete structures. *Electronic Journal of Structural Engineering*. 2001;1(1):2-14.

[46] Limbachiya M, Meddah MS, Ouchagour Y. Performance of Portland/silica fume cement concrete produced with recycled concrete aggregate. *ACI Materials Journal*. 2012;109(1):91-100.

[47] Leemann A, Lura P, Loser R. Shrinkage and creep of SCC-the influence of paste volume and binder composition. *Construction and Building Materials*. 2011;25:2283-9.

[48] Mazloom M, Ramezanianpour AA, Brooks JJ. Effect of silica fume on mechanical properties of high-strength concrete. *Cement and Concrete Composites*. 2004;26:347-57.

[49] Geng Y, Wang Y, Chen J. Creep behaviour of concrete using recycled coarse aggregates obtained from source concrete with different strengths. *Construction and Building Materials*. 2016;128:199-213.

[50] Sidorova A, Vazquez-Ramonich E, Barra-Bizinotto M, Roa-Rovira JJ, Jimenez-Pique E. Study of the recycled aggregates nature's influence on the aggregate–cement paste interface and ITZ. *Construction and Building Materials*. 2014;68:677-84.

[51] Medina C, Zhu W, Howind T, de Rojas MIS, Frías M. Influence of interfacial transition zone on engineering properties of the concrete manufactured with recycled ceramic aggregate. *Journal of Civil Engineering and Management*. 2015;21(1):83-93.

[52] Tam VW, Gao XF, Tam CM, Ng KM. Physio-chemical reactions in recycle aggregate concrete. *Journal of Hazardous Materials*. 2009;163:823-8.

[53] Kang SM, Na SH, Lee SH, Song MS, Lee WG, Song YJ. Effects of ettringite formation on the compressive strength of mortar during activation of blast furnace slag without ordinary Portland cement. *Materials Research Innovations*. 2015;19:545-8.

Statement of Authorship

Title of Paper	New formulations for mechanical properties of recycled aggregate concrete using gene expression programming
Publication Status	☑ Published ☐ Accepted for Publication ☐ Submitted for Publication ☐ Unpublished and Unsubmitted work written in manuscript style
Publication Details	Gholampour A, Gandomi AH, Ozbakkaloglu T. New formulations for mechanical properties of recycled aggregate concrete using gene expression programming. *Construction and Building Materials*. 2017;130:122-45.

Principal Author

Name of Principal Author (Candidate)	Aliakbar Gholampour		
Contribution to the Paper	Literature review, analysis and development of models, and preparation of the manuscript.		
Overall percentage (%)	70%		
Certification:	This paper reports on original research I conducted during the period of my Higher Degree by Research candidature and is not subject to any obligations or contractual agreements with a third party that would constrain its inclusion in this thesis. I am the primary author of this paper.		
Signature		Date	31/01/2019

Co-Author Contributions

By signing the Statement of Authorship, each author certifies that:

i. the candidate's stated contribution to the publication is accurate (as detailed above);

ii. permission is granted for the candidate in include the publication in the thesis; and

iii. the sum of all co-author contributions is equal to 100% less the candidate's stated contribution.

Name of Co-Author	Amir Hossein Gandomi		
Contribution to the Paper	Modelling and review of manuscript.		
Signature		Date	31/01/2019

Name of Co-Author	Togay Ozbakkaloglu		
Contribution to the Paper	Research supervision and review of manuscript.		
Signature		Date	31/01/2019

Please cut and paste additional co-author panels here as required.

New Formulations for Mechanical Properties of Recycled Aggregate Concrete using Gene Expression Programming

ABSTRACT

This paper presents new empirical models for prediction of the mechanical properties of recycled aggregate concrete (RAC) using gene expression programming (GEP) technique. A large and reliable test database containing the results of 650 compressive strength, 421 elastic modulus, 346 splitting tensile strength, and 152 flexural strength, tests of RACs containing no pozzolanic admixtures is collated through an extensive review of the literature. The performance of existing mechanical property models of RACs is then assessed using the database, and the results of this assessment are presented using selected statistical indicators. New expressions for the predictions of 28-day compressive strength, elastic modulus, flexural strength, and splitting tensile strength of RACs are developed based on the database. The assessment results indicate that the predictions of the proposed models are in close agreement with the test results, and the new models provide improved estimates of the mechanical properties of RACs compared to the existing models.

KEYWORDS: Recycled concrete aggregate; Recycled aggregate concrete (RAC); Compressive strength; Elastic modulus; Flexural strength; Splitting tensile strength; Gene expression programming (GEP).

INTRODUCTION

Rapid industrial and population growths have resulted in the increased rate of demolition of old structures in order to obtain new construction sites. Generation and disposal of the huge amount of construction and demolition waste in the landfills caused environmental problems by depleting the landfill areas [1–3]. Over the past two decades, the use of recycled concrete aggregates, obtained from construction and demolition waste, as an alternative to non-renewable natural aggregates in concrete has been considered to improve resource sustainability in the construction industry and minimize the environmental impact of the disposed construction and

demolition waste [4–6]. The use of recycled concrete as coarse aggregates in the new concrete mix is recognized as an attractive technology to conserve natural resources and reduce the environmental impact of the construction industry [2,3,7–9]. However, as a result of the variability in the characteristics of the recycled concrete aggregates the mechanical properties of RACs obtained using them varies from those of natural aggregate concrete (NAC). Therefore, understanding the relationship between the mechanical properties and mix proportions of RAC is essential before the material can widely be adopted by the construction industry.

The compressive strength, elastic modulus, flexural strength, and splitting tensile strength are the key material properties for the analysis and design of concrete structures. A comprehensive review of the existing studies on RAC has shown that a number of models have been reported in the literature to predict these mechanical properties for RAC [10–30]. However, because of the limitations in the parametric ranges of the considered experimental results, as well as the relatively small test databases used in the calibration of the models the existing models are often restricted to specific specimen subsets and they might not provide accurate predictions of the mechanical properties of RAC beyond these parametric spaces. Therefore, a large and carefully constructed database, covering a wide range of parameters, is needed to develop reliable and accurate expressions to predict the mechanical properties of RAC. Such a database is presented in the current paper.

Recent technological progress in artificial intelligence techniques has generated accurate and reliable computer-aided modelling procedures for structural engineering problems [31–39]. Application of machine learning and computational intelligence methods to predict the mechanical properties of RAC has also received recent research attention. Younis and Pilakoutas [9] proposed a strength model to predict the compressive strength of the RAC using multi-linear and non-linear regressing analysis. Duan et al. [40] and Sahoo et al. [41] utilized artificial neural networks (ANN) method to predict the compressive strength of the RAC. Deshpande et al. [42] modeled the compressive strength of the RAC by ANN, model tree, and nonlinear regression methods. Duan et al. [43] utilized ANN method to predict the elastic modulus of RAC. Behnood et al. [44] predicted elastic modulus of RAC using M5 model tree algorithm. Recently, Gonzalez-Taboada et al. [45]

proposed models to predict the compressive strength, elastic modulus, and splitting tensile strength of RAC using multivariable regression and genetic programming.

Pattern recognition of the computational intelligence methods plays a significant role in the application of them in the engineering applications. Most of the existing computational intelligence methods (e.g. ANN and support vector regression) are capable of providing complex pattern recognition through black-box models. However, the structure of these methods needs to be predefined by a base form, which requires extensive memory size [46,47]. Genetic Programming (GP) is a powerful optimization technique based on the genetic and natural selections. The main advantage of the GP-based methods is their ability to provide simple expressions without the need to assume a base form. GP provides a relatively new pattern recognition procedure for civil engineering applications [47,48]. Gene expression programming (GEP) introduced by Ferreira [49] is an extended GP-based method. In GEP, linear chromosomes as several genes with a fixed length encode a smaller program. Recent studies indicated that GEP can be an efficient alternative to the traditional GP method in civil engineering applications [46–51]. In these studies, GEP has been used for prediction of compressive strength of foam concrete, compressive strength of steel fiber reinforced concrete under triaxial compression, moment capacity of ferrocement members, shear strength of reinforced concrete deep beams, flow number of asphalt mixture, and liquefaction potential of soil. However, the use of GEP in structural engineering applications has remained limited, and no study to date has considered its application to predicting the mechanical properties of RAC.

In this study, empirical models are proposed using GEP technique to predict 28-day compressive strength, elastic modulus, flexural strength, and splitting tensile strength of RAC. In addition, 34 existing mechanical properties models of RAC collected from 21 published studies are reviewed and assessed through statistical analysis using a reliable and comprehensive database containing samples with a wide range of mixture proportions.

EXPERIMENTAL DATABASE

The RAC database presented in Appendix 1 was compiled from 69 experimental studies in the literature. The results included in the database were obtained from concrete specimens manufactured using mixes that contained no pozzolanic admixtures. The resulting database consists of 332 compressive strength results obtained from cube specimens ($f'_{c,cube}$), 318 compressive strength results obtained from cylinder specimens ($f'_{c,cylinder}$), 421 elastic modulus (E_c) results, 152 flexural strength (f_r) results, and 346 splitting tensile strength (f_{st}) results.

The database shown in Appendix 1 contains information for each dataset including the type and size of the specimens, the effective water-to-cement binder ratio (w_{eff}/c), aggregate-to-cement ratio (a/c), maximum particle size (Φ) of recycled concrete aggregates and NAs, air-dried density (ρ_{ad}) and saturated surface dry density of hardened concrete (ρ_{ssd}), strength of the parent concrete recycled concrete aggregate derived from ($f'_{c,p}$), recycled concrete aggregate replacement ratio (RCA%), water absorption of recycled concrete aggregates and NAs (WA_{RCA} and WA_{NA}, respectively), bulk density of coarse recycled concrete aggregate and NAs (ρ_{RCA} and ρ_{NA}, respectively), Los Angeles abrasion index of recycled concrete aggregates and NAs (LA_{RCA} and LA_{NA}, respectively), compressive strength of concrete (f'_c), elastic modulus of concrete (E_c), flexural strength of concrete (f_r), and splitting tensile strength of concrete (f_{st}). The distribution of the most influential parameters (i.e. w_{eff}/c and RCA%) are shown in Fig. 2.1 for the specimens in the database.

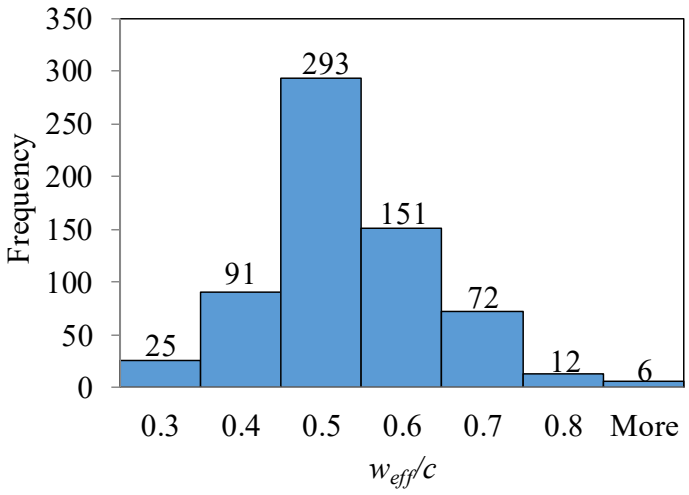

(a)

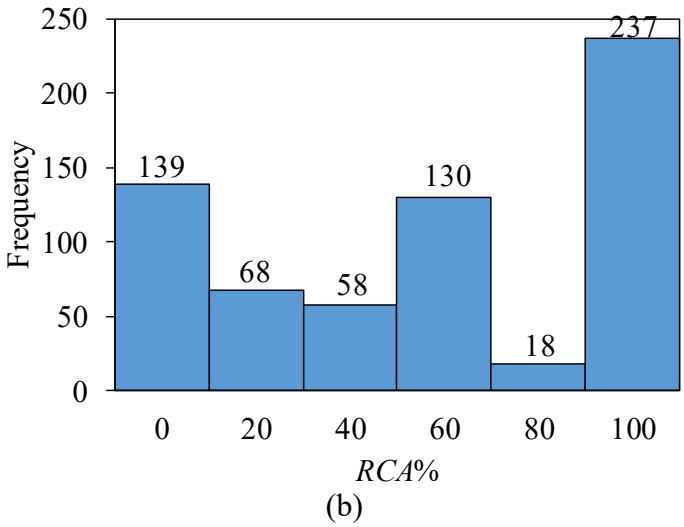

Figure 2.1. Distribution histograms of: (a) w_{eff}/c; (b) *RCA%*

Three types of specimens were used in obtaining the mechanical properties in Appendix 1; namely, cylinders, cubes, and beams. For each type of specimen, two different sizes were used in the tests, which are indicated by the labels. The cylinders had a diameter of either 100 or 150 mm and a height-to-diameter ratio of two, which are labeled as C_1 and C_2, respectively; cubes had a dimension of 100 or 150 mm, which are labeled as S_1 and S_2, respectively; and beams had a dimension of 100 × 100 × 500 mm or 150 × 150 × 750 mm, which are labeled as B_1 and B_2, respectively. In Appedix 1, w_{eff}/c of the specimens varied from 0.19 to 0.87, *RCA%* varied from 0 to 100, f'_c varied from 13.4 to 108.5 MPa, E_c varied from 12.5 to 50.4 GPa, f_r varied from and 1.9 to 10.2 MPa, and f_{st} varied from 1.1 to 6.3 MPa.

It should be noted that, as marked in Appendix 1, the datasets that deviated significantly from the global trends of the database (i.e. ± 50%) were excluded from the model assessment and were not used in the subsequent model development. This resulted in 508 compressive strength results, 251 from cube specimens and 257 from cylinder specimens; 351 elastic modulus results; 118 flexural strength results; and 307 splitting tensile strength results that were used in the model assessment and development.

EXISTING MODELS FOR PREDICTING MECHANICAL BEHAVIOUR OF RAC

Table 2.1 presents the existing models, obtained from 21 different studies in the literature, to predict the mechanical properties of RAC. These include the eight models for compressive strength [9-14], 16 models for elastic modulus [10,12,15-28], four models for flexural strength [10,17,21,23], and six models for splitting tensile strength [10,12,21,23,27,29]. All models contain closed-form equations, which were developed by regression analysis of the experimental test results, and hence their accuracy is dependent on the size, reliability, and parametric range of the test databases used in the model development.

GENE EXPRESSION PROGRAMMING

Gene expression programming (GEP) was developed by Ferreira [49] as a branch of genetic programming (GP) and it is based on five different components of: function and terminal sets, a fitness function, control parameters, and a terminal condition. A character string with a fixed length is used in the GEP algorithm in order to obtain the solution, whereas GP technique uses a parse tree structure, which can vary in length during the run in the computer program. The creation of the genetic variety in the GEP is extremely simple because of the genetic mechanism of this technique at the chromosome level. Furthermore, because of its multi-genic nature GEP allows the development of complex and nonlinear programs with several subprograms. In GEP, each gene consists of two types of symbols: a fixed length variables and constants as terminal set (e.g. {a,b,c,6}) and arithmetic operations as function set (e.g. {+,–,×,÷,log}). The key feature of the GEP is the creation of the chromosomes, which are capable of representing any parse tree using Karva language to read and express the information encoded in the chromosomes. The chromosomes are then translated to the branched structures of expression tree (ET). The transformation of the Karva expression (K-expression) to an ET initiates from the first position in the K-expression, as the root of ET, and continues through the string. In order to generate the string, the ET is inversely transformed to the K-expression using the record of the nodes from the root layer to the deepest layer. In the GEP algorithm,

Table 2.1. Summary of existing models to predict mechanical properties of RAC

Year	Model	Compressive strength (f'_c) (MPa)	Elastic modulus (E_c) (MPa)	Flexural strength (f_r) (MPa)	Splitting tensile strength (f_{st}) (MPa)
1985	Ravindrarajah and Tam [16]	–	$7770\ f'^{0.33}_{c,cube}$	–	–
1988	Kakizaki et al. [15]	–	$1.9 \cdot 10^5 \cdot \left(\frac{\rho_h}{2400}\right)^{1.5} \cdot \sqrt{\frac{f'_{c,cube}}{2000}}$	–	–
1993	Bairagi et al. [17]	–	$(5780 - 1340 \cdot RCA\%)\sqrt{f'_{c,cube}}$	$(0.82 - 0.16 \cdot RCA\%)\sqrt{f'_{c,cube}}$	–
1996	de Oliveira and Vazquez [18]	–	$2.15 \cdot 10^4 \sqrt[3]{0.1 f'_{c,cube}}$	–	–
1996	Tavakoli and Soroushian [21]	–	$378 f'_{c,cube} + 8242$	$0.62\sqrt{f'_{c,cube}}$ (ACI 318)	$0.5\sqrt{f'_{c,cube}}$
1998	Dillmann [19]	–	$634.43\ f'_{c,cube} + 3057.6$	–	–
1999	Dhir [20]	–	$370 f'_{c,cube} + 13100$	–	–
2001	Zilch and Roos [22]	–	$9100\ (f'_{c,cylinder} + 8)^{1/3} \cdot \left(\frac{\rho_h}{2400}\right)^2$	–	–
2005	Kheder and Al-Windawi [23]	–	$4993\ f'^{0.422}_{c,cylinder}$	$0.762\ f'^{0.473}_{c,cylinder}$	$0.568\ f'^{0.499}_{c,cylinder}$
2006	Xiao et al. [10]	$f'_{c,cube} = 0.069\rho_h - 116.1$	$\frac{10^5}{2.8 + \frac{40.1}{f'_{c,cube}}}$	$0.75\sqrt{f'_{c,cube}}$	$0.24\ f'^{0.65}_{c,cube}$
2006	Xiao et al. [29]	–	–	–	$(0.24 - 0.06 \cdot RCA\%)\ f'^{2/3}_{c,cube}$
2007	Rahal [24]	–	$\rho_h{}^{1.5} \cdot 0.043\sqrt{f'_{c,cylinder}}$	–	–
2010	Corinaldesi [25]	–	$18800 \cdot \sqrt[3]{0.083 \cdot f'_{c,ylinder}}$	–	–
2012	Sriravindrarajah et al. [11]	$f'_{c,cube} = 22.2\ e^{-0.052P}$ P is the porosity of the concrete	–	–	–

2012	Lovato et al. [12]	$f'_{c,cylinder} = 22.5\left(\frac{0.5}{w_{eff/c}}\right)^{0.67} \cdot \left(1 - \frac{RCA\%}{7.44}\right) \cdot FRA\% \cdot (1 - \frac{a/c}{8.61}) \cdot [1 - (-0.04 \cdot RCA\% \cdot a/c)] \cdot [1 - (0.008 \cdot FRA\% \cdot a/c)]$ where *FRA%* is fine recycled aggregate percentage	$13.49\left(\frac{0.5}{w_{eff/c}}\right)^{0.48} \cdot \left(1 - \frac{RCA\%}{5.76}\right) \cdot (1 - \frac{FRA\%}{5.49}) \cdot (1 - \frac{a/c}{8.67}) \cdot [1 - (-0.04 \cdot RCA\% \cdot a/c)]10^3$	–	$1.86\left(1 - \frac{RCA\%}{6.81}\right) \cdot (1 - \frac{FRA\%}{9.86}) \cdot (1 - \frac{a/c}{4.87}) \cdot [1 - (-0.016 \cdot RCA\% \cdot a/c)]$
2012	Hoffmann et al. [26]	–	$6800\sqrt[3]{f'_{c,ylinder}}$	–	–
2012	Pereira et al. [13]	$f'_{c,cube} = k_1/k_2^{(w_{eff/c})} \cdot (1 - k_3 \cdot WA_{RCA} \cdot RCA\%)$ k_1= 230.3, k_2 =25.9, k_3= -0.077 where WA_{RCA} is water absorption rate of recycled concrete aggregate	–	–	–
2012	Pereira et al.[27]	–	$4.228 \cdot {f'_{c,cube}}^{1/3}((1 - RCA\%) \cdot \rho_{NA} + RCA\% \cdot \rho_{RcA})\left[\frac{(0.55)}{(w_{eff/c})}\right]^{0.22}$	–	$0.096 \cdot {f'_{c,cube}}^{2/3}((1 - RCA\%) \cdot \rho_{NA} + RCA\% \cdot \rho_{RCA})\left[\frac{0.55}{(w_{eff/c})}\right]^{0.177}$
2013	Thomas et al.[14]	$f'_{c,ylinder} = -0.32 + 0.022 \cdot RCA\% + (1 - 0.0025 \cdot RCA\%) \cdot f'_{c-NA}$ f'_{c-NA} is the compressive strength of the companion NAC	–	–	–
2013	Younis and Pilakoutas [9]	$f'_{c,cube} = \left[13.7\frac{\rho_{RCA}}{\rho_{NA}} + 2.47\frac{LA_{RCA}}{LA_{NA}} - 0.2\frac{WA_{RCA}}{WA_{NA}} - 0.12RCA\% - 10.35\right] \cdot f'_{c-NA}$ $f'_{c,cube} = \left[-1.245\frac{\rho_{RCA}}{\rho_{NA}} + 3.22\frac{LA_{NA}}{LA_{RCA}} - 0.99\frac{WA_{NA}}{WA_{RCA}} - 0.13RCA\%\right] \cdot f'_{c-NA}$ $f'_{c,cube} = \left[f'_{c-NA} \cdot \left(\frac{\rho_{RCA}}{\rho_{NA}}\right)^{-0.15} \cdot \left(\frac{LA_{RCA}}{LA_{NA}}\right)^{-3.6} \cdot \left(\frac{WA_{RCA}}{WA_{NA}}\right)^{0.65}\right] \div (RCA\% + 1)^{0.12}$	–	–	–

		where LA_{RCA} and LA_{NA} , respectively, are the Los Angeles abrasion index for recycled concrete aggregate and NA, and WA_{NA} is water absorption rate of NA			
2014	Wardeh et al. [28]	–	$17553\left(0.1\cdot f'_{c,cube}\right)^{0.42}$	–	–

* In this table, f'_c, E_c, f_r, f_{st} and $f'_{c\text{-}NA}$ are in MPa; ρ_h, ρ_{RCA} and ρ_{NA} are in kg/m^3; P, WA_{RCA}, and WA_{NA} are in %.

because of the predefined and fixed length of the genes and the variability in the corresponding process of the genome. Therefore, the K-expression's length can be less than or equal to that of the GEP gene [46,48].

Figure 2.2 shows the schematic of the GEP algorithm. The algorithm starts with the random creation of the chromosome with the fixed length for each evolving program (individual). Subsequently, the chromosomes are declared, and the fitness of each individual is evaluated. Following this, the individuals are chosen based on their fitness results in order to apply the reproduction. The process is repeated with the new individual for a series of generations until a solution is found. In this approach, conversion in the population is provided by performing genetic operations, such as mutation, rotation, and crossover, on the selected program.

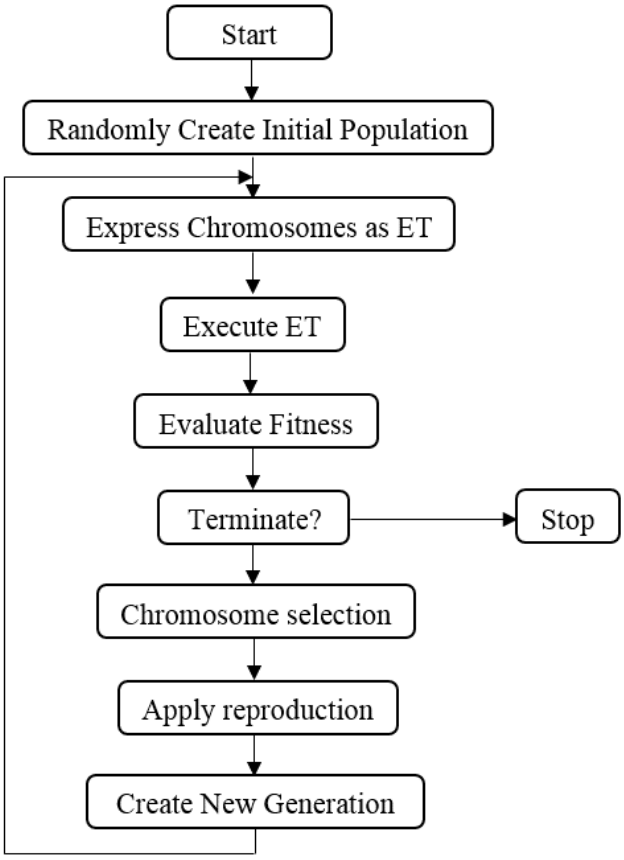

Figure 2.2. Schematic presentation of the GEP algorithm

PERFORMANCE MEASURES

To increase the accuracy of the developed models, the experimental database was randomly separated into three different subsets of learning, validation, and testing.

In this division, the learning data were used for the genetic development, the validation data for the final model selection, and the testing data for the determination of the accuracy of the GEP models in regard to the data that do not play any role in the structure of the models. The final models are selected using an objective function (OBJ) based on the best performance of both learning and validation data sets. The objective function, defined as Eq. 2.1 is minimized to select the best GEP models [47].

$$\mathrm{OBJ} = \left(\frac{n_L - n_V}{n_T}\right)\rho_L + \left(\frac{2n_V}{n_T}\right)\rho_V \tag{2.1}$$

where n is the number of the data points, ρ is the performance index, and subscripts L, V, and T are learning, validation, and testing data sets, respectively. Four statistical indexes including the average absolute error (AAE), root mean square error (RMSE), mean (M), and covariance (COV) are used to assess the model performance. The definitions of AAE, RMSE, M, COV, and ρ [47] are given in Eqs. 2.2-6.

$$\mathrm{AAE} = \frac{1}{n}\sum_{i=1}^{n}\frac{|t_i - u_i|}{t_i} \times 100 \tag{2.2}$$

$$\mathrm{RMSE} = \sqrt{\frac{\sum_{i=1}^{n}(t_i - u_i)^2}{n}} \tag{2.3}$$

$$\mathrm{M} = \frac{1}{n}\sum_{i=1}^{n}\frac{u_i}{t_i} \tag{2.4}$$

$$\mathrm{COV} = \frac{1}{\mathrm{M}}\sqrt{\frac{\sum_{i=1}^{n}\left(\frac{u_i}{t_i} - \frac{\bar{u}}{\bar{t}}\right)^2}{n-1}} \tag{2.5}$$

$$\rho = \frac{\mathrm{RMSE}/\bar{t}}{1 + \frac{\sum_{i=1}^{n}(u_i - \bar{u}_i)(t_i - \bar{t}_i)}{\sqrt{\sum_{i=1}^{n}(u_i - \bar{u}_i)^2 \sum_{i=1}^{n}(t_i - \bar{t}_i)^2}}} \tag{2.6}$$

where u_i and t_i are ith predicted and experimental outputs, respectively; $\bar{u}_i$ and $\bar{t}_i$ are ith average values of the predicted and experimental outputs, respectively; and $\bar{t}$ is the average value of the experimental output.

MODEL DEVELOPMENT USING GEP

In order to obtain the relationships between mechanical properties of RAC and the influential parameters with improved accuracy, the specimens in the database were closely studied and the main factors affecting the mechanical properties of RACs were determined. To evaluate the contribution of each input parameter on the mechanical properties, sensitivity analysis (SA) was performed through the determination of frequency values of the input parameters. The percentage of contribution of each input parameter is calculated using Eqs. 2.7-8 [113]:

$$L_i = f_{max}(x_i) - f_{min}(x_i) \tag{2.7}$$

$$\mathrm{SA}_i = \frac{L_i}{\sum_{j=1}^{n} L_j} \times 100 \tag{2.8}$$

where $f_{max}(x_i)$ and $f_{min}(x_i)$ are maximum and minimum of the predicted output based on the *i*th input domain when other input values are constant at the average value. Figures 2.3(a)–2.3(d) show the sensitivity analysis of compressive strength, elastic modulus, flexural strength, and splitting tensile strength, respectively. It can be seen in these figures that the most influential parameters on the mechanical properties of RAC are w_{eff}/c and *RCA%*. Figure 2.3 shows that the relative influences of w_{eff}/c and *RCA%* remain mostly constant across the mechanical properties investigated in this study.

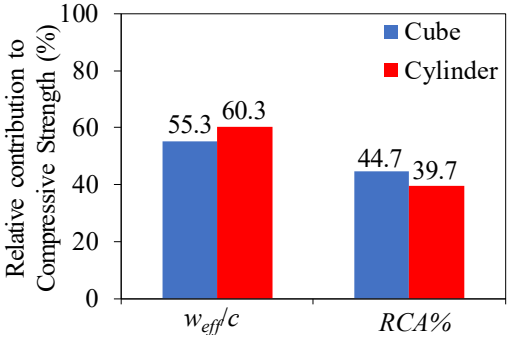

(a)

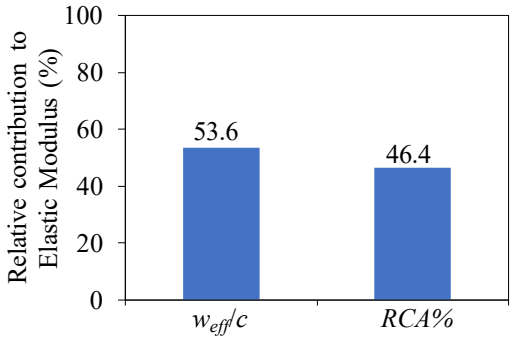

(b)

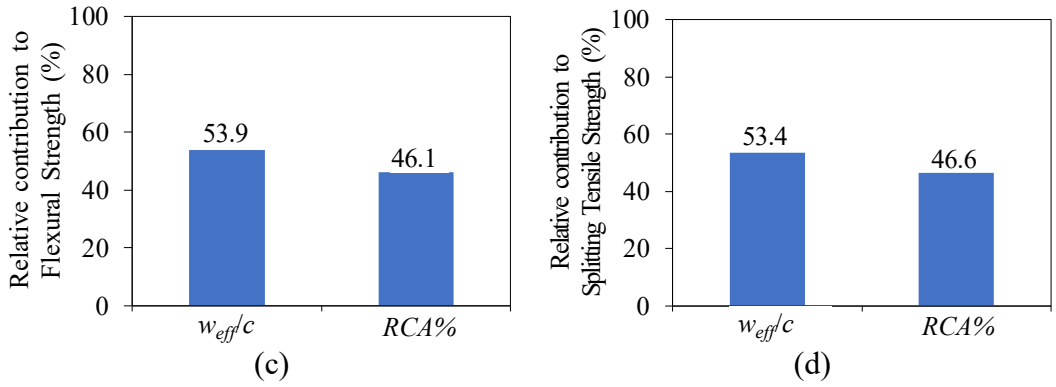

Figure 2.3. Sensitivity analysis of: (a) compressive strength, (b) elastic modulus, (c) flexural strength, and (d) splitting tensile strength of RAC

Consequently, the compressive strength (f_c'), elastic modulus (E_c), flexural strength (f_r), and splitting tensile strength (f_{st}) are considered to be a function of the following parameters:

$$f_c', E_c, f_r, \text{and } f_{st} = f\left(w_{eff}/c, RCA\%\right) \tag{2.9}$$

Based on Eq. 2.9, w_{eff}/c and $RCA\%$ were employed to generate the mechanical property models using the GEP algorithm. Several runs were performed to ensure adequate robustness and generalization of the models. The fitting parameters for the GEP algorithm were chosen based on the previously suggested values by Gandomi et al. [50,114] and a number of initial runs. Population size (i.e. number of chromosomes) sets the running time, with a larger size results in a longer time. Based on the number of possible solutions and complexity of the problem, three optimal levels were set for the population size, i.e. 50, 150, and 300. Head size and number of genes, which evolve the chromosome architectures of the models, specify the complexity of each gene and the number of sub-ET in the evolved model, respectively. The increase of the genes number usually results in overfitting and generation of a complex function. Based on the suggestion by Gandomi et al. [48], the head size was set as 1, and the number of genes was set as two in this study. The optimal values of the other parameters in the GEP algorithm are shown in Table 2.2. These values were obtained from 10 different runs for each combination adopting a trial-and-error method [48,115].

Table 2.2. Optimal parameter settings for GEP algorithm

Parameter	Settings
General	
Chromosomes	30
Genes	10
Gene size	7
Numerical constant	
Constants per gene	1
Data type	Floating number
Lower bound	-10
Upper bound	10

GEP-based formulation of the compressive strength of RAC

The performance of existing compressive strength models was assessed using the database to evaluate the accuracy and relative performance of the models. Based on the available input parameters in the database, only three compressive strength models, i.e. Xiao et al. [10], Pereira et al. [12], and Thomas et al. [14] models, could be used in the model assessment. Two of these models were given for cube specimens [10,13], and one for cylinder specimens [14]. The other compressive strength models (i.e. Refs. [9], [11], and [12]) required specific input parameters that were not available in the database.

In this study, two compressive strength models were developed; one to predict the cube strengths ($f'_{c,cube}$) and one to predict the cylinder ($f'_{c,cylinder}$) strengths. The proposed equations are obtained from 10 subprograms (i.e. genes), with each of them investigating an individual aspect of the problem [50]. The following expressions are proposed to predict the strengths at the age of 28 days for RACs with compressive strengths of up to 110 MPa:

$$f'_{c,cube}\ (\text{MPa}) = \frac{19.1\times 0.998^{RCA\%}\times\left(w_{eff}/c+0.33\right)}{w_{eff}/c^{1.5}} \tag{2.10}$$

$$f'_{c,cylinder}\ (\text{MPa}) = \frac{23.5\times 0.998^{RCA\%}\times\left(w_{eff}/c+0.09\right)}{w_{eff}/c^{1.7}} \tag{2.11}$$

Table 2.3 shows the prediction statistics of the proposed models together with those of the existing models. The size of the experimental database plays an important role in the reliability of the models. It can be seen in the table that the proposed models provide improved accuracy while also being applicable to a larger number of datasets than the existing models.

Table 2.3. Model predictions of compressive strength (f'_c) of RAC

Model	Number of datasets	AAE (%)	RMSE (MPa)	Mean	ρ	COV	Specimen type
Xiao et al. [10]	74	12.7	11.3	0.98	0.17	0.19	Cube
Pereira et al. [13]	157	22.2	11.8	1.14	0.15	0.24	Cube
Thomas et al. [14]	257	14.6	8.1	1.09	0.11	0.19	Cylinder
Proposed model	251	12.4	7.9	1.02	0.09	0.17	Cube
Proposed model	257	14.4	7.8	1.01	0.11	0.19	Cylinder

GEP-based formulation of the elastic modulus of RAC

As can be seen in Table 2.1, 16 models exist in the literature to predict the elastic modulus of RAC. In these models, the compressive strength (f'_c) is often considered as the sole parameter affecting the elastic modulus (E_c) of RACs. In the current study the following expression is proposed to predict the elastic modulus of RAC with E_c of up to 50 GPa as a function of $RCA\%$ and w_{eff}/c:

$$E_c\ (\text{GPa}) = 0.016 \times (6.1 - 0.015RCA\%) \times \left(5.3 - 1.7w_{eff}/c\right)^{3.9} \qquad (2.12)$$

Table 2.4 shows the prediction statistics of the proposed model together with those of the existing models. It can be seen from the table that the models by Xiao et al. [10], Ravindrarajah and Tam [16], Bairagi et al. [17], and Wardeh et al. [28] were the best performing elastic modulus models in the literature. However, the proposed model provides better accuracy than the existing models, while also being applicable to a larger number of datasets.

Table 2.4. Model predictions of elastic modulus (E_c) of RAC

Model	Number of datasets	AAE (%)	RMSE (GPa)	Mean	ρ	COV
Xiao et al. [10]	104	14.3	6.17	0.91	0.14	0.16
Kakizaki et al. [15]	33	10.9	4.51	0.92	0.08	0.13
Ravindrarajah and Tam [16]	104	13.1	5.62	0.93	0.12	0.16
Bairagi et al. [17]	104	19.1	6.76	1.15	0.13	0.16
de Oliveira and Vazquez [18]	104	22.3	7.14	1.20	0.15	0.16
Dillmann [19]	104	21.7	8.40	1.11	0.17	0.23
Dhir [20]	104	14.3	5.15	1.03	0.11	0.17
Tavakoli and Soroushian [21]	104	16.8	6.55	0.88	0.13	0.19
Pereira et al. [27]	82	31.1	10.54	1.29	0.22	0.17
Wardeh et al. [28]	104	17.2	5.79	1.13	0.12	0.16
Lovato et al. [12]	204	70.6	21.8	0.29	0.53	0.24
Zilch and Roos [22]	84	8.3	3.10	1.06	0.06	0.10
Kheder and Al-Windawi [23]	172	18.7	6.76	0.82	0.14	0.12
Rahal [24]	84	10.1	3.74	1.08	0.07	0.10
Corinaldesi [25]	172	10.1	3.85	0.96	0.08	0.12
Hoffmann et al. [26]	172	21.5	7.65	0.79	0.16	0.12
Proposed model	351	10.1	3.06	1.00	0.06	0.10

GEP-based formulation of the flexural strength of RAC

The following expression is proposed to predict the flexural strength (f_r) of RAC with f_r of up to 8 MPa:

$$f_r\ (\text{MPa}) = 0.022 \times (1.2 - 0.002RCA\%) \times \left(2.3 - 0.3w_{eff}/c\right)^{6.9} \quad (2.13)$$

Table 2.5 shows the prediction statistics of the proposed model together with those of the four existing models. It can be seen from the table that among the existing models, those by Xiao et al. [10] and Bairagi et al. [17] performed the best. It can also be seen in Table 2.5 that the proposed model provides further improvements to accuracy while also expanding the range of applicability.

Table 2.5. Model predictions of flexural strength (f_r) of RAC

Model	Number of datasets	AAE (%)	RMSE (MPa)	Mean	ρ	COV
Xiao et al. [10]	19	8.1	0.52	0.99	0.06	0.09
Bairagi et al. [17]	19	11.1	0.73	0.99	0.08	0.13
Tavakoli and Soroushian [21]	19	17.9	1.12	0.82	0.12	0.09
Kheder and Al-Windawi [23]	54	16.1	0.97	0.95	0.14	0.20
Proposed model	118	8.1	0.52	0.99	0.05	0.08

GEP-based formulation of the splitting tensile strength of RAC

The following expression is proposed to predict the splitting tensile strength (f_{st}) of RAC with f_{st} of up to 6 MPa:

$$f_{st}\ (\text{MPa}) = 0.012 \times (0.9 - 0.002RCA\%) \times \left(2.1 - 0.3w_{eff}/c\right)^{9.1} \qquad (2.14)$$

Table 2.6 shows the prediction statistics of the proposed model together with those of the six existing models. As can be seen in the table, among existing models those by Xiao et al. [10] and Bairagi et al. [17] performed the best. It can also be seen in Table 2.6 that further improvements to accuracy and range of applicability are achieved by the proposed model.

Table 2.6. Model predictions of splitting tensile strength (f_{st}) of RAC

Model	Number of datasets	AAE (%)	RMSE (MPa)	Mean	ρ	COV
Xiao et al. [10]	109	16.6	0.52	0.96	0.10	0.19
Tavakoli and Soroushian [21]	109	20.3	0.57	1.16	0.10	0.22
Pereira et al. [27]	58	17.3	0.78	1.12	0.15	0.24
Xiao et al. [29]	109	16.6	0.67	0.86	0.13	0.18
Lovato et al. [12]	149	76.4	2.50	0.23	0.62	0.43
Kheder and Al-Windawi [23]	139	23.1	0.77	1.20	0.16	0.18
Proposed model	307	15.8	0.51	0.99	0.10	0.17

PARAMETRIC INVESTIGATION OF THE PROPOSED MODELS

In order to further validate the proposed models, parametric analyses are performed for the proposed expressions based on the input parameters. The methodology is based on studying the variation of the model predictions with the change in a single input parameter, while the other variables are kept constant at the database average [116]. All datasets were first divided into four groups according to their recycled concrete aggregate replacement ratio (i.e., *RCA%* of 0%, 1–30%, 30–90%, and 100%) in order to study the effect of *RCA%* on the target mechanical properties. The robustness of the proposed expressions is determined by evaluating how well the predicted values agree with the mechanical properties of RAC. Figures 2.4 and 2.5 show the variation of the compressive strength of cube ($f'_{c,cube}$) and cylinder specimens ($f'_{c,cylinder}$), respectively, with w_{eff}/c at each *RCA%* interval. It is well understood that the compressive strength (f'_c) of concrete decreases with increasing w_{eff}/c and the results shown in Figs. 2.4 and 2.5 are in agreement with this [8,12,24,25,117]. Figures also illustrate that the compressive strength decreases with an increase in the *RCA%* for a given w_{eff}/c. As can be seen in Fig. 2.6, which shows the comparison of the compressive strength results with the model predictions, the proposed models accurately capture the influences of w_{eff}/c and *RCA%* to well reproduce the test results.

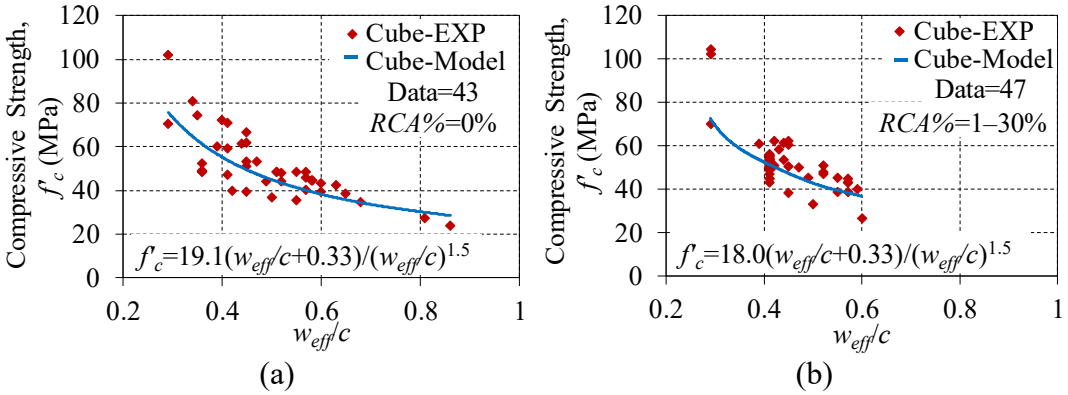

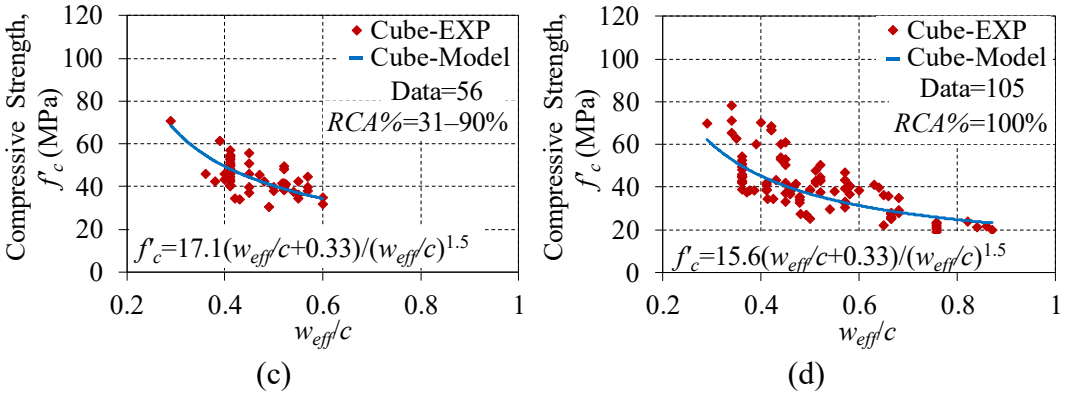

Figure 2.4. Variation in compressive strength of RAC with w_{eff}/c for cube specimens: (a) *RCA%*=0%, (b) *RCA%*=1-30%, (c) *RCA%*=31-90%, and (d) *RCA%*=100%

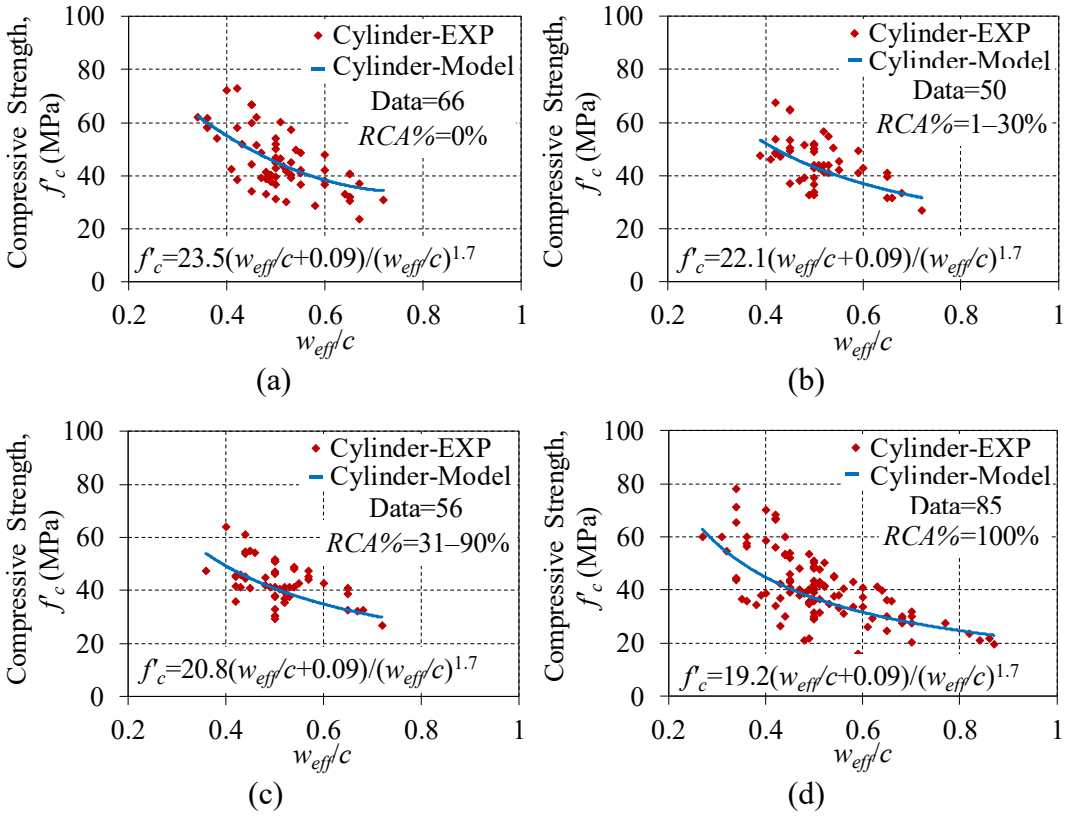

Figure 2.5. Variation in compressive strength of RAC with w_{eff}/c for cylinder specimens: (a) *RCA%*=0%, (b) *RCA%*=1-30%, (c) *RCA%*=31-90%, and (d) *RCA%*=100%

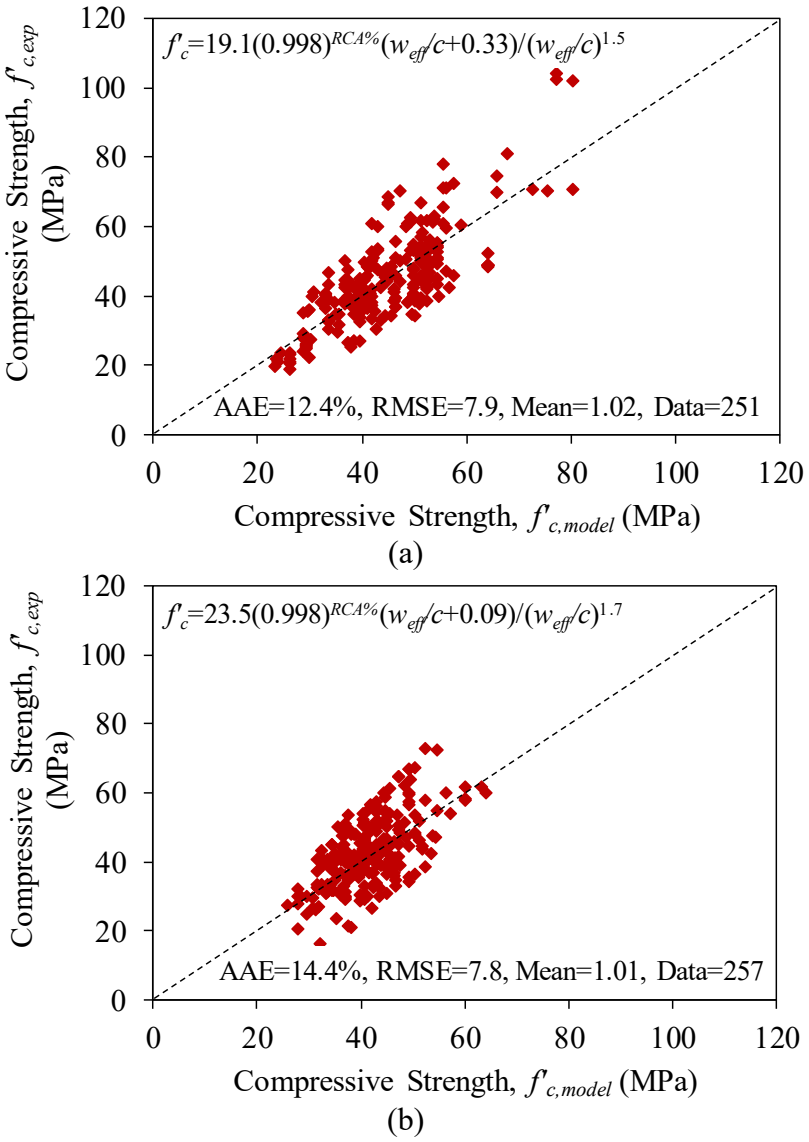

Figure 2.6. Comparison of concrete compressive strengths with model predictions: (a) cubes; (b) cylinders

Figure 2.7 shows the variation of the elastic modulus of RAC with w_{eff}/c at each *RCA*% interval. The comparison of the expressions in Fig. 2.7 shows that the elastic modulus of RAC decreases with increasing w_{eff}/c, which is in agreement with previous studies [10,12,13,17,23,25]. The figure also illustrates that the elastic modulus decreases with increasing *RCA*% for a given w_{eff}/c. It can be seen in Fig. 2.8, which shows the comparison of the elastic modulus results with the model predictions, that the proposed model provides close predictions accurately capturing the influences of w_{eff}/c and *RCA%*.

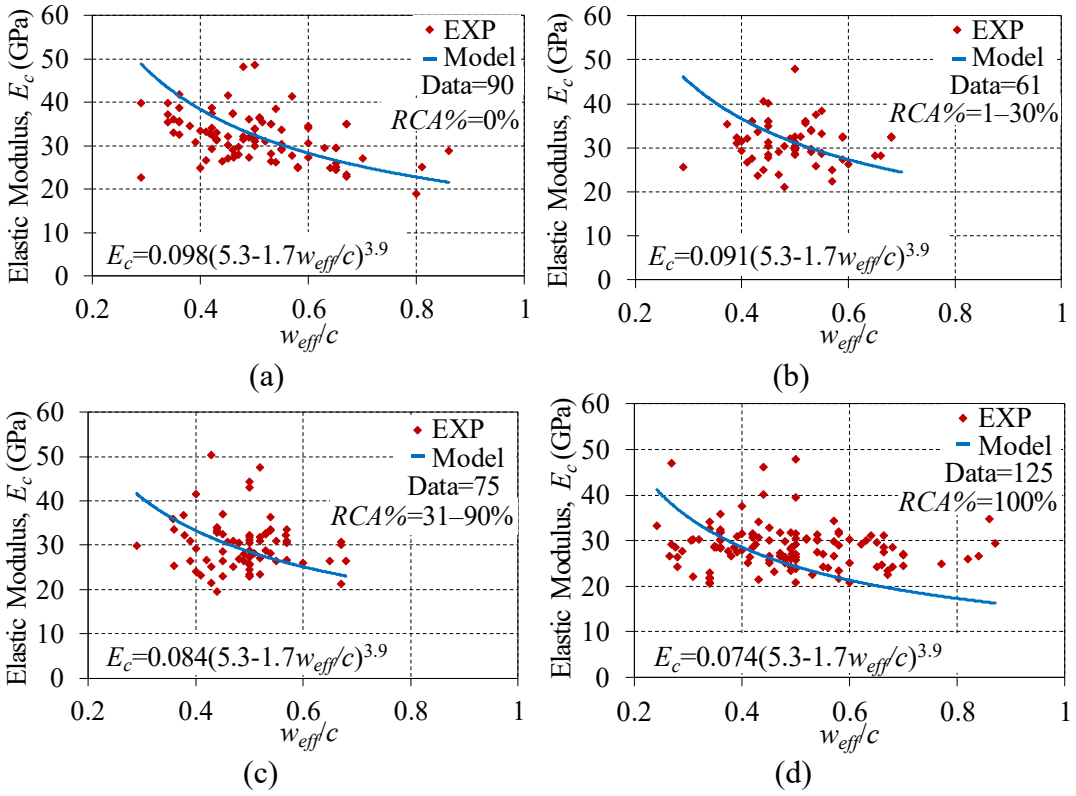

Figure 2.7. Variation in elastic modulus of RAC with w_{eff}/c: (a) $RCA\%$=0%, (b) $RCA\%$=1-30%, (c) $RCA\%$=31-90%, and (d) $RCA\%$=100%

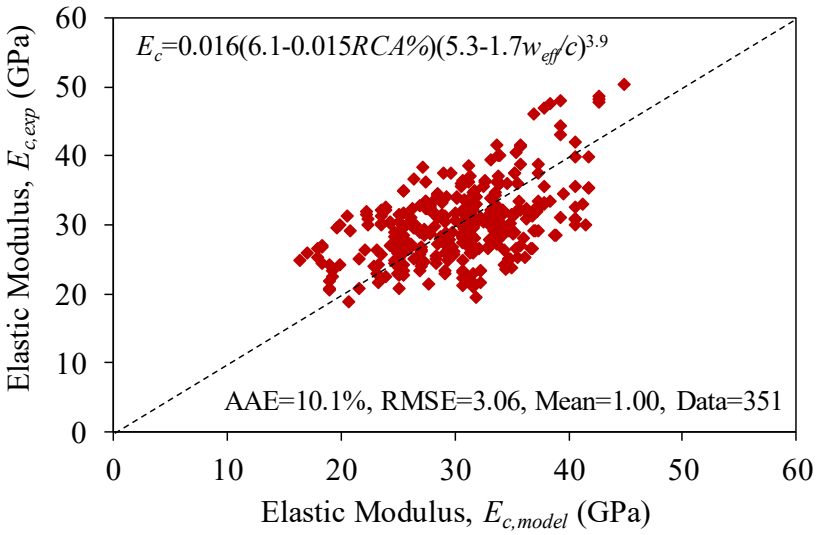

Figure 2.8. Comparison of concrete elastic modulus with model predictions

Figure 2.9 shows the variation of the flexural strength of RAC with w_{eff}/c at each $RCA\%$ interval. The comparison of the expressions in Fig. 2.9 shows that the flexural strength of RAC decreases with increasing w_{eff}/c, which is in agreement with previous studies [10,23]. The figure also illustrates that the flexural strength decreases with increasing $RCA\%$ for a given w_{eff}/c. The comparisons of the

experimental flexural strength results with the predictions of the proposed model are shown in Fig. 2.10. As can be seen in the figure the model predicts the results closely.

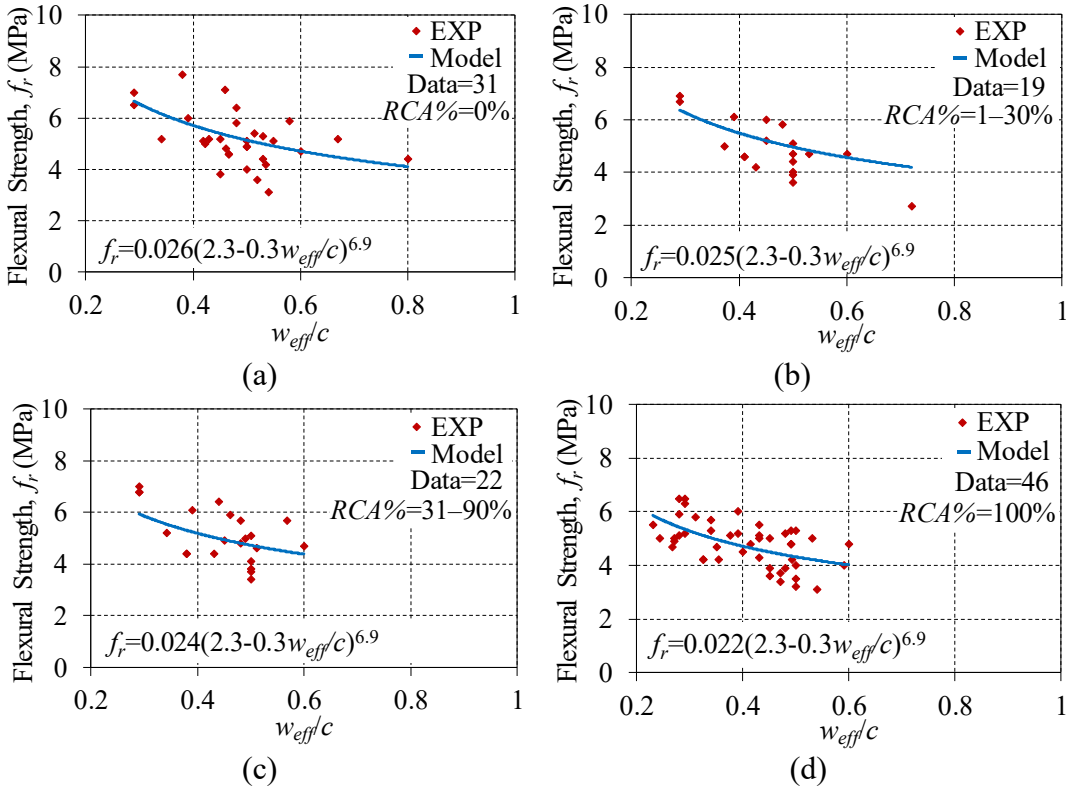

Figure 2.9. Variation in flexural strength of RAC with w_{eff}/c: (a) *RCA%*=0%, (b) *RCA%*=1-30%, (c) *RCA%*=31-90%, and (d) *RCA%*=100%

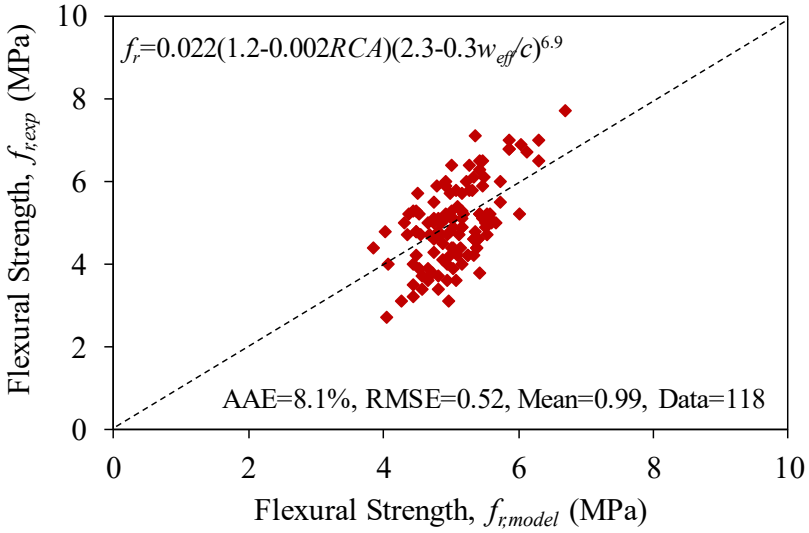

Figure 2.10. Comparison of concrete flexural strength with model predictions

Figure 2.11 shows the variation of the splitting tensile strength of RAC with w_{eff}/c at each *RCA*% interval. The comparison of the expressions in Fig. 2.11 shows that

the splitting tensile strength of RAC decreases with increasing w_{eff}/c, which is in agreement with the previous studies [8,23,29,117]. The figure also illustrates that the splitting tensile strength decreases with increasing *RCA*% for a given w_{eff}/c. The comparisons of the experimental splitting tensile strength results with the predictions of the proposed model are shown in Fig. 2.12. As can be seen in the figure the model predicts the results closely.

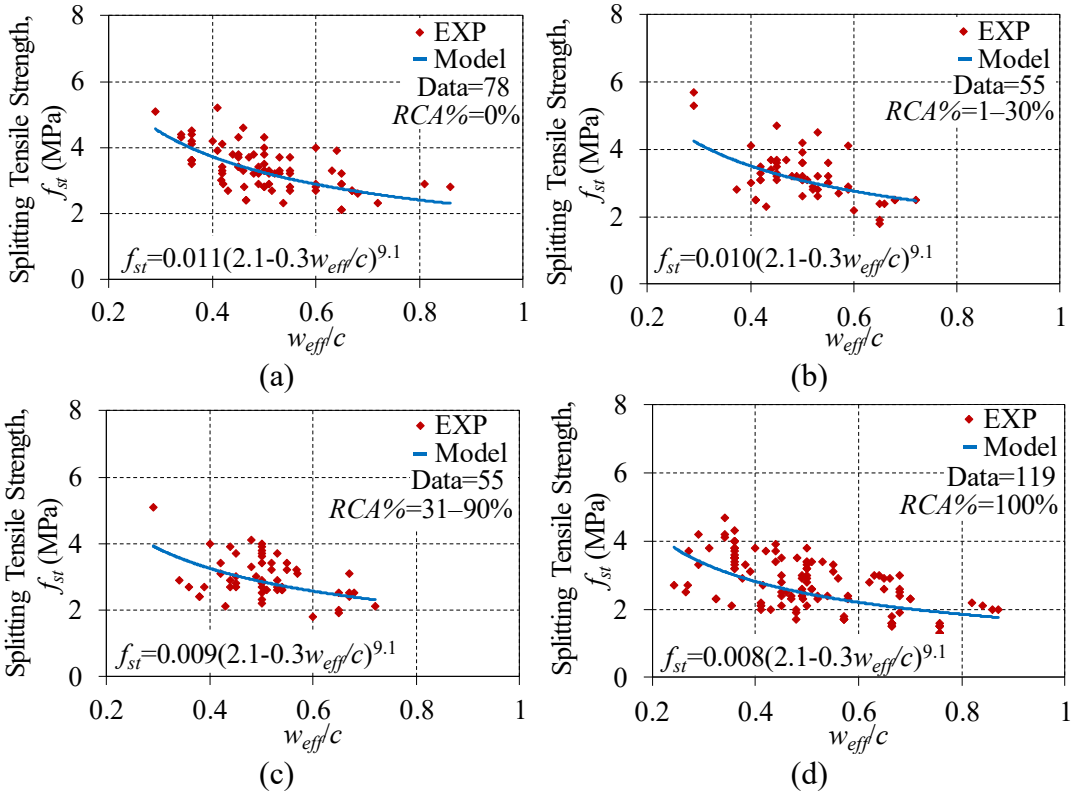

Figure 2.11. Variation in splitting tensile strength of RAC with w_{eff}/c: (a) *RCA*%=0%, (b) *RCA*%=1-30%, (c) *RCA*%=31-90%, and (d) *RCA*%=100%

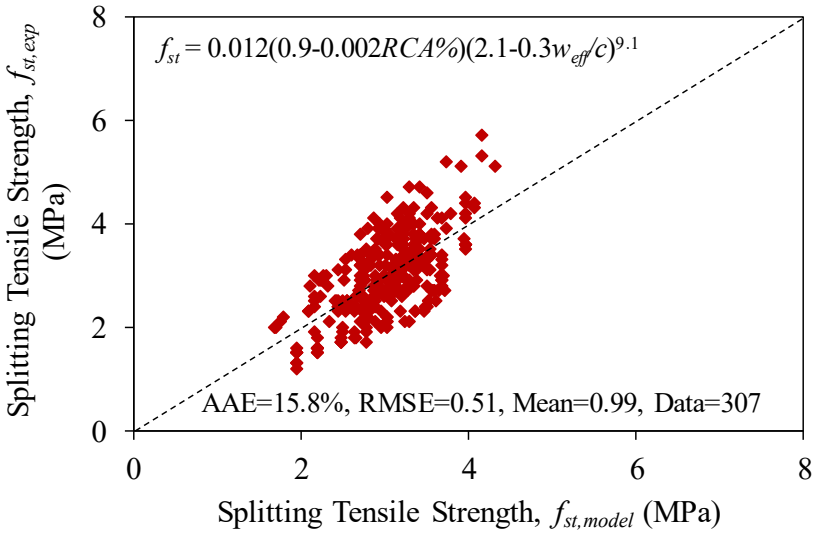

Figure 2.12. Comparison of concrete splitting tensile strength with model predictions

COMPARISON OF THE MODEL PREDICTIONS WITH DESIGN CODE EXPRESSIONS

A review of the existing design codes and standards [118–124] identified a number of models that were proposed to predict the mechanical properties of NAC based on $f'_{c,cylinder}$. The details of these models are summarized in Table 2.7. Figures 2.13(a)–2.13(c) show the predictions of the code expressions together with those of the models proposed in this study for the elastic modulus, flexural strength, and splitting tensile strength, respectively. The comparison of the results shows that, when applied to NAC (i.e. *RCA%*=0), the trends of the proposed models are in agreement with the overall trend of the existing code expressions. This observation validates the consistency of the proposed models with currently used expressions for NAC, which establishes a reliable baseline for the extension of the models to RAC through the incorporation of the aggregate replacement ratio.

Table 2.7. Summary of NAC mechanical property models given in current design codes

Model	Elastic modulus (E_c) (GPa)	Flexural strength (f_r) (MPa)	Splitting tensile strength (f_{st}) (MPa)
AS 3600-09 [118]	$4.3 \times 10^{-5}(\rho_h)^{1.5}\sqrt{f'_{cm}}$ * when $f'_{cm} \leq 40$ MPa $\left(2.4(\rho_h)^{1.5}\sqrt{f'_{cm}} + 12\right) \times 10^{-5}$ when $40 < f'_{cm} \leq 100$ MPa	$0.60\sqrt{f'_{c,cylinder}}$	$0.4\sqrt{f'_{c,cylinder}}$
ACI 318-11 [119]	$4.73\sqrt{f'_{c,cylinder}}$	$0.62\sqrt{f'_{c,cylinder}}$	$0.53\sqrt{f'_{c,cylinder}}$
CSA A23.3-04 [120]	$4.5\sqrt{f'_{c,cylinder}}$	$0.60\sqrt{f'_{c,cylinder}}$	–
Eurocode 2-04 [121]	$9.5{f'_{c,cylinder}}^{\frac{1}{3}}$	$0.435{f'_{c,cylinder}}^{2/3}$	$0.3\left(f'_{c,cylinder}\right)^{2/3}$
JSCE-07 [122]	$4.7\sqrt{f'_{c,cylinder}}$	–	$0.44\sqrt{f'_{c,cylinder}}$
JCI-08 [123]	$6.3{f'_{c,cylinder}}^{0.45}$	–	$0.13\left(f'_{c,cylinder}\right)^{0.85}$
NZS 3101:2006 [124]	$3.32(\sqrt{f'_{c,cylinder}}) + 6.9$	$0.60\sqrt{f'_{c,cylinder}}$	$0.44\sqrt{f'_{c,cylinder}}$

In this table, f'_c, f'_{cm}, f_r, and f_{st} are in MPa, E_c is in GPa, and ρ_h is in kg/m^3

* f'_{cm} is the mean in-situ compressive strength

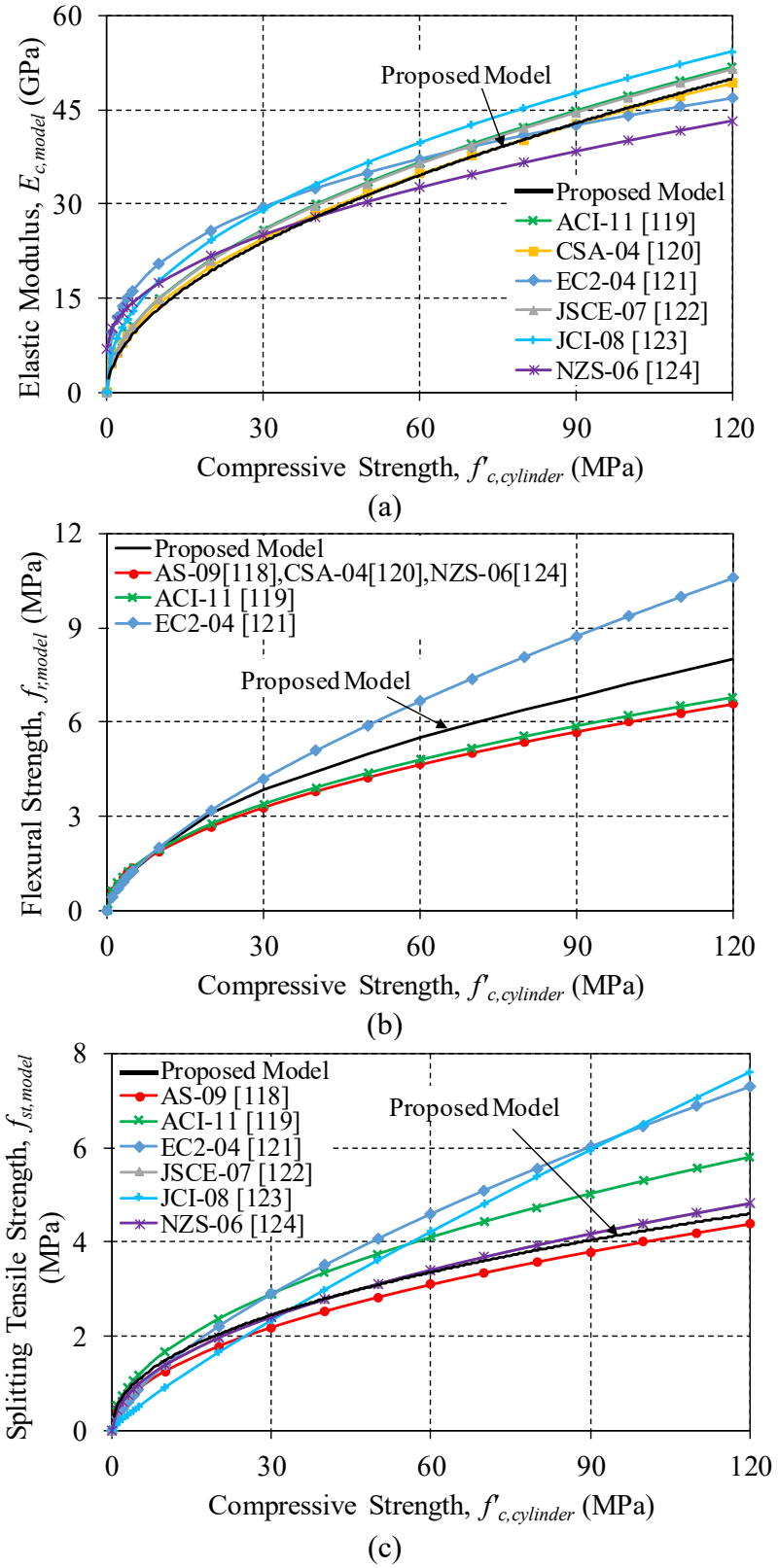

Figure 2.13. Comparisons of models of the present study with models given in design codes for conventional concrete: a) elastic modulus, b) flexural strength, c) splitting tensile strength

CONCLUSIONS

This paper has presented new models developed using GEP technique to predict the compressive strength, elastic modulus, flexural strength, and splitting tensile strength of recycled aggregate concrete. A comprehensive database containing results of 650 compressive strength, 421 elastic modulus, 346 splitting tensile strength, and 152 flexural strength, tests of RACs reported in 69 studies and covering a wide range of parameters was assembled through an extensive review of the literature. The database was used to assess the performance of 34 existing mechanical property models of RAC reported in 21 studies. The following are the main observations and conclusions resulting from this analytical study:

1- The results of the parametric and sensitivity analyses on the database show that w_{eff}/c and *RCA*% are the most influential parameters on mechanical properties of RAC.
2- The proposed models provide simple formulations by accurately establishing relative contributions of the most influential parameters while also being applicable to a larger number of datasets than the existing models.
3- The comparison of the proposed models with the existing code expressions shows that the trends of the proposed models are in agreement with the overall trend of the existing code expressions when applied to NAC (i.e. *RCA%*=0). This observation validates the consistency of the proposed models with currently used code expressions for NAC.
4- The assessment results show that the proposed models provide accurate predictions of the compressive strength, elastic modulus, flexural strength, and splitting tensile strength of RAC making them suitable for use in the pre-design of RACs.

ACKNOWLEDGEMENTS

The authors thank Mr Tianyu Xie for his assistance in the preparation of the test database supplied in the appendix.

REFERENCES

[1] Torgal FP, Jalali S. *Construction and Demolition (C&D) Wastes. In: Eco-efficient Construction and Building Materials*, Springer London, 2011, 51-73.

[2] Behera M, Bhattacharyya, SK, Minocha AK, Deoliya R, Maiti S. Recycled aggregate from C&D waste & its use in concrete–A breakthrough towards sustainability in construction sector: A review. *Construction and Building Materials*. 2014;68:501-16.

[3] Dilbas H, Şimşek M, Çakır Ö. An investigation on mechanical and physical properties of recycled aggregate concrete (RAC) with and without silica fume. *Construction and Building Materials*. 2014;61:50-9.

[4] Mehta PK, Meryman H. Tools for reducing carbon emissions due to cement consumption. *Structure Magazine*. 2009;1(1):11-5.

[5] Torgal FP, Ding Y, Miraldo S, Abdollahnejad Z, Labrincha JA. Are geopolymers moere suitable than portland cement to produce high volume recycled aggregates HPC. *Construction and Building Materials*. 2012;36:1048-52.

[6] Kou SC, Poon CS, Wan HW. Properties of concrete prepared with low-grade recycled aggregates. *Construction and Building Materials*. 2012;36:881-9.

[7] Topcu IB, Şengel S. Properties of concretes produced with waste concrete aggregate. *Cement and Concrete Research*. 2004;34(8):1307-12.

[8] Çakır Ö. Experimental analysis of properties of recycled coarse aggregate (RCA) concrete with mineral additives. *Construction and Building Materials*. 2014;68:17-25.

[9] Younis K. H., Pilakoutas K. Strength prediction model and methods for improving recycled aggregate concrete. *Construction and Building Materials*. 2013;49:688-701.

[10] Xiao JZ, Li JB, Zhang C. On relationships between the mechanical properties of recycled aggregate concrete: an overview. *Materials and Structures*. 2006;39(6):655-64.

[11] Sriravindrarajah R, Wang NDH, Ervin LJW. Mix Design for Pervious Recycled Aggregate Concrete. *International Journal of Concrete Structures and Materials*. 2012;6(4):239-46.

[12] Lovato PS, Possan E, Dal Molin DCC. Masuero ÂB, Ribeiro JLD. Modeling of mechanical properties and durability of recycled aggregate concretes. *Construction and Building Materials*. 2012;26(1):437-47.

[13] Pereira P, Evangelista L, De Brito J. The effect of superplasticisers on the workability and compressive strength of concrete made with fine recycled concrete aggregates. *Construction and Building Materials*. 2012;28(1):722-9.

[14] Thomas C, Setién J, Polanco JA, Alaejos P, de Juan MS. Durability of recycled aggregate concrete. *Construction and Building Materials*. 2013;40:1054-65.

[15] Kakizaki M, Harada M, Soshiroda T, Kubota S, Ikeda T, Kasai Y. Strength and elastic modulus of recycled aggregate concrete. *In Proceedings of the Second International RILEM Symposium on Demolition and Reuse of Concrete and Masonry*, 1988, Vol. 2, p. 565-74.

[16] Ravindrarajah RS, Tam CT. Properties of concrete made with crushed concrete as coarse aggregate. *Magazine of Concrete Research*. 1985;37(130):29-38.

[17] Bairagi NK, Ravande K, Pareek VK. Behaviour of concrete with different proportions of natural and recycled aggregates. *Resources, Conservation and Recycling*. 1993;9(1):109-26.

[18] de Oliveira MB, Vazquez E. The influence of retained moisture in aggregates from recycling on the properties of new hardened concrete. *Waste Management*. 1996;16(1):113-7.

[19] Dillmann R. Concrete with recycled concrete aggregate. Sustainable Construction: Use of Recycled Concrete Aggregate. *Producings of The International Symposium Held at Department of Trade and Industry Conference Centre*, London, UK, 1998, p.11-2.

[20] Dhir RK. Sustainability of Recycled Concrete Aggregate for Use IN BS 5328 Designated Mixes. *Proceedings of the ICE-Structures and Buildings*, 134(3), 1999, p. 257-74.

[21] Tavakoli M., Soroushian P. Strengths of recycled aggragate concrete made using field-demolished concrete as aggregate. *ACI Materials Journal*. 1996;93(2): 82-90.

[22] Zilch K, Roos F. An equation to estimate the modulus of elasticity of concrete with recycled aggregates. *Civil Engineers*. 2001;76(4):187–91.

[23] Kheder GF, Al-Windawi SA. Variation in mechanical properties of natural and recycled aggregate concrete as related to the strength of their binding mortar. *Materials and Structures*. 2005;38(7):701-9.

[24] Rahal K. Mechanical properties of concrete with recycled coarse aggregate. *Building and Environment*. 2007;42(1):407-15.

[25] Corinaldesi V. Mechanical and elastic behaviour of concretes made of recycled-concrete coarse aggregates. *Construction and Building Materials*. 2010;24(9):1616-20.

[26] Hoffmann C, Schubert S, Leemann A, Motavalli M. Recycled concrete and mixed rubble as aggregates: Influence of variations in composition on the concrete properties and their use as structural material. *Construction and Building Materials*. 2012;35:701-9.

[27] Pereira P, Evangelista L, de Brito J. The effect of superplasticizers on the mechanical performance of concrete made with fine recycled concrete aggregates. *Cement and Concrete Composites*. 2012;34(9):1044-52.

[28] Wardeh G, Ghorbel E, Gomart H. Mix Design and Properties of Recycled Aggregate Concretes: Applicability of Eurocode 2. *International Journal of Concrete Structures and Materials*. 2014;1-20.

[29] Xiao J, Li P, Qin W. Study on bond-slip between recycled concrete and rebars. *Journal of Tongji University*. 2006;34(1):13.

[30] Xuan DX, Houben LJM, Molenaar AAA, Shui ZH. Mechanical properties of cement-treated aggregate material–a review. *Materials & Design*. 2012;33:496-502.

[31] Mansouri I, Ozbakkaloglu T, Kisi O, Xie T. Predicting Behavior of FRP-Confined Concrete using Neuro Fuzzy, Neural Network, Multivariate Adaptive Regression Splines and M5 Model Tree Techniques. *Materials and Structures*. 2016;10.1617/s11527-015-0790-4.

[32] Mansouri I, Gholampour A, Kisi O, Ozbakkaloglu T. Evaluation of peak and residual conditions of actively confined concrete using neuro-fuzzy and neural computing techniques. *Neural Computing and Applications*. 2016;10.1007/s00521-016-2492-4.

[33] Lim JC, Karakus M, Ozbakkaloglu T. Evaluation of Ultimate Conditions of FRP-Confined Concrete Columns using Genetic Programming. *Computers and Structures*. 2016;162:28-37.

[34] Jalal M, Ramezanianpour AA, Pouladkhan AR, Tedro P. Application of genetic programming (GP) and ANFIS for strength enhancement modeling of CFRP-retrofitted concrete cylinders. *Neural Computing and Applications*. 2013;23:455-70.

[35] Mashrei MA, Seracino R, Rahman MS. Application of artificial neural networks to predict the bond strength of FRP-to-concrete joints. *Construction and Building Materials*. 2013;40:812-21.

[36] Sadrmomtazi A, Sobhani J, Mirgozar MA. Modeling compressive strength of EPS lightweight concrete using regression, neural network and ANFIS. *Construction and Building Materials*. 2013;42:205-16.

[37] Perera R, Tarazona D, Ruiz A, Martín A. Application of artificial intelligence techniques to predict the performance of RC beams shear strengthened with NSM FRP rods. Formulation of design equations. *Composites Part B*. 2014;66:162-73.

[38] Pham TM, Hadi MN. Predicting Stress and Strain of FRP-Confined Square/Rectangular Columns Using Artificial Neural Networks. *Journal of Composites for Construction*. 2014;18(6):04014019.

[39] Mashhadban H, Kutanaei SS, Sayarinejad MA. Prediction and modeling of mechanical properties in fiber reinforced self-compacting concrete using particle swarm optimization algorithm and artificial neural network. *Construction and Building Materials*. 2016;119:277-87.

[40] Duan Z. H., Kou S. C., Poon C. S. Prediction of compressive strength of recycled aggregate concrete using artificial neural networks. *Construction and Building Materials*. 2013;40:1200-6.

[41] Sahoo K., Sarkar P., Davis R. Artificial neural networks for prediction of compressive strength of recycled aggregate concrete. *International Journal of Chemical, Metallurgical and Civil Engineering*. 2016;3(1):81-5.

[42] Deshpande N., Londhe S., Kulkarni S. Modeling compressive strength of recycled aggregate concrete by Artificial Neural Network, Model Tree and Non-linear Regression. *International Journal of Sustainable Built Environment*. 2014;3:187-98.

[43] Duan ZH, Kou SC, Poon CS. Using artificial neural networks for predicting the elastic modulus of recycled aggregate concrete. *Construction and Building Materials*. 2013;44:524-32.

[44] Behnood A., Olek J., Glinicki M. A. Predicting modulus elasticity of recycled aggregate concrete using M5' model tree algorithm. *Construction and Building Materials*. 2015;94:137-47.

[45] Gonzalez-Taboada I., Gonzalez-Fonteboa B., Martinez-Abella F., Perez-Ordonez J. Prediction of the mechanical properties of structural recycled concrete using multivariable regression and genetic programming. *Construction and Building Materials*. 2016;106:480-99.

[46] Alavi AH, Gandomi AH. A robust data mining approach for formulation of geotechnical engineering systems. *Engineering Computations*. 2011;28(3):242–74.

[47] Gandomi AH, Roke DA. Assessment of artificial neural network and genetic programming as predictive tools, *Advances in Engineering Software*. 2015;88:63-72.

[48] Gandomi AH, Babanajad S, Alavi A, Farnam Y. Novel approach to strength modeling of concrete under triaxial compression. *Journal of Materials in Civil Engineering*. 2012;10.1061/(ASCE)MT.1943-5533.0000494.

[49] Ferreira C. Gene expression programming: A new adaptive algorithm for solving problems. *Complex Systems*. 2001;13(2):87-129.

[50] Gandomi AH, Alavi AH, Mirzahosseini MR, Nejad FM. Nonlinear genetic-based models for prediction of flow number of asphalt mixtures. *Journal of Materials in Civil Engineering*. 2011;23(3):248–63.

[51] Muduli PK, Das SK. Evaluation of liquefaction potential of soil based on standard penetration test using multi-gene genetic programming model. *Acta Geophysica*. 2014;62(3):529–43.

[52] Yoda K, Yoshikane T, Nakashima Y, Soshiroda, T. Recycled cement and recycled concrete in Japan. *Proceedings of the International Conference on Demolition and Reuse of Concrete and Masonry*, 1988, p. 527-36.

[53] Limbachiya MC, Leelawat T, Dhir RK. Use of recycled concrete aggregate in high-strength concrete. *Materials and Structures*. 2000;33(9):574-80.

[54] Ajdukiewicz A, Kliszczewicz A. Influence of recycled aggregates on mechanical properties of HS/HPC. *Cement and Concrete Composites*. 2002;24(2):269-79.

[55] Gómez-Soberón J. Porosity of recycled concrete with substitution of recycled concrete aggregate: an experimental study. *Cement and Concrete Research*. 2002;32(8):1301-11.

[56] Gonçalves A, Esteves A, Vieira M. Influence of recycled concrete aggregates on concrete durability. *International RILEM Conference on the Use of Recycled Materials in Buildings and Structures*, 2004;554-62.

[57] Poon CS, Shui, ZH, Lam L, Fok H, Kou SC. Influence of moisture states of natural and recycled aggregates on the slump and compressive strength of concrete. *Cement and Concrete Research*. 2004;34(1):31-6.

[58] Lin YH, Tyan YY, Chang, TP, Chang CY. An assessment of optimal mixture for concrete made with recycled concrete aggregates. *Cement and Concrete Research*. 2004;34(8):1373-80.

[59] Wei X. Experimental study on influence of recycled coarse aggregates contents on properties of recycled aggregate concrete. *Concrete*. 2006;9:13.

[60] Etxeberria M, Mari AR, Vazquez E. Recycled aggregate concrete as structural material. *Materials and Structures*. 2007;40(5):529-41.

[61] Etxeberria M, Vázquez E, Marí A, Barra M. Influence of amount of recycled coarse aggregates and production process on properties of recycled aggregate concrete. *Cement and Concrete Research*. 2007;37(5):735-42.

[62] Evangelista L, De Brito J. Mechanical behaviour of concrete made with fine recycled concrete aggregates. *Cement and Concrete Composites*. 2007;29(5):397-401.

[63] Poon CS, Kou, SC, Lam L. Influence of recycled aggregate on slump and bleeding of fresh concrete. *Materials and Structures*. 2007;40(9):981-8.

[64] Ajdukiewicz AB, Kliszczewicz AT. Comparative tests of beams and columns made of recycled aggregate concrete and natural aggregate concrete. *Journal of Advanced Concrete Technology.* 2007;5(2):259-73.

[65] Hu MP. Mechanical properties of concrete prepared with different recycled coarse aggregates replacement rate. *Chinese Concrete Journal*. 2007;2:52-4.

[66] Kou SC, Poon CS, Chan D. Influence of fly ash as cement replacement on the properties of recycled aggregate concrete. *Journal of Materials in Civil Engineering*. 2007;19(9):709-17.

[67] Wang ZW. Production and properties of high quality recycled aggregates. *Concrete*. 2007;3:74-7.

[68] Casuccio M, Torrijos MC, Giaccio G, Zerbino R. Failure mechanism of recycled aggregate concrete. *Construction and Building Materials*. 2008;22(7):1500-6.

[69] Hu MP. Mechanical properties of recycled aggregate concrete at early ages. *Concrete*. 2008;5:37-41.

[70] Kou SC, Poon CS, Chan D. Influence of fly ash as a cement addition on the hardened properties of recycled aggregate concrete. *Materials and Structures*. 2008;41(7):1191-201.

[71] Yang KH, Chung HS, Ashour AF. Influence of type and replacement level of recycled aggregates on concrete properties. *ACI Materials Journal*. 2008;105(3).

[72] Zhou H, Liu, BK, Guo LU. Experimental research on the basic mechanical properties of recycled aggregate concrete. *Journal of Anhui Institute of Architecture*. 2008;6:003.

[73] Domingo-Cabo A, Lázaro C, López-Gayarre F, Serrano-López MA, Serna P, Castaño-Tabares JO. Creep and shrinkage of recycled aggregate concrete. *Construction and Building Materials*. 2009;23(7):2545-53.

[74] Padmini AK, Ramamurthy K, Mathews MS. Influence of parent concrete on the properties of recycled aggregate concrete. *Construction and Building Materials*. 2009;23(2):829-36.

[75] Yang X, Wu J, Liang JG. Experimental study on relationship between tensile strength and compressive strength of recycled aggregate concrete. *Sichuan Building Science*. 2009;35:190-2.

[76] Ye H. Experimental study on mechanical properties of concrete made with high quality recycled aggregate. *Sichuan Building Science*. 2009;35:195-9.

[77] Kumutha R, Vijai K. Strength of concrete incorporating aggregates recycled from demolition waste. *ARPN Journal of Engineering and Applied Sciences*. 2010;5(5):64-71.

[78] Radonjanin V, Malešev M, Marinković S. Recycled concrete as aggregate for structural concrete production. *Sustainability*. 2010;2(5):1204-25.

[79] Zega CJ, Di Maio AA. Recycled Concretes Made with Waste Ready-Mix Concrete as Coarse Aggregate. *Journal of Materials in Civil Engineering*. 2010;23(3):281-6.

[80] Belén GF, Fernando MA, Diego, CL, Sindy SP. Stress–strain relationship in axial compression for concrete using recycled saturated coarse aggregate. *Construction and Building Materials*. 2011;25(5):2335-42.

[81] Fathifazl G, Razaqpur AG, Isgor OB, Abbas A, Fournier B, Foo S. Creep and drying shrinkage characteristics of concrete produced with coarse recycled concrete aggregate. *Cement and Concrete Composites*. 2011;33(10):1026-37.

[82] González-Fonteboa B, Martínez-Abella F, Eiras-López J, Seara-Paz S. Effect of recycled coarse aggregate on damage of recycled concrete. *Materials and Structures*. 2011;44(10):1759-71.

[83] Rao MC, Bhattacharyya SK, Barai SV. Influence of field recycled coarse aggregate on properties of concrete. *Materials and Structures*. 2011;44(1):205-20.

[84] Somna R, Jaturapitakkul C, Chalee W, Rattanachu P. Effect of the water to binder ratio and ground fly ash on properties of recycled aggregate concrete. *Journal of Materials in Civil Engineering*. 2011;24(1):16-22.

[85] Abd Elhakam A, Mohamed AE, Awad E. Influence of self-healing, mixing method and adding silica fume on mechanical properties of recycled aggregates concrete. *Construction and Building Materials*. 2012;35:421-7.

[86] Cui ZL, Lu SS, Wang ZS. Influence of Recycled Aggregate on Strength and Anti-carbonation Properties of Recycled Aggregate Concrete [J]. *Journal of Building Materials*. 2012;15(2):264-7.

[87] Li H. Xiao JZ. On Fatigue Strength of Recycled Aggregate concrete Based on Its Elastic Modulus. *Journal of Building Materials*. 2012;15(2):260-3.

[88] Limbachiya M, Meddah MS, Ouchagour Y. Performance of Portland/silica fume cement concrete produced with recycled concrete aggregate. *ACI Materials Journal*. 2012;109(1).

[89] Marinković S, Radonjanin V, Malešev M, gnjatović I. Comparative environmental assessment of natural and recycled aggregate concrete. *Waste Management*. 2010;30(11):2255-64.

[90] Barbudo A, de Brito J, Evangelista L, Bravo M, Agrela F. Influence of water-reducing admixtures on the mechanical performance of recycled concrete. *Journal of Cleaner Production*. 2013;59:93-8.

[91] Butler L, West, JS, Tighe SL. Effect of recycled concrete coarse aggregate from multiple sources on the hardened properties of concrete with equivalent compressive strength. *Construction and Building Materials*. 2013;47:1292-301.

[92] Chen ZP, Xu JJ, Zheng HH, Su YS, Xue JY, Li JT. Basic mechanical properties test and stress-strain constitutive relations of recycled coarse aggregate concrete. *Journal of Building Materials*. 2013;16(1):24-32.

[93] Hou YL. Zheng G. Mechanical Properties of Recycled Aggregate Concrete in Different Age. *Journal of Building Materials*. 2013;16(4):683-7.

[94] Ismail S, Ramli M. Engineering properties of treated recycled concrete aggregate (RCA) for structural applications. *Construction and Building Materials*. 2013;44:464-76.

[95] Manzi S, Mazzotti C, Bignozzi MC. Short and long-term behavior of structural concrete with recycled concrete aggregate. *Cement and Concrete Composites*. 2013;37:312-8.

[96] Matias D, de Brito J, Rosa A, Pedro D. Mechanical properties of concrete produced with recycled coarse aggregates–influence of the use of superplasticizers. *Construction and Building Materials*. 2013;44:101-9.

[97] Sheen YN, Wang HY, Juang YP, Le DH. Assessment on the engineering properties of ready-mixed concrete using recycled aggregates. *Construction and Building Materials*. 2013;45:298-305.

[98] Ulloa VA, García-Taengua E, Pelufo MJ, Domingo A, Serna P. New views on effect of recycled aggregates on concrete compressive strength. *ACI Materials Journal*. 2013;110(6).

[99] Xiao J, Li H, Yang Z. Fatigue behavior of recycled aggregate concrete under compression and bending cyclic loadings. *Construction and Building Materials*. 2013;38:681-8.

[100] Andreu G. Miren E. Experimental analysis of properties of high performance recycled aggregate concrete. *Construction and Building Materials*. 2014;52:227-35.

[101] Beltrán MG, Agrela F, Barbudo A, Ayuso J, Ramírez A. Mechanical and durability properties of concretes manufactured with biomass bottom ash and recycled coarse aggregates. *Construction and Building Materials*. 2014;72:231-8.

[102] Beltrán MG, Barbudo A, Agrela F, Galvín AP, Jiménez JR. Effect of cement addition on the properties of recycled concretes to reach control concretes strengths. *Journal of Cleaner Production*. 2014;79:124-33.

[103] Çakır Ö, Sofyanlı ÖÖ. Influence of silica fume on mechanical and physical properties of recycled aggregate concrete. *HBRC Journal*. 2015;11(2):157-66.

[104] Carneiro JA, Lima PRL, Leite MB, Toledo Filho RD. Compressive stress–strain behavior of steel fiber reinforced-recycled aggregate concrete. *Cement and Concrete Composites*. 2014;46:65-72.

[105] Duan ZH, Poon CS. Properties of recycled aggregate concrete made with recycled aggregates with different amounts of old adhered mortars. *Materials & Design*. 2014;58:19-29.

[106] Folino P, Xargay H. Recycled aggregate concrete–Mechanical behavior under uniaxial and triaxial compression. *Construction and Building Materials*. 2014;56:21-31.

[107] Gayarre FL, Pérez, CLC, López MAS, Cabo AD. The effect of curing conditions on the compressive strength of recycled aggregate concrete. *Construction and Building Materials*. 2014;53:260-6.

[108] Kang THK, Kim W, Kwak YK, Hong SG. Flexural Testing of Reinforced Concrete Beams with Recycled Concrete Aggregates (with Appendix). *ACI Structural Journal*. 2014;111(3).

[109] Pedro D, de Brito J, Evangelista L. Performance of concrete made with aggregates recycled from precasting industry waste: influence of the crushing process. *Materials and Structures*. 2014;1-14.

[110] Pepe M, Toledo Filho RD, Koenders EA, Martinelli E. Alternative processing procedures for recycled aggregates in structural concrete. *Construction and Building Materials*. 2014;69:124-32.

[111] Thomas C, Sosa I, Setién J, Polanco JA, Cimentada AI. Evaluation of the fatigue behavior of recycled aggregate concrete. *Journal of Cleaner Production*. 2014;65:397-405.

[112] Capitanio S, Hayes S, Mak M, Murdock M. *Design of RAC filled FRP tubers as columns for new construction*. Final Year Honor's Research Project Report, The University of Adelaide, 2014.

[113] Gandomi AH, Yun GJ, Alavi AH. An evolutionary approach for modeling of shear strength of RC deep beams. *Materials and Structures*. 2011;46(12):2109-19

[114] Gandomi AH, Alavi AH, Mousavi M, Tabatabaei SM. A hybrid computational approach to derive new ground-motion attenuation equations. *Engineering Applications of Artificial Intelligence*. 2011;24(4):717–32.

[115] Baykasoglu A, Gullub H, Canakcıb H, Ozbakırc L. Prediction of compressive and tensile strength of limestone via genetic programming. *Expert Systems with Applications*. 2008;35(1–2);111–23.

[116] Koza JR. *Genetic programming: On the programming of computers by means of natural selection*, MIT Press, Cambridge, MA, 1992.

[117] Mefteh H, Kebaïli O, Oucief H, Berredjem L, Arabi, N. Influence of moisture conditioning of recycled aggregates on the properties of fresh and hardened concrete. *Journal of Cleaner Production*. 2013;54:282-8.

[118] AS3600-2009. *Australian Standard for Concrete Structures*. S. A, North Sydney. 2009.

[119] ACI 318-11. *Building Code Requirements for Structural Concrete and Commentary, PCA notes on ACI 318-11: with design applications*. Farmington Hills, Mich: ACI International. 2011.

[120] Canadian Standard. C S A. A23.3-04. *Design of Concrete Structures*, Canadian Standard Association. 2004.

[121] British Standards Institution. *Eurocode 2: Design of Concrete Structures: Part 1-1: General Rules and Rules for Buildings*. British Standards Institution. 2004.

[122] Japan Society of Civil Engineers. *Standard Specification for Concrete Structure*. JSCE No. 15, Tokyo, Japan. 2007.

[123] Japanese Civil Institute. *Guidelines for Control of Cracking of Mass Concrete.* Japan Concrete Institute. 2008.

[124] New Zealand Standard. *Concrete structures standard*. NZS 3101:2006. The design of concrete structures, Wellington, New Zealand. 2006.

Statement of Authorship

Title of Paper	Evaluation of mechanical properties of concretes containing coarse recycled concrete aggregates using multivariate adaptive regression splines (MARS), M5 model tree (M5Tree), and least squares support vector regression (LSSVR) models
Publication Status	☑ Published ☐ Accepted for Publication ☐ Submitted for Publication ☐ Unpublished and Unsubmitted work written in manuscript style
Publication Details	Gholampour A, Mansouri I, Kisi O, Ozbakkaloglu T. Evaluation of mechanical properties of concretes containing coarse recycled concrete aggregates using multivariate adaptive regression splines (MARS), M5 model tree (M5Tree), and least squares support vector regression (LSSVR) models. *Neural Computing and Applications*. 2018;10.1007/s00521-018-3630-y.

Principal Author

Name of Principal Author (Candidate)	Aliakbar Gholampour		
Contribution to the Paper	Literature review, analysis and modelling, and preparation of the manuscript.		
Overall percentage (%)	60%		
Certification:	This paper reports on original research I conducted during the period of my Higher Degree by Research candidature and is not subject to any obligations or contractual agreements with a third party that would constrain its inclusion in this thesis. I am the primary author of this paper.		
Signature		Date	31/01/2019

Co-Author Contributions

By signing the Statement of Authorship, each author certifies that:

i. the candidate's stated contribution to the publication is accurate (as detailed above);

ii. permission is granted for the candidate in include the publication in the thesis; and

iii. the sum of all co-author contributions is equal to 100% less the candidate's stated contribution.

Name of Co-Author	Iman Mansouri		
Contribution to the Paper	Analysis and modelling.		
Signature		Date	31/01/2019

Name of Co-Author	Ozgur Kisi		
Contribution to the Paper	Analysis and modelling.		
Signature		Date	15/02/2019

Name of Co-Author	Togay Ozbakkaloglu		
Contribution to the Paper	Research supervision and review of manuscript.		
Signature		Date	15/02/2019

Please cut and paste additional co-author panels here as required.

Evaluation of Mechanical Properties of Concretes containing Coarse Recycled Concrete Aggregates using Multivariate Adaptive Regression Splines (MARS), M5 model tree (M5Tree), and Least Squares Support Vector Regression (LSSVR) Models

ABSTRACT

This paper investigates the application of three artificial intelligence methods, including multivariate adaptive regression splines (MARS), M5 model tree (M5Tree), and least squares support vector regression (LSSVR) for the prediction of the mechanical behaviour of recycled aggregate concrete (RAC). A large and reliable experimental test database containing the results of 650 compressive strength, 421 elastic modulus, 152 flexural strength, and 346 splitting tensile strength tests of RACs with no pozzolanic admixtures assembled from the published literature was used to train, test, and validate the three data-driven based models. The results of the model assessment show that the LSSVR model provides improved accuracy over the existing models in the prediction of the compressive strength of RACs. The results also indicate that, although all three models provide higher accuracy than the existing models in the prediction of the splitting tensile strength of RACs, only the performance of the LSSVR model exceeds those of the best performing existing models for the flexural strength of RACs. The results of this study indicate that MARS, M5Tree, and LSSVR models can provide close predictions of the mechanical behaviour of RACs by accurately capturing the influences of the key parameters. This points to the possibility of the application of these three models in the pre-design and modelling of structures manufactured with RACs.

KEYWORDS: Recycled aggregate concrete (RAC); Mechanical properties; Least squares support vector regression (LSSVR); M5Tree; Multivariate adaptive regression splines (MARS).

INTRODUCTION

The high demand for concrete because of the rapid growth in urbanization and industrialization has resulted in an increase in the consumption of natural aggregates, which typically makes up approximately 70% of the total volume of concrete [1]. Furthermore, rapid industrialization and urbanization have led to an increase in the generation of construction and demolition (C&D) wastes, which consequently resulted in the depletion of landfill space [2,3]. Over the past two decades, recycled aggregate concrete (RAC), obtained by crushing concrete sourced from C&D waste, has been considered as an alternative concrete material to conserve natural aggregate resources and to minimize the environmental impact of C&D waste [4,5]. During this period a large number of studies have been conducted to understand the mechanical behaviour of RACs (e.g. [6–9]). Existing studies confirmed that compressive strength, elastic modulus, flexural strength, and splitting tensile strength are the main mechanical properties for design and analysis of RACs [10–12]. In addition, a comprehensive literature review [1] revealed that a number of models have been proposed either based simply on experimental test results of the original study [13–30] or compiled databases from the results of previous studies [31–35] to predict the mechanical properties of RACs. However, owing to the limitations in the number of input parameters considered together with the use of relatively small number of test results in the calibration of most existing models, these models are not generalizable. Therefore, additional studies are needed to investigate the mechanical properties of RACs using computationally economical techniques based on a comprehensive test database containing key input parameters.

Machine learning-based models have been extensively used to predict the properties of concrete [36-39]. Recently, with the development of computer-aided modelling methods, the use of artificial intelligence techniques has been considered to predict the mechanical behaviour of RACs. Younis and Pilakoutas [40] used multilinear and nonlinear regression methods to develop a model for the prediction of the compressive strength of RAC. Duan et al. [41] and Sahoo et al. [42] predicted the compressive strength of RAC using artificial neural network (ANN) technique. Deshpande et al. [43] used ANN, M5Tree, and nonlinear regression method for the prediction of the compressive strength of RAC. Duan et al. [44] and Behnood et al.

[45] used ANN and M5Tree techniques for the prediction of the elastic modulus of RAC, respectively. Gonzalez-Taboada et al. [46] applied genetic programming and multivariable regression methods for the prediction of the compressive strength, elastic modulus, and splitting tensile strength of RAC. Recently, Ozbakkaloglu et al. [2] and Gholampour et al. [47] predicted the compressive strength, elastic modulus, flexural strength, and splitting tensile strength of RACs with the use of nonlinear regression and gene expression programming methods, respectively. However, most of these techniques were either computationally complex, unable to handle a large number of databases, or unable to accurately capture the influences of the key input parameters for solving nonlinear problems. Therefore, more robust and simple artificial intelligence techniques should be applied to predict the properties of concretes.

In recent years, data-driven techniques, such as Multivariate Adaptive Regression Splines (MARS), M5 model tree (M5Tree), and Least Squares Support Vector Regression (LSSVR) models, have received significant attention to solve critical civil engineering problems. MARS is a nonlinear and non-parametric regression method and its main advantages are efficiency and robustness to explore a large number of intricate nonlinear relations and rapid detection of interactions between them despite their complexity [48]. M5Tree model is a binary decision tree with a series of linear regression functions and its main advantages are the simple geometric structure and the ability to efficiently handle a large number of datasets with different attributes [49]. LSSVR is a statistical learning model, which adopts a least squares linear system as a loss function instead of the quadratic program in the original support vector machine (SVM) [50]. LSSVR solves a set of linear equations by linear programming that is computationally very simple [50]. Recent studies illustrated that because of their main advantages of i) easy handling of a large number of databases, ii) computational simplicity, and iii) strong ability of solving nonlinear problems, MARS, M5Tree, and LSSVR models can be efficient alternatives to existing artificial intelligence methods in solving key civil engineering problems. Cheng and Cao [51] used MARS model to predict the shear strength of reinforced concrete beams. Behnood et al. [45] applied M5Tree model for the prediction of the elastic modulus of RACs. Aiyer et al. [52] applied LSSVR model to predict the compressive strength of self-compacting concrete. Pham et al.

[53] predicted the compressive strength of high performance concretes using LSSVR model. However, no study has been reported to date on the application of LSSVR and MARS models for the prediction of the mechanical properties of RAC and only a single study on the application of M5Tree model for the prediction of the elastic modulus of RAC.

To address the above-mentioned research gaps, three robust artificial intelligence techniques, namely MARS, M5Tree, and LSSVR, were adopted in this study for the prediction of the compressive strength, elastic modulus, flexural strength, and splitting tensile strength of RAC. Existing experimental test database of RACs is initially presented, which is followed by the details of the three models developed in this study. Subsequently, an assessment of the prediction results of the new models is presented.

EXPERIMENTAL TEST DATABASE

The database of RAC, presented in Gholampour et al. [47], was assembled based on 69 experimental studies published in the open literature on RACs containing no pozzolanic admixtures. The RAC database consisted of 332, 318, 421, 152, and 346 datasets, respectively, for compressive strength of cube specimens ($f_{cm,cube}$), compressive strength of cylinder specimens ($f_{cm,cylinder}$), elastic modulus (E_c), flexural strength (f_r), and splitting tensile strength (f_{st}).

The cylinder specimens had either a 100 or 150 mm diameter and a 200 or 300 mm height; the cube specimens had a dimension of either 100 or 150 mm; and beams had a dimension of either 100×100×500 mm or 150×150×750 mm. Effective water-to-cement ratio (w_{eff}/c) of specimens varied from 0.19 to 0.87, coarse recycled concrete aggregate replacement ratio ($RCA\%$) varied from 0 to 100, aggregate-to-cement ratio (a/c) varied from 1.2 to 6.5, bulk density of recycled concrete aggregate (ρ_{RCA}) varied from 1946 to 2720 kg/m^3, water absorption of coarse recycled concrete aggregate (WA_{RCA}) varied from 1.5 to 11.9%. In addition, $f_{cm,cube}$, $f_{cm,cylinder}$, E_c, f_r, and f_{st} in the database ranged from 18.9 to 104.3 MPa, 26.6 to 61.2 MPa, 12.5 to 50.4 GPa, 1.9 to 10.2 MPa, and 1.1 to 6.3 MPa, respectively. The distribution of the

histogram of the key parameters (i.e. w_{eff}/c, *RCA%*, a/c, ρ_{RCA}, and WA_{RCA}) for the specimens in the database are illustrated in Fig. 3.1.

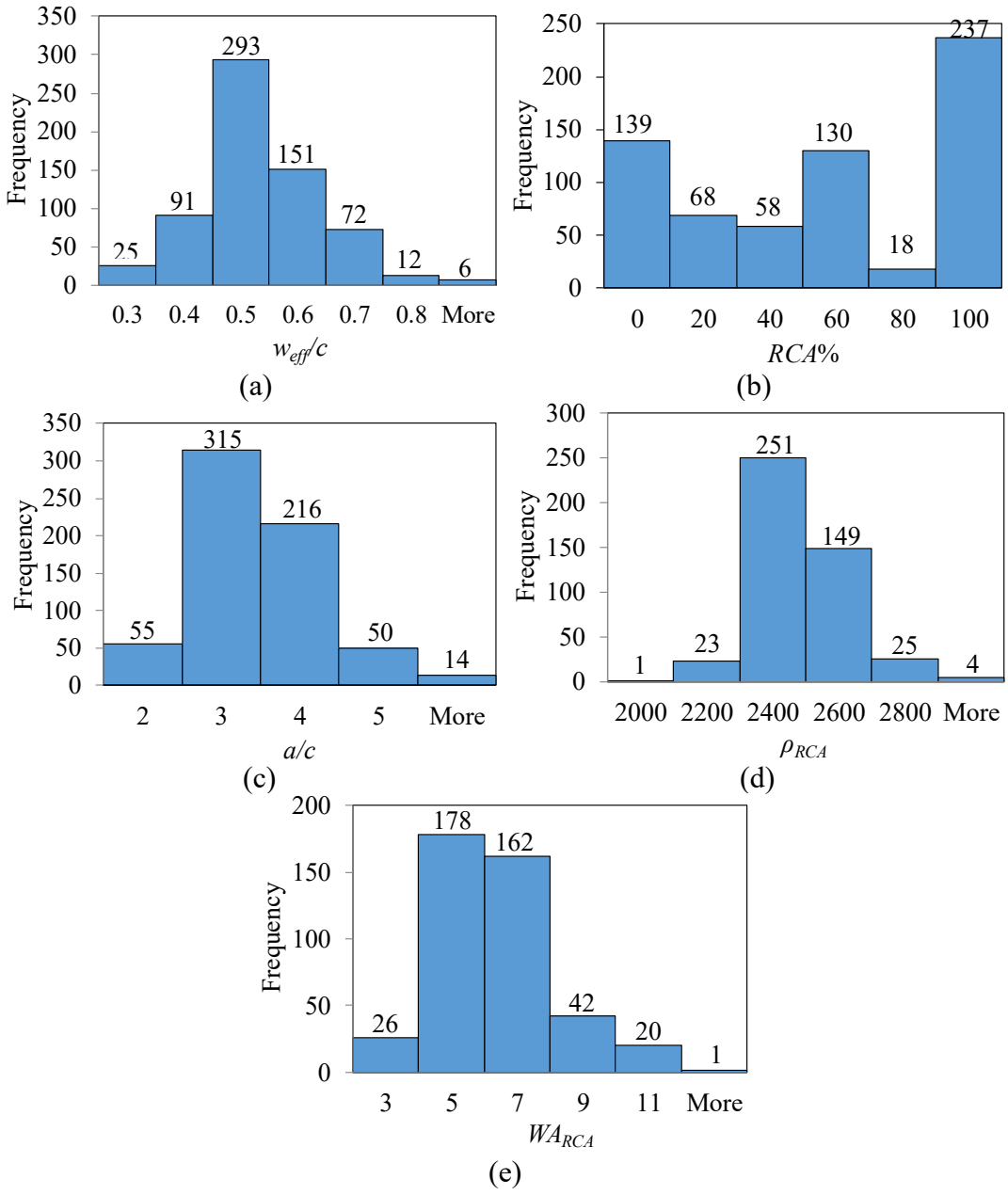

Figure 3.1. Histogram distribution of: (a) w_{eff}/c, (b) *RCA%*, (c) a/c, (d) ρ_{RCA}, and (e) WA_{RCA}

EXISTING MODELS FOR THE PREDICTION OF MECHANICAL PROPERTIES OF RAC

Models proposed to date for the prediction of the mechanical properties of RACs were assembled from 21 different studies, as previously presented in Gholampour

et al. [47]. All models contained closed-form expressions obtained from regression analysis of the test results. Furthermore, two sets of expressions recently proposed by Gholampour et al. [47] through the use of gene expression programming (GEP) and Ozbakkaloglu et al. [2] using regression analysis were also considered in the present study. Existing models include 11 models for compressive strength [2,24,25,28,32,33,40,47], 18 models for elastic modulus [2,13–20,22,23,26,27,30–32,47], six models for flexural strength [2,15,17,20,32,47], and eight models for splitting tensile strength [2,17,20,21,27,32,33,47] of RAC.

OVERVIEW OF LSSVR, MARS, AND M5TREE MODELS

Multivariate Adaptive Regression Splines (MARS)

MARS is a form of regression analysis that was developed by Friedman [48] for the prediction of continuous numerical outcomes. Its algorithm consists of a forward and backward stepwise procedure [54]. The backward procedure removes the unnecessary variables among the previous selected set in the forward procedure to improve the prediction accuracy. Therefore, the variable X is transferred to variable Y using either of the following equations by an inflection point along the input values [55]:

$$Y = \max(0, X - c) \quad \text{or} \quad \max(0, c - X) \tag{3.1}$$

in which c is a threshold value. In MARS, a function applies for each input variable in forward-backward stepwise procedure to find the location of the inflection point in which the function value changes. MARS is a non-parametric statistical technique in which piecewise curves and polynomials give flexible results that can handle not only linear but also nonlinear behaviour [54]. Detailed information about MARS is available in Ref. [55].

M5 model tree (M5Tree)

M5Tree model, which was originally proposed by Quinlan [49], is based on a binary decision tree with a series of linear regression functions at the terminal (leaf) nodes. In the first stage, a decision tree is created by splitting the data into subsets and assuming the standard deviation of class values that reach a node as a measure of

the error at that node. Subsequently, the expected reduction in the error as a result of testing each attribute at the node is calculated. The standard deviation reduction (SDR), which is used to describe the reduction in the error, is defined as follows [56]:

$$\text{SDR} = sd(T) - \sum \frac{|T_i|}{T} sd(T_i) \tag{3.2}$$

where T, T_i, and sd represent a set of examples that reach the node, subset of examples that have the ith outcome of the potential set, and standard deviation, respectively. Because of the splitting process, the standard deviation of data in child nodes (i.e. lower nodes) becomes lower than that of parent node. The split that maximizes the expected error reduction is selected after examining all possible splits [49].

Least Squares Support Vector Regression (LSSVR)

LSSVR, proposed by Suykens and Vandewalle [50], is a supervised learning method based on the principle of structural risk minimization. By considering a given training set of $\{x_k, y_k\}_{k=1}^{N}$ with input data of $x_k \in R^n$ and output data of $y_k \in R$ with class labels of $y_k \in \{-1, +1\}$, the linear classifier in the primal space is defined as:

$$y(x) = \text{sign}(w^T \varphi(x) + b) \tag{3.3}$$

in which b is a real constant. LSSVR is defined in dual space for nonlinear classification as:

$$y(x) = \text{sign}(\sum_{k=1}^{N} \alpha_k y_k K(x_k^T, x) + b) \tag{3.4}$$

in which α_k is a positive-real constant and $K(x_k^T, x)$ is a kernel function that is defined as $\langle \varphi(x_k), \varphi(x) \rangle$, where $\varphi(x)$ is nonlinear map from original space to the high dimensional space. The following expression is used to estimate a function:

$$y(x) = \sum_{k=1}^{N} \alpha_k K(x_k, x) + b \tag{3.5}$$

In order to use radial basis function (RBF) kernel in the modelling, two tuning parameters of γ and σ are added to Eq. 3.5, in which γ and σ are regularization constant and width of RBF kernel, respectively. The main advantage of LSSVR compared to Support Vector Regression (SVR) is the use of the linear squares

principle for the loss function in the LSSVR. In the SVR, however, quadratic programming is employed for this purpose, which is not computationally efficient. Consequently, LSSVR is faster than the SVR in computation [57]. Detailed information about LSSVR can be obtained from Ref. [58].

PREDICTION OF MECHANICAL PROPERTIES OF RAC

MARS, M5Tree, and LSSVR techniques were applied to estimate the compressive strength, elastic modulus, flexural strength, and splitting tensile strength of RAC. The main parameters influencing the mechanical properties of RACs were determined based on the accurate assessment of the specimens in the database. Based on this assessment it was found that w_{eff}/c, $RCA\%$, a/c, ρ_{RCA}, and WA_{RCA} are the most influential parameters on the mechanical behaviour of RACs. Therefore, these parameters were used as inputs to the models. The number of data points available for the validation and testing of the models were 171, 156, 224, 79, and 168 for $f_{cm,cylinder}$, $f_{cm,cube}$, E_c, f_r, and f_{st} of RACs, respectively. For each model, 80% of the database was used for training and validation of the models and remaining 20% was used for testing. The results of the models were subsequently compared with the existing models using the root mean square error (RMSE), mean absolute error (MAE), and mean absolute percentage error (MAPE) (is also referred to as the average absolute error, AAE, in previous studies) statistics to evaluate the performance of the models. Definitions of these statistical indicators are given as follows:

$$\text{RMSE} = \sqrt{\frac{1}{n}\sum_{i=1}^{n}(Mod_i - Exp_i)^2} \tag{3.6}$$

$$\text{MAE} = \frac{1}{n}\sum_{i=1}^{n}|Mod_i - Exp_i| \tag{3.7}$$

$$\text{MAPE} = \frac{1}{n}\sum_{i=1}^{n}\frac{|Mod_i - Exp_i|\times 100}{Exp_i} \tag{3.8}$$

where Mod_i and Exp_i are the estimated and experimental values of mechanical properties of RAC and n is the number of time steps.

An open source code (http://www.esat.kuleuven.be/sista/lssvmlab/) was used for the LSSVR model. Various numbers from 1 to 100 were tried for γ and σ control parameters. The optimal γ and σ values were calculated as 15.6 and 3.0 for $f_{cm,cube}$, 17.1 and 3.3 for $f_{cm,cylinder}$, 22.4 and 4.4 for E_c, 7.9 and 1.5 for f_r, and 16.8 and 3.3 for f_{st} of RAC, respectively. For MARS and M5Tree techniques, open source codes (http://www.cs.rtu.lv/jekabsons/regression.html) were used.

Compressive strength

In order to assess the accuracy of the compressive strength models, their performance was evaluated using the test database. Based on the available input parameters in the test database, only six compressive strength models [2,25,28,32,47] could be used in the model assessments, among which three of them were for cube specimens and three for cylinder specimens. The remaining models [24,33,40] required specific inputs that were not available in the database.

Table 3.1 shows the prediction statistics of MARS, M5Tree, and LSSVR models and existing models for $f_{cm,cube}$ of RAC. It can be seen in the table that the model by Gholampour et al. [47] was the best performing $f_{cm,cube}$ model in the literature. However, LSSVR model provided improved accuracy over the existing models in predicting $f_{cm,cube}$. This observation can be attributed to the ability of the model to accurately capture the influences of the key input parameters (i.e. w_{eff}/c, $RCA\%$, a/c, ρ_{RCA}, and WA_{RCA}) in the analysis. Figure 3.2 shows the comparison of MARS, M5Tree, and LSSVR model predictions with the experimental $f_{cm,cube}$ at the validation stage. As can be seen in the figure, LSSVR model developed a higher accuracy in predicting $f_{cm,cube}$ of RACs than that of MARS and M5Tree models.

Table 3.1. Model predictions of cube compressive strength ($f_{cm,cube}$) of RAC

Model	Number of all datasets	RMSE (MPa)	MAE (MPa)	MAPE (%)	Specimen type
Pereira et al. [25]	157	11.8	9.4	22.2	Cube
Xiao et al. [32]	74	11.3	4.7	12.7	Cube
Gholampour et al. [47]	156	8.9	5.5	12.7	Cube
MARS	156	9.1	5.4	13.0	Cube
M5Tree	156	8.3	5.9	14.2	Cube
LSSVR	156	7.7	4.6	12.6	Cube

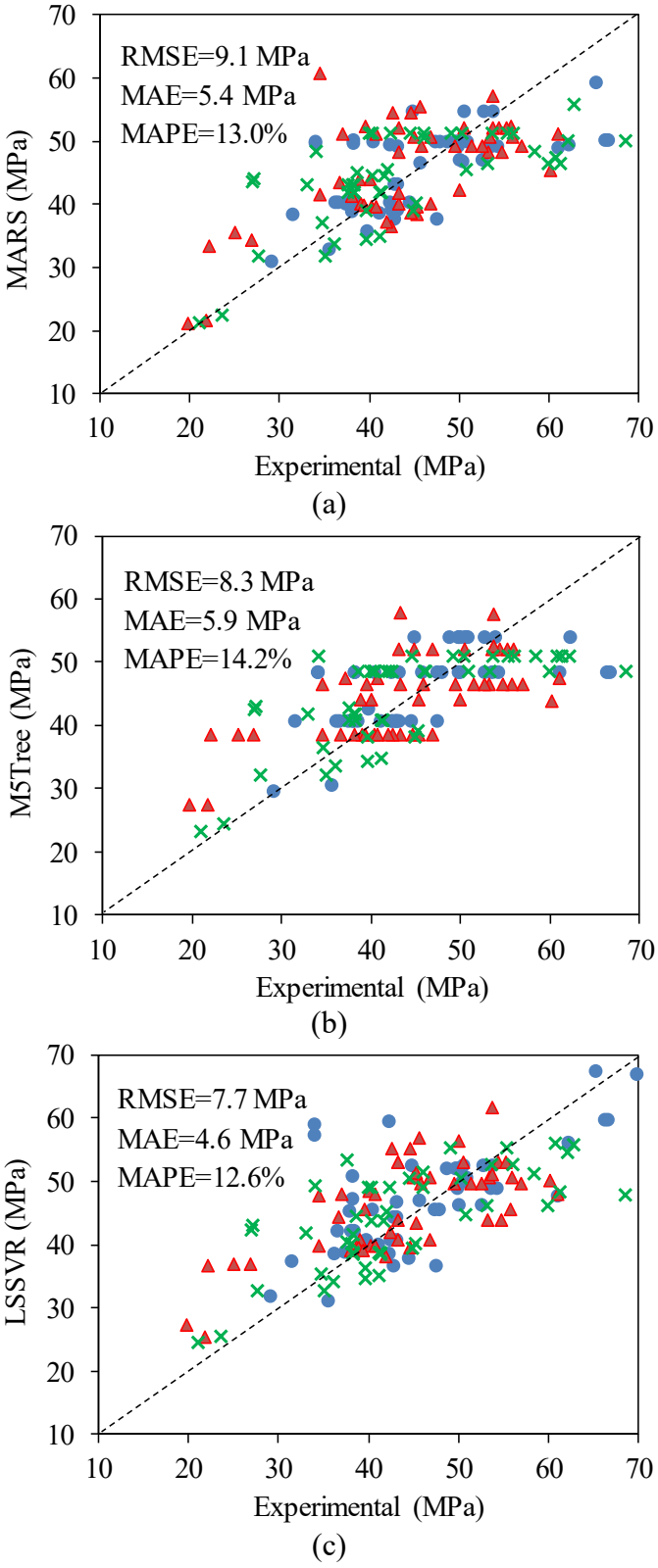

Figure 3.2. Compressive strength estimates of cube RAC ($f_{cm,cube}$) by (a) MARS, (b) M5Tree, and (c) LSSVR models at the validation stage. Circle, triangle, and cross shaped points are data points for validation set 1, 2, and 3, respectively.

Table 3.2 shows the prediction statistics of MARS, M5Tree, and LSSVR models and existing models for $f_{cm,cylinder}$ of RAC. As can be seen in the table, those by Gholampour et al. [47] showed the best performance among the existing models. It can be seen in Table 3.2 that only LSSVR model performed better than the existing models in predicting $f_{cm,cylinder}$. Figure 3.3 shows the comparison of MARS, M5Tree, and LSSVR model predictions with the experimental $f_{cm,cylinder}$ at the validation stage. As can be seen in the figure, similar to the case of $f_{cm,cube}$, LSSVR model exhibited a higher accuracy in the prediction of $f_{cm,cylinder}$ of RACs compared to that of MARS and M5Tree models. This is attributed to the fact that LSSVR is based on a learning method that is dependent on the statistical learning theory. In this method, the use of a regularization parameter helps to avoid over-fitting in the modelling [59].

Table 3.2. Model predictions of cylinder compressive strength ($f_{cm,cylinder}$) of RAC

Model	Number of all datasets	RMSE (MPa)	MAE (MPa)	MAPE (%)	Specimen type
Ozbakkaloglu et al. [2]	257	8.0	4.7	14.5	Cylinder
Thomas et al. [28]	257	8.1	4.8	14.6	Cylinder
Gholampour et al. [47]	171	7.9	5.3	14.5	Cylinder
MARS	171	8.4	6.4	16.3	Cylinder
M5Tree	171	8.2	6.4	16.5	Cylinder
LSSVR	171	7.4	4.6	14.3	Cylinder

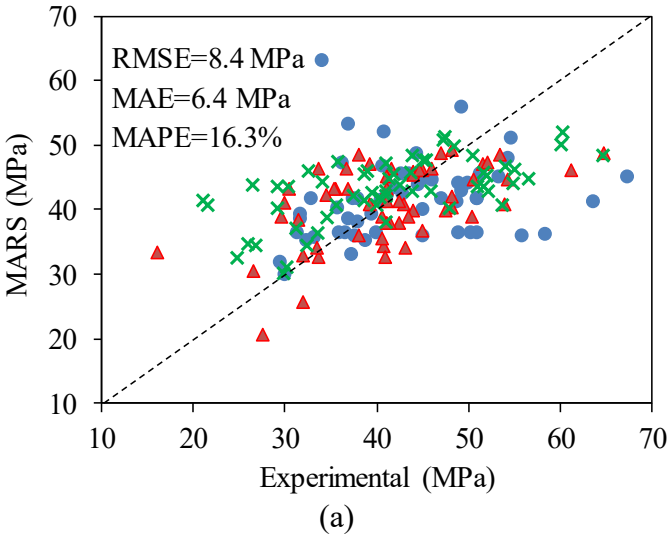

(a)

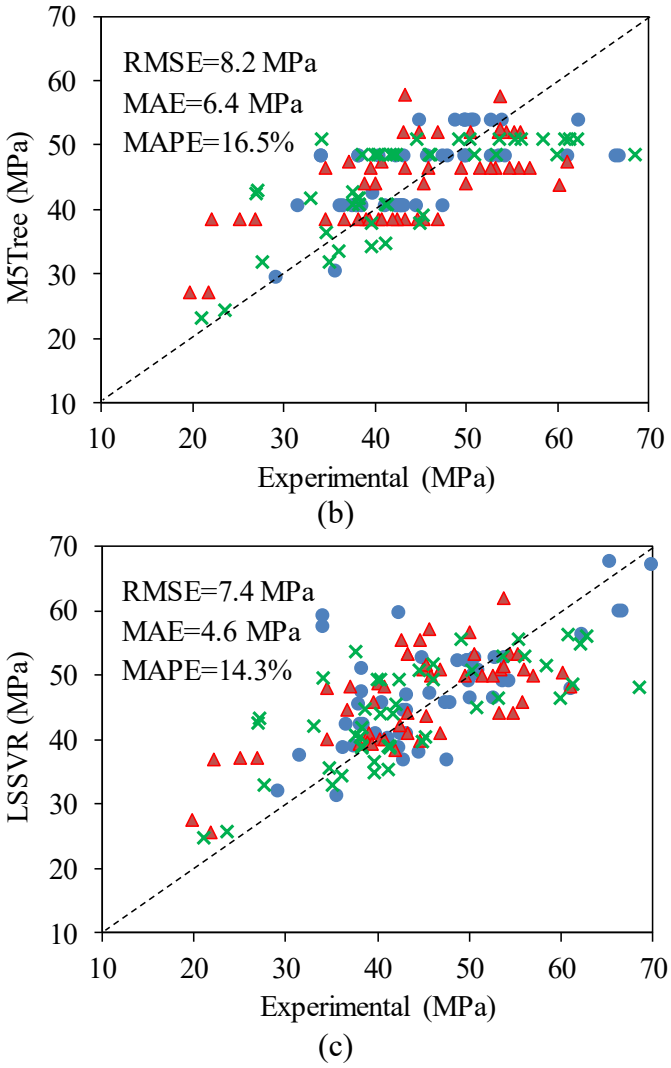

Figure 3.3. Compressive strength estimates of cylinder RAC ($f_{cm,cylinder}$) by (a) MARS, (b) M5Tree, and (c) LSSVR models at the validation stage. Circle, triangle, and cross shaped points are data points for validation set 1, 2, and 3, respectively.

Elastic modulus

Table 3.3 illustrates the prediction statistics of MARS, M5Tree, and LSSVR models and existing models for E_c of RACs. As can be seen in the table, Ozbakkaloglu et al. [2], Rahal [22], Corinaldesi [23], and Zilch and Roos [31] models showed the best performance among the models in the literature to predictE_c of RAC. As can also be seen in Table 3.3, MARS, M5Tree, and LSSVR models provide nearly identical accuracy to that of the best performing models in the literature in the prediction of E_c of RACs. Furthermore, MARS, M5Tree, and LSSVR models provided improved accuracy over Gholampour et al. [47] model in the prediction of f_{st} of RACs.

Table 3.3. Model predictions of elastic modulus (E_c) of RAC

Model	Number of all datasets	RMSE (GPa)	MAE (GPa)	MAPE (%)
Ozbakkaloglu et al. [2]	351	3.09	2.23	10.8
Ravindrarajah and Tam [13]	104	5.62	4.21	13.1
Kakizaki et al. [14]	33	4.51	3.64	10.9
Bairagi et al. [15]	104	6.76	5.55	19.1
de Oliveira and Vazquez [16]	104	7.14	6.19	22.3
Tavakoli and Soroushian [17]	104	6.55	5.29	16.8
Dillmann [18]	104	8.40	6.57	21.7
Dhir [19]	104	5.15	4.29	14.3
Kheder and Al-Windawi [20]	172	6.76	8.12	18.7
Rahal [22]	84	3.74	2.74	10.1
Corinaldesi [23]	172	3.85	3.13	10.1
Hoffmann et al. [26]	172	7.65	6.85	21.5
Pereira et al. [27]	82	10.54	9.07	31.1
Wardeh et al. [30]	104	5.79	4.86	17.2
Zilch and Roos [31]	84	3.10	2.23	8.3
Xiao et al. [32]	104	6.17	4.46	14.3
Lovato et al. [33]	204	21.80	21.40	70.6
Gholampour et al. [47]	224	4.44	3.41	14.4
MARS	224	3.78	2.66	11.5
M5Tree	224	3.74	2.71	11.7
LSSVR	224	3.25	2.35	10.7

Figure 3.4 shows comparison of MARS, M5Tree, and LSSVR model predictions with the experimental E_c of RACs at the validation stage. As can be seen in the figure, LSSVR model developed a higher accuracy in predicting the E_c of RAC than that of M5Tree and LSSVR models, confirming the suitability of the LSSVR model for this application.

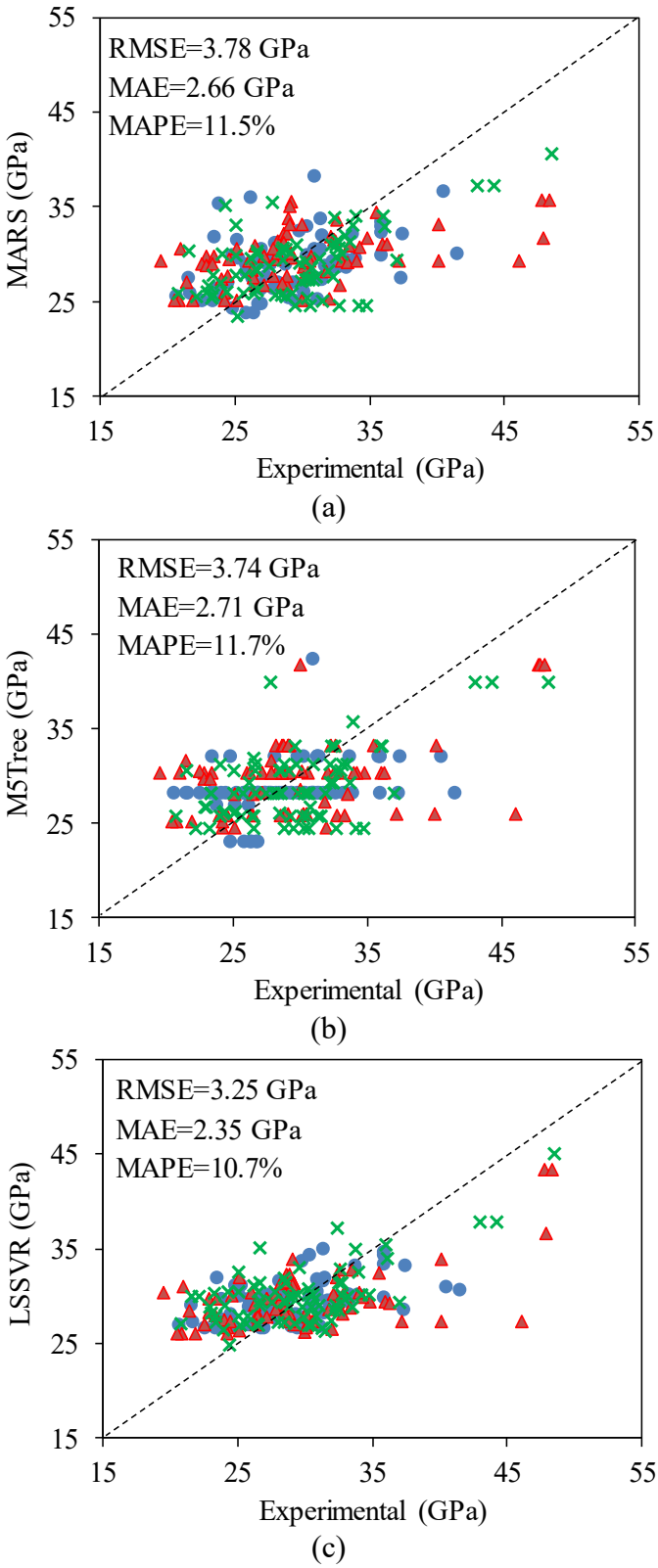

Figure 3.4. Elastic modulus (E_c) estimates of RAC by (a) MARS, (b) M5Tree, and (c) LSSVR models at the validation stage. Circle, triangle, and cross shaped points are data points for validation set 1, 2, and 3, respectively.

Flexural strength

Table 3.4 illustrates the prediction statistics of MARS, M5Tree, and LSSVR models and existing models for f_r of RACs. As can be seen in the table, the models by Ozbakkaloglu et al. [2], Xiao et al. [32], and Gholampour et al. [47] performed the best for the prediction of f_r of RAC among the existing models. It can be seen in Table 3.4 that LSSVR model provided slightly higher accuracy than those of the best performing models in the literature in the prediction of f_r of RACs. Comparison of MARS, M5Tree, and LSSVR model predictions with the experimental results shown in Fig. 3.5 further illustrates the better accuracy of the LSSVR model compared to that of MARS and M5Tree models in the prediction of the f_r of RACs.

Table 3.4. Model predictions of flexural strength (f_r) of RAC

Model	Number of all datasets	RMSE (MPa)	MAE (MPa)	MAPE (%)
Ozbakkaloglu et al. [2]	118	0.52	0.42	8.1
Bairagi et al. [15]	19	0.73	0.59	11.1
Tavakoli and Soroushian [17]	19	1.12	1.01	17.9
Kheder and Al-Windawi [20]	54	0.97	0.76	16.1
Xiao et al. [32]	19	0.52	0.45	8.1
Gholampour et al. [47]	79	0.54	0.45	8.3
MARS	79	0.58	0.49	9.2
M5Tree	79	0.55	0.48	8.6
LSSVR	79	0.52	0.41	8.0

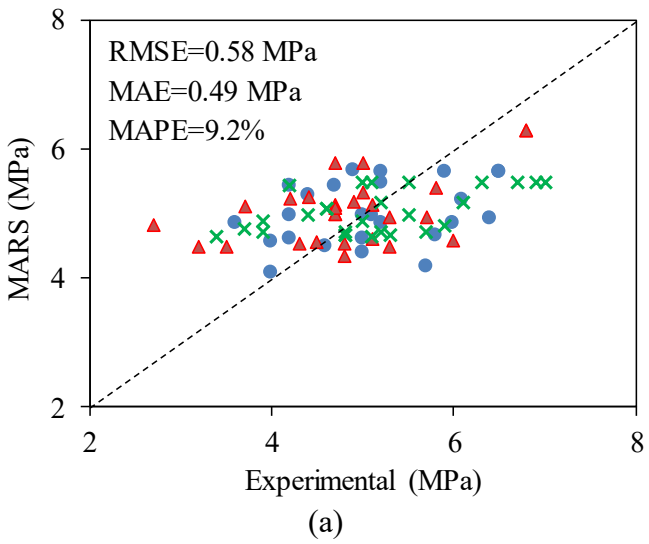

(a)

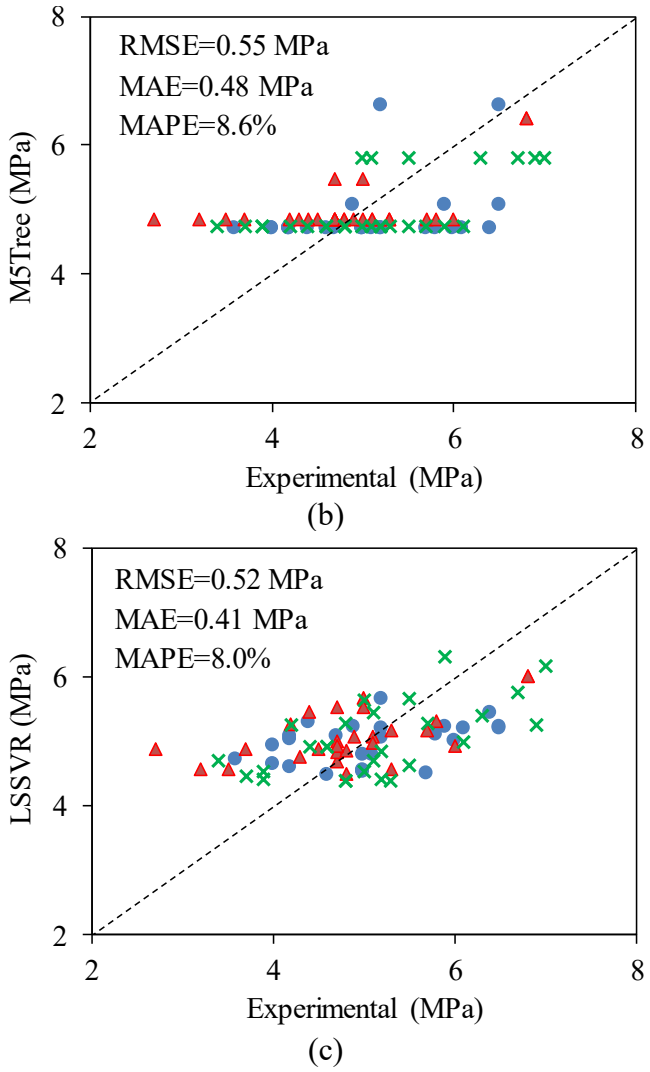

Figure 3.5. Flexural strength (f_r) estimates of RAC by (a) MARS, (b) M5Tree, and (c) LSSVR models at the validation stage. Circle, triangle, and cross shaped points are data points for validation set 1, 2, and 3, respectively.

Splitting tensile strength

Table 3.5 illustrates the comparison of prediction statistics of MARS, M5Tree, and LSSVR models with those of existing models in predicting the f_{st} of RAC. As can be seen in the table, Ozbakkaloglu et al. [2], Tavakoli and Soroushian [17], Xiao et al. [32], and Gholampour et al. [47] models performed the best among the existing models. It can also be seen in Table 3.5 that MARS, M5Tree, and LSSVR models provided improved accuracy over these best performing models in the prediction of f_{st} of RACs. The results suggest that all the three models are suitable for the prediction of the splitting tensile strength of RACs, which varies with the considered input parameters in a highly nonlinear fashion. However, in some cases, data-driven

models (e.g. MARS) may over-fit the data in training period and provide lower accuracy in test period compared to the simple models (e.g. regression method).

Table 3.5. Model predictions of splitting tensile strength (f_{st}) of RAC

Model	Number of all datasets	RMSE (MPa)	MAE (MPa)	MAPE (%)
Ozbakkaloglu et al. [2]	307	0.51	0.48	15.9
Tavakoli and Soroushian [17]	109	0.57	0.44	20.3
Kheder and Al-Windawi [20]	139	0.77	0.65	23.1
Xiao et al. [21]	109	0.67	0.52	16.6
Pereira et al. [27]	58	0.78	0.57	17.3
Xiao et al. [32]	109	0.52	0.46	16.6
Lovato et al. [33]	149	2.50	2.29	76.4
Gholampour et al. [47]	168	0.64	0.50	16.5
MARS	168	0.60	0.47	15.8
M5Tree	168	0.61	0.47	15.7
LSSVR	168	0.53	0.46	15.6

Figure 3.6 shows comparison of MARS, M5Tree, and LSSVR model predictions with the experimental f_{st} results of RACs in the validation stage. It can be seen in the figure that LSSVR model provided higher accuracy than that of MARS and M5Tree models in estimating the f_{st} of RAC.

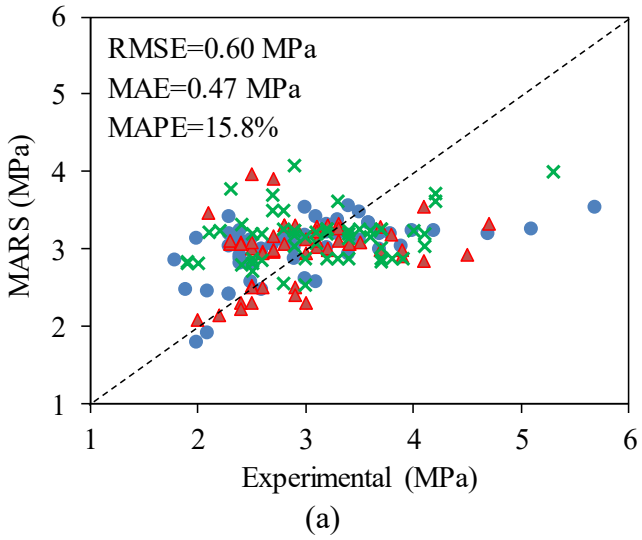

(a)

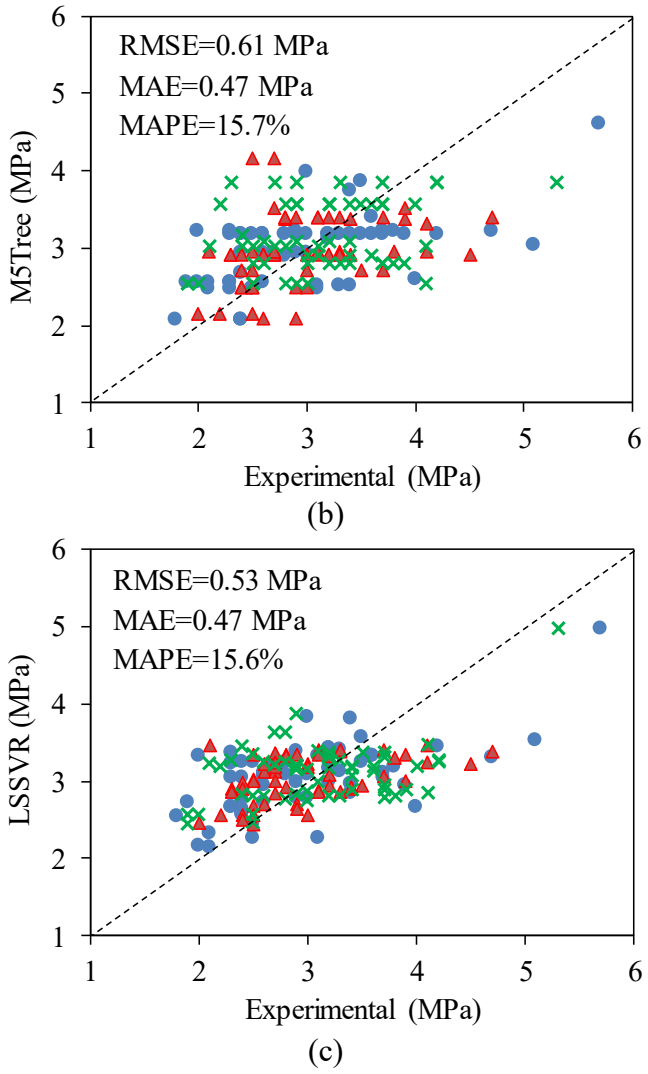

Figure 3.6. Splitting tensile strength (f_{st}) estimates of RAC by (a) MARS, (b) M5Tree, and (c) LSSVR models at the validation stage. Circle, triangle, and cross shaped points are data points for validation set 1, 2, and 3, respectively.

VARIATION OF MODEL PREDICTIONS WITH INFLUENTIAL PARAMETERS

In order to illustrate the variations of the model predictions with key input parameters within a physically meaningful framework, the variation of MARS, M5Tree, and LSSVR model predictions of $f_{cm,cube}$, $f_{cm,cylinder}$, E_c, f_r, and f_{st} with w_{eff}/c, *RCA%*, a/c, ρ_{RCA}, and WA_{RCA} are investigated. As was discussed in detail in Ref. [47], w_{eff}/c and *RCA%* have an accumulative effect on the mechanical properties of RACs. Therefore, the datasets used in the validation stage were divided into two subgroups based on their *RCA%* (i.e. *RCA%* of 0–50% and 51–100%) to better

isolate the individual effects of w_{eff}/c and *RCA%* on the mechanical behaviour of RACs.

Figures 3.7-3.11 show the variation of model predictions of $f_{cm,cube}$, $f_{cm,cylinder}$, E_c, f_r, and f_{st} of RACs with w_{eff}/c at each *RCA%* interval, respectively. As can be seen in the figures and as expected, an increase in w_{eff}/c resulted in a decrease in each mechanical property of RACs. It can also be seen in Figs. 3.7-3.11 that these properties decreased with increasing *RCA%* at a given w_{eff}/c. It can be seen in the figures that all the three models are able to accurately capture the effects of w_{eff}/c and *RCA%* on the mechanical behaviour of RACs to well reproduce the test results.

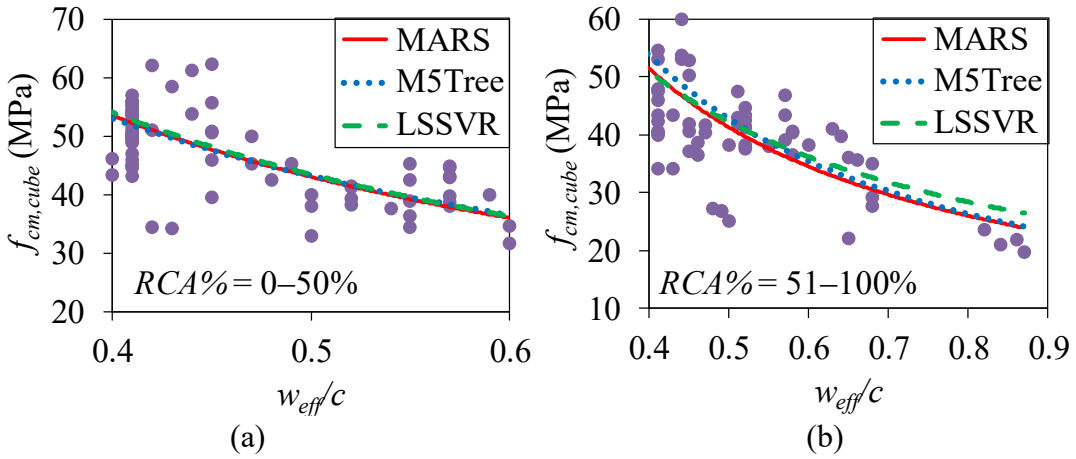

Figure 3.7. Variation of model predictions of $f_{cm,cube}$ with w_{eff}/c: (a) *RCA%* = 0–50%, (b) *RCA%* = 51–100%. Data points show experimental test results at the validation stage.

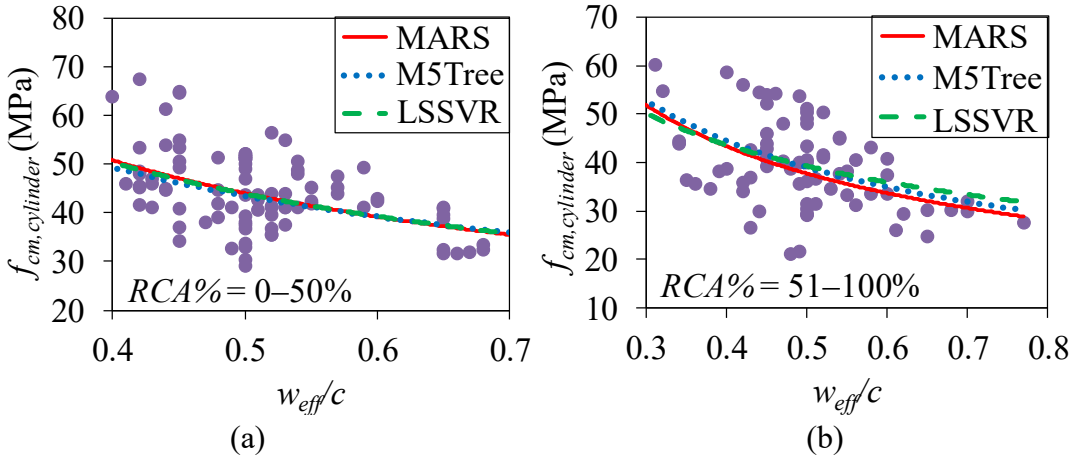

Figure 3.8. Variation of model predictions of $f_{cm,cylinder}$ with w_{eff}/c: (a) *RCA%* = 0–50%, (b) *RCA%* = 51–100%

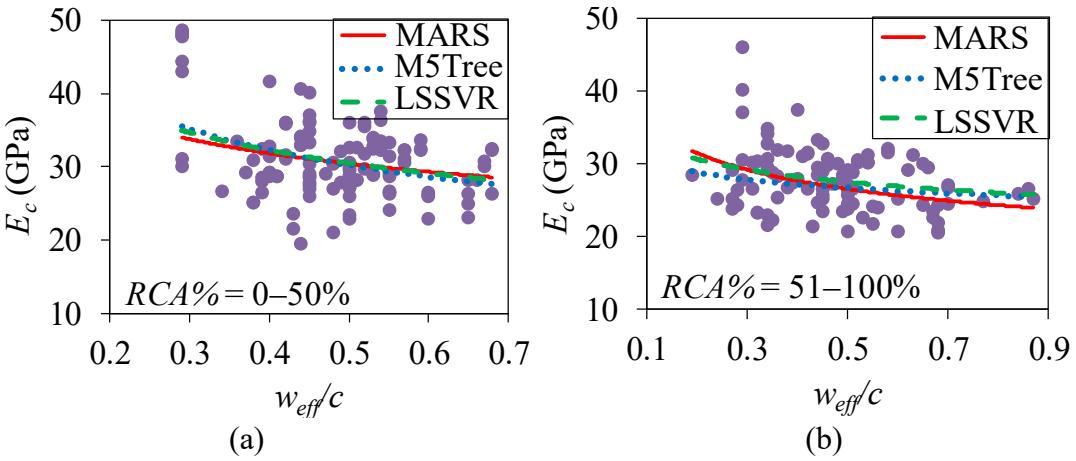

Figure 3.9. Variation of model predictions of E_c with w_{eff}/c: (a) *RCA%* = 0–50%, (b) *RCA%* = 51–100%

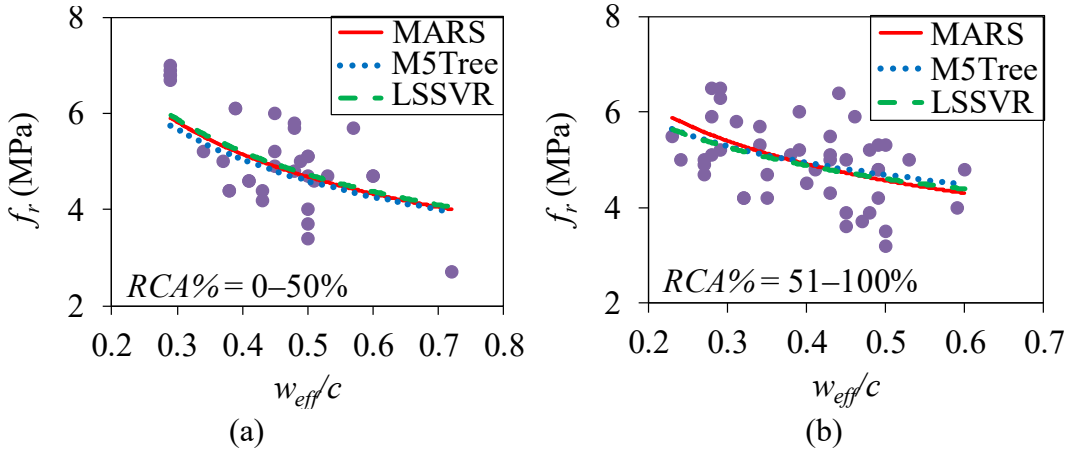

Figure 3.10. Variation of model predictions of f_r with w_{eff}/c: (a) *RCA%* = 0–50%, (b) *RCA%* = 51–100%

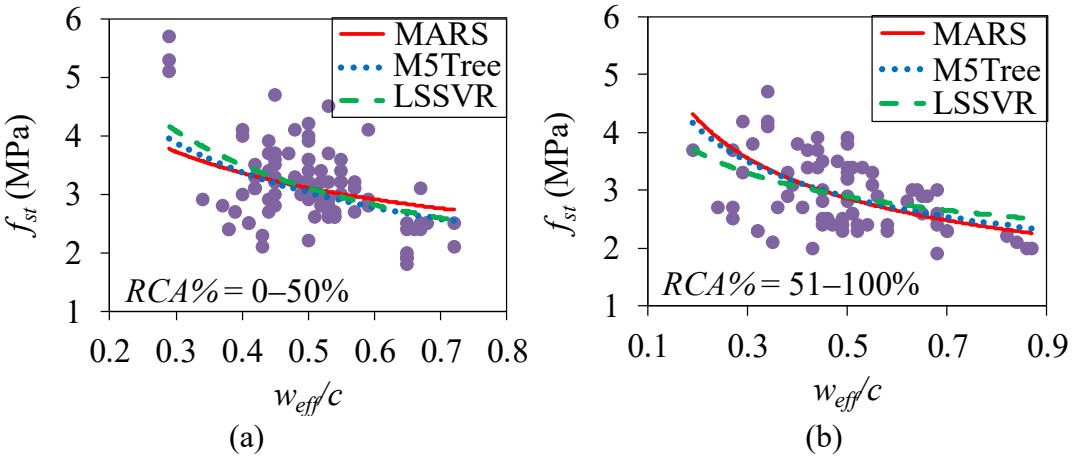

Figure 3.11. Variation of model predictions of f_{st} with w_{eff}/c: (a) *RCA%* = 0–50%, (b) *RCA%* = 51–100%

Figures 3.12-3.16, respectively, illustrate the variation of $f_{cm,cube}$, $f_{cm,cylinder}$, E_c, f_r, and f_{st} of RACs with a/c, ρ_{RCA}, and WA_{RCA}. As can be seen in the figures, an increase in a/c and ρ_{RCA} resulted in an increase in each mechanical property of RACs, whereas an increase in WA_{RCA} led to a decrease in the mechanical properties of RACs. These observations are in agreement with previous studies [23,60-69]. Therefore, all the three models are capable of accurately predicting the trend of the variation of the mechanical behaviour of RACs with key influential parameters.

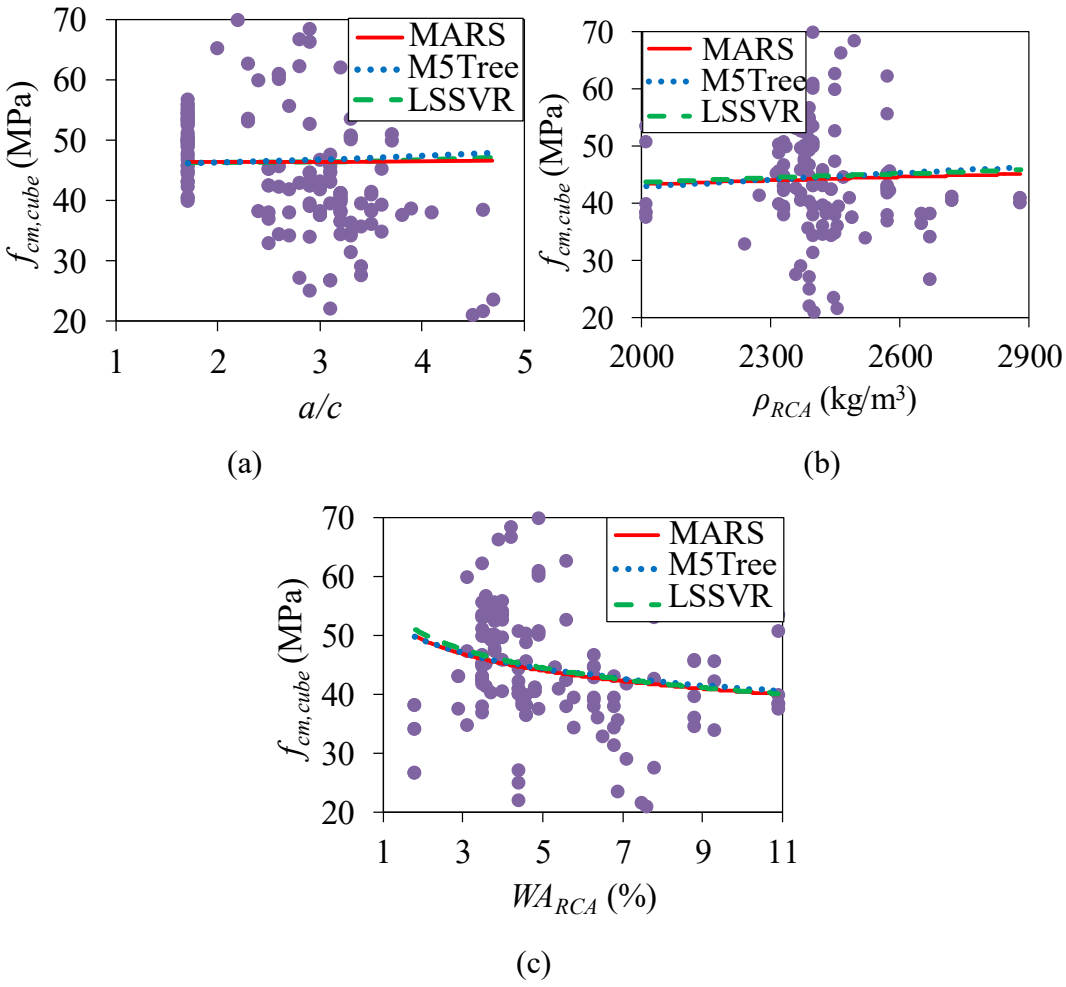

Figure 3.12. Variation of model predictions of $f_{cm,cube}$ with: (a) a/c, (b) ρ_{RCA}, and (c) WA_{RCA}

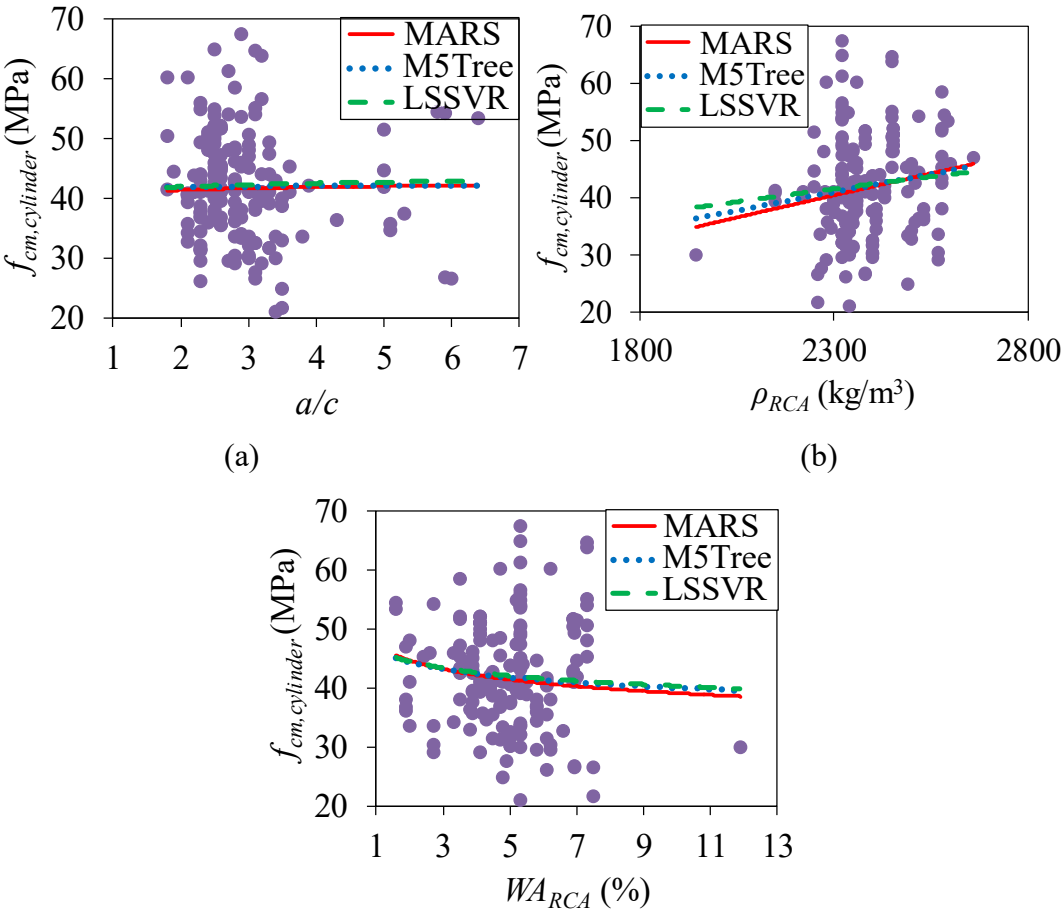

Figure 3.13. Variation of model predictions of $f_{cm,cylinder}$ with: (a) a/c, (b) ρ_{RCA}, and (c) WA_{RCA}

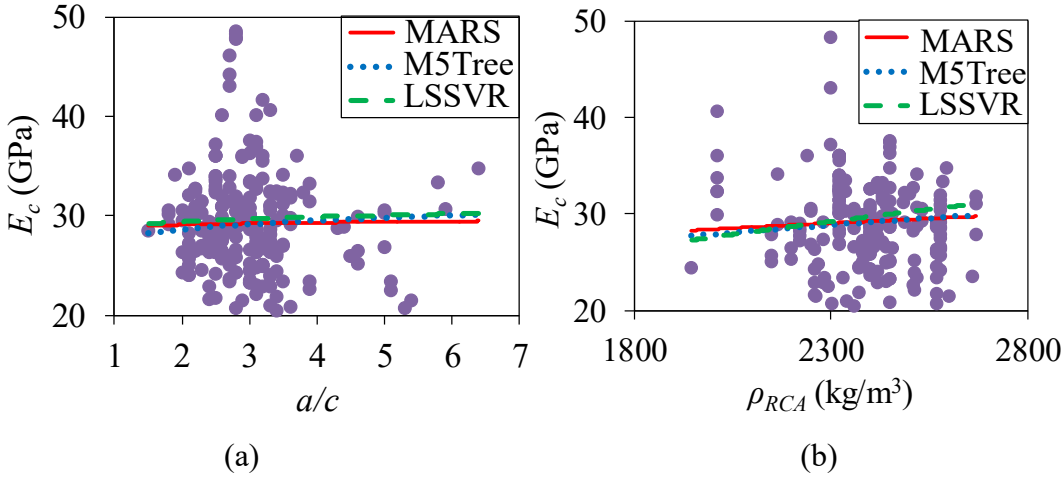

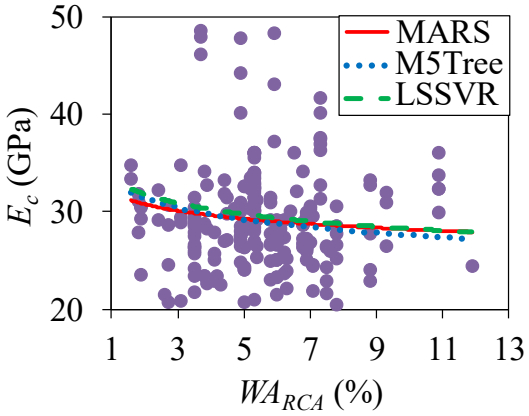

(c)

Figure 3.14. Variation of model predictions of E_c with: (a) a/c, (b) ρ_{RCA}, and (c) WA_{RCA}

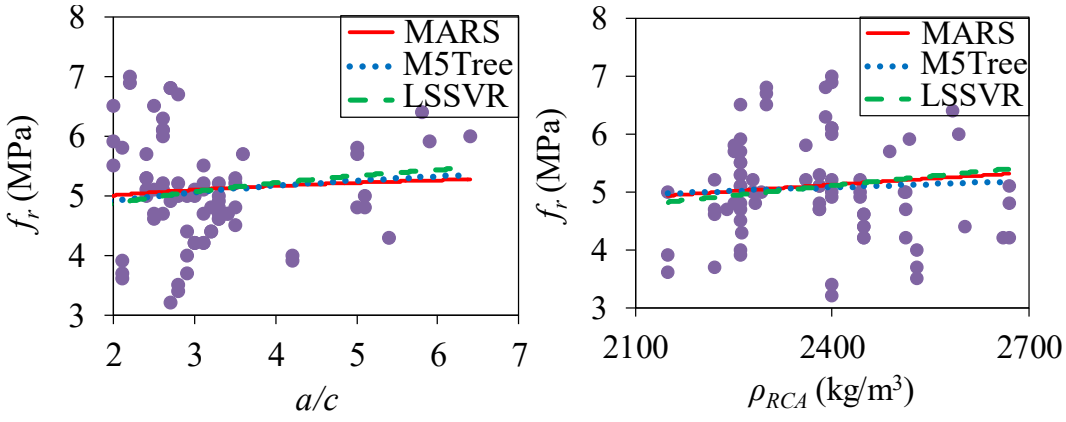

(a) (b)

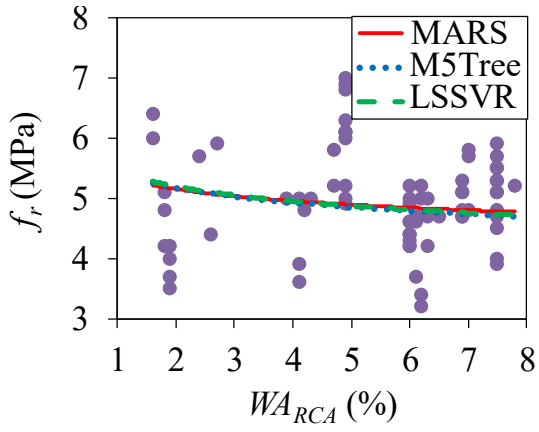

(c)

Figure 3.15. Variation of model predictions of f_r with: (a) a/c, (b) ρ_{RCA}, and (c) WA_{RCA}

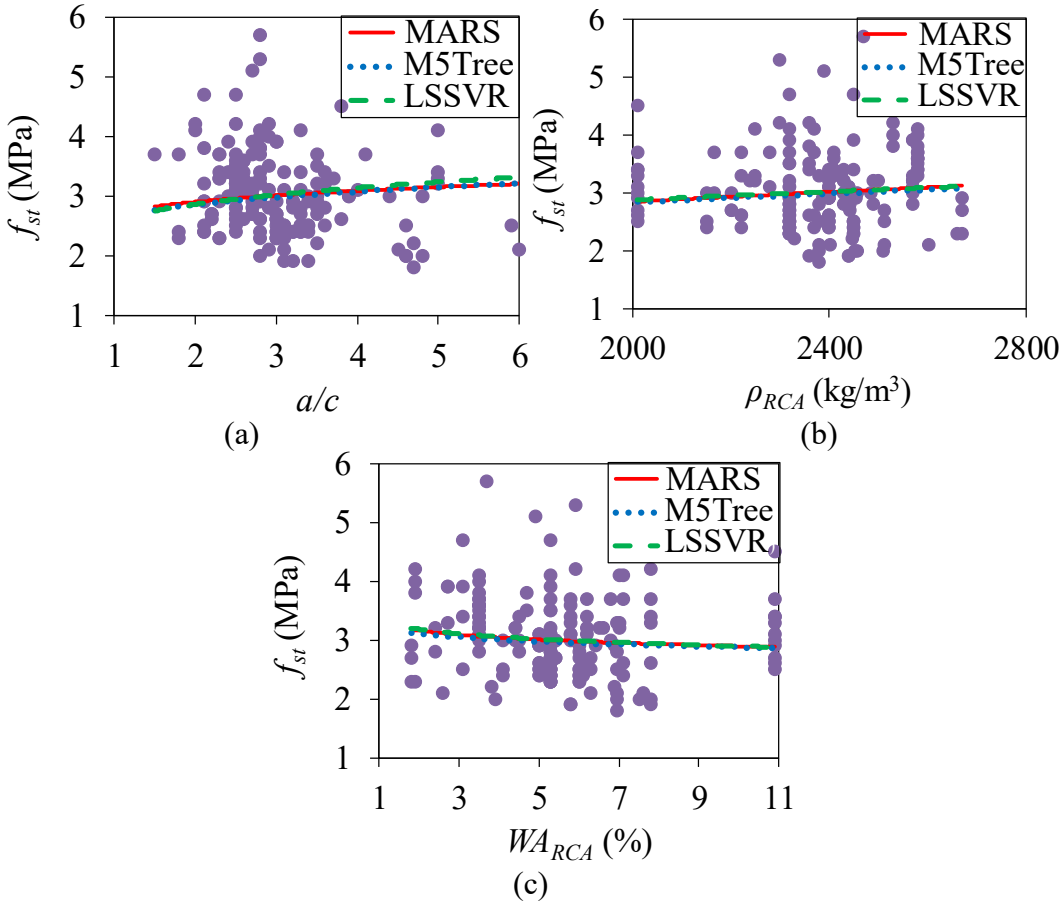

Figure 3.16. Variation of model predictions of f_{st} with: (a) a/c, (b) ρ_{RCA}, and (c) WA_{RCA}

COMPARISON OF MODEL PREDICTIONS WITH DESIGN CODE EXPRESSIONS

In order to investigate the agreement of predictions of MARS, M5Tree, and LSSVR models of mechanical properties of conventional concrete ($RCA\% = 0$) with those of existing design code and standard expressions, their overall trends were compared, as shown in Fig. 3.17. Table 3.6 shows the existing code expressions given for the prediction of E_c, f_r, and f_{st} of conventional concrete based on mean and characteristic cylinder compressive strength ($f_{cm,cylinder}$ and $f'_{c,cylinder}$). Figure 3.17 shows the variation of the predictions of E_c, f_r, and f_{st} by code expressions and MARS, M5Tree, and LSSVR models with $f'_{c,cylinder}$. The comparison of the results shown in Fig. 3.17 indicates that the trends of the MARS, M5Tree, and LSSVR models are consistent with the overall trend of the existing code expressions for conventional concrete.

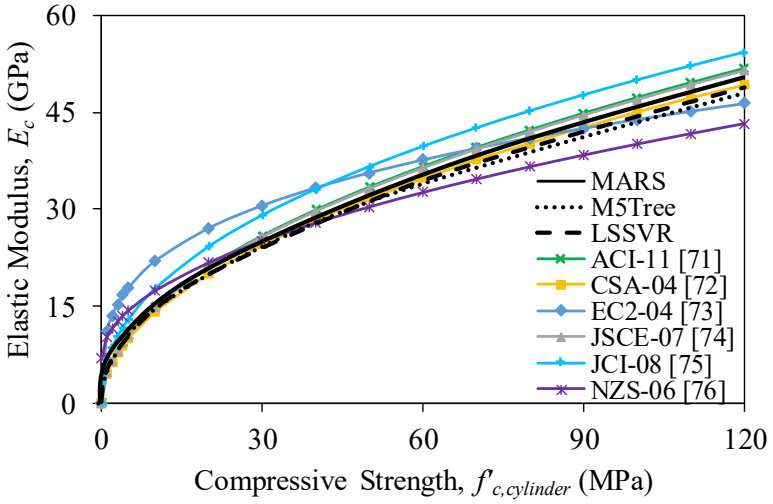

(a)

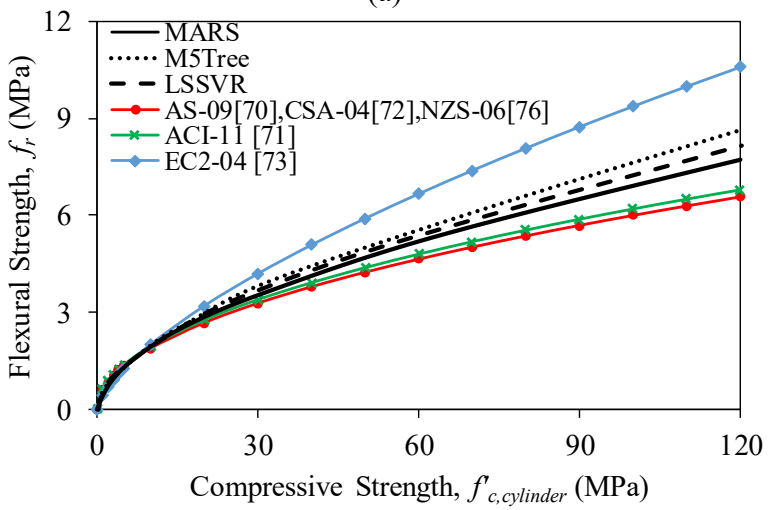

(b)

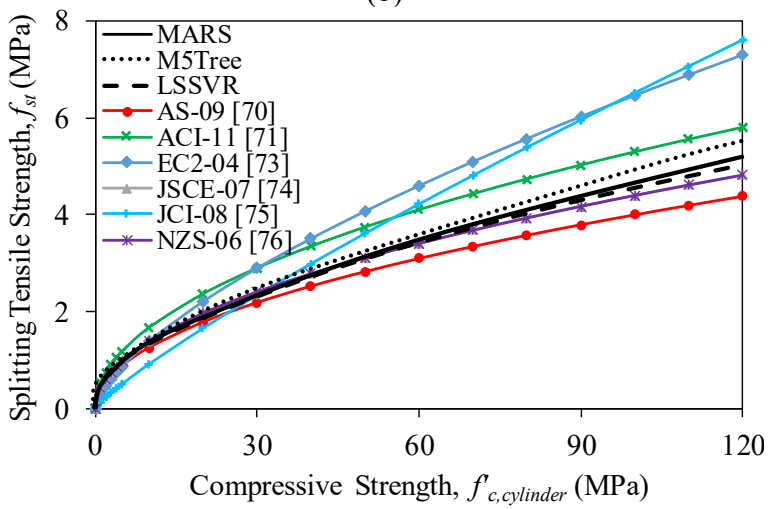

(c)

Figure 3.17. Comparisons of models of the present study with models given in design codes for conventional concrete: a) elastic modulus, b) flexural strength, c) splitting tensile strength

Table 3.6. Summary of conventional concrete mechanical property models given in current design codes

Model	Elastic modulus (E_c) (GPa)	Flexural strength (f_r) (MPa)	Splitting tensile strength (f_{st}) (MPa)
AS 3600-09 [70]	$4.3 \times 10^{-5}(\rho_h)^{1.5}\sqrt{f_{cm,cylinder}}$ when $f_{cm,cylinder} \leq 40$ MPa* $(2.4(\rho_h)^{1.5}\sqrt{f_{cm,cylinder}}+12) \times 10^{-5}$ when $40 < f_{cm,cylinder} \leq 100$ MPa	$0.60\sqrt{f'_{c,cylinder}}$	$0.4\sqrt{f'_{c,cylinder}}$
ACI 318-11 [71]	$4.73\sqrt{f'_{c,cylinder}}$	$0.62\sqrt{f'_{c,cylinder}}$	$0.53\sqrt{f'_{c,cylinder}}$
CSA A23.3-04 [72]	$4.5\sqrt{f'_{c,cylinder}}$	$0.60\sqrt{f'_{c,cylinder}}$	–
Eurocode 2-04 [73]	$22(f_{cm,cylinder}/10)^{0.3}$	$0.435{f'_{c,cylinder}}^{2/3}$	$0.3(f'_{c,cylinder})^{2/3}$
JSCE-07 [74]	$4.7\sqrt{f'_{c,cylinder}}$	–	$0.44\sqrt{f'_{c,cylinder}}$
JCI-08 [75]	$6.3{f'_{c,cylinder}}^{0.45}$	–	$0.13(f'_{c,cylinder})^{0.85}$
NZS 3101:2006 [76]	$3.32(\sqrt{f'_{c,cylinder}})+6.9$	$0.60\sqrt{f'_{c,cylinder}}$	$0.44\sqrt{f'_{c,cylinder}}$

$f'_{c,cylinder}$, $f_{cm,cylinder}$, f_r, and f_{st} are in MPa, E_c is in GPa, and ρ_h is in kg/m^3
* $f_{cm,cylinder}$ and $f'_{c,cylinder}$ are the mean and characteristic cylinder compressive strength, respectively ($f'_{c,cylinder} = f_{cm,cylinder} - 8$ MPa as per Eurocode 2).

CONCLUSIONS

This paper has presented an investigation into the capability of three artificial intelligence models, including MARS, M5Tree, and LSSVR, for the prediction of the compressive strength, elastic modulus, flexural strength, and splitting tensile strength of RACs. The test database of RAC was used to evaluate the performance of MARS, M5Tree, and LSSVR models and existing models in the literature. On the basis of assessment of modelling results, following conclusions can be drawn:

1- LSSVR model provides a higher accuracy for the prediction of the compressive strength of cube and cylinder RACs (MAPE=12.6% and 14.3%, respectively) compared to those of existing models.
2- The accuracy of MARS (MAPE=11.5%), M5Tree (MAPE=11.7%), and LSSVR (MAPE=10.7%) models for predicting the elastic modulus of RAC is nearly identical to that of best performing existing models.

3- MARS (MAPE=9.2%) and M5Tree (MAPE=8.6%) models predict the flexural strength of RACs with a slightly lower accuracy than that of the best performing existing models, whereas LSSVR model (MAPE=8.0%) performs better than the existing models.
4- All three models of MARS (MAPE=15.8%), M5Tree (MAPE=15.7%), and LSSVR (MAPE=15.6%) perform better than the existing models in the prediction of the splitting tensile strength of RACs.
5- LSSVR model performs better than MARS and M5Tree models in predicting the compressive strength, elastic modulus, flexural strength, and splitting tensile strength of RACs.
6- For conventional concrete, the predictions of the MARS, M5Tree, and LSSVR models are in agreement with those of the existing concrete design code expressions.

The results of this study indicate that MARS, M5Tree, and LSSVR models can provide close predictions of the mechanical behaviour of RACs by accurately capturing the influences of the key parameters, including the effective water-to-cement ratio, recycled concrete aggregate replacement ratio, aggregate-to-cement ratio, bulk density of recycled concrete aggregate, and water absorption of recycled concrete aggregate. These findings are promising and point to the possibility of the application of these techniques in the pre-design and modelling of structures manufactured with RACs.

REFERENCES

[1] Xie T, Gholampour A, Ozbakkaloglu T. Toward the development of sustainable concretes with recycled concrete aggregates: Comprehensive review of studies on mechanical properties. *Journal of Materials in Civil Engineering*. 2018;30(9):04018211.

[2] Ozbakkaloglu T, Gholampour A, Xie T. Mechanical and durability properties of recycled aggregate concrete: effect of recycled aggregate properties and content. *Journal of Materials in Civil Engineering*. 2018;30(2):04017275.

[3] Kou SC, Poon CS, Wan HW. Properties of concrete prepared with low-grade recycled aggregates. *Construction and Building Materials*. 2012;36:881-9.

[4] Torgal FP, Ding Y, Miraldo S, Abdollahnejad Z, Labrincha JA. Are geopolymers more suitable than portland cement to produce high volume recycled aggregates HPC. *Construction and Building Materials*. 2012;36:1048-52.

[5] Gholampour A, Ozbakkaloglu T. Time-dependent and long-term mechanical properties of concretes incorporating different grades of coarse recycled concrete aggregates. *Engineering Structures*. 2018;157:224-34.

[6] Somna R, Jaurapitakkul C, Chalee W, Rattanachu P. Effect of the water to binder ratio and ground fly ash on properties of recycled aggregate concrete. *Journal of Materials in Civil Engineering*. 2012;24(1):16-22.

[7] Limbachiya M, Meddah MS, Ouchagour Y. Performance of Portland/silica fume cement concrete produced with recycled concrete aggregate. *ACI Materials Journal*. 2012;109(1):91-100.

[8] Manzi S, Mazzotti C, Bignozzi MC. Short and long-term behavior of structural concrete with recycled concrete aggregate. *Cement and Concrete Composites*. 2013;37:312-8.

[9] de Brito J, Ferreira J, Pacheco J, Soares D, Guerreiro M. Structural, material, mechanical and durability properties and behaviour of recycled aggregates concrete. *Journal of Building Engineering*. 2015;6:1-16.

[10] Kou SC, Poon CS. Effect of the quality of parent concrete on the properties of high performance recycled aggregate concrete. *Construction and Building Materials*. 2015;77:501-8.

[11] Pedro D, de Brito J, Evangelista L. Evaluation of high-performance concrete with recycled aggregates: use of densified silica fume as cement replacement. *Construction and Building Materials*. 2017;147:803-14.

[12] Dimitriou G, Savva P, Petrou MF. Enhancing mechanical and durability properties of recycled aggregate concrete. *Construction and Building Materials*. 2018;158:228-35.

[13] Ravindrarajah RS, Tam CT. Properties of concrete made with crushed concrete as coarse aggregate. *Magazine of Concrete Research*. 1985;37(130):29-38.

[14] Kakizaki M, Harada M, Soshiroda T, Kubota S, Ikeda T, Kasai Y. Strength and elastic modulus of recycled aggregate concrete. *Proceedings of the Second International RILEM Symposium on Demolition and Reuse of Concrete and Masonry*. 1988;2:565-74.

[15] Bairagi NK, Ravande K, Pareek VK. Behaviour of concrete with different proportions of natural and recycled aggregates. *Resources, Conservation and Recycling*. 1993;9(1):109-26.

[16] de Oliveira MB, Vazquez E. The influence of retained moisture in aggregates from recycling on the properties of new hardened concrete. *Waste Management*. 1996;16(1):113-7.

[17] Tavakoli M, Soroushian P. Strengths of recycled aggragate concrete made using field-demolished concrete as aggregate. *ACI Materials Journal*. 1996;93(2):182-90.

[18] Dillmann R. Concrete with recycled concrete aggregate. Sustainable Construction: Use of Recycled Concrete Aggregate. *Producings of The International Symposium Held at Department of Trade and Industry Conference Centre*, London, UK. 1998;11-2.

[19] Dhir RK. Sustainability of Recycled Concrete Aggregate for Use IN BS 5328 Designated Mixes. *Proceedings of the ICE-Structures and Buildings*. 1999;134(3):257-74.

[20] Kheder GF, Al-Windawi SA. Variation in mechanical properties of natural and recycled aggregate concrete as related to the strength of their binding mortar. *Materials and Structures*. 2005;38(7):701-9.

[21] Xiao J, Li P, Qin W. Study on bond-slip between recycled concrete and rebars. *Journal of Tongji University*. 2006;34(1):13.

[22] Rahal K. Mechanical properties of concrete with recycled coarse aggregate. *Building and Environment*. 2007;42(1):407-15.

[23] Corinaldesi V. Mechanical and elastic behaviour of concretes made of recycled-concrete coarse aggregates. *Construction and Building Materials*. 2010;24(9):1616-20.

[24] Sriravindrarajah R, Wang NDH, Ervin LJW. Mix design for pervious recycled aggregate concrete. *International Journal of Concrete Structures and Materials*. 2012;6(4):239-46.

[25] Pereira P, Evangelista L, de Brito J. The effect of superplasticisers on the workability and compressive strength of concrete made with fine recycled concrete aggregates. *Construction and Building Materials*. 2012;28(1):722-9.

[26] Hoffmann C, Schubert S, Leemann A, Motavalli M. Recycled concrete and mixed rubble as aggregates: Influence of variations in composition on the

concrete properties and their use as structural material. *Construction and Building Materials*. 2012;35:701-9.

[27] Pereira P, Evangelista L, de Brito J. The effect of superplasticizers on the mechanical performance of concrete made with fine recycled concrete aggregates. *Cement and Concrete Composites*. 2012;34(9):1044-52.

[28] Thomas C, Setién J, Polanco JA, Alaejos P, de Juan MS. Durability of recycled aggregate concrete. *Construction and Building Materials*. 2013;40:1054-65.

[29] Serifou M, Sbartai ZM, Yotte S, Boffoue MO, Emeruwa E, Bos F. A study of concrete made with fine and coarse aggregates recycled from fresh concrete waste. *Journal of Construction Engineering*. 2013;1-5.

[30] Wardeh G, Ghorbel E, Gomart H. Mix design and properties of recycled aggregate concretes: applicability of Eurocode 2. *Internation Journal of Concrete Structures and Materials*. 2014;1-20.

[31] Zilch K, Roos F. An equation to estimate the modulus of elasticity of concrete with recycled aggregates. *ICE Proceedings Civil Engineering*. 2001;76(4):187–91.

[32] Xiao JZ, Li JB, Zhang C. On relationships between the mechanical properties of recycled aggregate concrete: an overview. *Materials and Structures*. 2006;39(6):655-64.

[33] Lovato PS, Possan E, Dal Molin DCC, Masuero AB, Ribeiro JLD. Modeling of mechanical properties and durability of recycled aggregate concretes. *Construction and Building Materials*. 2012;26(1):437-47.

[34] Xuan DX, Houben LJM, Molenaar AAA, Shui ZH. Mechanical properties of cement-treated aggregate material–a review. *Materials & Design*. 2012;33:496-502.

[35] Peng Y, Chu H, Pu J. Numerical simulation of recycled concrete using convex aggregate model and base force element method. *Advances in Materials Science and Engineering*. 2016;1-10.

[36] Taffese WZ, Sistonen E. Machine learning for durability and service-life assessment of reinforced concrete structures: recent advances and future directions. *Automation in Construction*. 2017;77:1-14.

[37] Hoang N, Chen C, Liao K. Prediction of chloride diffusion in cement mortar using multi-gene genetic programming and multivariable adaptive regression splines. *Measurement*. 2017;112:141-9.

[38] Yaseen ZM, Deo RC, Hilal A, Abd AM, Bueno LC, Salcedo-Sanz S, Nehdi ML. Predicting compressive strength of lightweight foamed concrete using extreme learning machine model. *Advances in Engineering Software*. 2018;115:112-25.

[39] Naderpour H, Rafiean AH, Fakharian P. Compressive strength prediction of environmentally friendly concrete using artificial neural networks. *Journal of Building Engineering*. 2018;16:213-9.

[40] Younis KH, Pilakoutas K. Strength prediction model and methods for improving recycled aggregate concrete. *Construction and Building Materials*. 2013;49:688-701.

[41] Duan ZH, Kou SC, Poon CS. Prediction of compressive strength of recycled aggregate concrete using artificial neural networks. *Construction and Building Materials*. 2013;40:1200-6.

[42] Sahoo K, Sarkar P, Davis R. Artificial neural networks for prediction of compressive strength of recycled aggregate concrete. *International Journal of Research in Chemical, Metallurgical and Civil Engineering*. 2016;3(1):81-5.

[43] Deshpande N, Londhe S, Kulkarni S. Modeling compressive strength of recycled aggregate concrete by Artificial Neural Network, Model Tree and Non-linear Regression. *Internationl Journal of Sustainable Built Environment*. 2014;3:187-98.

[44] Duan ZH, Kou SC, Poon CS. Using artificial neural networks for predicting the elastic modulus of recycled aggregate concrete. *Construction and Building Materials*. 2013;44:524-32.

[45] Behnood A, Olek J, Glinicki MA. Predicting modulus elasticity of recycled aggregate concrete using M5' model tree algorithm. *Construction and Building Materials*. 2015;94:137-47.

[46] Gonzalez-Taboada I, Gonzalez-Fonteboa B, Martinez-Abella F, Perez-Ordonez J. Prediction of the mechanical properties of structural recycled concrete using multivariable regression and genetic programming. *Construction and Building Materials*. 2016;106:480-99.

[47] Gholampour A, Gandomi AH, Ozbakkaloglu T. New formulations for mechanical properties of recycled aggregate concrete using gene expression programming. *Construction and Building Materials*. 2017;130:122-45.

[48] Friedman JH. Multivariate adaptive regression splines (with Discussion). *The Annuals of Statistics*. 1991;19(1):1-141.

[49] Quinlan JR. Learning with continuous classes. *Proceedings of the Fifth Australian Joint Conference on Artificial Intelligence*, Hobart, Australia, 16–18 November, World Scientific, Singapore. 1992;343-8.

[50] Suykens JAK, Vandewalle J. Least squares support vector machine classifiers. *Neural Processing Letters*. 1999;9(3):293–300.

[51] Cheng M, Cao M. Evolutionary multivariate adaptive regression splines for estimating shear strength in reinforced-concrete deep beams. *Engineering Applications of Artificial Intelligence*. 2014;28:86-96.

[52] Aiyer BG, Kim D, Karingattikkal N, Samui P, Rao PR. Prediction of compressive strength of self-compacting concrete using least square support vector machine and relevance vector machine. *KSCE Journal of Civil Engineering*. 2014;18(6):1753-8.

[53] Pham A, Hoang N, Nguyen Q. Predicting compressive strength of high-performance concrete using metaheuristic-optimized least squares support vector regression. *Journal of Computing in Civil Engineering*. 2016;30(3):06015002.

[54] Andres JD, Lorca P, de Cos Juez FJ, Sanchez-Lasheras F. Bankruptcy forecasting: a hybrid approach using fuzzy c-means clustring and multivariate adaptive regression splines (MARS). *Expert Systems with Applications*. 2010;38:1866-75.

[55] Sharda V, Prasher SO, Patel RM, Ojavasi PR, Prakash C. Modeling runoff from middle Himalayan watersheds employing artificial intelligence techniques. *Agricultural Water Management*. 2006;83:233-42.

[56] Pal M, Deswal S. M5 model tree based modelling of reference evapotranspiration. *Hydrological Processes*. 2009;23:1437-43.

[57] Adnan RM, Yuan X, Kisi O, Anam R. Improving accuracy of river flow forecasting using LSSVR with gravitational search algorithm. *Advances in Meteorology*. 2017;1-23.

[58] Suykens JAK, Van Gestel T, De Brabanter J, De Moor B, Vandewalle J. *Least squares support vector machines.* Singapore: Word Scientific. 2002.

[59] Cawley GC, Talbot NLC. On over-fitting in model selection and subsequent selection bias in performance evaluation. *Journal of Machine Learning Research*. 2010;11:2079-107.

[60] Kumutha R, Vijai K. Strength of concrete incorporating aggregates recycled from demolition waste. *ARPN Journal of Engineering and Applied Sciences*. 2010;5(5):64-71.

[61] Hou YL, Zheng G. Mechanical properties of recycled aggregate concrete in different age. *Journal of Building Materials*. 2013;16(4):683-7.

[62] Ismail S, Ramli M. Engineering properties of treated recycled concrete aggregate (RCA) for structural applications. *Construction and Building Materials*. 2013;44:464-76.

[63] Andreu G, Miren E. Experimental analysis of properties of high performance recycled aggregate concrete. *Construction and Building Materials*. 2014;52:227-35.

[64] Duan ZH, Poon CS. Properties of recycled aggregate concrete made with recycled aggregates with different amounts of old adhered mortars. *Materials & Design*. 2014;58:19-29.

[65] Casuccio M, Torrijos MC, Giaccio G, Zerbino R. Failure mechanism of recycled aggregate concrete. *Construction and Building Materials*. 2008;22(7):1500-6.

[66] Yang KH, Chung HS, Ashour AF. Influence of type and replacement level of recycled aggregates on concrete properties. *ACI Materials Journal*. 2008;105(3):289-96.

[67] Fathifazl G, Razaqpur AG, Isgor OB, Abbas A, Fournier B, Foo S. Creep and drying shrinkage characteristics of concrete produced with coarse recycled concrete aggregate. *Cement and Concrete Composites*. 2011;33(10):1026-37.

[68] Dilbas H, Simsek M, Çakır Ö. An investigation on mechanical and physical properties of recycled aggregate concrete (RAC) with and without silica fume. *Construction and Building Materials*. 2014;61:50-9.

[69] Ajdukiewicz A, Kliszczewicz A. Influence of recycled aggregates on mechanical properties of HS/HPC. *Cement and Concrete Composites*. 2002;24(2):269-79.

[70] AS3600-2009. *Australian Standard for Concrete Structures*. S. A, North Sydney, 2009.

[71] ACI 318-11. *Building Code Requirements for Structural Concrete and Commentary*, PCA notes on ACI 318-11: with design applications. Farmington Hills, Mich: ACI International, 2011.

[72] Canadian Standard. C S A. A23.3-04. *Design of concrete structures*, Canadian Standard Association, 2004.

[73] British Standards Institution. Eurocode 2: *Design of Concrete Structures: Part 1-1: General Rules and Rules for Buildings*. British Standards Institution, 2004.

[74] Japan Society of Civil Engineers. *Standard Specification for Concrete Structure*. JSCE No. 15, Tokyo, Japan, 2007.

[75] Japanese Civil Institute. *Guidelines for Control of Cracking of Mass Concrete*, Japan Concrete Institute, 2008

[76] New Zealand Standard. *Concrete Structures Standard*. NZS 3101:2006. The design of concrete structures, Wellington, New Zealand, 2006.

Chapter 2

Waste-based and geopolymer mortars and concretes

Publications:

Gholampour A, Ozbakkaloglu T. Performance of sustainable concretes containing very high volume class-F fly ash and ground granulated blast furnace slag. *Journal of Cleaner Production*. 2017;162:1407-17. ***Citations: 23***

Gholampour A, Ho VD, Ozbakkaloglu T. Ambient-cured geopolymer mortars prepared with waste-based sands: mechanical and durability-related properties and microstructure. *Composites Part B*. 2019;160:519-34. ***Citations: 4***

Gholampour A, Ozbakkaloglu T, Etemadi E, Vincent T. Mechanical properties and microstructure of waste-based mortars containing fly ash, ground granulated blast furnace slag, glass powder, and lead smelter slag. *Construction and Building Materials*. submitted on 14/01/2019. ***Citations: 0***

Statement of Authorship

Title of Paper	Performance of sustainable concretes containing very high volume class-F fly ash and ground granulated blast furnace slag
Publication Status	☑ Published ☐ Accepted for Publication ☐ Submitted for Publication ☐ Unpublished and Unsubmitted work written in manuscript style
Publication Details	Gholampour A, Ozbakkaloglu T. Performance of sustainable concretes containing very high volume class-F fly ash and ground granulated blast furnace slag. *Journal of Cleaner Production*. 2017;162:1407-17.

Principal Author

Name of Principal Author (Candidate)	Aliakbar Gholampour		
Contribution to the Paper	Literature review, analysis of test results, and preparation of the manuscript.		
Overall percentage (%)	80%		
Certification:	This paper reports on original research I conducted during the period of my Higher Degree by Research candidature and is not subject to any obligations or contractual agreements with a third party that would constrain its inclusion in this thesis. I am the primary author of this paper.		
Signature		Date	31/01/2019

Co-Author Contributions

By signing the Statement of Authorship, each author certifies that:

i. the candidate's stated contribution to the publication is accurate (as detailed above);

ii. permission is granted for the candidate in include the publication in the thesis; and

iii. the sum of all co-author contributions is equal to 100% less the candidate's stated contribution.

Name of Co-Author	Togay Ozbakkaloglu		
Contribution to the Paper	Research supervision and review of manuscript.		
Signature		Date	31/01/2019

Name of Co-Author			
Contribution to the Paper			
Signature		Date	

Please cut and paste additional co-author panels here as required.

Performance of Sustainable Concretes Containing Very High Volume Class-F Fly Ash and Ground Granulated Blast Furnace Slag

ABSTRACT

In recent years, with the aim of lowering the environmental impact of concrete, the partial replacement of cement in concrete with fly ash (FA) and ground granulated blast furnace slag (GGBS) has received significant attention. This paper presents the first experimental study on the properties of concrete containing ternary binders with high volume Class-F FA and GGBS partially replacing cement up to 90%. A total of 15 batches of concrete were manufactured with binary and ternary binders based on FA, GGBS, and cement. Experimental tests were performed to establish the density, workability, compressive strength, elastic modulus, flexural strength, splitting tensile strength, and water absorption of different mixes. The results indicate that the compressive strength of concrete containing FA decreases significantly with an increase in the FA content from 50% to 90%. The concretes containing GGBS at up to 90% cement replacement exhibit a similar compressive strength to that of conventional concrete after 28 days. It is found that ternary mixes with a 70% replacement ratio and relative FA to GGBS ratio (Ψ) of 1:2, and those with a 50% replacement ratio and Ψ of 1:1 develop a similar 28- and 90-day compressive strength to that of conventional concrete. A further increase in the replacement ratio and Ψ results in a decrease in the compressive strength. The results also show that GGBS mixes develop a slightly higher 28-day elastic modulus than that of conventional concrete mix. Although the elastic modulus of FA and the majority of the ternary mixes is lower than that of conventional concrete, ternary mixes with 70% (Ψ of 1:2) and 50% (Ψ of 1:1) replacement ratios develop a similar elastic modulus to that of conventional concrete. It is observed that an increase in the FA and GGBS content, respectively, results in a significant increase and moderate decrease in the water absorption of concrete. All ternary mixes with up to 90% cement replacement exhibit lower water absorption than conventional concrete mix. These highly promising findings suggest that the technology used in this study

can provide an attractive avenue for high volume use of FA and GGBS in concrete with the possibility of significantly reducing its environmental impact.

KEYWORDS: Fly ash (FA); Ground granulated blast furnace slag (GGBS); Concrete; Compressive strength; Mechanical properties; Water absorption.

INTRODUCTION

Concrete is the most widely used construction material. High volume use of concrete leads to the consumption of large amounts of energy on the production, transportation, and use of raw materials [1]. The production of the ordinary Portland cement (OPC) results in the release of a significant amount of greenhouse gases (essentially CO_2) into the atmosphere. It was reported that approximately one ton of CO_2 is generated and approximately 2.5 tons of materials are consumed to produce one ton of OPC [2]. It is estimated that the total amount of CO_2 produced by OPC production accounts for approximately 5–7% of global anthropogenic CO_2 emissions [3,4]. Therefore, it is recommended to seek an alternative material to replace cement in concrete to reduce the environmental impact of concrete.

One alternative to reduce the environmental impact of concrete is to use industrial by-products as mineral admixtures to replace the OPC in concrete [5]. Over the past three decades, fly ash (FA) and ground granulated blast furnace slag (GGBS) have been used as alternative cementitious materials to improve the green credentials of the construction industry. It is now recognized that the use of FA and GGBS in the concrete mixes is a highly promising technology to reduce the environmental impact of both the industrial by-products and concrete. It was reported that the worldwide generation of FA and GGBS is approximately 450 million and 530 million tons, respectively [6], with only about 25% of FA [7] and 65% of GGBS [8] are currently being used. Disposal of large volumes of FA and GGBS has become increasingly costly, while also causing environmental concerns [9].

In the past two decades, a large number of studies have been conducted to understand the performance of concrete containing FA and GGBS. Mo et al. [10] reported that the use of FA and GGBS reduces costs in the concrete production and

waste disposal, especially for high volume replacement. Bouzoubaa et al. [11] and Mehta [12] showed that the use of Class-F FA in the concrete modifies the properties of both fresh and hardened concrete, such as workability, strength, abrasion, heat evolution, shrinkage, and durability. Song and Saraswathy [13] and Atis and Bilim [14] showed that the inclusion of GGBS in concrete can reduce the porosity and increase the corrosion resistance of concrete. Siddique [15], Crouch et al. [16], and Kayali and Ahmed [17] showed that the compressive strength of concrete containing FA decreases with an increase in the FA replacement ratio. Chidiac and Panesar [18], Bilim et al. [19], and Mo et al. [20] found that the 28-day compressive strength of GGBS concrete increases with an increase in the GGBS replacement ratio up to 40–60% replacement level, beyond which the strength starts to decrease. Li and Zhao [21] and Berndt [22] reported that combined use of 25% of Class-F FA and 15–25% of GGBS in concrete resulted in a slightly lower or similar 28-day compressive strength to conventional concrete. Zhao et al. [6] and Berndt [22] showed that the elastic modulus of Class-F FA concrete decreases with an increase in the FA replacement ratio. They also reported that the elastic modulus of GGBS concrete increases with an increase in the GGBS content up to 50%, beyond which it starts to decrease. The tensile strength of concrete containing FA or GGBS has been shown to have a strong correlation with its compressive strength. Mehta [12], Berndt [22], and Yijin et al. [23] showed that the 28-day tensile strength of concretes decreases with an increase in the FA content and increases with an increase in the GGBS content up to 50% replacement level. Berndt [22] reported that beyond this replacement level the tensile strength of GGBS concrete starts to decrease with a similar trend to its compressive strength.

Most of the existing studies on the use of FA and GGBS in concrete were concerned with a relatively low volume replacement of cement (i.e., below 50%) with up to 30% and 40%, respectively. Although there are a number of studies that investigated the high volume Class-F [11,17,24] and Class-C [25,26] FA concrete (i.e., over 50% replacement), only one study [25] considered a replacement ratio of over 80%. As high volume FA concrete shows excellent workability and good long-term strength gain, attributed to the pozzolanic reaction of FA with calcium hydroxide of OPC resulting in a reduction in the porosity of the concrete in the longer term [16,17], the investigation of FA concrete at an ultra-high volume replacement is of significant

interest. Likewise, there are only a limited number of studies (i.e. [27-34]) on the high volume use (i.e., higher than 50%) of GGBS in concrete. The results of these studies showed that concretes containing high volume GGBS exhibit excellent mechanical properties and good long-term strength gain. Although there are a number of studies on the individual use of FA and GGBS in concrete, only two studies have investigated the properties of concrete with high volume replacement of cement by combined FA and GGBS (i.e. [25] (Class-C FA); [35] (Class-F FA)). Furthermore, only one study (i.e. [25]) to date has evaluated the mechanical properties, namely the compressive strength and elastic modulus, of concrete containing both FA (Class-C) and GGBS at a replacement ratio as high as 90%. However, the other important properties, such as the splitting tensile strength, flexural strength, and water absorption were not studied. As it is evident from the above review of the literature, additional experimental studies are required to understand the behaviour of concrete containing high volume Class-F FA and GGBS.

Water absorption is a key parameter in the investigation of the durability of concrete. Kungskulniti et al. [36] and Mukherjee et al. [37] showed that the water absorption of concrete significantly increases with an increase in the FA replacement ratio from 10% to 70%. This behaviour was attributed to the rough surface of FA as well as the presence of entrapped air on the surface of FA particles, which increase the porosity of concrete [36]. On the other hand, Atis and Bilim [14] and Sakai et al. [38] reported that the water absorption reduces with an increase in the amount of GGBS. This was explained by the reduction in the capillary pore volume and creation of a discontinuous capillary pore structure in the concrete with an increase in the GGBS content [38]. To date, only two studies have investigated the water absorption of the concrete containing high volume GGBS [28,29] and there has been no study on the water absorption of concrete containing the combination of FA and GGBS at high volume.

This paper presents the first experimental study to investigate the physical and mechanical properties of concretes containing high volume Class-F FA and GGBS binary and ternary binders with cement replacement ratios up to 90%. This study is also the first to investigate the splitting tensile strength, flexural strength, and water

absorption of concrete containing the combination of high volume FA and GGBS (i.e., replacement ratio > 50%). The paper initially provides a summary of the experimental program, including material properties, specimen properties, and testing procedures, which is followed by the results of the experimental program. A detailed discussion on the results is subsequently presented to discuss the effects of the cement replacement with FA and GGBS on the properties of concrete. The promising technology presented in this study allows the reduction of the environmental impact of both the industrial by-products and concrete and has the potential of significantly contributing toward a greener construction industry.

TEST PROGRAM

Materials

Natural aggregates

The physical properties of the natural aggregates are shown in Table 4.1. River sand was used as the fine aggregate and crushed basalt gravel, sourced from the McLaren Vale Quarry in Fleurieu Peninsula in South Australia, was used as the coarse aggregate.

Table 4.1. Properties of natural aggregates

Aggregate type	Maximum size (mm)	Bulk density (Loose) (t/m^3)	Bulk density (Compacted) (t/m^3)	Particle density (Apparent) (t/m^3)	Particle density (Dry) (t/m^3)	Particle density (SSD) (t/m^3)	Water absorption (%)	Fineness modulus
Coarse aggregate	9.5	1.48	1.61	2.74	2.60	2.65	2.0	5.4
Sand	2	1.42	1.55	2.63	2.60	2.61	0.4	2.5

Cement

In this study, high early strength cement (HESC) was used to minimize the effects of the low strength development at early curing stages of FA and GGBS concretes. The chemical composition and physical properties of the OPC and HESC used in this study are shown in Table 4.2.

Table 4.2. Chemical composition and physical properties of cementitious materials

Composition	Cementitious materials (%)			
	Ordinary Portland Cement	High Early Strength Cement	Fly ash	Granulated Blast Furnace Slag
Chemicals				
SiO_2	19.95	19.96	55.38	33.10
Al_2O_3	4.79	4.82	28.14	13.33
Fe_2O_3	3.14	3.09	3.31	0.69
CaO	63.28	63.58	3.45	42.83
MgO	2.03	1.97	1.85	5.57
Na_2O	0.29	0.28	2.30	0.27
K_2O	0.40	0.39	1.39	0.31
SO_3	2.69	2.69	0.32	1.81
P_2O_5	0.04	0.04	0.78	0.01
Compounds				
C3S	61.6	61.4	–	–
C2S	10.8	9.9	–	–
C3A	7.4	7.4	–	–
C4AF	9.5	9.2	–	–
Physical properties				
Specific gravity	3.01	3.04	2.62	2.91
Specific surface area (m^2/kg)	330	390	396	450

Fly ash (FA)

Class-F FA used in this study was sourced from the Port Augusta power station in South Australia. This fly ash is a by-product of combusting fine ground Leigh Creek Coal, which was extracted by electrostatic precipitators for the power station exhaust gases. The chemical composition and physical properties of FA shown in Fig. 4.1(a) is listed in Table 4.2. At least 75% of the FA particles were less than 45 μm and the moisture content of FA was less than 1%.

(a) (b)

Figure 4.1. Cementitious materials: a) Fly ash (FA); b) Ground granulated blast furnace slag (GGBS)

Ground Granulated Blast Furnace Slag (GGBS)

GGBS used in this study was produced as a by-product of iron and steel-making procedure at the Birkenhead Works in Adelaide. The chemical composition and physical properties of the GGBS shown in Fig. 4.1(b) is provided in Table 4.2.

Test specimens

15 unique batches of concrete, including: two control batches (one with OPC and one with HESC), three batches of concrete with binary mix of FA and HESC, three batches of concrete with binary mix of GGBS and HESC, and seven batches of concrete with ternary mix of FA, GGBS, and HESC, were prepared at the Concrete Materials Laboratory at the University of Adelaide. A series of tests including: the workability, compressive strength, elastic modulus, flexural strength, splitting tensile strength, and water absorption, was undertaken to evaluate the properties of fresh and hardened concretes. Two types of specimens were used in obtaining the mechanical properties; namely, beams and cylinders. The beam specimens were used for the flexural strength tests and they had a width and depth of 75 mm and length of 285 mm. The compressive strength, elastic modulus, and splitting tensile strength tests were established using 100 × 200 mm cylinders.

The test parameters included: the weight replacement ratio of cement with FA (*FA%*), GGBS (*GGBS%*), and combined FA and GGBS (*SCM%*; i.e., replacement ratio of cement with both supplementary cementitious materials), as well as the relative ratio of FA and GGBS (Ψ). Different *FA%*, *GGBS%*, and *SCM%* levels of 50%, 70%, and 90% were investigated, and Ψ was set as 1:1, 1:2, and 2:1. A constant water-to-binder ratio (*w/b*) of 0.56 was used in all mixes. The concrete mix proportions are shown in Table 4.3. Three nominally identical specimens were tested for each unique specimen configuration in each type of test.

Table 4.3. Mix proportions and physical properties of concrete

Concrete mix	OPC (kg/m^3)	HESC (kg/m^3)	FA (kg/m^3)	GGBS (kg/m^3)	Sand (kg/m^3)	Coarse aggregate (kg/m^3)	Water (kg/m^3)	SP (kg/m^3)	*w/b**	Slump (mm)	Fresh density (kg/m^3)	Hardened density (kg/m^3)
CS	350	0	0	0	740	1110	193	2	0.56	165	2385	2338
CSE	0	350	0	0	740	1110	193	2	0.56	155	2383	2349
FA50E	0	175	175	0	740	1110	193	2	0.56	220	2377	2315
FA70E	0	105	245	0	740	1110	193	2	0.56	230	2372	2315
FA90E	0	35	315	0	740	1110	193	2	0.56	245	2377	2317
G50E	0	175	0	175	740	1110	193	2	0.56	110	2395	2365
G70E	0	105	0	245	740	1110	193	2	0.56	80	2393	2361
G90E	0	35	0	315	740	1110	193	2	0.56	75	2394	2360
FA25G25E	0	175	87.5	87.5	740	1110	193	2	0.56	175	2386	2310
FA35G35E	0	105	122.5	122.5	740	1110	193	2	0.56	185	2388	2292
FA45G45E	0	35	157.5	157.5	740	1110	193	2	0.56	200	2383	2328
FA23G47E	0	105	80.5	164.5	740	1110	193	2	0.56	175	2384	2320
FA47G23E	0	105	164.5	80.5	740	1110	193	2	0.56	180	2368	2316
FA30G60E	0	35	105	210	740	1110	193	2	0.56	210	2385	2326
FA60G30E	0	35	210	105	740	1110	193	2	0.56	235	2392	2322

OPC: Ordinary Portland cement; HESC: High early strength cement; FA: Fly ash; GGBS: Ground granulated blast furnace slag; SP: Superplasticizer
* Including the water coming from the superplasticizer (i.e., 70% water by weight)

Specimen designation

The concrete series in Table 4.3 were labeled as follows: the letter CS stands for control samples with OPC and the additional letter E represents samples with HESC. The letters FA and G represent fly ash and ground granulated blast furnace slag, with the numbers following them indicating the percentage of cement replaced by the FA or GGBS.

Specimen preparation and testing

As shown in Table 4.3, the control groups (i.e., CS and CSE mixes) were designed to develop a 28-day compressive strength (f_{cm}) of 45 MPa. Once the specimens were demolded, they were cured in the fog room until test day at a constant temperature of 23±2°C according to ASTM C192 [39].

The experimental methods used in this paper to determine the concrete properties are shown in Table 4.4. The workability of fresh concrete was evaluated by a slump test, which was performed in accordance with ASTM C143 [40]. The fresh and hardened densities of concrete, respectively, were obtained in accordance with ASTM C138 [41] and ASTM C642 [42]. The mechanical properties, including the compressive strength [43], elastic modulus [44], splitting tensile strength [45], and flexural strength [46] of concrete were determined using a universal testing machine. The compressive strength of hardened concrete specimens was determined at the concrete ages of 3, 7, 28, and 90 days. All other tests were conducted at 28 days of curing. Prior to the compression tests, all cylinder specimens were ground by a surface-grinding machine to ensure uniform distribution of the applied load at the specimen ends. Water absorption tests were also carried out in all mixes in accordance with ASTM C642-13 [42].

Table 4.4. Experimental methods used to determine concrete properties

Target properties	Method
Slump test	ASTM C143/C143M–12 [40]
Fresh density	ASTM C138/C138M–14 [41]
Hardened density	ASTM C642–13 [42]
Compressive strength	ASTM C39/C39M–14 [43]
Modulus of elasticity	ASTM C469/C469M–14 [44]
Splitting tensile strength	ASTM C496/C496M–11 [45]
Flexural strength	ASTM C78/C78M–10 [46]
Water absorption	ASTM C642–13 [42]

TEST RESULTS AND EXPERIMENTAL OBSERVATIONS

Workability of fresh concrete

Figure 4.2 shows the slump test results of different mixes. As it can be seen in the figure, the concrete mixed with HESC (i.e., CSE) showed a slightly lower slump than that of the concrete mixed with OPC (i.e., CS). This reduction is attributed to the finer particle size and higher surface area of HESC than OPC [47]. It can also be seen in Fig. 4.2 that the slump increased with an increase in the *FA%*. The mix with 90% FA replacement developed a 58% higher slump than that of the control group (i.e., CSE). An increase in the workability of the specimens with an increase in the *FA%* is attributed to the spherical shape and smooth surface of FA [12,48,49]. Conversely, the slump decreased with an increase in the *GGBS%*. *GGBS%* of 50% and 90% resulted in 29% and 51% decreases in the slump, respectively. This decrease is attributed to the lower capillary pore volume of the GGBS mixes, which trapped some of the mixing water [50]. This observation is in agreement with the previous studies which investigated the use of the GGBS with up to 60% replacement level [33,51,52]. As shown in Fig. 4.2, the slump increased with an increase in the *SCM%* for all three Ψ ratios up to 51%. It is also notable that all ternary mixes had a higher slump than the control mixes and the mix FA60G30E developed the highest slump among all ternary mixes. These results suggest that FA had a more significant influence on the overall workability of the concrete than GGBS.

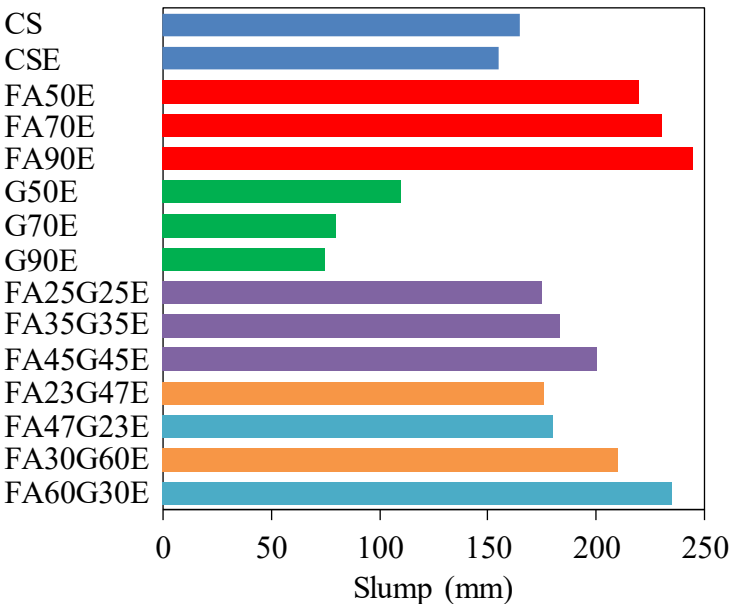

Figure 4.2. Slump test results of FA and GGBS mixes

Density of concrete

As can be seen in Table 4.3, the densities of CS and CSE mixes were similar both in fresh and hardened states (at 28 days). On the other hand, FA mixes had lower and GGBS mixes had higher densities in fresh and hardened states than those of the control groups (i.e., CS and CSE). Ternary concrete mixes containing FA, GGBS, and cement developed similar fresh and hardened densities compared to those of the control groups.

Mechanical properties of hardened concrete

Compressive strength

Figure 4.3 and Table 4.5 show the 3-, 7-, 28-, and 90-day compressive strengths of different mixes. As can be seen in Fig. 4.3, a comparable compressive strength (f_{cm}) was achieved by the control groups (i.e., CS and CSE) at the concrete age of 28-day. As expected, compared to CS, CSE developed a higher compressive strength at 3- and 7-day but lower at 90-day.

Table 4.5. Compressive strength of concrete

Concrete series	f_{cm} (3-day) (MPa)	f_{cm} (7-day) (MPa)	f_{cm} (28-day) (MPa)	f_{cm} (90-day) (MPa)
CS	29.6 (0.38)	35.0 (0.39)	43.2 (0.21)	49.5 (0.28)
CSE	32.8 (0.15)	39.4 (0.35)	43.5 (0.26)	46.7 (0.31)
FA50E	13.0 (0.21)	17.8 (0.36)	33.3 (0.31)	39.5 (0.33)
FA70E	8.3 (0.40)	8.9 (0.35)	22.1 (0.26)	30.2 (0.25)
FA90E	0.9 (0.32)	1.5 (0.31)	4.3 (0.23)	10.7 (0.27)
G50E	32.7 (0.25)	36.1 (0.21)	46.2 (0.27)	52.2 (0.26)
G70E	26.8 (0.30)	30.6 (0.22)	44.9 (0.25)	49.2 (0.32)
G90E	24.3 (0.15)	28.5 (0.28)	40.2 (0.29)	45.4 (0.34)
FA25G25E	16.6 (0.35)	27.4 (0.27)	41.4 (0.28)	44.9 (0.29)
FA35G35E	10.2 (0.21)	20.2 (0.34)	30.9 (0.32)	39.7 (0.14)
FA45G45E	7.1 (0.36)	16.5 (0.32)	30.7 (0.25)	39.8 (0.23)
FA23G47E	15.1 (0.18)	25.9 (0.40)	42.1 (0.39)	45.7 (0.35)
FA47G23E	13.3 (0.23)	16.7 (0.26)	31.5 (0.29)	40.6 (0.16)
FA30G60E	12.8 (0.35)	18.4 (0.28)	24.5 (0.27)	37.5 (0.27)
FA60G30E	7.5 (0.10)	11.2 (0.15)	22.0 (0.23)	34.3 (0.22)

* The values in parentheses represent the standard deviation of the compressive strengths

It can be seen in Fig. 4.3(a) that 50% FA replacement resulted in 23.4% and 15.4% strength reductions at 28- and 90-day, respectively, which are lower than those reported in previous studies (i.e., 37% and 29% at 28- and 90-day, respectively) [15-17]. Further increase in *FA%* led to a significant decrease in the compressive strength of concrete at a given curing age. This is attributed to the fact that Class-F FA has a significantly lower CaO content (i.e., < 5%) compared to OPC (i.e., > 60%). With an increase in the *FA%*, the CaO content was reduced, which led to a lower level of hydration [21]. This observation is in agreement with those reported in previous studies [15-17]. It can also be seen from Fig. 4.3(a) that the decrease in the compressive strength was higher at 3- and 7-day than at 28- and 90-day. This is attributed to the fact that FA is not a hydraulic material, i.e., hydration will not take place on its own, and it requires the use of an activator (e.g. OPC) to react with calcium hydroxide and as a result it has limited contribution toward the densification of concrete at early ages (i.e., 3- and 7-day) [21]. Following the hydration of OPC at early ages, FA starts to undergo pozzolanic reaction with calcium hydroxide and the

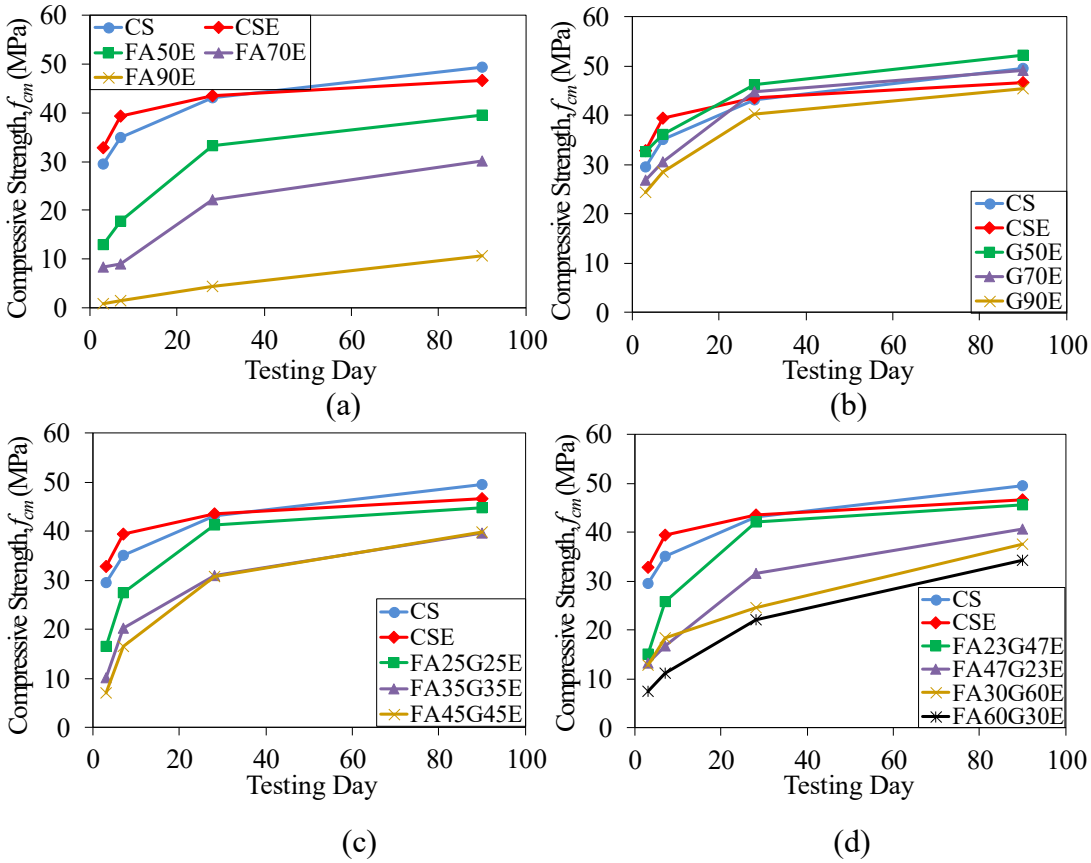

Figure 4.3. Compressive strength trends of mixes containing: a) FA; b) GGBS; c) FA & GGBS at 1:1 ratio; d) FA & GGBS at 1:2 and 2:1 ratios

hydration of both cement and FA lead to a reduction in the porosity of the concrete in longer term (i.e., 28- and 90-day), resulting in a higher compressive strength [15,53].

It can be seen from Fig. 4.3(b) that GGBS mixes developed slightly lower compressive strengths at early curing stage (i.e., 3- and 7-day), except for mix G50E at 3-day, but exhibited similar or slightly higher compressive strengths than that of the control group (i.e., CSE) in longer term (i.e., 28- and 90-day), except for mix G90E. The higher rate of strength gain of GGBS mixes compared to that of CSE after 7-day is due to the higher volume of SiO_2 (i.e., ~35%) and Al_2O_3 (i.e., ~13%) in the GGBS compared to those of OPC (i.e., < 20% and 5%, respectively), which leads to accelerated hydration as a result of the formation of high contents of tricalcium silicate (C_3S), dicalcium silicate (C_2S), and tricalcium aluminate (C_3A) in the mix [54]. It is seen that even G90E mix performed very well in comparison with the CSE, with a significantly lower strength reduction (i.e., 8% and 3% at 28- and 90-day, respectively) than that reported in the only previous study that investigated this very

high replacement level using Class-C FA (i.e., 44% and 27% at 28- and 112-day, respectively) [25]. It can also be observed from Fig. 4.3(b) that an increase in the *GGBS%* from 50% to 90% resulted in up to 25% and 13% decreases in the compressive strength of mixes at early (i.e., 3- and 7-day) and later ages (i.e., 28- and 90-day), respectively. This is attributed to the fact that GGBS has a lower CaO content (i.e., ~40%) compared to OPC (i.e., > 60%). With an increase in the *GGBS%*, the CaO content was reduced, which resulted in a lower level of hydration leading to lower early age strengths [21]. However, the higher SiO_2 and Al_2O_3 content of the GGBS compared to that of OPC resulted in accelerated hydration and a higher rate of strength gain in the GGBS mixes leading to the higher longer term (i.e., 28- and 90-day) strength of mixes with 50% and 70% *GGBS%* compared to that of CSE mix. This observation is in agreement with previous research [55].

It can be seen in Figs. 4.3(c) and 4.3(d) that the compressive strength of ternary mixes decreased with an increase in the *SCM%* at a given curing age. This is attributed to a decrease in the CaO content of the ternary mixes with an increase in the *SCM%*, which resulted in a lower level of hydration and strength as discussed previously. It can also be seen that the compressive strengths of the ternary mixes were significantly lower than the control groups (i.e., CSE) at or before 7 days of curing. However, the ternary mixes gained strength at a higher rate than those of the control groups (i.e., CS and CSE) after 7 days curing. This behaviour is attributed to the higher volume of SiO_2 and Al_2O_3 in the ternary mixes compared to those of control mixes, which lets –OH and –COOH groups interact with high contents of C_3S, C_2S, and C_3A, and consequently leads to the rapid growth of the hydration products of calcium silicate hydrate (C–S–H) [21]. Among all ternary mixes, FA23G47E mix had the highest 28- and 90-day compressive strengths, which were similar to those of the control mix (i.e., CSE). On the other hand, FA25G25E mix developed the highest 3- and 7-day compressive strength. These results indicate that properly designed ternary mixes can develop similar performances to conventional concrete even at replacement ratios as high as 70%. Figures 4.3(c) and 4.3(d) show that any increase beyond this replacement ratio results in significant decreases in the compressive strength at all Ψ ratios. However, the ternary mix with 90% *SCM%* (i.e., FA45G45E) experienced a lower strength reduction at 28-day (i.e., up to 27%) than that reported in the only previous

study (i.e., up to 51%) that investigated this very high replacement level using Class-C FA [25].

Elastic modulus

Figure 4.4 shows the 28-day elastic modulus of specimens. As can be seen in the figure, FA mixes developed a lower and GGBS mixes developed a higher elastic modulus than that of the control group (i.e., CSE). It can also be seen in Fig. 4.4 that an increase in the *FA%* and *GGBS%* from 50% to 90% resulted in significant (i.e., 57%) and slight (i.e., 4%) decreases in the elastic modulus of the FA and GGBS mixes, respectively. A larger decrease in the elastic modulus of FA mixes with an increase in the replacement ratio is in agreement with the results reported in the previous studies [15,17,22,52]. The influence of the replacement ratio on the elastic modulus of ternary mixes is also evident from Fig. 4.4, with mixes having a higher *SCM%* developing a lower elastic modulus at a given Ψ. Among all ternary mixes, FA23G47E mix had the highest elastic modulus, which was similar to that of the control mix (i.e., CSE), and FA60G30E mix developed the lowest elastic modulus. It is also seen that FA30G60E and FA45G45E mixes with 90% replacement level performed well with a reduction of only up to 14% in their elastic modulus compared to that of CSE. Although the trend of changes in the elastic modulus was similar to that seen in the compressive strength, the differences in the elastic moduli of different mixes were not as significant as those of the compressive strength. This is discussed further later where the experimental results were compared with the predictions of the existing design code expressions.

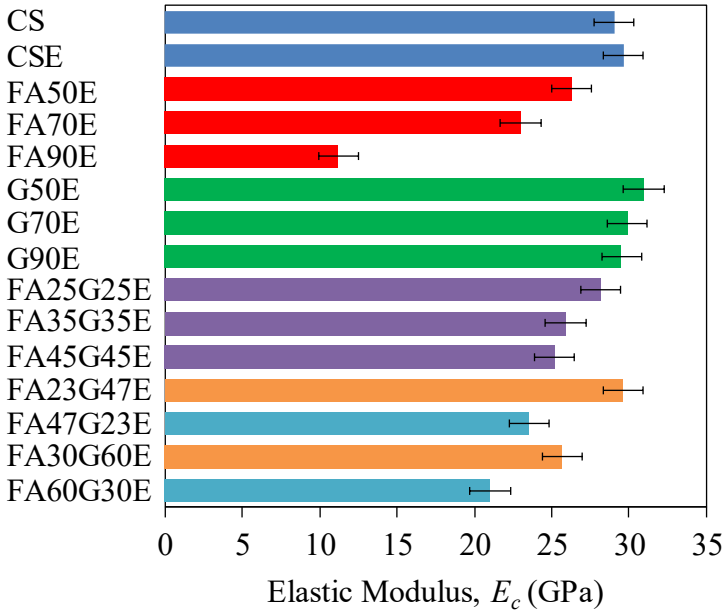

Figure 4.4. 28-day elastic modulus of FA and GGBS mixes

Flexural and splitting tensile strength

Figures 4.5(a) and 4.5(b), respectively, show the 28-day flexural and splitting tensile strength of conventional concretes and ternary mixes with Ψ of 1:1 and *SCM%* of 70% and 90%. As can be seen in the figures, CSE mix developed a slightly higher flexural strength and splitting tensile strength compared to those of CS mix. The figures also show that both the flexural and splitting tensile strength of ternary mixes were lower than that of the control CSE mix, which agree with the observations on the compressive strengths of these mixes. FA35G35E mix with *SCM%* of 70% developed 23% and 18%, and FA45G45E mix with *SCM%* of 90% developed 25% and 24% lower flexural and splitting tensile strength compared to that of CSE mix, respectively.

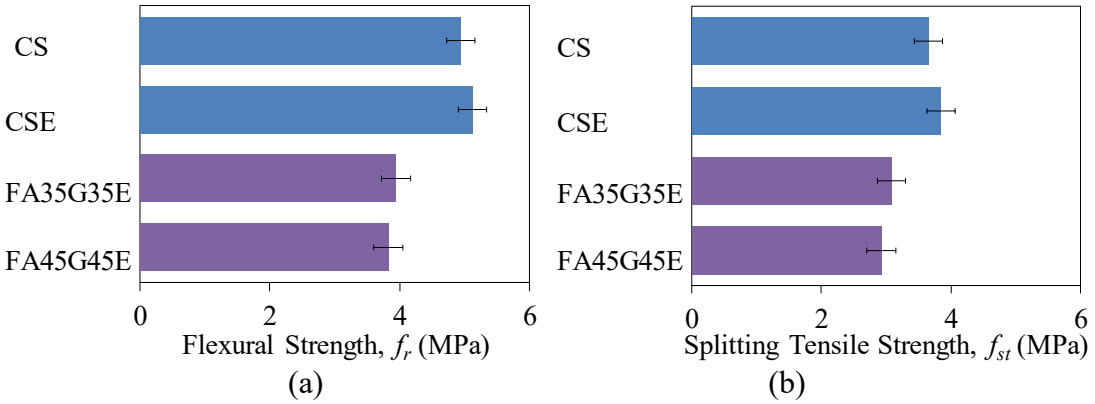

Figure 4.5. Comparison of 28-day: (a) flexural strength; (b) splitting tensile strength, of FA and GGBS mixes

Water absorption

Figure 4.6 shows the 28-day water absorption of the hardened concretes. As can be seen in the figure, CS mix developed a slightly higher water absorption compared to that of CSE mix. The water absorption of the mixes increased significantly with an increase in *FA%* (i.e., 109% increase over CSE mix with *FA%* of 90%) and decreased moderately with an increase in *GGBS%* (i.e., 33% decrease over CSE mix with *GGBS%* of 90%). This behaviour can be attributed to the fact that high porosity of the FA mixes allows water molecules to easily pass through the mix, whereas low capillary pore volume in the GGBS mixes results in a decrease in the water absorption of the mix [14,37,56]. However, the increase in the water absorption of FA mixes with up to 90% *FA%* was slightly lower than that reported previously (i.e., approximately 14%) [57]. Overall, the water absorption of ternary mixes was 9% to 27% lower than that of the control group (i.e., CSE) depending on *SCM%* and *Ψ*. As can be seen in Fig. 4.6, the water absorption decreased slightly with an increase in *SCM%* in mixes with *Ψ* of 1:1 and 1:2. However, in the case of mixes with *Ψ* of 2:1, the water absorption increased by 5% as *SCM%* increased from 70% to 90%. These results indicate that ternary mixes can be designed to develop reduced water absorption than conventional concrete even at replacement ratios as high as 90%, which is very positive for their durability performance.

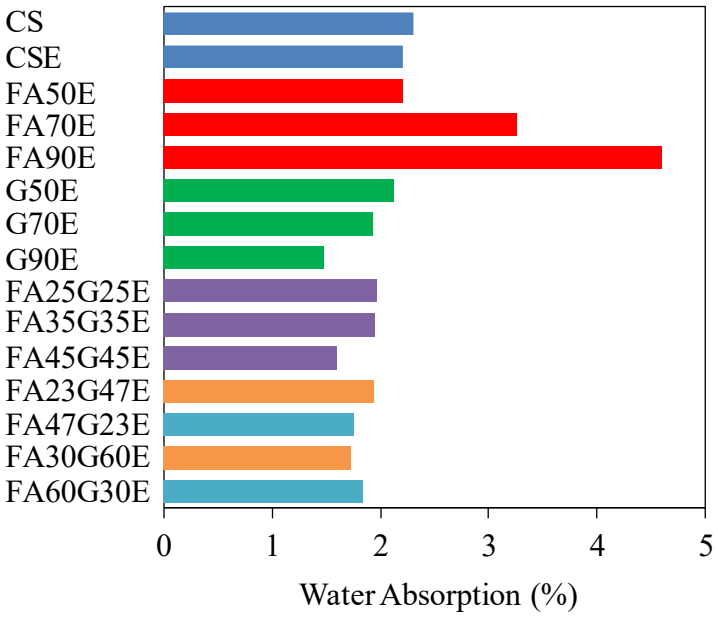

Figure 4.6. 28-day water absorption of hardened concretes

Comparison of the experimental results with design code expressions

A review of the existing design codes and standards [58-64] identified a number of models that were proposed to predict the elastic modulus (E_c), flexural strength (f_r), and splitting tensile strength (f_{st}) of concrete based on their compressive strength. These models are summarized in Table 4.6, and to investigate their applicability to FA and GGBS concretes, these expressions were used to predict E_c, f_r, and f_{st} of the specimens of the present study. Figure 4.7 shows the predictions of the code expressions together with the experimental results for 28-day E_c. The comparison of the results shows that the experimental results are in general agreement with the existing code predictions. A closer inspection of the results shows that EC-04 expression consistently overpredicts the E_c of all mixes. Likewise, JCI-08 expression slightly overpredicts the E_c, except for mixes FA70E, FA35G35E, FA30G60E, and FA60G30E. It is also seen that CSA A23.3-04 expression consistently underpredicts the E_c of all mixes. Likewise, NZS 3101 expression underpredicts the E_c, except for mix FA90E. It can be seen in Fig. 4.7 that ACI 318-11 and JSCE-07 expressions provide reasonably close predictions of the experimental results, except for mixes FA70E, FA35G35E, and FA30G60E. The differences in the prediction accuracies of the code expressions are attributed to the differences in the test databases used in their development. As can be seen in Fig. 4.7, among the existing code expressions, the closest predictions were provided by those by ACI 318-11, JSCE-07, and JCI-08. These three code expressions are able to provide relatively accurate predictions of the E_c of concrete containing FA and GGBS.

Table 4.6. Design equations recommended by existing codes and standards

Model	Elastic modulus (E_c) (GPa)	Flexural strength (f_r) (MPa)	Splitting tensile strength (f_{st}) (MPa)
AS 3600-09 [59]	$4.3 \times 10^{-5}(\rho_h)^{1.5}\sqrt{f_{cm}}$ when $f_{cm} \leq 40$ MPa $(\rho_h)^{1.5}\left(2.4\sqrt{f_{cm}} + 12\right) \times 10^{-5}$ when $40 < f_{cm} \leq 100$ MPa	$0.60\sqrt{f_c'}$	$0.40\sqrt{f_c'}$
ACI 318-11 [58]	$4.73\sqrt{f_c'}$	$0.62\sqrt{f_c'}$	$0.53\sqrt{f_c'}$
CSA A23.3-04 [60]	$4.5\sqrt{f_c'}$	$0.60\sqrt{f_c'}$	–
EC-04 [61]	$22(f_{cm}/10)^{0.3}$	$0.435{f_c'}^{2/3}$	$0.30(f_c')^{2/3}$
JSCE-07 [63]	$4.7\sqrt{f_c'}$	–	$0.44\sqrt{f_c'}$
JCI-08 [62]	$6.3{f_c'}^{0.45}$	–	$0.13(f_c')^{0.85}$
NZS 3101 [64]	$3.32(\sqrt{f_c'}) + 6.9$	$0.60\sqrt{f_c'}$	$0.44\sqrt{f_c'}$

f'_c, f_{cm}, f_r, and f_{st} are in MPa, E_c is in GPa, and ρ_h is in kg/m^3
f_{cm} and f'_c are the mean and characteristic compressive strength, respectively ($f'_c = f_{cm} - 8$ MPa, as per EC-04 [61]).

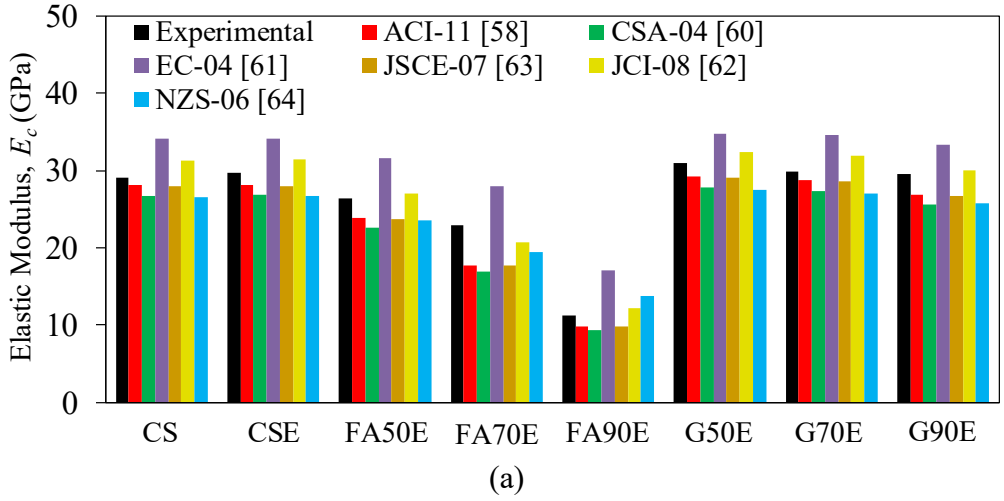

(a)

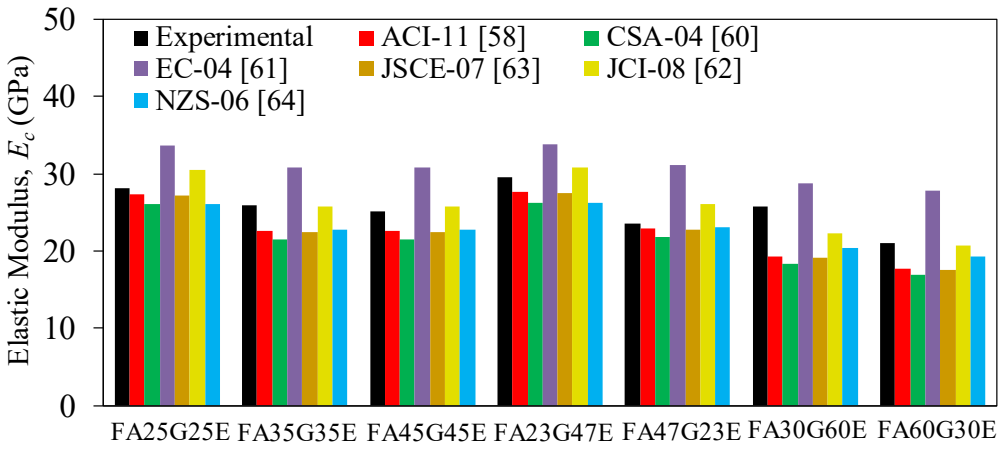

(b)

Figure 4.7. Comparisons of experimental values and design code predictions for elastic modulus of concretes with: a) FA or GGBS; b) FA & GGBS at 1:1, 1:2, and 2:1 ratios

Figures 4.8(a) and 4.8(b) show the predictions of the code expressions together with the experimental results for 28-day f_r and f_{st}, respectively. As can be seen in Fig. 4.8(a), the EC-04 expression provides relatively close predictions of the flexural strength of the ternary mixes, whereas the remaining models significantly underestimate the experimental results. It can be seen in Fig. 4.8(b) that both ACI 318-11 and EC-04 models slightly underestimate the splitting tensile strength of the ternary mixes, with the remaining models significantly underestimating the experimental results.

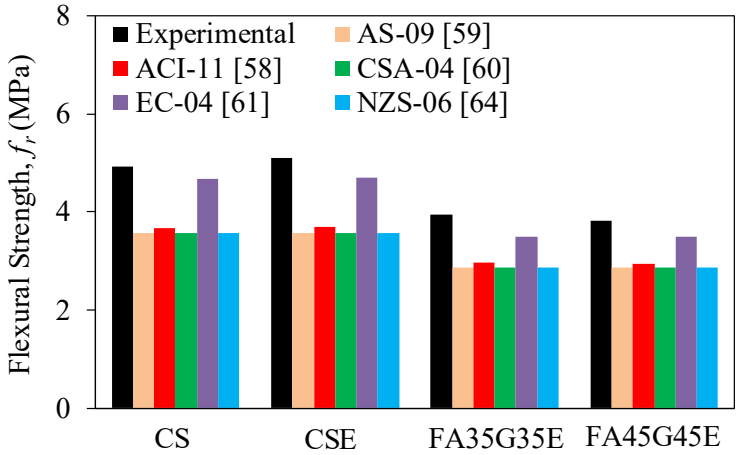

(a)

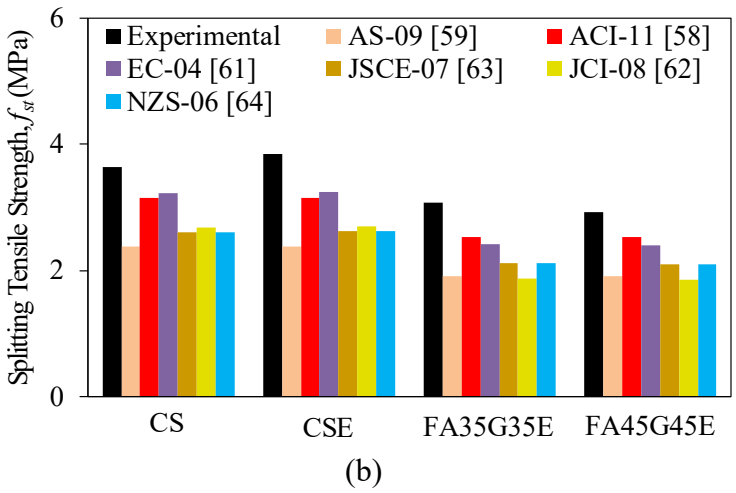

(b)

Figure 4.8. Comparisons of experimental values and design code predictions for: a) flexural strength; b) splitting tensile strength

CONCLUSIONS

This paper has presented the results of an experimental study on the properties of concretes containing different percentages of FA, GGBS, and their combinations as cement replacement. On the basis of the experimental results the following conclusions can be drawn:

1- Replacement of cement with 90% FA and GGBS, respectively, results in 58% increase and 51% decrease in the slump of the concrete. The workability of ternary mixes is higher than that of conventional concrete and it increases with an increase in *SCM%*.

2- GGBS mixes exhibit a similar 28- and 90-day compressive strength to that of conventional concrete, whereas FA mixes develop a lower strength that decreases with an increase in *FA%*. Ternary mixes with *SCM%* of 70% and Ψ of 1:2, and *SCM%* of 50% and Ψ of 1:1 develop similar 28- and 90-day compressive strength to conventional concrete.

3- FA and GGBS mixes, respectively, develop a lower and higher elastic modulus than that of conventional concrete. An increase in *FA%* and *GGBS%* from 50% to 90% results in a significant (i.e., 57%) and slight (i.e., 4%) decrease in the elastic modulus of concrete, respectively. In ternary mixes, the mix with *SCM%* of 70% and Ψ of 1:2 develops a similar elastic modulus to conventional concrete, and the elastic modulus of mixes with 90% *SCM%* and Ψ of 1:1 and 1:2 is only up to 14% lower than that of conventional concrete.

4- The flexural and splitting tensile strength of ternary mixes are lower than that of conventional concrete. Ternary mixes with *SCM%* of 90% and Ψ of 1:1 develop 25% lower flexural strength and 24% lower splitting tensile strength compared to those of conventional concrete.
5- FA and GGBS mixes, respectively, develop a higher and lower water absorption compared to that of conventional concrete. An increase in *FA%* and *GGBS%* up to 90%, respectively, results in a significant increase (i.e., up to 109%) and moderate decrease (i.e., up to 33%) in the water absorption compared to that of conventional concrete. Ternary mixes exhibit 9% to 27% lower water absorption is than that of conventional concrete depending on *SCM%* and Ψ.
6- The assessment results show that ACI 318-11, JSCE-07, and JCI-08 code expressions provide relatively accurate predictions of E_c of concrete containing FA and GGBS. EC-04 expression provides relatively close predictions of flexural strength of ternary mixes.

The findings of this study help better understand physical and mechanical behaviour of concrete containing high volume Class-F FA and GGBS. The experimental results show that properly designed mixes can develop properties that match those of conventional concrete. These findings are very promising as the high volume replacement of cement with FA and GGBS provides a highly attractive avenue to achieve resource sustainability in construction by reducing the environmental impact of both industrial by-products and conventional concrete. However, as FA and GGBS concretes exhibit different long-term hydration characteristics than those of conventional concretes, additional studies are recommended to investigate their time-dependent (e.g., drying shrinkage, creep) and long-term durability-related (e.g., acid and sulfate resistance, chloride penetration) properties.

ACKNOWLEDGEMENTS

The authors gratefully acknowledge the financial support from the National Natural Science Foundation of China through Grant No. 51650110495 and the University of Adelaide through a Research Excellence Grant awarded to the second author. The authors thank Messrs. Lim and Schiller for completing the tests reported in this paper as part of their Master's thesis and Messrs. Zheng and Gu for their assistance with the

analysis of the test results. The authors also thank Adelaide Brighton Cement Ltd. for their donation of the fly ash and ground granulated blast furnace slag used in this study.

REFERENCES

[1] Torgal FP, Ding Y, Miraldo S, Abdollahnejad Z, Labrincha JA. Are geopolymers more suitable than portland cement to produce high volume recycled aggregates HPC. *Construction and Building Materials*. 2012;36:1048-52.

[2] Mehta PK, Meryman H. Tools for reducing carbon emissions due to cement consumption. *Structure*. 2009;1(1):11-5.

[3] Huntzinger DN, Eatmon TD. A life-cycle assessment of cement manufacturing: comparing traditional process with alternative technologies. *Journal of Cleaner Production*. 2009;17(7):668–75.

[4] Turner LK, Collins FG. Carbon dioxide equivalent (CO2-e) emissions: A comparison between geopolymer and OPC cement concrete. *Construction and Building Materials*. 2013;43:125-30.

[5] Crossin E. The greenhouse gas implications of using ground granulated blast furnace slag as a cement substitute. *Journal of Cleaner Production*. 2015;95:101-8.

[6] Zhao H, Sun W, Wu X, Gao B. The properties of the self-compacting concrete with fly ash and ground granulated blast furnace slag mineral admixtures. *Journal of Cleaner Production.* 2015;95:66-74.

[7] Ahmaruzzaman M. A review on the utilization of fly ash. *Progress in Energy and Combustion Science*. 2010;36(3):327-63.

[8] Tsakiridis PE, Papadimitriou GD, Tsivilis S, Koroneos C. Utilization of steel slag for Portland cement clinker production. *Journal of Hazardous Materials*. 2008;152(2):805-11.

[9] Topcu IB. Physical and mechanical properties of concretes produced with waste concrete. *Cement and Concrete Research*. 1997;27(12):1817-23.

[10] Mo KH, Ling TC, Alengaram UJ, Yap SP, Yuen CW. Overview of supplementary cementitious materials usage in lightweight aggregate concrete. *Construction and Building Materials.* 2017;139:403-18.

[11] Bouzoubaa N, Zhang MH, Malhotra VM. Mechanical properties and durability of concrete made with high-volume fly ash blended cements using a coarse fly ash. *Cement and Concrete Research.* 2001;31(10):1393-402.

[12] Mehta PK. High-performance, high-volume fly ash concrete for sustainable development. *Proceedings of the international workshop on sustainable development and concrete technology* (pp. 3-14). Ames, IA, USA: Iowa State University, 2004.

[13] Song HW, Saraswathy V. Studies on the corrosion resistance of reinforced steel in concrete with ground granulated blast-furnace slag-an overview. *Journal of Hazardous Materials*. 2006;138(2):226-33.

[14] Atiş CD, Bilim C. Wet and dry cured compressive strength of concrete containing ground granulated blast-furnace slag. *Building and Environment*. 2007;42(8):3060-5.

[15] Siddique R. Performance characteristics of high-volume Class F fly ash concrete. *Cement and Concrete Research.* 2004;34(3):487-93.

[16] Crouch LK, Hewitt R, Byard B. High volume fly ash concrete. *World of Coal Ash (WOCA)*, 2007;1-14.

[17] Kayali O, Ahmed MS. Assessment of high volume replacement fly ash concrete–Concept of performance index. *Construction and Building Materials*. 2013;39:71-6.

[18] Chidiac SE, Panesar DK. Evolution of mechanical properties of concrete containing ground granulated blast furnace slag and effects on the scaling resistance test at 28 days. *Cement and Concrete Composites*. 2008;30(2):63-71.

[19] Bilim C, Atiş CD, Tanyildizi H, Karahan O. Predicting the compressive strength of ground granulated blast furnace slag concrete using artificial neural network. *Advances in Engineering Software.* 2009;40(5):334-40.

[20] Mo KH, Chin TS, Alengaram UJ, Jumaat MZ. Material and structural properties of waste-oil palm shell concrete incorporating ground granulated blast-furnace slag reinforced with low-volume steel fibres. *Journal of Cleaner Production*. 2016;133:414-26.

[21] Li G, Zhao X. Properties of concrete incorporating fly ash and ground granulated blast-furnace slag. *Cement and Concrete Composites*. 2003;25(3):293-9.

[22] Berndt ML. Properties of sustainable concrete containing fly ash, slag and recycled concrete aggregate. *Construction and Building Materials*. 2009;23(7):2606-13.

[23] Yijin L, Shiqiong Z, Jian Y, Yingli G. The effect of fly ash on the fluidity of cement paste, mortar, and concrete. *Proceedings of the International Workshop on Sustainable Development and Concrete Technology*, Beijing, 2004, pp. 339-345.

[24] Oner A, Akyuz S, Yildiz R. An experimental study on strength development of concrete containing fly ash and optimum usage of fly ash in concrete. *Cement and Concrete Research.* 2005;35:1165-71.

[25] Kuder K, Lehman D, Berman J, Hannesson G, Shogren R. Mechanical properties of self consolidating concrete blended with high volumes of fly ash and slag. *Construction and Building Materials.* 2012;34:285-95.

[26] Rivera F, Martínez P, Castro J, López M. Massive volume fly-ash concrete: A more sustainable material with fly ash replacing cement and aggregates. *Cement and Concrete Composites.* 2015;63:104-12.

[27] Bouikni A, Swamy RN, Bali A. Durability properties of concrete containing 50% and 65% slag. *Construction and Building Materials*. 2009;23(8):2836-45.

[28] Elchalakani M, Aly T, Abu-Aisheh E. Sustainable concrete with high volume GGBFS to build Masdar City in the UAE. *CASE Studies in Construction Materials*. 2014;1:10-24.

[29] Güneyisi E, Gesoğlu M. A study on durability properties of high-performance concretes incorporating high replacement levels of slag. *Materials and Structures*. 2008;41(3):479-93.

[30] Richardson DN. *Strength and durability characteristics of a 70% ground granulated blast furnace slag (GGBFS) concrete mix*. Organizational Results Research Report, Missouri Department of Transportation, 2006.

[31] Sivasundaram V, Malhotra VM. Properties of concrete incorporating low quantity of cement and high volumes of ground granulated slag. *Materials Journal*. 1992;89(6):554-63.

[32] Tomisawa T, Fujll M. Effects of High Fineness and Large Amounts of Ground Granulated Blast Furnace Slag on Properties and Microstructure of Slag Cements. *Special Publication*. 1995;153:951-74.

[33] Wang HY, Lin CC. A study of fresh and engineering properties of self-compacting high slag concrete (SCHSC). *Construction and Building Materials*. 2013;42:132-6.

[34] Yazıcı H, Yardımcı MY, Yiğiter H, Aydın S, Türkel S. Mechanical properties of reactive powder concrete containing high volumes of ground granulated blast furnace slag. *Cement and Concrete Composites*. 2010;32(8):639-48.

[35] Rashad AM. An investigation of high-volume fly ash concrete blended with slag subjected to elevated temperatures. *Journal of Cleaner Production*. 2015;93:47-55.

[36] Kungskulniti N, Thaisuchart N, Kongmuang U, Phornpimolthape C, Charoenca N. Application of bituminous fly ash for partial replacement of cement in producing hollow concrete blocks. *Asia Journal of Public Health*. 2011;2(3).

[37] Mukherjee S, Mandal S, Adhikari UB. Study on the physical and mechanical property of ordinary portland cement and fly ash paste. *International Journal of Civil and Structural Engineering.* 2012;2(3):731-6.

[38] Sakai K, Watanabe H, Suzuki M, Hamazaki K. Properties of granulated blast-furnace slag cement concrete. *Special Publication*. 1992;132:1367-84.

[39] ASTM C192/C192M-07. *Standard Practice for Making and Curing Concrete Test Specimens in the Laboratory*. American society for testing and materials. West Conshohocken, PA, USA: ASTM International, 2007.

[40] ASTM C143/C143M-12. *Standard Test Method for Slump of Hydraulic Cement Concrete.* American society for testing and materials. West Conshohocken, PA, USA: ASTM International, 2007.

[41] ASTM C138/C138M-16a. *Standard Test Method for Density (Unit Weight), Yield, and Air Content (Gravimetric) of Concrete*. American society for testing and materials. West Conshohocken, PA, USA: ASTM International, 2016.

[42] ASTM C642 – 13. *Standard Test Method for Density, Absorption, and Voids in Hardened Concrete*. American society for testing and materials. West Conshohocken, PA, USA: ASTM International. 2013.

[43] ASTM C39 / C39M-15. *Standard Test Method for Compressive Strength of Cylindrical Concrete Specimens.* American society for testing and materials. West Conshohocken, PA, USA: ASTM International, 2015.

[44] ASTM C469 / C469M-14. *Standard Test Method for Static Modulus of Elasticity and Poisson's Ratio of Concrete in Compression*. American society for testing and materials. West Conshohocken, PA, USA: ASTM International, 2015.

[45]ASTM C496/C496M-11. *Standard Test Method for Splitting Tensile Strength of Cylindrical Concrete Specimens*. American society for testing and materials. West Conshohocken, PA, USA: ASTM International, 2004.

[46] ASTM C78 / C78M-10. *Standard Test Method for Flexural Strength of Concrete (Using Simple Beam with Third-Point Loading).* American society for testing and materials. West Conshohocken, PA, USA: ASTM International, 2010.

[47] Sho KH, Park SJ, Kim YJ, Lee GC, Kim KM. Utilization of separator bag filter dust for high early strength cement production. *Construction and Building Materials*. 2011;25(5):2318-22.

[48] Jiang LH, Malhotra VM. Reduction in water demand of non-air-entrained concrete incorporating large volumes of fly ash. *Cement and Concrete Research.* 2000;30(11):1785-9.

[49] Malhotra VM, Mehta PK. High-performance, high-volume fly ash concrete. *Concrete International.* 2002;24(7):30-34.

[50] Bai Y, Ibrahim R, Basheer PM. Properties of lightweight concrete manufactured with fly ash, furnace bottom ash, and Lytag. *International workshop on sustainable development and concrete technology*, 2004, pp. 77-88.

[51] Collins FG, Sanjayan JG. Workability and mechanical properties of alkali activated slag concrete. *Cement and Concrete Research*. 1999;29(3):455-8.

[52] Siddique R, Kaur D. Properties of concrete containing ground granulated blast furnace slag (GGBFS) at elevated temperatures. *Journal of Advanced Research*. 2012;3(1):45-51.

[53] Siddique R. Effect of fine aggregate replacement with Class F fly ash on the mechanical properties of concrete. *Cement and Concrete Research*. 2003;33(4):539-47.

[54] Mohd Nasir NA, Abd Aziz FNA, Safiee NA. Hydration of the combinations of ground granulated blast furnace slag cements. *Australian Journal of Basic and Applied Sciences*. 2014;8(1):392-6.

[55] Oner A, Akyuz S. An experimental study on optimum usage of GGBS for the compressive strength of concrete. *Cement and Concrete Composites*. 2007;29(6):505-14.

[56] Dinakar P, Babu KG, Santhanam M. Durability properties of high volume fly ash self compacting concretes. *Cement and Concrete Composites*. 2008;30(10):880-6.

[57] Khatib JM. Performance of self-compacting concrete containing fly ash. *Construction and Building Materials.* 2008;22(9):1963-71.

[58] ACI 318-11. ACI Committee, *American Concrete Institute & International Organization for Standardization*. Building code requirements for structural concrete and commentary. American Concrete Institute, 2011.

[59] AS 3600. *Concrete Structures*. Standards Australia, Sydney, 2009.

[60] CSA. *Design of Concrete Structures* [electronic Resource]. Mississauga, Ont.: Canadian Standard Association, 2004.

[61] EC-04. B.S. Institution, *Eurocode 2: Design of Concrete Structures: Part 1-1: General Rules and Rules for Buildings*, British Standards Institution, 2004.

[62] J.C.I. *Guidelines for Control of Cracking of Mass Concrete*, Japan Concrete Institute, 2008.

[63] J.S.C.E. Engineers, *Standard Specification for Concrete Structure*, Japanese Society of Civil Engineering No. 15, Tokyo, 2007.

[64] N.Z. Standard. *Concrete Structures*. Standard: NZS 3101, 2006.

Statement of Authorship

Title of Paper	Ambient-cured geopolymer mortars prepared with waste-based sands: mechanical and durability-related properties and microstructure
Publication Status	☑ Published ☐ Accepted for Publication ☐ Submitted for Publication ☐ Unpublished and Unsubmitted work written in manuscript style
Publication Details	Gholampour A, Ho VD, Ozbakkaloglu T. Ambient-cured geopolymer mortars prepared with waste-based sands: mechanical and durability-related properties and microstructure. *Composites Part B*. 2019;160:519-34.

Principal Author

Name of Principal Author (Candidate)	Aliakbar Gholampour		
Contribution to the Paper	Literature review, analysis of test results, and preparation of the manuscript.		
Overall percentage (%)	70%		
Certification:	This paper reports on original research I conducted during the period of my Higher Degree by Research candidature and is not subject to any obligations or contractual agreements with a third party that would constrain its inclusion in this thesis. I am the primary author of this paper.		
Signature		Date	31/01/2019

Co-Author Contributions

By signing the Statement of Authorship, each author certifies that:

i. the candidate's stated contribution to the publication is accurate (as detailed above);

ii. permission is granted for the candidate in include the publication in the thesis; and

iii. the sum of all co-author contributions is equal to 100% less the candidate's stated contribution.

Name of Co-Author	Van Dac Ho		
Contribution to the Paper	Analysis and preparation of the manuscript.		
Signature		Date	31/01/2019

Name of Co-Author	Togay Ozbakkaloglu		
Contribution to the Paper	Research supervision and review of manuscript.		
Signature		Date	31/01/2019

Please cut and paste additional co-author panels here as required.

Ambient-cured geopolymer mortars prepared with waste-based sands: mechanical and durability-related properties and microstructure

ABSTRACT

In recent years, the use of industrial by-products and waste-based materials in the construction industry has received significant attention to develop eco-friendly and greener construction materials with the aim of reducing the impact of construction industry on the environment. The development of new concretes where cement is replaced with industrial by-products, such as ground granulated blast furnace slag (GGBS) and fly ash (FA), and natural sand (NS) is replaced with waste-based sands, such as lead smelter slag (LSS) and glass sand (GS), would lead to enormous environmental and health benefits by enabling the use of abundant wastes, reducing the extraction of non-renewable natural resources, and reducing the CO_2 emissions associated with concrete production. This paper presents an experimental study on the properties of geopolymer mortars prepared with FA/GGBS, LSS, and GS under ambient curing condition. A total of 12 batches of geopolymer mortars were manufactured and experimental tests were conducted to determine the flowability, hardened density, compressive strength, direct tensile strength, water absorption, and drying shrinkage of each batch together with the alkali-silica reaction (ASR) expansion of batches containing GS. Microstructural analysis was undertaken to describe the reasons for the obtained experimental results. The results show that the compressive and tensile strength of geopolymer mortars increase with an increase in the amount of GGBS. The results also show that an increase in the GGBS amount leads to a decrease in the water absorption of geopolymer mortars. Owing to the lower void amount at the binder-sand interaction zones, LSS- and GS-based geopolymer mortars containing up to 50% GGBS exhibit superior mechanical properties compared to those of their NS-based counterparts. These highly promising findings suggest that the full replacement of NS by LSS and GS can provide an attractive avenue to reduce the environmental impact of abundant waste products and conserve non-renewable natural resources.

KEYWORDS: Geopolymer mortars; Ground granulated blast furnace slag (GGBS); Fly ash; Lead smelter slag; Glass sand; Mechanical properties; Shrinkage; Microstructure.

INTRODUCTION

Cementitious materials are by far the most commonly used construction materials on earth [1]. The production of ordinary Portland cement (OPC), a core component of cementitious materials, releases a significant amount of greenhouse gases (essentially CO_2) into the atmosphere. As reported in Ref. [2], producing one ton of OPC generates approximately one ton of CO_2. It was also reported that approximately 1.35 billion tons of CO_2 annually produced from the production of OPC, which accounts for ~5–7% of the CO_2 emissions globally [3]. Therefore, in an effort to reduce emissions of CO_2 associated with the cement and concrete industry it is crucial to identify alternative materials that can replace OPC to produce a green concrete. Meanwhile, the high demand for natural river sand as fine aggregate in the construction industry has led to its over-exploitation, which results in harmful environmental issues such as depletion of non-renewable natural sand and negative effects on the ecosystem [4, 5]. Therefore, finding an alternative material to river sand has also become imperative.

The use of waste materials as binder and fine aggregate in the concrete is a viable strategy to develop an eco-friendly construction material that contributes toward cleaner production practices. Waste materials from industrial by-products, e.g. ground granulated blast furnace slag (GGBS) and fly ash (FA), can be considered as OPC replacement to reduce the negative environmental impact of OPC [6]. As was reported previously, the annual worldwide generation of GGBS and FA is approximately 530 million [7] and 750 million tons [8], respectively. However, it is believed that only 65% [9] and 25% [10] of the total GGBS and FA generated are currently being used, respectively. Furthermore, the use of waste-based sands such as glass sand (GS) [11, 12] and lead smelter slag (LSS) [13, 14] is currently being considered as a solution against the depletion of natural sand (NS), which has already become a major issue in a number of rapidly growing cities across the world

(e.g. Singapore; Shezhen, China). Existing studies have shown that GS and LSS, abundant waste products that are currently being landfilled, exhibit properties that make them suitable for use in structural concretes. It was reported that the global generation of waste glass was 130 million tons annually [15]. Disposal of a large amount of waste glass in landfill is costly and results in the depletion of the landfill space [16]. As reported in Ref. [17], the worldwide generation of the lead slag was approximately 3.9 million tons in 2009, and each ton generated 100 to 350 kg of LSS, only 15% of which was recycled. Therefore, there is significant potential for GS and LSS to be used as sand replacement in concrete for achieving resource sustainability in the construction industry while reducing the environmental impact of both abundant waste products and concrete. As the first systematic study on the topic, the current study examined the use of these materials in geopolymers.

In recent years, geopolymer, a new type of environmentally friendly material in which the OPC is replaced with alkali-activated binders, has received significant research attention. The production of geopolymers happens through the geopolymerization process by chemical reactions between materials with high aluminosilicate constituents and alkali activators [18]. Several researchers have investigated the properties of geopolymer mortars (e.g. [19-25]). As has been demonstrated in previous studies, geopolymer-based materials exhibit highly desirable mechanical and durability properties that are comparable to or better than those of their OPC-based counterparts [26, 27]. However, most of the existing studies have dealt with geopolymers cured under high temperatures (i.e. over 40°C) and only a few studies focused on ambient-cured geopolymers [17, 28-32]. A major challenge related to the use of FA in ambient-cured geopolymers is that they develop low strengths under such curing conditions. Owing to the relatively high calcium amount in GGBS, its addition to an ambient-cured FA-based geopolymer results in significant improvements in the mechanical properties and microstructure of the geopolymer [33]. To date, no study has been reported on the properties of geopolymer mortars containing GS or FA/GGBS-based geopolymer mortars containing LSS. Therefore, new experimental studies are needed to evaluate the properties of FA/GGBS-based geopolymer mortars containing LSS and GS.

The first experimental study on the properties of FA/GGBS-based geopolymer mortars containing LSS and GS is presented in this paper. A summary of the experimental program is first given. Test results and a detailed discussion on them are then presented, followed by the microstructural analysis of different mixes. The promising technology used in this study has a significant potential for contributing toward a green construction industry through i) conserving non-renewable natural resources, ii) reducing the large CO_2 footprint associated with the use of OPC, and iii) eliminating the negative impact of industrial by-product disposal on the environment.

TESTING PROGRAM

Materials

Ground granulated blast furnace slag (GGBS) and Fly ash (FA)

Ground granulated blast furnace slag (GGBS) and class-F fly ash (FA) with the chemical composition shown in Table 5.1 were provided by Adelaide Brighton Cement Ltd. GGBS was a by-product from Birkenhead Works and FA was a by-product from Leigh Creek Coal in South Australia.

Table 5.1. Chemical composition of cementitious materials and sands

Compounds	Fly ash (%)	Ground granulated blast furnace slag (%)	Glass sand (%)	Lead smelter slag (%)
SiO_2	55.38	33.10	99.10	21.39
Al_2O_3	28.14	13.33	0.50	3.56
Fe_2O_3	3.31	0.69	0.13	28.10
CaO	3.45	42.83	0.01	23.11
MgO	1.85	5.57	0.03	5.44
Na_2O	2.30	0.27	–	0.27
K_2O	1.39	0.31	0.06	0.26
SO_3	0.32	1.81	–	–
P_2O_5	0.78	0.01	–	–
TiO_2	–	–	0.07	0.25
ZnO	–	–	–	9.47
PbO	–	–	–	4.06
LOI	3.08	2.08	0.10	4.09

Natural sand (NS)

River sand with a 2.13-mm maximum particle size, sourced from McLaren Vale Quarry in Fleurieu Peninsula, was used as the natural sand (NS). The particle size distribution and physical properties of NS are shown in Fig. 5.1 and Table 5.2, respectively.

Table 5.2. Properties of fine aggregates

Aggregate type	Maximum size (mm)	Specific gravity (SSD)	Water absorption (%)	Fineness modulus
NS	2.13	2.63	0.4	2.56
LSS	1.94	3.30	0.6	2.51
GS	1.91	2.49	0.2	2.48

NS: natural sand
LSS: lead smelter slag
GS: glass sand

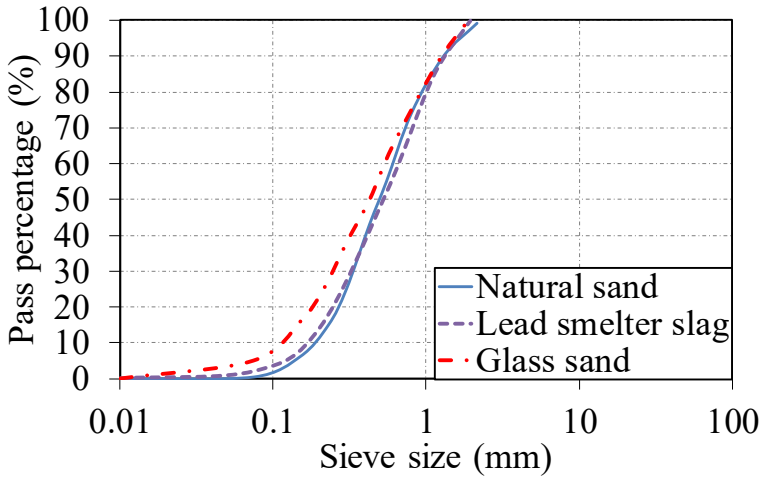

Figure 5.1. Sieving test results of fine aggregates: Particle Size Distribution (PSD)

Glass sand (GS)

Glass sand (GS) with a 1.91-mm maximum particle size was sourced from Glass Recovery Service in Victoria, and contained more than 99% silica as well as mineral and organic impurities, as supplied by the company. The particle size distribution, chemical composition, and physical properties of GS are shown in Fig. 5.1 and Tables 5.1 and 5.2, respectively.

Lead smelter slag (LSS)

Granulated lead smelter slag (LSS) with a 1.94-mm maximum particle size was obtained from Port Pirie in South Australia. The particle size distribution, chemical composition, and physical properties of LSS are shown in Fig. 5.1 and Tables 5.1 and 5.2, respectively. X-ray powder diffraction (XRD) analysis of LSS is shown in Fig. 5.2.

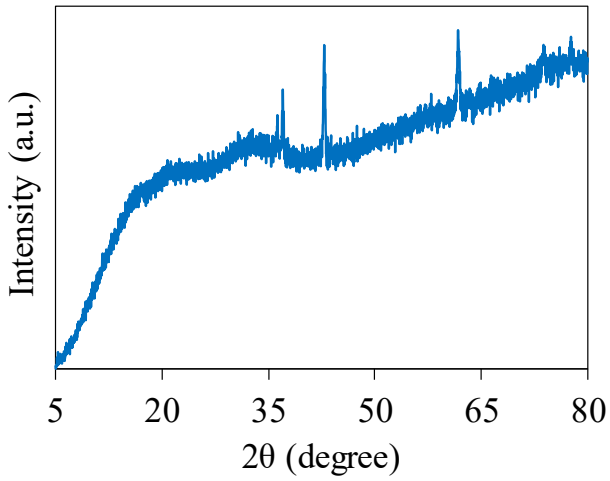

Figure 5.2. XRD pattern of LSS

Alkaline activator solution

The alkaline activator used in this study consisted of sodium hydroxide (NaOH) and sodium silicate (Na_2SiO_3) solutions that were premixed by a local supplier. The ratio of Na_2SiO_3 to NaOH in the alkaline activator solution was 2.5 by weight. In all mixes, the NaOH solution was used at 12 M concentration, and silicon dioxide-to-sodium oxide ratio (SiO_2/Na_2O) of the Na_2SiO_3 solution was 3 by weight. Before the mixing of geopolymer materials, the alkaline activator solution was premixed and left to rest at ambient temperature for 24 hr. The alkaline activator was pre-heated to 30°C before it was added to the mix to avoid rapid setting of the mortar.

Test specimens

A total of 12 unique mixes of geopolymer mortars were prepared, including four batches containing 100% natural sand, four batches containing 100% lead smelter slag, and four batches containing 100% glass sand. Binders were prepared using 100% FA (as FA100 mixes), 80% FA and 20% GGBS (as FA80G20 mixes), 50% FA and 50% GGBS (as FA50G50 mixes), and 100% GGBS (as G100 mixes). These

mixes were proportioned with different effective alkaline liquid-to-binder (l_{eff}/b) ratios to achieve workable mixes. An l_{eff}/b ratio of 0.45, 0.55, 0.75, and 1 were used in FA100, FA80G20, FA50G50, and G100 mixes, respectively. The test parameters included the weight percentage of GGBS (*GGBS%*) and FA (*FA%*) in the mortar. The mix proportions of geopolymer mortars are shown in Table 5.3. The weights of sands (shown in Table 5.3) were determined based on their saturated-surface dry (SSD) specific gravity. Different tests including: flowability, compressive strength, direct tensile strength, water absorption, and drying shrinkage were conducted on all batches to investigate the fresh and hardened properties of mortars. Alkali-silica reaction (ASR) expansion test was also performed on batches containing GS. For compression tests, 50 mm cube samples were used in accordance with the ASTM standard C109/C109M-07 [34]. A typical dog-bone shaped sample with a test region width and depth of 25±0.5 mm was used according to the ASTM standard C307-03 [35] for direct tension tests. Cylinders with a diameter of 75 mm and height of 50 mm were used for water absorption tests according to ASTM standard C1585-13 [36]. For shrinkage and ASR expansion tests, 25×25×285 mm prisms were used based on the ASTM standard C596-09 [37] and C1260-14 [38], respectively. For each unique specimen configuration and each type of test, three nominally identical specimens were used.

Specimen preparation and testing

In the preparation of mortar mixes, fine aggregates were in the SSD condition. Initially, fine aggregates and binders were mixed for approximately three minutes and then the liquid component of the mix (i.e. premixed alkaline activator solution) was gradually added to the mixes. Wet mixing continued for approximately five minutes. To ensure proper placement of mortars in the molds, gentle external vibration was used throughout the pouring processes of all mixes. All mixing and pouring processes were performed under the ambient temperature. The specimens were cured in a fog room under ambient temperature of 23 ± 2 °C until the testing day after they were demolded.

Table 5.3. Mix proportions and physical properties of mixes

Mix	FA (kg/m^3)	GGBS (kg/m^3)	NS (kg/m^3)	LSS (kg/m^3)	GS (kg/m^3)	Na_2SiO_3 (kg/m^3)	NaOH (kg/m^3)	l_{eff}/b	Hardened density (kg/m^3)
FA100NS	570	–	1425	–	–	183	73	0.45	2190
FA100LS	570	–	–	1788	–	183	73	0.45	2437
FA100GS	570	–	–	–	1349	183	73	0.45	2073
FA80G20NS	444	111	1425	–	–	218	87	0.55	2213
FA80G20LS	444	111	–	1788	–	218	87	0.55	2476
FA80G20GS	444	111	–	–	1349	218	87	0.55	2099
FA50G50NS	265	265	1425	–	–	284	114	0.75	2241
FA50G50LS	265	265	–	1788	–	284	114	0.75	2513
FA50G50GS	265	265	–	–	1349	284	114	0.75	2121
G100NS	–	500	1425	–	–	357	143	1.00	2292
G100LS	–	500	–	1788	–	357	143	1.00	2556
G100GS	–	500	–	–	1349	357	143	1.00	2175

The flowability of fresh mortars was established by a flow test [39] conducted immediately after the mixing of the mortars. The compressive strength of hardened mortar specimens was determined at 7, 28, and 56 days of curing age using a universal testing machine. ASR tests were performed on the specimens at 7, 10, and 14 days of curing age. The drying shrinkage of specimens was also determined at 7, 14, 21, and 28 days of curing age. Water absorption and direct tension tests were conducted at the 28 days of curing. Scanning electron microscopy (SEM) by High Resolution Field Emission Scanning Electron Microscope (FEI Quanta 450) was used to analyze the morphology of fine aggregates and binders as well as the surface microstructure of geopolymer mixes. Energy dispersive X-ray (EDX) spectroscopy was performed using TEAM EDS with SDD Detector to analyze the constituent elements of the mortar mixes.

Figures 5.3 and 5.4 show the failure photos of geopolymers mortar specimens under axial compression and tension loading, respectively. It should be noted that the failure photos of 100% GGBS group specimens under compression loading were unavailable.

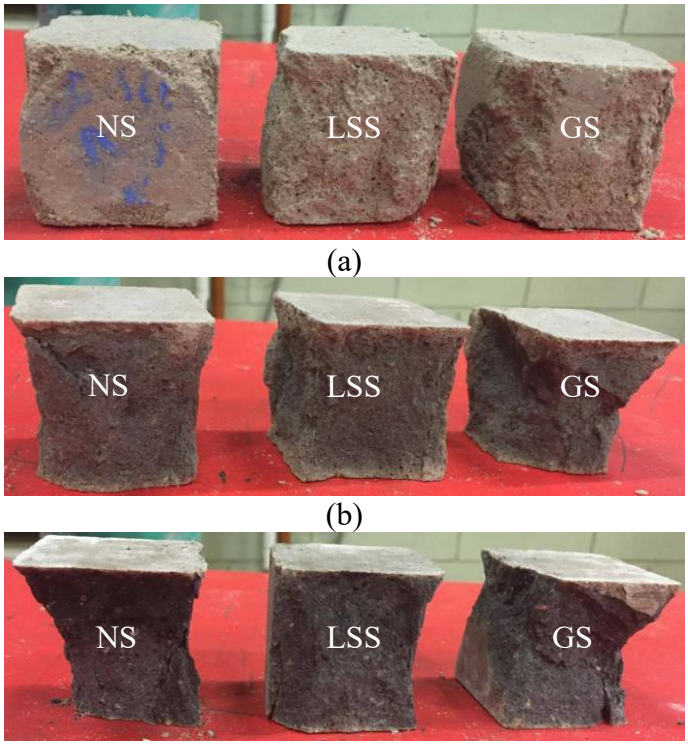

Figure 5.3. Failure mode of specimens under compression loading: (a) FA; (b) 80% FA and 20% GGBS; (c) 50% FA and 50% GGBS group

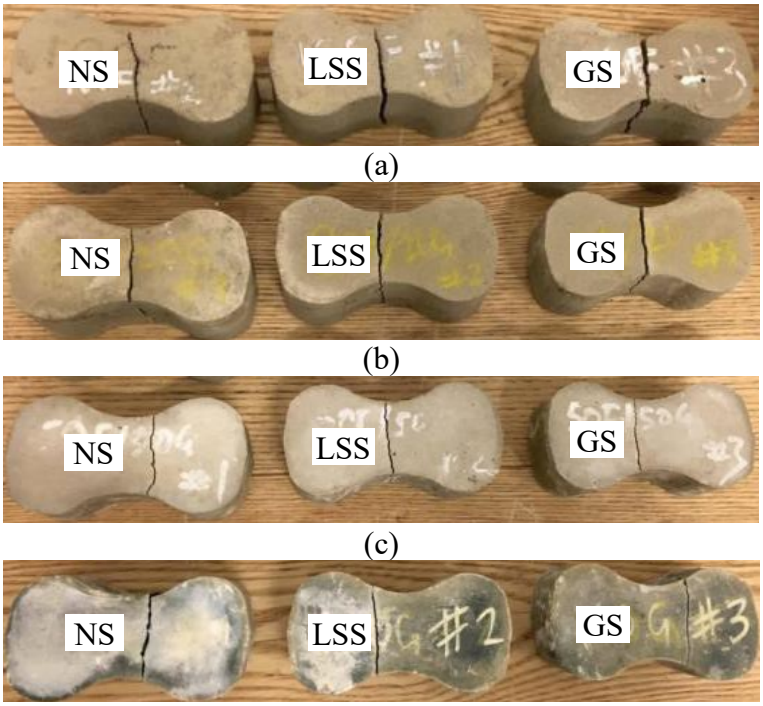

Figure 5.4. Failure mode of specimens under tension loading: (a) FA; (b) 80% FA and 20% GGBS; (c) 50% FA and 50% GGBS; (d) GGBS group

Geopolymer mixes shown in Table 5.3 are labelled as follows: the FA and G letters stand for FA and GGBS, respectively. The number after these letters indicates the weight percentage of each binder. The letters NS, LS, and GS stand for the natural sand, lead smelter slag, and glass sand group mixes, respectively. For example, FA80G20GS is a mortar mix prepared with GS and a blend of 80% FA and 20% GGBS.

RESULTS AND OBSERVATIONS

Flowability of fresh geopolymer mortar

Figure 5.5 shows the results of flowability tests for different mixes. It is evident from the figure that geopolymer mortars containing NS exhibited the highest flow for a given binder type, which was followed by mortars containing LSS and GS, respectively. The higher flowability of NS mixes than GS mixes is consistent with previous studies on conventional cement mortar [40, 41] and concrete [42, 43]. As discussed later in the section of SEM Analysis, the higher flowability of mixes containing NS is attributed to the lower angularity and slightly larger particle size

of NS compared to those of LSS and GS, resulting in a lower interparticle friction and formation of thicker water layers in NS mixes [44]. Furthermore, the lower flowability of GS mixes can be because of the slightly smaller particle size and higher angularity of GS compared to those of NS and LSS. As can also be seen in Fig. 5.5, the flowability of geopolymer mortars for a given sand type decreased with an increase in *GGBS%*. The NS, LSS, and GS mix with 100% GGBS developed 47%, 61%, and 47% lower flowability than that of 100% FA, respectively. Higher flowability of 100% FA mixes is in agreement with previous studies on geopolymer concretes containing FA and GGBS [45, 46]. The decrease in the flowability with an increase in *GGBS%* is because of the fact that GGBS reacts with the activator solution much more quickly than FA [7, 32].

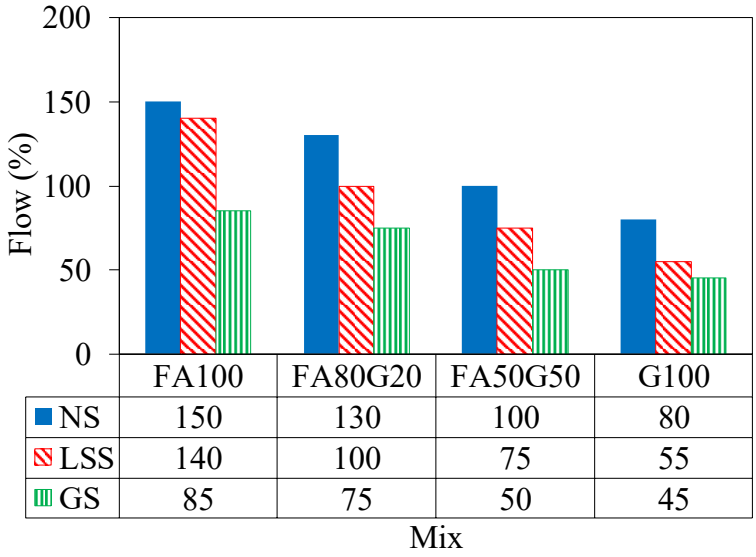

Figure 5.5. Flowability test results of different mixes

Density of hardened geopolymer mortar

The hardened density of different geopolymer mortars at 28 days of curing are presented in Table 5.3. It can be seen in the table that mixes containing LSS had the highest hardened density, which was followed by those containing NS and GS, respectively. This is because of the higher specific gravity of LSS than the NS and GS.

Mechanical properties of hardened geopolymer mortar

Compressive strength

Figures 5.6(a)-(d) show the compressive strength of geopolymer mortar mixes at 7, 28, and 56 days of curing age. As can be seen in the figures, the compressive strength of geopolymer mortars increased with an increase in *GGBS%* at all curing ages. As discussed in detail in the section of EDX Analysis, the lower strength of 100% FA mixes is because there is only one major hydration product of geopolymer gel (sodium aluminosilicate hydrate, N-A-S-H) in these mixes owing to the low content of calcium oxide (CaO) in FA. On the other hand, GGBS has a high amount of CaO, resulting in the creation of two hydration products of N-A-S-H and calcium silicate hydrate (C-S-H) [47, 48]. In NS mixes, the observed strength increases from 100% FA to 100% GGBS were 194%, 161%, and 139% at 7, 28, and 56 days, respectively, which were slightly higher than those seen in LSS (156%, 142%, and 120%, respectively) and GS (182%, 137%, and 131%, respectively) mixes. As discussed later in the section of EDX Analysis, this can be because NS mixes exhibited a lower content of hydration products (i.e. N-A-S-H) in the case of 100% FA, which resulted in a lower strength, but higher content of hydration products (i.e. C-S-H) in the case of 100% GGBS, which resulted in a higher strength increase in NS mixes compared to those of LSS and GS mixes. The higher percentage increase of strength from 100% FA mixes to 100% GGBS mixes at the early curing ages is because FA is not a hydraulic material at the ambient temperature and the formation of N-A-S-H takes longer, which results in the development of a very low strength in 100% FA mixes at early ages [33, 49]. When FA is replaced by GGBS, which has a significantly higher CaO content than that of FA, the C-S-H formation at early ages helps with the development of significantly higher strengths in mixes, which explains the significant strength increases between 100% FA and 100% GGBS mixes at early ages.

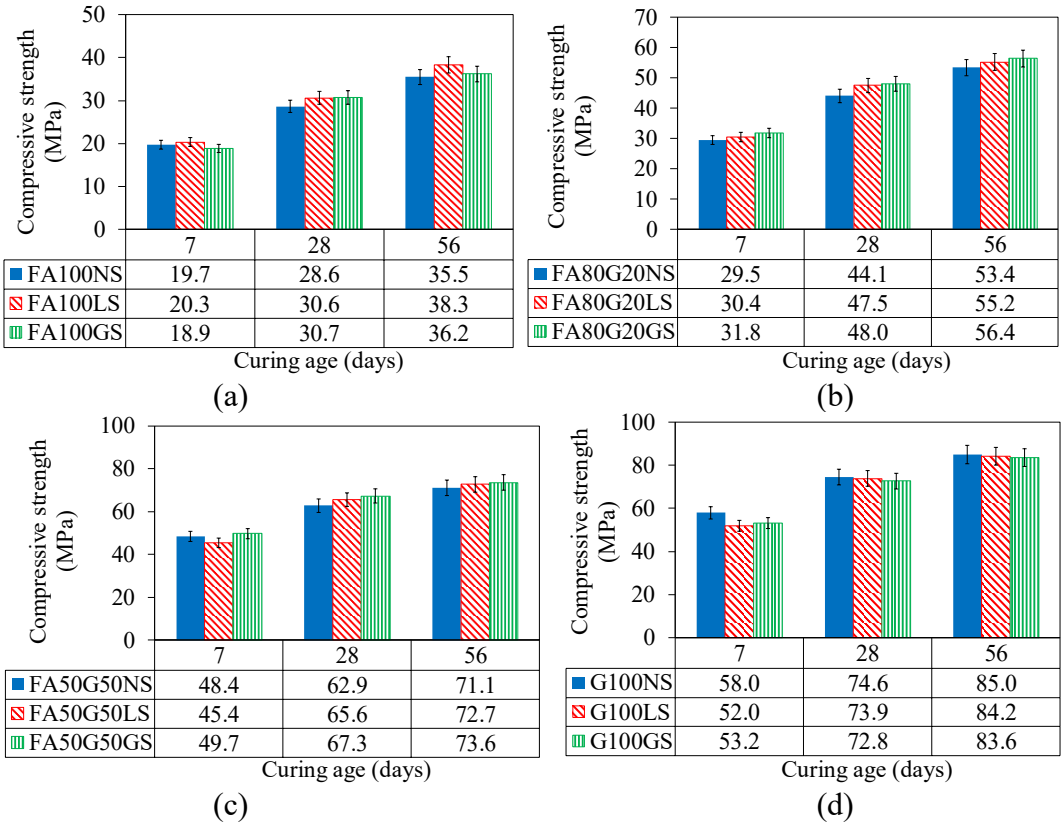

Figure 5.6. Variation of compressive strength of mixes with time: (a) FA; (b) 80% FA and 20% GGBS; (c) 50% FA and 50% GGBS; (d) GGBS group

Table 5.4 shows molar ratios of different geopolymer mortar mixes. As can be seen in the table, an increase in *GGBS%* resulted in an increase in sodium oxide/silicon dioxide (Na_2O/SiO_2), sodium oxide/aluminum oxide (Na_2O/Al_2O_3), SiO_2/Al_2O_3, CaO/SiO_2, and hydrogen oxide/sodium oxide (H_2O/Na_2O) molar ratios of geopolymer mortars. Figures 5.7(a) and (b) show the variation of the compressive strength with SiO_2/Al_2O_3 and CaO/SiO_2 molar ratios, respectively. SiO_2/Al_2O_3 and CaO/SiO_2 molar ratios have a close relationship with N-A-S-H and C-S-H hydration products. An increase in the SiO_2/Al_2O_3 and CaO/SiO_2 molar ratios leads to more compact N-A-S-H and C-S-H gels, which consequently results in a less porous microstructure [50-52]. As can be seen in the figures, the compressive strength of geopolymer mortars increased when *GGBS%* increased because of the increase in SiO_2/Al_2O_3 and CaO/SiO_2 molar ratios of the mixes.

Table 5.4. Molar ratios of geopolymer mortar mixes

Mix	Molar ratio				
	Na_2O/SiO_2	Na_2O/Al_2O_3	SiO_2/Al_2O_3	CaO/SiO_2	H_2O/Na_2O
FA100NS	0.134	0.522	3.89	0.057	11.2
FA100LS	0.134	0.522	3.89	0.057	11.2
FA100GS	0.134	0.522	3.89	0.057	11.2
FA80G20NS	0.156	0.654	4.19	0.195	12.3
FA80G20LS	0.156	0.654	4.19	0.195	12.3
FA80G20GS	0.156	0.654	4.19	0.195	12.3
FA50G50NS	0.202	0.983	4.87	0.417	13.5
FA50G50LS	0.202	0.983	4.87	0.417	13.5
FA50G50GS	0.202	0.983	4.87	0.417	13.5
G100NS	0.273	1.858	6.80	0.859	14.8
G100LS	0.273	1.858	6.80	0.859	14.8
G100GS	0.273	1.858	6.80	0.859	14.8

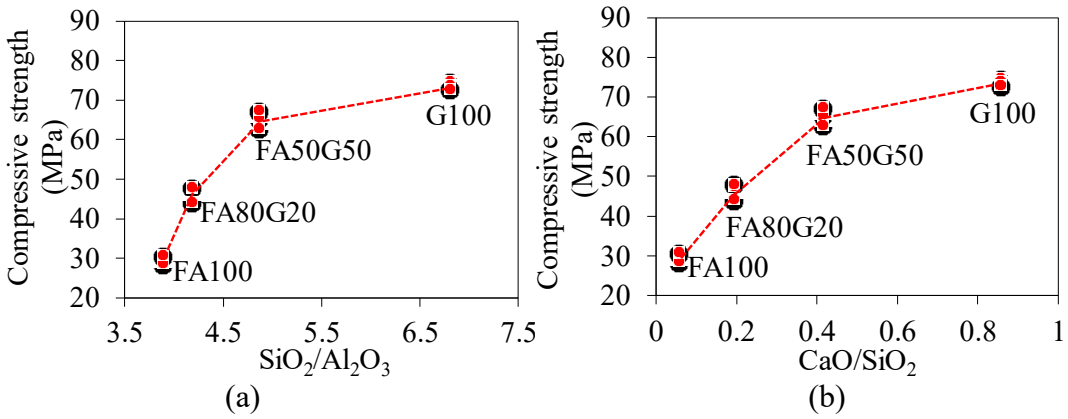

Figure 5.7. The variation of compressive strength with: (a) SiO_2/Al_2O_3; (b) CaO/SiO_2 ratio

It can be seen in Fig. 5.6 that, in all series of mixes, the compressive strength of mixes containing LSS and GS was generally close to those containing NS. However, mixes containing LSS tended to develop a slightly higher compressive strength than those containing NS and GS in the case of FA100, whereas mixes containing GS developed a slightly higher compressive strength than those containing NS and LSS in cases of FA80G20 and FA50G50. As can be seen in Fig. 5.6(a), the increase of the strength from mixes containing NS to that containing LSS had a tendency to increase with time from 3% at 7 days to 8% at 56 days in the case of 100% FA. As discussed later in the section of EDX Analysis, this observation can be because of the higher amount of hydration products (i.e. N-A-S-H and C-S-H) in LSS mixes

than those of NS mixes, which indicates that the LSS partly reacted with the activator solution. It can be seen in Fig. 5.6(c) that in the case of FA50G50 the compressive strength of mixes containing LSS was slightly lower (6%) at 7 days but slightly higher at 28 (4%) and 56 (2%) days than those containing NS. This can be because LSS mixes had a higher amount of N-A-S-H compared to that of NS mixes; consequently, because the formation of N-A-S-H takes longer LSS mixes developed a lower strength at 7 days but a higher strength at 28 and 56 days, which is discussed in detail in the section of EDX Analysis.

Direct tension strength

Figure 5.8 shows the tensile strengths of geopolymer mortar mixes at 28 days of curing age. As can be seen in the figure, for a given binder type, the replacement of NS with LSS and GS led to a slightly higher tensile strength, except for the mixes with 100% GGBS where mixes containing different sands developed nearly identical tensile strengths. This trend is consistent with that of compressive strength test results at 28 days of age. As can also be seen in Fig. 5.8, for a given sand type, the direct tensile strength of geopolymer mortars increased when *GGBS%* increased. The 100% GGBS mixes containing NS, LSS, and GS developed 40%, 33%, and 32% higher tensile strength than those of the corresponding 100% FA mixes, respectively. The lower increase in the tensile strength of GS and LSS mixes than that of NS mixes is in agreement with the compressive strength results.

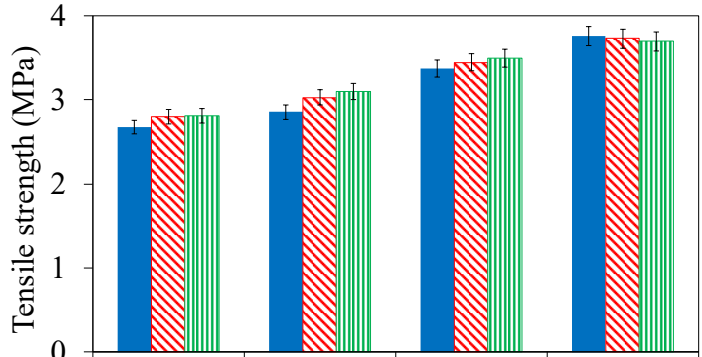

	FA100	FA80G20	FA50G50	G100
NS	2.68	2.86	3.38	3.76
LSS	2.80	3.03	3.45	3.73
GS	2.81	3.10	3.50	3.70

Figure 5.8. Direct tensile strength of different mixes at 28 days

Durability-related properties

Water absorption

Figure 5.9 shows the results of water absorption tests on hardened mixes after 28 days of curing. It can be seen in the figure that an increase in *GGBS%* resulted in a decrease in the water absorption of geopolymer mortars for a given sand type. 100% GGBS mixes containing NS, LSS, and GS developed 46%, 43%, and 53% lower water absorption than those of the corresponding 100% FA mixes, respectively. The lower water absorption of mixes with higher *GGBS%* is attributed to the higher content of hydration products in these mixes that consequently led to a more compact microstructure and a lower porosity, which is discussed in detail in the section of SEM Analysis.

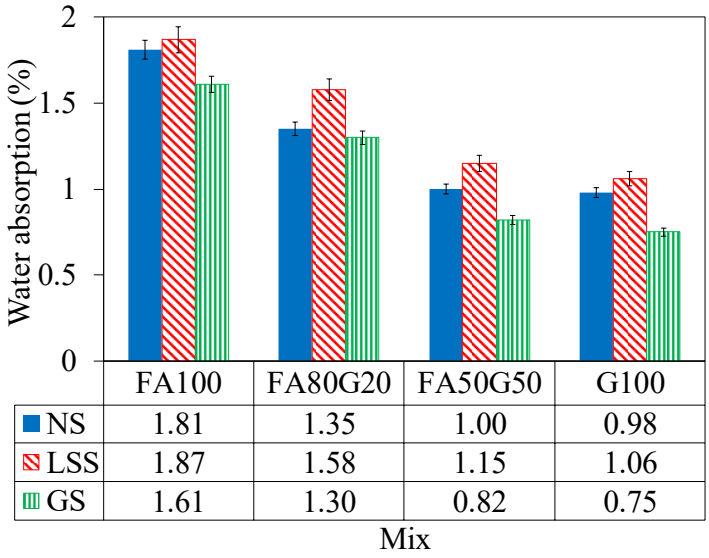

	FA100	FA80G20	FA50G50	G100
NS	1.81	1.35	1.00	0.98
LSS	1.87	1.58	1.15	1.06
GS	1.61	1.30	0.82	0.75

Figure 5.9. Water absorption of hardened mixes at 28 days

As can be seen in Fig. 5.9, for a given binder type, the replacement of NS with GS led to a lower water absorption and the replacement of NS with LSS led to a higher water absorption. This observation can be attributed to the lower water absorption of GS and higher water absorption of LSS (which has a honeycomb-like surface) compared to that of NS, as reported in Table 5.2.

Alkali-silica reaction (ASR) expansion

The expansion caused by alkali-silica reaction (ASR) in geopolymer mortars containing GS at 7, 10, and 14 days of curing age is shown in Fig. 5.10. It can be seen in the figure that the ASR expansion of all GS mixes was lower than the limit

value set up by ASTM C1260 [53]. For a given binder type, the ASR expansion of geopolymer mortars increased with an increase in the curing age. FA100, FA80G20, FA50G50, and G100 mixes at 14 days developed 800%, 550%, 440%, and 657% higher ASR expansion than those at 7 days, respectively. As can also be seen in Fig. 5.10, the ASR expansion of geopolymer mortars at a given curing age increased with an increase in *GGBS%*, which is in agreement with studies reported previously on the ASR behaviour of conventional OPC concrete [54], alkali-activated concrete [55], and OPC mortar [56]. This observation is because of the higher CaO content of GGBS compared to that of FA, which contributed to the formation of higher amount of hydroxyl (OH^-) ions from calcium hydroxide ($Ca(OH)_2$) in mixes with higher *GGBS%*, consequently leading to the generation of more alkali-silica expansion in the mix [57, 58].

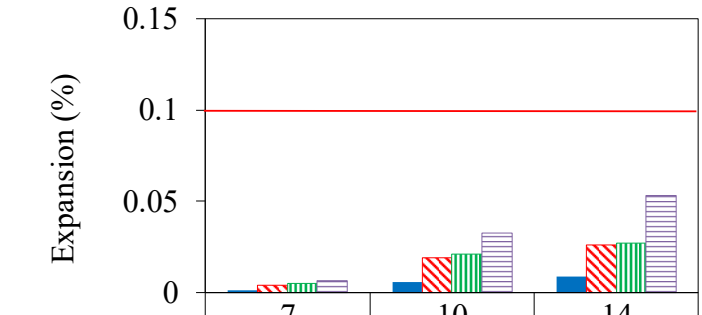

Figure 5.10. Variation of ASR (alkali–silica reaction) expansion of GS (glass sand) mixes with time. Red line shows the limit set up by ASTM C1260-14 at 14 days of curing age.

Drying shrinkage

Figure 5.11 shows the drying shrinkage of geopolymer mortar mixes at curing ages of 7, 14, 21, and 28 days. It should be noted that the drying shrinkage test results for G100NS and G100GS mixes were unavailable due to a problem encountered in their shrinkage measurement setup. It can be seen in Fig. 5.11 that, for a given sand type, the drying shrinkage of geopolymer mortars decreased with an increase in *GGBS%*, which is consistent with previous studies that investigated drying shrinkage of

ambient-cured geopolymer mortars [59] and concrete [60] containing NS. As discussed later in the section of Microstructural Analysis, this observation can be because of the higher amount of hydration products and microstructure compactness in mixes with higher *GGBS%*, resulting in a lower drying shrinkage. As can be seen in Fig. 5.11, for a given binder type, geopolymer mortars containing GS exhibited a higher drying shrinkage than those containing NS and LSS. This can be attributed to the lower permeability of GS than that of NS and LSS, resulting in the formation of more free water between sand particles in GS mixes than NS and LSS mixes that likely led to an increased moisture loss during the drying shrinkage process [61]. Figure 5.11 also revealed that, at a given curing age, LSS mixes had a lower shrinkage compared to that of the companion NS mixes. As discussed later in the section of SEM Analysis, this is because of the honeycomb surface of LSS, which allowed it to absorb and retain water thereby keeping the mortar in a moist condition during the drying shrinkage process.

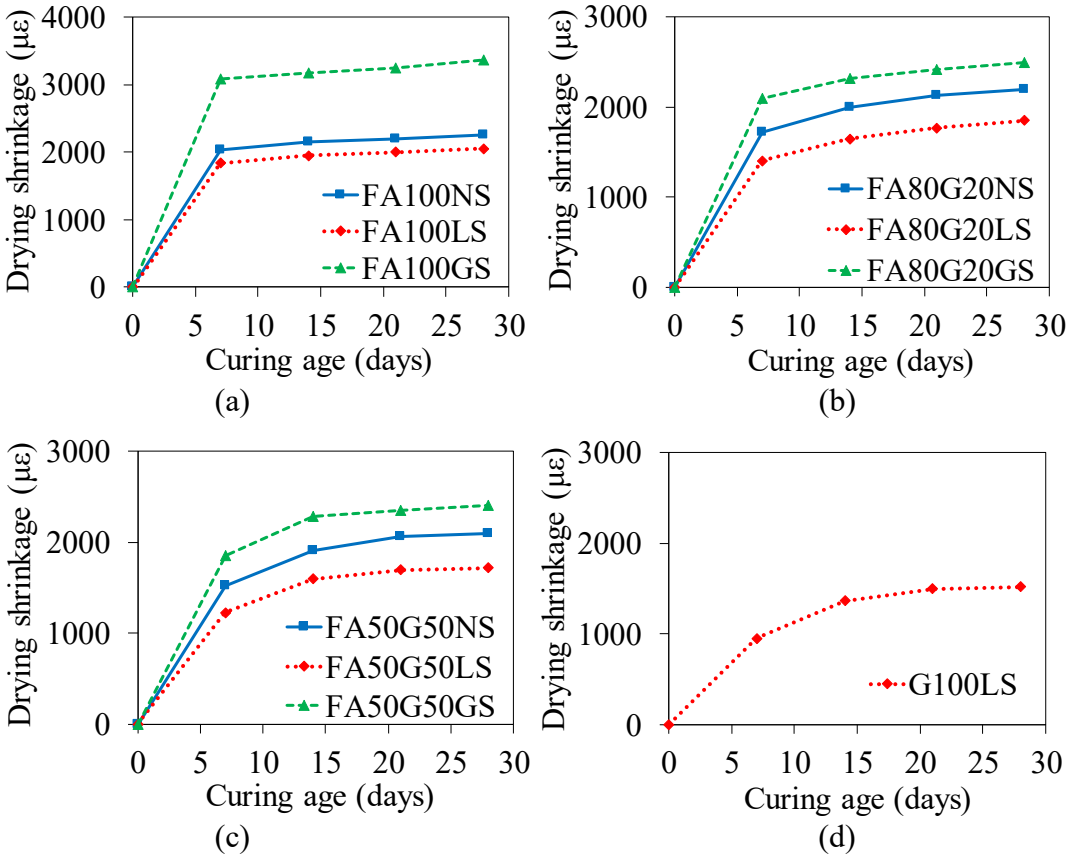

Figure 5.11. Variation of drying shrinkage of mixes with time: (a) FA; (b) 80% FA and 20% GGBS; (c) 50% FA and 50% GGBS; (d) GGBS group

It is worth noting that the paste (*l*+*b*)/sand ratio (*p/s*) of mixes were different (as shown in Table 5.3). As an increase in *p/s* ratio was accompanied with an increase in *GGBS%*, an increase in *p/s* ratio resulted in an increase in the strength but a decrease in the flowability, water absorption, and drying shrinkage of mortar mixes. This is attributed to the fact that GGBS particles react with solution more quickly than FA particles [7, 32] and mixes with higher *p/s* ratio had less void porosity and higher amount of hydration products than those with a lower *p/s* ratio, as discussed in the section of Microstructural Analysis. These results suggest that the effect of a change in *GGBS%* was more dominant than that of a change in *p/s* ratio.

Microstructural analysis of hardened geopolymer mortar

SEM analysis

Figures 5.12(a)-(e) show the SEM micrographs of the particle shapes of FA, GGBS, and the three fine aggregates. As can be seen in Figs. 5.12(a) and (b), FA particles were spherical in shape whereas GGBS particles had an irregular shape. As it is evident from Figs. 5.12(c)-(e), LSS had a more angular and irregular shape than NS and GS. Figures 5.13(a)-(c) show the SEM micrographs of the surface of NS, GS, and LSS, respectively. As can be seen in these images, the surface of GS had less voids than that of NS and LSS. It can also be seen in the figures that LSS had a honeycomb-like surface, which allows it to absorb water during the curing process. This resulted in a lower drying shrinkage in the LSS mixes owing to keeping the mortar in a moist condition during the shrinkage process (as discussed in the section of Drying Shrinkage).

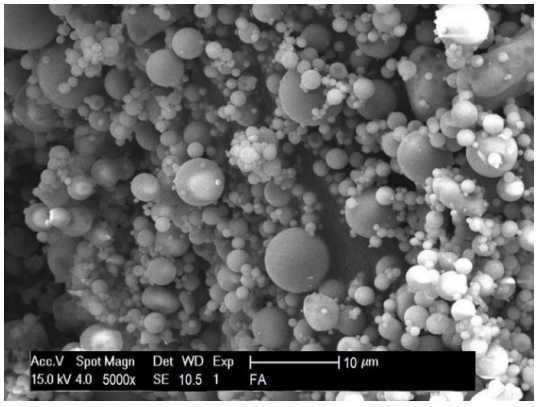

(a)

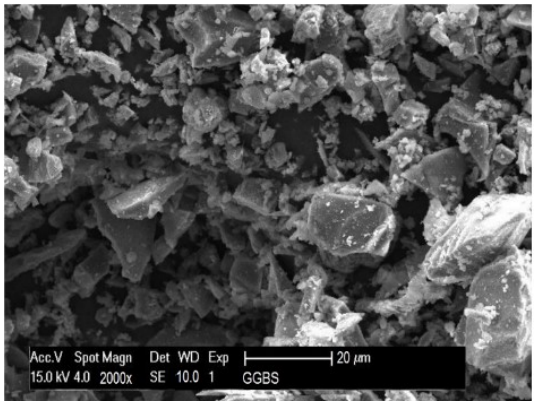

(b)

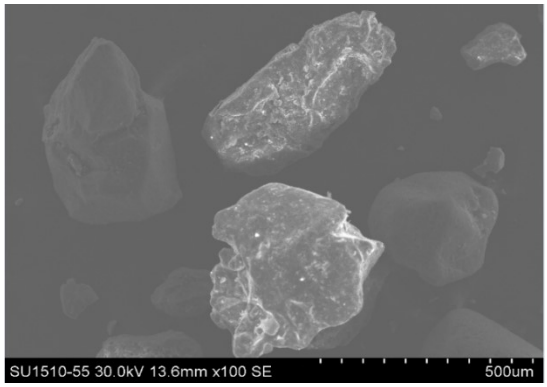

(c)

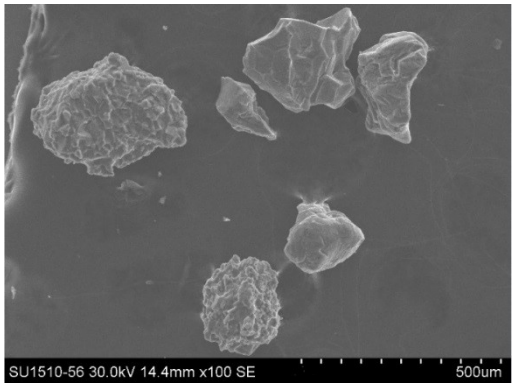

(d)

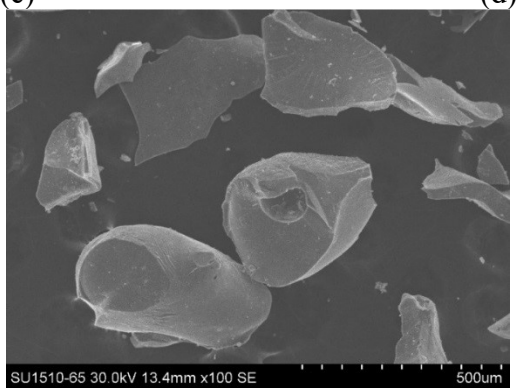

(e)

Figure 5.12. SEM micrographs of particle shapes of (a) FA, (b) GGBS, (c) NS, (d) GS, (e) LSS

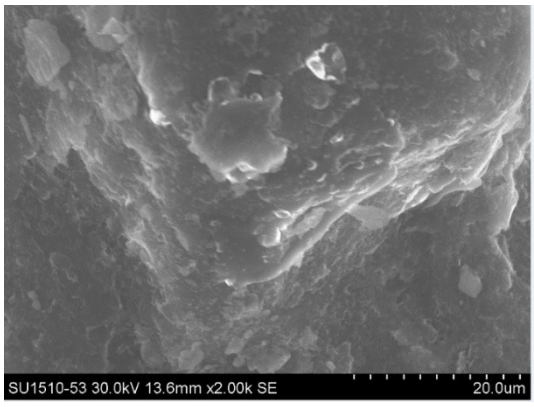

(a)

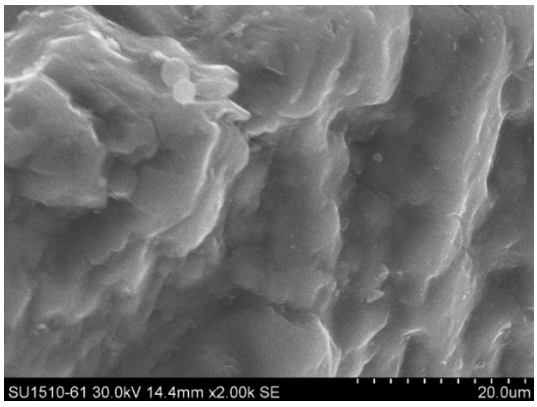

(b)

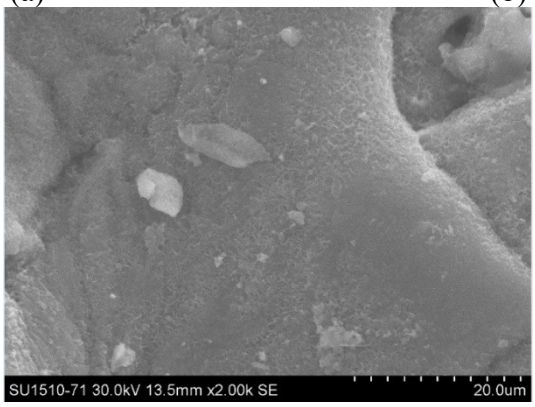

(c)

Figure 5.13. SEM micrographs of the surface of (a) NS, (b) GS, (c) LSS

Figures 5.14-5.17 show the SEM micrographs of the fresh-cut surface of different geopolymer mortars following the 28-day compression tests. It can be seen in the figures that FA100 and FA80G20 series mixes exhibited different microstructures compared to those of FA50G50 and G100 series mixes. It can be seen in Figs. 5.14-5.17 that FA50G50 and G100 series mixes had a larger number of capillary microcracks but exhibited a more compact microstructure than those of FA100 and FA80G20 series mixes. Presence of a larger number of capillary microcracks in the mix results in the evaporation of more free water during the drying shrinkage process, thereby leading to higher drying shrinkage [59, 62, 63]. On the other hand, formation of a higher amount of hydration products leads to a reduced amount of residual water in the structure of the mix, whose evaporation results in lower drying shrinkage [60, 64, 65]. Although FA50G50 and G100 series mixes had a higher amount of capillary microcracks than those of FA100 and FA80G20 series mixes, they exhibited a lower drying shrinkage. This is likely because of the increased amount of hydration products (as discussed in the section of EDX Analysis), and the resulting microstructure compactness appear to have had a more dominant positive effect on the shrinkage than the negative effect of the increased amount of capillary microcracks. Furthermore, the more compact microstructure of FA50G50 and G100 series mixes led to their higher mechanical properties compared to those of FA100 and FA80G20 series mixes, as discussed previously. As can be seen in Figs. 5.14 and 5.15, in FA100 and FA80G20 series mixes, geopolymer mortars containing LSS and GS exhibited a smaller amount of voids at the binder-sand interfacial transition zone (ITZ) than those containing NS, resulting in higher mechanical properties of LSS and GS mixes (as discussed in the section of Mechanical Properties). The SEM images in Fig. 5.16 show that, in FA50G50 series mixes, the microstructure of LSS and GS mixes was more compact than that of NS mixes, contributing to their higher mechanical properties. In the case of G100, it is not possible to explain by SEM images shown in Fig. 5.17 why such an increase was not observed when NS was replaced by GS and LSS. This becomes clear only after the EDX analysis showing that G100 mixes containing LSS and GS had a similar amount of hydration products to those containing NS.

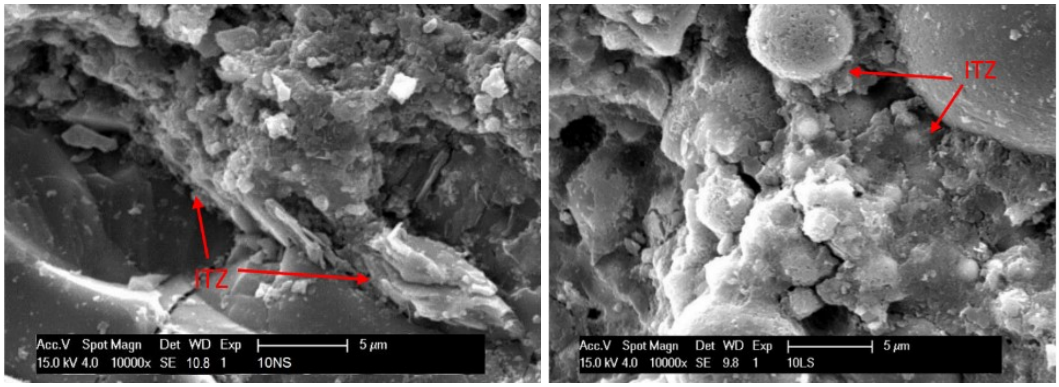

(a) (b)

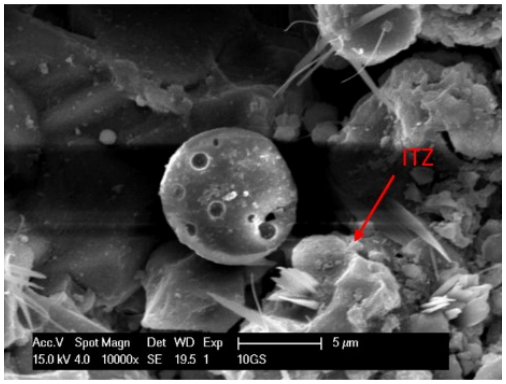

(c)

Figure 5.14. SEM micrographs of the fresh-cut surface of FA100 mixes containing: (a) NS, (b) LSS, and c) GS following compression tests

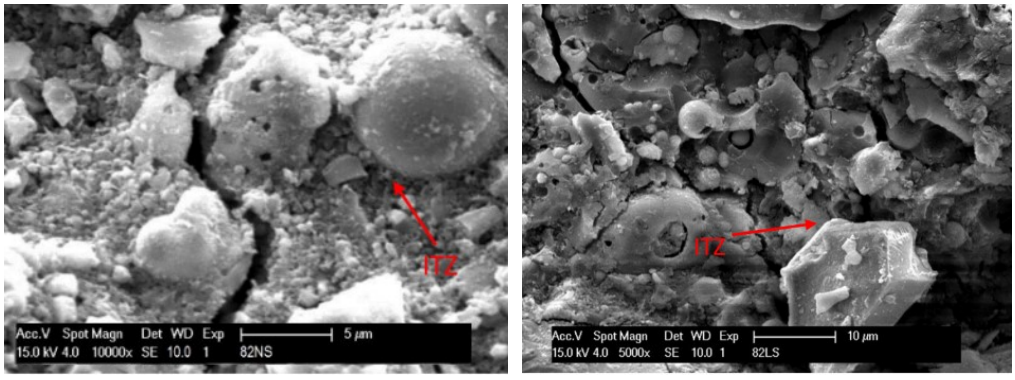

(a) (b)

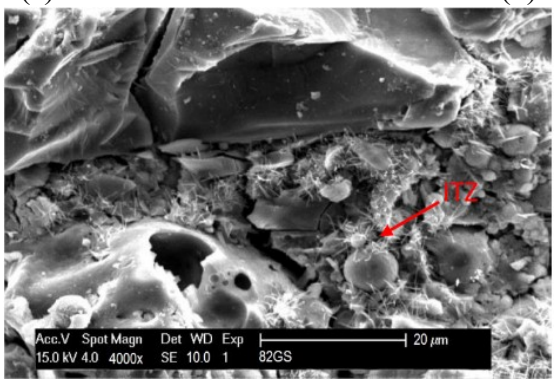

(c)

Figure 5.15. SEM micrographs of the fresh-cut surface of FA80G20 mixes containing: (a) NS, (b) LSS, and c) GS following compression tests

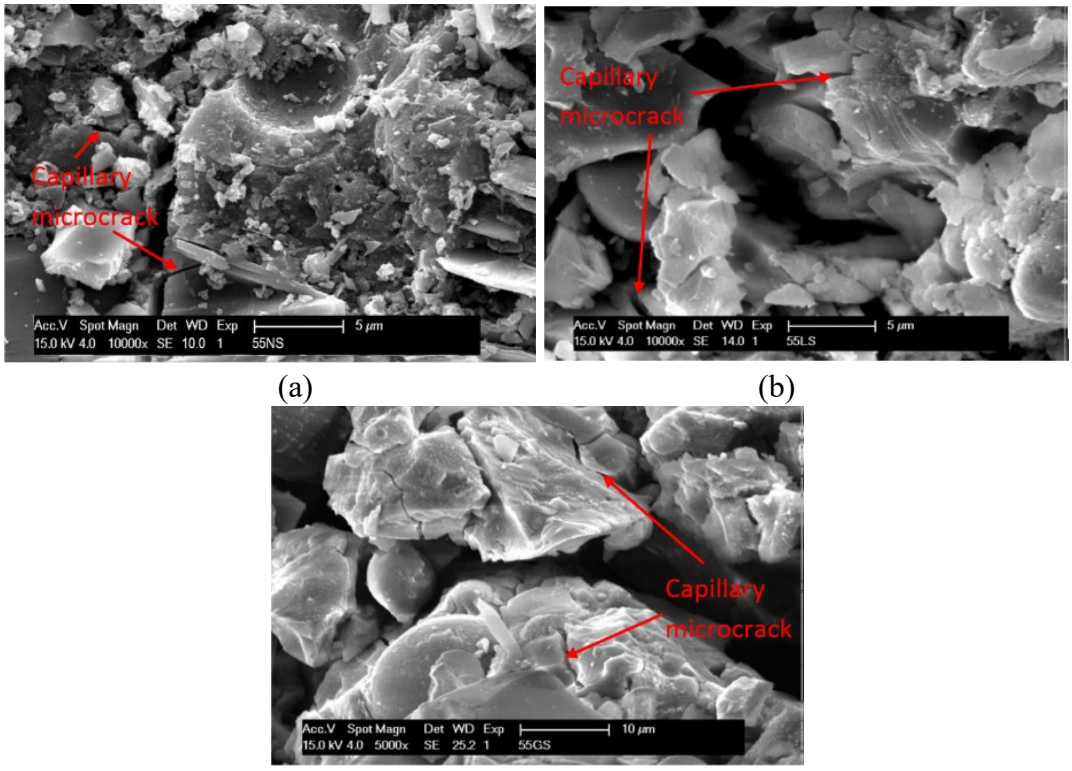

(a) (b)

(c)

Figure 5.16. SEM micrographs of the fresh-cut surface of FA50G50 mixes containing: (a) NS, (b) LSS, and c) GS following compression tests

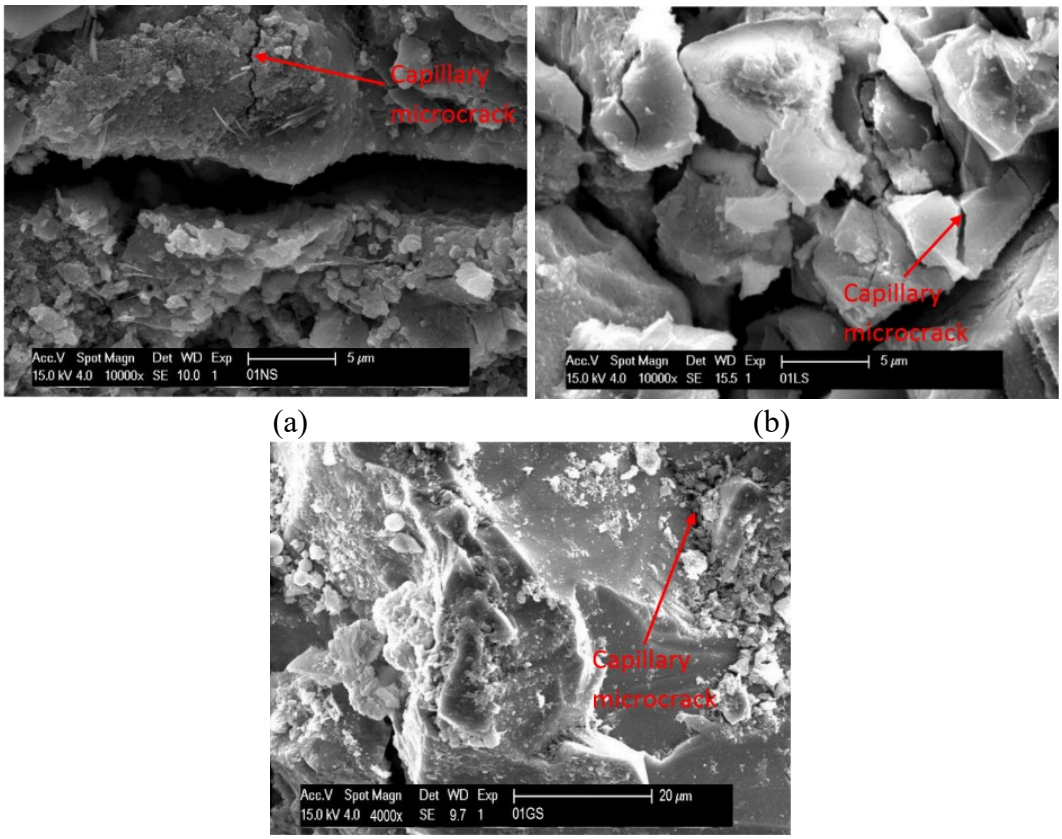

(a) (b)

(c)

Figure 5.17. SEM micrographs of the fresh-cut surface of G100 mixes containing: (a) NS, (b) LSS, and c) GS following compression tests

EDX analysis

Figures 5.18-5.21 show the EDX analysis results of different geopolymer mortar mixes at 28 days of curing age. In these figures the hydrogen constituent of the specimens was considered in the oxygen constituent. It should be noted that EDX results for FA100GS and FA80G20GS mixes were unavailable and the scale of images was not consistent. As can be seen in Figs. 5.18 and 5.19, in FA100 and FA80G20 mixes, main constituent elements of geopolymer mortars were sodium, silicon, aluminum, and oxygen. Therefore, their major hydration product was sodium aluminosilicate hydrate (N-A-S-H). It can also be seen in Figs. 5.18 and 5.19 that, in the case of FA100 and FA80G20, mixes containing LSS had a higher combined amount of silica, aluminum, and calcium (which are the principal elements of N-A-S-H and C-S-H hydration products) than those containing NS, resulting in the higher mechanical properties of LSS mixes. As was shown in Fig. 5.2, the XRD pattern of LSS had mostly amorphous structure. Therefore, LSS potentially contributed to the geopolymerization process through undergoing partial reaction with the activator solution, as previously discussed for different types of fine aggregates with amorphous structures in geopolymer mortars [66, 67].

Element	Weight %
Oxygen	26.3
Aluminum	22.3
Sodium	6.2
Silica	43.6
Calcium	1.2

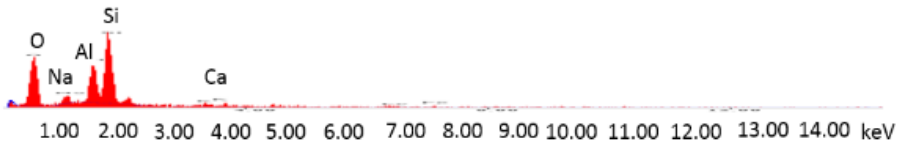

(a)

Element	Weight %
Oxygen	23.1
Aluminum	26.5
Sodium	6.5
Silica	41.2
Calcium	2.5

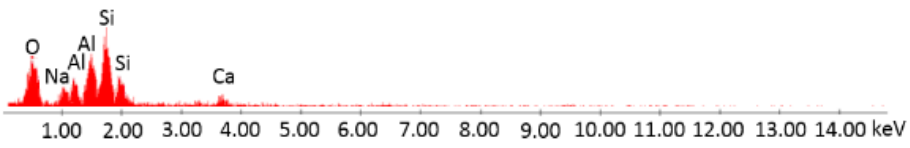

(b)

Figure 5.18. EDX composition analysis of FA100 mixes containing: (a) NS, (b) LSS

Element	Weight %
Oxygen	27.6
Aluminum	18.0
Sodium	9.2
Silica	38.3
Calcium	6.2

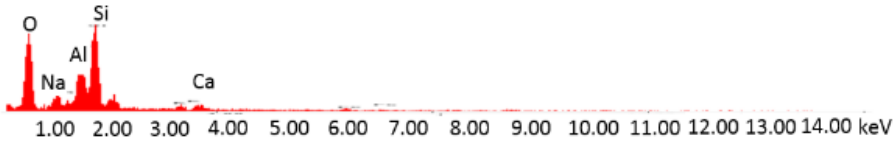

(a)

Element	Weight %
Oxygen	22.2
Aluminum	20.4
Sodium	10.4
Silica	36.8
Calcium	9.5

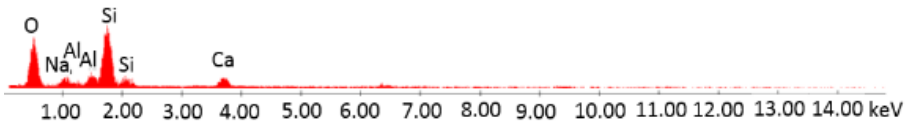

(b)

Figure 5.19. EDX composition analysis of FA80G20 mixes containing: (a) NS, (b) LSS

As can be seen in Figs. 5.20 and 5.21, in FA50G50 and G100 mixes, the principal constituent elements of geopolymer mortars included not only sodium, silicon, aluminum, and oxygen, but also calcium. Consequently, there were two hydration products of N-A-S-H and C-S-H gels in FA50G50 and G100 mixes. As it is evident from Fig. 5.20, in the case of FA50G50, LSS and GS mixes had a higher combined content of silicon, aluminum, and calcium compared to that of NS mixes, most likely due to the partial reaction of LSS and GS with the activator solution. This explains the higher 28-day strength of FA50G50 mixes containing LSS and GS than that of the companion mix containing NS. As can also be seen in Fig. 5.20, owing to the slightly higher combined content of silicon, aluminum, and calcium in the GS mix compared to that of the LSS mix, the GS mix developed a slightly higher compressive strength at 28 days as discussed in the section of Compressive Strength. As can be seen in Fig. 5.21, in the case of G100, LSS and GS mixes had a higher combined amount of silicon and aluminum but lower amount of calcium than those of NS mixes. This may explain why NS mixes developed a higher strength increases from 100% FA to 100% GGBS than those of LSS and GS mixes, as discussed in the

section of Compressive Strength. On the other hand, the similar mechanical properties of G100 mixes containing LSS and GS to those containing NS can be because of a similar combined content of silicon, aluminum, and calcium in LSS and GS mixes to that in NS mix.

Element	Weight %
Oxygen	15.5
Aluminum	6.2
Sodium	22.3
Silica	32.3
Calcium	22.5

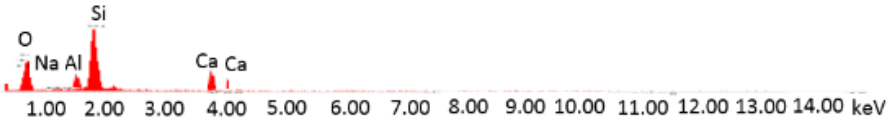

(a)

Element	Weight %
Oxygen	14.3
Aluminum	10.2
Sodium	20.0
Silica	30.1
Calcium	24.7

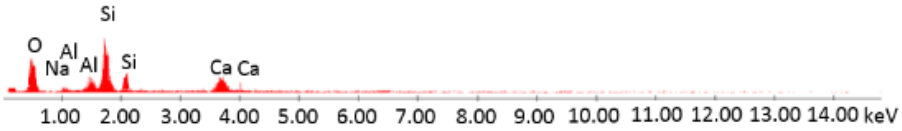

(b)

Element	Weight %
Oxygen	12.0
Aluminum	11.7
Sodium	21.1
Silica	31.5
Calcium	23.4

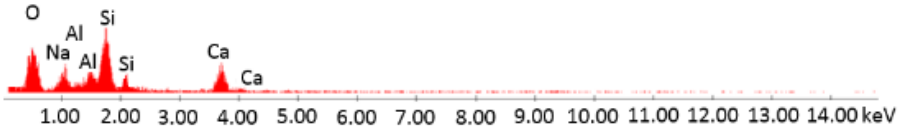

(c)

Figure 5.20. EDX composition analysis of FA50G50 mixes containing: (a) NS, (b) LSS, (c) GS

Element	Weight %
Oxygen	17.3
Aluminum	4.1
Sodium	18.0
Silica	25.2
Calcium	37.2

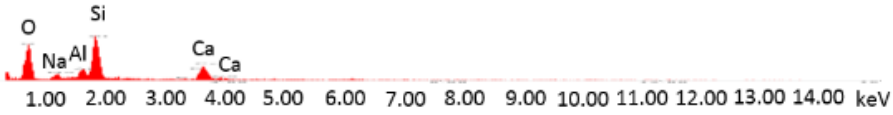

(a)

Element	Weight %
Oxygen	15.8
Aluminum	7.0
Sodium	19.3
Silica	24.1
Calcium	35.4

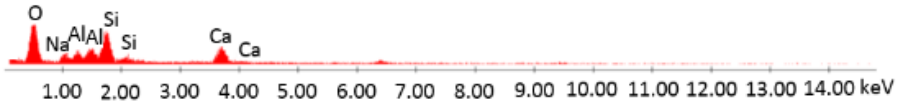

(b)

Element	Weight %
Oxygen	14.5
Aluminum	6.8
Sodium	19.7
Silica	24.6
Calcium	35.1

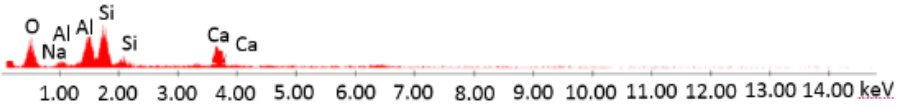

(c)

Figure 5.21. EDX composition analysis of G100 mixes containing: (a) NS, (b) LSS, (c) GS

CONCLUSIONS

The results of the first study on the properties of FA/GGBS-based geopolymer mortars containing LSS and GS have been presented. The following conclusions can be drawn based on the results and discussions presented in this study:

1- An increase in *GGBS%* results in a decrease in the flowability of geopolymer mortars owing to the the fact that GGBS reacts with the activator solution much more quickly than FA. Geopolymer mortars containing NS exhibit the highest flow, followed by those containing LSS and GS, respectively, owing to the less angular shape of NS particles compared to those of LSS and GS particles.
2- The compressive and tensile strength of geopolymer mortars increase with an increase in *GGBS%*. The mechanical properties of geopolymers containing LSS and GS are generally similar to those containing NS. LSS and GS geopolymer mortars containing up to 50% GGBS exhibit slightly higher mechanical properties compared to those of companion NS mortars, owing to their higher content of hydration products and lower porosity. LSS and GS mortars with a *GGBS%* over 50% exhibit very similar mechanical properties to those of companion NS mortars.
3- The water absorption of geopolymer mortars decreases when *GGBS%* increases, which is because of the increased microstructure compactness of the mix. Mortars containing LSS exhibit the highest water absorption owing to their honeycomb-like surface followed by those containing NS and GS, respectively.
4- The ASR expansion of GS geopolymer mortars increases when *GGBS%* increases. Even then, the ASR expansion of 100% GGBS geopolymer mortars with GS is lower than the limit value set up by ASTM standard C1260.
5- The drying shrinkage of geopolymer mortars decreases with an increase in *GGBS%*. Mortars containing GS develop the highest drying shrinkage, followed by those containing NS and LSS, respectively, owing to the lower permeability of GS than NS and LSS that causes an increase in the moisture loss of the mortar during the shrinkage process.

The promising findings of this study point to the possibility of the development of new composites offering significant environmental benefits through simultaneous replacement of NS by LSS and GS and cement by FA and GGBS. This is a viable strategy that contributes toward the development of an eco-friendly construction material, and cleaner and greener production practices aimed at reducing the impact of construction industry on the environment.

ACKNOWLEDGEMENTS

The authors thank Mesdames Dinh, Hariz, Rabbah, and Yin for completion of the tests reported in this paper as part of their Honour's thesis.

REFERENCES

[1] Low M-S. *Material flow analysis of concrete in the United States*: Massachusetts Institute of Technology; 2005.

[2] Mehta PK, Meryman H. Tools for reducing carbon emissions due to cement consumption. *Structure*. 2009;1(1):11-5.

[3] Golewski GL. Generalized fracture toughness and compressive strength of sustainable concrete including low calcium fly ash. *Materials*. 2017;10(12):1393.

[4] Sankh AC, Biradar PM, Naghathan S, Ishwargol MB. Recent trends in replacement of natural sand with different alternatives. *Proceedings of the International Conference on Advances in Engineering and Technology*. 2014. p. 59-66.

[5] Bravard J-P, Goichot M, Gaillot S. Geography of sand and gravel mining in the Lower Mekong River. First survey and impact assessment. *EchoGéo*. 2013(26).

[6] Gholampour A, Ozbakkaloglu T. Performance of sustainable concretes containing very high volume Class-F fly ash and ground granulated blast furnace slag. *Journal of Cleaner Production*. 2017;162:1407-17.

[7] Zhao H, Sun W, Wu X, Gao B. The properties of the self-compacting concrete with fly ash and ground granulated blast furnace slag mineral admixtures. *Journal of Cleaner Production*. 2015;95:66-74.

[8] Blissett R, Rowson N. A review of the multi-component utilisation of coal fly ash. *Fuel*. 2012;97:1-23.

[9] Tsakiridis P, Papadimitriou G, Tsivilis S, Koroneos C. Utilization of steel slag for Portland cement clinker production. *Journal of Hazardous Materials.* 2008;152(2):805-11.

[10] Prathik Gowda S, Latha MS. Environmental concrete - geopolymer of construction. *International Journal of Current Research*. 2017.

[11] Taha B, Nounu G. Utilizing waste recycled glass as sand/cement replacement in concrete. *Journal of Materials in Civil Engineering*. 2009;21(12):709-21.

[12] Park SB, Lee BC, Kim JH. Studies on mechanical properties of concrete containing waste glass aggregate. *Cement and Concrete Research*. 2004;34(12):2181-9.

[13] Tripathi B, Misra A, Chaudhary S. Strength and abrasion characteristics of ISF slag concrete. *Journal of Materials in Civil Engineering*. 2013;25(11):1611-8.

[14] Atzeni C, Massidda L, Sanna U. Use of granulated slag from lead and zinc processing in concrete technology. *Cement and Concrete Research.* 1996;26(9):1381-8.

[15] Islam G, Rahman M, Kazi N. Waste glass powder as partial replacement of cement for sustainable concrete practice. *International Journal of Sustainable Built Environment*. 2017;6(1):37-44.

[16] Aliabdo AA, Elmoaty AEMA, Aboshama AY. Utilization of waste glass powder in the production of cement and concrete. *Construction and Building materials.* 2016;124:866-77.

[17] Ogundiran M, Nugteren H, Witkamp G. Immobilisation of lead smelting slag within spent aluminate—fly ash based geopolymers. *Journal of hazardous materials.* 2013;248:29-36.

[18] Kheradmand M, Mastali M, Abdollahnejad Z, Pacheco-Torgal F. Experimental and numerical investigations on the flexural performance of geopolymers reinforced with short hybrid polymeric fibres. *Composites Part B*. 2017;126:108-18.

[19] Khan MZN, Hao Y, Hao H, Shaikh FUA. Experimental evaluation of quasi-static and dynamic compressive properties of ambient-cured high-strength plain and fiber reinforced geopolymer composites. *Construction and Building Materials*. 2018;166:482-99.

[20] Zhang HY, Kodur V, Wu B, Cao L, Wang F. Thermal behavior and mechanical properties of geopolymer mortar after exposure to elevated temperatures. *Construction and Building Materials*. 2016;109:17-24.

[21] Islam A, Alengaram UJ, Jumaat MZ, Bashar II. The development of compressive strength of ground granulated blast furnace slag-palm oil fuel ash-fly ash based geopolymer mortar. *Materials & Design*. 2014;56:833-41.

[22] Görhan G, Kürklü G. The influence of the NaOH solution on the properties of the fly ash-based geopolymer mortar cured at different temperatures. *Composites Part B.* 2014;58:371-7.

[23] Temuujin J, van Riessen A, MacKenzie K. Preparation and characterisation of fly ash based geopolymer mortars. *Construction and Building Materials*. 2010;24(10):1906-10.

[24] Chindaprasirt P, Chareerat T, Hatanaka S, Cao T. High-strength geopolymer using fine high-calcium fly ash. *Journal of Materials in Civil Engineering*. 2010;23(3):264-70.

[25] Sathonsaowaphak A, Chindaprasirt P, Pimraksa K. Workability and strength of lignite bottom ash geopolymer mortar. *Journal of Hazardous Materials.* 2009;168(1):44-50.

[26] Colangelo F, Roviello G, Ricciotti L, Ferone C, Cioffi R. Preparation and characterization of new geopolymer-epoxy resin hybrid mortars. *Materials*. 2013;6(7):2989-3006.

[27] Duxson P, Fernández-Jiménez A, Provis JL, Lukey GC, Palomo A, van Deventer JS. Geopolymer technology: the current state of the art. *Journal of Materials Science.* 2007;42(9):2917-33.

[28] Xie T, Ozbakkaloglu T. Influence of coal ash properties on compressive behaviour of FA-and BA-based GPC. *Magazine of Concrete Research.* 2015;67(24):1301-14.

[29] Xie T, Ozbakkaloglu T. Behavior of low-calcium fly and bottom ash-based geopolymer concrete cured at ambient temperature. *Ceramics International.* 2015;41(4):5945-58.

[30] Nath P, Sarker PK, Rangan VB. Early age properties of low-calcium fly ash geopolymer concrete suitable for ambient curing. *Procedia Engineering.* 2015;125:601-7.

[31] Albitar M, Ali MM, Visintin P, Drechsler M. Effect of granulated lead smelter slag on strength of fly ash-based geopolymer concrete. *Construction and Building Materials.* 2015;83:128-35.

[32] Nath P, Sarker PK. Effect of GGBFS on setting, workability and early strength properties of fly ash geopolymer concrete cured in ambient condition. *Construction and Building Materials.* 2014;66:163-71.

[33] Phoo-ngernkham T, Maegawa A, Mishima N, Hatanaka S, Chindaprasirt P. Effects of sodium hydroxide and sodium silicate solutions on compressive and shear bond strengths of FA–GBFS geopolymer. *Construction and Building Materials.* 2015;91:1-8.

[34] ASTM C109/C109M-07. *Standard Test Method for Compressive Strength of Hydraulic Cement Mortars*, ASTM International: USA 2008. 2008.

[35] ASTM C307-03. *Standard Test Method for Tensile Strength of Chemical-Resistant Mortar, Grouts, and Monolithic Surfacings*. 2012.

[36] ASTM C1585-13. *Standard Test Method for Measurement of Rate of Absorption of Water by Hydraulic-Cement Concretes.* 2013.

[37] ASTM C596-09. *Standard Test Method for Drying Shrinkage of Mortar Containing Hydraulic Cement*. 2017.

[38] ASTM C1260-14. *Standard Test Method for Potential Alkali Reactivity of Aggregates (Mortar-Bar Method).* 2014.

[39] ASTM C1437-15. *Standard Test Method for Flow of Hydraulic Cement Mortar.* 2015.

[40] Tan KH, Du H. Use of waste glass as sand in mortar: Part I–Fresh, mechanical and durability properties. *Cement and Concrete Composites.* 2013;35(1):109-17.

[41] Hui Z, Poon CS, Ling TC. Properties of mortar prepared with recycled cathode ray tube funnel glass sand at different mineral admixture. *Construction and Building Materials*. 2013;40:951-60.

[42] Wang H-Y. A study of the effects of LCD glass sand on the properties of concrete. *Waste Management*. 2009;29(1):335-41.

[43] Limbachiya MC. Bulk engineering and durability properties of washed glass sand concrete. *Construction and Building Materials.* 2009;23(2):1078-83.

[44] Tiwari A, Singh S, Nagar R. Feasibility assessment for partial replacement of fine aggregate to attain cleaner production perspective in concrete: A review. *Journal of Cleaner Production.* 2016;135:490-507.

[45] Deb PS, Nath P, Sarker PK. The effects of ground granulated blast-furnace slag blending with fly ash and activator content on the workability and strength properties of geopolymer concrete cured at ambient temperature. *Materials & Design (1980-2015).* 2014;62:32-9.

[46] Hadi MN, Farhan NA, Sheikh MN. Design of geopolymer concrete with GGBFS at ambient curing condition using Taguchi method. *Construction and Building Materials.* 2017;140:424-31.

[47] Nath P, Sarker P. Geopolymer concrete for ambient curing condition. *Australasian Structural Engineering Conference 2012: The past, present and future of Structural Engineering: Engineers Australia;* 2012. p. 225.

[48] Yip C, Van Deventer J. Microanalysis of calcium silicate hydrate gel formed within a geopolymeric binder. *Journal of Materials Science*. 2003;38(18):3851-60.

[49] Temuujin Jv, Van Riessen A, Williams R. Influence of calcium compounds on the mechanical properties of fly ash geopolymer pastes. *Journal of hazardous materials.* 2009;167(1):82-8.

[50] Phoo-ngernkham T, Sata V, Hanjitsuwan S, Ridtirud C, Hatanaka S, Chindaprasirt P. Compressive strength, bending and fracture characteristics of high calcium fly ash geopolymer mortar containing portland cement cured at ambient temperature. *Arabian Journal for Science and Engineering.* 2016;41(4):1263-71.

[51] Somna K, Jaturapitakkul C, Kajitvichyanukul P, Chindaprasirt P. NaOH-activated ground fly ash geopolymer cured at ambient temperature. *Fuel*. 2011;90(6):2118-24.

[52] Palomo A, Fernández-Jiménez A, Kovalchuk G, Ordoñez L, Naranjo M. OPC-fly ash cementitious systems: study of gel binders produced during alkaline hydration. *Journal of Materials Science*. 2007;42(9):2958-66.

[53] ASTM C1260. Standard test method for potential alkali reactivity of aggregates (mortar-bar method). *Section*. 2007;4:676-80.

[54] Al-Otaibi S. Durability of concrete incorporating GGBS activated by water-glass. *Construction and Building Materials.* 2008;22(10):2059-67.

[55] Bakharev T, Sanjayan J, Cheng Y-B. Resistance of alkali-activated slag concrete to alkali–aggregate reaction. *Cement and Concrete Research.* 2001;31(2):331-4.

[56] Du H, Tan KH. Use of waste glass as sand in mortar: Part II–Alkali–silica reaction and mitigation methods. *Cement and Concrete Composites.* 2013;35(1):118-26.

[57] Thomas M. The effect of supplementary cementing materials on alkali-silica reaction: A review. *Cement and Concrete Research*. 2011;41(12):1224-31.

[58] Kupwade-Patil K, Allouche E. Effect of alkali silica reaction (ASR) in geopolymer concrete. *World of Coal Ash (WOCA) conference.* 2011. p. 9-12.

[59] Neupane K, Kidd P, Chalmers D, Baweja D, Shrestha R. Investigation on compressive strength development and drying shrinkage of ambient cured

powder-activated geopolymer concretes. *Australian Journal of Civil Engineering.* 2016;14(1):72-83.

[60] Deb PS, Nath P, Sarker PK. Drying shrinkage of slag blended fly ash geopolymer concrete cured at room temperature. *Procedia Engineering.* 2015;125:594-600.

[61] Ling T-C, Poon C-S. Utilization of recycled glass derived from cathode ray tube glass as fine aggregate in cement mortar. *Journal of Hazardous Materials.* 2011;192(2):451-6.

[62] de Sa C, Benboudjema F, Thiery M, Sicard J. Analysis of microcracking induced by differential drying shrinkage. *Cement and Concrete Composites.* 2008;30(10):947-56.

[63] Palacios M, Puertas F. Effect of shrinkage-reducing admixtures on the properties of alkali-activated slag mortars and pastes. *Cement and Concrete Research.* 2007;37(5):691-702.

[64] Neto AAM, Cincotto MA, Repette W. Drying and autogenous shrinkage of pastes and mortars with activated slag cement. *Cement and Concrete Research.* 2008;38(4):565-74.

[65] Part WK, Ramli M, Cheah CB. An overview on the influence of various factors on the properties of geopolymer concrete derived from industrial by-products. *Construction and Building Materials.* 2015;77:370-95.

[66] Yip CK, Lukey G, Van Deventer J. The coexistence of geopolymeric gel and calcium silicate hydrate at the early stage of alkaline activation. *Cement and Concrete Research.* 2005;35(9):1688-97.

[67] Ahmari S, Zhang L. *The properties and durability of alkali-activated masonry units.* Handbook of Alkali-Activated Cements, Mortars and Concretes: Elsevier; 2015. p. 643-60.

Statement of Authorship

Title of Paper	Mechanical properties and microstructure of waste-based mortars containing fly ash, ground granulated blast furnace slag, glass powder, and lead smelter slag
Publication Status	☐ Published ☐ Accepted for Publication ☑ Submitted for Publication ☐ Unpublished and Unsubmitted work written in manuscript style
Publication Details	Gholampour A, Ozbakkaloglu T, Etemadi E, Vincent T. Mechanical properties and microstructure of waste-based mortars containing fly ash, ground granulated blast furnace slag, glass powder, and lead smelter slag. *Construction and Building Materials*. 2019.

Principal Author

Name of Principal Author (Candidate)	Aliakbar Gholampour		
Contribution to the Paper	Literature review, analysis of test results, and preparation of the manuscript.		
Overall percentage (%)	70%		
Certification:	This paper reports on original research I conducted during the period of my Higher Degree by Research candidature and is not subject to any obligations or contractual agreements with a third party that would constrain its inclusion in this thesis. I am the primary author of this paper.		
Signature		Date	31/01/2019

Co-Author Contributions

By signing the Statement of Authorship, each author certifies that:

i. the candidate's stated contribution to the publication is accurate (as detailed above);

ii. permission is granted for the candidate in include the publication in the thesis; and

iii. the sum of all co-author contributions is equal to 100% less the candidate's stated contribution.

Name of Co-Author	Togay Ozbakkaloglu		
Contribution to the Paper	Research supervision and review of manuscript.		
Signature		Date	31/01/2019

Name of Co-Author	Elahe Etemadi		
Contribution to the Paper	Preparation of the manuscript.		
Signature		Date	31/01/2019

Name of Co-Author	Thomas Vincent		
Contribution to the Paper	Review of manuscript.		
Signature		Date	31/01/2019

Please cut and paste additional co-author panels here as required.

Mechanical Properties and Microstructure of Waste-Based Mortars Containing Fly Ash, Glass Powder, Ground Granulated Blast Furnace Slag, and Lead Smelter Slag

ABSTRACT

The aim of the study being reported in this paper was to develop an eco-friendly concrete using waste products to reduce both the extraction of non-renewable natural resources and CO_2 emissions associated with concrete production. The development of a new eco-friendly concrete involved the replacement of cement with waste-based materials, such as fly ash (FA), glass powder (GP), and ground granulated blast furnace slag (GGBS), and the replacement of natural sand (NS) with waste-based sand, namely lead smelter slag (LSS). 24 batches of mortars were produced and tests were conducted to determine the flowability, compressive strength, and direct tensile strength of each batch. Microstructural analysis was undertaken to explain experimentally obtained properties of mortars. The results show that due to the higher angularity of LSS, waste-based mortars containing it exhibit lower flowability (i.e. up to 31%) compared to those containing NS. The results also show that the compressive and tensile strength of waste-based mortars containing LSS are similar to those containing NS. Owing to their nearly identical void amount and amount of hydration products at binder-sand interfacial transition zones, the mortars with 80% replacement of cement with GGBS and 100% replacement of NS with LSS show minimal strength reduction compared to the conventional mortar (i.e. 4%). The strength reduction of waste-based mortars with respect to the conventional mortar increases at 90% and 100% cement replacement levels but it remains limited to approximately 20% (at 90% GGBS) and 30% (at 100% GGBS), respectively. The promising findings of this study point to the possibility of the development of new structural grade mortars using full or near full replacement of cement with waste-based binders and full replacement of natural sand with waste-based sand.

KEYWORDS: Waste-based mortars; Lead smelter slag; Ground granulated blast furnace slag (GGBS); Glass powder; Fly ash; Microstructure.

INTRODUCTION

Concrete is the most commonly used construction material throughout the world owing to its favorable properties such as high compressive strength and low construction cost [1]. However, the production of conventional cement-based concretes requires energy intensive processes that generate approximately 5–7% of total greenhouse gases (essentially CO_2) emissions into the atmosphere contributing significantly to the global warming [2,3]. Therefore, to reduce the energy consumption and greenhouse gases emission associated with concrete production, it is crucial to identify environmentally friendly alternative materials to replace cement in concrete. Meanwhile, the high demand for natural river sand as fine aggregates in the construction industry that led to their over-exploitation, resulting in the depletion of this non-renewable material in a number of rapidly growing cities across the world (e.g. Singapore and Shenzhen, China), has and results in negative effects on the ecosystem [4,5]. Therefore, finding a suitable alternative material to river sand is also imperative.

The most common cement alternatives are pozzolanic waste materials including the fly ash (FA), waste glass powder (GP), and ground granulated blast furnace slag (GGBS) [6,7]. As was reported previously, the annual global generation of FA, GGBS, and waste glass is approximately 750 million [8], 530 million [9], and 130 million tons [10], respectively. However, only 25% [11], 65% [12], and 25% [13] of the total global FA, GGBS, and waste glass generation are currently being recycled, respectively. Therefore, there is significant potential for FA, GGBS, and GP to be used as cement replacement in the construction industry to reduce the environmental impact of both cement and waste materials. Furthermore, the use of waste-based sands such as lead smelter slag (LSS) is currently being considered as an alternative material to natural river sand (NS) [14]. Existing studies have shown that LSS, which is an abundant waste material that is currently being landfilled, exhibits properties that make it suitable for use in the production of structural concretes [15,16]. Therefore, there is significant potential for LSS to be used as sand replacement in concretes with the aim of improving mechanical properties of concretes. As the first systematic study on the topic, the current study examined the use of these waste-based materials together to generate 100% waste-based mortar.

A large number of studies were performed to investigate the mechanical properties of cement mortars incorporating waste-based materials (e.g. [10,17-27]). As has been shown in these studies, mortars containing waste-based materials can exhibit desirable mechanical and durability properties that are comparable to those of their cement-based counterparts. However, none of these studies focused on the full replacement of cement with waste-based binders, and to date no study has been reported on the properties of cement mortars containing LSS as sand replacement. Furthermore, the microstructure of waste-based mortars has not yet been investigated and is crucial to understand and explain the mechanisms behind the mechanical properties. Therefore, this study investigates the novel concept of full and simultaneous replacement of cement and natural sand with their waste-based counterparts.

The first experimental study on the properties of waste-based mortars with full and simultaneous replacement of cement with waste-based binders (i.e. FA, GGBS, and GP) and NS with LSS is presented in this paper. In addition to the mechanical tests, the microstructure of different mixes was investigated at 28 days of curing age. A summary of the experimental program and the test results are initially presented and a detailed discussion on the results is then provided. The promising technology reported in this study has a significant potential to contribute toward a green construction industry through i) conserving non-renewable natural sand resources, ii) reducing the large CO_2 footprint associated with the use of cement, and iii) eliminating the negative environmental impact associated with the disposal of waste-based materials.

TESTING PROGRAM

Materials

NS

River sand with a maximum particle size of 2.13 mm that was sourced from McLaren Vale Quarry, Fleurieu Peninsula, in South Australia was used as the NS. The physical properties and particle size distribution of NS are shown in Table 6.1 and Fig. 6.1, respectively.

Table 6.1. Properties of fine aggregates

Aggregate type	Maximum size (mm)	Specific gravity (SSD)	Water absorption (%)	Fineness modulus
Natural sand	2.13	2.63	0.4	2.56
Lead smelter slag	1.94	3.30	0.6	2.51

SSD: Saturated surface-dry

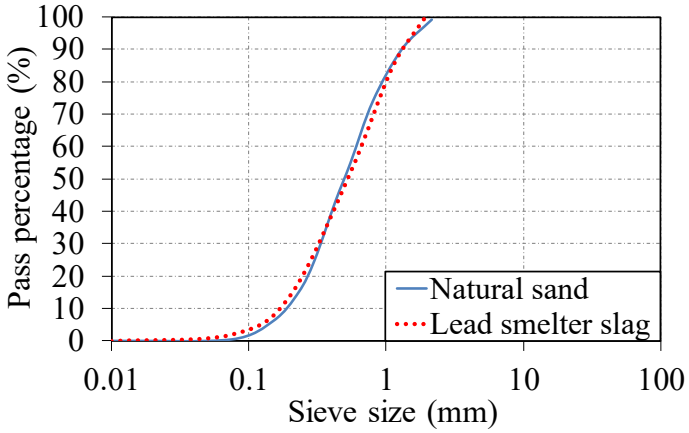

Figure 6.1. Sieving test results of fine aggregates: Particle Size Distribution (PSD)

LSS

Granulated LSS with a maximum particle size of 1.94 mm was obtained from Port Pirie in South Australia. The physical properties and particle size distribution of LSS are shown in Table 6.1 and Fig. 6.1, respectively.

High early strength cement (HESC)

High early strength cement (HESC) was provided by Adelaide Brighton Cement Ltd. The chemical composition of HESC used in this study is shown in Table 6.2.

Table 6.2. Chemical composition of cementitious materials

Composition	HESC (%)	Fly ash (%)	GGBS (%)	GP (%)
SiO_2	19.95	55.38	33.10	72.50
Al_2O_3	4.79	28.14	13.33	0.16
Fe_2O_3	3.14	3.31	0.69	0.20
CaO	63.28	3.45	42.83	9.18
MgO	2.03	1.85	5.57	3.35
Na_2O	0.29	2.30	0.27	13.20
K_2O	0.40	1.39	0.31	0.12
SO_3	2.69	0.32	1.81	0.39
P_2O_5	0.04	0.78	0.01	–
LOI	3.39	3.08	2.08	0.90
Specific surface area (m^2/kg)	390	396	450	217

HESC: High early strength cement
GGBS: ground granulated blast furnace slag
GP: Glass powder

FA

Class-F FA was provided by Adelaide Brighton Cement Ltd., who sourced the material from the Port Augusta power station in South Australia. This FA was a by-product of combusting fine ground Leigh Creek Coal and extracted by electrostatic precipitators from the exhaust gases. The chemical composition of FA is shown in Table 6.2.

GGBS

GGBS was provided by Adelaide Brighton Cement Ltd. and was a by-product of iron-making processes at the Birkenhead Works in Adelaide, South Australia. GGBS contained small amounts of gypsum and trace amounts of crystalline silica and hexavalent chromium. The chemical composition of GGBS is listed in Table 6.2.

GP

GP was provided by Glass Recovery Service in Victoria. GP was sieved from glass sand using vibrating sieve to obtain a particle size of less than 150 μm. The chemical composition of GP is shown in Table 6.2.

Test specimens

A total of 24 unique batches of waste-based mortars were prepared, which included: 13 batches containing 100% NS and 11 batches containing 100% LSS. Binders were prepared using 100% (as control mixes), 85%, 20%, 10%, and 0% HESC. An effective water-to-binder (w_{eff}/b) ratio of 0.65 was used in all the mixes. The test parameters were the weight percentage of HESC (HESC%), GGBS (GGBS%), FA (FA%), and GP (GP%) in the mortar. Table 6.3 shows the mix proportion of mortars. A series of tests were performed on each batch to investigate the properties of fresh and hardened mortar, including: flowability, compressive strength, and direct tensile strength. 50 mm cube samples were used for the compression tests according to the ASTM standard C109/C109M-07 [28]. For direct tension tests, typical dog-bone shaped samples with a test region width and depth of 25±0.5 mm were used in accordance with the ASTM standard C307-03 [29]. In each type of test three nominally identical specimens were tested for each unique specimen configuration.

It should be noted that test results for LSS mixes containing 75% GGBS/25% FA and 85% GGBS/15% GP were unavailable because of problems encountered during the preparation of these mixes.

Table 6.3. Mix proportions of mixes

Mix	HESC (kg/m^3)	FA (kg/m^3)	GGBS (kg/m^3)	GP (kg/m^3)	NS (kg/m^3)	LSS (kg/m^3)	Water (kg/m^3)	w_{eff}/b
H100N	500	–	–	–	1500	–	325	0.65
H85P15N	425	–	–	75	1500	–	325	0.65
H20G80N	100	–	400	–	1500	–	325	0.65
H20G70F10N	100	50	350	–	1500	–	325	0.65
H20G60F20N	100	100	300	–	1500	–	325	0.65
H20G70P10N	100	–	350	50	1500	–	325	0.65
H20G60F10P10N	100	50	300	50	1500	–	325	0.65
H10G90N	50	–	450	–	1500	–	325	0.65
H10G70F20N	50	100	350	–	1500	–	325	0.65
H10G75P15N	50	–	375	75	1500	–	325	0.65
G100N	–	–	500	–	1500	–	325	0.65
G75F25N	–	125	375	–	1500	–	325	0.65
G85P15N	–	–	425	75	1500	–	325	0.65
H100L	500	–	–	–	–	1882	325	0.65
H85P15L	425	–	–	75	–	1882	325	0.65
H20G80L	100	–	400	–	–	1882	325	0.65
H20G70F10L	100	50	350	–	–	1882	325	0.65
H20G60F20L	100	100	300	–	–	1882	325	0.65
H20G70P10L	100	–	350	50	–	1882	325	0.65
H20G60F10P10L	100	50	300	50	–	1882	325	0.65
H10G90L	50	–	450	–	–	1882	325	0.65
H10G70F20L	50	100	350	–	–	1882	325	0.65
H10G75P15L	50	–	375	75	–	1882	325	0.65
G100L	–	–	500	–	–	1882	325	0.65

Preparation of specimens and testing

In the preparation of mortar mixes, fine aggregates were used in the mix in the saturated surface-dry (SSD) condition. Once the specimens were demolded, they were cured in a fog room under the temperature of 23 ± 2 °C until the testing day.

The flowability of fresh mortars was investigated by a flow test [30] conducted instantly after the mixing of mortars. The compressive strength of hardened mortar

specimens was evaluated at curing ages of 7, 14, 28, and 56 days through the use of a universal testing machine. The direct tensile strength test was conducted on the specimens at the curing age of 28 days. Scanning electron microscopy (SEM) analysis by High Resolution Field Emission Scanning Electron Microscope (FEI Quanta 450) was used to investigate the morphology of fine aggregates and binders, and energy dispersive X-ray (EDX) spectroscopy by TEAM EDS with Silicon Drift Detector (SDD) was used to investigate the constituent elements of the mortars.

The mortar mix series in Table 6.3 were labelled as follows: the letters H, G, F, and P stand for HESC, GGBS, FA, and GP, respectively. The number after these letters indicates the weight percentage of each binder. The final letters N and L in the designation stand for the NS and LSS group mixes, respectively. For example, H20G60F10P10L is a mortar mix prepared with LSS and a blend of 20% HESC, 60% GGBS, 10% FA, and 10% GP.

TESTING RESULTS AND DISCUSSIONS

Flowability

Figure 6.2 shows flowability of different mixtures. It is shown in the figure that, for a given binder type, mortars containing LSS exhibited lower flow (between 14% in H85P15 and 31% in G100 mixes) than those containing NS. As discussed later in the section of Microstructural Analysis, the higher flowability of mixes containing NS is attributed to the lower angularity and slightly larger particle size of NS compared to those of LSS, resulting in a lower interparticle friction and formation of thicker water layers in NS mixes [31].

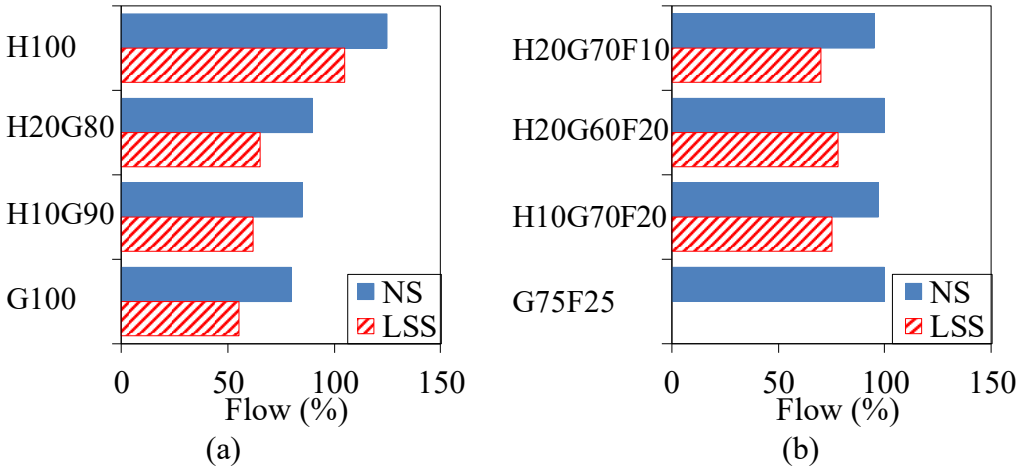

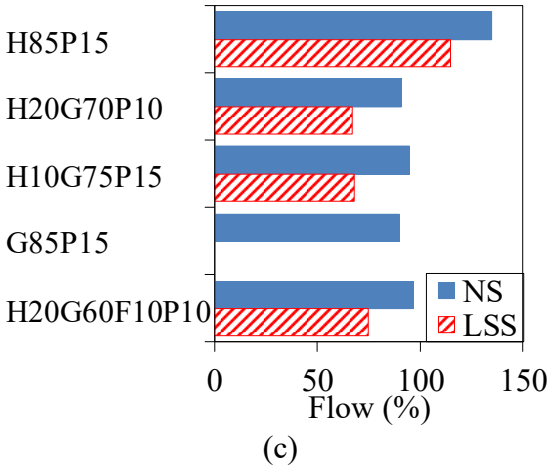

Figure 6.2. Flowability test results of different mixes: effect of (a) GGBS, (b) FA, and (c) GP addition

It is shown in Fig. 6.2(a) that an increase in GGBS% resulted in a decrease in the flowability of mortars for a given sand type, which is consistent with previous studies on NS mortars [20,23,32] and concretes [6,33,34] and is attributed to the more irregularity shape of GGBS than that of HESC as discussed in the section of SEM Analysis. The NS and LSS mix with 100% GGBS developed 36% and 48% lower flowability than that of the companion control mixes, respectively. It is shown in Fig. 6.2(b) that an increase in FA% resulted in a slight increase in the flowability of waste-based mortars, which is consistent with previous studies on NS mortars [24,35] and concretes [6,36-38] and is because of the spherical shape and smooth surface of FA as opposed to the irregular shape of HESC and GGBS [9,39,40], as discussed later in the section of SEM Analysis.

It can be seen in Fig. 6.2 that, for a given sand type, only H85P15 series of mixes exhibited a higher flowability than their companion control mixes (i.e. H100 series). The higher flowability of mortars containing GP than that of conventional mortars is consistent with previous studies on GP mortars [10,26] and concrete [41,42] containing NS. As discussed in the section of Microstructural Analysis in the presentation of the microstructural analysis, this is because of the larger particle size and lower water absorption (owing to the glassy surface of GP) of GP compared to HESC, resulting in the formation of thicker water layers in GP mixes [26,42]. As can be seen in Figs. 6.2(b) and (c), H20G70P10 mixes exhibited slightly lower flowability than H20G70F10 mixes, which is because higher angularity of GP

particles than FA particles had a more dominant negative affect on the flowability than the positive affect of the increased particle size of GP, as discussed later in the section of SEM Analysis.

Compressive strength

Figures 6.3(a)-(c) shows the influence of GGBS%, FA%, and GP% on the compressive strength of NS and LSS mixes at different curing ages, respectively. Figures show that, in all series, the compressive strength of LSS mixes was similar to those of the companion mixes containing NS. As discussed later in the section of SEM Analysis, this can be attributed to the partial reaction of LSS with water during the hydration process although LSS mixes had a less compact microstructure than that of companion NS mixes. As can be seen in Fig. 6.3, for a given sand type, control mixes with 100% HESC exhibited the highest compressive strength at all curing ages and, as expected, a decrease in HESC% resulted in a decrease in the compressive strength of mortars. However, it is noteworthy that the full replacement of cement by alternative binders did not reduce the strength of mortars dramatically (i.e. 32% to 37% strength reduction at 28 days of curing age). As discussed in the section of Microstructural Analysis, a decrease in the strength of mixes with a decrease in HESC% is attributed to the decrease in the amount of hydration products and increase in the porosity of the microstructure of mixes.

Figure 6.3(a) shows that 80% replacement of HESC with GGBS resulted in a slight decrease in the compressive strength. The strength reductions at 7, 14, 28, and 56 days in NS mixes were 12, 8, 7, and 5% and in LSS mixes were 8, 5, 4, and 3%, respectively. The higher rate of strength gain of H20G80 series mixes than that of H100 series mixes at ages beyond 7 days is because of the higher amount of silica and aluminum in H20G80 mixes, resulting in an extended period of hydration in the mix, which is discussed in the section of EDX Analysis. Figure 6.3(a) also shows that, at a given curing age, further increase in GGBS% over 80% resulted in a decrease in the compressive strength of mortar. This observation is consistent with previous studies on the compressive strength of concrete [6,43] and is attributed to the lower amount of hydration products and creation of higher amount of voids in

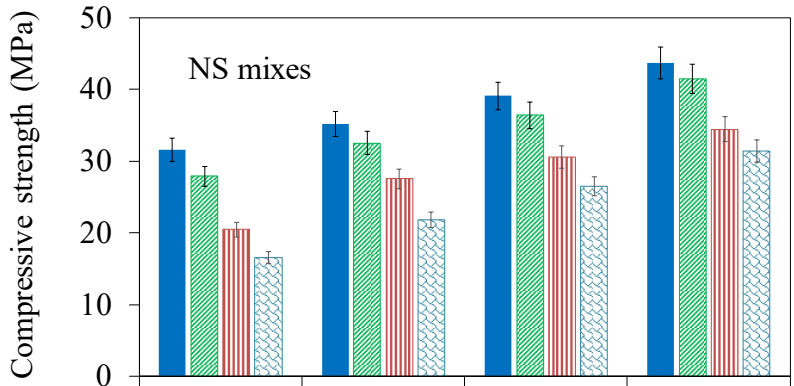

	7 days	14 days	28 days	56 days
H100N	31.6	35.2	39.1	43.7
H20G80N	27.9	32.5	36.4	41.5
H10G90N	20.5	27.5	30.6	34.4
G100N	16.5	21.8	26.5	31.4

Curing age (days)

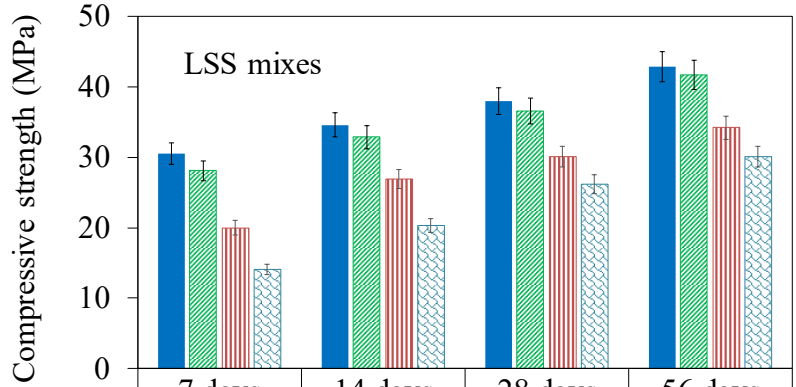

	7 days	14 days	28 days	56 days
H100L	30.5	34.6	38.0	42.9
H20G80L	28.1	32.9	36.6	41.7
H10G90L	20.0	26.9	30.1	34.2
G100L	14.1	20.3	26.2	30.1

Curing age (days)

(a)

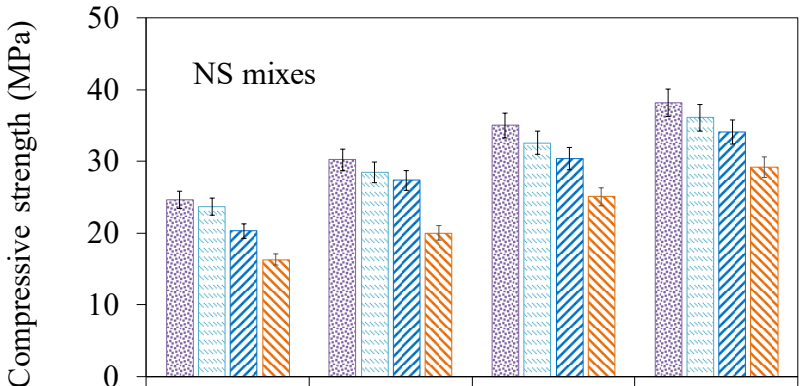

	7 days	14 days	28 days	56 days
H20G70F10N	24.6	30.2	35.0	38.2
H20G60F20N	23.7	28.5	32.6	36.1
H10G70F20N	20.3	27.4	30.4	34.1
G75F25N	16.3	20.0	25.1	29.2

Curing age (days)

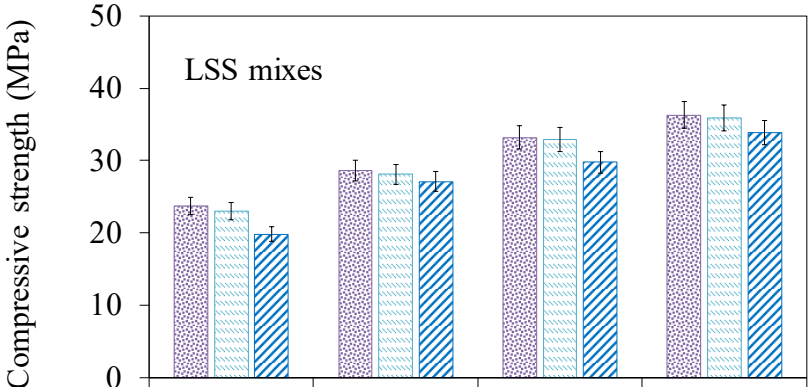

	7 days	14 days	28 days	56 days
H20G70F10L	23.7	28.6	33.2	36.3
H20G60F20L	23.0	28.1	32.9	35.9
H10G70F20L	19.8	27.1	29.8	33.9

Curing age (days)

(b)

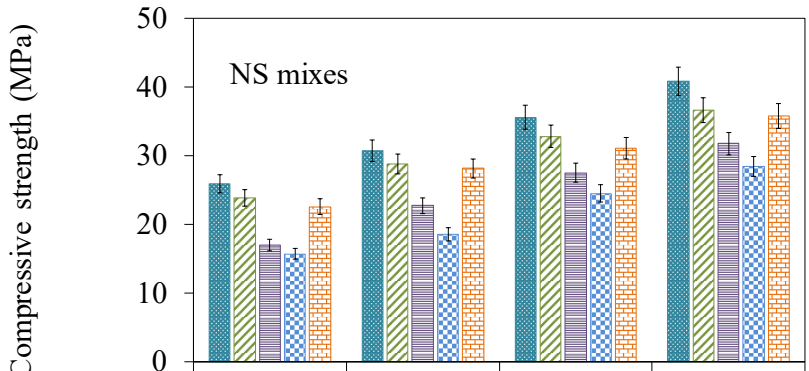

	7 days	14 days	28 days	56 days
H85P15N	25.9	30.7	35.6	40.8
H20G70P10N	23.9	28.8	32.8	36.6
H10G75P15N	17.0	22.7	27.5	31.8
G85P15N	15.7	18.6	24.5	28.4
H20G60F10P10N	22.6	28.2	31.1	35.8

Curing age (days)

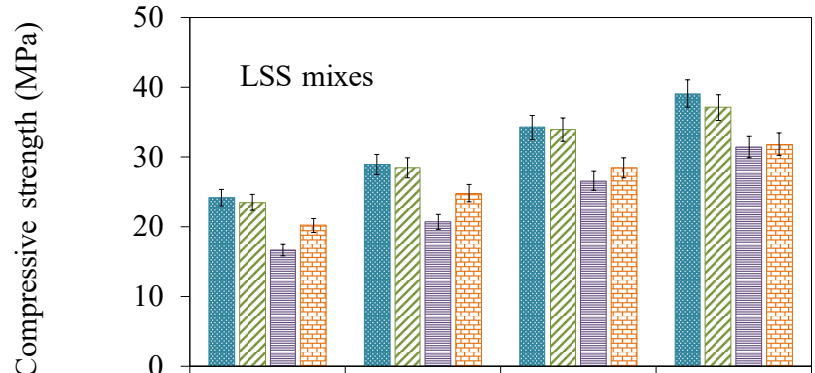

	7 days	14 days	28 days	56 days
H85P15L	24.2	29.0	34.2	39.1
H20G70P10L	23.5	28.5	33.9	37.1
H10G75P15L	16.6	20.7	26.6	31.4
H20G60F10P10L	20.2	24.8	28.4	31.8

Curing age (days)

(c)

Figure 6.3. Variation of compressive strength of mixes with time: effect of (a) GGBS, (b) FA, and (c) GP addition on the compressive strength

the microstructure of mixes with higher GGBS%, as discussed further in the section of Microstructural Analysis. Having said that, the strength loss for H10G90N and H10G90L mixes was limited to approximately 20% at 28 and 56 days when compared to the control mixes. Additionally, the G100 mixes performed well, with the strength reduction over the control mixes limited to approximately 30% at 28 and 56 days in both NS and LSS mixes.

As can be seen in Fig. 6.3(b), incorporation of FA in mortars containing HESC and GGBS resulted in a decrease in the compressive strength of the mortar. This is consistent with the previous study on the compressive strength of concrete containing FA, GGBS, and HESC [6]. H20G70F10N mix developed 12, 7, 4, and 8% lower strength than H20G80N mix, and H20G70F10L mix developed 16, 13, 9, and 13% lower strength than H20G80L mix at 7, 14, 28, and 56 days, respectively. Figure 6.3(b) also shows that with an increase in FA% from 10% to 20% the compressive strength of the mortar decreased further. This is attributed to the significantly lower CaO content of FA compared to HESC and GGBS, resulting in a lower hydration level in the mix [44]. However, as can be seen in Fig. 6.3(b), even with the full replacement of cement with 75% GGBS and 25% FA the strength loss was limited to 36 and 33% at 28 and 56 days, respectively.

It can be seen in Fig. 6.3(c) that incorporation of GP in mortars containing HESC and GGBS resulted in a decrease in the compressive strength of the mortar, which is because of the significantly lower CaO content of GP than HESC and GGBS [44]. As can also be seen in the figure, at the same cement replacement level of 80%, H20G70P10 mixes exhibited almost identical compressive strengths to those of H20G70F10 mixes (shown in Fig. 6.3(b)) for a given sand type. This observation may be explained by the nearly identical combined amount of CaO, SiO_2, and Al_2O_3 in FA and GP, as reported in Table 6.2. By comparison between Figs. 6.3(a) and 6.3(c), it can be seen that the compressive strengths of H85P15 series mixes (as mixes with the lowest cement replacement level) were identical to but slightly lower than those of H20G80 series mixes (as the best performing waste-based mortar mixes). As discussed later in the section of Microstructural Analysis, the higher compressive strength of H20G80 mixes (with 80% GGBS waste material) than that of H85P15 mixes (with only 15% GP waste material) is attributed to the more compact microstructure and presence of higher amount of hydration products in former mixes. Figure 6.3(c) shows that 80% replacement of cement with 60% GGBS, 10% FA, and 10% GP resulted in only approximately 23% and 22% decrease in the 28 and 56 days compressive strength of NS and LSS mortars, respectively. As can also be seen in Fig. 6.3(c), 90% replacement of cement with 75% GGBS and 15% GP and full replacement of NS with LSS resulted in only 32% decrease in the 28-day compressive strength compared to that of the conventional mortar. In

addition, full replacement of cement with 85% GGBS and 15% GP resulted in 37% and 35% decrease in the 28 and 56 days compressive strength of NS mortars, respectively.

In summary, at 80% cement replacement the compressive strength loss was minimal from approximately 4% (at 80% GGBS) and 23% (at 60% GGBS, 10% FA, and 10% GP) at 28 days to 3% (at 80% GGBS) and 22% (at 60% GGBS, 10% FA, and 10% GP) at 56 days. At 90% replacement of cement with GGBS, the losses in strength were limited to approximately 20%, which increased to 30% when the cement was fully replaced with GGBS. Even when 90% of cement was replaced with 70% GGBS and 20% FA or 75% GGBS and 15% GP the strength reduction was limited to 32%, which increased to 37% at full replacement of cement with 85% GGBS and 15% GP. These observations indicate the satisfactory strength development of mortars at very high cement and sand replacement ratio and point to the possibility of development of structural grade mortar using 100% waste-based materials.

Direct tensile strength

Figure 6.4 shows the tensile strengths of mortar mixes at 28 days of curing age. It can be seen in the figure that, for a given binder type, LSS mixes exhibited similar tensile strengths to those of NS mixes. This observation is consistent with that from compressive strength test results at 28 days of curing age. Figure 6.4 shows that, among the mortar mixes containing waste-based materials, H20G80 mixes developed only slightly lower tensile strength (7 and 3% in NS and LSS mixes, respectively) than H100 mixes. As can be seen in Fig. 6.4(a), for a given sand type, further increase in GGBS% over 80% resulted in a decrease in the tensile strength of the mortar, which is once again in agreement with the compressive strength results. As can be seen in Fig. 6.4(b), an increase in FA% resulted in a decrease in the direct tensile strength of the mortar. This trend in consistent with the results of previous studies on the splitting tensile and flexural strength of waste-based concretes [36,38]. It can be seen in Figs. 6.4(b) and (c) that, at the same FA% and GP%, H20G70F10 mixes developed an almost identical tensile strength to that of

H20G70P10 mixes, which is in agreement with the compressive strength test results of these mixes.

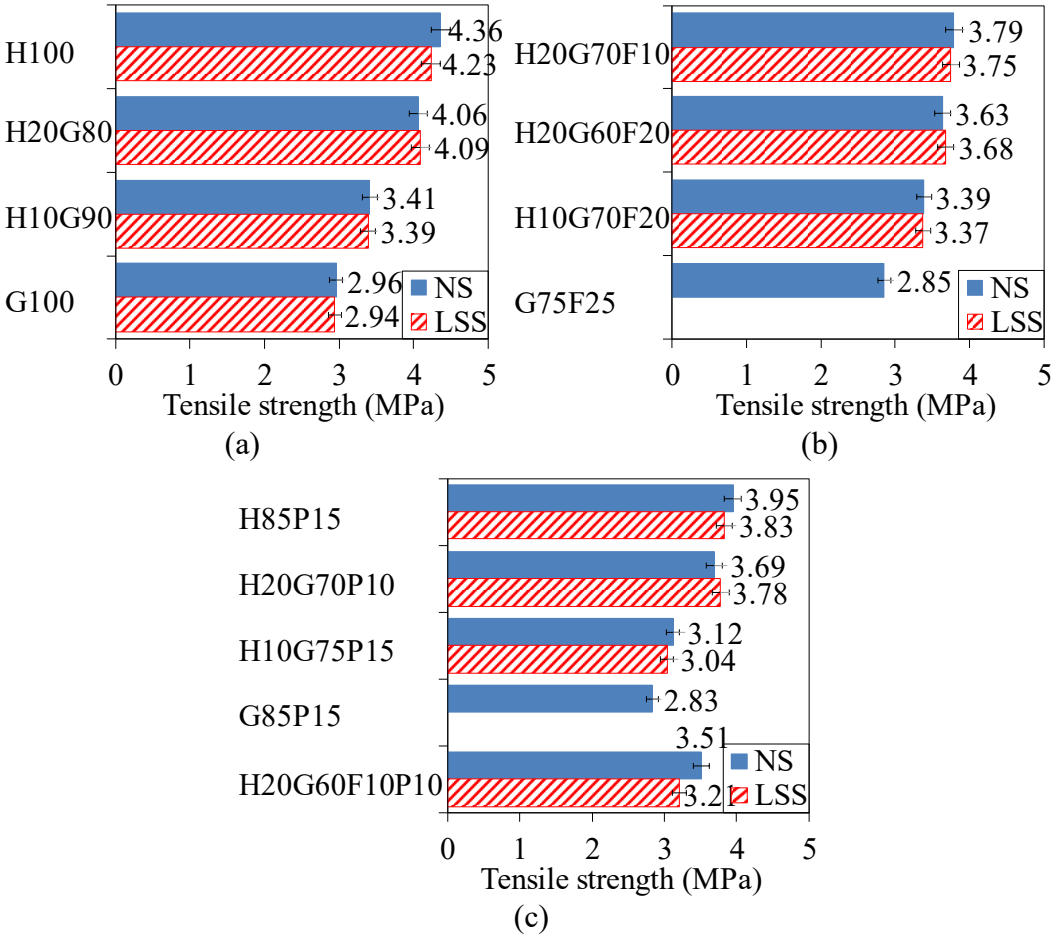

Figure 6.4. Direct tensile strength of different mixes at 28 days: effect of (a) GGBS, (b) FA, and (c) GP addition

By comparison between the tension test results presented in Figs. 6.4(a)-(c) it can be seen that, similar to the compressive strength trends, at 80% cement replacement the tensile strength loss was minimal (from approximately 5% for H20G80 series mixes to 22% for H20G60F10P10 series mixes). At 90% replacement of cement, the tensile strength losses were limited from 21% for H10G90 series mixes to 28% for H10G75P15 series mixes. Even at 100% cement replacement the tensile strength reduction was limited to 32% for G100 series mixes, which increased to 35% for G85P15 series mixes. These observations once again indicate the significant potential for the development of structural grade waste-based mortars through 80% cement replacement and possibility of developing such mortars with up to 100%

cement replacement if the strength loss of the mortar is acceptable or can be compensated by a reduction in water-to-binder ratio (*w/b*).

Microstructural analysis

SEM

Figures 6.5(a)-(f) show the SEM micrographs of the particle shapes of FA, GGBS, GP, HESC, and the two fine aggregates. It can be seen in Figs. 6.5(a) and (b) that both HESC and GP particles had an angular shape. However, GP particles were coarser than HESC particles, which caused mixes containing GP to develop a higher flowability than control mixes. Figures 6.5(c) and (d) show that FA particles were spherical in shape whereas GGBS particles had an irregular shape (with more irregularity than that of HESC). This resulted in a decrease in flowability with an increase in GGBS% and an increase in flowability with an increase in FA%. It can be seen in Figs. 6.5(e) and (f) that LSS had a more angular and irregular shape than NS. This resulted in the lower flowability of the LSS mixes owing to the higher interparticle friction between LSS particles than that of NS particles.

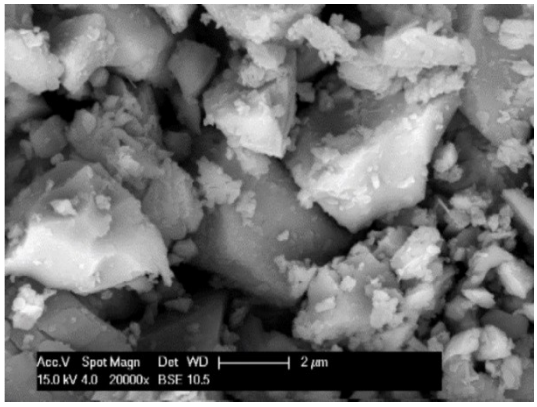

(a)

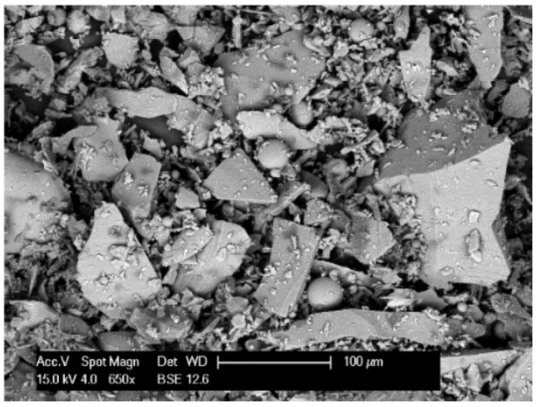

(b)

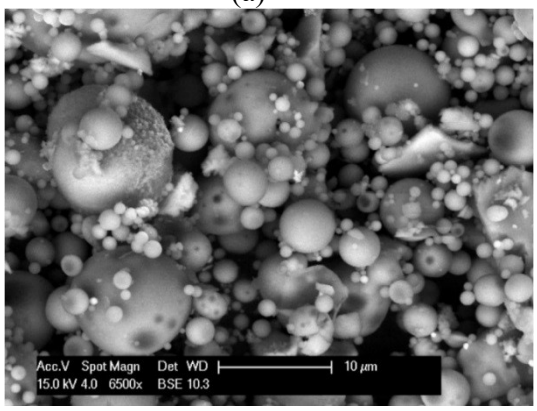

(c)

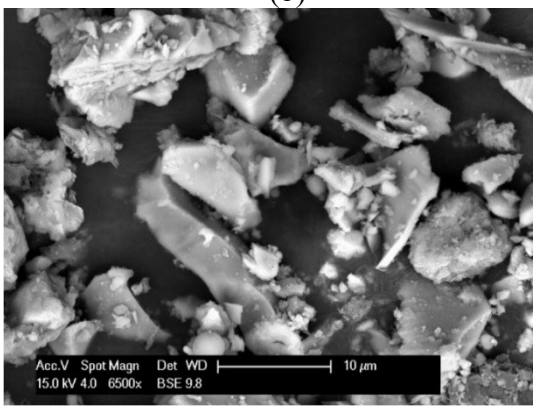

(d)

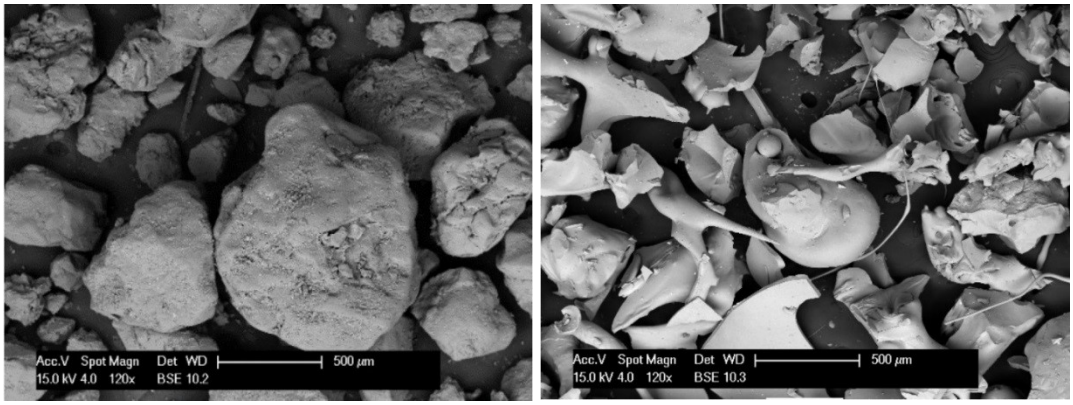

(e) (f)

Figure 6.5. SEM micrographs of particle shapes of (a) HESC, (b) GP, (c) FA, (d) GGBS, (e) NS, (f) LSS

Figure 6.6 shows the SEM micrographs of the fresh-cut surface of H100 mixes containing NS and LSS following the 28-day compression tests. The figure shows that LSS series mixes exhibited different microstructures compared to those of NS series mixes. It can also be seen in the figure that although NS mixes exhibited a more compact microstructure at the binder-sand interfacial transition zone (ITZ) than those of LSS mixes, LSS mixes had needle-shaped crystal hydrates that were well dispersed in their microstructure. This observation suggests that LSS partly reacted with water during the hydration process, which likely resulted in improvements in the mechanical properties of LSS mixes. This would explain the similar mechanical properties observed in companion of LSS and NS mixes, although the former mixes had a less compact microstructure.

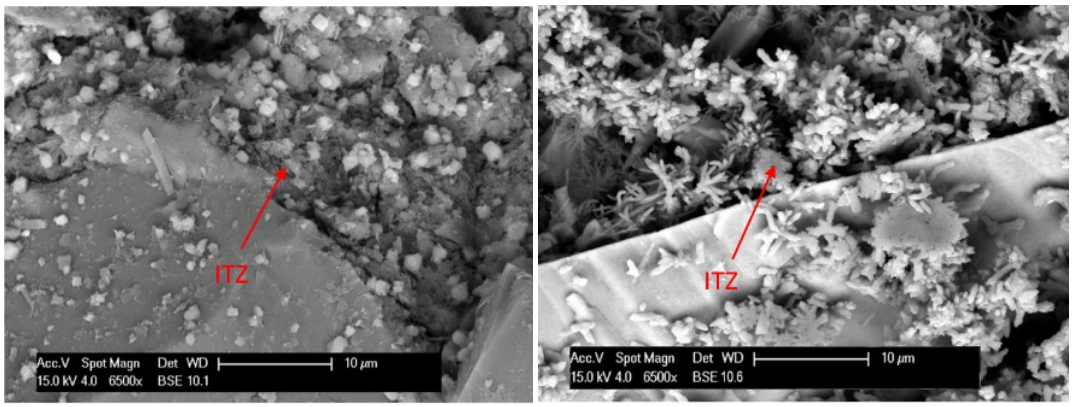

(a) (b)

Figure 6.6. SEM micrographs of the fresh-cut surface of 100% HESC mixes: (a) NS and (b) LSS group following compression tests

Figure 6.7 shows the SEM micrographs of the fresh-cut surface of NS mixes containing HESC and GGBS. Figure 6.7(a) shows that mortar mixes with 80% GGBS exhibited a well-compacted microstructure at the binder-sand ITZ, resulting in a comparable strength to mixes with 100% HESC. However, as can be seen in Figs. 6.7(b) and (c), further increase in GGBS% from 80% to 100% resulted in an increased void porosity in the microstructure of waste-based mortars, which is attributed to the reduced amount of hydration products, leading to not bridging of all the pores and gaps in the microstructure [45,46]. This provides reason to the observed decrease in strength for an increase in GGBS% beyond 80%, as previously discussed in the section of Compressive Strength.

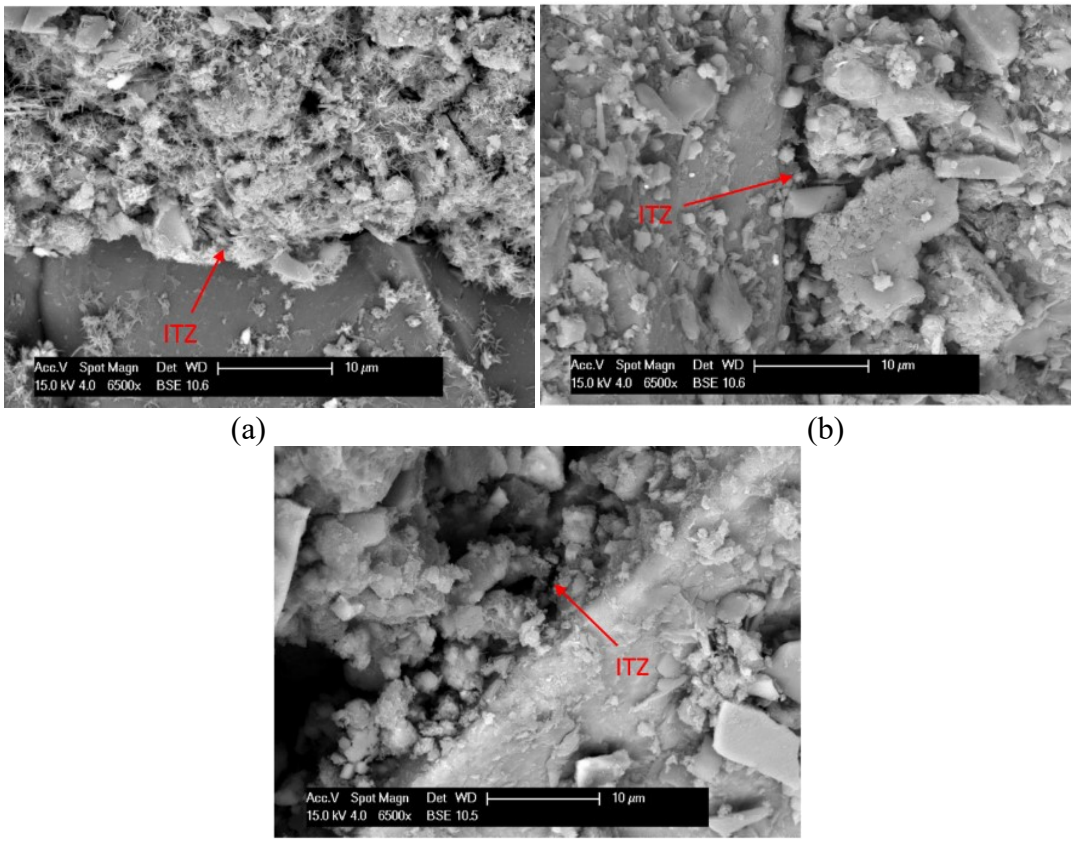

Figure 6.7. SEM micrographs of the fresh-cut surface of NS mixes with: (a) 20% HESC and 80% GGBS, (c) 10% HESC and 90% GGBS, and (d) 100% GGBS following compression tests

Figure 6.8 shows the SEM micrographs of NS mixes containing HESC, GGBS, and FA. As can be seen in the figure, H20G60F20 mixes exhibited a more compact binder-sand ITZ than H10G70F20 mixes, which resulted in a higher strength in the former mixes. Figure 6.9 shows the low- and high-magnification SEM micrographs of mixes containing HESC, GGBS, and GP. The figure shows that H20G70P10

mixes had a more compact microstructure than H10G75P15 mixes. These observations indicate that a decrease in HESC% below 20% led to an increase in the amount of voids in the microstructure of the mortar, which may be explained by the decrease in the amount of hydration products with a decrease in HESC% below 20%, resulting in a decrease in mechanical properties.

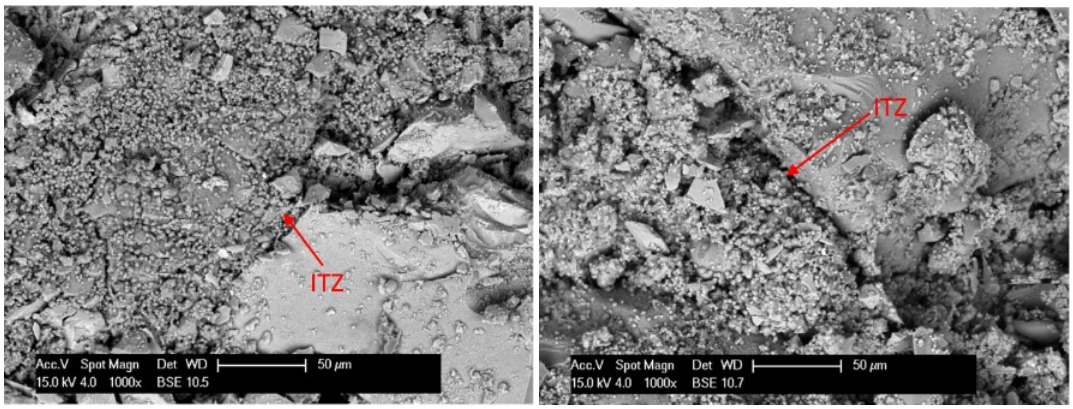

(a) (b)

Figure 6.8. SEM micrographs of the fresh-cut surface of NS mixes with: (a) 20% HESC, 60% GGBS, and 20% FA and (b) 10% HESC, 70% GGBS, and 20% FA following compression tests

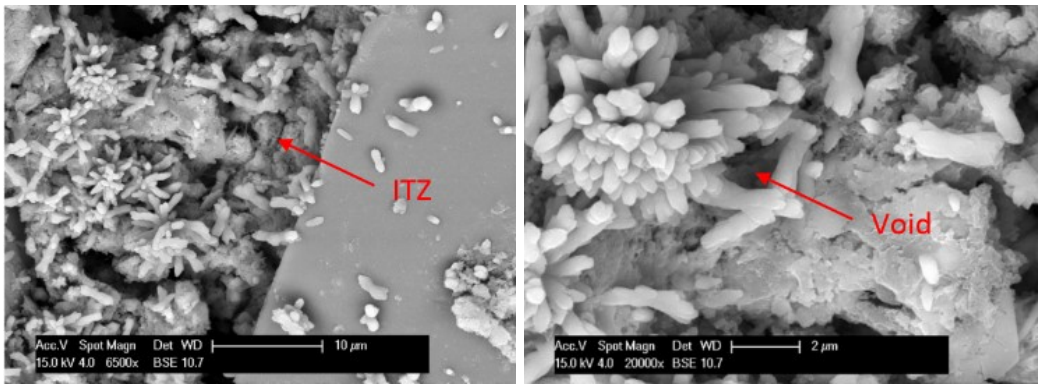

(a)

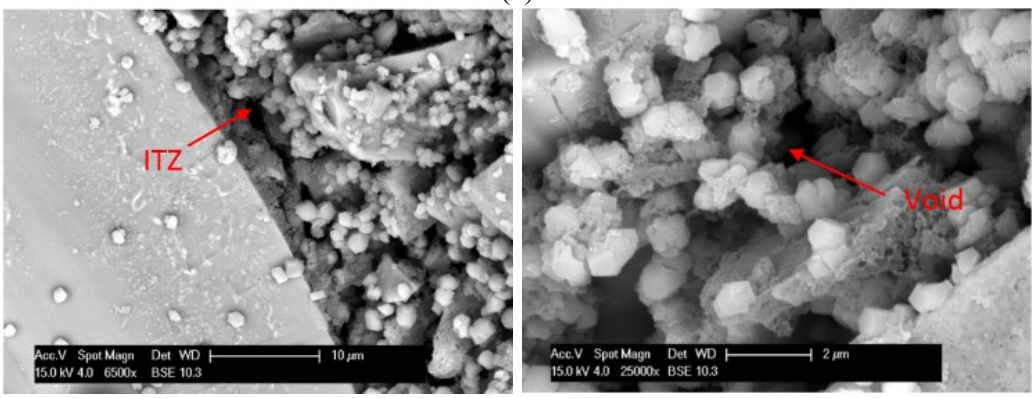

(b)

Figure 6.9. Low- and high-magnification SEM micrographs of the fresh-cut surface of NS mixes with: (a) 20% HESC, 70% GGBS, and 10% GP and (b) 10% HESC, 75% GGBS, and 15% GP following compression tests

Figure 6.10 shows the high-magnification SEM micrographs of H85P15N and H20G80N mixes. The figure shows that most of GP particles remained unreacted in the microstructure of the H85P15N mix, whereas GGBS particles in the H20G80N mix can be seen to have reacted in the mixture. This caused formation of a more compact microstructure in the H20G80N mix compared to that in the H85P15N mix, which resulted in the higher mechanical properties of the former mix as discussed previously. As was reported previously [47-49], glass powders at particle sizes below 75 μm can have pozzolanic reactivity with cement hydrates. As can be seen in Fig. 6.5(b), significant proportion of GP particles had particle sizes larger than 75 μm, which can explain why a large portion of GP particles remained unreacted.

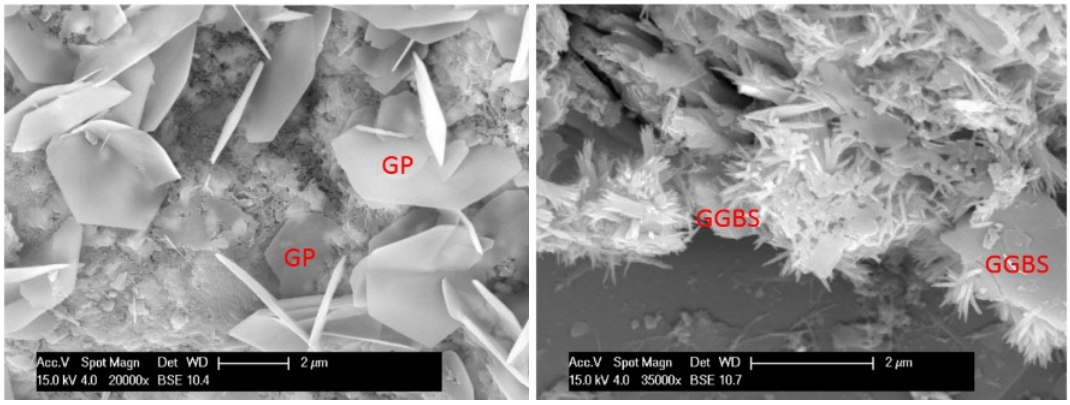

(a) (b)

Figure 6.10. SEM micrographs of the fresh-cut surface of NS mixes with: (a) 85% HESC and 15% GP and (b) 20% HESC and 80% GGBS following compression tests

EDX

Table 6.4 presents the EDX analysis results of different mortar mixes at 28 days of curing age. In this table the hydrogen constituent of the specimens was considered in the oxygen constituent. As shown in Table 6.4, oxygen, silica, aluminum, calcium, and sodium are main constituent elements of waste-based mortar mixes. As can be seen in the table, a decrease in HESC% resulted in a decrease in the combined amount of silica, aluminum, calcium, and sodium, which led to a decrease in the mechanical properties of mortars. The table also shows that an increase in GGBS% from 80% to 100% led to a decrease in the combined amount of silica, aluminum, calcium, and sodium from 70% to 66%, respectively, which indicates a decrease in the amount of hydration products with an increase in GGBS% over 80%.

As can also be seen in Table 6.4, H20G60F20N mix had a lower combined amount of silica, aluminum, calcium, and sodium (68%) compared to H20G80N mix (70%), indicating a reduced amount of hydration products. This is the reason why the strength of mortars decreased with the addition of FA. Table 6.4 shows that H20G80N mix had a slightly higher combined amount of silica, aluminum, calcium, and sodium (70%) compared to H85P15N mix (69%). This can explain the slightly higher 28-day strength of H20G80 series mixes than that of H85P15 series mixes. As can also be seen in the table that H85P15N and H20G80N mixes exhibited a higher amount of silica than H100N mix, causing pozzolanic reaction of GP and GGBS with calcium hydroxide of HESC [50,51]. This can explain why the strength gain of H85P15 and H20G80 series mixes continued at a higher rate than that of H100 series mixes beyond the 7 days of curing age, as discussed in the section of Compressive Strength.

Table 6.4. EDX composition analysis of mixes

Mix	O (wt%)	Si (wt%)	Al (wt%)	Ca (wt%)	Na (wt%)	Others (wt%)
H100N	27.5	19.4	7.56	41.1	3.50	0.93
H100L	25.8	18.2	7.23	42.7	3.61	2.59
H85P15N	27.8	22.6	6.12	34.0	6.77	2.77
H20G80N	27.7	20.2	9.42	38.0	2.65	2.09
H20G60F20N	27.1	23.1	16.5	26.1	2.71	4.44
H20G70P10N	26.1	21.1	8.75	35.8	3.55	4.58
H10G90N	28.3	21.4	10.4	33.5	2.53	3.75
H10G70F20N	28.1	24.8	17.7	22.7	2.66	3.95
H10G75P15N	28.9	23.7	8.97	29.0	5.97	3.42
G100N	30.8	22.1	11.2	30.2	2.55	3.07

CONCLUSIONS

The results of the first study on the properties of waste-based mortars with full and simultaneous replacement of cement with FA, GGBS, and GP and NS with LSS have been presented in this paper. Based on the experimental results and discussions, the following conclusions can be drawn:

1- Waste-based mortars containing NS exhibit higher flow than those containing LSS, owing to the less angular shape of NS particles compared to those of LSS

particles. An increase in GP% results in an increase in the flowability of waste-based mortars, which is because of the lower water absorption of GP than HESC. An increase in GGBS% results in a decrease in the flowability, whereas an increase in FA% results in an increase in the flowability of waste-based mortars owing to the irregular shape of GGBS as opposed to the spherical shape of FA.

2- Waste-based mortars containing 20% HESC and 80% GGBS exhibit very similar mechanical properties to mortars containing 100% HESC, owing to their nearly identical hydration product content and porosity. Even mortars with 90% cement replacement (i.e. 90% GGBS, 70% GGBS and 20% FA, and 75% GGBS and 15% GP) and 100% sand replacement exhibit satisfactory performance with strength reductions of only 20% (at 90% GGBS) to 32% (at 75% GGBS and 15% GP) when compared to that of conventional mortars.
3- Even at full replacement of cement with 100% GGBS, 75% GGBS and 25% FA, or 85% GGBS and 15% GP, the strength reduction over the conventional mortar is limited to the range of 30% (at 100% GGBS) to 37% (at 85% GGBS and 15% GP). This is a very promising observation toward the development of 100% waste-based mortars.
4- The SEM analysis of waste-based mortars revealed that although NS mixes exhibit a more compact microstructure at the binder-sand ITZ than that of LSS mixes, LSS mixes contained needle-shaped crystal hydrates, created by partial reaction of LSS with water during the hydration process and were well dispersed in the microstructure of the mortar. As a result, companion LSS mixes exhibit similar mechanical properties to those of NS mixes.

The promising findings of this study point to the possibility of the development of new structural grade mortars using full or near full replacement of cement with waste-based materials and full replacement of natural sand with waste-based sand. This would lead to the development of eco-friendly construction materials with significant environmental benefits.

ACKNOWLEDGEMENTS

The authors thank Messrs. Aquilina, Dalle-Nogare, Harris, and Pradhan for conducting the experimental tests reported in this paper as part of their Honour's thesis.

REFERENCES

[1] Kurda R, Silvestre JD, de Brito J, Ahmed H. Optimizing recycled concrete containing high volume of fly ash in terms of the embodied energy and chloride ion resistance. *Journal of Cleaner Production*. 2018;194:735-50.

[2] Mehta PK, Meryman H. Tools for reducing carbon emissions due to cement consumption. *Structure Magazine*. 2009;1:11-5.

[3] Golewski GL. Generalized fracture toughness and compressive strength of sustainable concrete including low calcium fly ash. *Materials*. 2017;10:1-22.

[4] Bravard JP, Goichot M, Gaillot S. Geography of sand and gravel mining in the Lower Mekong River. First survey and impact assessment. *EchoGéo*. 2013(26).

[5] Sankh AC, Biradar PM, Naghathan S, Ishwargol MB. Recent trends in replacement of natural sand with different alternatives, *Proceedings of the International Conference on Advances in Engineering and Technology*. 2014. P. 59-66.

[6] Gholampour A, Ozbakkaloglu T. Performance of sustainable concretes containing very high volume Class-F fly ash and ground granulated blast furnace slag. *Journal of Cleaner Production*. 2017;162:1407-17.

[7] Mastali M, Abdollahnejad Z, Pacheco-Torgal F. Performance of waste based alkaline mortars submitted to accelerated carbon dioxide curing. *Resources, Conservation and Recycling.* 2018;129:12-9.

[8] Blissett R, Rowson N. A review of the multi-component utilisation of coal fly ash. *Fuel*. 2012;97:1-23.

[9] Zhao H, Sun W, Wu X, Gao B. The properties of the self-compacting concrete with fly ash and ground granulated blast furnace slag mineral admixtures. *Journal of Cleaner Production*. 2015;95:66-74.

[10] Islam GMS, Rahman MH, Kazi N. Waste glass powder as partial replacement of cement for sustainable concrete practice. *International Journal of Sustainable Built Environment.* 2017;6:37-44.

[11] Prathik Gowda S, Latha MS. Environmental concrete - geopolymer of construction. *International Journal of Current Research*. 2017;9(12):62358-60.

[12] Tsakiridis P, Papadimitriou G, Tsivilis S, Koroneos C. Utilization of steel slag for Portland cement clinker production. *Journal of Hazardous Materials*. 2008;152:805-11.

[13] Ling TC, Poon CS, Wong HW. Management and recycling of waste glass in concrete products: current situations in Hong Kong. *Resources, Conservation and Recycling.* 2013;70:25-31.

[14] Tripathi B, Misra A, Chaudhary S. Strength and abrasion characteristics of ISF slag concrete. *Journal of Materials in Civil Engineering*. 2013;25:1611-8.

[15] Ogundiran M, Nugteren H, Witkamp G. Immobilisation of lead smelting slag within spent aluminate—fly ash based geopolymers. *Journal of Hazardous Materials.* 2013;248:29-36.

[16] Saca N, Radu L, Fugaru V, Gheorghe M, Petre I. Composite materials with primary lead slag content: Application in gamma radiation shielding and waste encapsulation fields. *Journal of Cleaner Production*. 2018;179:255-65.

[17] Chindaprasirt P, Homwuttiwong S, Sirivivatnanon V. Influence of fly ash fineness on strength, drying shrinkage and sulfate resistance of blended cement mortar. *Cement and Concrete Research*. 2004;34(7):1087-98.

[18] Shi C, Wu Y, Riefler C, Wang H. Characteristics and pozzolanic reactivity of glass powders. *Cement and Concrete Research*. 2005;35:987-93.

[19] Barnett SJ, Soutsos MN, Millard SG, Bungey JH. Strength development of mortars containing ground granulated blast-furnace slag: effect of curing temperature and determination of apparent activation energies. *Cement and Concrete Research.* 2006;36:434-40.

[20] Guneyisi E, Gesoglu M, Ozbay E. Effects of marble powder and slag on the properties of self compacting mortars. *Materials and Structures*. 2009;42:813-26.

[21] Zhong S, Ni K, Li J. Properties of mortars made by uncalcined FGD gypsum-fly ash-ground granulated blast furnace slag composite binder. *Waste Management.* 2012;32:1468-72.

[22] Yildirim K, Sumer M. Effects of sodium chloride and magnesium sulfate concentration on the durability of cement mortar with and without fly ash. *Composites Part B*. 2013;52:56-61.

[23] Isikdag B, Topcu IB. The effect of ground granulated blast-furnace slag on properties of Horasan mortar. *Construction and Building Materials*. 2013;40:448-54.

[24] Supit SWM, Shaikh FUA, Sarker PK. Effect of ultrafine fly ash on mechanical properties of high volume fly ash mortar. *Construction and Building Materials.* 2014;51:278-86.

[25] Tsai CJ, Huang R, Lin WT, Wang HN. Mechanical and cementitious characteristics of ground granulated blast furnace slag and basic oxygen furnace slag blended mortar. *Materials and Design*. 2014;60:267-73.

[26] Aliabdo AA, Elmoaty A, Aboshama AY. Utilization of waste glass powder in the production of cement and concrete. *Construction and Building Materials*. 2016;124:866-77.

[27] Tekin I, Durgun MY, Gencel O, Bilir T, Brostow W, Lobland HEH. Concretes with synthetic aggregates for sustainability. *Construction and Building Materials.* 2017;133:425-32.

[28] ASTM C109/C109M-07. *Standard Test Method for Compressive Strength of Hydraulic Cement Mortars,* ASTM International: USA 2008.

[29] ASTM C307-03. *Standard Test Method for Tensile Strength of Chemical-Resistant Mortar, Grouts, and Monolithic Surfacings*, ASTM International: USA 2012.

[30] ASTM C1437-15. *Standard Test Method for Flow of Hydraulic Cement Mortar,* ASTM International: USA 2015.

[31] Tiwari A, Singh S, Nagar R. Feasibility assessment for partial replacement of fine aggregate to attain cleaner production perspective in concrete: A review. *Journal of Cleaner Production*. 2016;135:490-507.

[32] Yang KH, Song JK, Ashour AF, Lee ET. Properties of cementless mortars activated by sodium silicate. *Construction and Building Materials*. 2008;22:1981-9.

[33] Guneyisi E, Gesoglu M, Ozbay E. Strength and drying shrinkage properties of self-compacting concretes incorporating multi-system blended mineral admixtures. *Construction and Building Materials*. 2010;24:1878-87.

[34] Wang C, Yang C, Liu F, Wan C, Pu X. Preparation of ultra-high performance concrete with common technology and materials. *Cement and Concrete Composites.* 2012;34:538-44.

[35] Hou PK, Kawashima S, Wang KJ, Corr DJ, Qian JS, Shah SP. Effects of colloidal nanosilica on rheological and mechanical properties of fly ash-cement mortar. *Cement and Concrete Composites*. 2013;35:12-22.

[36] Sahmaran M, Yaman IO, Tokyay M. Transport and mechanical properties of self consolidating concrete with high volume fly ash. *Cement and Concrete Composites*. 2009;31:99-106.

[37] Bingol AF, Tohumcu I. Effects of different curing regimes on the compressive strength properties of self compacting concrete incorporating fly ash and silica fume. *Materials and Design*. 2013;51:12-8.

[38] Jalal M, Pouladkhan A, Harandi OF, Jafari D. Comparative study on effects of class F fly ash, nano silica and silica fume on properties of high performance self compacting concrete. *Construction and Building Materials*. 2015;94:90-104.

[39] Nath P, Sarker PK. Effect of GGBFS on setting, workability and early strength properties of fly ash geopolymer concrete cured in ambient condition. *Construction and Building Materials*. 2014;66:163-71.

[40] Neupane K, Kidd P, Chalmers D, Baweja D, Shrestha R. Investigation on compressive strength development and drying shrinkage of ambient cured powder-activated geopolymer concretes. *Australian Journal of Civil Engineering.* 2016;14:72-83.

[41] Schwarz N, Cam H, Neithalath N. Influence of a fine glass powder on the durability characteristics of concrete and its comparison to fly ash. *Cement and Concrete Composites.* 2008;30:486-96.

[42] Soliman NA, Tagnit-Hamou A. Development of ultra-high-performance concrete using glass powder – Towards ecofriendly concrete. *Construction and Building Materials.* 2016;125:600-12.

[43] Kuder K, Lehman D, Berman J, Hannesson G, Shogren R. Mechanical properties of self consolidating concrete blended with high volumes of fly ash and slag. *Construction and Building Materials*. 2012;34:285-95.

[44] Gholampour A, Ho VD, Ozbakkaloglu T. Ambient-cured geopolymer mortars prepared with waste-based sands: Mechanical and durability-related properties and microstructure. *Composites Part B*. 2018.

[45] Yazici H, Yardimci MY, Yigiter H, Aydin S, Turkel S. Mechanical properties of reactive powder concrete containing high volumes of ground granulated blast furnace slag. *Cement and Concrete Composites*. 2010;32:639-48.

[46] Rashad AM. An investigation of high-volume fly ash concrete blended with slag subjected to elevated temperatures. *Journal of Cleaner Production*. 2015;93:47-55.

[47] Shao Y, Lefort T, Moras S, Rodriguez S. Studies on concrete containing ground waste glass. *Cement and Concrete Research*. 2000;30:91-100.

[48] Chen CH, Huang R, Wu JK, Yang CC. Waste E-glass particles used in cementitious mixtures. *Cement and Concrete Research*. 2006;36(3):449-56.

[49] Schwarz N, Neithalath N. Influence of a fine glass powder on cement hydration: Comparison to fly ash and modeling the degree of hydration. *Cement and Concrete Research.* 2008;38:429-36.

[50] Oner A, Akyuz S. An experimental study on optimum usage of GGBS for the compressive strength of concrete. *Cement and Concrete Composites*. 2007;29(6):505-14.

[51] Mohd Nasir NA, Abd Aziz FNA, Safiee NA. Hydration of the combinations of ground granulated blast furnace slag cements. *Australian Journal of Basic and Applied Sciences*. 2014;8(1):392-6.

Chapter 3

Graphene-cement mortar composites

Publications:

Gholampour A, Valizadeh Kiamahalleh M, Tran DNH, Ozbakkaloglu T, Losic D. Revealing the dependence of the physiochemical and mechanical properties of cement composites on graphene oxide concentration. *RSC Advances*. 2017;7(87):55148-56. ***Citations: 7***

Gholampour A, Valizadeh Kiamahalleh M, Tran DNH, Ozbakkaloglu T, Losic D. From graphene oxide to reduced graphene oxide: impact on the physiochemical and mechanical properties of graphene-cement composites. *ACS Applied Materials & Interfaces*. 2017;10.1021/acsami.7b16736. ***Citations: 13***

Statement of Authorship

Title of Paper	Revealing the dependence of the physiochemical and mechanical properties of cement composites on graphene oxide concentration
Publication Status	☑ Published ☐ Accepted for Publication ☐ Submitted for Publication ☐ Unpublished and Unsubmitted work written in manuscript style
Publication Details	Gholampour A, Valizadeh Kiamahalleh M, Tran DNH, Ozbakkaloglu T, Losic D. Revealing the dependence of the physiochemical and mechanical properties of cement composites on graphene oxide concentration. *RSC Advances*. 2017;7(87):55148-56.

Principal Author

Name of Principal Author (Candidate)	Aliakbar Gholampour		
Contribution to the Paper	Literature review, experimental testing, analysis of test results, and preparation of the manuscript.		
Overall percentage (%)	60%		
Certification:	This paper reports on original research I conducted during the period of my Higher Degree by Research candidature and is not subject to any obligations or contractual agreements with a third party that would constrain its inclusion in this thesis. I am the primary author of this paper.		
Signature		Date	31/01/2019

Co-Author Contributions

By signing the Statement of Authorship, each author certifies that:

i. the candidate's stated contribution to the publication is accurate (as detailed above);

ii. permission is granted for the candidate in include the publication in the thesis; and

iii. the sum of all co-author contributions is equal to 100% less the candidate's stated contribution.

Name of Co-Author	Meisam Valizadeh Kiamahalleh		
Contribution to the Paper	Experimental testing, analysis of test results, and preparation of the manuscript.		
Signature		Date	31/01/2019

Name of Co-Author	Diana N.H. Tran		
Contribution to the Paper	Review of manuscript.		
Signature		Date	31/01/2019

Name of Co-Author	Togay Ozbakkaloglu		
Contribution to the Paper	Research supervision and review of manuscript.		
Signature		Date	31/01/2019

Name of Co-Author	Dusan Losic		
Contribution to the Paper	Research supervision and review of manuscript.		
Signature		Date	27/02/2019

Please cut and paste additional co-author panels here as required.

Revealing the Dependence of the Physiochemical and Mechanical Properties of Cement Composites on Graphene Oxide Concentration

GRAPHICAL ABSTRACT

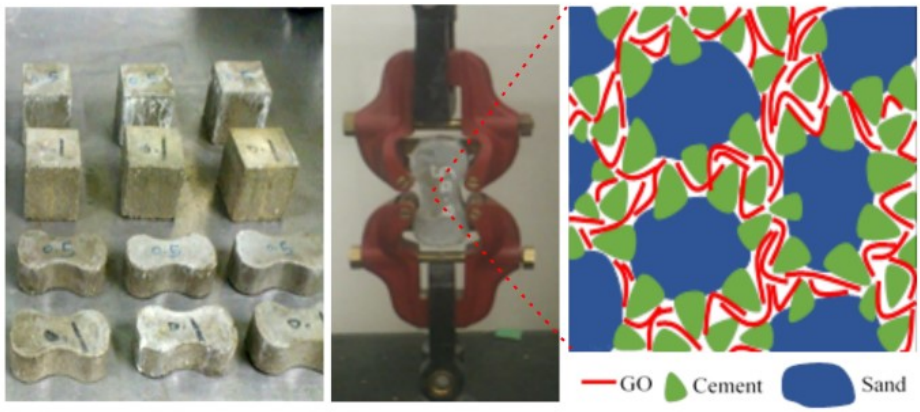

ABSTRACT

This paper presents a comprehensive study to evaluate the influence of graphene oxide (GO) concentration on the physiochemical and mechanical properties of cement mortar composites. Scanning electron micrographs (SEM), energy-dispersive X-ray spectroscopy (EDX), X-ray diffraction (XRD), thermogravimetric analysis (TGA), and Fourier transform infrared spectroscopy (FTIR) characterizations were performed to understand the correlation between physicochemical and observed axial tension and compression properties of GO–cement mortar composites. The results show considerable concentration dependence with the optimum concentration of 0.1% GO that increases the tensile and compressive strength of the composite by 37.5% and 77.7%, respectively. These results are explained by stronger bonding of calcium silicate hydrate (C–S–H) components in the cement matrix in the presence of GO sheets and dependence of their dispersions and possible aggregation.

KEYWORDS: Graphene oxide, cement mortar, mechanical strength, microstructure, chemical behaviour.

INTRODUCTION

Cementitious materials are the most widely used construction materials throughout the world. Although this type of material has relatively good compressive strength, brittleness, very low tensile strength and strain, and low flexural strength are their weaknesses [1,2]. Many researchers have tried to improve the mechanical properties of cementitious materials using different types of fibers and additives [3,4]. Recently, the use of nanoparticles in cementitious materials to improve their mechanical properties by controlling the nanoscale crack formation has received widespread attention.

A large number of studies conducted to date have shown that the use of nanoparticles in the cementitious materials results in the delay of the nanoscale cracks (at the initial stage of loading) in the material before generation of the microscale cracks [3,5-8]. As was reported by Chang et al. [7] and Madani et al. [8], a high specific surface area of nanoparticles (e.g. nanosilica and nanoclay) could result in the accelerated transformation of C–S–H surrounding the cement particles to the stable form through fast pozzolanic activity. This produces additional C–S–H gel, which improves internal paste-to-aggregate binding. The developments of graphene as a new type of carbon and 2-d materials with a unique 2-d structure, e.g. high surface area, good chemical, mechanical, and thermodynamic properties, presented a new opportunity to further improve properties of cementitious materials [9-12]. Graphene is usually prepared by exfoliating the graphite in water using sonication and with oxidation using strong oxidizing agents. Graphite oxide is separated into several single layers, as graphene oxide (GO), which is easily dispersible in water. Another form of graphene is reduced graphene oxide (rGO) prepared by reducing oxygen groups of pristine graphene, which is obtained directly from graphite. Graphene has an intrinsic strength and Young's modulus of up to 130 GPa and 1 TPa, respectively [13,14]. The surface area of the GO layer is theoretically 2600 m^2/g, which is higher than those of carbon nanotube and nanosilica (i.e. 1000 and 300 m^2/g, respectively) [15].

In recent years, several studies have proposed the significant potential of GO for enhancing mechanical properties of cementitious materials and designing new

composites for specific applications [5-6,10,16-21]. These studies indicated that GO can be dispersed in the cement matrix more homogeneously than graphene and graphite. The microstructure and mechanical properties of the GO–cement mortar have been studied by Lv et al. [5] and the results showed that the inclusion of GO in the cement mortar results in enhancements in its tensile, compressive, and flexural strengths through formation of the flower-like hydration crystals. Alkhateb et al. [16] showed that 0.5% addition of functionalized graphene nano-platelets in the cement paste resulted in a 23% increase in the elastic modulus. Fakhim et al. [17] reported that the tensile strength of the cement mortar increased by 48% after the addition of the optimum amount of 1.5% GO in the composite. Sharma and Kothiyal [18] found that inclusion of GO sheets with an average size of 900 nm at a rate of 1% results in 63% increase in the compressive strength of cement mortar composites. Slightly different results are reported by Pan et al. [6] showing that the addition of 0.05% GO improves the compressive strength and flexural strength of the GO–cement paste by 33% and 58%, respectively. Gong et al. [19] found that the degree of hydration of the cement paste is enhanced by addition of GO amount. They also reported that 0.03% GO in the cement composite exhibits 13.5% lower porosity than the normal cement paste. The addition of GO is confirmed to lower fluidity and improved compressive and flexural strengths for the GO–cement mortar composite in comparison with the conventional cement mortar [20]. Lu et al. [21] investigated the effect of the GO on the mechanical behaviour of the strain hardening cementitious composites, showing that addition of 0.08% GO by weight results in 24.8%, 37.7%, 80.6%, and 105% increases in the compressive strength, tensile strength, flexural strength, and flexural toughness of the cement mortar composite, respectively. The electrical behaviour of the GO–cement paste was also investigated by Singh et al. [10] showing that the addition of GO with an appropriate amount of ferrofluid results in an increase in the electrical conductivity of the cement paste. As evident from the results of the existing studies, improved mechanical and electrical properties along with the accessible source and highly dispersible properties in water, makes GO a promising material in the preparation of high performance cement mortar composites [6].

However, although significant progress has been made in previous studies, there is considerable inconsistency in these reports showing different effects of GO on the

mechanical properties of composite due to the use of different GO materials and preparation conditions, neither properly characterized. These studies were mainly focused on conducting mechanical tests to show the effect of GO on the mechanical properties of composite without presenting or exploring how properties of used GO materials including the concentration, size, number of layers, defects, and density of oxygen groups could influence these properties. As cementitious materials are complex mixtures involving many components and interactions, the study of the influence of the GO parameters on the molecular bonds, crystalline phases, and hydration degree of the composites is essential to understand and explain the observed impact on mechanical properties. The study of the effect of these GO parameters on the mechanical properties of cement mortar composites is currently missing and it is highly important to understand the mechanisms and fundamental aspects behind the improvements observed in the mechanical properties. Our research team is exploring the parameters of GO including concentration, size, chemistry, and surface modifications in order to improve existing knowledge and better understanding their influence at molecular-, and nano-, and micro-scale on mechanical properties of cementitious materials.

In this paper, we present the first in series of studies, with the aim of investigating the influence of GO contents on the physiochemical and mechanical properties of cement mortar composites. To find these correlations, GO–cement mortar composites were prepared using a broad range of GO dosages (i.e. 0–0.5% by weight of cement) and their physical, structural, chemical, and mechanical properties were comprehensively characterized using scanning electron micrographs (SEM), energy-dispersive X-ray spectroscopy (EDX), X-ray diffraction (XRD), thermogravimetric analysis (TGA), Fourier transform infrared spectroscopy (FTIR), and axial compression and tension tests. The results were used to find the optimal GO concentration that provides the best mechanical performance and to help us to gain better understanding of the mechanisms behind the improvements. Promising results from this study indicate that properties of cement mortar composites can be significantly enhanced by GO and potentially tailored in combination with other additives for specific applications.

EXPERIMENTAL SECTION

Materials

Preparation of GO

GO was produced from the oxidation of natural graphite using the improved Hummer's method [22]. A 9:1 mixture of concentrated sulphuric acid and phosphoric acid (120:13 ml) was cooled overnight to 4 °C. The cooled acid mixture was slowly added to the graphite powder (1 g) and potassium permanganate (6 g) during stirring at room temperature. Then, the mixture was heated to 50 °C for about 12 hours to form a thick paste. After the completion of the reaction, the paste was cooled down to room temperature and quickly poured onto the ice cubes (150 ml) with 30% hydrogen peroxide (1 ml) for an hour. The mixture was then washed and filtered with distilled water and hydrochloric acid (32%), followed by repeated washing with ethanol and eventually with Milli-Q water. For each wash, the obtained brown dispersion was centrifuged at 4400 rpm for two hours to remove residual salts and any un-exfoliated graphite oxide. The obtained GO was vacuum dried overnight at room temperature. Figure A1 (see Appendix 2) shows the graphite powder and final GO solution.

Graphite flakes were obtained from Valence Industries Ltd. Australia. Other chemicals, including 98% sulfuric acid (H_2SO_4, Sigma-Aldrich), 85% phosphoric acid (H_3PO_4, Chem-Supply), potassium permanganate ($KMnO_4$, Sigma-Aldrich), 30% hydrogen peroxide (H_2O_2, Chem-Supply), 35% hydrochloric acid (HCl, Merck), and ethanol (Chem-Supply) were used. Milli-Q water (Purelab option-Q, 18.2 MΩ-cm at 25 °C and a pH of 5.6) was used in all aqueous solutions.

Preparation of cement mortar

Ordinary Portland cement and graded river sand of 2–mm maximum size were used in the preparation of the cement mortars. Tables A1 and A2 (see Appendix 2) show the particle size distribution of the sand and chemical composition of the Portland cement used in this study, respectively. GO was added to the mortar mixes at eight different contents of 0% (as a control sample), 0.01%, 0.03%, 0.05%, 0.07%, 0.1%, 0.3%, and 0.5% by weight of cement for the preparation of the GO–cement mortar composites. These GO concentrations were determined based on a preliminary study

and careful review of the literature to establish an optimum amount of GO for improving the tensile and compressive strength of cement mortar composites [5,6,17,20,21]. All the mixes had a water to cement ratio (*w/c*) of 0.485. The mix proportions of these eight mixes are shown in Table A3 (see Appendix 2). Three nominally identical specimens were tested for each unique specimen configuration in direct tension and compression tests. Polycarboxylic ether polymer-based superplasticizer with the properties shown in Table A4 (see Appendix 2) was used in all mixes to increase the workability and ensure the uniform dispersion of GO particles in the composite. Flowability test was conducted on the fresh mortar mixes to investigate their workability according to the ASTM standard C1437 [23]. Table A5 (see Appendix 2) shows the results of flowability tests. For the direct tension tests, typical dog-bone shaped samples with a test region width and depth of 25±0.5 mm were used in accordance with the ASTM standard C307-03 [24]. 50 mm cube samples were used for the compression tests according to the ASTM standard C109/C109M-07 [25].

In order to improve the dispersion of GO in the mortar mixture, the following procedure was adopted. Firstly cement and sand were mixed together at a low speed of 40 rpm for 2 min. Then superplasticizer was added to the GO solution and the mixture was sonicated for 10 min. Finally GO solution was gradually added to the mix and the materials were mixed for 5 min before the mixtures were poured into the moulds. Once the specimens were demolded, they were cured in the fog room at a constant temperature of 23±2 °C until the test days. Figure A2 (see Appendix 2) shows the samples used in the direct tension and compression tests.

Characterizations

Transmission Electron Microscopy (TEM)

The morphology of GO particles was characterized with a transmission electron microscope (Phillips TEM CM200, FEI, USA) operating at an accelerating voltage of 160 kV. The sample was prepared by sonicating GO in water for 60 min and then drop casting the dispersion on a Lacey copper grid for analysis.

Scanning Electron Microscopy (SEM)

The dispersion and bonding properties between the GO sheets at the surface of the cement mortar were investigated by High Resolution Field Emission Scanning Electron Microscope (FEI Quanta 450). The SEM analysis was conducted after the 28-day mechanical tests and on the polished fresh cut surface of the specimens, which was cut with dimensions of approximately 8×4×3 mm. The specimens were then coated by a 10 nm-thick platinum layer to enhance the conductivity in the SEM analysis.

Atomic Force Microscopy (AFM)

The thickness of GO was characterized with a Ntegra Solaris atomic force microscopy (NT-MDT, Russia) in semi-contact (tapping) mode at room temperature using a NSG10 probe made of silicon nitride with a 10 nm tip radius. The sample was prepared by dispersing GO in ethanol, drop casted on a cleaned silicon wafer then left to dry in air before analysis.

Composition analysis

The composition of the mortar matrix was determined in two ways. Energy Dispersive X-Ray (EDX) spectroscopy was conducted on the polished fresh cut surface of specimens using TEAM EDS with SDD Detector to determine the constituent elements of the materials, whereas X-ray diffraction (XRD) was performed using X-ray diffractometer (Rigaku MiniFlex 600, Japan), at 40 kV and 15 mA in the range of 2θ = 5–80° with a scanning rate of 10 °C/min and CuKα radiation (λ= 1.540 Å), to determine the crystalline phases of the GO and GO-enriched hydrated cementitious composite materials.

Thermogravimetric analysis (TGA)

Thermal decomposition of GO was performed on the composites by a thermal gravimetric analyzer (TGA Q500, USA) under air atmosphere where the sample was heated from room temperature to 1000 °C at a heating rate of 20 °C/min. Also, in order to examine the influence of GO incorporation on the hydration properties of the cement paste, TGA was performed on the samples after 7 and 28 days of curing. Samples were kept in an alumina crucible and a Mettler Toledo TGA testing

machine was used for the analysis. In each test, approximately 25–35 mg of composite was heated from room temperature to 1000 °C under the flow of nitrogen with a heating rate of 10 °C/min.

In the TGA, two parameters of evaporable (free) and non-evaporable (bound) water contents are determined. The content of the evaporable water, which is the water on the outer surface of the composite particles, is recorded as a percentage of the weight loss for temperatures that ranged from room temperature to 145 °C. The content of non-evaporable water is determined as the percentage of the weight loss from 145 °C to 1000 °C, minus the weight loss from 600 °C and 800 °C, as a result of the CO_2 release by the calcite decomposition [19,26–29]. The non-evaporable water content of GO-cement composite is used to calculate the hydration degree of the sample (i.e. αTGA(t)) using the following equation [26]:

$$\alpha\text{TGA}(t)(\%)=(W_n(t))/(M_c\times W_n(\infty))\times 100 \quad (7.1)$$

where $W_n(\infty)$ is the non-evaporable water mass (g/g of cement) at the time $t\rightarrow\infty$. $t\rightarrow\infty$ corresponds to the time of full hydration of 1 g of cement, in which $W_n(\infty)$ is estimated as 0.2293 g from the mineralogical composition of cement [30]. $W_n(t)$ and M_c are the non-evaporable water mass at the time (t) and the initial anhydrous paste mass of the sample in g, respectively.

Fourier transform infrared spectroscopy (FTIR)

Vibrational stretching modes of different molecular bonds, including GO oxygen functional groups as well as the formation of $Ca(OH)_2$ and C–S–H in the GO–hydrated cementitious composite materials were confirmed by Fourier transform infrared spectroscopy (FTIR) analysis using Nicolet 6700 Thermo Fisher [29].

Raman spectra

Raman measurements were performed on a LabRAM HR Evolution Raman spectrometer (Horiba Scientific, Japan) with a 532 nm laser scanned from 750 to 3000 cm^{-1}. The parameters were set up as follows: a 50x objective, spot size of 100, 25% laser power, and 10 sec integration time for 3 accumulations.

Mechanical characterizations of tension and compression performances

To evaluate the mechanical behaviour of the mortar samples with different GO contents, prepared specimens were tested under axial tension and compression loadings with displacement control. Figure A3 (see Appendix 2) shows the equipment used in these tests. The ultimate tensile and compressive strengths were averaged from three tests on identical specimens for each mix proportions. The axial compressive strains of the specimens were measured by two linear variable displacement transformers (LVDTs) mounted at the corners of steel loading and supporting plates.

RESULTS AND DISCUSSION

Physical and chemical characterization of GO–cement mortar composites

Figure 7.1 shows the characterization results of GO sheets, used for making cement mortar composites. Figure 7.1(a) shows a typical TEM image of GO sheets showing their irregular shape and amorphous nature with a paper-like appearance with an approximate thickness of 1 nm, attributed to a single layer sheet (see Fig. A1 in Appendix 2). The crystal structure of GO was evaluated by XRD showing the characteristic 002 reflection peak at 2θ (scattering angle) = 11.1° (d-spacing = 0.79 nm, Fig. 7.1(b)) and TGA (Fig. 7.1(c)) confirmed the typical decomposition pattern of GO related to its oxygen functional groups [31-34].

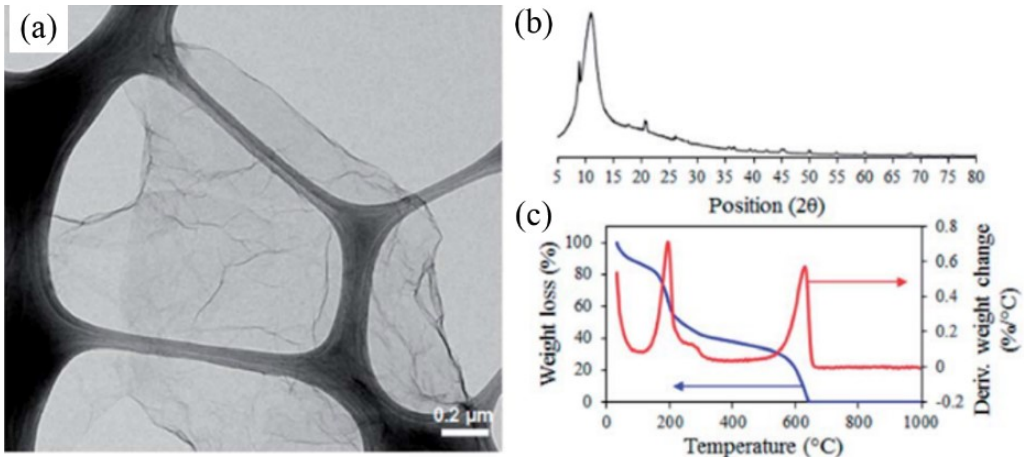

Figure 7.1. (a) TEM image, (b) XRD, and (c) TGA plots of GO material exfoliated from graphite and used for composite preparation

In order to explain the influence of the GO content on the mechanical behaviour of the cement mortar composite, SEM, EDX, XRD, TGA, and FTIR tests were performed on the composites with GO dosages of 0% (as the control sample), 0.03% (as representative effective low dosage), 0.1% (as the optimum dosage obtained from mechanical results), and 0.5% (as the maximum dosage).

Figure 7.2 shows the cracking patterns of the prepared cement mortar composites with GO contents of 0%, 0.03%, 0.1%, and 0.5% using low magnification SEM images. As shown in Fig. 7.2, the density of micro-cracks attributed to the poor bonding between the microparticles (sand and cementitious particles) in both cement mortar composites with 0% and 0.5% of GO incorporation is higher than those with 0.03% and 0.1% GO incorporation. This behaviour is attributed to the high dispersibility of GO sheets in the composite at up to an optimum GO concentration, which make them efficient in reinforcing the bridge of the micro-cracks and control the crack propagation from nanoscale to microscale [3,35]. Figure A4 (see Appendix 2) shows the enlarged cracks in cement mortar composites containing 0% and 0.5% GO.

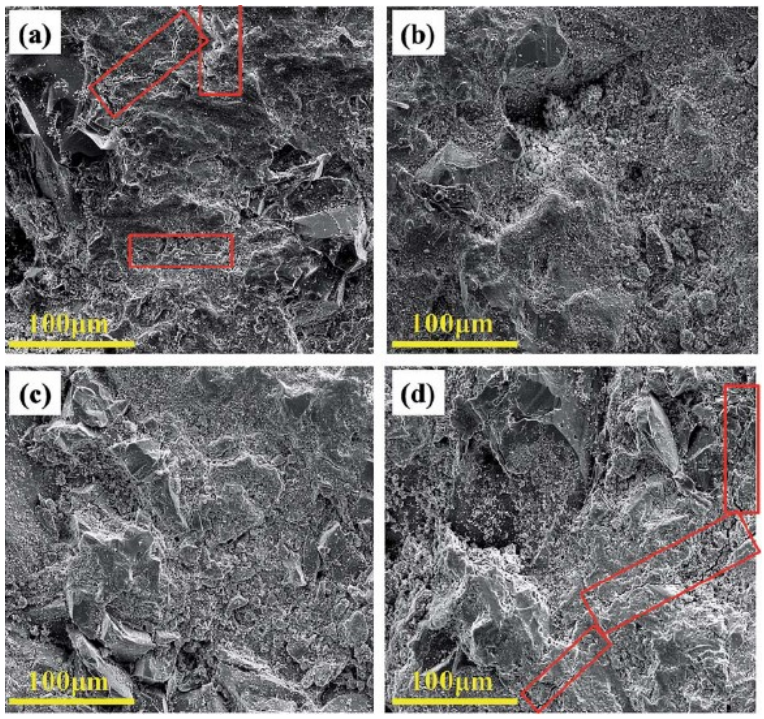

Figure 7.2. Low magnification SEM images of the cross-sectional structures of cement mortars with different GO contents (%): (a) 0%, (b) 0.03%, (c) 0.1%, and (d) 0.5%. Red boxes highlight the micro-cracks on the composite with no GO (a) and high concentration of GO (i.e. 0.5%) (d).

Figure 7.3 shows high magnification SEM images at the surface of the samples with GO contents of 0%, 0.03%, 0.1%, and 0.5%. Figure A5 (see Appendix 2) shows the enlarged SEM images of GO dispersion in cement mortar composites. As can be seen in Fig. 7.3(a), after hydration the plain mortar consists of pores, which were partially filled with the cement paste, and some gaps, which yet remained between the particles. By increasing the GO content to 0.03% and 0.1% (Figs. 7.3(b) and 7.3(c), respectively), the GO sheets were uniformly dispersed between the mortar materials without any aggregation in the cementitious mortar matrix. In these GO contents, the GO sheets were found to be embedded as an individual sheet in the paste that were strongly anchored on the particles and acted as bridges between hydrates and across the composite particles. It is seen from Fig. 7.3(d) that, with an increase in the GO content up to 0.5%, GO sheets are re-stacked and re-agglomerated to platelets, which resulted in the poor bond, interparticle interaction, and bridging in the mortar microstructure. This behaviour is attributed to the trapping of most of the GO in-plane oxygen groups between the GO layers, which prevents them from being able to contribute to the hydration and interaction with the C–S–H bonds [16,36]. The scheme to visualize the two stages with uniformly dispersed and aggregated GO sheets as a result of different GO concentration is presented in Fig. 7.3(e) (left and right, respectively). This is the first observation and report of the threshold GO concentration in cement composites. Considering that observed aggregation of GO sheets in cement mortar composites is not only dependent on GO concentration but also potentially on other parameters including the size of GO, their charge, condition of their mixing with mortar, and composition of mortar composites, this could explain the large discrepancy in results on the mechanical properties of these composites in previous reports.

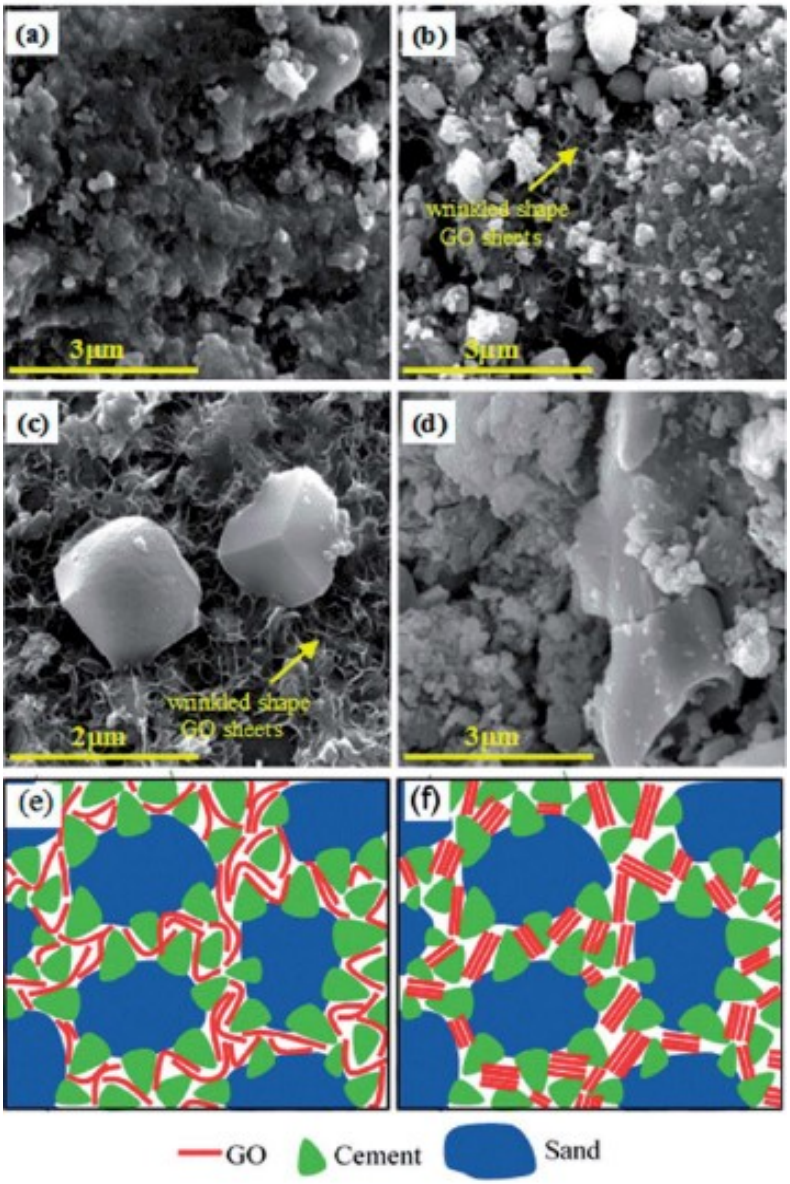

Figure 7.3. High magnification SEM micrographs of cement mortars with different GO contents (%): (a) 0%, (b) 0.03%, (c) 0.1%, and (d) 0.5%. (b) and (c) show the presence of GO sheets with good dispersion that are anchored to large cement and sand particles. GO sheets with high concentration in (d) stacks and takes flake shapes in the matrix. (e-f) shows the scheme to visualize uniformly dispersed GO sheets (left) and aggregated multi-layer GO sheets with poor dispersion (right) between cement mortar materials.

Figure 7.4 shows the EDX analysis results of different samples. As can be seen in the figure, although plain cement mortar does not have any GO, there is 10.5% carbon in its composite. This is due to the existence of carbon in superplasticiser. As can be seen in Fig. 7.4, the carbon content of the cement mortar composite increased with an increase in the GO concentration.

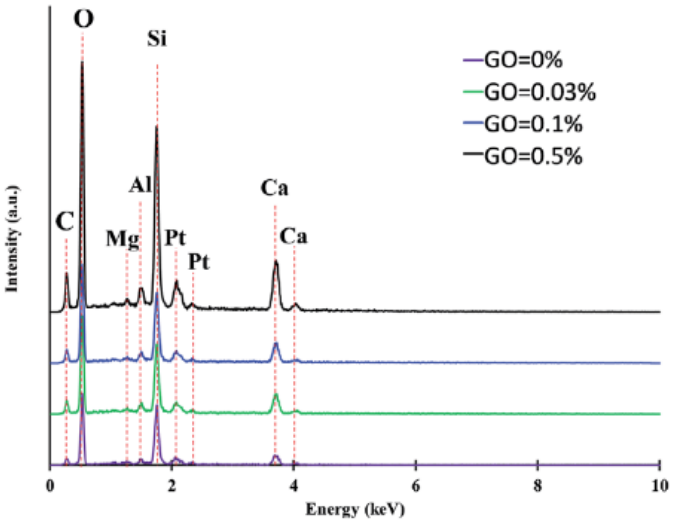

GO=0%

Element	Wt %	At %
C K	5.96	10.52
O K	39.65	52.50
MgK	0.60	0.52
AlK	1.92	1.50
SiK	33.45	25.23
CaK	18.42	9.73
Total	100	100

GO=0.03

Element	Wt %	At %
C K	7.23	12.70
O K	40.15	52.95
MgK	0.78	0.68
AlK	2.16	1.69
SiK	25.96	19.50
CaK	23.72	12.48
Total	100	100

GO=0.1%

Element	Wt %	At %
C K	8.24	14.35
O K	39.74	51.99
MgK	0.65	0.56
AlK	2.29	1.78
SiK	25.52	19.02
CaK	23.56	12.30
Total	100	100

GO=0.5%

Element	Wt %	At %
C K	9.72	16.65
O K	38.92	50.05
MgK	1.56	1.32
AlK	2.17	1.66
SiK	26.79	19.63
CaK	20.84	10.70
Total	100	100

Figure 7.4. EDX analysis of the GO–cement mortar composite with different GO contents

The influence of the GO concentration on the hydration degree of the GO–cement composites is shown in Fig. 7.5. The hydration degree values were calculated using Eq. 7.1. Each term of the equation was derived from the TGA plots provided in Fig. A6 (see Appendix 2). Figure 7.5 shows that the hydration degree of the samples increases with an increase in the curing time from 7- to 28-day regardless of the GO content in the cement paste composite. This observation is in agreement with the previous study by Gong et al. [19]. In addition, it is observed that the certain level of GO concentration in the composite plays a significant role in the hydration degree. The results show that the hydration degree increased by 8.2% and 11.9% at 28 days compared to the plain composite by increasing the GO dosages to 0.03% and 0.1%, respectively. Maximum wettability was achieved with 0.1% GO content, which is proportional to the hydration degree of the composite. This can be

attributed to the direct interaction of the GO individual sheets with the cement constituents. By increasing the GO dosage up to 0.5%, the wettability and hydration properties of the cement composite decreased due to the agglomeration of the GO sheets. The stacked GO sheets restricted the penetration of the water molecules into the GO interlayers.

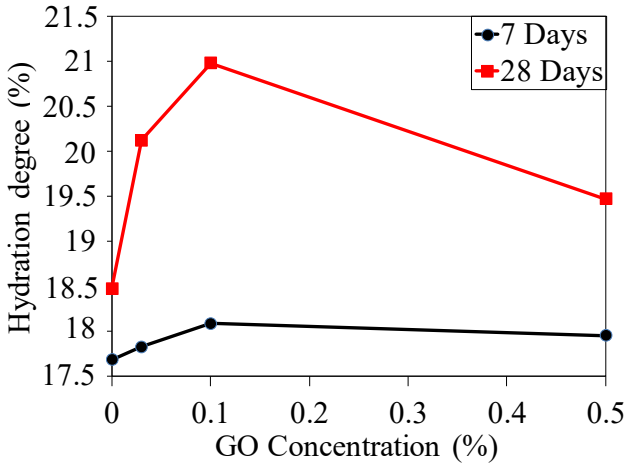

Figure 7.5. Hydration degree of the GO–cement composites prepared with different GO concentrations cured for 7 and 28 days

Comparative XRD spectra of Portland cement, sand, and GO–cement mortar mixes are shown in Fig. 7.6. As can be seen in the figure, the most dominant peaks detected in the XRD patterns are at the scattering angle (2θ) of 22° and 28° which is indicative from the quartz as this is the only crystalline phase of the sand [37,38]. It is seen from the insets (iii) and (iv) in Fig. 7.6 that after the formation of the tricalcium silicate C_3S (Ca_3SiO_5) and dicalcium silicate C_2S (Ca_2SiO_4), the hydration process continued to create the cement paste containing Portlandite $Ca(OH)_2$ and calcium silicate hydrate (C–S–H) [39]. This hydration process contributes to the enhancement of the strength and volume stability of the cementitious materials [40]. The XRD peaks shown in inset (i) at the scattering angles of about 18° and 34° correspond to the formation of $Ca(OH)_2$ [39,41,42]. As can be seen in inset (i), the $Ca(OH)_2$ peaks were intensified by an increase in the GO concentration up to 0.1%. A similar trend was also observed for the C–S–H as shown in inset (ii), where the cumulative intensity at 2θ of 29.6°, 45.7°, 50.3°, and 55.2° was the maximum for the cement mortar composite with 0.1% GO concentration. This further confirms that increasing the GO content in the cementitious composites enhances the wettability and hydration of the composite, which results in a higher strength. The

increased wettability of the composite with GO dosage of up to 0.1% can be attributed to the increase in the density of the oxygen functional groups (hydrophilic) located on the GO surface. With an increase in GO concentration in the composite beyond a certain level (i.e. 0.1%), the highly strong interlayer hydrogen bonds help the GO sheets to stack and agglomerate. Therefore, the GO interlayer distance drops to 6Å and the water molecules are hardly able to diffuse into the GO layers [43].

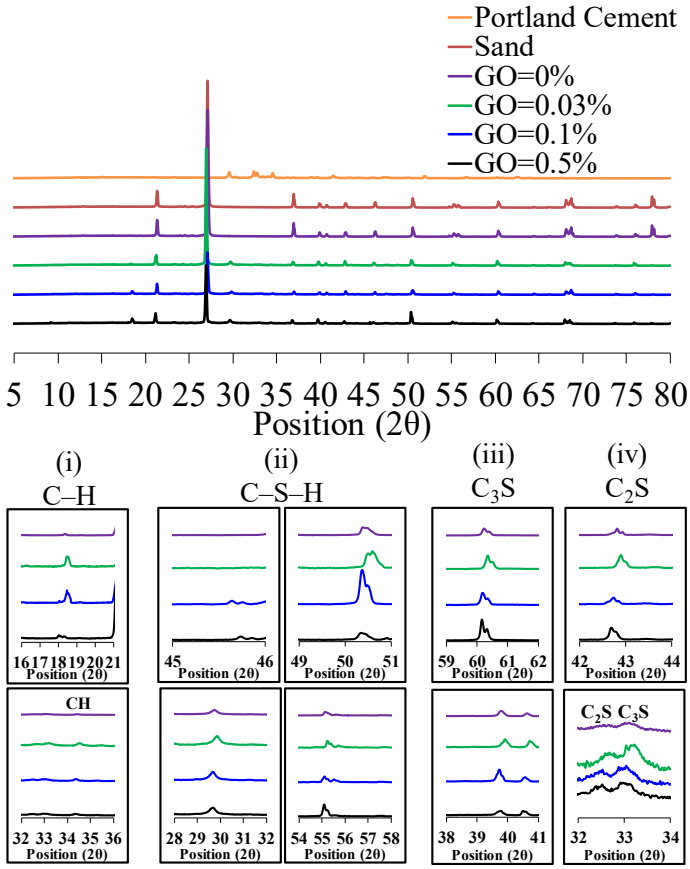

Figure 7.6. XRD patterns of Portland cement, sand, and GO–cement composites

In order to investigate the influence of the GO incorporation into the hydration of the cement mortar mix, the FTIR analysis was conducted on the specimens and the composite ingredients (i.e. GO, cement, and sand). Figure A7 shows the FTIR analysis results in Transmittance mode. Major peaks for the GO are: the O–H stretching vibrations from 3000 cm^{-1} to 3500 cm^{-1} as a broad peak and at 1413 cm^{-1} as a narrow peak; the stretching vibrations of C=O in carbonyl and carboxyl group at 1720 cm^{-1}; the in-plane C=C (sp^2 carbon) skeletal stretching vibrations at 1616 cm^{-1}; and the stretching peaks at 1225 cm^{-1} and 1050 cm^{-1} for the C–O (epoxy and alkoxy groups). These peaks are in agreement with those reported in the previous studies [31,32]. The FTIR spectra of the sand with its major stretching vibrations

peaks of ν_{as}(Si–O–Si), ν_s(Si–O–Si), and (Si–OH) are also consistent with those reported in literature [44,45]. For the Portland cement, the major stretching vibration bands are observed at about 875 cm^{-1} and 1410 cm^{-1}, which is attributed to the presence of CO_3 from $CaCO_3$ [46]. The peaks at the stretching bands of 450 cm^{-1} and 1080 cm^{-1} correspond to ν_4(O–Si–O) and ν_3(Si–O) stretching vibration, respectively, in SiO_4 tetrahedron [6]. The minor vibration band at about 3640 cm^{-1} corresponds to the O–H stretching band from $Ca(OH)_2$. This peak exists in all cement mortar composites spectra. These observations are also in agreement with the XRD analysis results in Fig. A7, which shows the formation of $Ca(OH)_2$ with the scattering angle of 18°.

As can be seen in Fig. 7.7, the most significant difference between the cement mortar composites, GO, the cement, and sand particles is the creation of a new broad band at about 980 cm^{-1}. This change can be attributed to the formation of the C–S–H phases in the Portland cement as well as the anhydrous phase and/or (Si–O) absorption bands of C2SH2 [47]. With regard to the GO–cement mortar composites, the intensity of the O–H stretching vibrations was increased compared to that of the plain cement mortar and the C=O stretching band shifted toward the right side (i.e. lower wavenumber). In other words, the addition of the GO into the plain cement mortar lets the –OH and –COOH groups interact preferentially with C3S, C2S, and tricalcium aluminate C3A (Ca3Al2O6), which results in the growth of the hydration products of C–S–H [5].

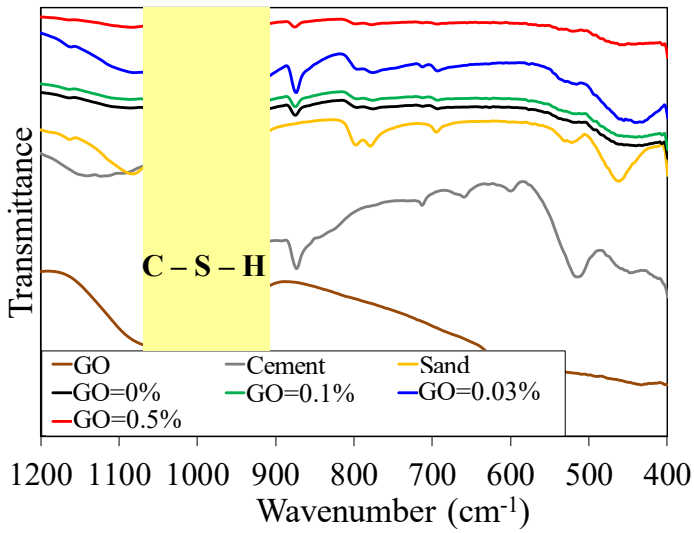

Figure 7.7. Creation of a new broad band in comparative FTIR spectra of GO–cement mortar composites

As can be seen from Fig. A7, the O–H stretching broad band at 3400 cm^{-1} and C=O band at 1640 cm^{-1} intensified with an increase in GO content up to 0.1%. This is not only due to the increase in the number of the oxygen groups interacting through the hydrogen bonds to the calcium silicate hydrate [21], but also because of the increase in the intercalated water in the well-dispersed GO in the cement mortar matrix [48]. It is also notable that the oxygen functional groups of the graphitic carbon allow the cement C–S–H components to be deposited on the graphitic surface and form a strong interaction between them. This can result in the improvement of the mechanical strength by enhancing the load transfer efficiency as well as the bond strength between the two surfaces (i.e. C–S–H and graphitic surfaces). The highest intensity of the O–H and C=O stretching peaks were found in the cement mortar mix with GO dosage of 0.1%. This also confirms the highest accessibility of the water to both the GO oxygen functional groups and the cement C–S–H phase, which resulted in the highest hydration degree for the mortar matrix and thus notable enhancements in the mechanical properties of GO–cement mortar composites.

In the case of the cement mortar composite with GO dosage of 0.5%, it can be seen from the Fig. A7 that the O–H and C=O stretching bands disappear. This behaviour is attributed to the diminution of GO and C–S–H intermolecular interaction. This result confirms the SEM observation that the in-plane oxygen functional groups of the highly concentrated GO sheets have the least exposure to the water molecules and almost no contact with the C–S–H phase. This further indicates the poor interaction between the GO oxygen functional groups and the C–S–H phase of the cement in the mortar matrix.

Mechanical behaviour of GO-cement mortar composites

The results of the tension and compression tests are summarized in Figs. 7.8 and 7.9, respectively, to investigate the influence of the GO concentration on the mechanical behaviour of the cement mortar composite. It can be seen from Fig. 7.8 that the inclusion of GO in the cement mortar results in an increase in the 7- and 28-day tensile strength for the composite. The tensile strength of the specimens also steadily increases with the addition of GO up to 0.1% then beyond this level the strength starts to decrease. The strength enhancement of the mix containing 0.1% GO

reached 44.4% at 7 days and 37.5% at 28 days. This observation is consistent with previous studies by Lv et al. [5] and Fakhim et al. [17] on the GO-cement mortar composite.

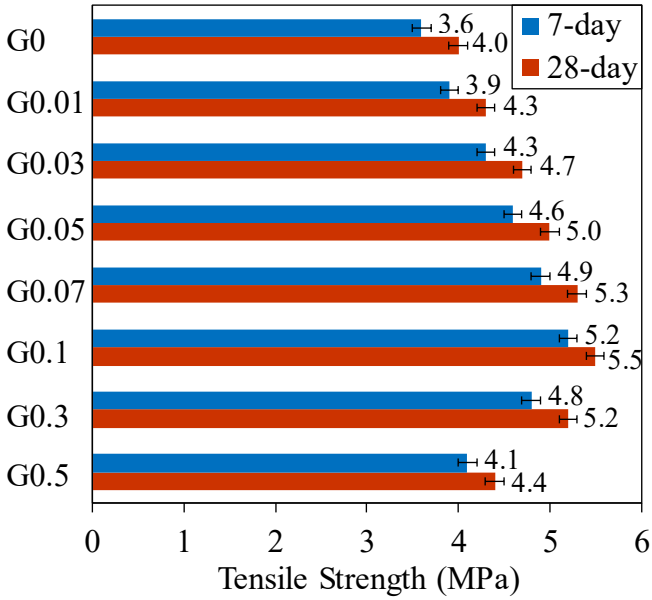

Figure 7.8. Variation of 7 and 28 days tensile strength of GO–cement mortar with different GO contents (0–0.5%). Number after letter G shows GO content of the mix in percentage.

The improvement in the tensile strength at the optimum concentration of GO in the cement mortar composites can be attributed to the improved bonding between the cement matrix and GO particles owing to the high dispersibility of GO sheets (as appearing like individual sheets) in the composite at the optimum GO concentration (see Fig. 7.3). High GO dispersion in the composite results in the interaction of cement hydration products (i.e. C–S–H) with higher surface area GO sheets leading to the enhanced interfacial load transfer between the GO sheets and cement matrix during the fiber pull out from the matrix [5,6,21]. However, further increase in the amount of GO results in the GO re-stacking due to van der Waals force, which results in poor dispersion of the GO in the matrix and reduces the bonding and internal friction within the composite as indicated in Scheme in Fig. 7.3(e). This in turn reduces the strength of the composite [6,21].

Figure 7.9 shows the 7- and 28-day compression test results of the different mixes. It can be seen from the figure that the compressive strength of the specimens steadily increased with the GO addition up to a concentration of 0.1%, and the strength decreased with a further increase in the GO content. This trend is consistent with

those reported by Cao et al. [20] and Du and Pang [51] on the GO-cement mortar composite. The compressive strength enhancement of the mix containing 0.1% GO reached 46% at 7 days and 77.7% at 28 days. It is worth noting that the maximum enhancement seen at the 28-day compressive strength is larger than those in previous studies by Lv et al. [5] (47.9%), Pan et al. [6] (24%), Cao et al. [20] (20.3%), and Lu et al. [21] (24.1%) on the GO-cement mortar composite. Comparison of Figs. 7.8 and 7.9 reveals that, for a given mix, compressive strength enhancements seen in GO mixes from 7 to 28 days are higher than those of tensile strength, indicating that the effect of GO on the tensile strength is mostly up to 7 days, whereas the compressive strength enhancement is more progressive and continues beyond the 7 days to 28 days curing age.

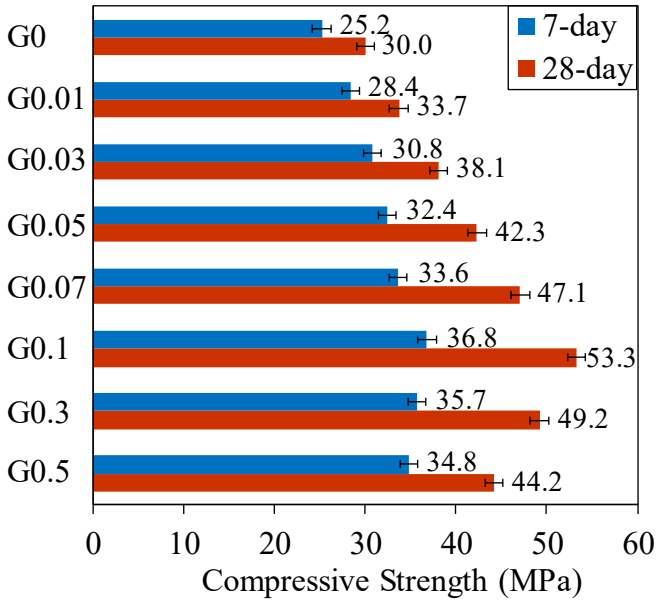

Figure 7.9. Variation of 7 and 28 days compressive strength of GO–cement mortar with different GO contents (0–0.5%)

The enhancement of the compressive strength is attributed to the good dispersibility of GO sheets in the composite that leads to the better interlocking behaviour between the GO and cement mortar and increased crack tip toughness, resulting in the prevention of the crack propagation from nanoscale to microscale [6,18,21]. However, an increase in the GO content over the optimum amount results in the aggregation of the GO in the matrix which provides poor dispersion and change in the thickness of the GO to multi layers [18,21]. Multi-layer GO obtains poor

interlocking cohesion between GO and the cement mortar, consequently reducing the strength of the composite [21].

Figure 7.10 shows the relationship between the axial compressive stress and strain for cement mortar composites with different GO concentrations at 28 days. The curves indicate that an increase in the GO content up to 0.1% results in an increase in the compressive strength of the composite. It is also notable from the figure that the elastic modulus and axial strain corresponding to the compressive strength of the cement mortars increased with an increase in the GO content up to 0.1%. The elastic modulus and axial strain corresponding to compressive strength enhancements of the mix containing 0.1% GO reached 109.6% and 41.9%, respectively. These increases are attributed to the well-known relationship between the compressive strength, elastic modulus, and axial strain corresponding to the compressive strength.

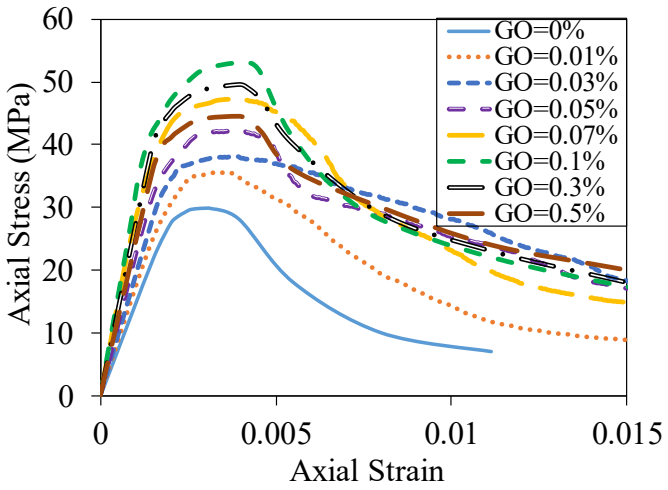

Figure 7.10. Variation of 28 days compressive axial stress-axial strain with different GO contents

CONCLUSIONS

In this work, the influence of GO concentration on physicochemical and mechanical properties of GO–cement mortar composites and explain how and why different GO concentrations affect these properties is revealed. The results show that the optimal percentage (i.e. 0.1%) of GO in the composite led to a 37.5% and 77.7% increase in the 28 days tensile and compressive strengths of GO–cement mortar composites compared to the plain cement mortar composite. Study revealed that GO not only prevent the crack propagation from the nanoscale to microscale and increase the

hydration degree of the cement mortar composites, but also improve accessibility of the water to the GO oxygen functional groups and cement C–S–H component, indicating the importance of having appropriate GO concentrations. We also discovered that there is a critical GO concentration (i.e. 0.1%) and increasing the amount of GO above this concentration leads to detrimental effects as observed by many micro-cracks related to restacking and aggregation of GO sheets in cement matrix. These observations with obtained mechanical properties that were validated by SEM, TGA, XRD, and FTIR analyses provide an essential link between structural, chemical, and mechanical properties and help better understand the influence of GO parameters. The positive influence of GO, as a promising additive for use as a nano reinforcement, and different oxygen functional groups on the phase composition and intermolecular interaction of cementitious materials to help early-age hydration characteristics of the composite is clearly demonstrated in this work. Further investigations on the effect of other GO parameters including particle size and surface chemistry on the properties of cement mortar composites are currently underway and will be presented as a separate study. Considering scalable production and low-cost availability of GO source, there is strong expectation for this material to be commercially applied for the development of a new generation of cementitious and construction materials with advanced performance for broad applications.

ACKNOWLEDGEMENTS

The authors gratefully acknowledge the support of the Australian Research Council through ARC IH 150100003 (ARC Research Hub for Graphene Enabled Industry Transformation). The authors also thank Schools of Chemical Engineering and Civil, Environment and Mining Engineering at the University of Adelaide for supporting this work.

REFERENCES

[1] Soranakom C, Mobasher B. Correlation of tensile and flexural responses of strain softening and strain hardening cement composites. *Cement and Concrete Composites*. 2008;30(6):465–77.

[2] Park SH, Kim DJ, Ryu GS, Koh KT. Tensile behavior of ultra high performance hybrid fiber reinforced concrete. *Cement and Concrete Composites*. 2012;34(2):172–84.

[3] Chuah S, Pan Z, Sanjayan JG, Wang CM, Duan WH. Nano reinforced cement and concrete composites and new perspective from graphene oxide. *Construction and Building Materials*. 2014;73:113–24.

[4] Wu Z, Shi C, Khayat KH. Influence of silica fume content on microstructure development and bond to steel fiber in ultra-high strength cement-based materials (UHSC). *Cement and Concrete Composites*. 2016;71:97–109.

[5] Lv S, Ma Y, Qiu C, Sun T, Liu J, Zhou Q. Effect of graphene oxide nanosheets of microstructure and mechanical properties of cement composites. *Construction and Building Materials*. 2013;49:121–7.

[6] Pan Z, He L, Qiu L, Habibnejad Korayem A, Li G, Zhu JW, Collins F, Li D, Duan WH, Wang MC. Mechanical properties and microstructure of a graphene oxide–cement composite. *Cement and Concrete Composites*. 2015;58:140–7.

[7] Chang TP, Shih JY, Yang K, Hsiao TC. Material properties of portland cement paste with nano-montmorillonite. *Journal of Materials Science*. 2007;42(17):7478–87.

[8] Madani H, Bagheri A, Parhizkar T. The pozzolanic reactivity of monodispersed nanosilica hydrosols and their influence on the hydration characteristics of Portland cement. *Cement and Concrete Research*. 2012;42(12):1563–70.

[9] Geim AK, Novoselov KS. The rise of graphene. *Nature Materials*. 2007;6(3):183-91.

[10] Singh AP, Mishra M, Chandra A, Dhawan SK. Graphene oxide/ferrofluid/cement composites for electromagnetic interference shielding application. *Nanotechnology*. 2011;22(46):465701.

[11] Ranjbar N, Mehrali M, Mehrali M, Alengaram UJ, Jumaat MZ. Graphene nanoplatelet-fly ash based geopolymer composites. *Cement and Concrete Research*. 2015;76:222–31.

[12] Lv SH, Deng LJ, Yang WQ, Zhou QF, Cui YY. Fabrication of polycarboxylate/graphene oxide nanosheet composites by copolymerization for reinforcing and toughening cement composites. *Cement and Concrete Composites*. 2016;66:1-9.

[13] Lee C, Wei X, Kysar JW, Hone J. Measurement of the elastic properties and intrinsic strength of monolayer graphene. *Science*. 2008;321(5887):385–8.

[14] Chu HY, Jiang JY, Sun W, Zhang M. Effects of graphene sulfonate nanosheets on mechanical and thermal properties of sacrificial concrete during high temperature exposure. *Cement and Concrete Composites*. 2017;82:252–64.

[15] Lambert TN, Chavez CA, Hernandez-Sanchez B, Lu P, Bell NS, Ambrosini A, Friedman T, Boyle TJ, Wheeler DR, Huber DL. Synthesis and characterization of titania-graphene nanocomposites. *Journal of Physical Chemistry C*. 2009;113(46):19812–23.

[16] Alkhateb H, Al-Ostsaz A, Cheng A, Li X. Materials genome for graphene-cement nanocomposites. *Journal of Nanomechanics and Micromechanics*. 2013;3(3):67−77.

[17] Fakhim B, Hassani A, Rashidi A, Ghodousi P. Preparation and Mechanical Properties of Graphene Oxide: Cement Nanocomposites. *Scientific World Journal*. 2014;1−10.

[18] Sharma S, Kothiyal NC. Influence of graphene oxide as dispersed phase in cement mortar matrix in defining the crystal patterns of cement hydrates and its effect on mechanical, microstructural and crystallization properties. *RSC Advances*. 2015;5:52642–57.

[19] Gong K, Pan Z, Korayem AH, Qiu L, Li D, Collins F, Wang CM, Duan WH. Reinforcing effects of graphene oxide on portland cement paste. *Journal of Materials in Civil Engineering*. 2014;27:A4014010.

[20] Cao ML, Zhang HX, Zhang C. Effect of graphene on mechanical properties of cement mortars. *Journal of Central South University*. 2016;23:919−25.

[21] Lu C, Lu Z, Li Z, Leung CKY. Effect of graphene oxide on the mechanical behavior of strain hardening cementitious composites. *Construction and Building Materials*. 2016;120:457–64.

[22] Marcano DC, Kosynkin DV, Berlin JM, Sinitskii A, Sun Z, Slesarev A, Alemany LB, Lu W, Tour JM. Improved synthesis of graphene oxide. *ACS Nano*. 2010;4:4806–14.

[23] ASTM C1437. Standard Test Method for Flow of Hydraulic Cement Mortar. American society for testing and materials, West Conshohocken, PA, USA: ASTM International, 2015.

[24] ASTM C307-03. Standard Test Method for Tensile Strength of Chemical-Resistant Mortar, Grouts, and Monolithic Surfacings. American society for testing and materials, West Conshohocken, PA, USA: ASTM International, 2012.

[25] ASTM C109/C109M-16a. Standard Test Method for Compressive Strength of Hydraulic Cement Mortars. American society for testing and materials, West Conshohocken, PA, USA: ASTM International, 2008.

[26] Mounanga P, Khelidj A, Loukili A, Baroghel-Bouny V. Predicting Ca(OH)2 content and chemical shrinkage of hydrating cement pastes using analytical approach. *Cement and Concrete Research*. 2004;34:255−65.

[27] Lothenbach B, Saout GL, Gallucci E, Scrivener K. Influence of limestone on the hydration of Portland cements. *Cement and Concrete Research*. 2008;38:848–60.

[28] Dilnesa BZ, Wieland E, Lothenbach B, Dahn R, Scrivener KL. Fe-containing phases in hydrated cements. *Cement and Concrete Research*. 2014;58:45–55.

[29] Scrivener K, Snellings R, Lothenbach B. A Practical Guide to Microstructural Analysis of Cementitious Materials. CRC Press. 2016, ISBN: 9781138747234.

[30] Czernin W. Cementkemi för Byggare. Svesnka Cement Föreningen, 1959.

[31] Tran DNH, Kabiri S, Losic D. A green approach for the reduction of graphene oxide nanosheets using non-aromatic amino acids. *Carbon*. 2014;76:193−202.

[32] Nine MJ, Cole MA, Johnson L, Tran DNH, Losic D. Robust superhydrophobic graphene-based composite coatings with self-cleaning and corrosion barrier properties. *ACS Applied Materials & Interfaces*. 2015;7:28482−93.

[33] Kabiri S, Tran DNH, Azari S, Losic D. Graphene-Diatom Silica Aerogels for Efficient Removal of Mercury Ions from Water. *ACS Applied Materials & Interfaces*. 2015;7:11815−23.

[34] Kabiri S, Tran DNH, Cole MA, Losic D. Functionalized three-dimensional (3D) graphene composite for high efficiency removal of mercury. *Environmental Science: Water Research & Technology*. 2016;2:390−402.

[35] Sedaghat A, Ram MK, Zayed A, Kamal R, Shanahan N. Investigation of physical properties of graphene-cement composite for structural applications. *Open Journal of Composite Materials*. 2014;4(1):12−21.

[36] Nicoleau L, Gadt T, Chitu L, Maier G, Paris O. Oriented aggregation of calcium silicate hydrate platelets by the use of comb-like copolymers. *Soft Matter*. 2013;9:4864−74.

[37] Raupp-Pereira F, Hotza D, Segadaes AM, Labrincha JA. Ceramic formulations prepared with industrial wastes and natural sub-products. *Ceramics International*. 2006;32:173−9.

[38] Amin NU, Alam S, Gul S. Assessment of pozzolanic activity of thermally activated clay and its impact on strength development in cement mortar. *RSC Advances*. 2015;5:6079−84.

[39] Wang R, Yao L, Wang P. Mechanism analysis and effect of styrene–acrylate copolymer powder on cement hydrates. *Construction and Building Materials*. 2013;41:538−44.

[40] Alizadeh R, Raki L, Makar JM, Beaudoin JJ, Moudrakovski I. Hydration of tricalcium silicate in the presence of synthetic calcium-silicate-hydrate. *Journal of Materials Chemistry.* 2009;19:7937−46.

[41] Yang N, Yue W. Handbook of a collection of illustrative plates of inorganic nonmetal materials. Wuhan: Wuhan University of Technology Publishing Company, 2000.

[42] Tkaczewska E. Mechanical Properties of Cement Mortar Containing Fine-Grained Fraction of Fly Ashes. *Open Journal of Civil Engineering*. 2013;3(2a):54−68.

[43] Buchsteiner A, Lerf A, Pieper J. Water Dynamics in Graphite Oxide Investigated with Neutron Scattering. *Journal of Physical Chemistry B*. 2006;110:22328−38.

[44] Mourhly A, Khachani M, El Hamidi A, Kacimi M, Halim M, Arsalane S. The Synthesis and Characterization of Low-cost Mesoporous Silica SiO2 from Local Pumice Rock. *Nanomaterials and Nanotechnology*. 2015;5(35):1−7.

[45] Bera A, Kumar T, Ojha K, Mandal A. Adsorption of surfactants on sand surface in enhanced oil recovery: Isotherms, kinetics and thermodynamic studies. *Applied Surface Science*. 2013;284:87−99.

[46] Li GY, Wang PM, Zhao X. Mechanical behavior and microstructure of cement composites incorporating surface-treated multi-walled carbon nanotubes. *Carbon*. 2005;43:1239−45.

[47] Cerveny S, Barroso-Bujans F, Alegria Á, Colmenero J. Dynamics of Water Intercalated in Graphite Oxide. *Journal of Physical Chemistry C.* 2010;114:2604−12..

[48] Du H, Pang SD. Enhancement of barrier properties of cement mortar with graphene nanoplatelet. *Cement and Concrete Research*. 2015;76:10−9.

Statement of Authorship

Title of Paper	From graphene oxide to reduced graphene oxide: impact on the physiochemical and mechanical properties of graphene-cement composites
Publication Status	☑ Published ☐ Accepted for Publication ☐ Submitted for Publication ☐ Unpublished and Unsubmitted work written in manuscript style
Publication Details	Gholampour A, Valizadeh Kiamahalleh M, Tran DNH, Ozbakkaloglu T, Losic D. From graphene oxide to reduced graphene oxide: impact on the physiochemical and mechanical properties of graphene-cement composites. *ACS Applied Materials & Interfaces*. 2017; 10.1021/acsami.7b16736.

Principal Author

Name of Principal Author (Candidate)	Aliakbar Gholampour		
Contribution to the Paper	Literature review, experimental testing, analysis of test results, and preparation of the manuscript.		
Overall percentage (%)	60%		
Certification:	This paper reports on original research I conducted during the period of my Higher Degree by Research candidature and is not subject to any obligations or contractual agreements with a third party that would constrain its inclusion in this thesis. I am the primary author of this paper.		
Signature		Date	31/01/2019

Co-Author Contributions

By signing the Statement of Authorship, each author certifies that:

i. the candidate's stated contribution to the publication is accurate (as detailed above);

ii. permission is granted for the candidate in include the publication in the thesis; and

iii. the sum of all co-author contributions is equal to 100% less the candidate's stated contribution.

Name of Co-Author	Meisam Valizadeh Kiamahalleh		
Contribution to the Paper	Experimental testing, analysis of test results, and preparation of the manuscript.		
Signature		Date	31/01/2019

Name of Co-Author	Diana N.H. Tran		
Contribution to the Paper	Experimental testing and review of manuscript.		
Signature		Date	31/01/2019

Name of Co-Author	Togay Ozbakkaloglu		
Contribution to the Paper	Research supervision and review of manuscript.		
Signature		Date	31/01/2019

Name of Co-Author	Dusan Losic		
Contribution to the Paper	Research supervision and review of manuscript.		
Signature		Date	27/02/2019

Please cut and paste additional co-author panels here as required.

From Graphene Oxide to Reduced Graphene Oxide: Impact on the Physiochemical and Mechanical Properties of Graphene–Cement Composites

GRAPHICAL ABSTRACT

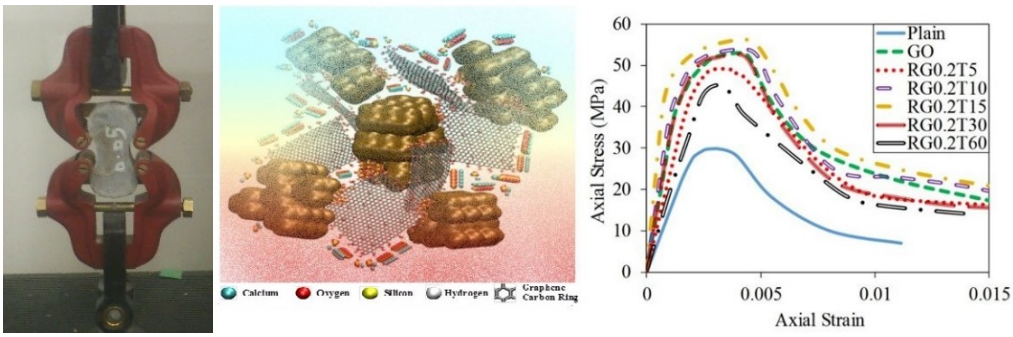

ABSTRACT

Graphene materials have been extensively explored and successfully used to improve performances of cement composites. These formulations were mainly optimized based on different dosages of graphene additives, but with lack of understanding how other parameters such as surface chemistry, size, charge, and defects of graphene structures could impact on physiochemical and mechanical properties of final material. This paper presents the first experimental study to evaluate the influence of oxygen functional groups of graphene and defectiveness of graphene structures on the axial tension and compression properties of graphene–cement mortar composites. Series of reduced graphene oxide (rGO) samples with different levels of oxygen groups (high, mild, and low) were prepared by reduction of GO using different concentration of hydrazine (wt%, 0.1, 0.15, 0.2, 0.3, and 0.4%) and reduction time (5, 10, 15, 30, and 60 minutes) and added to cement mortar composites at optimal concentration of 0.1 %. Series of characterization methods including scanning electron micrographs (SEM), energy-dispersive X-ray spectroscopy (EDX), X-ray diffraction (XRD), thermogravimetric analysis (TGA), and Fourier transform infrared spectroscopy (FTIR) characterizations were performed to determine the distribution and mixing of prepared rGO in cement matrix and correlated with observed mechanical properties of rGO–cement mortar

composites. The measurement of axial tension and compression properties revealed that oxygen level of rGO additives has a significant influence on mechanical properties of cement composites. An addition of 0.1% rGO prepared by 15 min reduction and 0.2% (wt%) hydrazine with mild level of oxygen groups resulted in a maximum enhancement of 45.0% and 83.7%, respectively, in the 28 days tensile and compressive strengths in comparison with the plain cement mortar and were higher compared to the composite prepared with GO (37.5% and 77.7%, respectively). These results indicate that there is a strong influence a level of oxygen groups and crystallinity of graphene structures on physiochemical and mechanical properties. The influence of these two parameters are interconnected and their careful balancing is required to provide an optimum level of oxygen groups on rGO sheets to ensure that there is sufficient bonding between the calcium silicate hydrate (C–S–H) components in the cement matrix and minimum level of defects and higher crystallinity of graphene structures, which will improve the mechanical properties of composites. The finding this optimized balance between these two parameters are required to formulate of graphene cement composites with the highest performance.

KEYWORDS: Graphene oxide, reduced graphene oxide (rGO), cement composites, mechanical properties, tensile and compressive strengths.

INTRODUCTION

A large number of studies on the mechanical properties of cementitious materials containing nanoscale materials have been conducted in recent years. Among them, the use of carbon-based nanomaterials was shown that could delay the formation of nanoscale cracks during the initial stage of tension and compression loading and their progression into microscale cracks that is a significant problem in construction industry [1-4]. Recently, graphene, as a type of carbon 2D material with unique planar structures, outstanding high surface area (2600 m^2/g), chemical, mechanical, and thermodynamic properties, has offered new opportunities to further improve the properties of cementitious materials [5-10].

Graphene materials have different forms, morphologies, and chemical compositions. Graphene oxide (GO) and pristine or reduced graphene oxide (rGO)

are two main forms explored for many industrial applications [9]. Graphene sheets have very low dispersibility in water due to their hydrophobicity, high surface area, and high surface energy, resulting in agglomeration that limits their applications [11]. Graphene oxide, as oxygenated derivate of graphene prepared by acid oxidation of graphite, contains a large amount of hydroxyl, carboxyl, epoxide, and carbonyl functional groups and is water compatible and highly dispersible. This is one of the reasons why GO was preferentially explored as an additive for making cementitious composites to improve their mechanical performances [12,13]. However, GO is amorphous with many defects and mechanical properties of considerably lower than those of pristine graphene or reduced graphene oxide that can be generated by chemical or thermal reduction of GO [14]. The resulting material, which is referred as reduced GO, exhibits properties of both pristine graphene (i.e. high surface area and strength) and GO (i.e. high dispersible in water). Therefore, the superior properties of graphene, can be partly restored by reducing the oxygen functional groups of GO. Most of existing studies on the microstructure and mechanical properties of graphene–cement mortar composites considered the use of GO and showed the significant potential of GO to enhance the mechanical properties of cementitious materials [1-3,6,15-20]. However, these studies were focused on optimization of concentration dependence of GO on tensile and compression properties on cement composites without considering other critical parameters, such as particles size, number of layers, surface chemistry, charge, defects, and crystallinity that could have a significant impact.

Only two studies have been conducted on cementitious materials and their alternatives (e.g. geopolymers) containing rGO [21,22]. Saafi et al. [21] showed that incorporation of 0.35% rGO (prepared by dispersion of 1.1 nm thick GO in 100 g of NaOH solution (10M) under 1 h sonication) by weight of fly ash into geopolymer paste resulted in 134%, 376%, and 56% higher flexural strength, Young's modulus, and flexural toughness compared to those of conventional geopolymer paste, respectively. Murugan et al. [22] reported that the addition of 0.02% rGO (prepared by dispersion of the 5 nm thick GO in hydrazine solution at 100°C for 24 h) by weight of cement into the cement paste increased the 7- and 28-day flexural strengths by 70% and 23% respectively compared to the control paste. In addition, they found that rGO substantially decreased the size of voids in the paste more than

other nanoparticles such as aluminium oxide and colloidal silicon dioxide. As it is evident from the results of the existing studies, improved mechanical properties make rGO a promising material in the preparation of high performance cementitious composites. However, the existing studies were on the rGO-paste composite and the properties of cement mortar composites containing rGO have not been studied yet. These results are not surprising and indicate significant potential of rGO for further enhancing the mechanical properties of cementitious materials and developing new and advanced composites for structural applications. Nevertheless, to formulate these products it is critical to have better understanding of key parameters of GO, rGO, and pristine graphene on physiochemical and mechanical properties of cementitious materials that include not only dosage, but also many other parameters such as particle size, chemical composition, level of oxygen, carbon/oxygen (C/O) ratio, defectiveness, and crystal structure, which were not considered before.

To address these existing research gaps, this paper presents the first experimental study to explore the impact of oxygen functionalities and defectiveness/crystallinity of rGO on physiochemical and mechanical properties of rGO–cement mortar composites. Our recent experimental study demonstrated the strong dependence of the axial tension and compression properties of GO-cement mortars on the GO dosage [23]. It was found that inclusion of the optimal GO concentration (0.1%) in the cement mortar composite results in 37.5% and 77.7% increase in the tensile and compressive strength of the composite compared to those of plain composite, respectively. Considering that 0.1% is an optimal concentration, in this work we designed the study based on this dosage using series rGO samples with different levels of oxygen groups (high, mild, and low) that are prepared by controlled reduction of GO solution using different concentration (wt%) of hydrazine (0.1, 0.15, 0.2, 0.3, and 0.4%) and reduction time (5, 10, 15, 30, and 60 min). This preparation methods provide a broad range of graphene materials with different properties from GO with the highest level of oxygen and lowest mechanical strength to rGO with the lowest level of oxygen and highest mechanical strength. Physical, structural, chemical, and mechanical properties of the prepared composites with GO to rGO additives were comprehensively characterized using scanning electron micrographs (SEM), energy-dispersive X-ray spectroscopy (EDX), X-ray diffraction (XRD), thermogravimetric analysis (TGA), Fourier transform infrared

spectroscopy (FTIR), zeta potential, and axial compression and tension tests. The obtained results were analyzed to reveal the optimal combination of rGO reduction parameters that provide the best mechanical performance and to gain better understanding of the mechanisms behind the improvements and future formulations.

EXPERIMENTAL SECTION

Preparation of rGO

GO dispersion was produced by a modified Hummers' method [24] as originally presented by Kovtyukhova and colleagues using graphite as a starting material [25]. GO was converted back to rGO using series of experimental conditions with different hydrazine weight percentages in GO solution (0.1, 0.15, 0.2, 0.3, and 0.4%), which are outlined in Table A6 (see Appendix 3), and reduction time (5, 10, 15, 30, and 60 min).

Preparation of the graphene-cement mortar composite

Ordinary Portland cement and graded river sand of 2–mm maximum size were used in the preparation of the cement mortars. Tables A7 and A8 (see Appendix 3) show the particle size distribution of the sand and chemical composition of the cement used in this study, respectively. Our previous study was conducted on the mechanical properties of GO–cement mortar composites at eight GO contents of 0%, 0.01%, 0.03%, 0.05%, 0.07%, 0.1%, 0.3%, and 0.5% by weight of cement to establish the optimum amount of GO to improve the tensile and compressive strength of cement mortar composites [23]. It was found that incorporation of 0.1% GO by weight of cement resulted in the largest improvements in the tensile and compressive strength. Therefore, this dosage was used in the current study in investigating the effect of the oxygen reduction on the mechanical properties of the cement mortar composite. Two parameters, namely the reduction time and weight percentage (by weight of GO) of oxygen reducing agent (hydrazine), were used to determine the optimal oxygen reduction condition leading to the largest improvements in mechanical properties of the composite. To this end, rGO dispersions were prepared by fixing one parameter and varying the other. In the initial phase, GO was reduced using 0.2% weight percentage of hydrazine at

different reduction times of 5, 10, 15, 30, and 60 minutes. In the subsequent phase, additional rGO dispersions were prepared using the optimum reduction time determined in the first phase with different hydrazine weight percentages (i.e. 0.1, 0.15, 0.2, 0.3, and 0.4%). The mix proportions of different mixes are shown in Table A9 (see Appendix 3). Three nominally identical specimens were tested for each unique specimen configuration in direct tension and compression tests. Polycarboxylic ether polymer-based superplasticizer was used to improve their workability and ensure uniform dispersion of rGO particles in the composite. Once the specimens were demolded, they were cured in the fog room at a constant temperature of 23±2°C until the test day. For the direct tension tests, typical dog-bone shaped samples with a test region width and depth of 25±0.5 mm were used in accordance with ASTM C307-03 [26]. 50 mm cube samples were used for the compression tests according to ASTM C109/C109M-07 [27].

Characterizations

Transmission Electron Microscopy (TEM)

A transmission electron microscope (TEM Tecnai G2 Spirit, USA) operating at an accelerating voltage of 100 kV was used for characterization of the morphology of rGO sheets. The sample was prepared by drop casting the rGO dispersion on a Lacey copper grid straight after the reaction was completed for analysis.

Scanning Electron Microscopy (SEM)

The dispersion and bonding properties between the rGO at the surface of the cement mortar were evaluated by a Field Emission Scanning Electron Microscope (Philips XL30). The SEM analysis was conducted following the 28-day mechanical tests and on the polished fresh surface of the specimens, which was cut with dimensions of approximately 8×4×3 mm. The specimens were then coated by a 10 nm-thick platinum layer to enhance the conductivity in the SEM analysis.

Contact Angle measurement

Thin films of GO and rGO were prepared by vacuum filtration of the corresponding dispersion. Contact angle measurements (using an Attension Theta optical tensiometer) were conducted on GO/rGO films to establish the correlation between

the GO reduction process and material hydrophobicity. The measured angle was reported as an average of the angles read from both sides of the bubble stabilized on each GO/rGO film.

Zeta Potentials measurement

As a quantitative method, the zeta potentials of the GO/rGO dispersions were measured in triplicate by Zetasizer-NANO-ZS (Malvern Instruments) to confirm and track the loss of oxygen functionalities of the aqueous dispersions after reducing the GO by varying different reduction parameters. All dispersions were left undisturbed overnight to check their stability before being added to the mortar mixes.

Composition analysis

The composition of the mortar matrix was determined in two ways. Energy Dispersive X-Ray (EDX) spectroscopy was conducted on the specimens using Genesis EDAX with a Backscattered Electron (BSE) Detector to determine the constituent elements of the materials, and X-ray diffraction (XRD) was performed using X-ray diffractometer (Rigaku MiniFlex 600, Japan), at 40 kV and 15 mA in the range of $2\theta = 5–80°$ with a scanning rate of 10 degree/min and CuKα radiation (λ= 1.540 Å), to determine the crystalline phases of the GO, rGO, and rGO-enriched hydrated cementitious composite materials.

Thermogravimetric analysis (TGA)

Thermal decomposition of rGO was conducted by a thermal gravimetric analyzer (TGA Q500, TA Instruments, USA) under air atmosphere where the samples were heated from room temperature to 1000 °C at a heating rate of 20 °C/min. Also, in order to examine the influence of rGO incorporation on the hydration properties of the cement mortar composite, TGA was performed on the samples after 7 and 28 days of curing. Samples were kept in a platinum (Pt) pan for the analysis. In each test, approximately 25–35 mg of composite was heated from room temperature to 900 °C under the flow of nitrogen with a heating rate of 10 °C/min. In the TGA analysis, the non-evaporable (bound) water content was used to calculate the hydration degree of the sample excluding the sand mass losses.

Fourier transform infrared spectroscopy (FTIR)

Fourier transform infrared spectroscopy (FTIR) analysis in transmittance mode via Nicolet 6700 Thermo Fisher used to investigate the vibrational stretching modes of different molecular bonds, including rGO oxygen functional groups as well as the formation of $Ca(OH)_2$ and C–S–H in the rGO–hydrated cementitious composite materials.

Mechanical characterizations

Tension and compressions tests were conducted on the specimens to evaluate the mechanical behaviour of the samples with different GO oxygen reductions. Figure A8 (see Appendix 3) shows the testing machines used in these tests. The ultimate tensile and compressive strengths were averaged from three tests on nominally identical specimens for each mix. The axial compressive strains of the specimens were measured by two linear variable displacement transformers (LVDTs) mounted at the corners of steel loading and supporting plates of the compression test machine.

Specimen designation

The specimens in this study were labelled as follows: plain and GO are plain cement mortar (control specimen) and GO–cement mortar composite, respectively. The letter RG is used for specimens containing rGO solution, which was followed by a number indicating the weight percentage of hydrazine solution used for GO oxygen reduction. The next letter, T, is followed by a number showing the reduction time in minutes. For example, RG0.2T15 presents the mix containing rGO solution reduced by 0.2% hydrazine at 15 min reduction.

RESULTS AND DISCUSSION

Characterization of prepared GO and rGO materials

The characterization results of prepared GO material obtained by TEM, XRD, TGA, and Atomic Force Microscopy (AFM) used in this study are shown in Fig. A9 (see Appendix 3). The typical TEM image of GO sheets shows their irregular shape and amorphous nature with a paper-like appearance. The average size of GO sheets was

approximately 1 μm. The AFM image and height profile of GO shows an approximate thickness of 1 nm, which is attributed to a few layers graphene sheets.

To confirm the conversion of GO to rGO, TEM, XRD, and TGA analyses were performed to show the changes in morphology. Figure 8.1(a) shows a TEM image of rGO sheets that are typically formed during a chemical reduction process when GO is used as the starting material. TGA analysis of GO and rGO measured as a function of time clearly shows that rGO is highly stable up to 600°C as expected (Fig. 8.1(b)). The major mass losses in GO are due to the decomposition of its oxygen functional groups which rGO does not contain in its structure and was removed during the reduction process. XRD analysis shown in Fig. 8.1(c) further confirms the change in the structure of GO to rGO as the characteristic 002 reflection peak at 2θ (scattering angle) = 11.1° has shifted, which is evidently broader. This phenomenon is due to the removal of the carboxylic acid (-COOH) groups as the crystalline sizes of GO are reduced [28].

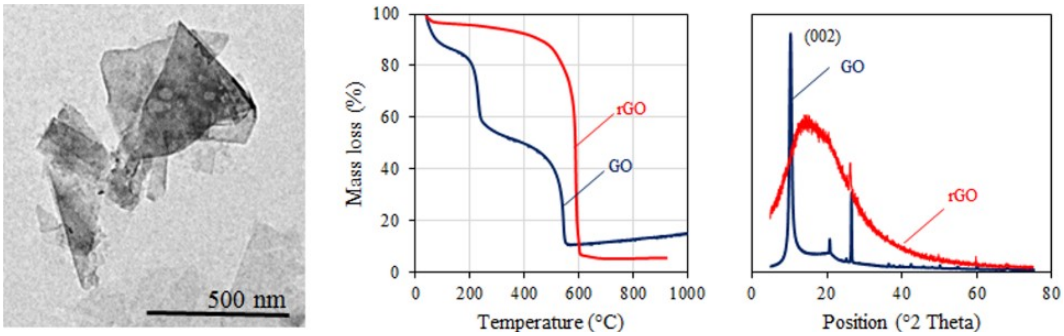

(a) (b) (c)

Figure 8.1. (a) TEM image of folded rGO sheets, (b) TGA plots, and (c) XRD spectra of GO and rGO

The measurements of water contact angle (wettability) (CA) were conducted as a qualitative method in order to confirm the reduction of GO or removal of oxygen groups and increasing the hydrophobicity. The interfacial properties of graphene have a significant influence on its distribution in the composite, interaction with the hydrophilic matrix, and potential aggregation. Figure A10 (see Appendix 3) shows the wettability of the rGO films prepared by fixing one parameter and varying the other. Super-hydrophilic GO film demonstrated the average contact angle as low as 23.06°. The top row of Fig. A10 represents the samples prepared with a constant

weight percentage of hydrazine (0.2%) at different reduction times. The average water contact angles of the rGO films treated with 0.2% hydrazine for 5, 15 and 60 min were 32.00°, 69.09°, and 82.78°, respectively. In the case of fixing the reduction time at 15 min, the average contact angles on rGO film surface were 41.19°, 73.65°, and 81.64° for being treated with 0.1, 0.2, and 0.4% hydrazine, respectively. Clearly, the rGO surface showed the higher hydrophobicity, indicating a high degree of reduction and more removal of oxygen content by increasing either the reduction time or hydrazine weight percentage.

In order to further confirm and monitor level of the loss of oxygen containing group throughout the GO reduction process, zeta potential experiments were conducted on six representative rGO dispersions along with the starting dispersion of GO. Figures 8.2(a) and (b) show the influences of the reduction time and amount of hydrazine on the degree of oxygen group removal. Regardless of the influencing parameter, the brown GO dispersion became darker and darker as soon as the reduction experiment began and progressed. The plots at the bottom of Figs. 8.2(a) and (b) show that all the samples were negatively charged to some extent indicating that the GO had a significant loss of oxygen functionalities (negative charge) as the hydrazine amount and reduction time were increased. The zeta potential of GO was initially around –70.9 mV, but it started decreasing after adding more hydrazine and increasing the reduction time, contributing to the elimination of the oxygen-containing functional groups. According to basic principles of colloidal science [29], the minimum absolute value of zeta potentials has to be 30 mV to ensure there is sufficient repulsion to reach to the colloidal stability. The American Standard Test Methods (ASTM) [30], on the other hand, defines that colloids possess “good stability” if they have zeta potentials of higher than 40 mV. All dispersions prepared at increased reduction time up to 15 min and with hydrazine percentage as high as 0.2% presented zeta potentials larger than these minimum values. The samples prepared at the lower (i.e. 0.1% hydrazine or 5 min reduction time), intermediate (i.e. 0.2% hydrazine or 15 min reduction time), and higher (0.4% hydrazine or 60 min reduction time) range of parameters were called slightly, moderately, and highly reduced GO. The zeta potentials of highly reduced GO were even below -30 mV, thereby reducing the electrostatic repulsions; these dispersions are with low colloidal stability and consequently expected to agglomerate if left undisturbed for

days or weeks. For this reason, all dispersions were used fresh as soon as the reduction process accomplished.

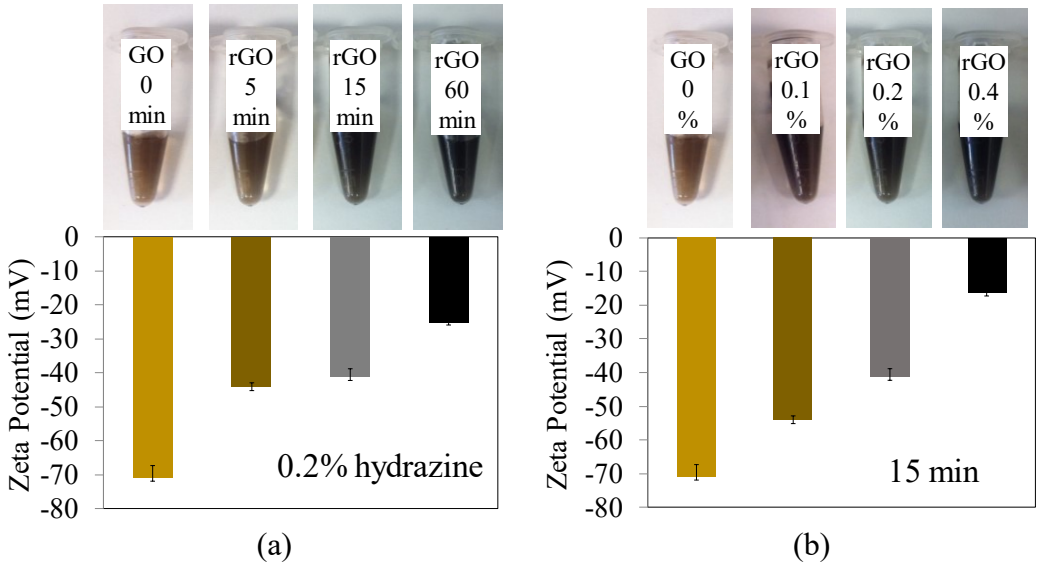

Figure 8.2. Top row) the photo images of the collected GO and rGO dispersions; (Bottom row) the zeta potential measurements of the collected sample dispersions prepared by different reduction conditions: (a) fixed hydrazine concentration (0.2 wt%), different reduction times (5, 15, and 60 min); (b) fixed reduction time (15 min), different hydrazine concentration (0.1, 0.2, and 0.4 wt%)

The changes of oxygen functional groups through reduction process of GO to rGO using different reduction conditions (reduction time and hydrazine concentrations) were unveiled by FTIR analyses and summarized in Figs. 8.3(a) and (b). The GO and rGO films of slightly, moderately, and highly reduced similar to those used in the contact angle measurement were used for FTIR experiments. FTIR graphs of GO, show the characteristic peaks for hydroxyl (−OH stretching group at ~3218 cm^{-1}), carbonyl C═O stretching (1730 cm^{-1}), aromatic C═C (1620 cm^{-1}), carboxy C−O (1415 cm^{-1}), epoxy C−O (1228 cm^{-1}), and C−O (1070 cm^{-1}), which are all in the agreement reported in previous studies [31-33]. The slightly reduced GOs treated with the lower ranges of reduction parameters (i.e. 5 min in Fig. 8.3(a) and 0.1% hydrazine in Fig. 8.3(b)) demonstrated substantial losses of their oxygen containing groups with the C−O bonds stretching in particular in the form of epoxy and hydroxyl groups. However, the intensity of the loss in the sample prepared at 5 min with 0.2% hydrazine was significantly higher than that of 15 min reduction with 0.1% hydrazine, indicating the dependency of the reduction process to the amount of reducing agent in comparison with the reduction time. This is in agreement with

zeta potential measurements of these two specimens, where the slightly reduced GO prepared at 5 min with 0.2% hydrazine (see Fig. 8.2(a)) had 10 mV loss of potential more than that of the slightly reduced GO produced with 0.1% hydrazine (see Fig. 8.2(b)). The moderately reduced GOs prepared at 15 min with 0.2% hydrazine exhibited losses of similar groups but with greater intensities. Our FTIR results are in agreement with the literature on the chemical reduction of GO dispersions [34, 35].

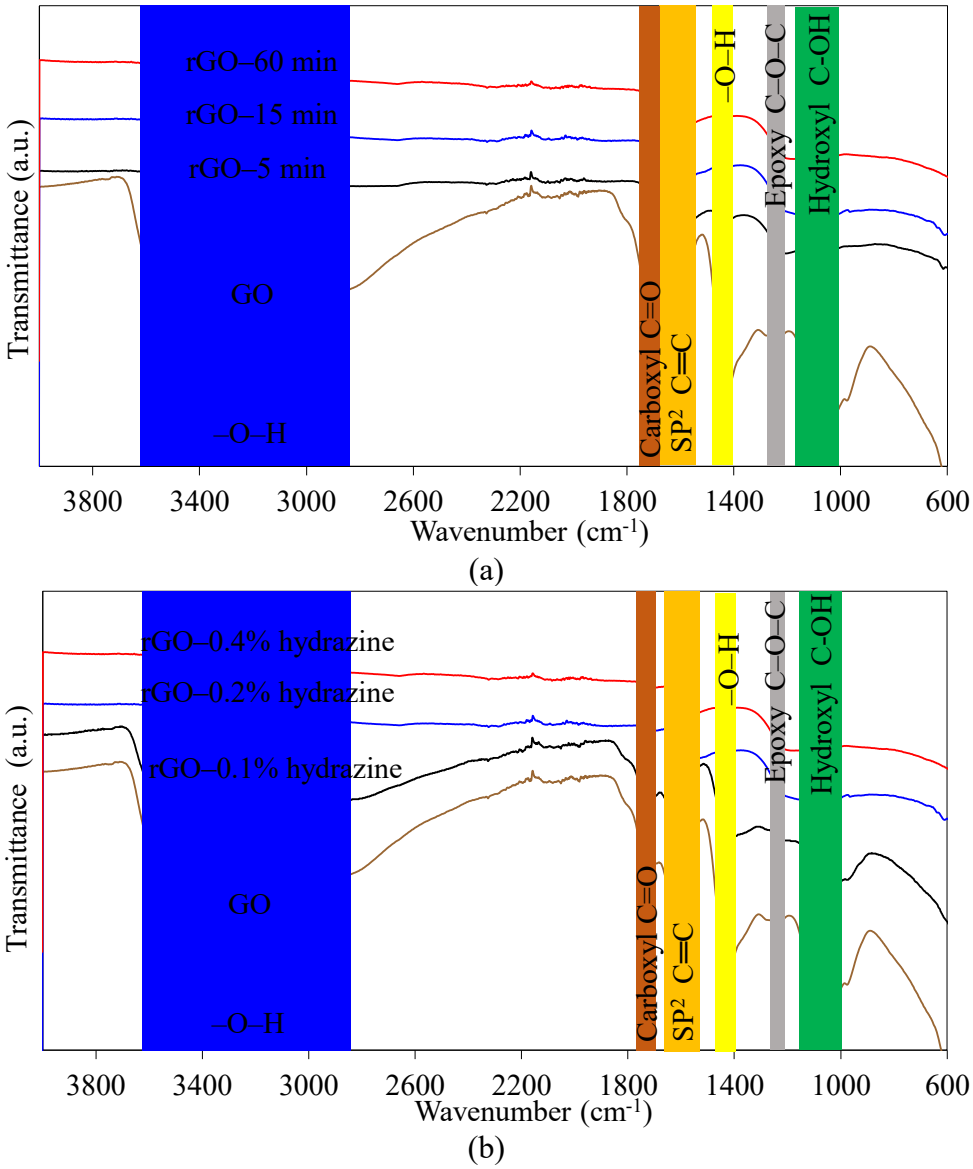

Figure 8.3. Comparative FTIR spectra of GO and rGO prepared by different reduction conditions: (a) fixed hydrazine percentage (0.2 wt%), different reduction times (5, 15, and 60 min); (b) fixed reduction time (15 min), different hydrazine percentages (0.1, 0.2, and 0.4 wt%)

Chemically reduced GO, particularly when treated with hydrazine, loses the majority of the oxidized groups, including the hydroxyl and epoxy groups, whereas most of carboxyl groups remain untouched. It is noteworthy that carboxyl groups are unlikely to be reduced by hydrazine [36,37], particularly under the reaction conditions in this study, where a shorter reaction time and a lower hydrazine/GO ratio were used compared to those of literature [38,39]. The evidences to such claim are the FTIR peaks at the wavenumber about 1415 cm^{-1} and 1730 cm^{-1} in Figs. 8.3(a) and (b), representing the remaining carboxyl group in the form of –COO– on rGO while being reduced in the basic environment. In the instance of highly reduced GO, where the hydrazine amount (0.4%) or reduction time (60 min) was set at its higher end, the intensity of characteristic peaks for the oxygen containing groups was reduced efficiently. The remaining significant peaks in Figs. 8.3(a) and (b) are attributed to the aromatic carbon double bonds (C═C) group and a minor C═O stretching which represents the presence of carboxyl group. In the highly reduced GO dispersion, where the C═C stretching peak becomes dominant, the pi (π) electrons of benzene aromatic rings lead to strong π−π stacking interactions and aggregation of graphene sheet.

Characterization of physicochemical properties GO and rGO-cement composite

Figures 8.4(a) and (b) show the morphology of the prepared cement mortar composites with reduced GO contents at 5, 15 and 60 min with 0.2% hydrazine imaged in secondary electron (SE) and backscattering electron (BSE) mode, respectively. As can be seen in Fig. 8.4(a), the cement composites with GO reduced at 5 and 15 min are similarly showing a uniform surface with less micro cracks compared to GO reduced at 60 min. The micro cracks are more evidently seen in Fig. 8.4(b) when imaged in BSE mode due to their high energy scattered electrons, which reveals information on the contrast in atomic number of the sample. For example, regions that contain atoms with high atomic number (e.g. Si, Mg, Ca) can be seen as bright regions, and those with low atomic number, such as carbon (C) as dark regions. The darker regions (red star) seen in Fig. 8.4(b) for slightly reduced GO at 5 min is silica (Si, 51.62% from EDAX) and not carbon. There were no graphene sheets seen on the surface of all the fractured cement mortar composites,

indicating that graphene exists as individual sheet was uniformly distributed in the composite structure. EDAX analysis of the full frame of the SEM images (in BSE mode) as shown in Fig. 8.4(c) further confirmed that the graphene sheets were uniformly distributed. The percentage of carbon detected in the cement composite containing moderately reduced GO (31.41%) was similar to the slightly reduced GO (30.45%). Interestingly, the cement composite mixed with highly reduced GO at a greater reduction time (60 min) detected less carbon (23.22%), which could be due to the fact that the graphene sheets are in a stacked form rather than individual sheets.

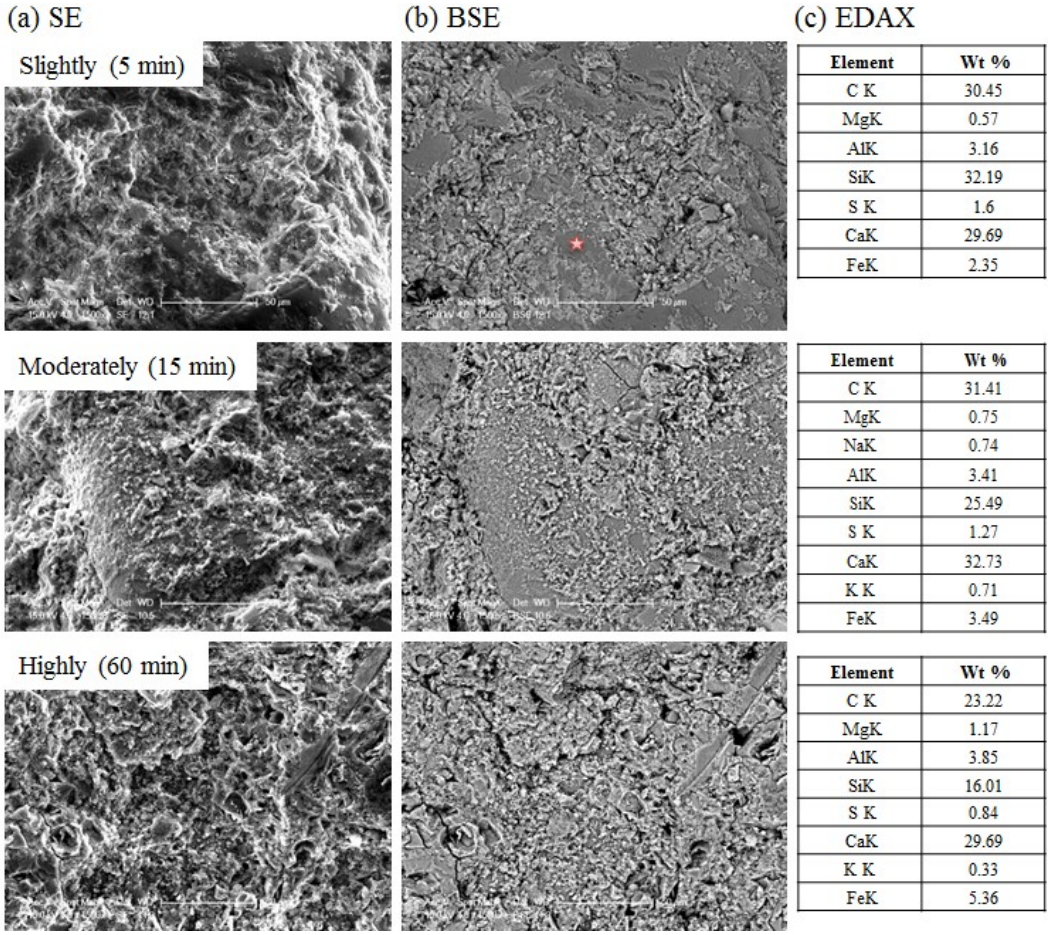

Element	Wt %
C K	30.45
MgK	0.57
AlK	3.16
SiK	32.19
S K	1.6
CaK	29.69
FeK	2.35

Element	Wt %
C K	31.41
MgK	0.75
NaK	0.74
AlK	3.41
SiK	25.49
S K	1.27
CaK	32.73
K K	0.71
FeK	3.49

Element	Wt %
C K	23.22
MgK	1.17
AlK	3.85
SiK	16.01
S K	0.84
CaK	29.69
K K	0.33
FeK	5.36

Figure 8.4. The low magnification SEM images of slightly, moderately, and highly reduced GO with different density level of oxygen groups (high, mild, and low) prepared by fixed hydrazine percentage (0.2%) at different reduction times of 5, 15, and 60 min, respectively: (a) secondary electron (SE), (b) backscattered electron (BSE) mode, (c) EDAX analysis of the full frame in BSE mode. Red star (in (b) of slightly) refers to the EDAX region which confirmed the composition to be silica (Si) and not carbon (C).

Figures 8.5(a) and (b) show the fractured surface of the cement mortar composites with 0.1% and 0.4% hydrazine used in the reduction process of GO at 15 min. The surface topography of the two samples are similar in roughness and once more graphene sheets were not seen as they were uniformly distributed. As can be seen in Fig. 8.5(c), highly reduced GO using a large amount of hydrazine (0.4%) has probably caused the graphene sheets to re-stack than exist as individual sheets due to the lower carbon content (22.61%) compared to the slightly reduced GO (0.1% hydrazine) where 28.55% was measured. The threshold for the reduction time and weight percentage of hydrazine required for the reduction of GO is 15 min and 0.2%, respectively, as the GO sheets are uniformly and individually dispersed and wrapped in the mortar composite without any aggregation in the cement mortar structure.

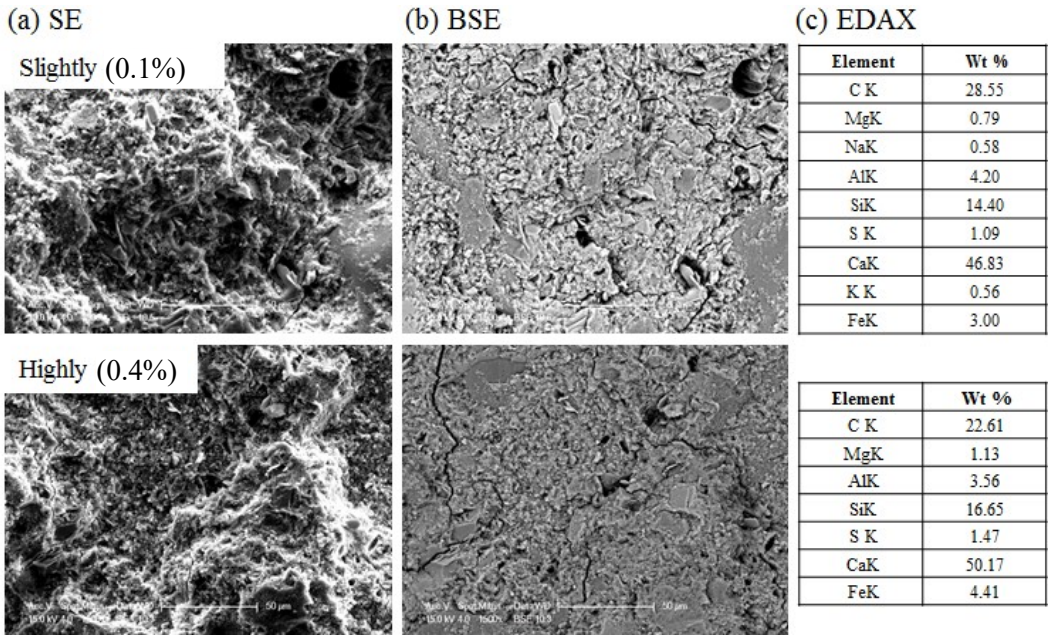

Element	Wt %
C K	28.55
MgK	0.79
NaK	0.58
AlK	4.20
SiK	14.40
S K	1.09
CaK	46.83
K K	0.56
FeK	3.00

Element	Wt %
C K	22.61
MgK	1.13
AlK	3.56
SiK	16.65
S K	1.47
CaK	50.17
FeK	4.41

Figure 8.5. The low magnification SEM images of slightly and highly reduced GO with high and low density level of oxygen groups prepared by fixed reduction time (15 min) at different hydrazine percentages (0.1% and 0.4%, respectively): (a) secondary electron (SE), (b) backscattered electron (BSE) mode, (c) EDAX analysis of the full frame in BSE mode

Figure 8.6 shows the influences of the rGO reduction on the hydration degree of the rGO–cement composites after 7 and 28 days of curing treatment. TGA plots of all composites shown in Fig. A11 (see Appendix 3) were used to calculate the hydration degree values. The hydration degree of the specimens found to be dependent to the

presence of oxygen groups obtained by both GO reduction conditions (concentration of reducing agent and time), showing the optimum at mild level of reduction. The reduction time, as shown in Fig. 8.6(a), found to be an influential factor on the hydration degree by reducing the hydration degree for both 7 and 28 days treated samples from 5 min to 60 min reduction time, however, with an optimum point at 15 min with similar reason provide for other factor, slightly reduced GO (at 5 min) and highly reduced GO (at 60 min) accommodate less water molecules compared to that of moderately reduced GO (at 15 min). This result indicates that there is an optimum threshold of density of oxygen groups in rGO that provides the highest hydration degree. The drop of the hydration degree from the highest value obtained for GO at the initial stage of reduction process to the lowest value (10 min, 0.2% hydrazine) similar to completely reduced GO (60 min, 0.2% hydrazine) was surprising. Figure A10 (see Appendix 3) exhibited the contact angle of 15 min reduced GO to be larger than 5 min reduced and smaller than 60 min reduced GO. This further confirms that 15 min reduced GO is more hydrophobic than that of 5 min reduced and less hydrophobic compared to the 60 min reduced GO. Reduction of GO, even though introduces some defects on the graphene surface by increasing the water permeability [40]. The GO sheets with heavily oxidized regions on basal plane cannot provide a frictionless pathway and subsequently affect the water flow and cause instability. On the contrary, graphene planar surface bare of oxygen functional groups makes the sheet super-hydrophobic and non-permeable [41]. Thus, rGO with an optimum reduction degree could be of better option for flowing, accommodating and stable residing of water on a graphitic surface. Moreover, highly reduced rGO sheets behave very similar to pristine graphene nanosheets; they can heavily re-stack and aggregate in water due to the existence of large-area π-π interactions as well as strong van der Waals interactions between the graphene layers, which result in rejection of the water [11,42].

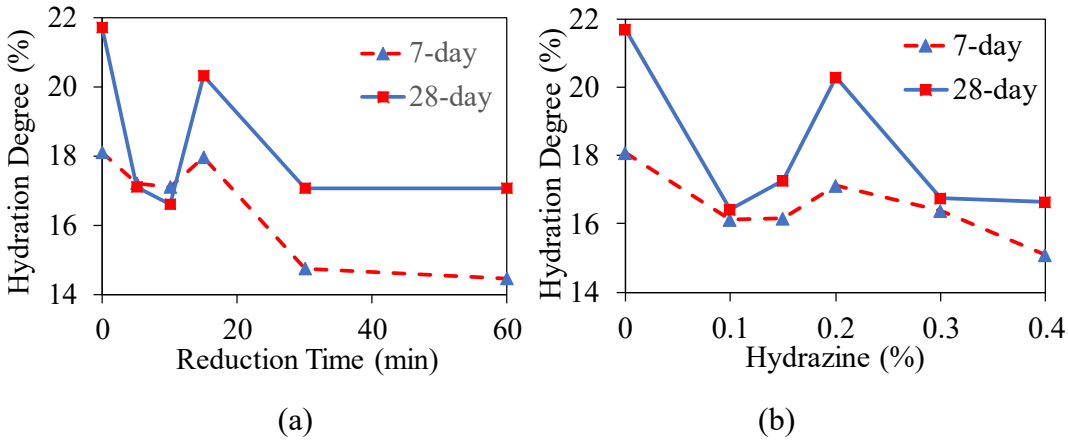

Figure 8.6. Hydration degrees of the rGO-cement composites by different reduction conditions: (a) fixed hydrazine percentage (0.2 wt%), different reduction times (5, 10, 15, 30, and 60 min); (b) fixed reduction time (15 min), different hydrazine percentages (0.1, 0.15, 0.2, 0.3, and 0.4 wt%)

As can be seen in Fig. 8.6(b), increasing the hydrazine percentage up to 0.15% resulted in a significant decrease in the hydration degrees of both 7 and 28 days treated samples. This can be attributed to graphene sheets' becoming more hydrophobic after the loss of more oxygen functionalities with the introduction of a larger amount of hydrazine. Adding more hydrazine up to 0.2% by weight of GO surprisingly elevated the hydration degree, but the addition of hydrazine from this point forward again led to a decrease in the hydration degree. Although with a higher reduction of the GO a higher hydrophobicity of the sample is expected, the possible reason for having the highest hydration degree at optimum hydrazine percentage of 0.2% can be attributed to the generation of more available space between the GO functional groups to accommodate more water molecules. This is identified as the optimum level, as beyond this point the graphene sheet becomes super-hydrophobic developing water-repellent properties, thereby reducing the hydration degree. The water contact angle measurements shown in Fig. A10 are also in support of this explanation.

The comparative XRD spectra of GO- and rGO-cement mortar composites are shown in Fig. 8.7. All spectra were normalized for easier and more accurate comparison. As can be seen in Figs. 8.7(a) and (b), the most dominant peaks observed at the scattering angle (2θ) of 22° and 28° are indicative from the quartz

as this constitutes the major crystalline phase of the sand [43,44]. All spectra evidenced the formation of the tricalcium silicate C_3S (Ca_3SiO_5) and dicalcium silicate C_2S (Ca_2SiO_4) as well as the initiation of the hydration process creating the cement paste containing Portlandite $Ca(OH)_2$ abbreviated as CH at about 18° and 34° [45-47] and calcium silicate hydrate (C–S–H) at 2θ of 29.6°, 45.7°, 50.3°, and 55.2° [46]. The cumulative intensity of all these peaks for the rGO-mortar mix of the optimum preparation condition showed to be higher than that of other mixes, regardless of parameters which were varied. Creation of C–H and C–S–H significantly contributes to hydration process and ultimately to the enhancement of the strength and volume stability of the cementitious materials [48]. The XRD and TGA results well agree each other in introducing the rGO-mortar mix of 60 min reduction time with 0.2% hydrazine with the highest chance of hydration compared to other specimens. Figure 8.7(c) compares the crystalline phase 7 and 28 days treated mortar specimens prepared at optimum condition and emphasizes the influence of curing process on the elevation of the hydration level as well as the enhancement of the mechanical strength. They are of the similar crystalline phase with higher intensity of the hydration peaks for the 28 days cured specimens.

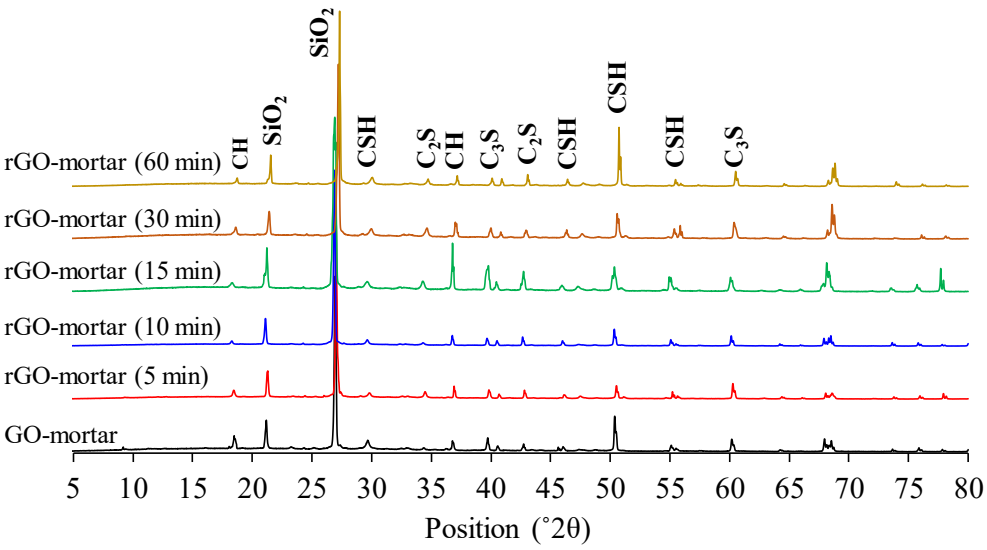

(a)

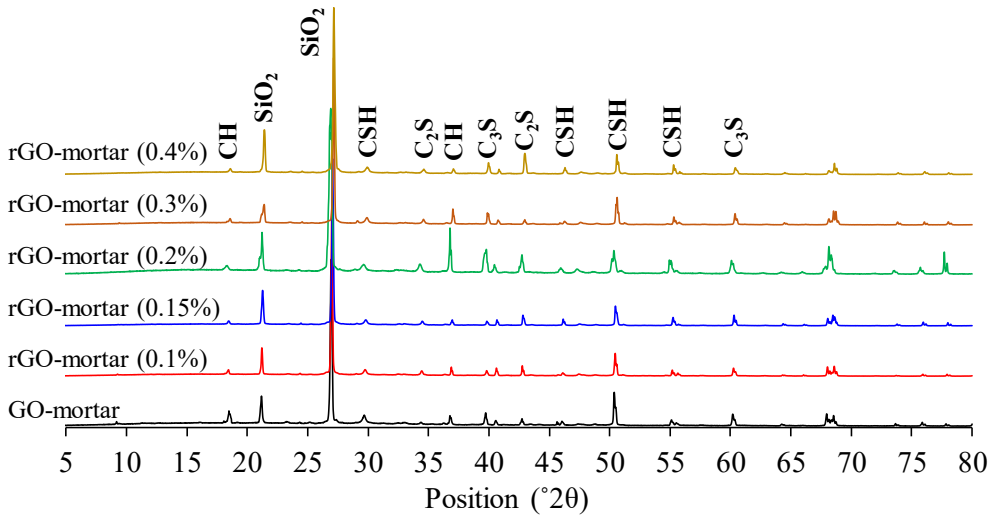

(b)

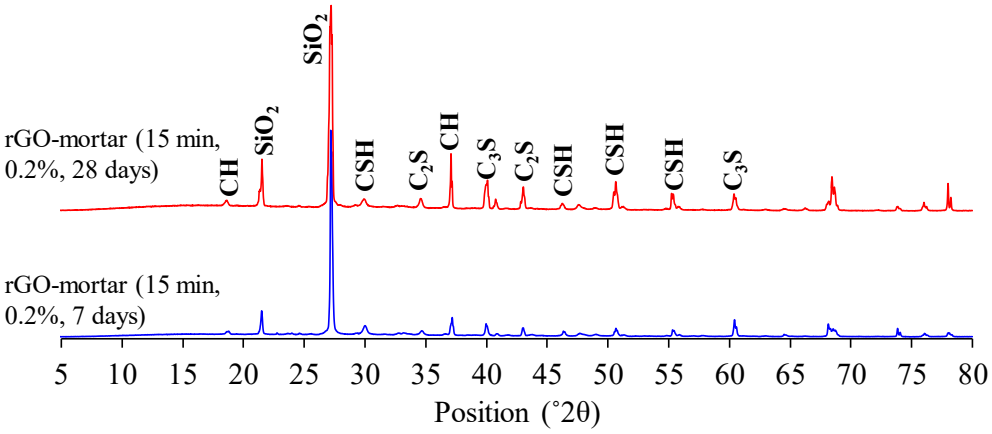

(c)

Figure 8.7. The XRD spectra of the GO- and rGO-cement mortar composites at 28 days: (a) fixed hydrazine percentage (0.2 wt%), different reduction times (5, 10, 15, 30, and 60 min); (b) fixed reduction time (15 min), different hydrazine percentages (0.1, 0.15, 0.2, 0.3, and 0.4 wt%). (c) The XRD spectra of the rGO-cement mortar prepared with rGO reduced at 15 min by 0.2 wt% hydrazine cured for 7 and 28 days

FTIR analyses in transmittance mode were conducted in order to investigate the influence of the GO and rGO incorporation into the hydration of the cement mortar mix. The influences of reduction time and hydrazine amount were shown in Fig. 8.8. Unlike the TGA and XRD, the FTIR is more of quantitative analytical technique, which can comment more on the existence of bond stretching and interactions rather than their extent. Figures 8.8(a) and (b) similarly show characteristic peaks of GO and rGO, which are the broad peak of O–H stretching vibrations from 3000 cm^{-1} to 3500 cm^{-1} and narrow peak of the in-plane C=C (sp^2 carbon) skeletal stretching

vibrations at 1616 cm^{-1}; and the stretching peaks at 1225 cm^{-1} and 1050 cm^{-1} for the C–O (epoxy and alkoxy groups) [49]. Regardless of the reduction parameters, Fig. 8.8 confirmed the loss of oxygen containing group (mainly hydroxyl and epoxy) and remaining of the C=C (sp^2 carbon) in rGO mixes compared with GO mix. This finding attributes to the successful reduction process of GO, which was explained in detail previously in GO/rGO FTIR analyses. The major stretching vibration bands observed at about 875 cm^{-1} and 1410 cm^{-1} attribute to the presence of CO_3 from $CaCO_3$ for the Portland cement [50]. The characteristic peaks which evidenced the influences of the GO and rGO incorporation in mortar mixes are the minor vibration band at about 3640 cm^{-1} and a major band at about 980 cm^{-1} correspond to the O–H stretching and C–S–H bands, respectively. The former and latter bands in agreement with the XRD analysis confirm the formation of the $Ca(OH)_2$ and C–S–H phases in the Portland cement, respectively. Figure 8.8(c) shows the comparative FTIR spectra of the rGO-cement mortar mixes prepared at optimum rGO condition and being cured for 7 and 28 days. Both spectra showed similar shapes of peaks without any notable difference confirming the chemical stability of the mixes over the time. In another word, prolonging the curing process does not affect the chemical structure of the mixes, given that the hydration levels for the two mixes are different.

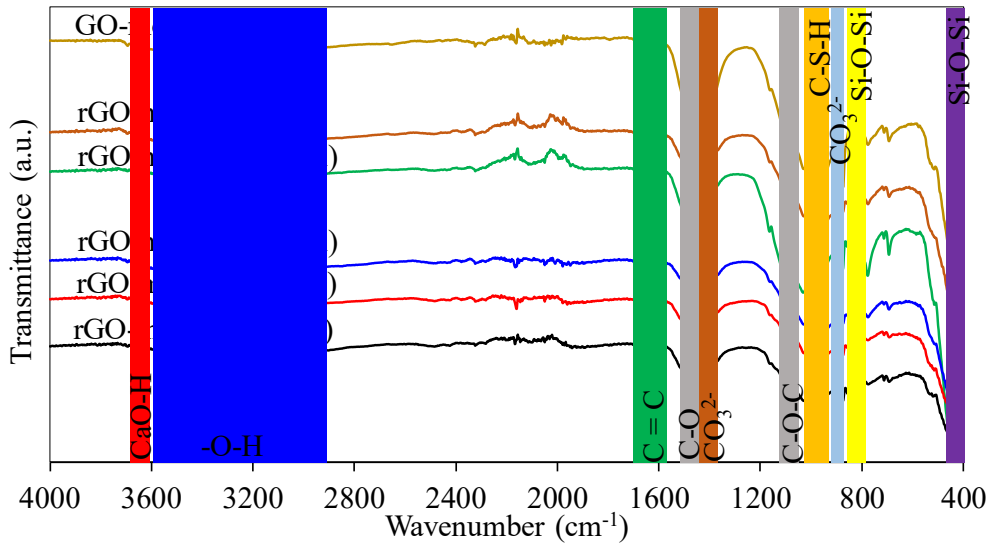

(a)

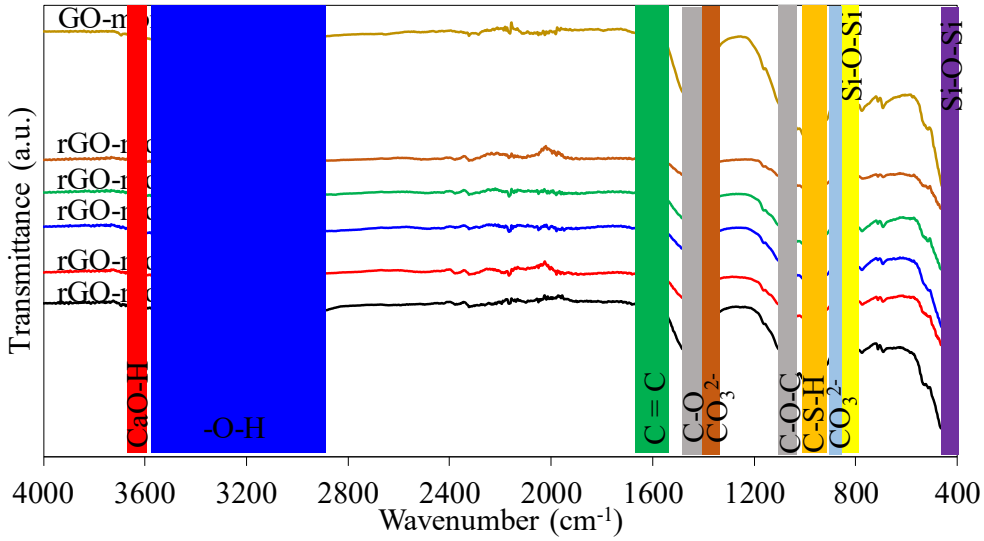

(b)

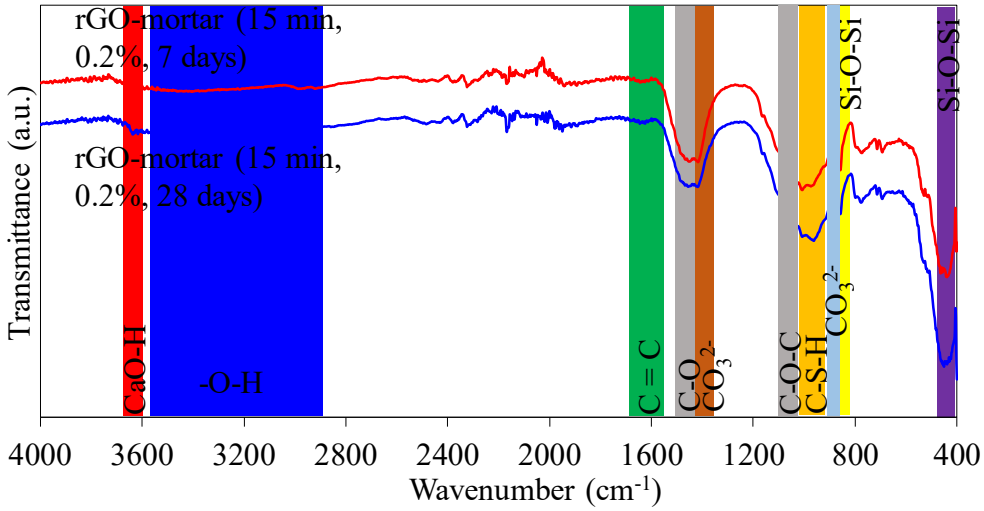

(c)

Figure 8.8. The FTIR spectra of the GO- and rGO-cement mortar composites at 28 days: (a) fixed hydrazine percentage (0.2 wt%), different reduction times (5, 10, 15, 30, and 60 min); (b) fixed reduction time (15 min), different hydrazine percentages (0.1, 0.15, 0.2, 0.3, and 0.4 wt%). (c) FTIR spectra of the rGO-cement mortar mixes prepared with rGO reduced at 15 min by 0.2 wt% hydrazine cured for 7 and 28 days

Characterization of mechanical properties of rGO-cement composites

Figures 8.9(a) and (b) show the variation of tensile strength of cement mortar composites with level of oxygen groups of GO and rGO obtained by different reduction conditions including the reduction time (0–60 min at 0.2 wt% hydrazine) and hydrazine concentration (0–0.4 wt% at 15 min), respectively. Experimental

results and the strength enhancements compared to the plain mortar are shown in Table A10 (see Supporting Information). As can be seen in Fig. 8.9 and Table A10, the inclusion of 0.1% GO in the cement mortar resulted in a 44.4% and 37.5% increase in the 7- and 28-day tensile strength of the composite, respectively. It can be seen in Fig. 8.9(a) that, at a constant hydrazine percentage level of 0.2%, the tensile strength of the mortar mixes steadily increased with an increase in the reduction time up to 15 min, and beyond this time the strength started to decrease. In addition, as can be seen in Fig. 8.9(b), at the same reduction time of 15 min, the tensile strength of the mixes increased with an increase in the hydrazine percentage up to 0.2% and beyond this level the strength started to decrease. The results show that the inclusion of the rGO with 0.2% hydrazine at 15 min reduction resulted in the highest tensile strength development. The strength enhancement of the mix containing rGO with 15 min reduction by 0.2% hydrazine (as the optimum reduction condition) reached 47.2% and 45.0% at 7 and 28 days compared to the plain mortar, respectively, which are higher than those of the GO mix. It is worth noting that the increase in the mechanical properties over those of the GO mix was limited due to the lower dispersibility of rGO than that of GO as discussed in hydration degree section. It can also be seen in Fig. 8.9 that all the rGO mixes obtained significantly higher 7- and 28-day tensile strength compared to those of plain cement mortar. It is also worth noting that the enhancements seen (in Table A10) in the slightly (i.e. 0.2% hydrazine at 5 min reduction) and highly (i.e. 0.2% hydrazine at 60 min reduction and 0.4% hydrazine at 15 min reduction) reduced rGO conditions were lower than those attained through the addition of GO. As discussed in detail in physiochemical characterization section, this observation is attributed to the weaker bonding between the cement matrix and graphene sheets at the slightly and highly reduced rGO mixes compared to that of GO mix, as slightly reduced rGO mix exhibited a reduced degree of hydration and highly reduced rGO mix had graphene sheets with super-hydrophobic and re-stack properties that gave rise to a higher density of micro cracks in the composite.

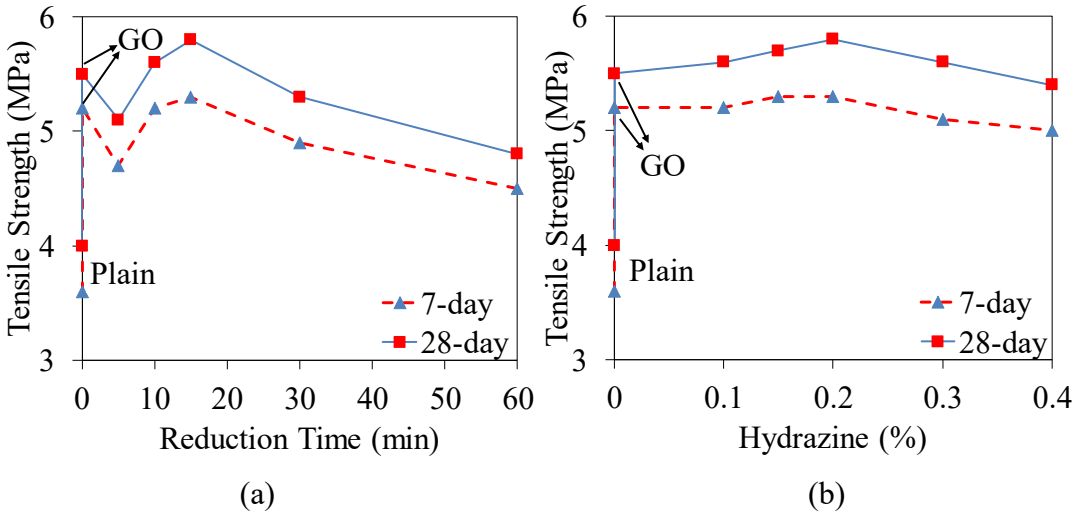

Figure 8.9. The variation of 7 and 28 days tensile strength of cement mortar composites with level of oxygen groups of GO and rGO additives prepared by different conditions including (a) the reduction time (0–60 min at 0.2 wt% hydrazine) and (b) hydrazine concentration (0–0.4 wt% at 15 min)

Figures 8.10(a) and (b) show the variation of compressive strength of cement mortar composites with level of oxygen groups of GO and rGO prepared by different conditions including the reduction time (0–60 min at 0.2 wt% hydrazine) and hydrazine concentration (0–0.4 wt% at 15 min). It can be seen in Fig. 8.10 and Table A10 that addition of GO by 0.1% weight of cement in the mortar resulted in a 46.0% and 77.7% increase in the 7- and 28-day compressive strength of the composite, respectively. As can be seen in Fig. 8.10(a), at a constant hydrazine percentage level of 0.2%, the compressive strength of the specimens steadily increased with an increase in the reduction time up to 15 min, and beyond this time the strength started to decrease. It can be seen in Fig. 8.10(b) that, at the same reduction time of 15 min, the compressive strength of the mixes increased with an increase in the hydrazine percentage up to 0.2% and beyond this level the strength started to decrease. The compressive strength enhancement of the mix containing rGO with 15 min reduction by 0.2% hydrazine reached 51.6% and 83.7% at 7 and 28 days, respectively, indicating that enhancements seen in the mix with the optimum rGO condition (i.e. 0.2% hydrazine at 15 min reduction) are higher than those with GO. As can be seen in Table A10 (see Appendix 3), comparison of the compression and tension test results show that, for a given mix, compressive strength enhancements in rGO mixes from 7 to 28 days curing age are higher than those of tensile strength. This indicates that the effect of graphene on the tensile strength is experienced mostly up to 7 days

and after that no further improvement is evident, whereas the compressive strength enhancement is more progressive and continues beyond the 7 days to 28 days curing age. It can be seen in Table A10 that the enhancements seen in the slightly (i.e. 0.2% hydrazine at 5 min reduction) and highly (i.e. 0.2% hydrazine at 60 min reduction and 0.4% hydrazine at 15 min reduction) reduced rGO conditions were lower than those attained through the addition of GO. This is attributed to the better interlocking action between the GO and C–S–H products owing to the higher hydration degree of GO mix compared to that of slightly and highly reduced rGO mixes.

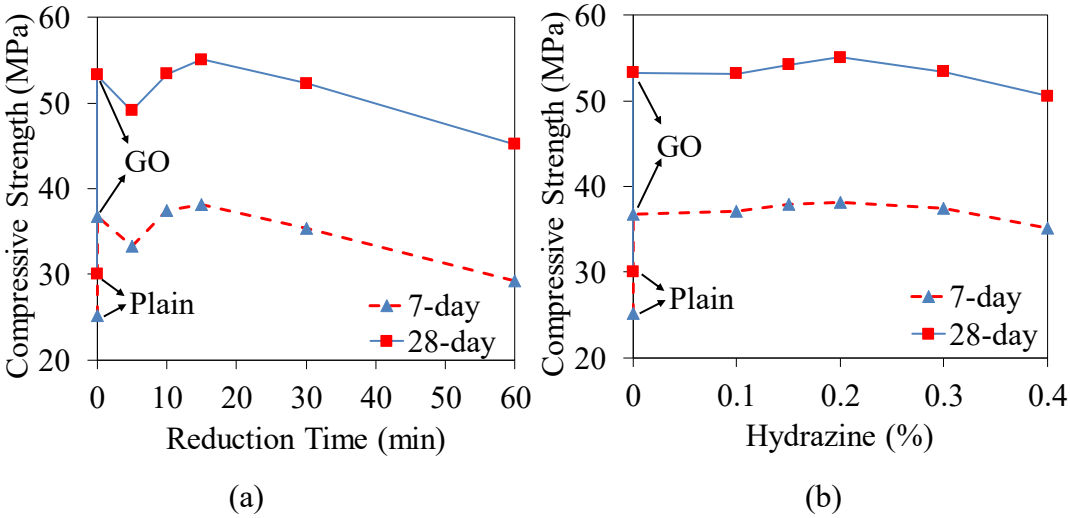

Figure 8.10. The variation of 7 and 28 days compressive strength of cement mortar composites with level of oxygen groups of GO and rGO obtained by different conditions including (a) the reduction time (0–60 min at 0.2 wt% hydrazine) and (b) hydrazine concentration (0–0.4 wt% at 15 min)

The observed improvements in the tensile and compressive strengths of cement mortar composites at the optimum condition of rGO (i.e. 0.2% hydrazine at 15 min reduction) can be linked to the two factors of graphene structure, as established based on the FTIR, SEM, XRD, and TGA results. The first factor is the level of oxygen that is critical for the bonding between the cement C–S–H and graphene sheets. Mechanical results suggest that there is an optimal threshold of required oxygen groups for the interactions between the graphene sheets and C–S–H. Highly reduced rGO behaves mechanically similar to pristine graphene; it is super-hydrophobic (as shown in Fig. A9) and hence accommodates less water molecules between the graphene layers. Therefore, highly reduced rGO sheets with the lowest level of oxygen (i.e. 0.4% hydrazine or 60 min reduction) could easily re-stack and

agglomerate in the mix owing to the strong van der Waals interactions between the graphene layers, which limits their dispersion and results in an increased micro crack density at the surface of the composite (as shown in Figs. 8.4 and 8.5). On the other hand, slightly reduced rGO with a high level of oxygen (i.e. 0.1% hydrazine or 5 min reduction) is highly hydrophilic and dispersible, and hence provides frictionless pathway for the flow of water molecules, which subsequently leads to water instability on the GO sheets and in the microstructure of the composite (refer to TGA analysis). Reduction of some oxygen functional groups can be beneficial to generate gaps and frictional pathways to trap and accommodate stable water into the graphene sheets. The second contributing factor is the level of mechanical strength of the graphene structures, which changes considerably from the lowest at GO to the highest at fully reduced rGO. The changes in the mechanical strength of graphene through the reduction process results in changes in defectiveness and crystallinity of GO and rGO with the level of oxygen groups, and rearrangement of graphitic structures. It would be reasonable to expect that the use of fully reduced rGO with the highest mechanical strength would lead to the highest tensile and compressive strength in the composite, but this was not the case, suggesting that the influence of oxygen level is also important and the optimal balance between these two factors needs to be established. Therefore, finding the optimum oxygen condition and balances between different parameters of graphene additives in cement composites is of vital importance that needs to be considered to achieve the best physiochemical and mechanical properties.

Figure 8.11 shows the relationship between the axial compressive stress and strain for cement mortar composites with GO and rGO inclusions at 28 days. As can be seen in Figs. 8.11(a) and (b), the elastic modulus and axial strain corresponding to the compressive strength (strain at peak) of the rGO-cement mortars steadily increased with an increase in the oxygen reduction level up to the optimum condition (reduction time up to 15 min and hydrazine up to 0.2 wt%), but decreased with a further decrease in the oxygen level (increased reduction time and hydrazine percentage). It can also be seen in the figures that mixes containing slightly and highly reduced rGO exhibited lower elastic modulus and peak strain compared to those of GO. As can be seen in Figs. 8.11(a) and (b), the variation in the elastic modulus and peak strain of mixes with oxygen level (reduction time and hydrazine

percentage) is consistent with the changes in compressive strength, which is attributed to the well-known relationship between the compressive strength, elastic modulus, and axial strain of cementitious materials. It can also be seen in the figures that the presence and reduction rate of GO do not have a significant effect on the second branch trend of the axial stress-strain curves of the cement mortar composite.

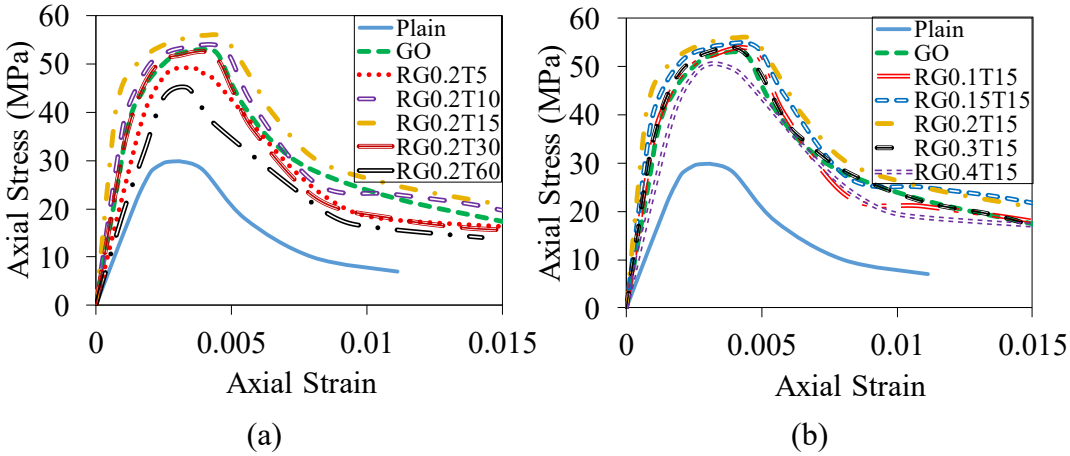

Figure 8.11. Variation of 28 days compressive axial stress-axial strain relationships of cement mortar composites with: (a) reduction time at fixed hydrazine percentage (0.2%); (b) hydrazine percentage at fixed reduction time (15 min)

CONCLUSIONS

This paper has demonstrated that oxygen functionalities of graphene structure have significant influence on physicochemical and mechanical properties of cement composites, which need to be considered in the formulation of these materials. The results show that the use of rGO with 0.1% dosage with the optimal reduction condition (i.e. 15 min reduction by 0.2% hydrazine) leads to a 45.0% and 83.7% increase in the 28-day tensile and compressive strengths of rGO–cement mortar composites compared to those of the plain cement mortar composite. These enhancements in the tensile and compressive strength are larger than those containing 0.1% GO (37.5% and 77.7% increase compared to the plain cement mortar composite, respectively). Study revealed that rGO reduced by optimal conditions not only reduce the micro crack density and increase the hydration degree of the composite, but also improve accessibility of the water to the GO oxygen functional groups and cement C–S–H component, indicating the importance of establishing an appropriate GO oxygen functionality level. This is attributed to the

fact that reduction of GO with the higher end of each influential parameter (reduction time and weight percentage of hydrazine) provides graphene sheets with the improved mechanical properties but presents hydrophobic and re-stack properties. On the other hand, rGO prepared at the lower end condition of each influential parameter possesses highly dense spread of oxygen functionalities, which provides frictionless pathway for flowing of water molecules, and subsequently lead to water instability on the GO sheets and in composite microstructures. These results suggest that it is critical to balance these two parameters to achieve optimized physiochemical and mechanical properties of graphene cement composite. These observations from mechanical properties that were validated by SEM, TGA, XRD, and FTIR analyses provide an essential link between structural, chemical, and mechanical properties of rGO–cement mortar composites and help to better understand the influence of oxygen functionality reducing parameters. This work presents an important contribution toward the understanding of the key parameters of GO and rGO additives for the formulation of next-generation of cementitious composites with advanced properties.

ACKNOWLEDGMENTS

The authors gratefully acknowledge the support of the Australian Research Council through ARC IH 150100003 (Research Hub for Graphene Enabled Industry Transformation) and The University of Adelaide. T.A. acknowledges support from a Research Excellence Grant. The authors also thank Schools of Chemical Engineering and Civil, Environment and Mining Engineering at the University of Adelaide for supporting this work.

REFERENCES

[1] Lv S, Ma Y, Qiu C, Sun T, Liu J, Zhou Q. Effect of graphene oxide nanosheets of microstructure and mechanical properties of cement composites. *Construction and Building Materials*. 2013;49:121–7

[2] Chuah S, Pan Z, Sanjayan JG, Wang CM, Duan WH. Nano reinforced cement and concrete composites and new perspective from graphene oxide. *Construction and Building Materials.* 2014;73:113-24.

[3] Pan Z, He L, Qiu L, Habibnejad Korayem A, Li G, Zhu JW, Collins F, Li D, Duan WH, Wang MC. Mechanical properties and microstructure of a graphene oxide–cement composite. *Cement and Concrete Composites*. 2015;58:140-7.

[4] Dvorkin D, Peled A. Effect of reinforcement with carbon fabrics impregnated with nanoparticles on the tensile behavior of cement-based composites. *Cement and Concrete Research*. 2016;85:28–38.

[5] Geim AK, Novoselov KS. The rise of graphene. *Nature Materials*. 2007;6(3):183-91.

[6] Singh AP, Mishra M, Chandra A, Dhawan SK. Graphene oxide/ferrofluid/cement composites for electromagnetic interference shielding application. *Nanotechnology*. 2011;22(46):465701.

[7] Ranjbar N, Mehrali M, Mehrali M, Alengaram UJ, Jumaat MZ. Graphene nanoplatelet-fly ash based geopolymer composites. *Cement and Concrete Research*. 2015;76:222–31.

[8] Lee C, Wei X, Kysar JW, Hone J. Measurement of the elastic properties and intrinsic strength of monolayer graphene. *Science*. 2008;321(5887):385–8.

[9] Kuilla T, Bhadra S, Yao D, Kim NH, Bose S, Lee JH. Recent advances in graphene based polymer composites. *Progress in Polymer Science*. 2010;35(11):1350–75.

[10] Lambert TN, Chavez CA, Hernandez-Sanchez B, Lu P, Bell NS, Ambrosini A, Friedman T, Boyle TJ, Wheeler DR, Huber DL. Synthesis and characterization of titania-graphene nanocomposites. *Journal of Physical Chemistry C.* 2009;113(46):19812–23.

[11] Yang K, Wang J, Chen B. Facile fabrication of stable monolayer and few-layer graphene nanosheets as superior sorbents for persistent aromatic pollutant management in water. *Journal of Materials Chemistry A.* 2014;2:18219-24.

[12] Stankovich S, Piner RD, Nguyen ST, Ruoff RS. Synthesis and exfoliation of isocyanate-treated graphene oxide nanoplatelets. *Carbon*. 2006;44:3342−7.

[13] Kim DH, Yun YS, Jin HJ. Difference of dispersion behavior between graphene oxide and oxidized carbon nanotubes in polar organic solvents. *Current Applied Physics*. 2012;12(3):637–42.

[14] Khoei AR, Khorrami MS. Mechanical properties of graphene oxide: A molecular dynamics study. *Fullerenes, Nanotubes and Carbon Nanostructures*. 2016;24(9):594-603.

[15] Alkhateb H, Al-Ostsaz A, Cheng A, Li X. Materials genome for graphene-cement nanocomposites. *Journal of Nanomechanics and Micromechanics*. 2013;3(3):67−77.

[16] Fakhim B, Hassani A, Rashidi A, Ghodousi P. Preparation and Mechanical Properties of Graphene Oxide: Cement Nanocomposites. *Scientific World Journal*. 2014;1-10.

[17] Sharma S, Kothiyal NC. Influence of graphene oxide as dispersed phase in cement mortar matrix in defining the crystal patterns of cement hydrates and its effect on mechanical, microstructural and crystallization properties. *RSC Advances*. 2015;5:52642–57.

[18] Gong K, Pan Z, Korayem AH, Qiu L, Li D, Collins F, Wang CM, Duan WH. Reinforcing effects of graphene oxide on portland cement paste. *Journal of Materials in Civil Engineering*. 2014;27:A4014010.

[19] Cao ML, Zhang HX, Zhang C. Effect of graphene on mechanical properties of cement mortars. *Journal of Central South University*. 2016;23:919−25.

[20] Lu C, Lu Z, Li Z, Leung CKY. Effect of graphene oxide on the mechanical behavior of strain hardening cementitious composites. *Construction and Building Materials.* 2016;120:457–64.

[21] Saafi M, Tang L, Fung J, Rahman M, Liggat J. Enhanced properties of graphene/fly ash geopolymeric composite cement. *Cement and Concrete Research.* 2015;67:292-9.

[22] Murugan M, Santhanam M, Gupta SS, Pradeep T, Shah SP. Influence of 2D rGO nanosheets on the properties of OPC paste. *Cement and Concrete Composites.* 2016;70:48-59.

[23] Gholampour A, Valizadeh Kiamahalleh M, Tran DNH, Ozbakkaloglu T, Losic D. Revealing the dependence of the physiochemical and mechanical properties of cement composites on graphene oxide concentration. *RSC Advances.* 2017;7:55148-56.

[24] Hummers WS, Offeman RE. Preparation of graphitic oxide. *Journal of American Chemical Society.* 1985;80:1339.

[25] Kovtyukhova N, Ollivier PJ, Martin BR, Mallouk TE, Chizhik SA, Buzaneva EV, Gorchinskiy AD. Layer-by-layer assembly of ultrathin composite films from micron-sized graphite oxide sheets and polycations. *Chemistry of Materials*. 1999;11:771-8.

[26] ASTM C307-03. *Standard Test Method for Tensile Strength of Chemical-Resistant Mortar, Grouts, and Monolithic Surfacings*. American society for testing and materials, West Conshohocken, PA, USA: ASTM International, 2012.

[27] ASTM C109/C109M-16a. *Standard Test Method for Compressive Strength of Hydraulic Cement Mortars*. American society for testing and materials, West Conshohocken, PA, USA: ASTM International, 2008.

[28] Huh SH. *Thermal reduction of graphene oxide, Physics and Applications of Graphene-Experiments*, Dr. Sergey Mikhailov (Ed.), ISBN: 978-953-307-217-3, 2011.

[29] Gregory J. The matter in suspension. *Nature*. 1989;338:182.

[30] ASTM D4187-82. *Methods of Test for Zeta Potential of Colloids in Water and Waste Water.* American society for testing and materials, USA: ASTM International, 1985.

[31] Park S, An J, Piner RD, Jung I, Yang D, Velamakanni A, Nguyen ST, Ruoff RS. Aqueous suspension and characterization of chemically modified graphene sheets. *Chemistry of Materials*. 2008;20:6592-4.

[32] Chen W, Yan L, Bangal PR. Chemical reduction of graphene oxide to graphene by sulfur-containing compounds. *Journal of Physical Chemistry C.* 2010;114:19885-90.

[33] Xue L, Shen C, Zheng M, Lu H, Li N, Ji G, Pan L, Cao J. Hydrothermal synthesis of graphene–ZnS quantum dot nanocomposites. *Materials Letters*. 2011;65:198-200.

[34] Haubner K, Murawski J, Olk P, Eng LM, Ziegler C, Adolphi B, Jaehne E. The route to functional graphene oxide. *ChemPhysChem*. 2010;11:2131-9.

[35] Xu C, Yuan RS, Wang X. Selective reduction of graphene oxide. *Xinxing Tan Cailiao/New Carbon Materials.* 2014;29:61-6.

[36] Li D, Muller MB, Gilje S, Kaner RB, Wallace GG. Processable aqueous dispersions of graphene nanosheets. *Nature Nanotechnology*. 2008;3:101-5.

[37] Paul H, Mohanta D. Hydrazine reduced exfoliated graphene/graphene oxide layers and magnetoconductance measurements of Ge-supported graphene layers. *Applied Physics A*. 2011;103:395-402.

[38] Peng-Gang R, Ding-Xiang Y, Xu J, Tao C, Zhong-Ming L. Temperature dependence of graphene oxide reduced by hydrazine hydrate. *Nanotechnology*. 2011;22:055705.

[39] Choi J, Tu NDK, Lee SS, Lee H, Kim JS, Kim H. Controlled oxidation level of reduced graphene oxides and its effect on thermoelectric properties. *Macromolecular Research*. 2014;22:1104-8.

[40] Lin LC, Grossman JC. Atomistic understandings of reduced graphene oxide as an ultrathin-film nanoporous membrane for separations. *Nature Communications.* 2015;6:8335.

[41] Mi B. *New Materials for Emerging Desalination Technologies*. Frontiers of Engineering: Reports on Leading-Edge Engineering from the 2016 Symposium. Washington, DC: The National Academies Press, 2017.

[42] Wang J, Chen Z, Chen B. Adsorption of polycyclic aromatic hydrocarbons by graphene and graphene oxide nanosheets. *Environmental Science & Technology.* 2014;48:4817-25.

[43] Raupp-Pereira F, Hotza D, Segadaes AM, Labrincha JA. Ceramic formulations prepared with industrial wastes and natural sub-products. *Ceramics International.* 2006;32:173−9.

[44] Amin NU, Alam S, Gul S. Assessment of pozzolanic activity of thermally activated clay and its impact on strength development in cement mortar. *RSC Advances.* 2015;5:6079−84.

[45] Wang R, Yao L, Wang P. Mechanism analysis and effect of styrene–acrylate copolymer powder on cement hydrates. *Construction and Building Materials*. 2013;41:538−44.

[46] Yang N, Yue W. *Handbook of a collection of illustrative plates of inorganic nonmetal materials.* Wuhan: Wuhan University of Technology Publishing Company, 2000.

[47] Tkaczewska E. Mechanical Properties of Cement Mortar Containing Fine-Grained Fraction of Fly Ashes. *Open Journal of Civil Engineering*. 2013;3(2a):54−68.

[48] Alizadeh R, Raki L, Makar JM, Beaudoin JJ, Moudrakovski I. Hydration of tricalcium silicate in the presence of synthetic calcium-silicate-hydrate. *Journal of Materials Chemistry.* 2009;19:7937−46.

[49] Nine MJ, Cole MA, Johnson L, Tran DNH, Losic D. Robust superhydrophobic graphene-based composite coatings with self-cleaning and corrosion barrier properties. *ACS Applied Materials & Interfaces*. 2015;7:28482-93.

[50] Li GY, Wang PM, Zhao X. Mechanical behavior and microstructure of cement composites incorporating surface-treated multi-walled carbon nanotubes. *Carbon*. 2005;43:1239-45.

Chapter 4

Confinement of normal- and high-strength concretes

Publications:

Gholampour A, Ozbakkaloglu T, Ng CT. Ambient- and oven-cured geopolymer concretes under active confinement. *Construction and Building Materials.* submitted on 26/11/2018. ***Citations: 0***

Gholampour A, Ozbakkaloglu T. Understanding the compressive behavior of shape memory alloy (SMA)-confined normal- and high-strength concrete. *Composite Structures*. 2018;202:943-53. ***Citations: 2***

Gholampour A, Ozbakkaloglu T. Fiber-reinforced concrete containing ultra high-strength micro steel fibers under active confinement. *Construction and Building Materials*. 2018;187:299-306. ***Citations: 1***

Gholampour A, Ozbakkaloglu T. Behavior of steel fiber-reinforced concrete-filled FRP tube columns: experimental results and a finite element model. *Composite Structures.* 2018;194:252-62. ***Citations: 3***

Statement of Authorship

Title of Paper	Ambient- and oven-cured geopolymer concretes under active confinement
Publication Status	☐ Published ☐ Accepted for Publication ☑ Submitted for Publication ☐ Unpublished and Unsubmitted work written in manuscript style
Publication Details	Gholampour A, Ozbakkaloglu T, Ng CT. Ambient- and oven-cured geopolymer concretes under active confinement. *Construction and Building Materials*. 2019.

Principal Author

Name of Principal Author (Candidate)	Aliakbar Gholampour		
Contribution to the Paper	Literature review, analysis of test results, and preparation of the manuscript.		
Overall percentage (%)	70%		
Certification:	This paper reports on original research I conducted during the period of my Higher Degree by Research candidature and is not subject to any obligations or contractual agreements with a third party that would constrain its inclusion in this thesis. I am the primary author of this paper.		
Signature		Date	31/01/2019

Co-Author Contributions

By signing the Statement of Authorship, each author certifies that:

i. the candidate's stated contribution to the publication is accurate (as detailed above);

ii. permission is granted for the candidate in include the publication in the thesis; and

iii. the sum of all co-author contributions is equal to 100% less the candidate's stated contribution.

Name of Co-Author	Togay Ozbakkaloglu		
Contribution to the Paper	Research supervision and review of manuscript.		
Signature		Date	31/01/2019

Name of Co-Author	Ching-Tai Ng		
Contribution to the Paper	Review of manuscript.		
Signature		Date	31/01/2019

Please cut and paste additional co-author panels here as required.

Ambient- and Oven-Cured Geopolymer Concretes under Active Confinement

ABSTRACT

The axial compressive behaviour of actively confined geopolymer concretes (GPCs) is investigated. Two different batches of GPCs were manufactured using either 80% fly ash (FA)/20% ground granulated blast furnace slag (GGBS) (80/20 series) or 50% FA/50% GGBS (50/50 series). Two different curing conditions of ambient (at 23°C) and oven (at 70°C) curing were considered to evaluate the influence of the curing condition on the axial compressive behaviour of GPCs. GPCs were confined actively by a Hoek cell at different confining pressures ranging from 5 to 25 MPa. Axial compression tests were conducted on unconfined and actively confined geopolymers to investigate the influence of the composition of the GPC mix, curing condition, and confining pressure on the behaviour of GPCs. It is found that 50/50 series mixes exhibit slightly higher axial peak stress and strain than 80/20 series mixes. The results also show that oven-cured GPCs exhibit a slightly higher axial strength but a slightly lower peak axial strain than ambient-cured GPCs. At a given confining pressure, the GGBS content and curing condition also affect the trend of descending branch of the axial stress-axial strain curve of GPCs. The descending branch slope of GPCs tends to decrease with an increase in GGBS content, and oven-cured GPCs exhibit a slightly steeper descending branch than their ambient-cured counterparts. It is also found that, at a given axial strain, GPCs with a higher GGBS content develop a slightly higher lateral strain, indicating the increased dilation rate of GPCs at a higher GGBS content. These promising findings indicate the possibility of the use of GPC in structural columns in which the concrete will be subjected to lateral confinement.

KEYWORDS: Geopolymer concrete (GPC); Ground granulated blast furnace slag (GGBS); Fly ash; Axial compression; Active confinement; Dilation.

INTRODUCTION

The production of ordinary Portland cement (OPC) as a core component of concrete releases a large amount of greenhouse gases (especially CO_2) into the atmosphere. As reported in Ref. [1], production of one ton of OPC leads to the generation of approximately one ton of CO_2. It was also reported that approximately 1.35 billion tons of CO_2 annually produced from the production of OPC, which accounts for about 5–7% of the global CO_2 emissions [2]. Therefore, in an effort to reduce emission of CO_2 associated with the production of cement and concrete, it is important to identify alternative materials to replace OPC in concrete. The use of waste materials as binder in the concrete is a viable strategy to develop an environmentally-friendly construction material. Waste materials from industrial by-products, e.g. ground granulated blast furnace slag (GGBS) and fly ash (FA), can be considered as OPC replacements to reduce the negative environmental impact of OPC [3]. As was reported previously, the annual worldwide generation of GGBS and FA is approximately 530 million [4] and 750 million tons [5], respectively. However, it is believed that only 65% [6] and 25% [7] of the total GGBS and FA generated are currently being used, respectively.

In recent years, geopolymer as a new type of environmentally-friendly material, in which the OPC is replaced with alkali-activated binders, has received significant research attention. The production of geopolymer happens through the geopolymerization process by chemical reactions between materials with high aluminosilicate constituents and alkali activators [8]. A large number of studies were conducted on the properties of geopolymer concretes (GPCs) (e.g. [9-20]). As has been shown in previous studies, GPCs exhibit highly desirable mechanical and durability properties that are comparable to or better than those of their OPC-based counterparts [21, 22]. However, most of the existing studies focused on GPCs containing FA but some also investigated GPCs prepared with a combination of FA and GGBS [23-33]. A major challenge related to the use of FA in ambient-cured GPCs is that they develop low strengths. Owing to the relatively high calcium amount in GGBS, its addition to an FA-based GPC results in significant improvements in the properties of the GPC [28].

As has been reported in previous studies [34-43], active confinement of concrete, where the concrete is subjected to constant lateral confining pressure, significantly improves its ductility and compressive strength. The only existing studies on the behaviour of GPCs under confinement [30, 44], which investigated the confinement of GPC with fiber-reinforced polymer (FRP), revealed that the confined GPC exhibits desirable properties making it an attractive candidate for use in structural column applications. However, no study has been conducted to date on the behaviour of actively confined GPC, which is of vital importance to investigate the possibility of the use of this material in structural columns, where constant lateral confining pressure is applied to the concrete (such as in the case of steel-confined concrete when the confining pressure remains nearly constant after yielding of lateral steel reinforcement), especially in the case of columns designed for blast and seismic resistance.

The first experimental study on the properties of actively confined GPCs containing FA and GGBS under axial compression is presented. The main aim of the study was to investigate the possibility of the application of GPC in structural systems, which would lead to significant reductions in both the large CO_2 footprint associated with the use of OPC in construction and negative impact of industrial by-product disposal on the environment.

TESTING PROGRAM

Materials

GGBS and FA

GGBS and class-F FA with the chemical composition shown in Table 9.1 were provided by Adelaide Brighton Cement Ltd. GGBS was a by-product of iron-making processes at the Birkenhead Works and FA was combustion by-product of fine ground Leigh Creek Coal in South Australia, extracted by electrostatic precipitators from the power station exhaust gases.

Table 9.1. Chemical composition of cementitious materials

Compounds	Fly ash (%)	Ground granulated blast furnace slag (%)
SiO_2	55.38	33.10
Al_2O_3	28.14	13.33
Fe_2O_3	3.31	0.69
CaO	3.45	42.83
MgO	1.85	5.57
Na_2O	2.30	0.27
K_2O	1.39	0.31
SO_3	0.32	1.81
P_2O_5	0.78	0.01
LOI	3.08	2.08

Fine and coarse aggregates

River sand with a 2-mm nominal maximum particle size, sourced from Price Pit in South Australia, was used as the fine aggregate. Crushed basalt stone with a 10-mm maximum particle size was used as the coarse aggregate in the mixes, which was sourced from McLaren Vale Quarry, South Australia.

Alkaline activator solution

The alkaline activator used in this study consisted of sodium hydroxide (NaOH) and sodium silicate (Na_2SiO_3) solutions that were premixed by a local supplier. The ratio of Na_2SiO_3 to NaOH in the alkaline activator solution was 2.5 by weight. In all mixes, the NaOH solution was used at 12 M concentration, and silicon dioxide-to-sodium oxide ratio (SiO_2/Na_2O) of the Na_2SiO_3 solution was 3 by weight. Before the mixing of GPCs, the alkaline activator solution was premixed and left to rest at room temperature for 24 hr. The alkaline activator was pre-heated to 30°C before it was added to the mix to avoid rapid setting of the concrete.

Test specimens

Two unique batches of GPCs (i.e. 80/20 and 50/50) were prepared, in which 80/20 mixes were GPCs with FA weight percentage (FA%) of 80% and GGBS weight percentage (GGBS%) of 20%, and 50/50 mixes were GPCs with FA% of 50% and GGBS% of 50%. The mix proportions of GPCs are shown in Table 9.2. 80/20 and

50/50 mixes were designed with a alkaline liquid-to-binder (*l/b*) ratio of 0.55 and 0.75, respectively, to achieve workable mixes.

Table 9.2. Mix proportions of the concrete

Concrete mix	80/20	50/50
Fly ash (kg/m^3)	320	200
GGBS (kg/m^3)	80	200
Sand (kg/m^3)	680	680
Coarse Aggregate (kg/m^3)	1000	1000
Na_2SiO_3 (kg/m^3)	157	214
NaOH (kg/m^3)	63	86
Na_2SiO_3/NaOH	2.5	2.5
l/b	0.55	0.75
Slump flow (mm)	210	200

* GGBS: Ground granulated blast furnace slag

The specimens had a height of 126 mm and a diameter of 63 mm as was dictated by the geometry of the Hoek cell. To obtain orthogonal specimen ends with respect to the longitudinal axis and remove irregularities, the specimen ends were ground by a grinding machine. Five different constant lateral pressures (f^*_l) (i.e. 5, 10, 15, 20, and 25 MPa) were applied to the specimens through the Hoek cell.

Specimen preparation and testing

In the preparation of GPC mixes, fine and coarse aggregates and binders were initially mixed for about three minutes and then the premixed alkaline activator solution, as the liquid component of the mix, was gradually added to the mixes. Wet mixing continued for about five minutes. To ensure proper placement of concretes in the molds, gentle external vibration was used in the pouring processes of all the mixes. All mixing and pouring processes were performed under the ambient temperature. The slump flow of fresh concretes was established by a flow test [45] conducted immediately after the mixing of the GPCs.

Two different curing conditions of ambient curing at temperature of 23 °C and oven curing at temperature of 70 °C were considered to study the influence of the curing condition on the axial compression behaviour of GPCs. Oven-cured specimens were cured in the oven until the testing day (i.e. 28 days) after they were demolded.

The axial compression tests on hardened specimens were conducted according to ASTM C39/C39M-16b [46] using a 1000-kN universal testing machine under displacement control at a rate of 24 microstrain per second. Figures 9.1(a) and (b) show the Hoek cell and testing machine utilized in this study, respectively. To measure the axial strain of the GPCs, two linear variable displacement transformers (LVDTs) were used at the corners of steel loading and supporting plates. An axial strain gauge was also placed at the mid-height of the specimens in order to validate and correct the measurements obtained by the LVDTs at early stages of the loading. Two lateral strain gauges were also mounted at the mid-height of the specimens at a 180-degree interval to record the lateral strains of the specimens. To prevent any damage to the strain gauges through the use of the cell, the strain gauges were coated by a lubricating wax.

(a) (b)

Figure 9.1. (a) Hoek cell and (b) universal testing machine

GPCs shown in Tables 9.3 and 9.4 are labelled as follows: the letters A and O stand for ambient and oven curing conditions, respectively. The numbers 80/20 and 50/50 after these letters indicate GPC mixes with 80% FA/20% GGBS and 50% FA/50% GGBS, respectively. Finally, the letter F stands for the lateral confinement and the number after that indicates f^*_l in MPa. For example, O50/50-F15 is a GPC with a blend of 50% FA and 50% GGBS, cured under 70°C in the oven and confined by f^*_l = 15 MPa.

RESULTS AND OBSERVATIONS

Unconfined GPC

The results of flowability tests on GPCs are shown in Table 9.2. It is evident from the table that the GPC with a higher GGBS content exhibited a lower flow. The lower flowability of 50/50 mixes than 80/20 mixes can be attributed to the fact that GGBS reacts with the activator solution much more quickly than FA [4, 27].

Table 9.3 presents the compressive strength (f'_{co}) of unconfined GPCs ($f^*_l = 0$) at 7, 14, and 28 days and the corresponding axial strain (ε_{co}) at 28 days. Figure 9.2 illustrates the axial stress-axial strain and lateral strain-axial strain curves of unconfined GPCs at 28 days. As expected, it can be seen in the figure and table that 50/50 mixes exhibited a slightly higher f'_{co} and ε_{co} compared to those of 80/20 mixes. At 28 days, A50/50 and O50/50 mixes experienced 7.2% and 3.3% higher strength compared to those of A80/20 and O80/20 mixes, respectively. The corresponding axial strain enhancements of A50/50 and O50/50 mixes over A80/20 and O80/20 mixes were 7.7% and 4.0%, respectively. As can also be seen in Fig. 9.2 and Table 9.3, oven-cured GPCs had a slightly higher f'_{co} and a slightly lower ε_{co} than those of ambient-cured GPCs. At 28 days, 80/20 and 50/50 mixes experienced a strength increase of 9.4% and 5.4% and corresponding axial strain decrease of 3.8% and 7.1% when they were oven-cured at 70°C compared to those cured in the room temperature, respectively. The higher strength of oven-cured mixes is because at room temperature the FA reacts with the activator solution at a low rate but the reaction is accelerated when the temperature increases [47, 48]. The lower strain of oven-cured GPCs than that of ambient-cured GPCs can be explained by the increased stiffness of the GPC matrix as a result of oven curing [49, 50].

Table 9.3. Compression test results of unconfined specimens

Mix	f'_{co} (MPa)			ε_{co} (%)
	7-day	14-day	28-day	28-day
A80/20	30.8	37.1	41.5	0.26
A50/50	34.8	40.9	44.5	0.28
O80/20	40.3	44.7	45.4	0.25
O50/50	42.6	45.8	46.9	0.26

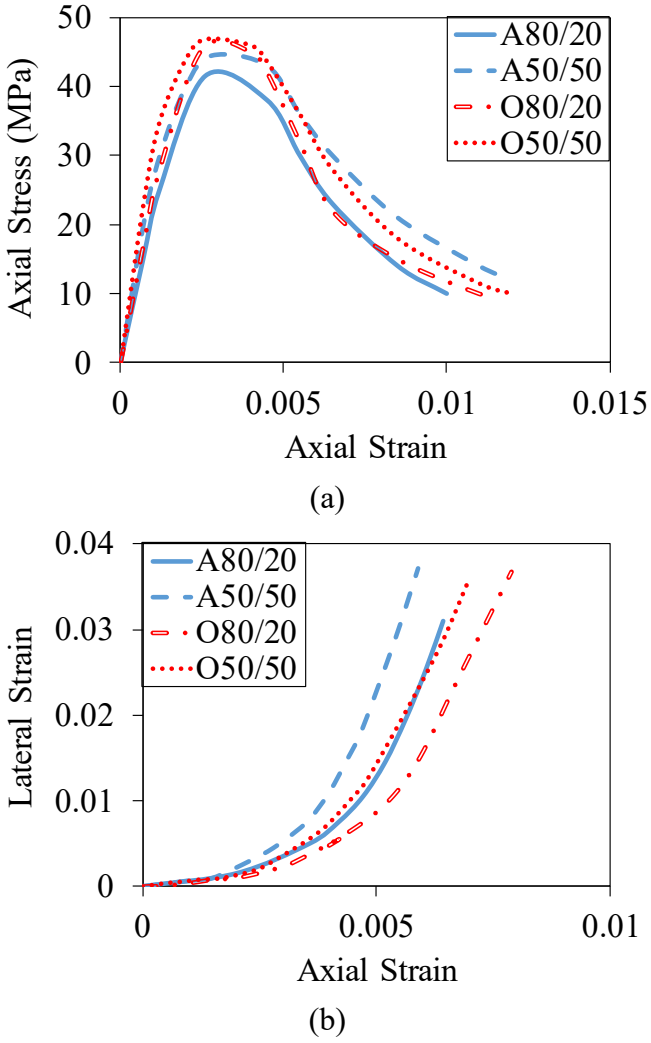

Figure 9.2. 28-day (a) axial stress-strain relationships, (b) lateral strain-axial strain relationships of unconfined specimens

As can be seen in Fig. 9.2(a), 50/50 mixes exhibited axial stress-axial strain relationships with a slightly shallower descending branch than that of 80/20 mixes, suggesting that 50/50 mixes were slightly less brittle than 80/20 mixes, which can be because of the more compact microstructure of 50/50 mixes [51]. The more compact microstructure of 50/50 mixes than that of 80/20 mixes is because of the higher amount of calcium oxide (CaO) in GGBS than that in FA, which resulted in the creation of two hydration products of geopolymer gel (i.e. sodium aluminosilicate hydrate) and calcium silicate hydrate (C-S-H) in concrete [52, 53]. It can also be seen in the figure that oven-cured GPCs had axial stress-axial strain curves with a slightly more steeply declining second branch than that of ambient-cured GPCs, suggesting that oven curing slightly increased the brittleness of GPCs. Figure 9.2(b) shows that, at a given axial strain, 50/50 mixes had a slightly higher

lateral strain than 80/20 mixes. This points to a higher dilation rate of GPCs with a FA/GGBS ratio of 50/50 than that of 80/20, which is because of the less brittle behaviour of 50/50 mixes than 80/20 mixes. It can also be seen in the figure that oven-cured GPCs had a slightly lower lateral strain than ambient-cured GPCs at a given axial strain. This observation indicates that the lateral dilation rate of oven-cured specimens was lower than that of ambient-cured specimens.

Figure 9.3 shows the failure patterns of unconfined GPCs. It can be seen in the figure that curing condition and composition of GPC mixes had an influence on the failure mode of GPCs. As can be seen in Fig. 9.3, 80/20 specimens exhibited heterogenic microcracks, accompanied by a major diagonal shear crack formed along the mid-height of the specimen. On the other hand, in 50/50 specimens microcracks were formed and progressed only along the vertical axis of the specimen. It can also be seen in Fig. 9.3 that ambient-cured GPCs remained intact until the failure but oven-cured specimens experienced surface spalling of concrete, resulting in the more brittle behaviour of oven-cured GPCs as discussed previously.

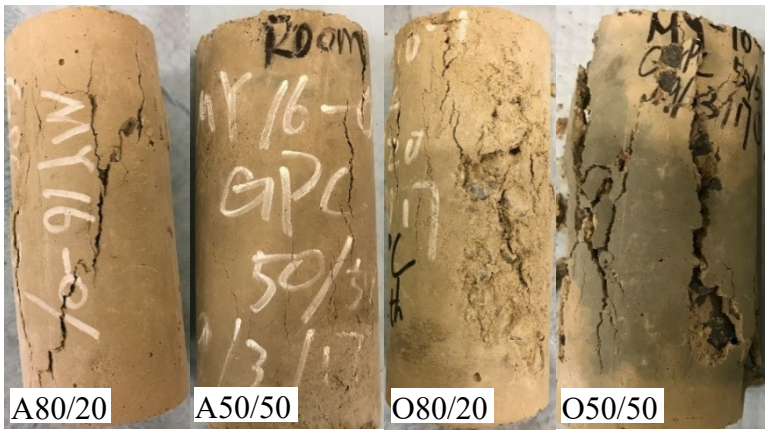

Figure 9.3. Failure modes of different unconfined GPC specimens

Confined GPC

Table 9.4 shows the peak and residual stress and strain of GPCs under different confinement levels. In this table, f^*_{cc} and ε^*_{cc} are the peak axial stress and strain and $f_{c,res}$ and $\varepsilon_{c,res}$ are the residual axial stress and strain of confined specimens, respectively. $f_{c,res}$ is the strength that corresponds to the stabilized plateau region on the axial stress-axial strain curve following the descending branch, and $\varepsilon_{c,res}$ is the axial strain corresponding to the beginning of this plateau zone. It can be seen in Table 9.4 that, as expected, an increase in f^*_l resulted in an increase in the peak stress

ratio (f^*_{cc}/f'_{co}), peak strain ratio ($\varepsilon^*_{cc}/\varepsilon_{co}$), residual stress ratio ($f_{c,res}/f'_{co}$), and residual strain ratio ($\varepsilon_{c,res}/\varepsilon_{co}$) of GPCs. An increase in f^*_l from 5 MPa to 25 MPa led to an approximately 133%, 185%, 233%, and 119% increase in f^*_{cc}/f'_{co}, $\varepsilon^*_{cc}/\varepsilon_{co}$, $f_{c,res}/f'_{co}$, and $\varepsilon_{c,res}/\varepsilon_{co}$ of GPCs, respectively. As it can also be seen in the table, at a given f^*_l, 50/50 mixes had a slightly lower f^*_{cc}/f'_{co} and $\varepsilon^*_{cc}/\varepsilon_{co}$ but slightly higher $f_{c,res}/f'_{co}$ and $\varepsilon_{c,res}/\varepsilon_{co}$ than 80/20 mixes. Lower f^*_{cc}/f'_{co} and $\varepsilon^*_{cc}/\varepsilon_{co}$ of 50/50 mixes than those of 80/20 mixes is because of the lower confining pressure ratio (f^*_l/f'_{co}) of 50/50 mixes compared to that of 80/20 mixes as caused by the higher f'_{co} of 50/50 mixes. On the other hand, higher $f_{c,res}/f'_{co}$ and $\varepsilon_{c,res}/\varepsilon_{co}$ of 50/50 mixes than those of 80/20 mixes is a result of less brittle behaviour of 50/50 mixes than that of 80/20 mixes, as discussed previously. It can be seen in Table 9.4 that oven-cured mixes generally had a slightly lower peak and residual stress and strain ratios than those of ambient-cured mixes, which can be because of the lower f^*_l/f'_{co} of oven-cured mixes (caused by their higher f'_{co}) than that of ambient-cured mixes.

Figure 9.4 shows the axial stress-axial strain and lateral strain-axial strain relationships of GPCs under different confinement levels. It can be seen in the figure that, under a given f^*_l and curing condition, 50/50 mixes had axial stress-axial strain curves with a slightly less steep post-peak descending branch than that of 80/20 mixes. This is attributed to the less brittle behaviour of GPCs with a FA/GGBS ratio of 50/50 compared to that of 80/20, as discussed previously. As can also be seen in Fig. 9.4, ambient-cured GPCs experienced a slightly shallower descending branch in their axial stress-axial strain curves compared to oven-cured GPCs at a given f^*_l and FA/GGBS content, which can be because of the higher f^*_l/f'_{co} and slightly lower brittleness of ambient-cured GPCs than that of oven-cured GPCs.

As can be seen in the lateral strain-axial strain curves of GPCs shown in Fig. 9.4, at a given f^*_l and curing condition, 50/50 mixes experienced a slightly higher lateral strain at a given axial strain than 80/20 mixes. This observation is attributed to the increased rate of lateral dilation of GPCs with a higher GGBS%, as discussed previously. It can also be seen in the figure that, under a given f^*_l and FA/GGBS content, oven-cured GPCs exhibited a slightly lower lateral strain at a given axial strain than that of ambient-cured GPCs. This observation indicates that oven-cured GPCs had a lower dilation rate than that of ambient-cured GPCs.

Table 9.4. 28-day compression test results of the confined specimens

Specimens	f_l^* (MPa)	f_{cc}^* (MPa)	f_{cc}^*/f_{co}'	ε_{cc}^* (%)	$\varepsilon_{cc}^*/\varepsilon_{co}$	$f_{c,res}$ (MPa)	$f_{c,res}/f_{co}'$	$\varepsilon_{c,res}$ (%)	$\varepsilon_{c,res}/\varepsilon_{co}$
A80/20-F5	5	68.5	1.65	0.63	2.42	38.0	0.92	2.43	9.3
A50/50-F5	5	72.6	1.63	0.67	2.39	46.1	1.04	2.72	9.7
O80/20-F5	5	72.9	1.61	0.58	2.32	46.6	1.03	2.25	9.0
O50/50-F5	5	75.2	1.60	0.6	2.31	52.7	1.12	2.45	9.4
A80/20-F10	10	97.1	2.34	1.01	3.88	67.1	1.62	3.10	11.9
A50/50-F10	10	102.4	2.30	1.06	3.79	75.3	1.69	3.45	12.3
O80/20-F10	10	103.2	2.27	0.89	3.56	75.7	1.67	2.77	11.1
O50/50-F10	10	106.5	2.27	0.92	3.54	82.5	1.76	3.02	11.6
A80/20-F15	15	119.2	2.87	1.38	5.31	92.0	2.22	3.91	15.0
A50/50-F15	15	126.5	2.84	1.45	5.18	102.1	2.29	4.51	16.1
O80/20-F15	15	127.8	2.81	1.18	4.72	101.8	2.24	3.44	13.8
O50/50-F15	15	131.2	2.80	1.24	4.77	107.5	2.29	3.88	14.9
A80/20-F20	20	142	3.42	1.65	6.35	119.5	2.88	4.80	18.5
A50/50-F20	20	150.1	3.37	1.73	6.18	131.5	2.96	5.46	19.5
O80/20-F20	20	151.3	3.33	1.43	5.72	125.3	2.76	4.39	17.6
O50/50-F20	20	155.5	3.32	1.49	5.73	133.5	2.85	4.81	18.5
A80/20-F25	25	159.1	3.83	1.85	7.12	142.0	3.42	5.35	20.6
A50/50-F25	25	168.8	3.79	1.93	6.89	152.6	3.43	5.97	21.3
O80/20-F25	25	170.7	3.76	1.61	6.44	151.7	3.34	4.85	19.4
O50/50-F25	25	176.4	3.76	1.67	6.42	160.4	3.42	5.33	20.5

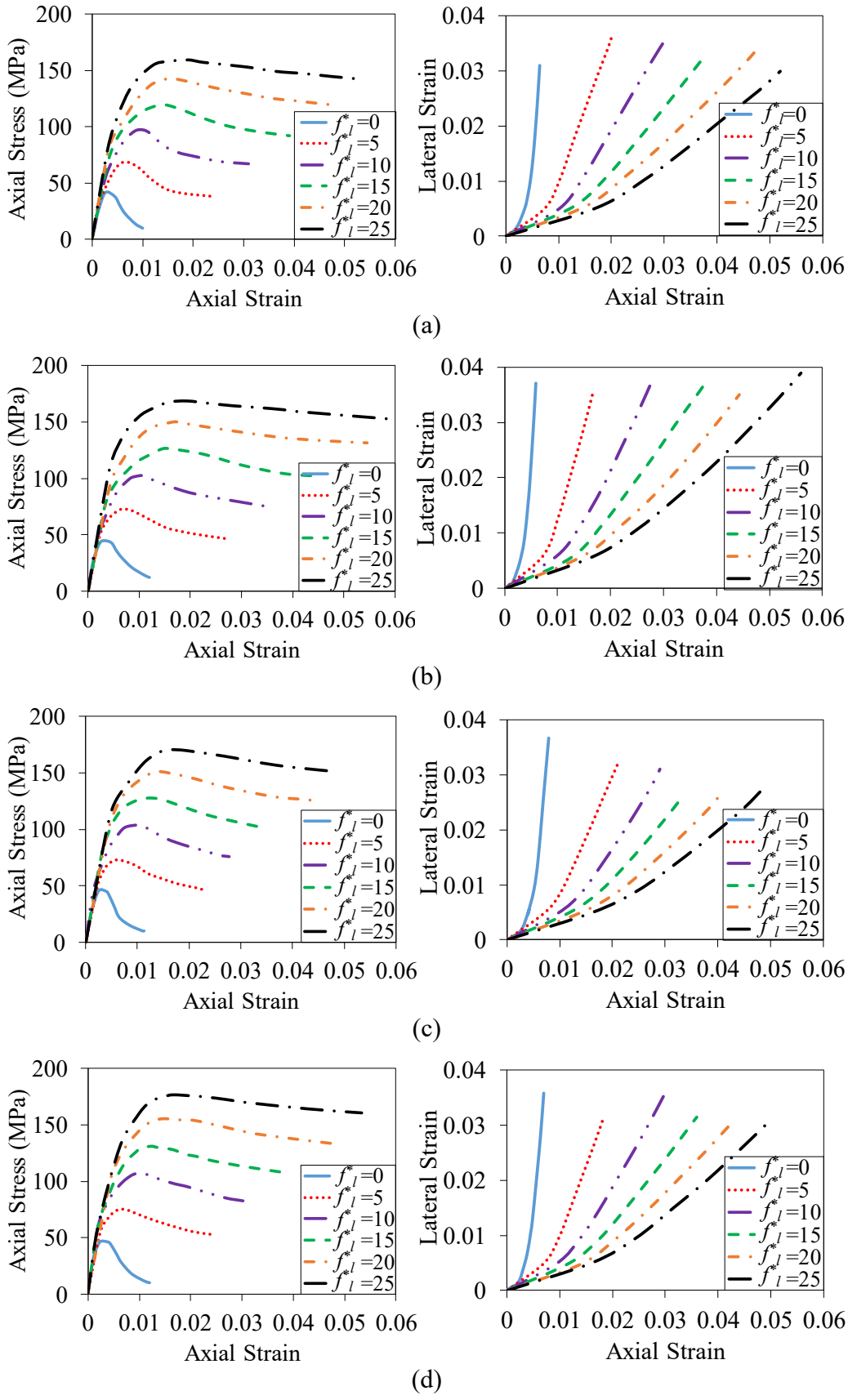

Figure 9.4. Variation of axial stress-axial strain and lateral strain-axial strain relationships with the level of confinement: a) A80/20; b) A50/50; c) O80/20; d) O50/50 mix

Figure 9.5 shows the variation of strength (k_1) and strain enhancement coefficient (k_2) of different concretes with confinement level to assess the effectiveness of confinement in GPCs. For simplicity, k_1 and k_2 are defined by the widely adopted linear expressions of $(f^*_{cc}/f'_{co}-1)/(f^*_l/f'_{co})$ and $(\varepsilon^*_{cc}/\varepsilon_{co}-1)/(f^*_l/f'_{co})$, respectively. It can be seen in the figure that, for a given f^*_l and curing condition, 50/50 mixes had a higher k_1 and k_2 than 80/20 mixes. This observation indicates the higher effectiveness of confinement in 50/50 mixes than that in 80/20 mixes. This can, once again, be attributed to the less brittle behaviour observed in 50/50 mixes. It can also be seen in Fig. 9.5 that oven-cured GPCs experienced a slightly higher k_1 but a lower k_2 compared to ambient-cured GPCs under a given f^*_l and FA/GGBS content. The higher k_1 of oven-cured GPCs than that of ambient-cured GPCs can be explained by the improved microstructure of oven-cured GPCs than that of ambient-cured GPCs, which consequently increased the effectiveness of confinement on the strength gain of oven-cured GPCs. The lower k_2 of oven-cured GPCs is attributed to the increased stiffness in the matrix of oven-cured GPCs compared to that of ambient-cured GPCs, as discussed previously for unconfined specimens.

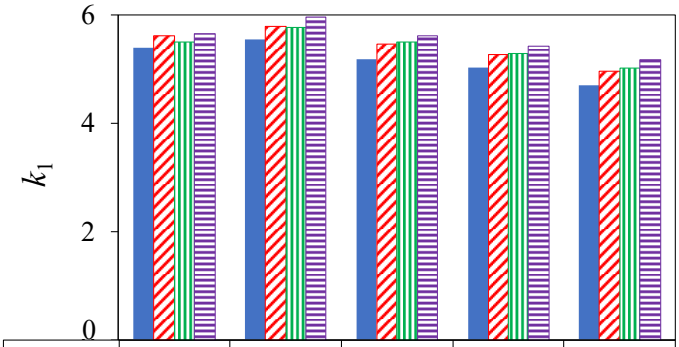

f^*_l (MPa)	5	10	15	20	25
A80/20	5.40	5.56	5.18	5.03	4.70
A50/50	5.62	5.79	5.47	5.28	4.97
O80/20	5.50	5.78	5.49	5.30	5.01
O50/50	5.66	5.96	5.62	5.43	5.18

(a)

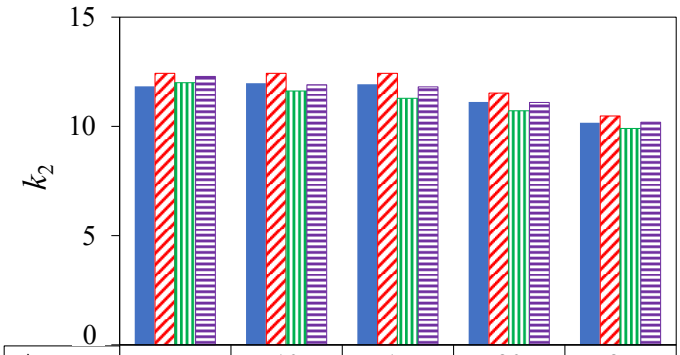

f^*_l (MPa)	5	10	15	20	25
A80/20	11.8	12.0	11.9	11.1	10.2
A50/50	12.4	12.4	12.4	11.5	10.5
O80/20	12.0	11.6	11.3	10.7	9.9
O50/50	12.3	11.9	11.8	11.1	10.2

(b)

Figure 9.5. Variation of (a) strength enhancement coefficient (k_1) and (b) strain enhancement coefficient (k_2) of different mixes with confining pressure (f^*_l)

CONCLUSIONS

The results of the first experimental investigation on the axial compressive behaviour of actively confined GPC have been presented. Based on the presented results and discussions, the following conclusions can be drawn:

1- An increase in the confinement level leads to an increase in the peak and residual axial stress and strain of GPCs. Under a given confining pressure and curing condition, an increase in the GGBS content from 20% to 50% leads to a slight increase in the peak and residual stress and strain of GPCs produced with FA and GGBS. In addition, oven-cured GPCs exhibit a slightly higher peak and residual stress but a slightly lower peak and residual strain than ambient-cured GPCs at a given confining pressure and FA/GGBS ratio.

2- An increase in the GGBS content from 20% to 50% leads to an axial stress-axial strain curve with a less steeply descending second branch. Furthermore, oven-cured GPCs exhibit a slightly less shallow descending branch than ambient-cured GPCs. These differences are because of the less brittle behaviour of GPCs with a higher GGBS content and those cured under ambient conditions.

3- An increase in the amount of GGBS from 20% to 50% results in a slight increase in the lateral dilation rate of GPCs under a given confining pressure and curing condition. In addition, ambient-cured GPCs exhibit a slightly higher dilation rate

than oven-cured GPCs. These are, once again, attributed to the less brittle behaviour of GPCs with a higher GGBS content and those cured under ambient conditions.

4- GPCs with a higher amount of GGBS exhibit a higher strength and strain enhancement coefficients, indicating increased effectiveness of confinement in GPCs with a higher GGBS content. Ambient-cured GPCs develop a higher strain enhancement coefficient but a lower strength enhancement coefficient than oven-cured GPCs. The lower strain enhancement coefficient of oven-cured GPCs is because of the increased stiffness in the matrix of oven-cured GPCs compared to that of ambient-cured GPCs and the higher strength enhancement coefficient of oven-cured GPCs is attributed to the improved microstructure of oven-cured GPCs and the resulting increase in the effectiveness of confinement.

The promising findings of this study point to the possibility of the use of GPC in new laterally confined structural columns that are designed to undergo large deformations for resilience against extreme events such as earthquakes. The use of GPC in place of ordinary Portland cement-based concrete in such applications would lead to significant environmental benefits.

ACKNOWLEDGEMENTS

The authors thank Mr. Liu and Mesdames Yang and Liu for completing the tests reported in this paper as part of their Master's thesis.

REFERENCES

[1] Mehta PKH, Meryman. Tools for reducing carbon emissions due to cement consumption. *Structure Magazine*. 2009;11-5.

[2] Golewski GL. Generalized fracture toughness and compressive strength of sustainable concrete including low calcium fly ash. *Materials*. 2017;10(12):1393.

[3] Gholampour A, Ozbakkaloglu T. Performance of sustainable concretes containing very high volume Class-F fly ash and ground granulated blast furnace slag. *Journal of Cleaner Production*. 2017;162:1407-17.

[4] Zhao H, Sun W, Wu X, Gao B. The properties of the self-compacting concrete with fly ash and ground granulated blast furnace slag mineral admixtures. *Journal of Cleaner Production*. 2015;95:66-74.

[5] Blissett R, Rowson N. A review of the multi-component utilisation of coal fly ash. *Fuel*. 2012;97:1-23.

[6] Tsakiridis P, Papadimitriou G, Tsivilis S, Koroneos C. Utilization of steel slag for Portland cement clinker production. *Journal of Hazardous Materials.* 2008;152(2):805-11.

[7] Prathik Gowda SL, MS. Environmental concrete - geopolymer of construction. *International Journal of Current Research*. 2017;9(12):62358-60.

[8] Kheradmand M, Mastali M, Abdollahnejad Z, Pacheco-Torgal F. Experimental and numerical investigations on the flexural performance of geopolymers reinforced with short hybrid polymeric fibres. *Composites Part B*. 2017;126:108-18.

[9] Hardjito D, Wallah SE, Sumajouw DM, Rangan BV. On the development of fly ash-based geopolymer concrete. *Materials Journal*. 2004;101(6):467-72.

[10] Kong DL, Sanjayan JG. Effect of elevated temperatures on geopolymer paste, mortar and concrete. *Cement and Concrete Research*. 2010;40(2):334-9.

[11] Vijai K, Kumutha R, Vishnuram B. Effect of types of curing on strength of geopolymer concrete. *International Journal of Physical Sciences*. 2010;5(9):1419-23.

[12] Diaz-Loya EI, Allouche EN, Vaidya S. Mechanical properties of fly-ash-based geopolymer concrete. *ACI Materials Journal*. 2011;108(3):300.

[13] Ryu GS, Lee YB, Koh KT, Chung YS. The mechanical properties of fly ash-based geopolymer concrete with alkaline activators. *Construction and Building Materials.* 2013;47:409-18.

[14] Sarker PK, Haque R, Ramgolam KV. Fracture behaviour of heat cured fly ash based geopolymer concrete. *Materials & Design*. 2013;44:580-6.

[15] Ganesan N, Abraham R, Raj SD, Sasi D. Stress–strain behaviour of confined Geopolymer concrete. *Construction and Building Materials*. 2014;73:326-31.

[16] Feng KN, Ruan D, Pan Z, Collins F, Bai Y, Wang C, et al. Mechanical behavior of geopolymer concrete subjected to high strain rate compressive loadings. *Materials and Structures*. 2015;48(3):671-81.

[17] Xie T, Ozbakkaloglu T. Behavior of low-calcium fly and bottom ash-based geopolymer concrete cured at ambient temperature. *Ceramics International.* 2015;41(4):5945-58.

[18] Xie T, Ozbakkaloglu T. Influence of coal ash properties on compressive behaviour of FA-and BA-based GPC. *Magazine of Concrete Research.* 2015;67(24):1301-14.

[19] Ding Y, Dai J-G, Shi C-J. Mechanical properties of alkali-activated concrete: A state-of-the-art review. *Construction and Building Materials.* 2016;127:68-79.

[20] Junaid MT, Kayali O, Khennane A. Response of alkali activated low calcium fly-ash based geopolymer concrete under compressive load at elevated temperatures. *Materials and Structures.* 2017;50(1):50.

[21] Duxson P, Fernández-Jiménez A, Provis JL, Lukey GC, Palomo A, van Deventer JS. Geopolymer technology: the current state of the art. *Journal of Materials Science.* 2007;42(9):2917-33.

[22] Singh B, Ishwarya G, Gupta M, Bhattacharyya S. Geopolymer concrete: A review of some recent developments. *Construction and Building Materials.* 2015;85:78-90.

[23] Oh JE, Monteiro PJ, Jun SS, Choi S, Clark SM. The evolution of strength and crystalline phases for alkali-activated ground blast furnace slag and fly ash-based geopolymers. *Cement and Concrete Research*. 2010;40(2):189-96.

[24] Lee N, Lee H. Setting and mechanical properties of alkali-activated fly ash/slag concrete manufactured at room temperature. *Construction and Building Materials.* 2013;47:1201-9.

[25] Bagheri A, Nazari A. Compressive strength of high strength class C fly ash-based geopolymers with reactive granulated blast furnace slag aggregates designed by Taguchi method. *Materials & Design (1980-2015).* 2014;54:483-90.

[26] Deb PS, Nath P, Sarker PK. The effects of ground granulated blast-furnace slag blending with fly ash and activator content on the workability and strength properties of geopolymer concrete cured at ambient temperature. *Materials & Design (1980-2015).* 2014;62:32-9.

[27] Nath P, Sarker PK. Effect of GGBFS on setting, workability and early strength properties of fly ash geopolymer concrete cured in ambient condition. *Construction and Building Materials.* 2014;66:163-71.

[28] Phoo-ngernkham T, Maegawa A, Mishima N, Hatanaka S, Chindaprasirt P. Effects of sodium hydroxide and sodium silicate solutions on compressive and shear bond strengths of FA–GBFS geopolymer. *Construction and Building Materials.* 2015;91:1-8.

[29] Marjanović N, Komljenović M, Baščarević Z, Nikolić V, Petrović R. Physical–mechanical and microstructural properties of alkali-activated fly ash–blast furnace slag blends. *Ceramics International.* 2015;41(1):1421-35.

[30] Lokuge W, Karunasena W. Ductility enhancement of geopolymer concrete columns using fibre-reinforced polymer confinement. *Journal of Composite Materials.* 2016;50(14):1887-96.

[31] Nath P, Sarker PK. Fracture properties of GGBFS-blended fly ash geopolymer concrete cured in ambient temperature. *Materials and Structures.* 2017;50(1):32.

[32] Venu M, Rao TG. An Experimental Investigation of the Stress-Strain Behaviour of Geopolymer Concrete. *Slovak Journal of Civil Engineering.* 2018;26(2):30-4.

[33] Farhan NA, Sheikh MN, Hadi MN. Investigation of engineering properties of normal and high strength fly ash based geopolymer and alkali-activated slag concrete compared to ordinary Portland cement concrete. *Construction and Building Materials.* 2019;196:26-42.

[34] Lim JC, Ozbakkaloglu T. Investigation of the influence of the application path of confining pressure: Tests on actively confined and FRP-confined concretes. *Journal of Structural Engineering.* 2014;141(8):04014203.

[35] Lim JC, Ozbakkaloglu T. Stress–strain model for normal-and light-weight concretes under uniaxial and triaxial compression. *Construction and Building Materials.* 2014;71:492-509.

[36] Rousakis TC, Tourtouras IS. RC columns of square section–passive and active confinement with composite ropes. *Composites Part B*. 2014;58:573-81.

[37] Lim JC, Ozbakkaloglu T, Gholampour A, Bennett T, Sadeghi R. Finite-element modeling of actively confined normal-strength and high-strength concrete under uniaxial, biaxial, and triaxial compression. *Journal of Structural Engineering.* 2016;142(11):04016113.

[38] Gholampour A, Ozbakkaloglu T, Hassanli R. Behavior of rubberized concrete under active confinement. *Construction and Building Materials.* 2017;138:372-82.

[39] Mohammadi M, Wu Y-F. Triaxial test for concrete under non-uniform passive confinement. *Construction and Building Materials.* 2017;138:455-68.

[40] Gholampour A, Ozbakkaloglu T. Fiber-reinforced concrete containing ultra high-strength micro steel fibers under active confinement. *Construction and Building Materials*. 2018;187:299-306.

[41] Gholampour A, Ozbakkaloglu T. Behavior of steel fiber-reinforced concrete-filled FRP tube columns: Experimental results and a finite element model. *Composite Structures*. 2018;194:252-62.

[42] Mansouri I, Gholampour A, Kisi O, Ozbakkaloglu T. Evaluation of peak and residual conditions of actively confined concrete using neuro-fuzzy and neural computing techniques. *Neural Computing and Applications*. 2018;29(3):873-88.

[43] Gholampour A, Ozbakkaloglu T. Understanding the compressive behavior of shape memory alloy (SMA)-confined normal-and high-strength concrete. *Composite Structures*. 2018.

[44] Ozbakkaloglu T, Xie T. Geopolymer concrete-filled FRP tubes: Behavior of circular and square columns under axial compression. *Composites Part B.* 2016;96:215-30.

[45] ASTM-C1437-15. *Standard Test Method for Flow of Hydraulic Cement Mortar.* West Conshohocken, PA: ASTM International; 2015.

[46] ASTM-C39/C39M-16b. *Standard Test Method for Compressive Strength of Cylindrical Concrete Specimens*. West Conshohocken, PA: ASTM International; 2016.

[47] Puertas F, Martínez-Ramírez S, Alonso S, Vazquez T. Alkali-activated fly ash/slag cements: strength behaviour and hydration products. *Cement and Concrete Research.* 2000;30(10):1625-32.

[48] Wang K, Shah SP, Mishulovich A. Effects of curing temperature and NaOH addition on hydration and strength development of clinker-free CKD-fly ash binders. *Cement and Concrete Research*. 2004;34(2):299-309.

[49] Kim JK, Han SH, Song YC. Effect of temperature and aging on the mechanical properties of concrete - Part I. Experimental results. *Cement and Concrete Research.* 2002;32(7):1087-94.

[50] Shi MX, Wang Q, Zhou ZK. Comparison of the properties between high-volume fly ash concrete and high-volume steel slag concrete under temperature

matching curing condition. *Construction and Building Materials*. 2015;98:649-55.

[51] Ohno M, Li VC. A feasibility study of strain hardening fiber reinforced fly ash-based geopolymer composites. *Construction and Building Materials*. 2014;57:163-8.

[52] Yip C, Van Deventer J. Microanalysis of calcium silicate hydrate gel formed within a geopolymeric binder. *Journal of Materials Science*. 2003;38(18):3851-60.

[53] Nath P, Sarker PK. Geopolymer concrete for ambient curing condition. *Australasian Structural Engineering Conference 2012: The past, present and future of structural engineering: Engineers Australia.* 2012. p. 225.

Statement of Authorship

Title of Paper	Understanding the compressive behavior of shape memory alloy (SMA)-confined normal- and high-strength concrete
Publication Status	☑ Published ☐ Accepted for Publication ☐ Submitted for Publication ☐ Unpublished and Unsubmitted work written in manuscript style
Publication Details	Gholampour A, Ozbakkaloglu T. Understanding the compressive behavior of shape memory alloy (SMA)-confined normal- and high-strength concrete. *Composite Structures*. 2018;202:943-53.

Principal Author

Name of Principal Author (Candidate)	Aliakbar Gholampour		
Contribution to the Paper	Literature review, analysis of test results, and preparation of the manuscript.		
Overall percentage (%)	80%		
Certification:	This paper reports on original research I conducted during the period of my Higher Degree by Research candidature and is not subject to any obligations or contractual agreements with a third party that would constrain its inclusion in this thesis. I am the primary author of this paper.		
Signature		Date	31/01/2019

Co-Author Contributions

By signing the Statement of Authorship, each author certifies that:

i. the candidate's stated contribution to the publication is accurate (as detailed above);

ii. permission is granted for the candidate in include the publication in the thesis; and

iii. the sum of all co-author contributions is equal to 100% less the candidate's stated contribution.

Name of Co-Author	Togay Ozbakkaloglu		
Contribution to the Paper	Research supervision and review of manuscript.		
Signature		Date	31/01/2019

Name of Co-Author			
Contribution to the Paper			
Signature		Date	

Please cut and paste additional co-author panels here as required.

Understanding the Compressive Behaviour of Shape Memory Alloy (SMA)-Confined Normal- and High-Strength Concrete

ABSTRACT

This paper presents the first experimental study on the axial compressive behaviour of high-strength concrete (HSC) confined by shape memory alloy (SMA) wire. Concrete cylinders that were prepared using two different grades of concrete, namely normal-strength concrete (NSC) and HSC, were confined with SMA spirals having a pitch spacing of 36 and 20 mm, respectively. Preliminary material tests were performed on SMA wires to investigate the tensile strength and strain of SMA in martensitic and austenitic phases and the effect of the temperature on the recovery stress. The confining pressure was applied on concrete cylinders by SMA spirals that were prestrained at 0, 5.5, and 9.5%. The material test results show that an increase in the prestrain level from 5.5% to 9.5% leads to an increase in the recovery stress of SMA wire at temperatures higher than the austenitic finish temperature (90°C). The compression test results on SMA-confined concrete specimens show that an increase in the prestrain level leads to an increase in the peak axial stress and corresponding axial strain of SMA-confined concrete. Confinement of NSC and HSC specimens by 9.5% prestrained SMA spirals results in a 38.1% and 23.6% higher peak axial stress and a 333% and 346% higher corresponding axial strain, respectively, compared to those of unconfined specimens. It is also shown that because of the more brittle behaviour of HSC specimens, SMA-confined HSC fails at a lower axial strain compared to SMA-confined NSC. The lower ultimate axial strain of HSC specimens is also attributed to the lower confinement ratio of the HSC specimens of the current study compared to that of NSC specimens. The promising findings of this study point to the significant potential for the use of SMA spirals in the construction industry for the development of high-performance composite structural members and for strengthening and retrofit of existing concrete members.

KEYWORDS: Shape memory alloy (SMA); Active confinement; Concrete; High-strength concrete (HSC); Axial compression; Prestrain.

INTRODUCTION

It is now well understood that through lateral confinement the strength and ductility of concrete can be greatly enhanced [1-10]. In most general terms, the lateral confinement can be classified under two categories, namely as active and passive confinement. In passive confinement, the confining pressure develops under lateral dilation of concrete subjected to axial compression, whereas in active confinement, a constant confining pressure is present independent of the lateral expansion of the concrete [11-14]. It has been shown that active confinement is more effective in enhancing the compressive strength of concrete compared to passive confinement [15-17].

Most of the existing studies in the literature on the behaviour of actively confined concrete used mechanically prestressed materials or triaxial testing devices to provide confining pressure on the concrete [6,18-26]. However, because of practical limitations related to the high cost and extensive labor and equipment in prestressing the concrete, the application of active confinement in practice has so far been limited [23]. In recent years, a new class of smart material known as shape memory alloy (SMA) has been used to actively confine the concrete specimens. SMA, a class of metallic alloys, is known for its ability to recover its original shape after experiencing a large strain because of its shape memory effect resulting from the weak asymmetric parallelogram structure in martensitic phase and superelastic behaviour resulting from a strong body centered cube crystal structure in austenitic phase [27-31]. The behaviour of concrete confined by unstrained SMA spiral is not very different than that of the behaviour of concrete confined by steel wire. However, nitinol (Ni-Ti) SMA spirals have the main advantage of having the ability of applying prestress through its shape memory effect, as well as offering higher corrosion resistance and biocompatibility, higher strength-to-weight ratio (or a similar ratio in the case of ultra high-strength steel), and superior fatigue performance under cycling loading compared to steel wires [28,32-35]. Although this type of smart material is relatively expensive, as suggested by the current trends, it is expected that progress in technology and increase in production demands will lead to significant reductions in the cost of SMA [36,37].

In recent years, a number of studies have been conducted to understand the mechanical performance of concrete confined by SMAs. Andrawes and Shin [38] introduced the use of Ni-Ti SMA spirals to provide active confinement for concrete bridge columns. They found that the concrete column retrofitted by SMA spirals (with initial confining pressure (f_{li}) of 2.93 MPa and ultimate confining pressure (f_{lu}) of 4.34 MPa) developed a lower maximum lateral drift compared to those retrofitted by carbon fiber reinforced polymer (CFRP) sheets (with f_{lu} = 4.34 MPa) under the same ground motion excitation, attributed to a relatively higher column effective stiffness obtained under SMA confinement. Choi et al. [30] applied Ni-Ti SMA wires in austenitic and martensitic phases to confine concrete and found that the use of SMA at both phases resulted in a similar enhancement in the failure strain and energy dissipation of concrete confined by SMA. Shin and Andrawes [39] investigated the feasibility of the use of niobium-nitinol (Ni-Ti-Nb) SMA spirals with a diameter of 2 mm to actively confine concrete specimens (with unconfined compressive strength (f'_{co}) of 39.2 MPa) through heating prestrained SMA spirals (to a strain of 6.4%) with a 13 mm pitch spacing up to the austenite finish temperature. They reported a 21% and 24% increase in the peak stress and corresponding strain, respectively, of SMA-confined concrete compared to those of unconfined concrete. Choi et al. [33] compared the confining effectiveness of two types of SMA wire jackets (i.e. Ni-Ti and Ni-Ti-Nb) with the same wire diameter of 1 mm and reported that concrete (with f'_{co} = 30.2 MPa) confined by Ni-Ti-Nb SMA wires (with f_{lu} = 3.73 MPa) developed higher peak stress (16.6%) compared to that of Ni-Ti SMA wires (with f_{lu} = 1.69 MPa). This was attributed to the higher ultimate confining pressure provided by Ni-Ti-Nb compared to that by Ni-Ti at the same prestrain level (5%). In 2011, Park et al. [40] reported that concrete columns confined by Ni-Ti-Nb SMA wires with diameter of 1 mm, spiral pitch space of 2 mm, and prestrain level of 4.6% exhibited higher energy dissipation than that of companion columns confined by a steel tube with a thickness of 1.5 mm and yield strength of 250 MPa. Later, Dommer and Andrawes [41] studied the possibility of the use of Ni-Ti-Nb SMA for active confinement of concrete by investigating its thermomechanical characteristics. They reported that Ni-Ti-Nb SMA spirals had a great potential to be used for confinement of concrete columns because typical changes in ambient temperature (from -10°C to 50°C) had not effect on its thermoremechanical behaviour. Tran et al. [42] compared the behaviour of

unconfined, actively confined, and passively confined (obtained by unstressed SMA in austenite phase) concrete cylinders (with f'_{co} = 26.5 MPa) using Ni-Ti SMA wires with a diameter of 1 mm and pitch spacing of 2 mm under uniaxial compression. They reported that SMA-confined concrete under active confinement (with prestrain level of 5% and f_{lu} = 1.80 MPa) developed 70% and 59% higher peak stress compared to that of unconfined and passively confined concrete (with f_{lu} = 1.80 MPa), respectively. Finally, Chen and Andrawes [43] studied the compressive behaviour of Ni-Ti-Nb SMA-confined concrete (with f'_{co} = 39.6 MPa) with four different spiral pitch space of 6.4 (f_{li} = 3.92 MPa), 12.7 (f_{li} = 1.92 MPa), 19.1 (f_{li} = 1.23 MPa), and 25.4 mm (f_{li} = 0.91 MPa). The SMA wire had a diameter of 1.8 mm, tensile strength of 1270 MPa, and prestrain level of 6%. They reported that SMA-confined concrete with 6.4, 12.7, 19.1, and 25.4 mm pitch space developed 51.0%, 24.5%, 16.2%, and 13.9% higher peak axial stress and 218%, 72.7%, 45.4%, and 22.7% higher corresponding axial strain compared to those of unconfined concrete, respectively. It is evident from the results of the existing studies that SMA is a promising material for concrete confinement for the development of new generation of high-performance composite columns as well as for use in the easy to apply and efficient retrofit of existing columns. However, the studies reported to date on SMA-confined concrete dealt only with the behaviour of normal-strength concrete (NSC). Over the past decade, high-strength concrete (HSC) has been finding increasingly wide applications in the construction industry owing to the superior performance and economy offered by the material over NSC. Therefore, experimental studies are needed to understand the behaviour of SMA-confined HSC and investigate the feasibility of the use of SMA confinement for this type of concrete.

This paper presents the first experimental study on the compressive behaviour of HSC columns confined by SMA spirals. The paper initially provides a summary of the experimental program, including material properties, specimen properties, and testing procedures, which is followed by the results of the experimental tests on the SMA material and SMA-confined concrete specimens. A detailed discussion on the results is subsequently presented to discuss the effect of the SMA confinement on the axial compressive behaviour of both NSC and HSC cylinders. The results of this study contribute strongly to the development of this novel confinement technique

intended for the construction of the next generation of high-performance composite structural members and retrofit existing concrete members.

TEST PROGRAM

Materials

Concrete

The concrete specimens were manufactured using concrete mixtures of two different grades (referred to here as NSC and HSC). These mixes consisted of crushed basalt stone with a nominal maximum size of 10 mm as the coarse aggregate, and river sand with a 0.4-mm nominal maximum size as the fine aggregate. Ordinary Portland cement, supplied by Adelaide Brighton Cement Ltd., was used as the binder in both mixes. Table 10.1 shows the mix proportions of the NSC and HSC mixes. As can be seen from the table, NSC and HSC mixes had a water-to-cement ratio (*w/c*) of 0.74 and 0.44, respectively, and to ensure sufficient workability a polycarboxylic ether polymer-based superplasticizer was added to the HSC mix.

Table 10.1. Mix proportions of concrete

Concrete mix	NSC	HSC
Cement (kg/m^3)	280	375
Sand (kg/m^3)	745	760
Gravel (kg/m^3)	1118	1140
Water (kg/m^3)	207	162
Superplasticizer (kg/m^3)	0	4
w/c ratio *	0.74	0.44

* Including the water coming from the superplasticizer (i.e. 70% water by weight)

NSC and HSC mixes were designed to develop a 28-day unconfined compressive strength (f'_{co}) of 25 and 65 MPa, respectively. Once the specimens were demolded, they were cured in the fog room until test day at a constant temperature of 23 ± 2°C according to ASTM C192 [44].

SMA spirals

A Ni-Ti SMA spiral was used in this study. Tables 10.2 and 10.3 show the material properties and chemical composition of SMA material, respectively. As can be seen

in Table 10.3, the SMA material was composed nearly equal amount of nickel (Ni) and titanium (Ti).

Table 10.2. Material properties of SMA wire (provided by manufacturer)

Diameter (mm)	Transition Temperature (°C)	Tensile Strength (MPa)	Tensile Load (kN)	Yield Strength (MPa)	Yield Load (kN)	Elongation (%)
3.5	77 ± 5	1021	9.82	254	2.44	18

Table 10.3. Chemical composition of SMA wire

Ni	Fe	C	O	N	H	CO	Cu	Cr	Nb	Ti
50.2	0.014	0.044	0.03	0.006	0.001	0.074	0.01	< 0.01	< 0.01	Remainder

* Values are in percentage by weight

Test specimens

16 concrete cylinders were prepared in eight groups at the Concrete Materials Laboratory of the University of Adelaide. These included two control groups (unconfined NSC and HSC), two NSC and HSC groups confined with unstrained SMA spirals, two NSC and HSC groups confined with 5.5% prestrained SMA spirals, and two NSC and HSC groups confined with 9.5% prestrained SMA spirals. The cylinder specimens were 100 mm in diameter and 200 mm in height, and two nominally identical specimens were tested for each confinement configuration.

The concrete series in this study were labeled as follows: each label starts with the letters “A” and “B” for first and second nominally identical specimen configuration and is followed by letters “N” and “H” for NSC and HSC mixes, respectively. SMA-confined specimens were followed by numbers 0, 5.5, and 9.5, which indicate the level of prestrain applied to the SMA spirals. For instance, A-H-5.5 is the first of the two identical SMA-confined HSC specimens confined with an SMA spiral prestrained to 5.5%.

Testing

Tests on SMA material

In order to measure thermomechanical properties of SMA material, preliminary tests were conducted on SMA wires. As can be seen in Fig. 10.1, tensile strength test was performed using a Meccano apparatus on unstrained SMA wires at both martensitic

and austenitic phases to determine the stress-strain relationship and tensile strength and ultimate tensile strain of SMA wires. To investigate the relationship between the SMA prestrain level, rupture strain, and recovery stress, five prestraining levels ranging from 2.5% to 12.5% at an increment of 2.5% were considered. Thermomechanical tests were subsequently performed on SMA wires using a universal testing machine (Fig. 10.2). To ensure uniform heating on the SMA wires during the thermomechanical test, an electrical setup was used as shown in Fig. 10.3. Variac and transformer were used to control the amount of volts and amps on the wire, respectively. A thermocouple was attached to the center point of the SMA wire to monitor its temperature while electricity was passing through. The voltage was incrementally increased until the transformer reached its upper threshold of 30 amps. Because SMA wires typically contract elastically after unloading, they were strained to prestrain levels that were slightly above the target levels. They were then unloaded and allowed to elastically contract to the desired prestrain levels. In their restrained position, the SMA wires were then heated with the electrical current to temperatures above the austenitic finish temperature (approximately 90°C) and the recovery stress was measured and recorded by the load cell attached to the Meccano apparatus. Once the recovery stress (the stress recovered when the deformed wire is heated beyond its transition temperature from martensitic to austenitic phase; i.e. austenitic start temperature) was recorded, the SMA wire was strained until failure at the austenitic phase to investigate the effect of prestrain on the tensile strength of SMA wires.

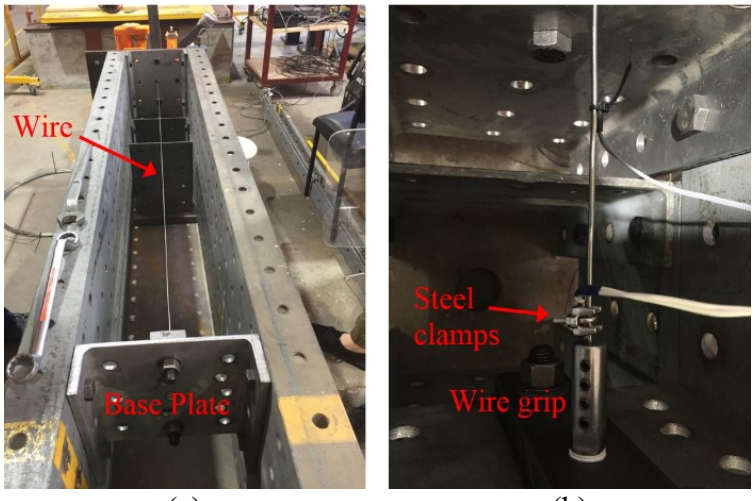

(a) (b)

Figure 10.1. Prestraining the SMA wire: (a) Meccano apparatus; (b) Wire grip connected with two remote controlled electric scissor jacks

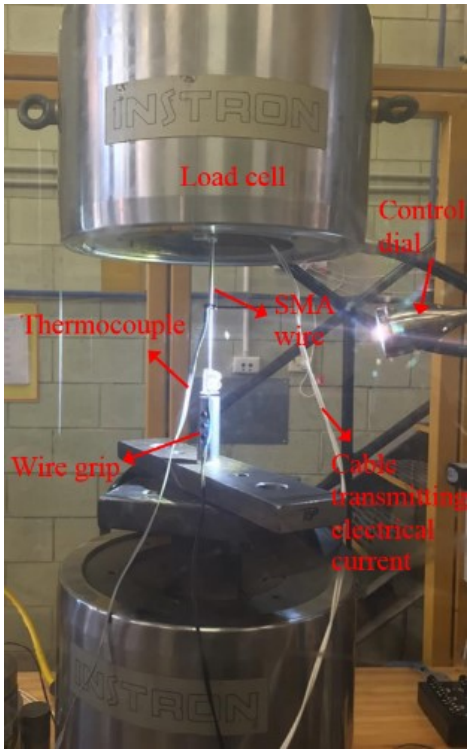

Figure 10.2. Thermomechanical testing of a prestrained SMA wire

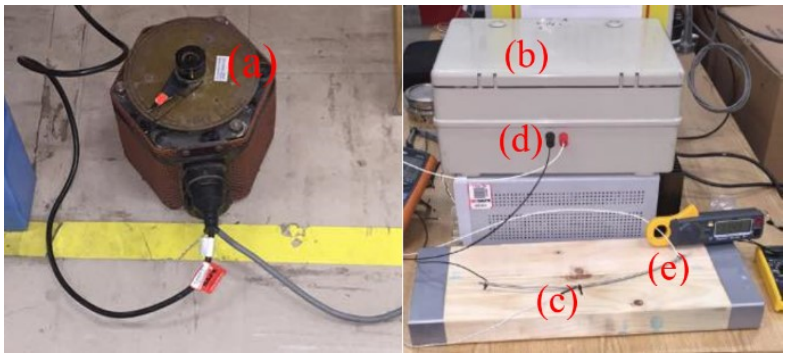

Figure 10.3. Electrical Setup: (a) Variac; (b) Transformers; (c) Thermocouple; (d) Flexi cables; (e) SMA wire

Two prestress levels (as recovery stress) were selected as 35% and 70% of the austenitic rupture stress (referred to as the tensile strength in this paper) based on the fact that they correspond to approximately 1/3 and 2/3 of f_{lu}, respectively. It was determined from the stress-strain relationship of the SMA wire in austenitic phase that to develop these prestress levels the SMA wire had to be strained to 5.5% and 9.5%, respectively. Table 10.4 shows the prestraining matrix of SMA wires based on the SMA spiral pitch space for each concrete mix. It can be seen in the table that initial SMA wire lengths were dependent on the compressive strength of concrete (as it affected the spiral pitch spacing) and the prestrain level. The SMA elongation

required to achieve the correct level of prestrain was calculated using the prestrain level and strain losses. The SMA wires were then strained in the universal testing machine at a displacement controlled rate of 1 mm/min (Fig. 10.4). After the desired strains were reached, the wire was unloaded and the final prestrain (Table 10.4) was confirmed. Through tension tests on the SMA wire it was determined that to achieve a 5.5% and 9.5% prestrain after the wire was released it had to be extended up to 6.3% and 11.7%, respectively. Final thermomechanical tests were conducted on each SMA wire to investigate the effect of the temperature on the recovery stress of SMA and to confirm that the required recovery stress could be achieved at the target prestrains. The results are presented and discussed in detail in the section of Thermomechanical Tests.

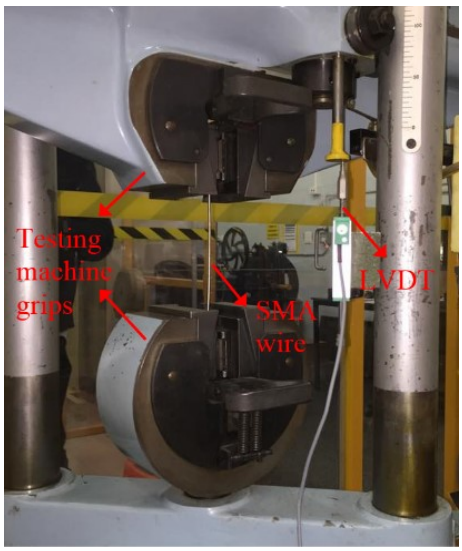

Figure 10.4. Uniaxial tension test of SMA wire

Table 10.4. Prestrain matrix of SMA wires

Type of specimen	Target prestrain (%)	Percentage of rupture strength	Tensile strain under loading (%)*	Actual prestrain (%)		Initial length (mm)		Final length (mm)
				Specimen A	Specimen B	Specimen A	Specimen B	
NSC	0	0	0	0	0	2057	2057	2057
	5.5	35	6.3	5.18	5.28	1956	1954	2057
	9.5	70	11.7	8.63	9.11	1894	1885	2057
HSC	0	0	0	0	0	3448	3448	3448
	5.5	35	6.3	5.76	5.54	3260	3267	3448
	9.5	70	11.7	8.64	8.89	3174	3166	3448

* Required tensile strain under loading to achieve the target prestrain level

Axial compression tests on SMA-confined concrete

Figure 10.5 shows an individual SMA spiral as well as NSC and HSC concrete specimens confined by SMA spirals. As can be seen in the figure, a single continuous SMA spiral was wrapped around the concrete cylinders. A wire gripping steel platen was placed at the top and bottom of the concrete cylinders to keep the SMA spiral attached to the concrete specimen. The use of custom designed and made wire gripping steel platens to anchor SMA spirals at each end of the concrete cylinders ensured that the prestrain losses in SMA-confined concrete specimens were negligible. An SMA spiral pitch space of 36 and 20 mm was used for NSC and HSC specimens, respectively. A lower spiral pitch space was used in HSC specimens to address the increased confinement demand of the concrete as a result of an increase in its compressive strength [45-48]. The axial compression tests were conducted on the SMA-confined concrete specimens in accordance with ASTM C39 [49]. Figure 10.6 shows the SMA-confined concrete specimen configuration under the uniaxial compressive test. A small load of approximately 5 kN was initially applied to the specimen to fix its position between the steel plates. The SMA spiral was then heated using a variable AC transformer (with low voltage and high current supply) to the austenitic finish temperature by passing an electrical current through the wire. Subsequently, the concrete specimens were compressed at a displacement controlled rate of 0.18 mm/min using a 1000-kN capacity universal testing machine. The axial strain of the specimens was measured by two linear variable displacement transformers (LVDTs) mounted at the corners of steel loading and supporting plates. Two axial strain gauges mounted at the mid-height of the specimen were also used to validate and correct the LVDT measurements at the early stages of the loading.

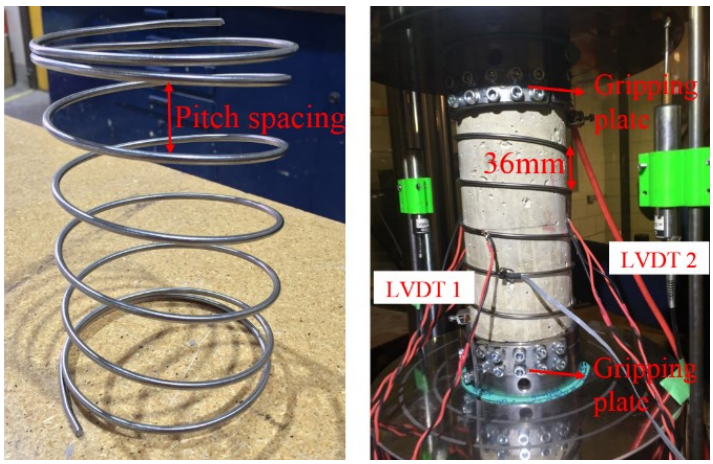

(a) (b)

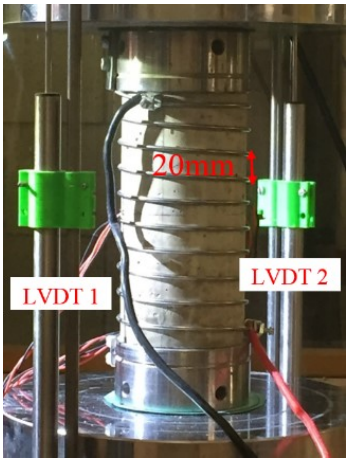

(c)

Figure 10.5. Concrete specimens: (a) SMA spirals; (b) NSC cylinder confined with SMA spirals; (c) HSC cylinder confined with SMA spirals

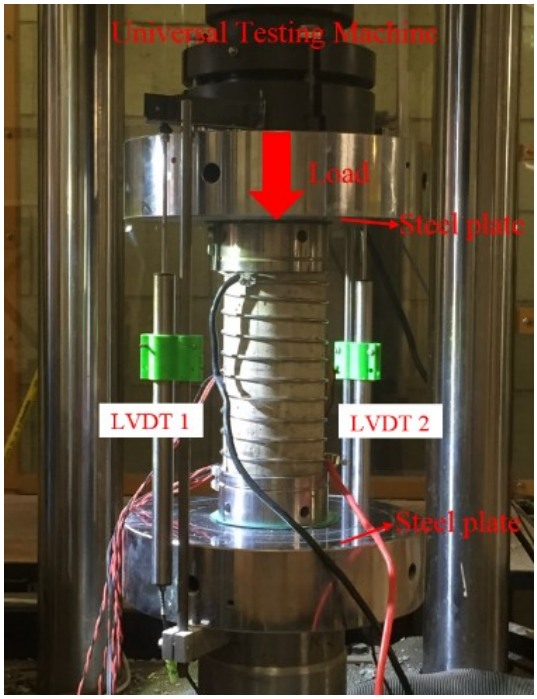

Figure 10.6. Uniaxial compression test setup

TEST RESULTS AND EXPERIMENTAL OBSERVATIONS

SMA material testing results

Tensile strength tests

Figure 10.7 shows the tensile stress-strain relationship of SMA wire in martensitic and austenitic phases. As can be seen in the figure, SMA behaves differently in martensitic and austenitic phases, owing to different crystal structures at different

phases (i.e. weak asymmetric parallelogram structure in martensitic and strong body centered cube crystal structure of SMA in austenitic phase). As can be seen in Fig. 10.7, a plateau was created in the stress-strain curve of SMA wire in martensitic phase between the axial strains of 0.01 and 0.04, owing to the detwinning of the martensite. After perfect detwinning, the plateau is followed by a steep hardening behaviour and the wire eventually ruptured at an ultimate tensile stress of 880 MPa and the corresponding axial strain of 0.34. As can be seen in Fig. 10.7, in austenitic phase, SMA wire failed at an ultimate tensile stress of 795 MPa and the corresponding strain of 0.21. This observation indicates that SMA developed a 10.2% and 38.2% lower tensile strength and strain, respectively, in austenitic phase than in martensitic phase, revealing that the difference in the tensile strain is more significant than the tensile strength. Lower tensile strength and strain of SMA in austenitic phase compared to those of martensitic phase is due to the fact that in austenitic phase SMA material contains crystal lattices with a stable structure and low strength, resulting in a more solid-state phase in the material [50].

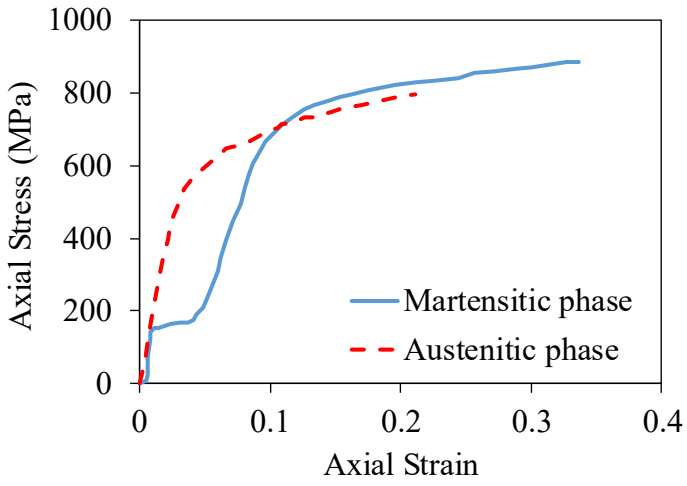

Figure 10.7. Tensile stress-strain relationship of SMA wire at martensitic and austenitic phases

Table 10.5 shows the summary of the tension test results of SMA wires. As can be seen in the table, prestrained SMA wires exhibited an average tensile strength of approximately 795 MPa, which is similar to that of unstrained SMA wire in austenitic phase. This observation indicates that the tensile strength of SMA is independent of the magnitude of the prestrain induced on the wire. However, as

expected, the ultimate tensile strain obtained at the rupture of the SMA wire decreased with an increase in the level of prestrain.

Table 10.5. Results of tensile strength tests on SMA wires

Type of test	Phase	Temperature* (°C)	Level of prestrain (%)	σ_{max} (MPa)	ε_{max} (%)
Uniaxial	Martensitic	17	0	880	34.0
Cyclic	Martensitic	17	0	900	18.0
Uniaxial	Austenitic	90	0	795	21.0
Uniaxial	Austenitic	90	5.5	800	15.5
Uniaxial	Austenitic	90	7.5	788	13.5
Uniaxial	Austenitic	90	9.5	794	11.5

* Temperature of SMA wire at the beginning of tension test
σ_{max} = tensile strength; ε_{max} = tensile rupture strain

Thermomechanical tests

Thermomechanical tests were conducted on SMA wires to investigate the influence of the temperature on the recovery stress of SMA material. As was discussed in the section of Tests on SMA Material, a recovery stress of 279 MPa (35% of tensile strength) and 558 MPa (70% of tensile strength) was required to strain the SMA wire to the target prestrain of 5.5% and 9.5%, respectively. Figures 10.8(a) and 10.8(b) show the variation of the recovery stress of SMA wire and temperature with time under prestrain levels of 5.5% and 9.5%, respectively. As can be seen in the figures, when SMA was initially loaded and unloaded at the ambient temperature (before increasing the temperature), the recovery stress had a nonlinear behaviour. It can be seen in Fig. 10.8(a) that the SMA wire developed a recovery stress of 315 MPa at the austenitic finish temperature (i.e. 90°C), which was higher than the required stress (i.e. 279 MPa) for the 5.5% prestrain level. An analysis of the recorded data indicated that a temperature of 85°C would provide the required recovery stress corresponding to the 5.5% prestrain, and hence this temperature was adopted in the test of SMA-confined concrete specimens. As can be seen in Fig. 10.8(b), the required recovery stress (558 MPa) at 9.5% prestrain level was obtained at 120°C. Based on this observation the SMA wire was heated to 120°C in the test of SMA-confined concrete specimens under 9.5% prestrain.

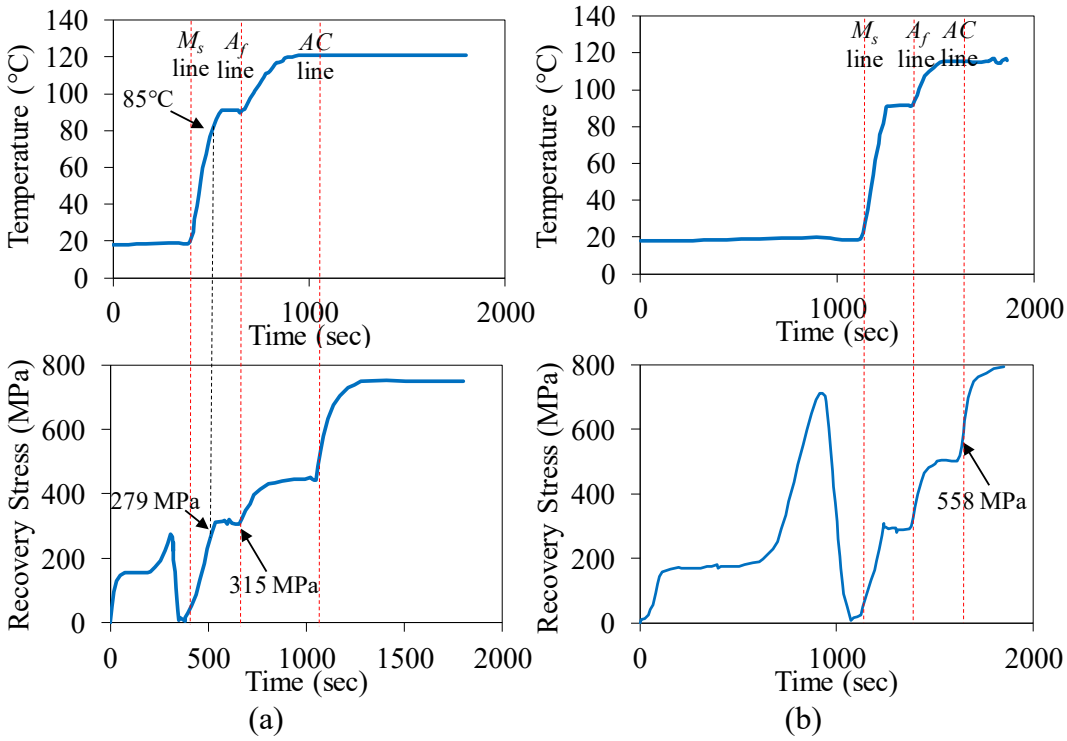

Figure 10.8. Variation of recovery stress and temperature with time for (a) 5.5% and (b) 9.5% prestraining level. M_s, A_f, and AC lines are the lines corresponding to martensite start temperature (17°C), austenite finish temperature (90°C), and AC transformer maximum temperature (120°C).

Figure 10.9 shows the influence of the prestraining level on the recovery stress of the SMA wires at 90°C (as the austenitic finish temperature) and 120°C (as the maximum temperature of the AC transformer). As can be seen in the figure, at a given prestrain level the SMA wire exhibited a higher recovery stress at 120°C compared to that at 90°C (i.e. austenitic finish temperature). This agrees with previous research [51] and suggests that the temperature at which SMA completes its austenitic transformation is affected by the presence of an applied external load. It can also be seen in Fig. 10.9 that, an increase in the prestrain level from 5.5% to 9.5% at 90°C resulted in a 5.8% decrease in the recovery stress, whereas the same increase in the prestrain level led to a 21.1% increase in the recovery stress at 120°C. This, once again, indicates that the SMA wire was not fully austenitic at 90°C in its deformed shape under the application of an external load. A similar observation was reported in a previous study [52] that, although the austenitic finish temperature of the used Ni-Ti SMA wire was 87°C, the recovery stress decreased with an increase in the prestrain level at temperatures between ~74°C and 100°C, suggesting that the material used in that study too was not fully austenitic between 87°C and 100°C

under the applied load. The temperature dependence of the effect of prestrain on the recovery stress (Fig. 10.9) can be attributed to the fact that at temperatures higher than its austenitic finish temperature SMA releases all of its stored energy to return to its original shape, whereas in the state at which the SMA is not fully austenitic all the energy does not get released, owing to the constrained deformation, and parts of it get stored as the residual stress [52].

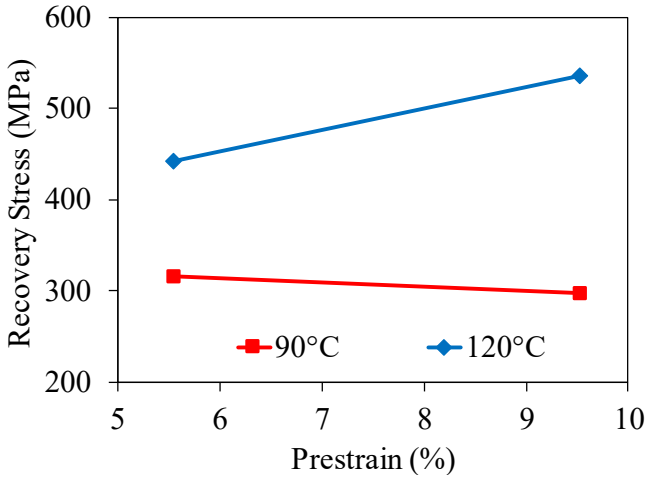

Figure 10.9. Variation of recovery stress of SMA wire with prestrain level at 90°C and 120°C

Compression tests on SMA-confined concrete specimens

Failure modes

Figures 10.10(a) and 10.10(b), respectively, show the typical failure modes of SMA-confined NSC and HSC specimens during compression tests. It can be seen in Fig. 10.10(a) that, in NSC specimens, heterogenic micro-cracks were formed and progressed leading to the surface spalling of concrete, which was accompanied by the formation of a more major shear crack along the mid-height of the specimen. However, it is evident from the figure that the specimen remained mostly intact until the concrete failure after excessive lateral expansion owing to the presence of confining pressure applied by the SMA spiral. On the other hand, HSC specimens failed as a result of the formation of a major diagonal macro-crack, which progressed to the rupture of the SMA wire under a large lateral strain caused by excessive lateral expansion of concrete (Fig. 10.10(b)).

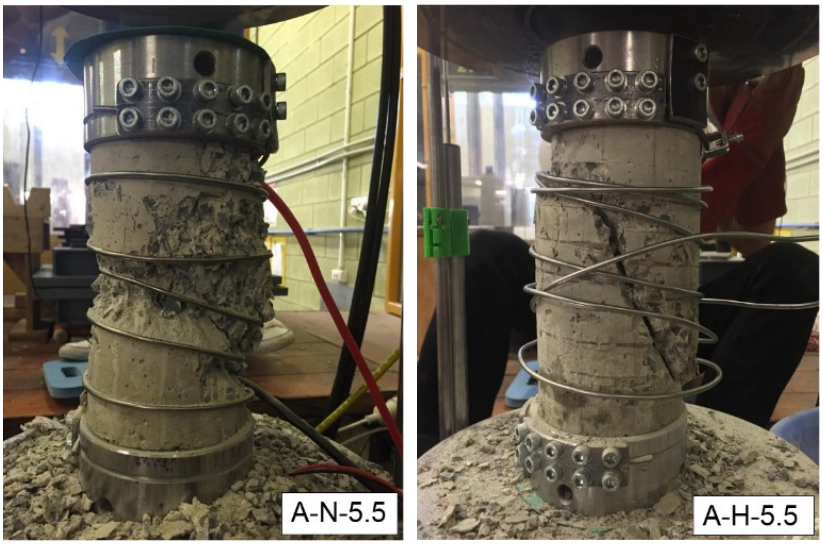

(a) (b)

Figure 10.10. Typical failure modes of SMA-confined (a) NSC and (b) HSC

Axial stress-strain relationships

Tables 10.6 and 10.7 show the compression test results of unconfined concrete and SMA-confined concrete specimens, respectively. The initial (f_{li}) and ultimate confining pressure (f_{lu}) were calculated using the recovery stress (279 MPa for 5.5% and 558 MPa for 9.5% prestrain level) and tensile strength (795 MPa) of the SMA wire, respectively. The difference between f_{li} and f_{lu} indicates that the confining pressure provided by SMA spiral consists of two components, namely active (i.e. initial constant confining pressure defined by f_{li}) and passive (additional confining pressure, over f_{li} up to f_{lu}, exerted by the SMA spiral as triggered by concrete dilation) confinement. As can be seen in the tables, an increase in the prestrain level resulted in an increase in the average (the average of specimens A and B test results) peak axial stress (f^*_{cc}) and corresponding axial strain (ε^*_{cc}) of the specimens. It can be seen in Table 10.7 that confinement of NSC specimens with 0%, 5.5%, and 9.5% prestrained SMA spirals resulted in an average increase of 17.7%, 24.5%, and 38.1% in f^*_{cc} and 179%, 267%, and 333% in ε^*_{cc} compared to those of unconfined NSC specimens, respectively. These observations indicate that the strength and strain increases observed in NSC specimens approximately doubled from zero to 9.5% prestrain level. It is worth noting that NSC specimens confined by unstrained SMA spirals exhibited a lower strength enhancement and a similar strain enhancement to those of NSC specimens confined by high-strength steel wires [35,53] under a

similar confinement level. However, the strain enhancement of NSC specimens confined by prestrained SMA spirals was significantly higher than that of the companion high-strength steel wire-confined specimens. Furthermore, the axial stress-strain curves of high-strength steel wire-confined specimens experienced a sudden drop after reaching f^*_{cc}, indicating the lower deformability of these specimens compared to that of the companion SMA spiral-confined specimens.

Table 10.6. Results of uniaxial compression tests on unconfined concrete specimens

Specimen	f'_{co} (MPa)	Average f'_{co} (MPa)	ε_{co} (%)	Average ε_{co} (%)
A-N	24.4	24.9	0.23	0.24
B-N	25.3		0.24	
A-H	64.8	63.5	0.28	0.29
B-H	62.1		0.29	

It can also be seen in Tables 10.6 and 10.7 that confinement of HSC specimens with 0%, 5.5%, and 9.5% prestrained SMA spirals led to an average increase of 6.8%, 9.3%, and 23.6% in f^*_{cc} and 143%, 164%, and 346% in ε^*_{cc}, respectively, than those of unconfined HSC specimens. These results indicate that increasing the prestraining level for HSC specimens from zero to 9.5% results in even higher strength and strain increases compared to those seen in NSC specimens. The enhancement in f^*_{cc} and ε^*_{cc} with an increase in the prestrain level of SMA spirals is attributed to the presence and magnitude of the active confining pressure on specimens confined by prestrained SMA spirals. An increase in the prestrain level results in an increase in the active confining pressure, leading to a more controlled crack growth experienced by concrete in the presence of a higher confining pressure [15,47]. Similar observations were also reported in previous studies [39,40].

Table 10.7. Results of uniaxial compression tests on SMA-confined concrete specimens

Specimen	f'_{co} (MPa)	ε_{co} (%)	Level of prestrain (%)	s (mm)	f_{li} (MPa)	f_{lu} (MPa)	f^*_{cc} (MPa)	Average f^*_{cc} (MPa)	Strength enhancement (%)	ε^*_{cc} (%)	Average ε^*_{cc} (%)	Strain enhancement (%)	k_1	k_2
A-N-0	24.9	0.24	0	36	0	4.25	28.3	29.3	17.7	0.71	0.67	179	0.80	12.59
B-N-0					0		30.3			0.62			1.27	9.73
A-H-0	63.5	0.29	0	20	0	7.65	68.8	67.8	6.8	0.73	0.68	143	0.69	11.47
B-H-0					0		66.7			0.63			0.42	9.28
A-N-5.5	24.9	0.24	5.5	36	1.40	4.25	31.0	31.0	24.5	0.97	0.88	267	1.43	17.82
B-N-5.5					1.43		31.0			0.78			1.43	13.18
A-H-5.5	63.5	0.29	5.5	20	2.81	7.65	69.8	69.4	9.3	0.74	0.74	164	0.82	12.88
B-H-5.5					2.70		69.0			0.73			0.72	12.59
A-N-9.5	24.9	0.24	9.5	36	2.71	4.25	35.2	34.4	38.1	1.14	1.04	333	2.42	24.62
B-N-9.5					2.86		33.5			0.94			2.02	26.33
A-H-9.5	63.5	0.29	9.5	20	4.88	7.65	78.7	78.5	23.6	1.15	1.18	307	1.99	21.97
B-H-9.5					5.03		78.3			1.21			1.93	17.09

s = pitch spacing of SMA spiral; f_{li} = initial confining pressure; f_{lu} = ultimate confining pressure; f^*_{cc} = peak axial stress; ε^*_{cc} = axial strain corresponding to f^*_{cc}; k_1 = strength enhancement coefficient; k_2=strain enhancement coefficient

Figures 10.11 and 10.12 show the axial stress-axial strain curves of NSC and HSC specimens under different levels of SMA prestrain, respectively. Comparison of Figs. 10.11 and 10.12 indicates that SMA confinement of NSC specimens led to a more shallow descending branch in the post-peak curve of the axial stress-strain relationship compared to that of HSC specimens, although they were under a lower level of lateral confinement (as defined by f_{lu}). This is partly attributed to the higher confinement ratio (f_{lu}/f'_{co}) (i.e. 0.17 and 0.12 for NSC and HSC specimens, respectively) of NSC specimens compared to that in HSC specimens and partly to more brittle behaviour of HSC [45-48]. It can also be seen in the figures that the failure of SMA-confined HSC specimens took place at a lower axial strain compared to that of SMA-confined NSC specimens. This can be attributed to the more brittle behaviour of HSC and the fact that HSC specimens had a lower f_{lu}/f'_{co} as the ultimate axial strain of confined concrete is a function of f_{lu}/f'_{co}. Effects of f'_{co} and f_{lu}/f'_{co} on the compressive behaviour of confined concrete were discussed in detail in previous studies [45-48]. As can be seen in Fig. 10.12, the ultimate axial strain of HSC specimens decreased with an increase in f_{li}. This observation is attributed to the failure mode of HSC specimens, which was caused by the rupture of the SMA spiral, and the fact that prestraining the spiral naturally reduced its available strain capacity when functioning as concrete confinement. It is worth noting that the reduced available strain capacity of SMA would not have any detrimental effect on the structural performance of these members, as evident from the fact that even specimens confined with 9.5% prestrained SMA developed approximately 5% ultimate axial strain, which is extremely high.

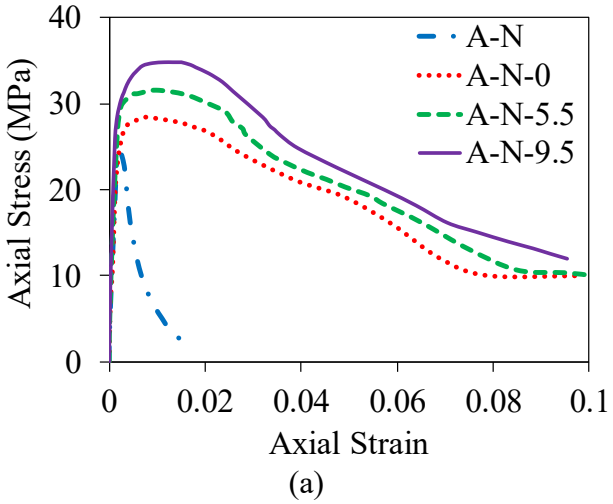

(a)

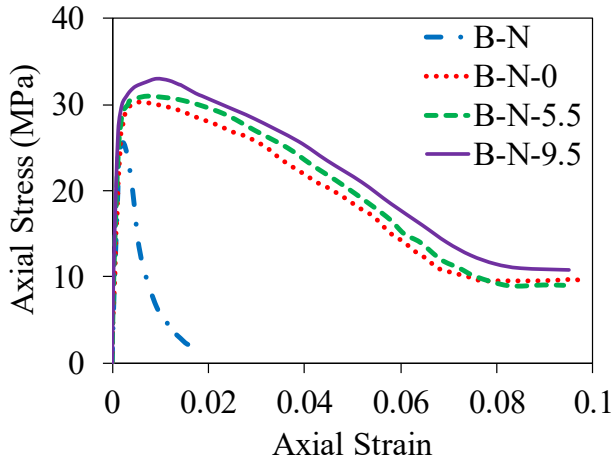

(b)

Figure 10.11. Axial stress-strain curves of SMA-confined NSC: (a) Series A; (b) Series B

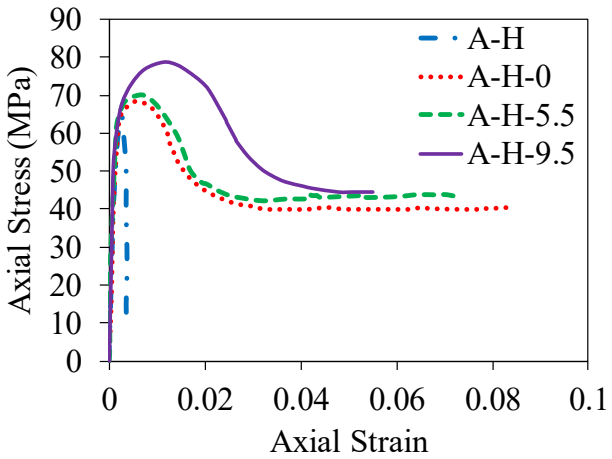

(a)

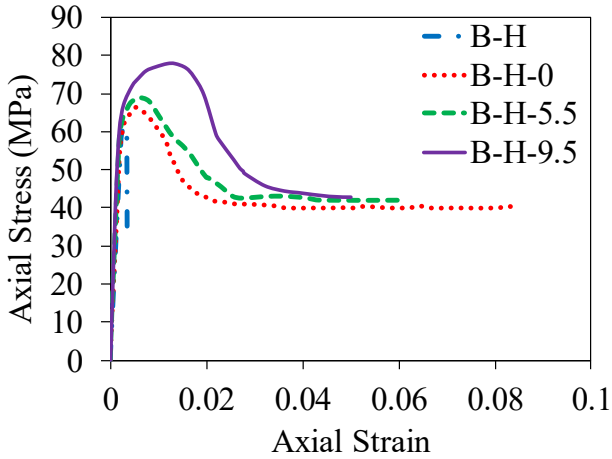

(b)

Figure 10.12. Axial stress-strain curves of SMA-confined HSC: (a) Series A; (b) Series B

As was defined in previous studies [22,54], the axial strain corresponding to 85% of f^*_{cc} (i.e. at 15% drop of the maximum bearing load) on the descending branch of the axial stress-strain curve can be used an indicator of the ductility of concrete. The results presented in Figs. 10.11 and 10.12 show that NSC specimens confined by 0%, 5.5%, and 9.5% prestrained SMA spirals exhibited an average axial strain corresponding to $0.85f^*_{cc}$ of 2.88%, 3.01%, and 3.15%, whereas HSC specimens confined by 0%, 5.5%, and 9.5% prestrained SMA spirals exhibited an average axial strain corresponding to $0.85f^*_{cc}$ of 1.22%, 1.35%, and 2.11%, respectively. These observations indicate that an increase in the prestrain level resulted in an increase in the ductility of concrete, which was more pronounced in the case HSC specimens.

Figures 10.13(a) and 10.13(b) show the variation of strength enhancement ratio (f^*_{cc}/f'_{co}) and strain enhancement ratio ($\varepsilon^*_{cc}/\varepsilon_{co}$) with prestrain level, respectively. As can be seen in the figure, SMA-confined NSC had a higher f^*_{cc}/f'_{co} and $\varepsilon^*_{cc}/\varepsilon_{co}$ than those of SMA-confined HSC, indicating that NSC specimens experienced higher improvements in strength and ductility than their HSC counterparts at a given prestrain level. It can also be seen in the figure that an increase in the SMA prestrain level led to an increase in f^*_{cc}/f'_{co} and $\varepsilon^*_{cc}/\varepsilon_{co}$ of both NSC and HSC specimens. The strength and strain enhancement in NSC specimens under 9.5% prestrain were 2.11 and 1.88 times higher than those of unstrained specimens, respectively. Likewise, the strength and strain enhancements of HSC specimens under 9.5% prestrain were 3.43 and 2.29 times higher than those of unstrained specimens, respectively, indicating that specimens at a higher prestrain level experienced significantly higher strength and deformability.

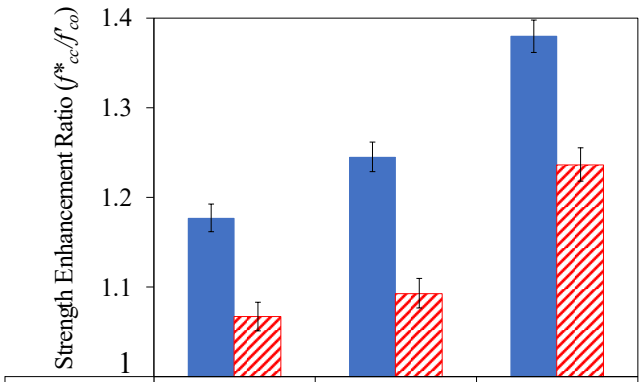

Prestrain (%)	0	5.5	9.5
NSC	1.18	1.24	1.38
HSC	1.07	1.09	1.24

(a)

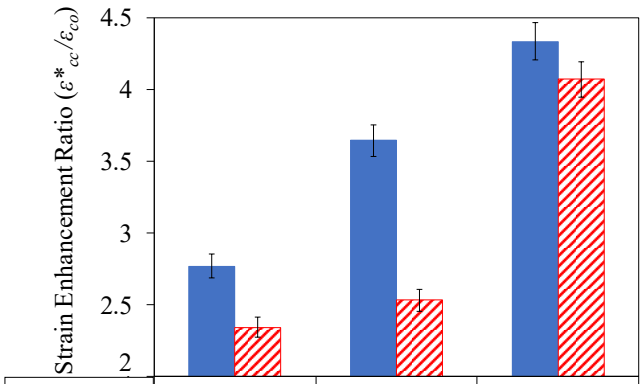

Prestrain (%)	0	5.5	9.5
NSC	2.77	3.65	4.33
HSC	2.34	2.53	4.07

(b)

Figure 10.13. Variation of (a) strength enhancement ratio (f^*_{cc}/f'_{co}) and (b) strain enhancement ratio ($\varepsilon^*_{cc}/\varepsilon_{co}$) with SMA prestrain level

In order to investigate the confinement effectiveness of SMA under different levels of prestrain, the relationship between strength and strain enhancement ratios and confinement ratio is studied. The values of strength (k_1) and strain enhancement coefficient (k_2), which were established respectively using the following simple expressions that are commonly used in the literature, are shown in Table 10.7.

$$f^*_{cc}/f'_{co} = 1 + k_1(f_{lu}/f'_{co}) \quad (10.1)$$

$$\varepsilon^*_{cc}/\varepsilon_{co} = 1 + k_2(f_{lu}/f'_{co}) \quad (10.2)$$

As can be seen in the table, at a given f'_{co}, an increase in f_{li} obtained from an increase in the level of prestrain resulted in substantial increases in both k_1 and k_2 of the specimens, indicating that SMA confinement of concrete with a higher level of prestrain leads to a significant increase in the confinement effectiveness of the system.

CONCLUSIONS

The experimental study on the axial compressive behaviour of NSC together with the first study on HSC under SMA confinement has been presented. On the basis of the experimental results and discussions the following conclusions can be drawn:

1- Ni-Ti SMA wires develop lower tensile strength and strain in austenitic phase compared to they do in martensitic phase, which is because in austenitic phase SMA is in more solid-state than it is in martensitic phase. The difference in the tensile strength is relatively small (i.e. 795 MPa vs 880 MPa), whereas that in the tensile strain is significant (i.e. 0.21 vs 0.34).
2- An increase in the temperature of the SMA wire results in a higher recovery stress at a given prestrain level, attributing to the fact that the SMA becomes more austenitic (superelastic) at higher temperatures.
3- An increase in the prestrain level from 5.5% to 9.5% leads to a decrease and increase in the recovery stress of the SMA wire at 90°C and 120°C, respectively, pointing to the dependence of the effect of prestrain on the recovery stress on the level of austenitic transformation.
4- SMA confinement, especially when applied through prestrained wires, significantly increases the compressive strength and corresponding axial strain of NSC and HSC. NSC and HSC specimens confined by 9.5% prestrained SMA spirals respectively exhibit an increase of 38.1% and 23.6% in their compressive strength and 333% and 346% in the corresponding axial strain compared to those of unconfined specimens.
5- An increase in the prestrain level results in an increase in the peak axial stress and corresponding axial strain of SMA-confined concretes. SMA-confined NSC and HSC specimens under 9.5% prestrain level respectively exhibit 2.1 and 3.4 times the strength enhancement and 1.9 and 2.3 times the strain enhancement compared to those of the unstrained specimens.
6- SMA-confined HSC develops a lower ultimate axial strain compared to SMA-confined NSC owing to the more brittle behaviour of HSC specimens. It is worth noting that the lower ultimate axial strain of HSC is also partly attributed to the lower confinement ratio of the HSC specimens of the current study (0.12) compared to that of NSC specimens (0.17).

The promising findings of this study point to the possibility of the use of SMA spirals as a novel confinement technique to develop high-performance composite structural members and as an efficient prestressing technique to strengthen and retrofit existing concrete members.

ACKNOWLEDGEMENTS

The authors thank Messrs. Giannini, Koch, Lim, and Shaw for completing the tests reported in this paper as part of their Honour's thesis and Messrs. Fang and Gu for their assistance with the analysis of some of the test results.

REFERENCES

[1] Karabinis AI, Rousakis TC. Concrete confined by FRP material: a plasticity approach. *Engineering Structures*. 2002;24(7):923-32.

[2] Lokuge WP, Sanjayan JG, Setunge S. Stress-strain model for laterally confined concrete. *Journal of Materials in Civil Engineering*. 2005;17(6):607-16.

[3] Ilki A, Peker O, Karamuk E, Demir C, Kumbasar N. FRP retrofit of low and medium strength circular and rectangular reinforced concrete columns. *Journal of Materials in Civil Engineering*. 2008;20(2):169-88.

[4] Wu YF, Wang LM. Unified strength model for square and circular concrete columns confined by external jacket. *Journal of Structural Engineering*. 2009;135(3):253-61.

[5] Smith ST, Kim SJ, Zhang HW. Behavior and effectiveness of FRP wrap in the confinement of large concrete cylinders. *Journal of Composites for Construction*. 2010;14(5):573-82.

[6] Lim JC, Ozbakkaloglu T. Investigation of the influence of application path of confining pressure: tests on actively confined and FRP-confined concretes. *Journal of Structural Engineering*. 2015;10.1061/(ASCE)ST.1943-541X.0001177.

[7] Dundar C, Erturkmen D, Tokgoz S. Studies on carbon fiber polymer confined slender plain and steel fiber reinforced concrete columns. *Engineering Structures.* 2015;102:31-9.

[8] Ozbakkaloglu T, Gholampour A, Lim JC. Damage–plasticity model for FRP-confined normal-strength and high-strength. *Journal of Composites for Construction.* 2016;10.1061/(ASCE)CC.1943-5614.0000712.

[9] Xie T, Ozbakkaloglu T. Behavior of recycled aggregate concrete-filled basalt and carbon FRP tubes. *Construction and Building Materials*. 2016;105:132-43.

[10] Ozbakkaloglu T, Saatcioglu M. Displacement-based model to predict lateral drift capacities of concrete-filled FRP tube columns. *Engineering Structures*. 2017;147:345-55.

[11] Lim JC, Ozbakkaloglu T. Lateral strain-to-axial strain relationship of confined concrete. *Journal of Structural Engineering*. 2015;10.1061/(ASCE)ST.1943-541X.0001094.

[12] Mansouri I, Gholampour A, Kisi O, Ozbakkaloglu T. Evaluation of peak and residual conditions of actively confined concrete using neuro-fuzzy and neural computing techniques. *Neural Computing and Applications*. 2016; 10.1007/s00521-016-2492-4.

[13] Lim JC, Ozbakkaloglu T, Gholampour A, Bennett T, Sadeghi R. Finite-element modeling of actively confined normal-strength and high strength concrete under uniaxial, biaxial, and triaxial compression. *Journal of Structural Engineering.* 2016;10.1061/(ASCE)ST.1943-541X.0001589.

[14] Gholampour A, Ozbakkaloglu T, Hassanli R. Behavior of rubberized concrete under active confinement. *Construction and Building Materials*. 2017;138:372-82.

[15] Lim JC, Ozbakkaloglu O, Unified stress-strain model for FRP and actively confined normal-strength and high-strength concrete. *Journal of Composites for Construction.* 2014;10.1061/(ASCE)CC.1943-5614.0000536.

[16] Lim JC, Ozbakkaloglu T. Stress-strain model for normal- and light-weight concretes under uniaxial and triaxial compression. *Construction and Building Materials*. 2014;71:492-509.

[17] Lim JC, Ozbakkaloglu T. Influence of size and slenderness on compressive strain softening of confined and unconfined concrete. *Journal of Materials in Civil Engineering.* 2016;28(2):06015010.

[18] Saatcioglu M, Yalcin C. External prestressing concrete columns for improved seismic shear resistance. *Journal of Structural Engineering*. 2003;129(8):1057-70.

[19] Nesheli KN, Meguro K. External prestressing concrete columns with fibrous composite belts. *7th International Symposium on Fiber-Reinforced (FRP) Polymer Reinforcement for Concrete Structures*, 2005, ACI, SP-230-92:1631.

[20] Tamuzs V, Tepfers R, Chi-Sang You, Rousakis T, Repelis I, Skruls V, Vilks U. Behavior of concrete cylinders confined by carbon-composite tapes and

prestressed yarns 1. Experimental data. *Mechanics of Composite Materials*. 2006;42(1):13-32.

[21] Yan Z, Pantelides CP, Reaveley LD. Posttensioned FRP composite shells for concrete confinement. *Journal of Composites for Construction*. 2007;11(1):81–90.

[22] Janke L, Czaderski C, Ruth J, Motavalli M. Experiments on the residual load-bearing capacity of prestressed confined concrete columns. *Engineering Structures*. 2009;31:2247-56.

[23] Moghaddam H, Samadi M, Pilakoutas K, Mohebbi S. Axial compressive behaviour of concrete actively confined by metal strips; A: experimental study. *Materials and Structures*. 2010;43:1369-81.

[24] Cinina I, Zıle E, Zıle O. Mechanical behavior of concrete columns confined by basalt FRP windings. *Mechanics of Composite Materials*. 2012;48(5):539-46.

[25] Rousakis TC, Tourtouras IS. RC Columns of square section – passive and active confinement with composite ropes. *Composites Part B*. 2014;58:573-81.

[26] Rousakis TC, Tourtouras IS. Modeling of passive and active external confinement of RC columns with elastic material. *ZAMM Journal*. 2015;95(10):1046-57.

[27] Vokoun D, Kafka V, Hu CT. Recovery stresses generated by NiTi shape memory wires under different constraint conditions. *Smart Materials and Structures*. 2003;12:680-5.

[28] DesRoches R, McCormick J, Delemont M, Cyclic properties of superelastic shape memory alloy wires and bars. *Journal of Structural Engineering*. 2004;130(1):38-46.

[29] Janke L, Czaderski C, Motavalli M, Ruth J. Applications of shape memory alloys in civil engineering structures – overview, limits and new ideas. *Materials and Structures*. 2005;38:578-92.

[30] Choi E, Nam TH, Cho SC, Chung YS, Park T. The behavior of concrete cylinders confined by shape memory alloy wires. *Smart Materials and Structures.* 2008;17(6):065032.

[31] Li J, Zu L, Zhong G, He M, Yin H, Tan Y. Stiffness characteristics of soft finger with embedded SMA fibers. *Composite Structures*. 2017;160:758-64.

[32] Assa B, Nishiyama M, Watanabe F. New approach for modeling confined concrete. I: circular columns. *Journal of Structural Engineering*. 2001;127(7):743-50.

[33] Choi E, Chung YS, Choi JH, Kim HT, Lee H. The confining effectiveness of NiTiNb and NiTi SMA wire jackets for concrete. *Smart Materials and Structures.* 2010;19(3):035024.

[34] Song D, Kang G, Kan Q, Yu C, Zhang C. The effect of martensite plasticity on the cyclic deformation of super-elastic NiTi shape memory alloy. *Smart Materials and Structures.* 2014;23:015008.

[35] Wei Y, Wu YF. Compression behavior of concrete columns confined by high strength steel wire. *Construction and Building Materials*. 2014;54:443-53.

[36] Chen Q, Andrawes B. Cyclic stress-strain behavior of concrete confined with NiTiNb-shape memory alloy spirals. *Journal of Structural Engineering*. 2017;143(5):04017008.

[37] Panton B, Oliveira JP, Zeng Z, Zhou YN, Khan MI. Thermomechanical fatigue of post-weld heat treated NiTi shape memory alloy wires. *International Journal of Fatigue*. 2016;92:1-7.

[38] Andrawes B, Shin M. Seismic retrofitting of bridge columns using shape memory alloys. *Proc. SPIE - The International Society for Optical Engineering*, May 2008;6928.

[39] Shin M, Andrawes B. Experimental investigation of actively confined concrete using shape memory alloys. *Journal of Structural Engineering*. 2010;32(3):656-64.

[40] Park J, Choi E, Park K, Kim HT. Comparing the cyclic behavior of concrete cylinders confined by shape memory alloy wire or steel jackets. *Smart Materials and Structures*. 2011;20(9):094008.

[41] Dommer K, Andrawes B. Thermomechanical characterization of NiTiNb shape memory alloy for concrete active confinement applications. *Journal of Materials in Civil Engineering.* 2012;24(10):1274-82.

[42] Tran H, Balandraud X, Destrebecq JF. Improvement of the mechanical performances of concrete cylinders confined actively or passively by means of SMA wires. *Archives of Civil and Mechanical Engineering*. 2015;15:292-9.

[43] Chen Q, Andrawes B, Sehitoglu H. Thermomechanical testing of FeNiCoTi shape memory alloy for active confinement of concrete. *Smart Materials and Structures.* 2014;23:055015.

[44] ASTM C192/C192M-07. *Standard Practice for Making and Curing Concrete Test Specimens in the Laboratory*. American society for testing and materials. West Conshohocken, PA, USA, 2007.

[45] Ozbakkaloglu T. Axial compressive behavior of square and rectangular high-strength concrete-filled FRP tubes. *Journal of Composites for Construction*. 2013;17(1):151-61.

[46] Lim JC, Ozbakkaloglu T. Hoop strains in FRP-confined concrete columns: Experimental observations. *Materials and Structures*. 2015;48(9):2839-54.

[47] Vincent T, Ozbakkaloglu T. Compressive behavior of prestressed high-strength concrete-filled aramid FRP tube columns: Experimental observations. *Journal of Composites for Construction.* 2015;19(6):04015003.

[48] Vincent T, Ozbakkaloglu T. Influence of overlap configuration on compressive behavior of CFRP-confined normal-and high-strength concrete. *Materials and Structures.* 2016;49(4):1245-68.

[49] ASTM C39/C39M-15. *Standard Test Method for Compressive Strength of Cylindrical Concrete Specimens*. American society for testing and materials. West Conshohocken, PA, USA, 2015.

[50] McKelvey AL, Ritchie RO. Fatigue-crack growth behavior in the superelastic and shape memory alloy Nitinol. *Metallurgical and Materials Transactions A.* 2001;32(13):731-43.

[51] Andrawes B, Shin M, Wierschem N. Active confinement of reinforced concrete bridge columns using shape memory alloys. *Journal of Bridge Engineering*. 2010;15(1):81-9.

[52] Li Y, Cui LS, Xu HB, Yang DZ. Constrained phased-transformation of a TiNi shape-memory alloy. *Metallurgical and Materials Transactions A.* 2003;34A:219-23.

[53] Wu YF, Wei Y. General stress-strain model for steel- and FRP-confined concrete. *Journal of Composites for Construction*. 2015;19(4):04014069.

[54] Ozbakkaloglu T, Oehlers D. Manufacture and testing of a novel FRP tube confinement system. *Engineering Structures*. 2008;30:2448-59.

Statement of Authorship

Title of Paper	Fiber-reinforced concrete containing ultra high-strength micro steel fibers under active confinement
Publication Status	☑ Published ☐ Accepted for Publication ☐ Submitted for Publication ☐ Unpublished and Unsubmitted work written in manuscript style
Publication Details	Gholampour A, Ozbakkaloglu T. Fiber-reinforced concrete containing ultra high-strength micro steel fibers under active confinement. *Construction and Building Materials*. 2018;187:299-306.

Principal Author

Name of Principal Author (Candidate)	Aliakbar Gholampour		
Contribution to the Paper	Literature review, analysis of test results, and preparation of the manuscript.		
Overall percentage (%)	80%		
Certification:	This paper reports on original research I conducted during the period of my Higher Degree by Research candidature and is not subject to any obligations or contractual agreements with a third party that would constrain its inclusion in this thesis. I am the primary author of this paper.		
Signature		Date	31/01/2019

Co-Author Contributions

By signing the Statement of Authorship, each author certifies that:

i. the candidate's stated contribution to the publication is accurate (as detailed above);

ii. permission is granted for the candidate in include the publication in the thesis; and

iii. the sum of all co-author contributions is equal to 100% less the candidate's stated contribution.

Name of Co-Author	Togay Ozbakkaloglu		
Contribution to the Paper	Research supervision and review of manuscript.		
Signature		Date	31/01/2019

Name of Co-Author			
Contribution to the Paper			
Signature		Date	

Please cut and paste additional co-author panels here as required.

Fiber-Reinforced Concrete containing Ultra High-Strength Micro Steel Fibers under Active Confinement

ABSTRACT

This paper presents an experimental study on the compressive behaviour of steel fiber-reinforced concrete (SFRC) under active confining pressure. Four different SFRC mixes containing ultra high-strength micro steel fibers at two volume fractions of 1% and 2% were prepared to produce concretes with two different target compressive strengths of 50 and 100 MPa. The active confining pressure was applied on SFRC using a Hoek cell at different confinement levels of 5, 10, 15, and 25 MPa. The effects of confining pressure and steel fiber volume fraction on the compressive behaviour of concrete were examined through the axial compression tests on unconfined and actively confined SFRCs. The results show that the axial strength and peak axial strain of SFRCs increase with an increase in the fiber volume fraction. The volume fraction also affects the post-peak branch trend of the axial stress-strain relationships of SFRCs under a given confinement level. SFRCs with a higher volume fraction exhibit more shallow post-peak branches than those of SFRCs with a lower volume fraction. The results also show that the axial strain of SFRC at a given lateral strain increases with an increase in the volume fraction, indicating a reduced rate of dilation of SFRCs at a higher volume fraction. These promising findings point to the great potential of the use of ultra high-strength micro steel fibers in the development of high-performance composite structural members in applications where the concrete will be subjected to lateral confinement.

KEYWORDS: Steel fiber-reinforced concrete (SFRC); High-strength concrete (HSC); Active Confinement; Dilation Behaviour; Axial compression; Ultra high-strength micro steel fiber.

INTRODUCTION

In recent years, high-strength concrete (HSC) has become a promising alternative in the construction of new high performance columns owing to its superior structural properties over normal-strength concrete (NSC) [1,2]. However, because of the

inherent brittleness of conventional HSC, its application has been somewhat limited especially in constructions undertaken in seismically active zones [3]. On the other hand, studies have shown that the use of steel fibers can improve the brittle behaviour of conventional concrete [4-10]. The distribution of internal steel fibers in the concrete decreases isolated major crack formations by reinforcing the bridge of microcracks, which leads to a more even and controlled crack propagation [7]. This thereby results in improvements in the ductility and strength of concrete.

A large number of experimental investigations have been conducted to understand the mechanical behaviour of steel fiber-reinforced concrete (SFRC) columns (e.g. [3,11-22]). Existing studies have shown that the steel fiber parameters, the volume fraction (V_f) and aspect ratio (A_R), influence the stress-strain relationship of SFRC. It was shown that at a given V_f, the compressive strength (f'_{co}) and corresponding axial strain (ε_{co}) of concrete decrease with an increase in A_R. On the other hand, it was shown that an increase in V_f at a given A_R leads to an increase in f'_{co} and ε_{co}. It was also shown that when steel fibers are uniformly dispersed in the concrete, significant improvements can be obtained in the mechanical properties of concrete [18,21]. Therefore, due to their superior performance compared to that of conventional concrete, SFRC has a great potential to serve as a high performance concrete in structural applications.

It is now well known that significant improvements in the ductility and compressive strength of concrete can be achieved by its lateral confinement [23-34]. Active confinement is a confinement method in which a constant lateral confining pressure is applied to concrete [35]. In order to understand the mechanical behaviour of SFRCs under lateral confinement, the study of the actively confined concrete is of vital importance to simulate the behaviour of concrete under constant confining pressure (e.g. steel-confined concrete) and varying confining pressure (e.g. fiber-reinforced polymer (FRP)-confined concrete). Although a number of experimental studies have been performed to date to understand the mechanical behaviour of confined SFRCs under axial compression (e.g. [5,7,30,36,37]), only two of these studies have dealt with the mechanical behaviour of actively confined SFRC [38,39]. However, the dilation behaviour of concrete, which is crucial for understanding and modelling the behaviour of concrete in triaxial compression, has

not been evaluated in these two studies. Therefore, it is clear that there is need for new experimental studies to improve understanding on the behaviour of SFRCs under active confinement. Furthermore, the existing studies on actively confined SFRC investigated the behaviour of only the concrete columns with unconfined concrete strength of up to 70 MPa. Studies focusing on higher strength concretes are needed to understand the feasibility of the use of this material in ultra high-performance composite structural members where lateral confining pressure is to be applied to concrete, such as columns designed for seismic and blast resistance.

This paper presents an experimental study on the compressive behaviour of actively confined SFRCs containing ultra high-strength micro steel fibers together with the first study on the dilation behaviour of SFRCs under different confining pressures. Axial compression tests were performed on the specimens to study the effect of fiber volume fraction and confinement level on the compressive behaviour of actively confined SFRC. The results show that the axial strain of SFRC at a given lateral strain increases with an increase in the volume fraction, which indicates a reduced rate of dilation of SFRCs at a higher volume fraction. The results of this study point to the significant potential of the use of ultra high-strength micro steel fibers in the development of high-performance composite structural members, especially columns designed for seismic and blast resistance.

EXPERIMENTAL PROGRAM

Materials

Coarse and fine aggregates

Coarse aggregates (crushed basalt stone) used in the concrete mixes had a nominal maximum size of 10 mm and were sourced from McLaren Vale Quarry in South Australia. Sand having a 2-mm maximum nominal size was obtained from Price Pit in South Australia and used as the fine aggregate.

Cement and pozzolanic admixture

Table 11.1 shows the chemical composition and physical properties of the ordinary Portland cement (OPC) and silica fume used in the preparation of concrete mixes.

Table 11.1. Chemical composition and physical properties of cementitious materials

Item	Cementitious materials (%)	
	Ordinary Portland cement	Silica fume
SiO_2	21.4	92.5
$ZrO_2 + HfO_2$	–	5.50
Al_2O_3	5.55	0.35
Fe_2O_3	3.46	0.40
P_2O_5	–	0.30
CaO	64.0	0.03
MgO	1.86	–
SO_3	1.42	0.90
K_2O	0.54	0.02
Na_2O	0.26	0.02
	Compounds	
C_3S	51.0	–
C_2S	23.1	–
C_3A	8.85	–
C_4AF	10.5	–
	Fineness	
Surface area (m^2/kg)	330	18,000

Steel fibers

Ultra high-strength micro steel fibers with a length of 13 mm and diameter of 0.18 mm were added to the SFRC mixes at 1% and 2% volume fractions. Table 11.2 shows their material properties as supplied by the manufacturer.

Table 11.2. Material properties of ultra high-strength micro steel fibers

Length (mm)	Diameter (mm)	Aspect ratio	Tensile strength (MPa)
13	0.18	73	2850

Test specimens and mix design

Four unique mixes of SFRC (i.e. two C50 and two C100) were prepared, in which C50 and C100 mixes were designed to develop a 28-day compressive strength of 50 MPa and 100 MPa, respectively. The mix proportions of different SFRCs used in this study are shown Table 11.3. C50 and C100 mixes had a water-to-binder ratio (*w/b*) of 0.479 and 0.295, respectively. Steel fibers were added to the mixes at two fiber volume fractions (V_f) of 1% and 2% by replacement of coarse aggregates. Silica

fume was used in C100 mixes and a polycarboxylic ether polymer-based superplasticizer was added to all mixtures to achieve workable mixes. Slump tests were conducted according to ASTM C143/C143M [40] on fresh SFRCs to evaluate their workability. The hardened density of SFRC was also obtained according to ASTM C642-13 [41].

Table 11.3. Mix proportions of the concrete

Concrete mix	C50-1	C50-2	C100-1	C100-2
Cement (kg/m^3)	375	375	506	506
Silica fume (kg/m^3)	–	–	44	44
Sand (kg/m^3)	720	720	700	700
Coarse Aggregate (kg/m^3)	1053	1026	1023	996
Water (kg/m^3)	176	176	145	145
Superplasticizer (kg/m^3)	5	5	25	25
w/b *	0.479	0.479	0.295	0.295
Volume Fraction (V_f) (%)	1	2	1	2
Fiber (kg/m^3)	78	156	78	156
Slump (mm)	140	125	175	130
Hardened Density (kg/m^3)	2449	2526	2476	2555

* Including the water coming from the superplasticizer (i.e. 70% water by weight)

Figure 11.1 shows the SFRC specimens. The geometry of the specimens was determined based on the geometry of the Hoek cell (i.e. 126 mm in height and 63 mm in diameter). Both ends of the specimens were ground by a surface grinding machine in order to remove irregularities and obtain orthogonal specimen ends with respect to the longitudinal axis. Specimens were kept in a fog room at a constant temperature of 23±2°C until test day in accordance with ASTM C192/C192M [42]. The specimens were confined by a Hoek cell using four different constant hydrostatic pressures (f^*_l) of 5, 10, 15, and 25 MPa.

Figure 11.1. SFRC specimens

Instrumentation and testing

Axial compression tests were conducted according to ASTM C39/C39M-16b [43]. A 1000-kN capacity universal testing machine was used for testing, which was conducted under a displacement control at a rate of 0.18 mm/min. Figure 11.2 shows the testing machine used in this study. The axial strain of the specimens was measured by two linear variable displacement transformers (LVDTs) that were mounted at the corners of steel loading and supporting plates. One axial strain gauge mounted at the mid-height of the specimen was used to correct and validate the LVDT measurements at the early stages of the loading. Two lateral strain gauges were also placed at the mid-height of the specimen to obtain the lateral strains. A thin coating of lubricating wax was used on the strain gauges to prevent damages to the strain gauges by the Hoek cell membrane.

Figure 11.2. Universal testing machine

Specimen designation

The labelling of specimens in Table 11.5 is as follows: C50 and C100 represent mixes with target compressive strengths (f'_{co}) of 50 MPa and 100 MPa, respectively, followed by a number showing the steel fiber volume fraction (V_f) and a subsequent number indicating the confining pressure (f^*_l) in MPa. For instance, C50-2-F15 represents an SFRC mix with a 50 MPa target f'_{co} and V_f of 2% and f^*_l of 15 MPa.

TEST RESULTS AND DISCUSSIONS

Unconfined specimens

The slump and density test results are shown in Table 11.3. As expected, the results show a decrease in the workability and increase in the hardened density of SFRCs with an increase in the V_f from 1% to 2%. Table 11.4 presents the 7-, 14-, and 28-day compressive strength (f'_{co}) and the corresponding 28-day axial strain (ε_{co}) of the unconfined SFRCs (i.e. $f^*_l = 0$). Figure 11.3 shows the axial stress-strain and lateral-axial strain relationships of unconfined SFRC specimens at 28 days. As can be seen in the table and figure, f'_{co} and ε_{co} of SFRCs increased with an increase in V_f. At 28 days, C50 and C100 mixes experienced a strength increase of 24.0% and 10.0% respectively with an increase in V_f from 1% to 2%. The corresponding increases of the axial strains of C50 and C100 mixes were 6.7% and 5.7%, respectively.

Table 11.4. Compression test results of unconfined specimens

Mix	f'_{co} (MPa)			ε_{co} (%)
	7-day	14-day	28-day	28-day
C50-1	32.1	43.5	51.7	0.30
C50-2	47.7	58.3	64.1	0.32
C100-1	74.7	90.1	103.2	0.35
C100-2	79.7	96.6	113.5	0.37

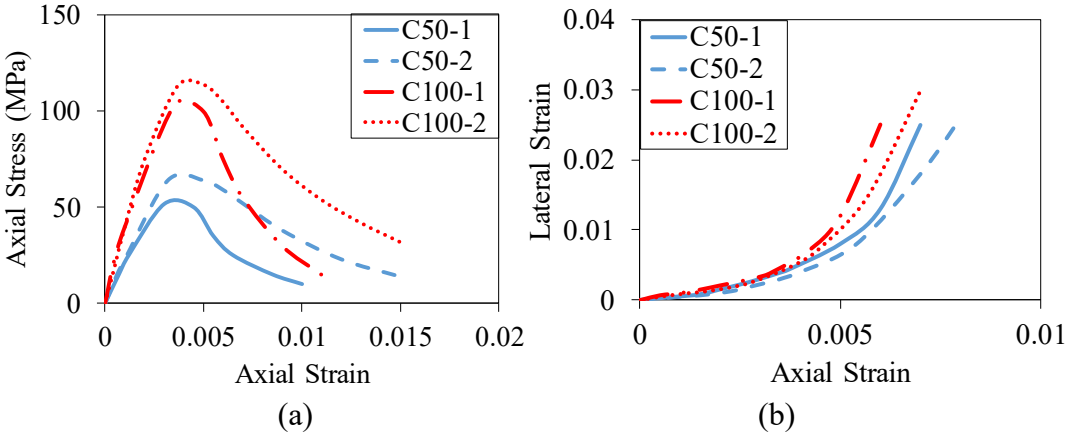

Figure 11.3. 28-day (a) axial stress-strain relationships, (b) lateral strain-axial strain relationships of unconfined specimens

It can be seen in Fig. 11.3(a) that an increase in V_f resulted in a decrease in the second branch slope of the axial stress-strain curve, suggesting that the ductility of unconfined SFRCs (defined as the area under the plastic portion of the axial stress-

strain curve) increased with an increase in V_f. As can be seen in Fig. 11.3(b), an increase in V_f led to an increase in the axial strain of SFRC at a given lateral strain. This is because of the reduced rate of lateral expansion of SFRC with higher V_f owing to the bridging effect of steel fibers across the cracks, which results in a more controlled cracking of concrete under axial compression [7,39].

Confined specimens

Failure modes

Figure 11.4 illustrates the failure modes of actively confined SFRC specimens under f^*_l of 10 MPa. It can be seen in Fig. 11.4 that the failure mode of C50 and C100 specimens were different to each other. C50 specimens experienced a series of cracks, whereas the concrete crushing in C100 specimens was localized around a single macrocrack. As can also be seen in Fig. 11.4, there was no major difference between the failure modes of SFRC specimens with V_f of 1% and 2%.

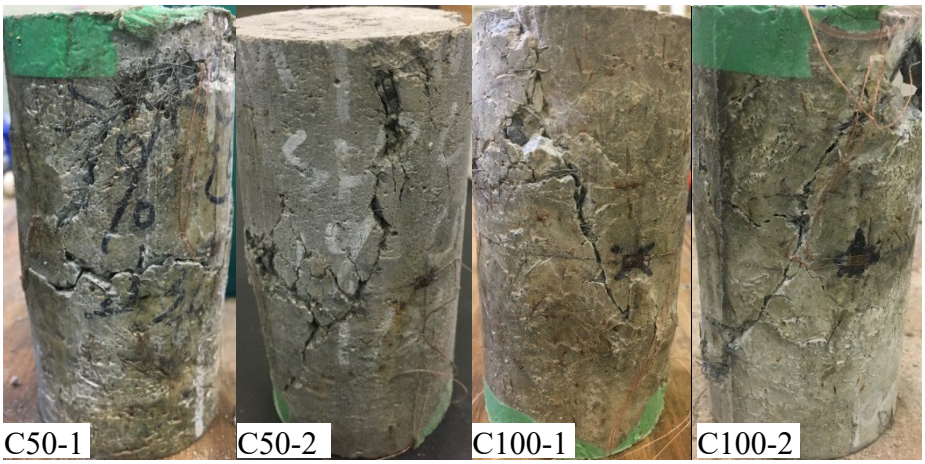

Figure 11.4. Failure modes of different SFRC mixes under f^*_l=10 MPa

Axial stress-strain and lateral-axial strain relationships

Figure 11.5 shows axial stress-strain and lateral-axial strain relationships of actively confined SFRCs under different levels of confining pressure. As can be seen in the figure, axial stress-strain curves of SFRCs with V_f = 2% had a slightly more shallow post-peak descending branch compared to those of SFRCs with V_f = 1%. This can be because of the increased internal confinement provided through internal steel fibers with an increase in V_f, which is discussed in detail in the following section. As can also be seen in Fig. 11.5, the axial stress-strain curves of C50 mixes exhibited

a more shallow descending branch than those of C100 mixes, which is attributed to the higher f^*_l/f'_{co} of C50 mixes [1]. As can be seen in the lateral-axial strain relationships shown in Fig. 11.5, under a given f^*_l, the axial strain of SFRCs increased with an increase in V_f at a given lateral strain. This observation indicates a reduced rate of dilation of concrete at a higher V_f, which is attributed to the bridging effect of steel fibers across the cracks that becomes more pronounced with an increase in V_f [39,44].

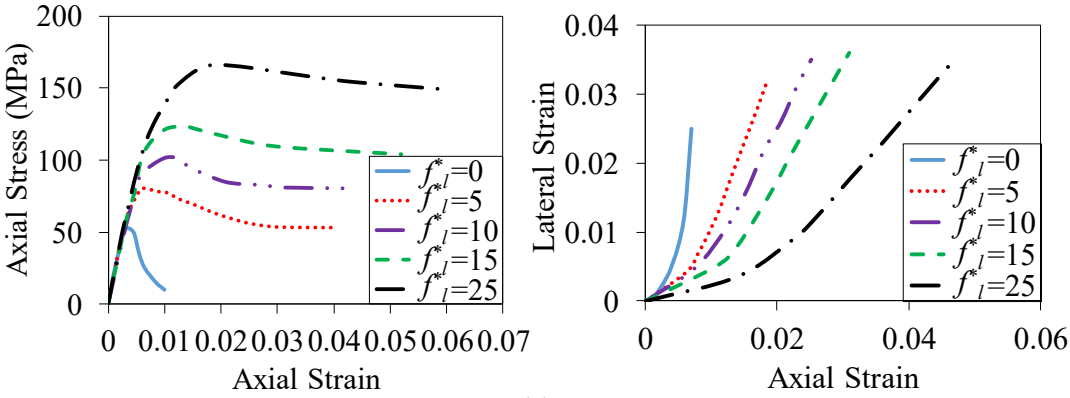

(a)

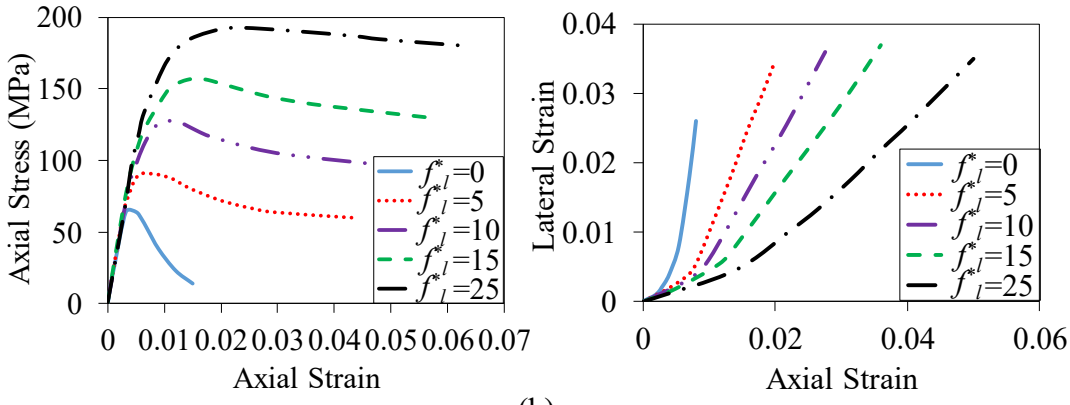

(b)

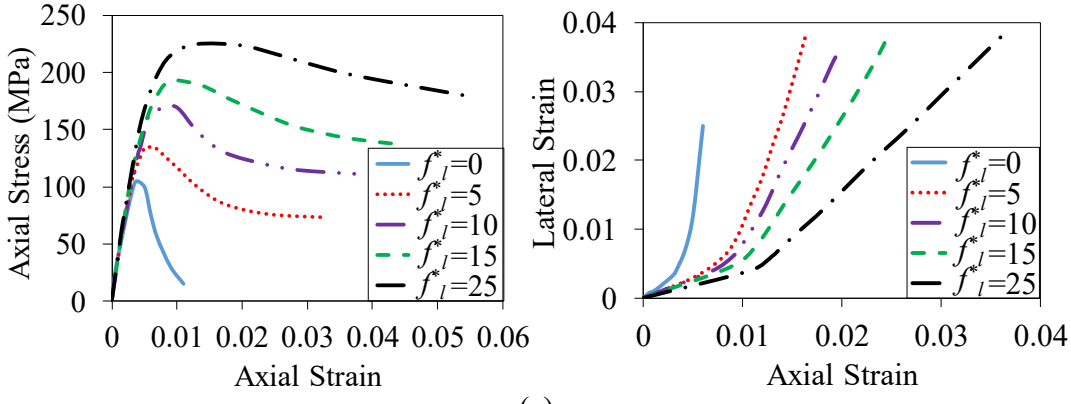

(c)

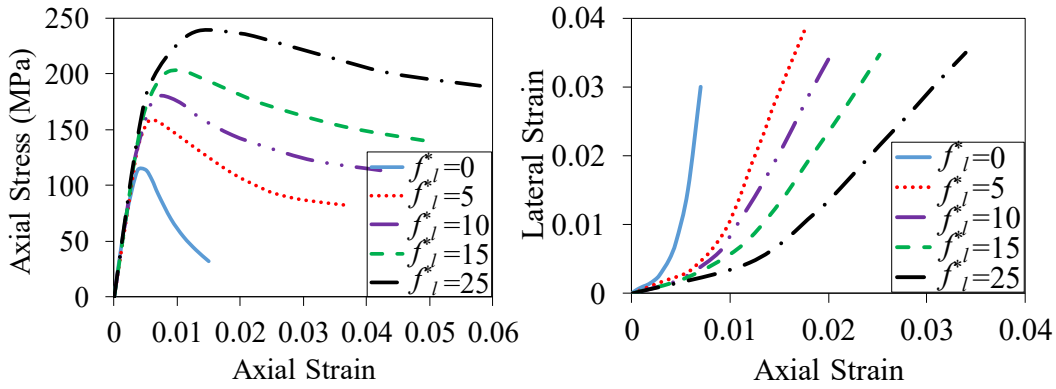

(d)

Figure 11.5. Variation of axial stress-axial strain and lateral strain-axial strain relationships with the level of confinement: a) C50-1; b) C50-2; c) C100-1; d) C100-2 mix

Peak and residual conditions

Table 11.5 presents the peak and residual stress and strain of actively confined SFRCs tested under different confining pressures. The peak state of the actively confined concrete is specified by the peak axial stress (f^*_{cc}) and peak axial strain (ε^*_{cc}), whereas the residual state is specified by the residual stress ($f_{c,res}$) and corresponding residual strain ($\varepsilon_{c,res}$). $f_{c,res}$ is defined as the strength of damaged concrete, generated through frictional actions, and it manifests as a stabilized plateau in the axial stress-strain curve, with the axial strain corresponding to the start of the plateau region is defined as $\varepsilon_{c,res}$.

Table 11.5. 28-day compression test results of the confined specimens

Specimens	f_l^* (MPa)	f_{cc}^* (MPa)	f_{cc}^*/f'_{co}	ε_{cc}^* (%)	$f_{c,res}$ (MPa)	$f_{c,res}/f_{cc}^*$	$\varepsilon_{c,res}$ (%)
C50-1-F5	5	80.3	1.55	0.63	53.1	0.66	3.95
C50-2-F5	5	94.1	1.47	0.64	60.1	0.64	4.27
C100-1-F5	5	134.7	1.31	0.51	73.1	0.54	3.31
C100-2-F5	5	145.7	1.28	0.54	78.1	0.53	3.70
C50-1-F10	10	112.1	2.17	0.98	80.3	0.72	4.36
C50-2-F10	10	127.4	1.99	0.99	90.8	0.71	4.67
C100-1-F10	10	167.1	1.62	0.69	110.6	0.66	3.91
C100-2-F10	10	178.1	1.57	0.73	113.4	0.64	4.22
C50-1-F15	15	134.6	2.60	1.39	109.2	0.81	5.20
C50-2-F15	15	151.3	2.36	1.40	122.5	0.80	5.61
C100-1-F15	15	192.2	1.86	0.88	136.5	0.71	4.50
C100-2-F15	15	203.2	1.79	0.92	140.3	0.69	4.92
C50-1-F25	25	165.5	3.20	2.25	149.1	0.90	6.02
C50-2-F25	25	185.1	2.89	2.26	166.5	0.89	6.40
C100-1-F25	25	225.7	2.19	1.29	179.3	0.79	5.49
C100-2-F25	25	238.3	2.10	1.33	186.2	0.78	5.81

Peak condition

In order to investigate the confinement effectiveness of SFRCs, the relationship between the strength (k_1) and strain (k_2) enhancement coefficient and f^*_l is studied. Figures 11.6(a) and (b) shows the variation of k_1 and k_2 with f^*_l, respectively. k_1 and k_2 are defined by the following simple expressions, which are widely used in the literature:

$$f^*_{cc}/f'_{co} = 1 + k_1(f^*_l/f'_{co}) \tag{11.1}$$

$$\varepsilon^*_{cc}/\varepsilon_{co} = 1 + k_2(f^*_l/f'_{co}) \tag{11.2}$$

It can be seen in Fig. 11.6 that k_1 and k_2 of both C50 and C100 series SFRCs increased with an increase in V_f at a given f^*_l, owing to the additional confining pressure provided by the internal steel fibers [7]. As can also be seen in Fig. 11.6, C50 group mixes had a slightly lower k_1 but a higher k_2 than those of C100 group mixes.

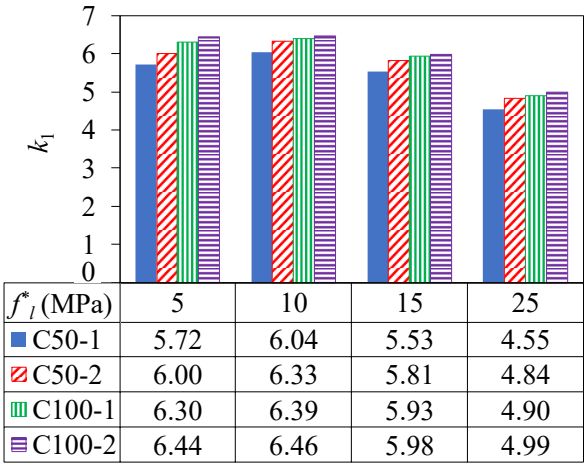

f^*_l (MPa)	5	10	15	25
C50-1	5.72	6.04	5.53	4.55
C50-2	6.00	6.33	5.81	4.84
C100-1	6.30	6.39	5.93	4.90
C100-2	6.44	6.46	5.98	4.99

(a)

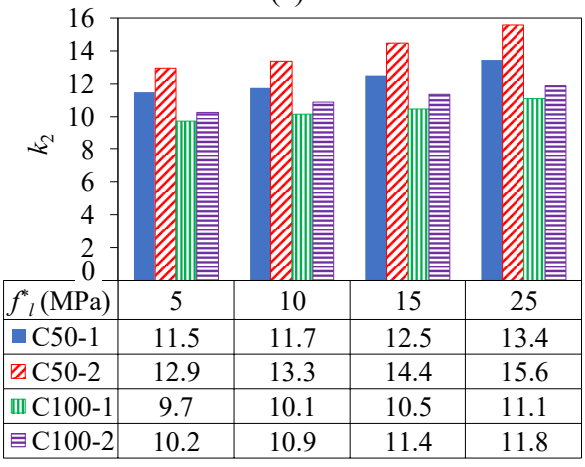

f^*_l (MPa)	5	10	15	25
C50-1	11.5	11.7	12.5	13.4
C50-2	12.9	13.3	14.4	15.6
C100-1	9.7	10.1	10.5	11.1
C100-2	10.2	10.9	11.4	11.8

(b)

Figure 11.6. Variation of (a) strength enhancement coefficient (k_1) and (b) strain enhancement coefficient (k_2) of different mixes with confining pressure (f^*_l)

Figures 11.7(a) and (b) show the effect of the confinement level on the peak stress ratio (f^*_{cc}/f'_{co}) and peak strain ratio ($\varepsilon^*_{cc}/\varepsilon_{co}$) of different SFRC mixes, respectively. It can be seen in Figs. 11.7(a) and (b) that, in both C50 and C100 mixes, f^*_{cc}/f'_{co} and $\varepsilon^*_{cc}/\varepsilon_{co}$ increased with an increase in f^*_l at a given V_f. An increase in f^*_l from 5 to 25 MPa resulted in a 106%, 97%, 67%, and 64% increase in f^*_{cc}/f'_{co} and 255%, 252%, 151%, and 149% increase in $\varepsilon^*_{cc}/\varepsilon_{co}$ of C50-1, C50-2, C100-1, and C100-2 mixes, respectively. Higher increases observed in f^*_{cc} and ε^*_{cc} of C50 mixes compared to those of C100 mixes are attributed to the higher confinement ratio (f^*_l/f'_{co}) of C50 mixes than that of C100 mixes. As can also be seen in the figures, f^*_{cc}/f'_{co} and $\varepsilon^*_{cc}/\varepsilon_{co}$ of the C50 and C100 group mixes slightly decreased with an increase in V_f at a given f^*_l and the reduction became more pronounced with an increase in f^*_l. This observation is attributed to the higher f'_{co} and ε_{co} of mixes with $V_f = 2\%$ compared to those of companion mixes with $V_f = 1\%$; although, SFRCs with $V_f = 2\%$ exhibited a higher confinement effectiveness (i.e. higher k_1 and k_2) than those with $V_f = 1\%$.

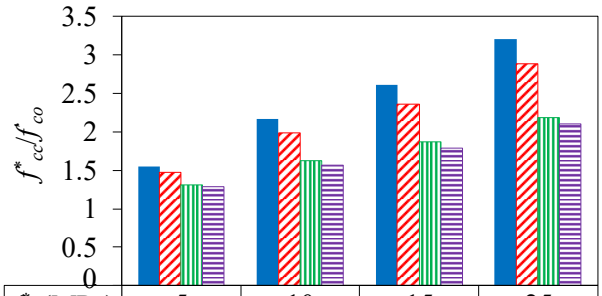

f^*_l (MPa)	5	10	15	25
C50-1	1.55	2.17	2.60	3.20
C50-2	1.47	1.99	2.36	2.89
C100-1	1.31	1.62	1.86	2.19
C100-2	1.28	1.57	1.79	2.10

(a)

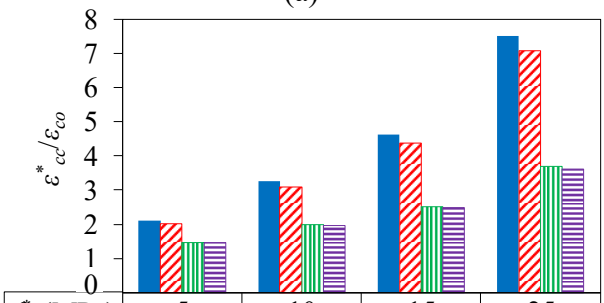

f^*_l (MPa)	5	10	15	25
C50-1	2.11	3.27	4.62	7.50
C50-2	2.01	3.08	4.38	7.07
C100-1	1.47	1.98	2.52	3.69
C100-2	1.45	1.96	2.50	3.61

(b)

Figure 11.7. Variation of (a) peak stress ratio (f^*_{cc}/f'_{co}) and (b) peak strain ratio ($\varepsilon^*_{cc}/\varepsilon_{co}$) of different mixes with confining pressure (f^*_l)

Residual condition

Figures 11.8(a) and (b) illustrate the variation of the residual strength ratio ($f_{c,res}/f'_{co}$) and residual strain ratio ($\varepsilon_{c,res}/\varepsilon_{co}$) of different mixes with f^*_l, respectively. It can be seen in the figures that, at a given V_f, $f_{c,res}/f'_{co}$ and $\varepsilon_{c,res}/\varepsilon_{co}$ of SFRCs increased with an increase in f^*_l. An increase in f^*_l from 5 to 25 MPa led to a 180%, 177%, 145%, and 138% increase in $f_{c,res}/f'_{co}$ of C50-1, C50-2, C100-1, and C100-2 mixes, respectively, indicating that the increases in $f_{c,res}/f'_{co}$ of C50 mixes with an increase in f^*_l were more significant than those of C100 mixes. This is, once again, attributed to the higher f^*_l/f'_{co} of C50 mixes compared to that of C100 mixes. As can also be seen in Fig. 11.8(a), at a given f^*_l, $f_{c,res}/f'_{co}$ of SFRCs decreased with an increase in V_f, which is attributed to the higher f'_{co} of SFRCs with V_f = 2% in comparison with those of companion mixes with V_f = 1%. Furthermore, at a given f^*_l, although SFRCs with V_f = 2% had a slightly lower $f_{c,res}/f^*_{cc}$ (shown in Table 11.5) than those with V_f = 1%, the post-peak descending branch of SFRCs with V_f = 2% exhibited a lower slope owing to their significantly higher $\varepsilon_{c,res}$ than those of companion mixes with V_f = 1%. Figure 11.8(b) shows that the increases seen in $\varepsilon_{c,res}/\varepsilon_{co}$ of C50 mixes (~51%) with an increase in f^*_l from 5 MPa to 25 MPa were less than those of C100 mixes (~60%). As can also be seen in Fig. 11.8(b), $\varepsilon_{c,res}/\varepsilon_{co}$ of C50 and C100 mixes slightly increased with an increase in V_f at a given f^*_l. This observation is, once again, because of the higher additional confinement actions provided by steel fibers in SFRCs with V_f = 2%, although f^*_l/f'_{co} of these specimens was lower.

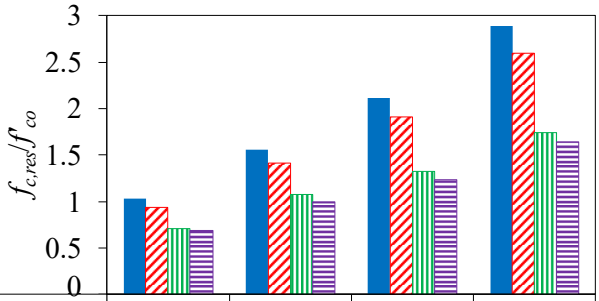

f^*_l (MPa)	5	10	15	25
C50-1	1.03	1.55	2.11	2.88
C50-2	0.94	1.42	1.91	2.60
C100-1	0.71	1.07	1.32	1.74
C100-2	0.69	1.00	1.24	1.64

(a)

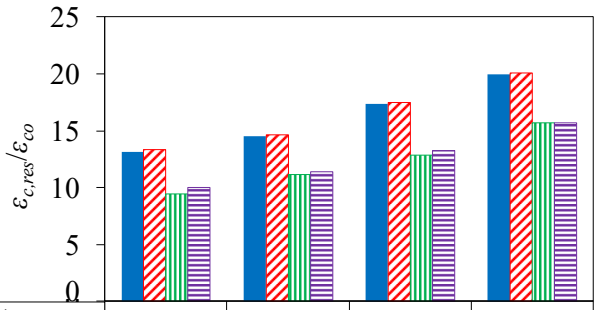

f^*_l (MPa)	5	10	15	25
C50-1	13.2	14.6	17.3	20.0
C50-2	13.3	14.6	17.5	20.1
C100-1	9.5	11.2	12.9	15.7
C100-2	10.0	11.4	13.3	15.7

(b)

Figure 11.8. Variation of (a) residual strength ratio ($f_{c,res}/f'_{co}$) and (b) residual strain ratio ($\varepsilon_{c,res}/\varepsilon_{co}$) of different mixes with confining pressure (f^*_l)

CONCLUSIONS

An experimental study on the compressive behaviour of actively confined SFRCs under axial compression has been presented. The following conclusions can be drawn based on the results and discussions presented in this study:

1- The peak and residual axial stress and strain of SFRCs increase with an increase in the confinement level. At a given confinement level, an increase in the steel fiber volume fraction results in an increase in the peak and residual stress and strain of SFRCs.

2- Axial stress-strain curves of SFRCs with a higher steel fiber volume fraction exhibit a more shallow post-peak descending branch than those of SFRCs with a lower steel fiber volume fraction. This improved behaviour is because of the higher additional confinement actions provided by internal steel fibers in SFRCs with a higher steel fiber volume fraction.

3- Under a given confining pressure, the dilation rate of SFRCs decreases with an increase in the steel fiber volume fraction, which is attributed to the bridging effect of steel fibers across the cracks that becomes more pronounced at a higher steel fiber volume fraction.

4- An increase in the steel fiber volume fraction results in an increase in strength and strain enhancement coefficients of SFRCs at a given confining pressure.

Findings of this study suggest that ultra high-strength micro steel fibers can be successfully incorporated into concrete for the development of high-performance composite structural members where the concrete is to be subjected to lateral confinement, such as columns designed for seismic and blast resistance.

ACKNOWLEDGEMENTS

The authors thank Mr. Liu and Mesdames Yang and Liu for completing the tests reported in this paper as part of their Master's thesis.

REFERENCES

[1] Vincent T, Ozbakkaloglu T. Influence of concrete strength and confinement method on axial compressive behavior of FRP confined high- and ultra high strength concrete. *Composites Part B*. 2013;50:413–28.

[2] Lim JC, Ozbakkaloglu T. Unified stress-strain model for FRP and actively confined normal-strengh and high-strength concrete. *Journal of Composites for Construction.* 2014;19(4):04014072.

[3] Caballero-Morrison KE, Bonet JL, Navarro-Gregori J, Serna-Ros P. An experimental study of steel fiber-reinforced high-strength concrete slender columns under cyclic loading. *Engineering Structures*. 2013;57:565-77.

[4] Bencardino F, Rizzuti L, Spadea G, Swamy RN. Stress-strain behavior of steel fiber-reinforced concrete in compression. *Journal of Materials in Civil Engineering.* 2008;20(3):255-63.

[5] Zohrevand P, Mirmiran A. Stress-strain model of ultrahigh performance concrete confined by fiber-reinforced polymers. *Journal of Materials in Civil Engineering.* 2013;25(12):1822-9.

[6] Madandoust R, Ranjbar MM, Ghavidel R, Shahabi F. Assessment of factors influencing mechanical properties of steel fiber reinforced self-compacting concrete. *Materials & Design*. 2015;83:284-94.

[7] Xie T, Ozbakkaloglu T. Behavior of steel fiber-reinforced high-strength concrete-filled FRP tube columns under axial compression. *Engineering Structures.* 2015;90:158-71.

[8] Afroughtsabet V, Ozbakkalgolu T. Mechanical and durability properties of high-strength concrete containing steel and polypropylene fibers. *Construction and Building Materials.* 2015;94:73-82.

[9] Afroughtsabet V, Biolzi L, Ozbakkaloglu T. High-performance fiber-reinforced concrete: a review. *Journal of Materials Science*. 2016;51:6517-51.

[10] Afroughtsabet V, Biolzi L, Ozbakkaloglu T. Influence of double hooked-end steel fibers and slag on mechanical and durability properties of high perfoemance recycled aggregate concrete. *Composite Structures*. 2017;181:273-84.

[11] Ayan E, Saatcioglu O, Turanli L. Parameter optimization on compressive strength of steel fiber reinforced high strength concrete. *Construction and Building Materials.* 2011;25(6):2837–44.

[12] Ou YC, Tsai MS, Liu KY, Chang KC. Compressive behavior of steel-fiber reinforced concrete with a high reinforcing index. *Journal of Materials in Civil Engineering.* 2011;24(2):207–15.

[13] Hassan AMT, Jones SW, Mahmud GH. Experimental test methods to determine the uniaxial tensile and compressive behaviour of ultra high performance fibre reinforced concrete (UHPFRC). *Construction and Building Materials.* 2012;37:874–82.

[14] Tokgoz S, Dundar C. Tests of eccentrically loaded L-shaped section steel fibre high strength reinforced concrete and composite columns. *Engineering Structures.* 2012;38:134–41.

[15] Oliver J, Mora DF, Huespe AE, Weyler R. A micromorphic model for steel fiber reinforced concrete. *International Journal of Solids and Structures*. 2012;49(21):2990-3007.

[16] Kaïkea A, Achoura D, Duplan F, Rizzuti L. Effect of mineral admixtures and steel fiber volume contents on the behavior of high performance fiber reinforced concrete. *Materials & Design*. 2014;63:493-9.

[17] Dügenci O, Haktanir T, Altun F. Experimental research for the effect of high temperature on the mechanical properties of steel fiber-reinforced concrete. *Construction and Building Materials*. 2015;75:82-8.

[18] Wu Z, Shi C, He W, Wu L. Effects of steel fiber content and shape on mechanical properties of ultra high performance concrete. *Construction and Building Materials.* 2016;103:8-14.

[19] Hannawi K, Bian H, Prince-Agbodjan W, Raghavan B. Effect of different types of fibers on the microstructure and the mechanical behavior of ultra-high performance fiber-reinforced concretes. *Composites Part B*. 2016;86:214-20.

[20] Gesoglu M, Güneyisi E, Muhyaddin GF, Asaad DS. Strain hardening ultra-high performance fiber reinforced cementitious composites: Effect of fiber type and concentration. *Composites Part B*. 2016;103:74-83.

[21] Li B, Xu L, Chi Y, Huang B, Li C. Experimental investigation on the stress-strain behavior of steel fiber reinforced concrete subjected to uniaxial cyclic compression. *Construction and Building Materials*. 2017;140:109-18.

[22] Wu Z, Shi C, He W, Wang D. Static and dynamic compressive properties of ultra-high performance concrete (UHPC) with hybrid steel fiber reinforcements. *Cement and Concrete Composites* . 2017;79:148-57.

[23] Rousakis T, Karabinis A, Kiousis P, Tepfers R. Analytical modelling of plastic behavior of uniformly FRP confined concrete members. *Composites Part B.* 2008;39(7-8):1104-13.

[24] Ilki A, Peker O, Karamuk E, Demir C, Kumbasar N. FRP retrofit of low and medium strength circular and rectangular reinforced concrete columns. *Journal of Materials in Civil Engineering.* 2008;20(2):169-88.

[25] Kusumawardaningsih Y, Hadi MNS. Comparative behaviour of hollow columns confined with FRP composites. *Composite Structures*. 2010;93(1):198-205.

[26] Smith ST, Kim SJ, Zhang H. Behavior and effectiveness of FRP wrap in the confinement of large concrete cylinders. *Journal of Composites for Construction.* 2010;14(5):573-82.

[27] Wu YF, Jiang JF. Effective strain of FRP for confined circular concrete columns. *Composite Structures*. 2013;95:479–91.

[28] Ozbakkaloglu T, Vincent T. Axial compressive behavior of circular high-strength concrete-filled FRP tubes. *Journal of Composites for Construction*. 2014;18(2):04013037.

[29] Dundar C, Erturkmen D, Tokgoz S. Studies on carbon fiber polymer confined slender plain and steel fiber reinforced concrete columns. *Engineering Structures*. 2015;102:31-9.

[30] Deng ZC, Qu JL. The experimental studies on behavior of ultrahigh-performance concrete confined by hybrid fiber-reinforced polymer tubes. *Advances in Materials Science and Engineering*. 2015.

[31] Mansouri I, Gholampour A, Kisi O, Ozbakkaloglu T. Evaluation of peak and residual conditions of actiely confined concrete using neuro-fuzzy and neural computing techniques. *Neural Computing and Applications*. 2016;10.1007/s00521-016-2492-4.

[32] Ozbakkaloglu T, Gholampour A, Lim JC. Damage-plasticity model for FRP-confined normal-strength and high-strength concrete. *Journal of Composites for Construction.* 2016;10.1061/(ASCE)CC.1943-5614.0000712.

[33] Lim JC, Ozbakkaloglu T, Gholampour A, Bennett T, Sadeghi R. Finite-element modeling of actively confined normal-strength and high-strength concrete under uniaxial, biaxial, and triaxial compression. *Journal of Structural Engineering.* 2016;10.1061/(ASCE)ST.1943-541X.0001589.

[34] Gholampour A, Ozbakkaloglu T, Hassanli R. Behavior of rubberized concrete under active confinement. *Construction and Building Materials*. 2017;138:372-82.

[35] Gholampour A, Ozbakkaloglu T. Understanding the compressive behavior of shape memory alloy (SMA)-confined normal- and high-strength concrete. *Composite Structures*. 2018;202:943-53.

[36] Ramesh K, Seshu DR, Prabhakar M. Constitutive behaviour of confined fibre reinforced concrete under axial compression. *Cement and Concrete Composites.* 2003;25:343-50.

[37] Lu Y, Liu Z, Li S, Hu J. Axial compression behavior of hybrid fiber reinforced concrete filled steel tube stub column. *Construction and Building Materials*. 2018;174:96-107.

[38] Lu X, Hsu CT. Behavior of high strength concrete with and without steel fiber reinforcement in triaxial compression. *Cement and Concrete Research*. 2016;36:1679-85.

[39] Wang ZL, Zhu HH, Wang JG, Zhu B. Experimental study on macroscopic mechanical behavior of SFRC under triaxial compression. *Mechanics of Advanced Materials and Structures*. 2012;19(8):653-62.

[40] ASTM C143/C143M-12, *Standard Test Method for Slump of Hydraulic-Cement Concrete*, West Conshohocken, ASTM International, 2012.

[41] ASTM C642-13, *Standard Test Method for Density, Absorption, and Voids in Hardened Concrete*, West Conshohocken, ASTM International, 2013.

[42] ASTM C192/C192M-07, *Standard Practice for Making and Curing Concrete Test Specimens in the Laboratory*, West Conshohocken, PA, USA, ASTM International, 2007.

[43] ASTM C39/C39M-16b, *Standard Test Method for Compressive Strength of Cylindrical Concrete Specimens*, West Conshohocken, PA, USA, ASTM International, 2016.

[44] Gholampour A, Ozbakkaloglu T. Behavior of steel fiber-reinforced concrete-filled FRP tube columns: experimental results and a finite element model. *Composite Structures*. 2018;194:252-62.

Statement of Authorship

Title of Paper	Behavior of steel fiber-reinforced concrete-filled FRP tube columns: experimental results and a finite element model
Publication Status	☑ Published ☐ Accepted for Publication ☐ Submitted for Publication ☐ Unpublished and Unsubmitted work written in manuscript style
Publication Details	Gholampour A, Ozbakkaloglu T. Behavior of steel fiber-reinforced concrete-filled FRP tube columns: experimental results and a finite element model. *Composite Structures*. 2018;194:252-62.

Principal Author

Name of Principal Author (Candidate)	Aliakbar Gholampour		
Contribution to the Paper	Literature review, modelling and analysis, and preparation of the manuscript.		
Overall percentage (%)	80%		
Certification:	This paper reports on original research I conducted during the period of my Higher Degree by Research candidature and is not subject to any obligations or contractual agreements with a third party that would constrain its inclusion in this thesis. I am the primary author of this paper.		
Signature		Date	31/01/2019

Co-Author Contributions

By signing the Statement of Authorship, each author certifies that:

i. the candidate's stated contribution to the publication is accurate (as detailed above);

ii. permission is granted for the candidate in include the publication in the thesis; and

iii. the sum of all co-author contributions is equal to 100% less the candidate's stated contribution.

Name of Co-Author	Togay Ozbakkaloglu		
Contribution to the Paper	Research supervision and review of manuscript.		
Signature		Date	31/01/2019

Name of Co-Author			
Contribution to the Paper			
Signature		Date	

Please cut and paste additional co-author panels here as required.

Behaviour of Steel Fiber-Reinforced Concrete-Filled FRP Tube Columns: Experimental Results and a Finite Element Model

ABSTRACT

This paper presents the results of an experimental study together with the first finite element (FE) model for the compressive behaviour of fiber-reinforced polymer (FRP)-confined steel fiber-reinforced concrete (SFRC). 73 existing experimental test results of FRP-confined and actively confined SFRC specimens tested under axial compression were initially assembled. Additional axial compression tests were conducted on 16 actively confined SFRC specimens to address the gaps in the existing test database to compile a reliable database for the FE modelling of FRP-confined SFRCs. The analysis of experimental test results revealed that the compressive behaviour of FRP-confined SFRCs is influenced by the steel fiber volume fraction and aspect ratio. New expressions were developed for the hoop rupture strain of the FRP jacket, axial strain-lateral strain relationship of FRP-confined and actively confined SFRC, and relationship between the confining pressure and the compressive strength of actively confined SFRC by considering the influences of the volume fraction and aspect ratio of internal steel fibers. A recently developed concrete damage-plasticity model, which was shown to be the most accurate currently available model for confined plain concrete, was adopted for the prediction of the compressive behaviour of FRP-confined SFRC. The failure surface and flow rule of the model were modified based on the results from actively and FRP-confined SFRC. The results show that model predictions of the axial stress-axial strain, lateral strain-axial strain, axial stress-volumetric strain, plastic volumetric strain-axial plastic strain, and plastic dilation angle-axial plastic strain relationships are in good agreement with the experimental results of FRP-confined SFRC. The new model provides improved accuracy over the best performing existing models of FRP-confined plain concrete in predicting the behaviour of FRP-confined SFRC.

KEYWORDS: Steel fiber-reinforced concrete (SFRC); Fiber-reinforced polymer (FRP); Confined concrete; Stress-strain relationship; Concentric compression; Finite element (FE) modelling.

INTRODUCTION

The addition of internal steel fibers to concrete is a popular technique that is used for improving the inherent brittle behaviour of plain concrete [1-4]. Likewise, lateral confinement of concrete results in a significant improvement in the ductility of concrete under compression [5-17]. Therefore, fiber-reinforced polymer (FRP)-confined steel fiber reinforced concrete (SFRC), as an ultra-high performance system, can be considered as a higher performance alternative with further enhanced mechanical properties to conventional FRP-confined plain concrete. As shown previously, the existence of steel fiber decreases isolated major crack formations in the concrete and results in a more even and controlled cracking [18]. In the case of FRP-confined SFRC, this in turn leads to reduced stress concentrations on the FRP jacket leading to higher FRP hoop rupture strains and ductility [19].

A number of experimental studies have been performed recently to understand the mechanical behaviour of FRP-confined SFRCs [19-22]. Only the two of these studies experimentally investigated the mechanical behaviour of FRP-confined SFRCs confined under concentric axial compression [19,20]. The remaining two were concerned with FRP-confined SFRC containing internal steel reinforcing bars under eccentric loading [21] and SFRCs confined by hybrid FRP tubes [22]. Existing studies have shown that steel fiber parameters (i.e. volume fraction (V_f) and aspect ratio (A_R)) influence the stress-strain relationship of the concrete. It was shown that at a given V_f, an increase in A_R leads to a decrease in the compressive strength (f'_{cc}), ultimate axial strain (ε_{cu}), and hoop rupture strain ($\varepsilon_{h,rup}$) of concrete. On the other hand, an increase in V_f at a given A_R resulted in an increase in f'_{cc}, ε_{cu}, and $\varepsilon_{h,rup}$ [19].

Finite element (FE) method has been extensively used to accurately model the mechanical behaviour of confined plain concrete. Although a relatively large number of studies have been reported on the FE modelling of FRP-confined plain

concrete [23-31], no study has been reported to date on the FE modelling of the FRP-confined SFRC. Furthermore, most of the existing FE models for FRP-confined plain concrete were based on an approach that was recently shown to be inaccurate, especially for high-strength concrete (HSC) [32,33]. Therefore, there is a clear need for additional numerical studies to better understand the constitutive behaviour of FRP-confined SFRC. As discussed in detail in Refs. [31,34], concrete damage-plasticity approach, which was proposed by Lubliner et al. [35] and later modified by Lee and Fenves [36], provides a more accurate prediction of the constitutive behaviour of confined concretes than the pure plasticity and damage approaches. In order to investigate the constitutive behaviour of the FRP-confined concrete by damage-plasticity approach, it is required to establish experimental databases for both FRP-confined and actively confined concrete [31]. The review of the literature indicates that only two experimental studies have investigated the compressive behaviour of actively confined SFRCs [1,37], the results of which would not be sufficient for the development of an accurate FE model. To address this research gap, in the current study additional experimental tests were performed on actively confined SFRCs to compile a reliable database that would enable FE modelling of FRP-confined SFRCs.

This paper presents the first study on FE modelling of FRP-confined SFRC. Existing experimental test results of FRP-confined and actively confined SFRC specimens tested under axial compression were initially assembled and additional axial compression tests were conducted on actively confined SFRC specimens to address the gaps in the existing test database to provide a reliable database for the constitutive behaviour of FRP-confined SFRCs. The new concrete damage-plasticity model with developed failure surface and flow rule is implemented in a FE program ABAQUS [38] through the use of a script (given in Appendix 4) for the prediction of: i) axial stress-axial strain, ii) lateral strain-axial strain, iii) axial stress-volumetric strain, iv) plastic volumetric strain-axial plastic strain, and v) plastic dilation angle-axial plastic strain relationships. The FE modelling results show that model predictions are in good agreement with the experimental results of FRP-confined SFRC. Comparisons between the FE modelling and experimental results show that the new model provides improved accuracy compared to the predictions of Lim and Ozbakkaloglu's model [39], which was originally proposed for

conventional concrete and shown to provide the most accurate predictions of FRP-confined plain concrete among existing models. The availability of such an accurate model is of vital importance for practical applications of this highly promising FRP-confined SFRC composite system.

EXPERIMENTAL TEST DATABASES

Existing test database

The databases of FRP-confined and actively confined SFRCs were assembled based on the results available in the open literature. Tables 12.1 and 12.2 show the details of these databases. The FRP-confined and actively confined SFRCs databases contained 32 and 41 datasets respectively, obtained from four experimental studies published between 2006 and 2015 [1,19,20,37].

The FRP-confined SFRC database is composed of specimens confined by three types of FRP materials: carbon FRP (CFRP), glass FRP (GFRP), and aramid FRP (AFRP). FRP confinement was provided by manual wet lay-up technique in the hoop direction. The FRP-confined SFRC database presented in Table 12.1 consists of the following information for each specimen: specimen's geometric properties (diameter D and height H), total fiber thickness (t_f), tensile strength of fibers in FRP jacket (f_f), unconfined concrete strength (f'_{co}), steel fiber volume fraction (V_f), steel fiber aspect ratio ($A_R = l_f/d_f$, where l_f is the steel fiber length and d_f is the equivalent fiber diameter), tensile strength of internal steel fibers (f_{sf}), compressive strength (f'_{cc}), and ultimate axial strain (ε_{cu}). The actively confined SFRC database presented in Table 12.2 consists of the following information for each specimen: specimen's geometric properties (D and H), f'_{co}, V_f, A_R, f_{sf}, and peak compressive strength (f^*_{cc}) and corresponding axial strain (ε^*_{cc}). Five steel fiber volume fractions (V_f) of 0%, 1%, 1.5%, 2%, and 2.5% and three steel fiber aspect ratios (A_R) of 37, 60, and 67 were used in the specimens included in this database.

Table 12.1. Existing test results of FRP-confined SFRC

Study	Group	Specimen ID	Specimen Dimension (mm)	FRP Type	t_f (mm)	f_f (MPa)	f'_{co} (MPa)	V_f (%)	A_R	l_f (mm)	d_f (mm)	Steel Fiber Type	f_{Sf} (MPa)	f'_{cc} (MPa)	ε_{cu} (%)	$\varepsilon_{h,rup}$ (%)
Xie and Ozbakkaloglu [19]	U120-1	V1.5A67F28	ø152 × 305	AFRP	1.2	2600	131.6	1.5	67	60	0.90	Hooked end	1050	179.8	1.91	1.23
		V1.5A67F27					124.6							171.3	1.78	1.19
		V1.5A67F26					132.7							169.7	1.68	1.14
		V2.5A67F31					123.9	2.5						191.6	2.00	1.37
		V2.5A67F38					131.4							204.7	2.50	1.68
		V2.5A67F26					124.2							191.2	1.95	1.11
	U120-2	V1.5A37F32					124.0	1.5	37	31	0.85	Hooked end	1200	191.8	2.05	1.40
		V1.5A37F33					127.1							188.1	1.82	1.42
		V1.5A37F28					126.4							185.2	1.95	1.20
		V2.5A37F40					122.5	2.5						199.9	2.65	1.75
		V2.5A37F34					126.4							195.3	2.16	1.49
		V2.5A37F42					124.8							204.1	2.31	1.86
	U120-3	V0A0F22					123.5	0	0	–	–	–	–	174.0	2.07	0.96
		V0A0F24					125.7							180.6	2.16	1.07
Zohrevand and Mirmiran [20]	U190-1	V2.0A65F20	ø108 × 191	GFRP	3.06*	610*	194.0	2.0	67	13	0.19	Straight	2800	226.6	0.86	1.20
		V2.0A65F26			4.08*		185.0							273.5	1.06	1.35
		V2.0A65F33			5.10*		190.0							298.9	1.15	1.40
	U190-2	V2.0A65F21		CFRP	2.04*	850*	185.4							254.1	0.68	0.69
		V2.0A65F41			4.08*		185.4							372.2	1.05	0.80

f_f is the tensile strength of fibers in FRP jacket; f_{sf} is the tensile strength of internal steel fibers
* Properties of FRP tube

Table 12.2. Existing test results of actively confined SFRC

Study	Specimen ID	Specimen Dimension (mm)	f'_{co} (MPa)	V_f (%)	A_R	l_f (mm)	d_f (mm)	Steel Fiber Type	f_{Sf} (MPa)	f^*_{cc} (MPa)	ε^*_{cc} (%)
Lu and Hsu [1]	V0A0F*3.5	ø100 × 200	67.0	0	0	–	–	–	–	84.9	0.47
	V0A0F*7									99.0	0.78
	V0A0F*14									130.7	1.24
	V0A0F*14									132.7	1.25
	V0A0F*14									134.9	1.34
	V0A0F*14									135.5	1.37
	V0A0F*21									154.0	1.66
	V0A0F*21									157.1	1.83
	V0A0F*21									161.2	1.94
	V0A0F*28									180.2	2.50
	V0A0F*28									179.9	2.41
	V0A0F*42									229.1	3.20
	V0A0F*56									276.0	4.10
	V1A60F*7	ø100 × 200	69.0	1	60	30	0.50	Hooked end	1100	105.2	0.71
	V1A60F*14									136.8	1.27
	V1A60F*14									139.0	1.21
	V1A60F*21									164.1	1.70
	V1A60F*21									162.3	2.02
	V1A60F*28									186.5	2.57
	V1A60F*28									189.6	2.74
	V1A60F*28									191.6	2.44
	V1A60F*28									191.8	2.40
	V1A60F*28									189.6	2.52
	V1A60F*42									239.0	3.33
	V1A60F*56									282.2	4.22
	V1A60F*63									308.2	4.51
	V1A60F*70									324.1	4.82

"–" indicates there is not any steel fiber in the mix.

New tests on actively confined SFRC specimens

To extend the existing database of actively confined SFRC, four different batches of SFRCs were prepared and confined under hydraulic pressure applied by a Hoek cell. The geometry of the cylindrical specimens was prescribed by the geometry of the Hoek cell (i.e. 63×126 mm). Ultra high-strength micro steel fibers with A_R of 73 (l_f =13 mm and d_f=0.18 mm) were added to the SFRC mixes at two different V_f of 1% and 2%. Table 12.3 shows the concrete mix proportions of SFRC specimens. Natural sand and crushed basalt stone with a nominal maximum size of 10 mm were

used in the mixes as fine and coarse aggregates, respectively. C50 and C100 mixes were designed to develop a 28-day compressive strength of 50 MPa and 100 MPa and they had a water-to-binder ratio (*w/b*) of 0.479 and 0.295, respectively. Silica fume was used in C100 mixes to achieve a high compressive strength and polycarboxylic ether polymer-based superplasticizer was used in both C50 and C100 mixes in order to achieve sufficient workability. The workability of fresh SFRC was evaluated by a slump test, which was performed in accordance with ASTM C143/C143M [40].

Table 12.3. Mix proportions of the concrete

Concrete mix	C50-1	C50-2	C100-1	C100-2
Cement (kg/m^3)	375	375	506	506
Silica fume (kg/m^3)	–	–	44	44
Sand (kg/m^3)	720	720	700	700
Coarse Aggregate (kg/m^3)	1053	1026	1023	996
Water (kg/m^3)	176	176	145	145
Superplasticizer (kg/m^3)	5	5	25	25
w/b *	0.479	0.479	0.295	0.295
Volume Fraction (V_f) (%)	1	2	1	2
Fiber (kg/m^3)	78	156	78	156
Slump (mm)	140	125	175	130

* Including the water coming from the superplasticizer (i.e. 70% water by weight)

Constant confining pressures (f^*_l) of 5, 10, 15, and 25 MPa were applied on the specimens using a Hoek cell to investigate the effect of different confinement levels ranging from low to high level on the behaviour of SFRC. Axial compression tests were conducted with a displacement control at a rate of 0.18 mm/min using a 1000-kN capacity universal testing machine in accordance with ASTM C39/C39M-16b [41]. Figure 12.1 shows the instrumentation and test setup of specimens under compression loading. The axial strain of the specimens was measured by two linear variable displacement transformers (LVDTs) mounted at the corners of steel loading and supporting plates. One axial strain gauge mounted at the mid-height of the specimen was also used to validate and correct the LVDT measurements at the early stages of the loading. Two lateral strain gauges were also placed at the mid-height of the specimen to obtain the lateral strains. Table 12.4 presents the compression test results of actively confined SFRCs. In the table, ε^*_{lc} is the lateral strain corresponding to f^*_{cc} and ε^*_{cc}.

Figure 12.1. Instrumentation and test setup used in compression tests

Table 12.4. 28-day compression test results of actively confined SFRC

Specimens	f'_{co} (MPa)	V_f (%)	A_R	l_f (mm)	d_f (mm)	Steel Fiber Type	f_{Sf} (MPa)	f^*_l (MPa)	f^*_{cc} (MPa)	ε^*_{cc} (%)	ε^*_{lc} (%)
C50-V1F*5	51.7	1	73	13	0.18	Straight	2850	5	80.3	0.63	0.43
C50-V2F*5	64.1	2							94.1	0.64	0.45
C100-V1F*5	103.2	1							134.7	0.51	0.25
C100-V2F*5	113.5	2							145.7	0.54	0.29
C50-V1F*10	51.7	1						10	112.1	0.98	0.68
C50-V2F*10	64.1	2							127.4	0.99	0.72
C100-V1F*10	103.2	1							167.1	0.69	0.39
C100-V2F*10	113.5	2							178.1	0.73	0.44
C50-V1F*15	51.7	1						15	134.6	1.39	0.79
C50-V2F*15	64.1	2							151.3	1.40	0.84
C100-V1F*15	103.2	1							192.2	0.88	0.45
C100-V2F*15	113.5	2							203.2	0.92	0.53
C50-V1F*25	51.7	1						25	165.5	2.25	1.00
C50-V2F*25	64.1	2							185.1	2.26	1.07
C100-V1F*25	103.2	1							225.7	1.29	0.67
C100-V2F*25	113.5	2							238.3	1.33	0.79

Specimen designation

In specimen labels in Tables 12.1, 12.2, and 12.4 the numbers after V, A, F, and F* represent the V_f in percentage, A_R, actual ultimate confining pressure ($f_{lu,a}$) of FRP jacket, and f^*_l of Hoek cell in MPa, respectively. For example, V1.5A67F28 represents the FRP-confined SFRC specimen with V_f of 1.5%, A_R of 67, and $f_{lu,a}$ of 28 MPa.

COMPRESSIVE BEHAVIOUR OF FRP-CONFINED SFRC

Figure 12.2 shows typical axial stress-axial strain and lateral strain-axial strain curves of actively confined and FRP-confined concretes. As can be seen in the figure, the peak condition of actively confined concrete is characterized by the peak stress (f^*_{cc}) and corresponding axial strain (ε^*_{cc}) and lateral strain (ε^*_{lc}). It can also be seen in Fig. 12.2 that the ultimate condition of the FRP-confined concrete is characterized by the compressive strength (f'_{cc}) and corresponding axial strain (ε_{cu}) and lateral strain ($\varepsilon_{h,rup}$) recorded at the rupture of the FRP jacket.

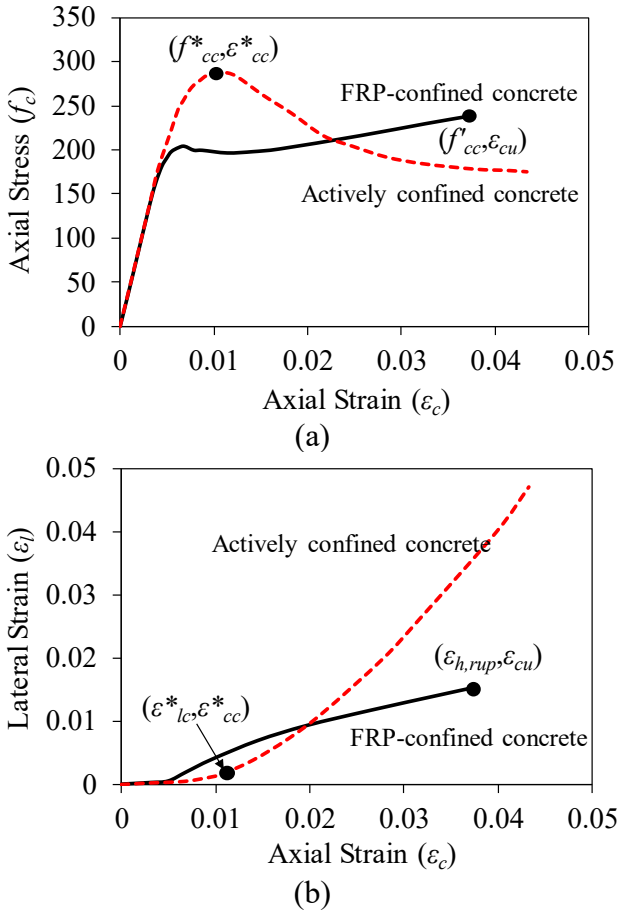

Figure 12.2. (a) Typical axial stress-axial strain curves and (b) lateral strain-axial strain curves of FRP-confined and actively confined concrete (adopted from Ref. [32])

As discussed in detail in Xie and Ozbakkaloglu [19], V_f and A_R have a notable influence on the compressive behaviour of FRP-confined SFRC. It was shown in Xie and Ozbakkaloglu [19] that, at a given A_R, an increase in V_f resulted in an increase in f'_{cc}, ε_{cu}, and $\varepsilon_{h,rup}$ of FRP-confined SFRC, and an increase in A_R at a given V_f led to a decrease in these properties. These observations suggest that existing models of FRP-confined plain concrete would not be able to accurately capture the compressive behaviour of FRP-confined SFRC. In this study, new expressions were developed for the hoop rupture strain, dilation relationship, and relationship between the confining pressure and the compressive strength by considering the influences of V_f and A_R on the Lim and Ozbakkaloglu's [39] expressions, which was shown to provide the most accurate predictions for FRP-confined plain concrete. It should be noted that, based on the initial assessment of experimental test results, the results of specimens containing crimped steel fibers were inconsistent with those of hooked end and straight steel fibers. Therefore, only the experimental database of hooked end and straight steel fibers were considered in the modelling. In addition, the experimental results of study by Wang et al. [37] were excluded from the modelling as these results exhibited significant fluctuations and in most cases were in disagreement with the overall trend of the database.

Hoop rupture strain of FRP jacket of FRP-confined SFRC

The expression proposed by Lim and Ozbakkaloglu [11] for $\varepsilon_{h,rup}$ of FRP jacket was modified by the incorporation of the hoop rupture strain coefficient (K_1) to allow for the important influences of V_f and A_R observed in FRP-confined SFRC.

$$\varepsilon_{h,rup} = k_{\varepsilon,rup}\varepsilon_f = \left[K_1\left(0.9 - 2.3f'_{co} \times 10^{-3} - 0.75E_f \times 10^{-6}\right)\right]\varepsilon_f \qquad (12.1)$$

where $k_{\varepsilon,rup}$ and ε_f are FRP hoop strain reduction factor and ultimate tensile strain of fibers in the FRP jacket, respectively. Figures 12.3(a) and 12.3(b) show the variation of experimentally determined K_1 with V_f at different A_R for FRP-confined concrete containing hooked end and straight steel fibers, respectively. The experimental values of K_1 were obtained by dividing the experimental $k_{\varepsilon,rup}$ of SFRCs with the experimental $k_{\varepsilon,rup}$ of the companion plain concrete. It can be seen in Fig. 12.3 that the trend of the experimental K_1 of specimens containing hooked end steel fibers is consistent with that of straight steel fibers, and at a given A_R, K_1

gradually increases with an increase in V_f. This observation can be attributed to the fact that, in SFRC with higher V_f, bridges formed by steel fibers across the cracks inside the concrete lead to a more even and controlled cracking of concrete, which in turn results in the reduction of isolated major cracks in concrete and associated stress concentrations on the FRP jacket [19]. Therefore, specimens with higher V_f exhibited higher FRP hoop rupture strains. On the other hand, as can be seen in Fig. 12.3(a), K_1 decreases with an increase in A_R at a given V_f. This can be attributed to the ability of steel fibers with lower aspect ratios to more effectively control the initiation and propagation of major cracks in concrete than their counterparts with a higher aspect ratio [37]. Based on these observations K_1 is defined as in Eq. 12.2 through the regression analysis of the test results.

$$K_1 = 1 + 6.1V_f/A_R \tag{12.2}$$

in which V_f is in percentage (%).

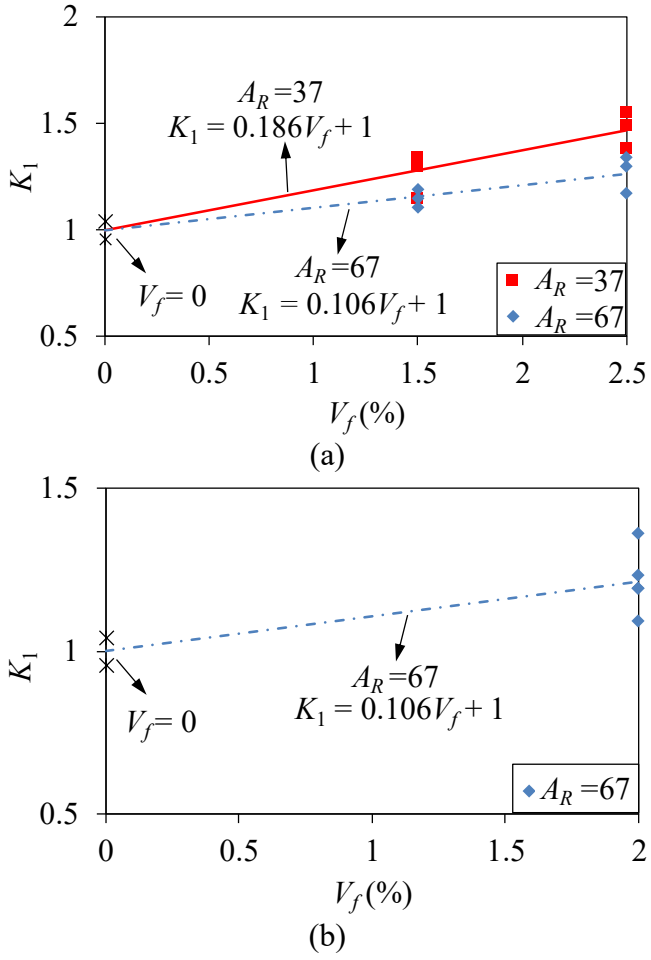

Figure 12.3. Variation of experimental values of K_1 with volume fraction (V_f): concrete containing (a) hooked end; (b) straight steel fibers

Figures 12.4(a) and 12.4(b) show comparisons of the experimental values of $k_{\varepsilon,rup}$ with the predictions obtained by the proposed expression for $k_{\varepsilon,rup}$ (Eq. 12.1) and $k_{\varepsilon,rup}$ determined by Lim and Ozbakkaloglu [11] expression, respectively. As can be seen in the figures, incorporation of K_1 into $k_{\varepsilon,rup}$ expression led to a higher accuracy over the existing model by Lim and Ozbakkaloglu [11].

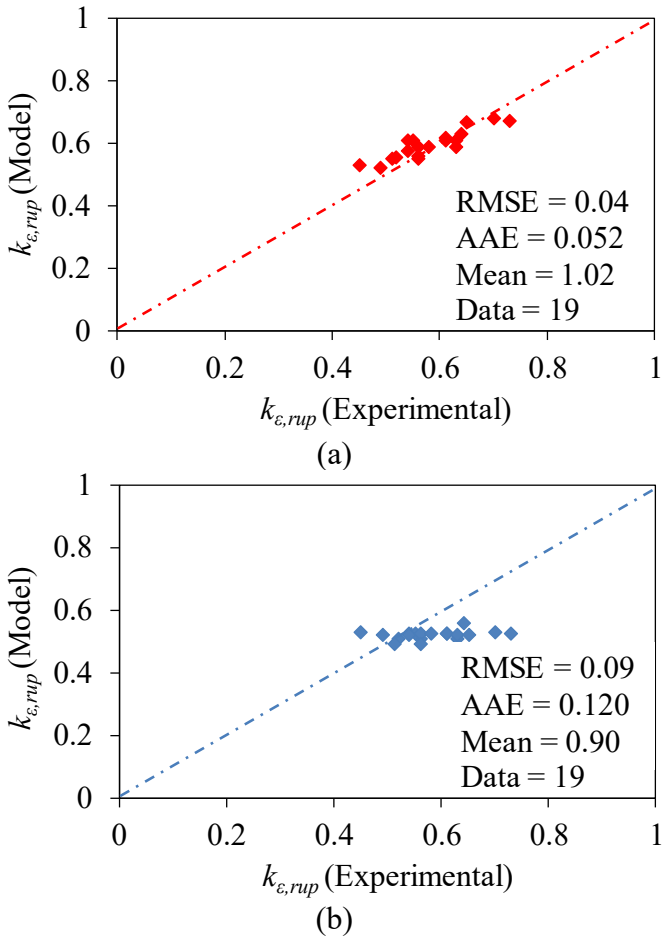

Figure 12.4. Comparison of the experimental values of FRP hoop strain reduction factor ($k_{\varepsilon,rup}$) with: (a) predictions of the proposed model; (b) predictions of model by Lim and Ozbakkaloglu [39]

Dilation behaviour of confined SFRC

Analysis of the test databases of FRP-confined and actively confined SFRC revealed that the steel fiber parameters of V_f and A_R had an influence on the dilation behaviour of SFRCs. It was found that the lateral strains corresponding to ε_{cu} in FRP-confined SFRC and ε^*_{cc} in actively confined SFRC increased with an increase in V_f and a decrease in A_R. The dilation relationship between lateral strain (ε_l) and axial strain (ε_c) proposed by Lim and Ozbakkaloglu [39], which was shown to be highly

accurate for both actively and FRP-confined plain concrete, was modified by incorporating the dilation coefficient (K_2) into the expression to consider the key influences of steel fiber parameters.

$$\varepsilon_c = \frac{\varepsilon_l}{\upsilon\left(1+\left(\frac{\varepsilon_l}{\upsilon\varepsilon_{co}}\right)^n\right)^{\frac{1}{n}}} + 0.04{\varepsilon_l}^{0.7}K_2\left(1 + 21\left(\frac{f_l}{f'_{co}}\right)^{0.8}\right) \quad (12.3)$$

where υ, ε_{co}, n, and f_l are the initial Poisson's ratio of concrete, axial strain corresponding to f'_{co}, curve shape parameter, and confining pressure, respectively. In Eq. 12.3, f_l is a variable parameter for the FRP-confined SFRC that gradually increases with an increase in ε_l until $\varepsilon_{h,rup}$ (determined using Eq. 12.1) is reached and the resulting $f_{lu,a}$ is developed. υ, ε_{co}, and n were adopted from Lim and Ozbakkaloglu [39], which are expressed as:

$$\upsilon = 8 \times 10^{-6}{f'_{co}}^2 + 0.0002f'_{co} + 0.138 \quad (12.4)$$

$$\varepsilon_{co} = \frac{{f'_{co}}^{0.225}}{1000}\left(\frac{152}{D}\right)^{0.1}\left(\frac{2D}{H}\right)^{0.13} \quad (12.5)$$

$$n = 1 + 0.03f'_{co} \quad (12.6)$$

in which f'_{co} is in MPa and D and H are in mm. Figures 12.5(a) and 12.5(b) show the variation of experimental K_2 with V_f at different A_R for FRP-confined concrete containing hooked end and straight steel fibers, respectively. As can be seen in Fig. 12.5, the trend of experimental K_2 of specimens containing hooked end steel fibers is consistent with that of straight steel fibers, and at a given A_R, K_2 gradually increases with an increase in V_f. This observation can be attributed to the lateral expansion of SFRC with higher V_f at a reduced rate due to the bridging effect of steel fibers [19,37]. It can also be seen in the figure that K_2 decreases with an increase in A_R at a given V_f, which can be explained by the lower internal confinement efficiency of steel fibers with higher A_R, leading to an increased lateral dilation rate of the resulting SFRC [19]. Based on the regression analysis, the following expression is proposed for K_2:

$$K_2 = 1 + 0.23V_f{A_R}^{-0.5} \quad (12.7)$$

where V_f is in percentage (%).

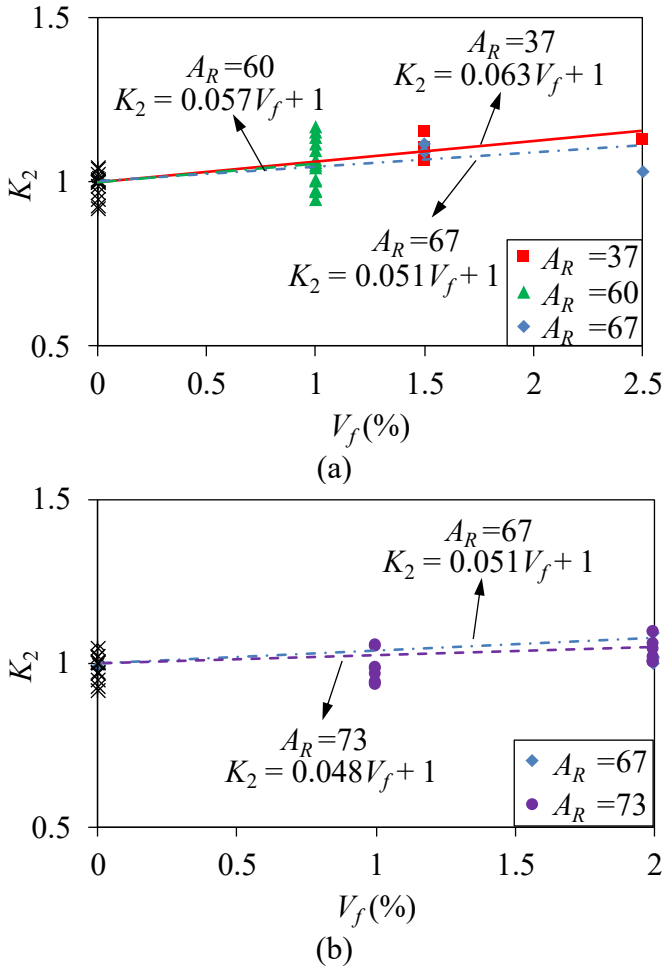

Figure 12.5. Variation of experimental values of K_2 with volume fraction (V_f): concrete containing (a) hooked end; (b) straight steel fibers

Figure 12.6 shows comparisons of the experimental values of ε_{cu} for FRP-confined SFRC and ε^*_{cc} for actively confined SFRC with the predictions obtained by the proposed expression for the dilation behaviour of confined SFRC (Eq. 12.3). In the calculation of ε_{cu} and ε^*_{cc} the corresponding lateral strains $\varepsilon_{h,rup}$ and ε^*_{lc} were used in Eq. 12.3, which were obtained from lateral strain gauges placed at the mid-height of the specimens. The experimental values of ε_{cu} and ε^*_{cc} shown in Fig. 12.6 were obtained from LVDTs. As can be seen in Fig. 12.6, incorporation of K_2 into the dilation relationship resulted in a higher prediction accuracy of the dilation behaviour of FRP-confined SFRC compared to that of the model by Lim and Ozbakkaloglu [39].

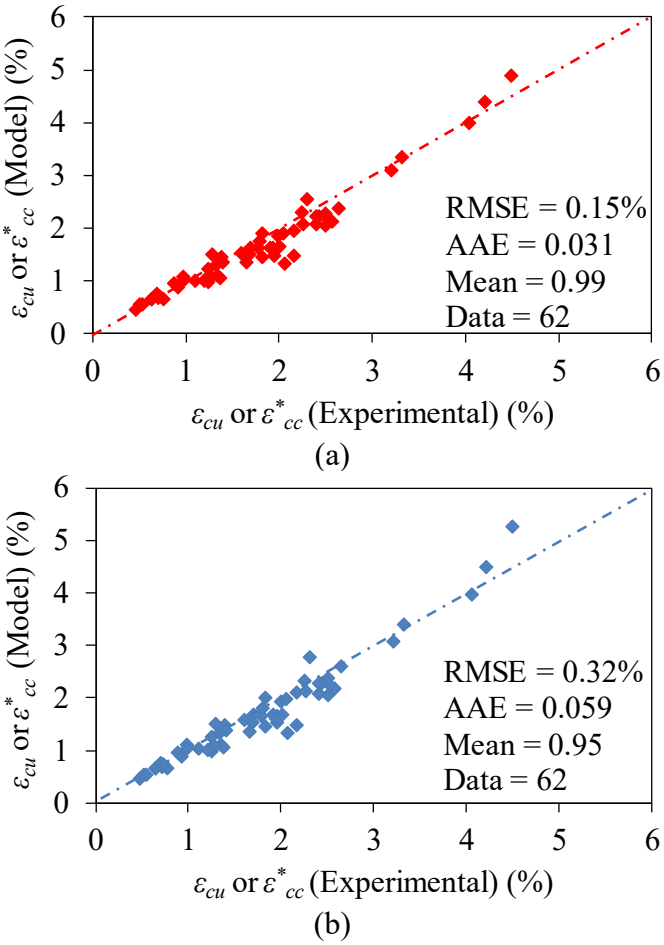

Figure 12.6. Comparison of the experimental values of ultimate axial strain (ε_{cu}) or peak axial strain (ε^*_{cc}) with: (a) predictions of the proposed model; (b) predictions of model by Lim and Ozbakkaloglu [39]

Axial stress-strain relationship of FRP-confined SFRC

Through the unifying confining pressure gradient concept introduced by Lim and Ozbakkaloglu [39], the axial stress (f_c) of FRP-confined concrete can be obtained from the axial stress-strain relationship of actively confined concrete by considering the proposed confining pressure gradient ($\Delta f_l = f_l - f^*_l$, in which f_l and f^*_l are the confining pressure by FRP confinement and corresponding confining pressure by active confinement, respectively). In this study, actively confined concrete model proposed by Lim and Ozbakkaloglu [42], which was modified from Popovics model [43], was used to obtain the axial stress-strain curves of actively confined concretes. Defining the axial stress-strain curve of actively confined concrete requires the accurate determination of the coordinates of the curve corresponding to the peak stress (i.e. f^*_{cc} and ε^*_{cc}). Based on the analysis of the test database it is found that

steel fiber properties, such as V_f and A_R, did not have a significant influence on ε^*_{cc} of actively confined SFRCs. Therefore, in the current study a new expression was developed only for f^*_{cc} of SFRCs and it is recommended that the ε^*_{cc} expression given by Lim and Ozbakkaloglu [39] (i.e. $\varepsilon^*_{cc} = \varepsilon_{co} + 0.045\left(f^*_l/f'_{co}\right)^{1.15}$) for actively confined plain concrete can also be applied to actively confined SFRC. f^*_{cc} expression proposed by Lim and Ozbakkaloglu [39] for plain concrete was modified by incorporating the strength coefficient (K_3) into the expression.

$$f^*_{cc} = f'_{co} + 5.2K_3 f'^{0.91}_{co}\left(\frac{f^*_l}{f'_{co}}\right)^a \quad \text{where} \quad a = f'^{-0.06}_{co} \tag{12.8}$$

Figures 12.7(a) and 12.7(b) show the variation of experimental K_3 with V_f for FRP-confined concrete containing hooked end and straight steel fibers, respectively. As can be seen in the figures, K_3 gradually increases with an increase in V_f, which is attributed to the additional confinement provided by the internal steel fibers resulting in enhancements in the compressive strength of SFRCs [37]. The regression analysis showed that V_f was the only influential parameter for f^*_{cc}. However, it is worth noting that this observation is limited to mixes prepared with a relatively narrow range of A_R spanning from 60 to 73 due to the limitations of the current database. Accordingly, K_3 is defined through Eq. 12.9 as a function of V_f.

$$K_3 = 1 + 0.065V_f \tag{12.9}$$

in which V_f is in percentage (%).

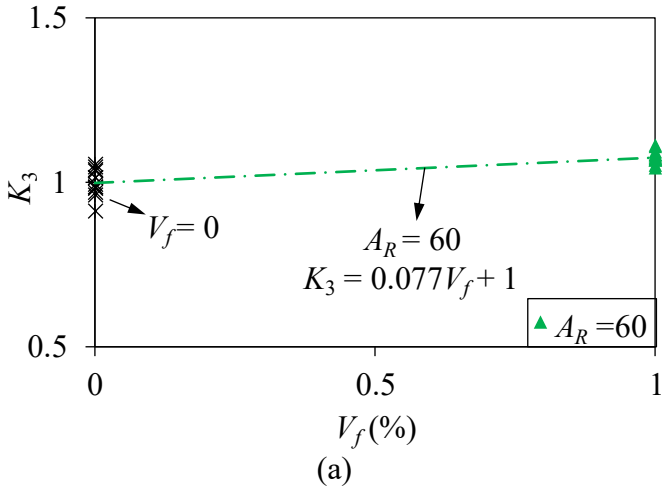

(a)

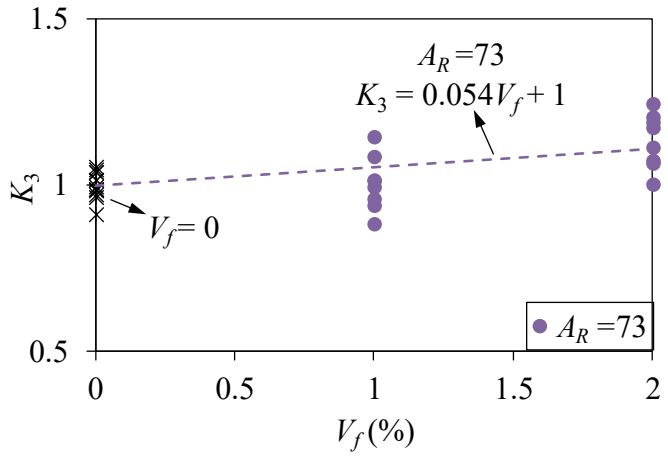

(b)

Figure 12.7. Variation of experimental values of K_3 with volume fraction (V_f): concrete containing (a) hooked end; (b) straight steel fibers

Figures 12.8(a) and 12.8(b) show comparisons of the experimental values of f^*_{cc} with the predictions obtained by the proposed expression for f^*_{cc} (Eq. 12.5) and f^*_{cc} determined by Lim and Ozbakkaloglu [39] expression, respectively. As can be seen in the figures, incorporation of K_3 into f^*_{cc} expression led to a higher a prediction accuracy compared with that of the model by Lim and Ozbakkaloglu [39].

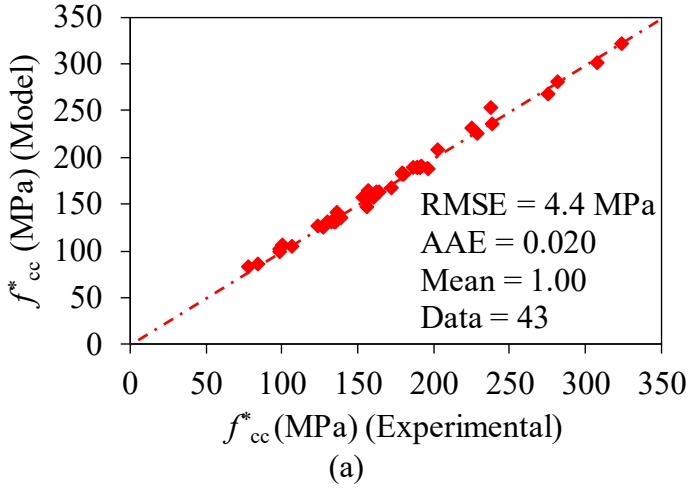

(a)

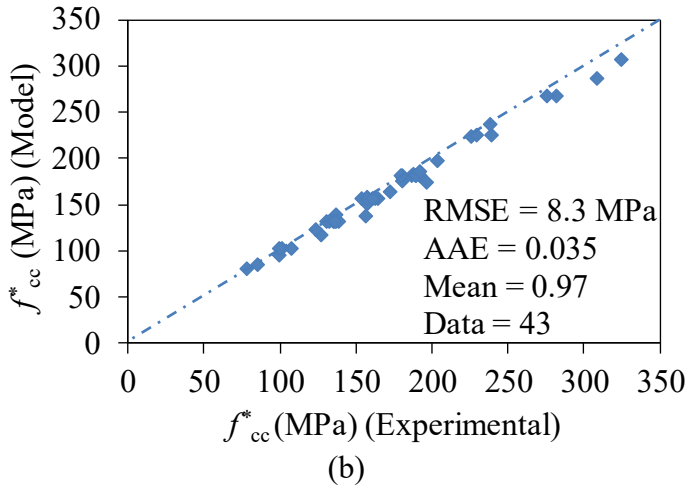

(b)

Figure 12.8. Comparison of the experimental values of peak axial stress (f^*_{cc}) with: (a) predictions of the proposed model; (b) predictions of model by Lim and Ozbakkaloglu [39]

FE MODELLING OF COMPRESSIVE BEHAVIOUR OF FRP-CONFINED SFRC

As was discussed in Refs. [31,34], different theories of plasticity, damage, and coupled damage-plasticity have been proposed for FE modelling of concrete [26,35,36,44-47]. Plasticity approach only considers a plasticity failure surface and does not address the degradation of the material stiffness [26]. Conversely, the damage approach only applies the degradation of the material stiffness without considering the irreversible deformations and inelastic volumetric expansion in compression [44]. On the other hand, the concrete damage-plasticity approach combines the benefits of both plasticity and damage approaches in the failure surface and flow rule. Therefore, the concrete damage-plasticity method, which was developed by Ozbakkaloglu et al. [31] and Lim et al. [34], was adopted in the present study for FE modelling of FRP-confined SFRCs.

Appendix 5 presents the details of the concrete damage-plasticity method given in Refs. [31,34]. The new expressions proposed in the current study for f^*_{cc} (Eq. 12.8), $\varepsilon_{h,rup}$ (Eq. 12.1), and the axial strain-lateral strain relationship (Eq. 12.3) were adopted to improve the failure surface and flow rule of the concrete damage-plasticity model for FRP-confined SFRC. The improved failure surface and flow rule were achieved through the use of Eq. 12.8 in Eq. A8 (in Appendix 5) and Eq.

12.3 in Eq. A11 (in Appendix 5), respectively. The proposed model is applicable to confined SFRCs containing hooked end and straight steel fibers with up to 194 MPa unconfined compressive stregth.

COMPARISON OF PROPOSED MODEL PREDICTIONS WITH EXPERIMENTAL RESULTS

The FRP-confined SFRC specimens were modeled in FE program ABAQUS using the proposed constitutive model. As was done previously in Refs. [31,34], boundary conditions were assigned to the axis-symmetric planes and were considered to be pinned-end to simulate the specimen boundary conditions in the test setup. A tie constraint was used to model the interaction between the FRP sheet and concrete, through which the nodes on both surfaces were constrained to displace similarly. FRP sheets were modeled by four-node shell elements with reduced integration (S4R) and the concrete core was modeled as the eight-node brick element (C3D8R). To capture the post-peak softening behaviour of concrete, axial compression was applied as a uniform axial displacement to the nodes along the top of the specimen. Compressive stresses and strains were defined to be positive. Figure 12.9 shows a typical FRP-confined SFRC specimen modeled in ABAQUS. In order to validate the proposed model, the predictions obtained from the FE analysis based on the model were compared with the experimental results of FRP-confined SFRC and predictions of the model by Lim and Ozbakkaloglu [39] proposed for FRP-confined plain concrete. Four groups of FRP-confined SFRC specimens (i.e. U120-1, U120-2, U190-1, and U190-2) were used in the validation of the FE model. Figures 12.10 and 12.11 show the axial stress-strain, lateral strain-axial strain, axial stress-volumetric strain, plastic volumetric strain-axial plastic strain, and plastic dilation angle-axial plastic strain relationships for the group U120-1 and U120-2 specimens (refer to Table 12.1 for specimen properties), whereas Fig. 12.12 shows the axial stress-strain relationships for the group U190-1 and U190-2 specimens.

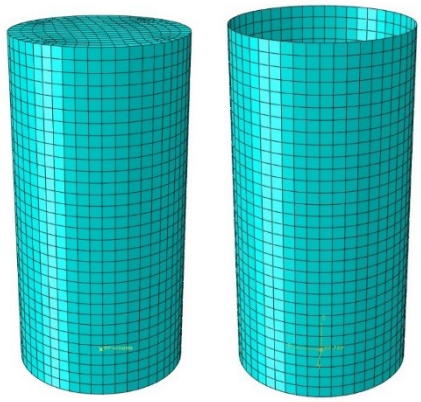

(a) (b)

Figure 12.9. FE modelling of FRP-confined SFRC: (a) SFRC; (b) FRP tube

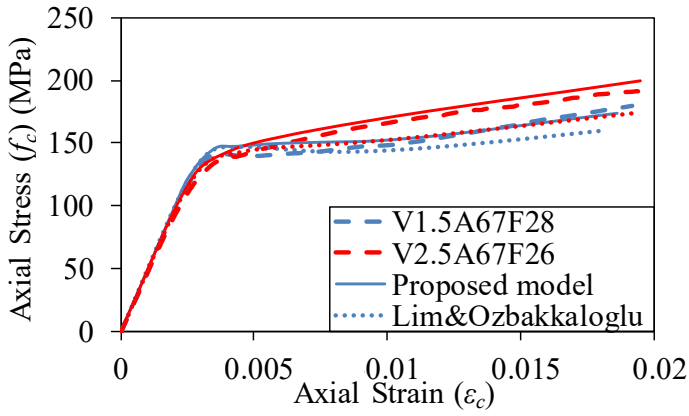

(a)

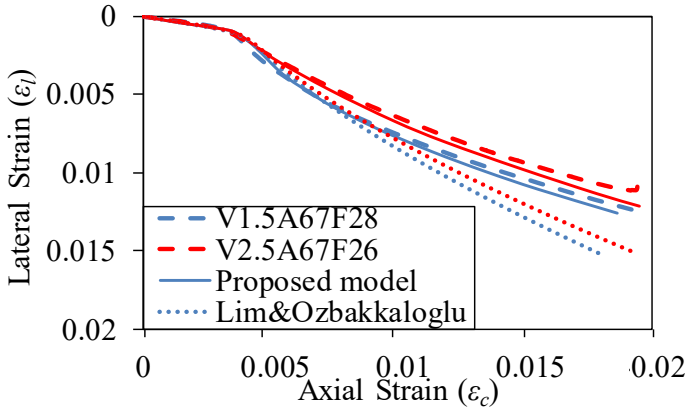

(b)

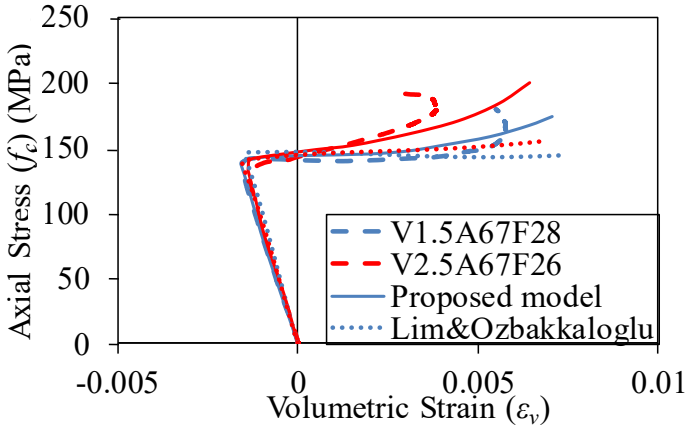

(c)

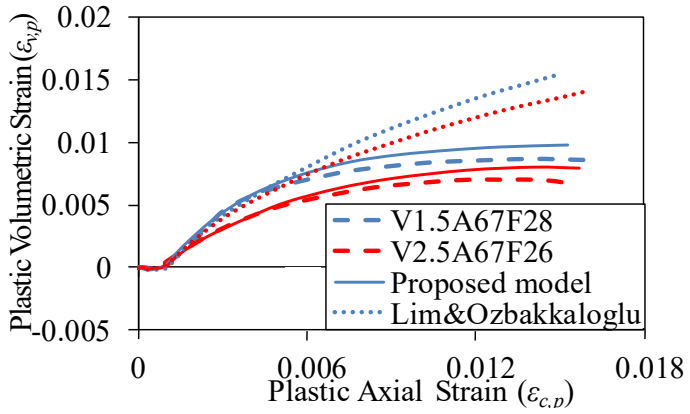

(d)

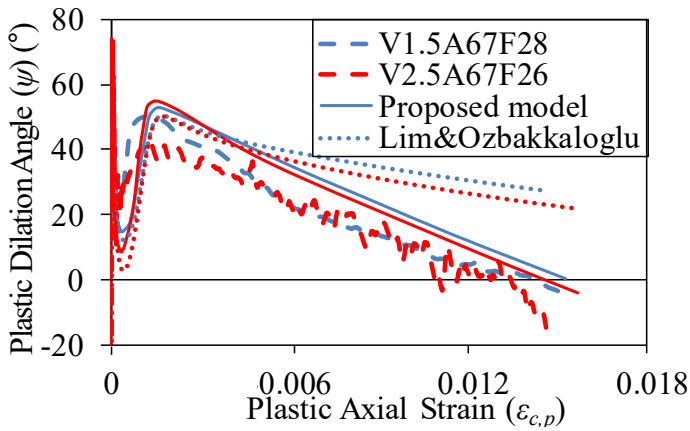

(e)

Figure 12.10. Variation of: (a) axial stress-axial strain; (b) lateral strain-axial strain; (c) axial stress-volumetric strain; (d) plastic volumetric strain-axial plastic strain; (e) plastic dilation angle-axial plastic strain relationships of Group U120-1

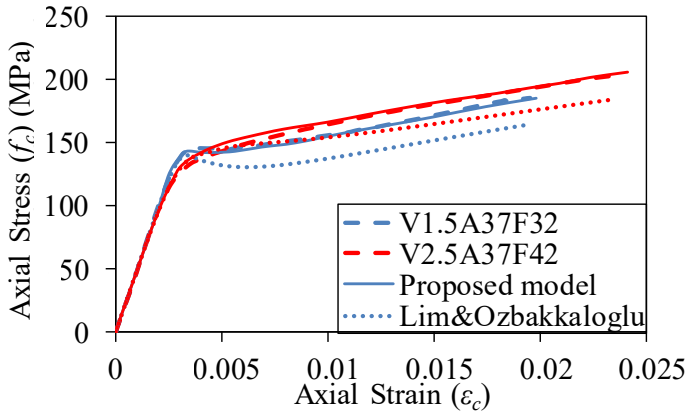
Axial Stress (f_c) (MPa)
250
200
150
100
50
0
0
0.005
0.01
0.015
0.02
0.025
Axial Strain (ε_c)
V1.5A37F32
V2.5A37F42
Proposed model
Lim&Ozbakkaloglu

(a)

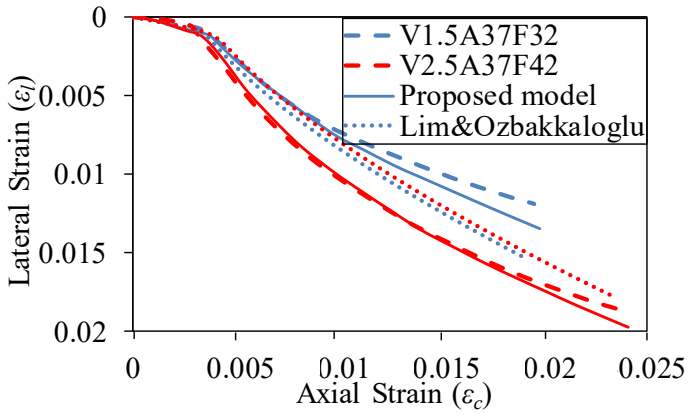
Lateral Strain (ε_l)
0
0.005
0.01
0.015
0.02
0
0.005
0.01
0.015
0.02
0.025
Axial Strain (ε_c)
V1.5A37F32
V2.5A37F42
Proposed model
Lim&Ozbakkaloglu

(b)

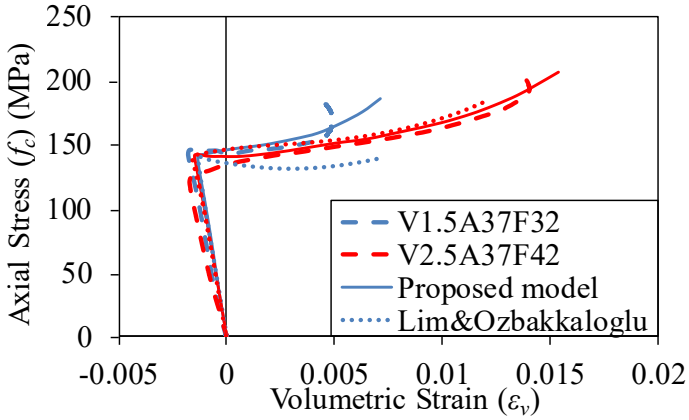
Axial Stress (f_c) (MPa)
250
200
150
100
50
0
-0.005
0
0.005
0.01
0.015
0.02
Volumetric Strain (ε_v)
V1.5A37F32
V2.5A37F42
Proposed model
Lim&Ozbakkaloglu

(c)

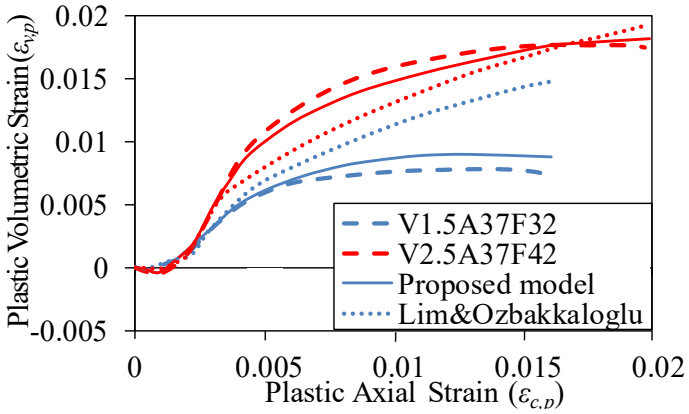
Plastic Volumetric Strain ($\varepsilon_{v,p}$)
0.02
0.015
0.01
0.005
0
-0.005
0
0.005
0.01
0.015
0.02
Plastic Axial Strain ($\varepsilon_{c,p}$)
V1.5A37F32
V2.5A37F42
Proposed model
Lim&Ozbakkaloglu

(d)

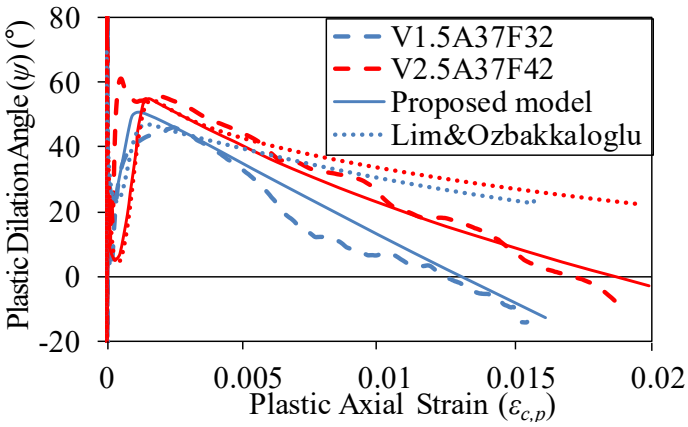

(e)

Figure 12.11. Variation of: (a) axial stress-axial strain; (b) lateral strain-axial strain; (c) axial stress-volumetric strain; (d) plastic volumetric strain-axial plastic strain; and (e) plastic dilation angle-axial plastic strain relationships of Group U120-2

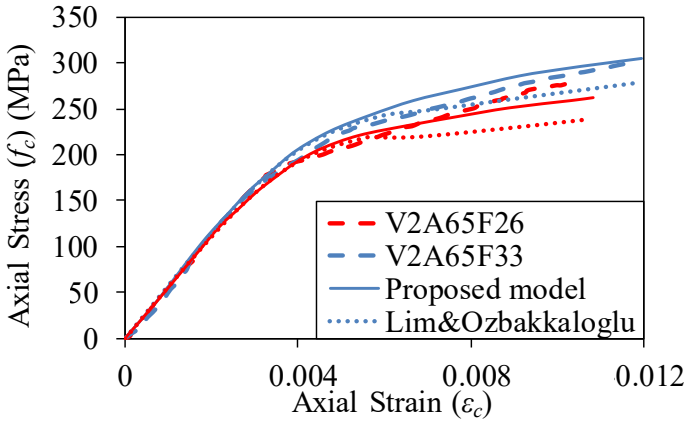

(a)

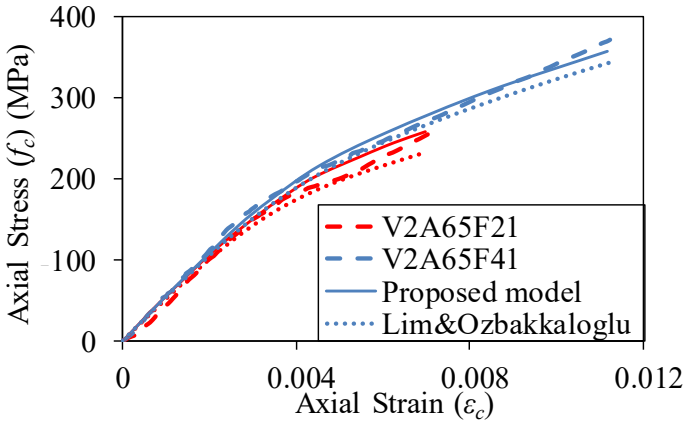

(b)

Figure 12.12. Variation of axial stress-axial strain relationships for Groups: (a) U190-1; (b) U190-2

As can be seen in Figs. 12.10-12.12, the proposed model closely predicts the mechanical behaviour of FRP-confined SFRCs and it provides higher accuracy than the predictions of the model by Lim and Ozbakkaloglu, which shows considerable deviations from the experimental test results of FRP-confined SFRCs. The accuracy of the proposed model was achieved by the incorporation of the key internal steel properties (i.e. V_f and A_R) into the accurate failure surface and flow rule models given for plain concrete in Refs. [31,34]. As can be seen in Figs. 12.10(a) and 12.11(a), model by Lim and Ozbakkaloglu significantly underestimated the stresses in the axial stress-axial strain relationship of FRP-confined SFRCs, especially for specimens with a higher steel fiber volume fraction. Figures 12.10(b) and 12.11(b) show the lateral strain-axial strain relationships of FRP-confined SFRC specimens of the group U120-1 and U120-2, respectively. The higher accuracy of the proposed FE model compared to the model by Lim and Ozbakkaloglu in prediction of the dilation behaviour of FRP-confined SFRC is because of the incorporation of the steel fiber parameters (V_f and A_R) in the prediction of the hoop rupture strain and relationship between axial and lateral strains.

Figures 12.10(c) and 12.11(c) show the axial stress-volumetric strain relationships of FRP-confined SFRC under different steel fiber parameters and levels of confinement. As can be seen in the figures, inelastic volumetric contraction occurred at the beginning of the plastic flow and followed by dilation. It means that the volume of each SFRC specimen contracted until the specimen reached its unconfined compressive strength. After this point, the lateral restraint resulted in a change from contraction to expansion throughout the loading history. As can be seen in Figs. 12.10(d) and 12.11(d), which show the plastic volumetric strain-plastic axial strain relationships for FRP-confined SFRC, the sign of the tangential slope of the curve changed from negative to positive at an inflection point (transition point from the first to second part of the curve), which verifies the transition from contraction to expansion seen in Figs. 12.10(c) and 12.11(c). It can be seen in Figs. 12.10(e) and 12.11(e), which show the plastic dilation angle-plastic axial strain relationships for FRP-confined SFRC, that plastic dilation angle (ψ) decreases with an increase in the plastic axial strain until the inflection point of Figs. 12.10(d) and 12.11(d) and then it rapidly increases until the plastic volumetric strain becomes zero, which corresponds to the transition from contraction to expansion seen in Figs. 12.10(c)

and 12.11(c). With an increase in the level of confining pressure under FRP confinement, the concrete dilatancy has a tendency to change towards densification, which can be seen as the reduction in ψ with a further increase in the plastic axial strain in Figs. 12.10(e) and 12.11(e).

Figure 12.12 shows the axial stress-axial strain curves of FRP-confined ultra-high strength SFRC, from which it can be seen that the curves obtained by the proposed model are in close agreement with the experimental curves. These results indicate that the proposed FE model can be applied to predict the compressive behaviour of circular FRP-confined SFRC specimens with an unconfined concrete strength of up to 194 MPa.

SUMMARY AND CONCLUSIONS

This paper has presented the first FE model to predict the compressive behaviour of FRP-confined SFRCs in circular sections. A test database containing 73 datasets from axial compression tests of FRP-confined and actively confined SFRC was assembled based on the results available in the literature. Additional axial compression tests were conducted on 16 actively confined SFRC specimens to address the gaps in the existing test database. The analysis of the experimental test results indicated that the compressive behaviour of FRP-confined SFRC is influenced by the steel fiber volume fraction and aspect ratio. Therefore, the model by Lim and Ozbakkaloglu, which was proposed for FRP-confined plain concretes, was extended to predict the compressive behaviour of FRP-confined SFRCs by considering the influences of steel fiber volume fraction and aspect ratio. In the proposed model, the hoop rupture strain of the FRP jacket, dilation relationship between axial strain and lateral strain of actively and FRP-confined SFRC, and relationship between the confining pressure and the compressive strength of actively confined SFRC were established by modifying the previously proposed models by Lim and Ozbakkaloglu for confined plain concrete. The improved failure surface and flow rule of the concrete damage-plasticity model was achieved by incorporating the effects of steel fiber volume fraction and aspect ratio into the accurate failure surface and flow rule models given for plain concrete in Refs.

[31,34]. The comparison of model predictions with the experimental results shows that the new models closely predict the axial stress-axial strain, lateral strain-axial strain, axial stress-volumetric strain, plastic volumetric strain-axial plastic strain, and plastic dilation angle-axial plastic strain relationships of FRP-confined SFRC. The analysis results also indicate that the new FE model provides improved accuracy in predicting the compressive behaviour of FRP-confined SFRCs compared to the predictions of the model given by Lim and Ozbakkaloglu for conventional concrete. The availability of such an accurate model is of vital importance for practical applications of FRP-confined SFRC columns.

Because of the influence of the steel fiber parameters on the mechanical behaviour of FRP-confined SFRC, the application of the models of FRP-confined plain concrete to predict the behaviour of FRP-confined SFRC is not recommended. Therefore, additional targeted studies are recommended on the FRP-confined and actively confined SFRC columns to expand the existing test database to enable the development of additional models for FRP-confined SFRCs with a broader range of applicability, such as those for square and rectangular columns.

ACKNOWLEDGEMENTS

The authors gratefully acknowledge the financial support from the National Natural Science Foundation of China through Grant No. 51650110495 and the University of Adelaide through a Research Excellence Grant awarded to the second author. The authors also thank Mr. Liu and Mesdames Yang and Liu for completing the tests reported in this paper as part of their Master's thesis.

REFERENCES

[1] Lu X, Hsu CT. Behavior of high strength concrete with and without steel fiber reinforcement in triaxial compression. *Cement and Concrete Research*. 2006;36:1679-85.

[2] Bencardino F, Rizzuti L, Spadea G, Swamy RN. Stress-strain behavior of steel fiber-reinforced concrete in compression. *Journal of Materials in Civil Engineering*. 20089;20(3):255-63.

[3] Kaïkea A, Achoura D, Duplan F, Rizzuti L. Effect of mineral admixtures and steel fiber volume contents on the behavior of high performance fiber reinforced concrete. *Materials & Design*. 2014;63:493-9.

[4] Madandoust R, Ranjbar MM, Ghavidel R, Shahabi F. Assessment of factors influencing mechanical properties of steel fiber reinforced self-compacting concrete. *Materials & Design*. 2015;83:284-94.

[5] Ilki A, Peker O, Karamuk E, Demir C, Kumbasar N. FRP retrofit of low and medium strength circular and rectangular reinforced concrete columns. *Journal of Materials in Civil Engineering.* 2008;20(2):169-88.

[6] Doran B, Koksal HO, Turgay T. Nonlinear finite element modeling of rectangular/square concrete columns confined with FRP. *Materials & Design*. 2009;30(8):3066-75.

[7] Kusumawardaningsih Y, Hadi MNS. Comparative behaviour of hollow columns confined with FRP composites. *Composite Structures*. 2010;93(1):198-205.

[8] Smith ST, Kim SJ, Zhang H. Behavior and Effectiveness of FRP Wrap in the Confinement of Large Concrete Cylinders. *Journal of Composites for Construction*. 2010;14(5):573-82.

[9] Rousakis T, Karabinis A, Kiousis P, Tepfers R. Analytical modeling of plastic behavior of uniformly FRP confined concrete members. *Composites Part B*. 2008;39(7-8):1104-13.

[10] Wu YF, Jiang JF. Effective strain of FRP for confined circular concrete columns. *Composite Structures*. 2013;95:479–91.

[11] Ozbakkaloglu T, Lim JC. Axial compressive behavior of FRP-confined concrete: Experimental test database and a new design-oriented model. *Composites Part B*. 2013;55:607-34.

[12] Vincent T, Ozbakkaloglu T. Influence of concrete strength and confinement method on axial compressive behavior of FRP confined high- and ultra high-strength concrete. *Composites Part B.* 2013;50:413-28.

[13] Lim JC, Ozbakkaloglu T. Confinement model for FRP-confined high-strength concrete. *Journal of Composites for Construction*. 2014;18(4):04013058.

[14] Ozbakkaloglu T, Vincent T. Axial compressive behavior of circular high-strength concrete-filled FRP tubes. *Journal of Composites for Construction*. 2014;18(2):04013037.

[15] Ozbakkaloglu T. A novel FRP-dual grade concrete-steel composite column system. *Thin-Walled Structures*. 2015;96:295-306.

[16] Mansouri I, Gholampour A, Kisi O, Ozbakkaloglu T. Evaluation of peak and residual conditions of actiely confined concrete using neuro-fuzzy and neural computing techniques. *Neural Computing and Applications*. 2016;96:10.1007/s00521-016-2492-4.

[17] Ozbakkaloglu T, Louk Fanggi BA, Zheng J. Confinement model for concrete in circular and square FRP-concrete-steel double skin-composite columns. *Materials & Design*. 2016;96:458-69.

[18] Afroughsabet V, Biolzi L, Ozbakkaloglu T. High performance fiber-reinforced concrete: A review. *Journal of Materials Science*. 2016;51(14):6517-51.

[19] Xie T, Ozbakkaloglu T, Behavior of steel fiber-reinforced high-strength concrete-filled FRP tube columns under axial compression. *Engineering Structures*. 2015;90:158-71.

[20] Zohrevand P, Mirmiran A. Stress-strain model of ultrahigh performance concrete confined by fiber-reinforced polymers. *Journal of Materials in Civil Engineering.* 2013;25(12):1822-9.

[21] Dundar C, Erturkmen D, Tokgoz S. Studies on carbon fiber polymer confined slender plain and steel fiber reinforced concrete columns. *Engineering Structures.* 2015;102:31-9.

[22] Deng ZC, Qu JL. The experimental studies on behavior of ultrahigh-performance concrete confined by hybrid fiber-reinforced polymer tubes. *Advances in Materials Science and Engineering*. 2015;10.1155/2015/201289.

[23] Mirmiran A, Zagers K, Yuan WQ. Nonlinear finite element modeling of concrete confined by fiber composites. *Finite Elements in Analysis and Design.* 2000;35(1):79-96.

[24] Malvar LJ, Morrill KB, Crawford JE. Numerical modeling of concrete confined by fiber-reinforced composites. *Journal of Composites for Construction.* 2004;8(4):315-22.

[25] Karabinis AI, Rousakis TC, Manolitsi GE. 3D finite-element analysis of substandard RC columns strengthened by fiber-reinforced polymer sheets. *Journal of Composites for Construction*. 2008;12(5):531-40.

[26] Yu T, Teng JG, Wong YL, Dong SL. Finite element modeling of confined concrete-I: Drucker-Prager type plasticity model. *Engineering Structures*. 2010;32(3):665-79.

[27] Yu T, Teng JG, Wong YL, Dong SL. Finite element modeling of confined concrete-II: Plastic-damage model. *Engineering Structures*. 2010;32(3):680-91.

[28] Csuka B, Kollar LP. Analysis of FRP confined columns under eccentric loading. *Composite Structures*. 2012;94(3):1106-16.

[29] Jiang JF, Wu YF. Identification of material parameters for Drucker-Prager plasticity model for FRP confined circular concrete columns. *International Journal of Solids and Structures*. 2012;49(3-4):445-56.

[30] Youssf O, ElGawady MA, Mills JE, Ma X. Finite element modelling and dilation of FRP-confined concrete columns. *Engineering Structures.* 2014;79:70–85.

[31] Ozbakkaloglu T, Gholampour A, Lim JC. Damage-plasticity model for FRP-confined normal-strength and high-strength concrete. *Journal of Composites for Construction*. 2016;10.1061/(ASCE)CC.1943-5614.0000712.

[32] Lim JC, Ozbakkaloglu T. Investigation of the influence of application path of confining pressure: tests on actively confined and FRP-confined concretes. *Journal of Structural Engineering*. 2015;10.1061/(ASCE)ST.1943-541X.0001177.

[33] Lim JC, Ozbakkaloglu T. Lateral strain-to-axial strain relationship of confined concrete. *Journal of Structural Engineering*. 2015;10.1061/(ASCE)ST.1943-541X.0001094.

[34] Lim JC, Ozbakkaloglu T, Gholampour A, Bennett T, Sadeghi R. Finite-element modeling of actively confined normal-strength and high-strength concrete under uniaxial, biaxial, and triaxial compression. *Journal of Structural Engineering.* 2016;10.1061/(ASCE)ST.1943-541X.0001589.

[35] Lubliner J, Oliver J, Oller S, Onate E. A plastic-damage model for concrete. *International Journal of Solids and Structures*. 1989;25(3):299-326.

[36] Lee J, Fenves GL. Plastic-damage model for cyclic loading of concrete structures. *Journal of Engineering Mechanics*. 1998;124(8):892-900.

[37] Wang ZL, Zhu HH, Wang JG, Zhu B. Experimental study on macroscopic mechanical behavior of SFRC under triaxial compression. *Mechanics of Advanced Materials and Structures.* 2012;19(8):653-62,

[38] ABAQUS, *ABAQUS Analysis User's Manual*, version 6.12, Dassault Systèmes Simulia Corp., Providence, RI, USA, 2012.

[39] Lim JC, Ozbakkaloglu T. Unified stress-strain model for FRP and actively confined normal-strengh and high-strength concrete. *Journal of Composites for Construction.* 2015;19(4):04014072.

[40] ASTM C143/C143M-12. *Standard Test Method for Slump of Hydraulic-Cement Concrete*, West Conshohocken, ASTM International, 2012.

[41] ASTM C39/C39M-16b. *Standard Test Method for Compressive Strength of Cylindrical Concrete Specimens*, West Conshohocken, PA, USA, ASTM International, 2016.

[42] Lim JC, Ozbakkaloglu T. Stress-strain model for normal- and light-weight concretes under uniaxial and triaxial compression. *Construction and Building Materials*. 2014;71:492-509.

[43] Popovics S. A numerical approach to the complete stress-strain curves for concrete. *Cement and Concrete Research*. 1973;3(5):583-99.

[44] Lubarda VA, Kracjinvovic D, Mastilovic S. Damage model for brittle elastic solids with unequal tensile and compressive strength. *Engineering Fracture Mechanics.* 1994;49:681-97.

[45] Imran I, Pantazopoulou SJ. Plasticity model for concrete under triaxial compression. *Journal of Engineering Mechanics*. 2001;127(3):281-90.

[46] Karabinis AI, Rousakis TC. Concrete confined by FRP material: a plasticity approach. *Engineering Structures.* 2002;24(7):923-32.

[47] Zheng F, Wu Z, Gu C, Bao T, Hu J. A plastic damage model for concrete structure cracks with two damage variables. *Science China Technological Sciences.* 2012;55(11):2971-80.

Conclusions and Recommendations

Conclusions

This thesis has focused on the development of eco-friendly and high performance construction materials and technologies. The novel findings and major research contributions of the thesis are listed as follows:

1- Recycled aggregate concrete

- Parent concrete strength of recycled concrete aggregates significantly affects time-dependent and long-term mechanical properties of recycled aggregate concretes (RACs). High-strength RACs, prepared with full replacement of natural coarse aggregates with recycled concrete aggregates having a high parent concrete strength, exhibit properties that are similar to or better than those of companion natural aggregate concretes.
- By incorporating the contribution of effective water-to-cement ratio and recycled concrete aggregate replacement ratio, proposed empirical models using gene expression programming (GEP) technique exhibits improved estimates of mechanical properties of RACs compared to the existing models. This makes these models suitable for use in the pre-design of RACs.
- By accurately capturing the influences of key parameters, multivariate adaptive regression splines (MARS), M5 model tree (M5Tree), and least squares support vector regression (LSSVR) techniques can provide close predictions of the mechanical properties of RACs for the pre-design and modelling purposes.

2- Waste-based and geopolymer mortars and concretes

- Replacement of cement with ground granulated blast furnace slag (GGBS) at up to 90% develops a similar compressive strength to those of conventional concrete. Ternary concretes with cement replacement of 70% and fly ash (FA)-to-GGBS ratio of 1:2, and cement replacement of 50% and FA-to-GGBS ratio of 1:1 exhibit similar compressive strength to conventional concrete.

- Lead smelter slag (LSS)- and glass sand (GS)-based geopolymer mortars containing up to 50% GGBS exhibit superior compressive and tensile strength compared to their natural sand (NS)-based counterparts. Geopolymer mortars containing LSS develop a lower drying shrinkage than those containing NS.
- The compressive and tensile strength of waste-based mortars with full replacement of NS with LSS are similar to those of conventional mortar. At full replacement of cement with GGBS, FA, and glass powder (GP), the strength reduction of LSS mortar over the conventional mortar is limited to only 30%, which is a very promising observation toward the development of 100% waste-based mortars.

3- Graphene-cement mortar composites

- Addition of 0.1% dosage of graphene oxide (GO) by weight of cement in the cement mortar results in 37.5% and 77.7% increase in the 28-day tensile and compressive strength of the mortar, respectively. This is the optimal dosage and increasing the amount of GO above this leads to detrimental effects related to restacking and aggregation of GO sheets in cement matrix.
- Reduction of oxygen functional groups of GO by 0.2% (wt%) hydrazine at 15 min results in 45.0% and 83.7% increase in the 28-day tensile and compressive strength of the cement mortar, respectively, which are higher than the strength increases seen in the mortar prepared with GO without oxygen reduction.

4- Confinement of normal- and high-strength concretes

- Ambient-cured geopolymer concretes (GPCs) exhibit a slightly higher ductility and lateral dilation than oven-cured GPCs, indicating the great potential of the use of ambient-cured geopolymers in new laterally confined structural columns designed to undergo large deformations.
- Confinement of high-strength concrete (HSC) by prestrained shape memory alloy (SMA) spirals leads to a higher peak axial stress and corresponding axial strain than those of unconfined HSC. This indicates that SMA spiral can be efficiently used as a prestressing technique to strengthen and retrofit existing concrete members.

- Steel fibre-reinforced concretes (SFRCs) with a higher steel fibre volume fraction exhibit more ductile behaviour and less lateral dilation than SFRCs with a lower steel fibre volume fraction.
- Considering the influence of fibre volume fraction and aspect ratio on the mechanical properties of SFRCs, the developed concrete damage-plasticity model provides an improved accuracy over the best performing existing models of fibre-reinforced polymer (FRP)-confined plain concrete in predicting the behaviour of FRP-confined SFRC.

Recommendations

Further studies are recommended as follows to contribute toward the development of the next-generation of eco-friendly and high performance construction materials aimed at reducing the impact of construction industry on the environment:

1- The influence of the full replacement of cement and natural sand with waste-based materials in this research was studied at mortar scale. It is recommended to investigate the behaviour of 100% waste-based concrete as well.

2- Because waste-based concretes exhibit different long-term hydration characteristics than those of conventional concretes, new studies are recommended to investigate their time-dependent (e.g. drying shrinkage, creep) and long-term durability-related (e.g. acid and sulfate resistance, chloride penetration) properties.

3- Based on the preliminary studies, particle size and surface chemistry of GO exhibit a significant influence on properties of cement mortar. Further research is suggested to investigate the influence of these two parameters. Furthermore, additional studies are recommended to investigate the influence of incorporation of GO with different dosages and oxygen functionalities in concretes.

4- The proposed concrete damage-plasticity model can be extended to different types of concretes. Therefore, further research is recommended to develop a model applicable to different types of concretes, such as rubberized concrete, waste-based concrete, and geopolymer concrete. In addition, new studies are recommended to investigate the bending performance of composite structural beam members made with the developed materials in chapters 1 to 3.

Appendix

Appendix 1. Experimental database of recycled aggregate concrete

Year	Source	Geometric properties of specimens				Concrete mix properties			Properties of coarse aggregate								Physical properties of concrete		Mechanical properties of concrete			
		Compressive strength tests	Elastic modulus tests	Flexural strength tests	Splitting tensile strength tests	Effective water-to-cement ratio (w_{eff}/c)	Aggregate-to-cement ratio (a/c)	RCA replacement ratio (RCA %)	Parent concrete strength (MPa)	Nominal maximum RCA size (mm)	Nominal maximum NA size (mm)	Bulk density of RCA (kg/m^3)	Bulk density of NA (kg/m^3)	Water absorption of RCA (WA_{RCA}) (%)	Water absorption of NA (WA_{NA}) (%)	Los Angeles abrasion of RCA (LA_{RCA})	Los Angeles abrasion of NA (LA_{NA})	Density of hardened concrete AD (ρ_{ad}) (kg/m^3)	Density of hardened concrete SSD (ρ_{SSD}) (kg/m^3)	Compressive strength (f'_c) (MPa)	Elastic modulus (E_c) (MPa)	Flexural strength (f'_r) (MPa)	Splitting tensile strength (f'_{st}) (MPa)
1988	Yoda et al. [52]	C_1	C_1			0.50	2.6	0		20	20									42.8	32153		
		C_1	C_1			0.50	2.5	20		20	20									42.7	31178		
		C_1	C_1			0.50	2.5	50		20	20									41.3	31204		
		C_1	C_1			0.50	2.3	100		20	20									41.8	31589		
2000	Limbachiya et al. [53]	S_1	C_2	B_2		0.45	3.3	0		20	30		2610		2.5					51.2	27000	5.2	
		S_1	C_2	B_2		0.45	3.3	30		20	30	2400	2610	4.9	2.5					50.6	27000	5.2	
		S_1	C_2	B_2		0.45	3.3	50		20	30	2400	2610	4.9	2.5					50.8	27500	4.9	
		S_1	C_2	B_2		0.45	3.3	100		20	30	2400		4.9						50.2	26500	5.0	
		S_1	C_2	B_2		0.39	2.6	0		20	30		2610		2.5					60.3	28500	6.0	
		S_1	C_2	B_2		0.39	2.6	30		20	30	2400	2610	4.9	2.5					60.8	28000	6.1	
		S_1	C_2	B_2		0.39	2.6	50		20	30	2400	2610	4.9	2.5					61.2	28500	6.1	
		S_1	C_2	B_2		0.39	2.6	100		20	30	2400		4.9						60.2	27500	6.0	
		S_1	C_2	B_2		0.29	2.2	0		20	30		2610		2.5					70.5	30000*	7.0	
		S_1	C_2	B_2		0.29	2.2	30		20	30	2400	2610	4.9	2.5					70.2	30000	6.9	
		S_1	C_2	B_2		0.29	2.2	50		20	30	2400	2610	4.9	2.5					70.8	31000	7.0	
		S_1	C_2	B_2		0.29	2.2	100		20	30	2400		4.9						70.0	30500	7.2*	
2002	Ajdukiewicz and Kliszczewicz [54]	S_2	C_2		C_2	0.36	2.4	0	41.6	16	16							2400		48.4	30000		4.1
		S_2	C_2		C_2	0.36	2.3	100	41.6	16	16							2320		44.5	27400		4.0
		S_2	C_2		C_2	0.36	2.2	100	41.6	16	16							2230		38.7	22300		3.5

		S_2	C_2	C_2	0.36	2.4	0	50.6	16	16					2390	48.9	30900	3.6
		S_2	C_2	C_2	0.36	2.3	100	50.6	16	16					2350	46.1	28100	3.4
		S_2	C_2	C_2	0.36	2.2	100	50.6	16	16					2260	42.4	23200	3.2
		S_2	C_2	C_2	0.36	2.4	0	63.2	16	16					2390	48.9	30900	3.6
		S_2	C_2	C_2	0.36	2.3	100	63.2	16	16					2330	52.5	30100	4.0
		S_2	C_2	C_2	0.36	2.2	100	63.2	16	16					2260	50.7	24900	3.6
		S_2	C_2	C_2	0.36	2.4	0	35.6	16	16					2390	48.9	30900	3.6
		S_2	C_2	C_2	0.36	2.3	100	35.6	16	16					2370	45.2	27500	3.5
		S_2	C_2	C_2	0.36	2.2	100	35.6	16	16					2240	42.0	21300	3.2
		S_2	C_2	C_2	0.36	2.4	0	66.0	16	16					2390	48.9	30900	3.6
		S_2	C_2	C_2	0.36	2.3	100	66.0	16	16					2280	49.6	28500	3.8
		S_2	C_2	C_2	0.36	2.2	100	66.0	16	16					2210	45.1	23300	3.5
		S_2	C_2	C_2	0.36	2.7	0	72.3	16	16					2530	52.3	39800	4.2
		S_2	C_2	C_2	0.36	2.4	100	72.3	16	16					2380	54.4	36500	4.0
		S_2	C_2	C_2	0.36	2.3	100	72.3	16	16					2280	48.2	29800	3.8
2002	Gómez-Soberón [55]	C_2	C_2	C_2	0.47	2.5	0	38.4	20	20		2590		0.9		39.0	29700	3.7
		C_2	C_2	C_2	0.47	2.5	15	38.4	20	20	2410	2590	5.8	0.9		38.1	29100	3.7
		C_2	C_2	C_2	0.45	2.5	30	38.4	20	20	2410	2590	5.8	0.9		37.0	27800	3.6
		C_2	C_2	C_2	0.42	2.4	60	38.4	20	20	2410	2590	5.8	0.9		35.8	26600	3.4
		C_2	C_2	C_2	0.38	2.3	100	38.4	20	20	2410		5.8			34.5	26700	3.3
2004	Gonçalves et al. [56]	S_2			0.60	4.6	0		15	20		2670		0.5		43.5		
		S_2			0.60	4.1	100		15	20	2450		5.6			38.2		
		S_2			0.45	3.3	0		15	20		2670		0.5		61.7		
		S_2			0.45	2.9	100		15	20	2450		5.6			52.8		
		S_2			0.35	2.6	0		15	20		2670		0.5		74.4		
		S_2			0.35	2.3	100		15	20	2450		5.6			62.8		
		S_2			0.45	3.2	25		15	20		2670		0.5		60.7		
		S_2			0.45	3.1	50		15	20	2450		5.6			59.4*		
2004	Poon et al. [57]	S_1			0.57	3.1	0		20	25		2620		1.3		48.3		
		S_1			0.57	3.1	20		20	25	2330	2620	6.3	1.3		44.9		
		S_1			0.57	3.1	50		20	32	2330	2620	6.3	1.3		44.7		
		S_1			0.57	3.0	100		20	32	2330		6.3			46.8		
		S_1			0.57	3.0	0		20	32		2620		1.3		40.2		

		S_1				0.57	3.1	20		20	32	2330	2620	6.3	1.3			43.2			
		S_1				0.57	2.9	50		20	32	2330	2620	6.3	1.3			39.7			
		S_1				0.57	2.9	100		20	32	2330		6.3				43.3			
		S_1				0.57	3.0	0		20	20		2620		1.3			46.0			
		S_1				0.57	2.8	20		20	20	2330	2620	6.3	1.3			43.0			
		S_1				0.57	2.7	50		20	20	2330	2620	6.3	1.3			38.1			
		S_1				0.57	2.9	100		20	20	2330		6.3				39.1			
2004	Lin et al. [58]	C_1				0.50	2.4	100		25	20							30.2			
		C_1				0.50	2.3	100		25	20							36.2			
		C_1				0.70	3.3	100		25	20							27.7			
		C_1				0.70	3.2	100		25	20							20.4			
2006	Xiao et al. [10]	S_1				0.43	3.0	0		32	19		2820		0.4		2402	35.9*			
		S_1				0.43	2.9	33		32	19	2520	2820	9.3	0.4		2368	34.1			
		S_1				0.43	2.8	53		32	19	2520	2820	9.3	0.4		2345	29.6*			
		S_1				0.43	2.8	72		32	19	2520	2820	9.3	0.4		2316	30.3*			
		S_1				0.43	2.7	100		32	19	2520		9.3			2280	26.7*			
2006	Wei [59]	S_2	C_1	B_1	C_1	0.42	3.0	0		32	32		2786		0.3			36.8*	31880	5.0	2.9
		S_2	C_1	B_1	C_1	0.37	2.9	30		32	32	2442	2786	6.0	0.3			37.2*	29132	5.0	2.8
		S_2	C_1	B_1	C_1	0.34	2.8	50		32	32	2442	2786	6.0	0.3			37.8*	26620	5.2	2.9
		S_2	C_1	B_1	C_1	0.38	2.0	70		32	32	2442	2786	6.0	0.3			36.7*	25433*	5.1*	2.7*
		S_2	C_1	B_1	C_1	0.27	2.7	100		32	32	2442		6.0				35.2*	25111	4.9	2.7
2007	Etxeberria et al. [60]	C_2	C_2		C_2	0.55	4.0	0		25	19		2670		0.9			42.0	33700		2.7
		C_2	C_2		C_2	0.55	3.9	25		25	19	2430	2670	4.4	0.9			42.0	33200		3.0
		C_2	C_2		C_2	0.52	3.6	50		25	19	2430	2670	4.4	0.9			41.0	31800		3.2
		C_2	C_2		C_2	0.50	3.5	100		25	19	2430		4.4				40.0	27000		3.2
2007	Etxeberria et al. [61]	S_2	C_2		C_2	0.55	4.0	0		25	19		2670		0.9		2420	35.5	32437		2.8
		S_2	C_2		C_2	0.55	3.9	25		25	19	2430	2670	4.5	0.9		2400	38.8	31427		3.0
		S_2	C_2		C_2	0.52	3.6	50		25	19	2430	2670	4.5	0.9		2390	39.4	29758		3.4
		S_2	C_2		C_2	0.50	3.5	100		25	19	2430	2670	4.5			2340	38.3	27063		2.8
2007	Evangelista and De Brito [62]	S_2	C_2		C_2	0.41	3.1	0		20	25		2564		0.8			59.4	35500		3.9
		S_2				0.42	3.2	10		20	25	2165	2564	6.8	0.8			62.2			
		S_2				0.43	3.4	20		20	25	2165	2564	6.8	0.8			58.4			
		S_2	C_2		C_2	0.44	3.5	30		20	25	2165	2564	6.8	0.8			61.3	34200		3.7

		S_2				0.45	3.7	50		20	25	2165	2564	6.8	0.8			60.8*			
		S_2	C_2		C_2	0.45	4.4	100		20	25	2165		6.8				61.0	28900		3.0
2007	Poon et al. [63]	S_1				0.51	2.6	0		20	20		2620		1.1			48.6			
		S_1				0.49	2.5	20		20	20	2570	2620	3.5	1.1			45.3			
		S_1				0.48	2.5	50		20	20	2570	2620	3.5	1.1			42.5			
		S_1				0.46	2.5	80		20	20	2570	2620	3.5	1.1			39.2*			
		S_1				0.45	2.5	100		20	20	2570		3.5				37.1			
2007	Ajdukiewicz and Kliszczewicz [64]	C_2	C_2		C_2	0.49	4.7	0		16	20	2270					2350	37.7	31900		2.9
		C_2	C_2		C_2	0.49	3.9	100		16	20	2270					2250	34.6	25900		2.6
		C_2	C_2		C_2	0.36	2.4	0		16	20	2270					2380	57.9	35600		3.5
		C_2	C_2		C_2	0.36	2.2	100		16	20	2270					2310	56.4	31800		3.3
		C_2	C_2		C_2	0.49	3.7	0		16	25	2780					2390	39.8	27300		3.2
		C_2	C_2		C_2	0.49	4.4	100		16	25	2780					2310	40.1	24300		2.9
		C_2	C_2		C_2	0.36	2.4	0		16	25	2780					2390	58.3	32500		4.4
		C_2	C_2		C_2	0.36	2.3	100		16	25	2780					2290	60.2	28500		4.3
		C_2	C_2		C_2	0.49	5.1	0		16	16	2565					2550	40.1	36200		3.4
		C_2	C_2		C_2	0.49	4.2	100		16	16	2565					2400	35.3	31700		3.0
		C_2	C_2		C_2	0.36	2.7	0		16	16	2565					2530	61.8	41900		4.5
		C_2	C_2		C_2	0.36	2.4	100		16	16	2565					2430	57.5	35900		3.7
2007	Hu [65]	S_2	C_1	B_1	C_1	0.47	3.3	0		32	22		2788		0.3			31.2*	30296	4.6	2.4
		S_2	C_1	B_1	C_1	0.41	3.3	30		32	22	2449	2788	6.0	0.3			31.0*	28620	4.6	2.5
		S_2	C_1	B_1	C_1	0.38	3.2	50		32	22	2449	2788	6.0	0.3			29.3*	25119	4.4	2.4
		S_2	C_1	B_1	C_1	0.36	3.1	70		32	22	2449	2788	6.0	0.3			28.4*	23378*	4.4*	2.4*
		S_2	C_1	B_1	C_1	0.32	3.0	100		32	22	2449		6.0				27.2*	23297	4.2	2.3
2007	Kou et al. [66]	S_1	C_1		C_1	0.45	2.8	0		20	19		2620		1.1			66.8	38700		3.4
		S_1	C_1		C_1	0.45	2.8	20		20	19	2570	2620	3.5	1.1			62.4	29100		3.2
		S_1	C_1		C_1	0.45	2.7	50		20	19	2570	2620	3.5	1.1			55.8	26000		3.0
		S_1	C_1		C_1	0.45	2.7	100		20	32	2570		3.5				42.0	23400		2.8
		S_1	C_1		C_1	0.55	2.6	0		20	32		2620		1.1			48.6	30000		3.3
		S_1	C_1		C_1	0.55	2.5	20		20	32	2570	2620	3.5	1.1			45.3	28800		3.2
		S_1	C_1		C_1	0.55	2.5	50		20	32	2570	2620	3.5	1.1			42.5	26300		3.2
		S_1	C_1		C_1	0.55	2.5	100		20	32	2570		3.5				38.1	21700		3.1
2007	Rahal [24]	S_1	C_2			0.65	3.1	0		19	25		2860		0.7			21.8*	11400*		
		S_1	C_2			0.65	3.1	100		19	25	2390		4.4				22.1	12400*		

		S_1	C_2			0.50	2.9	0		19	25		2860		0.7				26.7*	14900*		
		S_1	C_2			0.50	2.9	100		19	25	2390		4.4					25.1	11300*		
		S_1	C_2			0.48	2.8	0		19	25		2860		0.7				28.9*	15700*		
		S_1	C_2			0.48	2.8	100		19	25	2390		4.4					27.2	14900*		
		S_1	C_2			0.43	2.6	0		19	25		2860		0.7				31.1*	17800*		
		S_1	C_2			0.43	2.6	100		19	25	2390		4.4					28.7*	14700*		
		S_1	C_2			0.40	2.4	0		19	19		2860		0.7				33.7*	17100*		
		S_1	C_2			0.40	2.4	100		19	19	2390		4.4					29.5*	13400*		
2007	Wang [67]	S_2				0.54	3.1	0		32	25		2840		0.4				26.8*			
		S_2				0.35	3.1	100		32	25	2512		6.3					24.6*			
		S_2				0.49	3.1	100		32	25	2670		1.8					26.9			
		S_2				0.46	2.7	0		32	25		2840		0.4				34.3*			
		S_2				0.31	2.7	100		32	32	2512		6.3					30.2*			
		S_2				0.43	2.7	100		32	32	2670		1.8					34.2			
		S_2				0.42	2.4	0		32	32		2840		0.4				38.6*			
		S_2				0.28	2.4	100		32	32	2512		6.3					35.5*			
		S_2				0.39	2.4	100		32	32	2670		1.8					38.4			
2008	Casuccio et al. [68]	C_1	C_1			0.70	4.1	0		30	10		2700		0.5		28.0		18.1*	27100		
		C_1	C_1			0.67	3.9	100		30	10	2520		3.8		34			18.0*	23400		
		C_1	C_1			0.67	3.9	100		30	10	2510		3.9		39			15.4*	22600		
		C_1	C_1			0.35	3.1	0		30	10		2700		0.5		28.0		37.5*	33100		
		C_1	C_1			0.35	4.3	100		30	10	2520		3.8		34			36.4	28800		
		C_1	C_1			0.36	2.1	100		30	10	2510		3.9		39			35.7	28300		
		C_1	C_1			0.34	2.1	0		30	19		2700		0.5		28.0		48.4*	39900		
		C_1	C_1			0.34	1.9	100		30	19	2520		3.8		34			44.4	34200		
		C_1	C_1			0.34	2.2	100		30	30	2510		3.9		39			43.8	32700		
2008	Hu [69]	S_2	C_1	B_1	C_1	0.47	3.3	0		32	22		2788		0.3				31.2*	30296	4.6	2.4
		S_2	C_1	B_1	C_1	0.41	3.3	30		32	22	2449	2788	6.0	0.3				31.0*	28620	4.6	2.5
		S_2	C_1	B_1	C_1	0.38	3.2	50		32	22	2449	2788	6.0	0.3				29.3*	25119	4.4	2.4
		S_2	C_1	B_1	C_1	0.36	3.1	70		32	22	2449	2788	6.0	0.3				28.4*	23378*	4.4*	2.4*
		S_2	C_1	B_1	C_1	0.32	3.0	100		32	25	2449		6.0					27.2*	23297	4.2	2.3
2008	Kou et al. [70]	C_1	C_1		C_1	0.55	2.6	0		20	20		2620		1.1				48.6	30300		3.7
		C_1	C_1		C_1	0.55	2.6	20		20	20	2580	2620	3.5	1.1				45.3	28650		3.6
		C_1	C_1		C_1	0.55	2.5	50		20	20	2580	2620	3.5	1.1				42.5	26400		3.4

		C_1	C_1		C_1	0.55	2.5	100		20	20	2580		3.5					38.1	24200		3.3
		C_1	C_1		C_1	0.50	2.6	0		20	20		2620		1.1				54.1	31100		3.8
		C_1	C_1		C_1	0.50	2.6	20		20	20	2580	2620	3.5	1.1				51.7	29570		3.6
		C_1	C_1		C_1	0.50	2.6	50		20	20	2580	2620	3.5	1.1				47.1	27510		3.6
		C_1	C_1		C_1	0.50	2.6	100		20	20	2580		3.5					43.4	25670		3.4
		C_1	C_1		C_1	0.45	2.8	0		20	20		2620		1.1				66.8	32210		3.8
		C_1	C_1		C_1	0.45	2.8	20		20	20	2580	2620	3.5	1.1				62.4*	30370		3.7
		C_1	C_1		C_1	0.45	2.7	50		20	20	2580	2620	3.5	1.1				56.8*	28540		3.7
		C_1	C_1		C_1	0.45	2.5	100		20	20	2580		3.5					52.1	26600		3.5
		C_1	C_1		C_1	0.40	2.9	0		20	20		2620		1.1				72.3	33470		4.2
		C_1	C_1		C_1	0.40	2.8	20		20	20	2580	2620	3.5	1.1				69.6*	31400		4.1
		C_1	C_1		C_1	0.40	2.8	50		20	20	2580	2620	3.5	1.1				65.3*	29200		4.0
		C_1	C_1		C_1	0.40	2.8	100		20	20	2580		3.5					58.5	27850		3.8
2008	Yang et al. [71]	C_1	C_1	B_2	C_1	0.50	2.9	0		25	20		2600		1.4				39.5	31722	4.0	4.3
		C_1	C_1	B_2	C_1	0.50	2.9	30		25	20	2530	2600	1.9	1.4				36.7	30374	4.0	4.2
		C_1	C_1	B_2	C_1	0.50	2.9	50		25	20	2530	2600	1.9	1.4				38.0	30520	3.7	4.0
		C_1	C_1	B_2	C_1	0.50	2.8	100		25	32	2530		1.9					36.0	29223	3.5	3.8
		C_1	C_1	B_2	C_1	0.50	2.8	30		25	32		2600		1.4				32.6	28361	3.6	3.6
		C_1	C_1	B_2	C_1	0.50	2.8	50		25	32	2400	2600	6.2	1.4				30.4	25885	3.4	3.4
		C_1	C_1	B_2	C_1	0.50	2.7	100		25	32	2400		6.2					29.5	23717	3.2	3.2
2008	Zhou et al. [72]	S_1				0.58	3.2	0		32	32		2970		0.8				44.6			
		S_1				0.52	3.2	50		32	22	2720	2970	4.8	0.8				41.4			
		S_1				0.45	3.2	100		32	22	2720		4.8					40.7			
		S_1				0.52	3.2	50		32	22	2650	2970	4.6	0.8				38.3			
		S_1				0.46	3.2	100		32	22	2650		4.6					36.6			
		S_1				0.52	3.2	50		32	22	2880	2970	4.4	0.8				41.2			
		S_1				0.47	3.2	100		32	22	2880		4.4					40.3			
2009	Domingo-Cabo et al. [73]	C_2	C_2			0.41	2.6	0		20	20		2647		1.0		27.8	2360	42.3	33308		
		C_2	C_2			0.39	2.5	20		20	20	2338	2647	5.2	1.0	40.2	27.8	2350	47.4	32360		
		C_2	C_2			0.36	2.5	50		20	20	2338	2647	5.2	1.0	40.2	27.8	2340	47.3	33516		
		C_2	C_2			0.32	2.3	100		20	20	2338		5.2		40.2		2320	54.8	30337		
2009	Padmini et al. [74]	S_2				0.52	2.9	0		22	20								48.0			
		S_2				0.52	2.9	10		22	20								46.9			

		S_2				0.52	2.8	20	22	20		47.7				
		S_2				0.52	2.8	30	22	20		50.8				
		S_2				0.52	2.8	40	22	20		48.0				
		S_2				0.52	2.8	50	22	25		49.5				
		S_2				0.52	2.7	100	22	25		50.3				
		S_2	C_2	B_2		0.54	3.2	0	22	25		23.5*	36200	3.1		
		S_2	C_2	B_2		0.54	3.1	25	22	25		21.6*	34100	2.9*		
		S_2	C_2	B_2		0.54	3.1	100	22	20		20.5*	32100	3.1		
2009	Yang et al. [75]	S_2			C_1	0.76	4.5	100	30	32		21.1*				1.2
		S_2			C_1	0.76	4.5	100	30	32		22.0				1.6
		S_2			C_1	0.76	4.5	100	30	32		23.1				1.5
		S_2			C_1	0.76	4.5	100	30	32		23.5				1.3
		S_2			C_1	0.76	4.5	100	30	32		20.4				1.5
		S_2			C_1	0.76	4.5	100	30	32		18.9				1.3
		S_2			C_1	0.76	4.5	100	30	32		21.2				1.5
		S_2			C_1	0.66	3.9	100	30	32		25.7				1.6
		S_2			C_1	0.66	3.9	100	30	32		28.0				1.6
		S_2			C_1	0.66	3.9	100	30	32		25.1				1.5
		S_2			C_1	0.66	3.9	100	30	32		27.5				1.6
		S_2			C_1	0.66	3.9	100	30	32		26.1				1.5
		S_2			C_1	0.66	3.9	100	30	32		27.4				1.1*
		S_2			C_1	0.66	3.9	100	30	32		27.7				1.6
		S_2			C_1	0.66	3.9	100	30	32		25.0				1.8
		S_2			C_1	0.57	3.3	100	30	32		30.5				1.7
		S_2			C_1	0.57	3.3	100	30	30		32.7				1.7
		S_2			C_1	0.57	3.3	100	30	30		32.8				1.7
		S_2			C_1	0.57	3.3	100	30	30		33.1				1.8
		S_2			C_1	0.48	2.7	100	30	30		35.3				2.0
		S_2			C_1	0.48	2.7	100	30	30		35.2				1.4*
		S_2			C_1	0.48	2.7	100	30	30		32.5				1.9
		S_2			C_1	0.48	2.7	100	30	30		33.8				1.7
		S_2			C_1	0.41	2.2	100	30	30		41.9				2.1
		S_2			C_1	0.41	2.2	100	30	30		38.4				2.0
		S_2			C_1	0.41	2.2	100	30	30		38.7				2.1
		S_2			C_1	0.41	2.2	100	30	30		41.2				2.2

2009	Ye [76]	S_2	C_1	B_1	C_1	0.54	3.1	0	32	32		2840		0.4				26.8*	28500	4.2	2.3
		S_2	C_1	B_1	C_1	0.35	3.1	100	32	32	2512		6.3					24.6*	22180	4.2	2.1
		S_2	C_1	B_1	C_1	0.49	3.1	100	32	32	2670		1.8					26.9	27900	4.2	2.3
		S_2	C_1	B_1	C_1	0.46	3.3	0	32	32		2840		0.4				34.3*	31230	4.8	2.8
		S_2	C_1	B_1	C_1	0.27	3.3	100	32	32	2512		6.3					30.2*	23860	4.7	2.5
		S_2	C_1	B_1	C_1	0.41	3.3	100	32	32	2670		1.8					34.2	31070	4.8	2.7
		S_2	C_1	B_1	C_1	0.42	3.0	0	32	32		2840		0.4				38.6*	32500	5.1	3.0
		S_2	C_1	B_1	C_1	0.24	3.0	100	32	32	2512		6.3					35.5*	25200	5.0	2.7
		S_2	C_1	B_1	C_1	0.38	3.0	100	32	32	2670		1.8					38.4	31800	5.1	2.9
2010	Corinaldesi [25]	S_1	C_1			0.40	3.1	50	12	30	2420	2570	6.8	3.0				43.3	28600		
		S_1	C_1			0.45	3.1	50	12	30	2400	2570	6.8	3.0				39.6	28600		
		S_1	C_1			0.50	3.2	50	12	30	2400	2570	6.8	3.0				38.1	27200		
		S_1	C_1			0.55	3.2	50	12	30	2400	2570	6.8	3.0				34.5	26700		
		S_1	C_1			0.60	3.3	50	12	30	2400	2570	6.8	3.0				31.6	26400		
		S_1	C_1			0.40	3.1	50	22	30	2420	2570	8.8	3.0				46.1	32700		
		S_1	C_1			0.45	3.1	50	22	30	2420	2570	8.8	3.0				45.8	33300		
		S_1	C_1			0.50	3.2	50	22	30	2420	2570	8.8	3.0				39.9	27700		
		S_1	C_1			0.55	3.3	50	22	20	2420	2570	8.8	3.0				36.3	24000		
		S_1	C_1			0.60	3.3	50	22	20	2420	2570	8.8	3.0				34.7	22900		
2010	Kumutha and Vijai [77]	S_1	C_2	B_1	C_2	0.50	3.5	0	20	20		2870					2610	28.3*	27665	4.9	3.3
		S_1	C_2	B_1	C_2	0.50	3.5	20	20	20	2400	2870					2559	27.2*	27078	3.9	3.1
		S_1	C_2	B_1	C_2	0.50	3.5	40	20	20	2400	2870					2510	26.5*	26222	2.9*	2.8
		S_1	C_2	B_1	C_2	0.50	3.5	60	20	20	2400	2870					2488	25.4*	25527	2.7*	2.7
		S_1	C_2	B_1	C_2	0.50	3.5	80	20	20	2400	2870					2478	25.1*	25250*	2.6*	2.2*
		S_1	C_2	B_1	C_2	0.50	3.5	100	20	20	2400						2454	20.4*	22681	2.4*	2.1
		S_1	C_2	B_1	C_2	0.50	3.8	20	20	20	2630	2870					2602	26.4*	25927	4.4	2.6
		S_1	C_2	B_1	C_2	0.50	4.1	40	20	20	2630	2870					2582	25.9*	25782	4.1	2.5
		S_1	C_2	B_1	C_2	0.50	4.5	60	20	20	2630	2870					2558	23.5*	25113	3.8	2.3
		S_1	C_2	B_1	C_2	0.50	4.8	80	20	20	2630	2870					2538	15.4*	18048*	3.4*	2.0*
2010	Radonjanin et al. [78]	C_1	C_1	B_1	C_1	0.51	3.6	0	32	20		2671		0.3		29.2		43.4	35550	5.4	2.7
		C_1	C_1	B_1	C_1	0.57	3.6	50	32	20	2489	2671	2.4	0.3	34	29.2		45.2	32250	5.7	3.2
		C_1	C_1	B_1	C_1	0.62	3.6	100	32	20	2489		2.4		34			45.7*	29100	5.2*	2.8
2010	Zega and Di Maio [79]	S_1	C_2		C_2	0.65	3.3	0	19	20		2720		0.2		25.0		20.2*	25000		2.1

		S_1	C_2	C_2	0.65	3.2	25	19	20	2440	2720	5.8	0.2	33.6	25.0		18.5*	24900		1.9
		S_1	C_2	C_2	0.65	3.1	50	19	20	2440	2720	5.8	0.2	33.6	25.0		18.0*	23000		1.9
		S_1	C_2	C_2	0.65	3.1	75	19	20	2440	2720	5.8	0.2		25.0		16.5*	20500*		1.4*
		S_1	C_2	C_2	0.42	2.7	0	19	20		2720		0.2	33.6	25.0		40.0	33500		3.2
		S_1	C_2	C_2	0.42	2.7	25	19	20	2440	2720	5.8	0.2	33.6	25.0		33.0*	31500		3.1
		S_1	C_2	C_2	0.42	2.6	50	19	20	2440	2720	5.8	0.2	33.6	25.0		34.5	31000		3.1
		S_1	C_2	C_2	0.42	2.5	75	19	20	2440	2720	5.8	0.2	33.6	25.0		34.0*	30000*		2.9*
2011	Belén et al. [80]	C_1	C_1	C_1	0.65	3.4	0	16	20		2730		2.5			2340	31.9	29569		2.9
		C_1	C_1	C_1	0.66	3.3	20	16	20	2400	2730	5.0	2.5			2330	31.7	28190		2.4
		C_1	C_1	C_1	0.68	3.1	50	16	20	2400	2730	5.0	2.5			2310	32.4	26352		2.5
		C_1	C_1	C_1	0.68	2.8	100	16	20	2400		5.0				2270	30.1	24261		2.6
		C_1	C_1	C_1	0.50	2.6	0	16	20		2730		2.5			2360	44.8	33875		2.8
		C_1	C_1	C_1	0.51	2.5	20	16	20	2400	2730	5.0	2.5			2330	43.7	32594		3.1
		C_1	C_1	C_1	0.53	2.3	50	16	20	2400	2730	5.0	2.5			2310	37.5	28817		2.9
		C_1	C_1	C_1	0.56	2.1	100	16	20	2400		5.0				2270	40.5	23994		2.9
2011	Fathifazl et al. [81]	C_2			0.45	1.9	0	19	25	2420		5.4	0.9			2324	35.2*			
		C_2			0.45	3.4	64	19	25	2420	2740	5.4	0.9			2303	41.4*			
		C_2			0.45	2.3	100	19	25	2420	2740	5.4				2290	43.9			
		C_2			0.45	2.1	0	19	25	2500		3.3	0.9			2322	34.1			
		C_2			0.45	3.1	64	19	25	2500	2740	3.3	0.9			2364	44.8*			
		C_2			0.45	2.5	100	19	25	2500	2740	3.3				2348	45.9			
2011	González-Fonteboa et al. [82]	C_2	C_2	C_2	0.65	3.4	0	16	20		2720		2.0		23.0	2340	31.9	29569		2.9
		C_2	C_2	C_2	0.65	3.3	20	16	20	2400	2720	5.0	2.0	34	23.0	2320	31.7	28190		2.4
		C_2	C_2	C_2	0.65	3.1	50	16	20	2400	2720	5.0	2.0	34	23.0	2300	32.4	26352		2.5
		C_2	C_2	C_2	0.65	2.8	100	16	20	2400		5.0		34		2270	30.1	24261		2.6
		C_2	C_2	C_2	0.50	2.6	0	16	20		2720		2.0		23.0	2360	44.8	33875		2.8
		C_2	C_2	C_2	0.50	2.5	20	16	20	2400	2720	5.0	2.0	34	23.0	2330	43.7	32594		3.1
		C_2	C_2	C_2	0.50	2.8	50	16	20	2400	2720	5.0	2.0	34	23.0	2310	37.5	28817		2.9
		C_2	C_2	C_2	0.50	2.1	100	16	20	2400		5.0		34		2270	40.5	23994		2.9
2011	Rao et al. [83]	C_2	C_2	C_2	0.43	3.1	0	20	20		2620		1.1		21.6	2146	51.8	31220	5.2	2.7
		C_2	C_2	C_2	0.43	3.0	25	20	20	2661	2620	1.9	1.1		21.6	2329	47.0	23570	4.2	2.3
		C_2	C_2	C_2	0.43	2.9	50	20	20	2602	2620	2.6	1.1		21.6	2302	46.0	21540	4.4	2.1

		C_2	C_2	C_2	0.43	2.8	100		20	20	2510		3.9		38.8		2175	42.5	20350*	5.0	2.0
2011	Somna et al. [84]	C_1			0.45	2.3	0		19	25		2730		0.45		23		44.4			
		C_1			0.45	2.3	100		19	25	2490		4.8		37			41.0			
		C_1			0.55	2.9	0		19	25		2730		0.45		23		36.7			
		C_1			0.55	2.9	100		19	25	2490		4.8		37			33.3			
		C_1			0.65	3.5	0		19	25		2730		0.45		23		30.4			
		C_1			0.65	3.5	100		19	25	2490		4.8		37			24.8			
2012	Abd Elhakam et al. [85]	S_2		C_1	0.60	4.6	0		19	20								25.0*			2.7
		S_2		C_1	0.60	4.6	25		19	20								26.7			2.2
		S_2		C_1	0.60	4.5	50		19	20								21.5*			1.8
		S_2		C_1	0.60	4.5	75		19	20								21.4*			1.4*
		S_2		C_1	0.60	4.4	100		19	20								20.0*			1.2*
		S_2		C_1	0.45	2.6	0		19	20								39.5			3.4
		S_2		C_1	0.45	2.6	25		19	20								38.3			3.1
		S_2		C_1	0.45	2.5	50		19	20								37.0			2.7
		S_2		C_1	0.45	2.5	75		19	19								35.0*			2.5*
		S_2		C_1	0.45	2.5	100		19	19								33.3			2.1
2012	Cui et al. [86]	S_2			0.49	3.1	0		25	16		2710		0.8				44.3			
		S_2			0.37	3.0	100	26.3	25	16	2490		2.9					37.6			
		S_2			0.43	3.0	100	42.7	25	16	2570		2.9					43.3			
		S_2			0.36	2.9	100	42.7	25	16	2440		5.6					42.6			
		S_2			0.36	2.9	100	65.3	25	16	2470		5.3					44.7			
2012	Hoffmann et al. [26]	C_2	C_2	B_2	0.53	6.5	0		32	15		2650		0.2				39.3	26500	4.4	
		C_2	C_2	B_2	0.43	5.4	100		32	15	2263		6.0					33.2*	21450	4.3	
		C_2	C_2	B_2	0.49	5.1	100		32	15	2283		4.2					35.6	23400	4.8	
		C_2	C_2	B_2	0.53	5.1	100		32	15	2292		4.3					34.6	22550	5.0	
		C_2	C_2	B_2	0.60	5.3	100		32	15	2301		5.0					37.3	20700	5.1*	
		C_2	C_2	B_2	0.54	6.4	90		32	15	2609	2650	1.5	0.2				45.4*	32433*	4.4*	
		C_2	C_2	B_2	0.46	5.9	60		32	15	2518	2650	2.7	0.2				54.3	30667	5.9	
		C_2	C_2	B_2	0.44	5.8	60		32	15	2584	2650	1.6	0.2				54.4	33333	6.4	
		C_2	C_2	B_2	0.45	6.4	25		32	32	2594	2650	1.6	0.2				53.4	34800	6.0	
2012	Li and Xiao [87]	S_1	C_1		0.43	3.0	0		32	25								34.8*	26568		
		S_1	C_1		0.47	2.9	30		32	32								31.9*	26552		

		S_1	C_1		0.49	2.8	50		32	32							30.6	26333	
		S_1	C_1		0.54	2.7	100		32	32							29.7	25650	
2012	Limbachiya et al. [88]	C_2	C_2		0.66	4.6	0		20	22		2510		1.4			21.0*	19500*	
		C_2	C_2		0.66	4.6	30		20	22	2340	2510	5.3	1.4			20.0*	17500*	
		C_2	C_2		0.61	4.3	50		20	22	2340	2510	5.3	1.4			19.0*	15500*	
		C_2	C_2		0.58	4.0	100		20	22	2340		5.3				18.0*	12500*	
		C_2	C_2		0.55	3.8	0		20	22		2510		1.4			21.0*	18800*	
		C_2	C_2		0.55	3.8	30		20	22	2340	2510	5.3	1.4			23.0*	17000*	
		C_2	C_2		0.51	3.5	50		20	22	2340	2510	5.3	1.4			24.0*	16500*	
		C_2	C_2		0.48	3.4	100		20	22	2340		5.3				21.0	14000*	
		C_2	C_2		0.50	3.5	0		20	22		2510		1.4			31.0	23500*	
		C_2	C_2		0.50	3.5	30		20	22	2340	2510	5.3	1.4			25.0*	18500*	
		C_2	C_2		0.47	3.2	50		20	22	2340	2510	5.3	1.4			29.0*	17000*	
		C_2	C_2		0.44	3.0	100		20	22	2340		5.3				30.0	16500*	
		C_2	C_2		0.48	3.3	0		20	22		2510		1.4			33.0	22000*	
		C_2	C_2		0.48	3.3	30		20	12	2340	2510	5.3	1.4			39.0	21000	
		C_2	C_2		0.44	3.1	50		20	22	2340	2510	5.3	1.4			31.0*	19500	
		C_2	C_2		0.42	2.9	100		20	22	2340		5.3				34.0	16000*	
2012	Marinković et al. [89]	C_1			0.60	4.3	0		32	20		2381					36.6		
		C_1			0.60	3.8	100		32	20	2264		2.0				33.6		
		C_1			0.52	3.6	0		32	20		2389					41.8		
		C_1			0.52	3.2	100		32	25	2276		2.0				41.1		
		C_1			0.47	3.0	0		32	25		2387					48.6		
		C_1			0.47	2.7	100		32	25	2273		2.0				48.1		
2012	Pereira et al. [27]	S_2	C_2	C_2	0.60	3.0	0	37.3	12	20		2720		0.6	2394		39.5	34400	2.9
		S_2	C_2	C_2	0.59	3.2	10	37.3	12	20	2010	2720	10.9	0.6	2377		40.0	33700	2.9
		S_2	C_2	C_2	0.57	3.5	30	37.3	12	20	2010	2720	10.9	0.6	2362		38.6	32300	2.7
		S_2	C_2	C_2	0.54	3.8	50	37.3	12	20	2010	2720	10.9	0.6	2349		37.6	32300	2.6
		S_2	C_2	C_2	0.46	4.6	100	37.3	12	20	2010		10.9		2308		38.6	29900	2.5
		S_2	C_2	C_2	0.45	3.2	0	37.3	12	20		2720		0.6	2450		53.3	41300	3.7
		S_2	C_2	C_2	0.44	3.3	10	37.3	12	20	2010	2720	10.9	0.6	2430		53.7	40600	3.4
		S_2	C_2	C_2	0.42	3.7	30	37.3	12	20	2010	2720	10.9	0.6	2406		51.0	36000	3.3
		S_2	C_2	C_2	0.67	4.0	50	37.3	12	20	2010	2720	10.9	0.6	2388		47.8*	35000*	3.1

		S_2	C_2		C_2	0.68	4.8	100	37.3	12	20	2010		10.9			2369	45.1*	34200*		3.0
		S_2	C_2		C_2	0.67	3.3	0	37.3	12	20		2720		0.6		2475	65.2*	43900*		4.5*
		S_2	C_2		C_2	0.70	3.4	10	37.3	12	20	2010	2720	10.9	0.6		2454	64.6*	43900*		4.2*
		S_2	C_2		C_2	0.53	3.8	30	37.3	12	20	2010	2720	10.9	0.6		2445	65.4*	41900*		4.5
		S_2	C_2		C_2	0.53	4.1	50	37.3	12	20	2010	2720	10.9	0.6		2428	63.2*	40200*		3.7
		S_2	C_2		C_2	0.53	5.0	100	37.3	12	20	2010		10.9			2417	63.0*	39700*		3.4
2013	Barbudo et al. [90]	C_2	C_2			0.54	3.0	0	41.4	20	22		2581		1.2		24.8		49.8	38480		
		C_2	C_2			0.54	3.0	20	41.4	20	22	2451	2581	7.3	1.2	40	24.8		50.5	37550		
		C_2	C_2			0.54	3.0	50	41.4	20	22	2451	2581	7.3	1.2	40	24.8		48.1	36280		
		C_2	C_2			0.54	2.9	100	41.4	20	22	2451		7.3		40			45.2	31280		
		C_2	C_2			0.45	3.1	0	41.4	20	22		2581		1.2		24.8		59.7	41630		
		C_2	C_2			0.45	3.1	20	41.4	20	22	2451	2581	7.3	1.2	40	24.8		64.7	40100		
		C_2	C_2			0.45	3.1	50	41.4	20	22	2451	2581	7.3	1.2	40	24.8		55.0	37000		
		C_2	C_2			0.45	3.1	100	41.4	20	22	2451		7.3		40			53.9	32750		
		C_2	C_2			0.40	3.2	0	41.4	20	22		2581		1.2		24.8		78.7*	48800*		
		C_2	C_2			0.40	3.2	20	41.4	20	22	2451	2581	7.3	1.2	40	24.8		69.9*	45700*		
		C_2	C_2			0.40	3.2	50	41.4	20	22	2451	2581	7.3	1.2	40	24.8		63.8	41630		
		C_2	C_2			0.40	3.1	100	41.4	20	22	2451		7.3		40			62.8*	37440		
2013	Butler et al. [91]	C_1	C_1	B_2	C_1	0.48	4.1	0		10	20		2670		1.5		11.9	2388	38.9	32090	5.8	3.2
		C_1	C_1	B_2	C_1	0.48	3.5	100		10	20	2360		4.7		15.1		2316	38.6	29920	5.2	3.5
		C_1	C_1	B_2	C_1	0.39	3.1	100		10	20	2280		6.2		22.1		2256	38.1	27370	5.2	3.1
		C_1	C_1	B_2	C_1	0.29	2.6	100		10	20	2220		7.8		25		2270	39.3*	27770	5.2	3.3
		C_1	C_1	B_2	C_1	0.34	2.3	0		10	20		2670		1.5		11.9	2407	61.9	35380	5.2	4.4
		C_1	C_1	B_2	C_1	0.31	2.1	100		10	20	2360		4.7		15.1		2341	60.1	30250	5.8	3.8
		C_1	C_1	B_2	C_1	0.27	1.8	100		10	20	2280		6.2		22.1		2285	60.2	29140	5.0	3.7
		C_1	C_1	B_2	C_1	0.19	1.5	100		10	20	2220		7.8		25		2294	62.8*	28490	4.4*	3.7
2013	Chen et al. [92]	S_2				0.52	3.0	100		25	20	2490		4.9					37.6			
		S_2				0.52	3.0	100		25	20	2570		2.9					43.3			
		S_2				0.52	2.9	100		25	20	2440		5.6					42.6			
		S_2				0.52	2.9	100		25	32	2470		5.3					44.7			
		S_2				0.52	3.1	0		25	32		2710		0.83				44.3			
2013	Hou and Zheng [93]	S_1				0.58	3.2	0		32	16		2970		0.8				44.6			
		S_1				0.52	3.2	53		32	16	2720	2970	4.8	0.8				41.4			

		S_1	0.58	3.2	100	32	16	2720		4.8			40.7
		S_1	0.52	3.2	54	32	25	2650	2970	4.6	0.8		38.3
		S_1	0.58	3.2	100	32	25	2650		4.6			36.6
		S_1	0.52	3.2	53	32	25	2880	2970	4.4	0.8		41.2
		S_1	0.58	3.2	100	32	25	2880		4.4			40.3
2013	Ismail and Ramli [94]	S_1	0.41	1.7	15	20	32	2330	2600	4.4	0.7	2378	50.8
		S_1	0.41	1.7	30	20	32	2330	2600	4.4	0.7	2368	44.9
		S_1	0.41	1.7	45	20	32	2330	2600	4.4	0.7	2369	44.6
		S_1	0.41	1.7	60	20	32	2330	2600	4.4	0.7	2354	42.4
		S_1	0.41	1.7	15	20	32	2370	2600	4.0	0.7	2393	54.0
		S_1	0.41	1.7	30	20	32	2370	2600	4.0	0.7	2404	56.0
		S_1	0.41	1.7	45	20	32	2370	2600	4.0	0.7	2435	54.4
		S_1	0.41	1.7	60	20	32	2370	2600	4.0	0.7	2347	40.6
		S_1	0.41	1.7	15	20	20	2390	2600	3.6	0.7	2383	55.2
		S_1	0.41	1.7	30	20	20	2390	2600	3.6	0.7	2374	53.5
		S_1	0.41	1.7	45	20	20	2390	2600	3.6	0.7	2365	56.9
		S_1	0.41	1.7	60	20	20	2390	2600	3.6	0.7	2345	54.7
		S_1	0.41	1.7	15	20	20	2320	2600	4.6	0.7	2388	50.5
		S_1	0.41	1.7	30	20	20	2320	2600	4.6	0.7	2383	48.9
		S_1	0.41	1.7	45	20	20	2320	2600	4.6	0.7	2380	45.8
		S_1	0.41	1.7	60	20	20	2320	2600	4.6	0.7	2346	40.0
		S_1	0.41	1.7	15	20	20	2390	2600	3.7	0.7	2379	54.4
		S_1	0.41	1.7	30	20	20	2390	2600	3.7	0.7	2371	50.2
		S_1	0.41	1.7	45	20	20	2390	2600	3.7	0.7	2372	49.5
		S_1	0.41	1.7	60	20	20	2390	2600	3.7	0.7	2355	40.4
		S_1	0.41	1.7	15	20	20	2390	2600	3.5	0.7	2376	45.0
		S_1	0.41	1.7	30	20	20	2390	2600	3.5	0.7	2374	46.9
		S_1	0.41	1.7	45	20	20	2390	2600	3.5	0.7	2378	51.4
		S_1	0.41	1.7	60	20	20	2390	2600	3.5	0.7	2348	53.2
		S_1	0.41	1.7	15	20	20	2380	2600	3.8	0.7	2380	55.3
		S_1	0.41	1.7	30	20	20	2380	2600	3.8	0.7	2364	55.9
		S_1	0.41	1.7	45	20	20	2380	2600	3.8	0.7	2366	52.6
		S_1	0.41	1.7	60	20	20	2380	2600	3.8	0.7	2351	48.0
		S_1	0.41	1.7	15	20	20	2380	2600	3.8	0.7	2384	49.1

		S_1			0.41	1.7	30		20	20	2380	2600	3.8	0.7		2366		49.9			
		S_1			0.41	1.7	45		20	20	2380	2600	3.8	0.7		2356		50.3			
		S_1			0.41	1.7	60		20	20	2380	2600	3.8	0.7		2359		47.5			
		S_1			0.41	1.7	15		20	20	2400	2600	3.5	0.7		2388		43.2			
		S_1			0.41	1.7	30		20	20	2400	2600	3.5	0.7		2367		53.7			
		S_1			0.41	1.7	45		20	20	2400	2600	3.5	0.7		2363		50.0			
		S_1			0.41	1.7	60		20	20	2400	2600	3.5	0.7		2352		43.3			
		S_1			0.41	1.7	15		20	20	2370	2600	4.0	0.7		2383		52.9			
		S_1			0.41	1.7	30		20	20	2370	2600	4.0	0.7		2362		49.9			
		S_1			0.41	1.7	45		20	20	2370	2600	4.0	0.7		2358		53.7			
		S_1			0.41	1.7	60		20	20	2370	2600	4.0	0.7		2349		46.0			
2013	Manzi et al. [95]	C_1	C_1	B_1	0.48	5.1	0	36.0	25	20		2570		1.2			2380	41.3	31400	6.4	3.8
		C_1	C_1	B_1	0.48	5.0	27	36.0	25	20	2250	2570	7.0	1.2			2320	51.4	30300	5.8	3.2
		C_1	C_1	B_1	0.48	4.9	64	36.0	25	20	2250	2570	7.0	1.2			2200	45.6*	24900*	4.9*	3.0*
		C_1	C_1	B_1	0.48	5.0	37	36.0	25	20	2250	2570	7.0	1.2			2270	44.7	26900	4.8	4.1
		C_1	C_1	B_1	0.48	5.0	37	36.0	25	20	2250	2570	7.0	1.2			2300	41.9	30600	5.7	3.3
2013	Matias et al. [96]	C_2			0.50	2.4	100		25	32	2452		4.1			2267		51.0			
		C_2			0.50	2.4	100		25	32	2452		4.1			2237		49.0			
		C_2			0.50	2.4	100		25	32	2452		4.1			2239		48.0			
		C_2			0.50	2.6	0		25	32	2452	2652	4.1	0.8		2350		52.0			
		C_2			0.50	2.5	50		25	32	2452	2652	4.1	0.8		2300		51.0			
		C_2			0.50	2.5	50		25	32	2452	2652	4.1	0.8		2284		51.0			
		C_2			0.50	2.5	50		25	32	2452	2652	4.1	0.8		2296		51.0			
		C_2			0.50	2.5	25		25	32	2452	2652	4.1	0.8		2332		52.0			
		C_2			0.50	2.5	25		25	25	2452	2652	4.1	0.8		2340		50.0			
		C_2			0.50	2.5	25		25	25	2452	2652	4.1	0.8		2308		49.0			
2013	Sheen et al. [97]	C_1	C_1	B_1	0.38	2.0	0		25	38		2630		1.2				54.1	34500	7.7	
		C_1	C_1	B_1	0.28	2.0	100		25	38	2260		7.5					38.3*	26300	6.5	
		C_1	C_1	B_1	0.28	2.0	100		25	38	2260		7.5					32.9*	24300	5.9	
		C_1	C_1	B_1	0.23	2.0	100		25	38	2260		7.5					33.2*	23500*	5.5	
		C_1	C_1	B_1	0.46	2.4	0		25	38		2630		1.2				42.2	29000	7.1	
		C_1	C_1	B_1	0.34	2.4	100		25	38	2260		7.5					31.3*	22900	5.7	
		C_1	C_1	B_1	0.34	2.4	100		25	38	2260		7.5					28.4*	21600	5.3	
		C_1	C_1	B_1	0.28	2.4	100		25	38	2260		7.5					28.0*	21500*	5.1	
		C_1	C_1	B_1	0.58	3.1	0		25	25		2630		1.2				28.8	24800	5.9	

		C_1	C_1	B_1		0.43	3.1	100		25	25	2260		7.5					26.5	19300*	5.5	
		C_1	C_1	B_1		0.43	3.1	100		25	25	2260		7.5					23.3*	17100*	5.1	
		C_1	C_1	B_1		0.35	3.1	100		25	25	2260		7.5					21.6*	17200*	4.7	
		C_1	C_1	B_1		0.67	3.5	0		25	25		2630		1.2				23.6	22800	5.2	
		C_1	C_1	B_1		0.49	3.5	100		25	25	2260		7.5					21.6	16500*	5.3	
		C_1	C_1	B_1		0.49	3.5	100		25	25	2260		7.5					18.0*	16200*	4.8	
		C_1	C_1	B_1		0.40	3.5	100		25	25	2260		7.5					18.8*	15300*	4.5	
		C_1	C_1	B_1		0.80	4.2	0		25	25		2630		1.2				17.3*	18900	4.4	
		C_1	C_1	B_1		0.59	4.2	100		25	25	2260		7.5					16.1	15100*	5.2*	
		C_1	C_1	B_1		0.59	4.2	100		25	25	2260		7.5					13.4*	13800*	4.0	
		C_1	C_1	B_1		0.48	4.2	100		25	25	2260		7.5					13.9*	14100*	3.9	
2013	Thomas et al. [14]	C_2	C_2		C_2	0.60	3.6	0		20	20		2540		1.8		31.0		38.0	34500		2.8
		C_2	C_2		C_2	0.59	3.3	20		20	20	2320	2540	5.3	1.8	42	31.0		41.0	32500		2.8
		C_2	C_2		C_2	0.57	3.3	50		20	20	2320	2540	5.3	1.8	42	31.0		44.0	31000		3.1
		C_2	C_2		C_2	0.54	3.0	100		20	20	2320		5.3		42	31.0		45.0	30200		2.4
		C_2	C_2		C_2	0.46	2.6	0		20	20		2540		1.8	42			51.5	37500		3.3
		C_2	C_2		C_2	0.45	2.5	20		20	20	2320	2540	5.3	1.8		31.0		50.5	36000		3.5
		C_2	C_2		C_2	0.44	2.5	50		20	20	2320	2540	5.3	1.8	42	31.0		45.0	33000		2.7
		C_2	C_2		C_2	0.42	2.3	100		20	20	2320		5.3		42			56.0	31500		3.7
		C_2	C_2		C_2	0.67	3.6	0		20	19		2540		1.8		31.0		37.0	35000		2.7
		C_2	C_2		C_2	0.68	3.4	20		20	19	2320	2540	5.3	1.8	42	31.0		33.5	32500		2.5
		C_2	C_2		C_2	0.67	3.0	50		20	19	2320	2540	5.3	1.8	42	31.0		32.0	30800		2.5
		C_2	C_2		C_2	0.70	2.3	100		20	19	2320		5.3		42			32.0	27000		2.3
		C_2	C_2		C_2	0.53	2.7	0		20	19		2540		1.8		31.0		45.0	35000		3.2
		C_2	C_2		C_2	0.53	2.5	20		20	19	2320	2540	5.3	1.8	42	31.0		44.0	34000		2.8
		C_2	C_2		C_2	0.53	2.2	50		20	19	2320	2540	5.3	1.8	42	31.0		41.0	32500		2.6
		C_2	C_2		C_2	0.52	1.8	100		20	19	2320		5.3		42			41.5	30500		2.3
		C_2	C_2		C_2	0.51	3.1	0		20	20		2540		1.8		31.0		46.5	36500		2.9
		C_2	C_2		C_2	0.52	3.2	20		20	20	2320	2540	5.3	1.8	42	31.0		44.0	36000		2.8
		C_2	C_2		C_2	0.54	3.0	50		20	20	2320	2540	5.3	1.8	42	31.0		41.0	33500		2.7
		C_2	C_2		C_2	0.58	2.8	100		20	20	2320		5.3		42			33.5	32000		2.3
		C_2	C_2		C_2	0.42	2.7	0		20	20		2540		1.8		31.0		58.0	37500		3.4
		C_2	C_2		C_2	0.42	2.9	20		20	20	2320	2540	5.3	1.8	42	31.0		53.5	36000		3.1
		C_2	C_2		C_2	0.44	2.7	50		20	20	2320	2540	5.3	1.8	42	31.0		54.0	34000		3.9

		C_2	C_2	C_2	0.49	2.5	100		20	20	2320		5.3		42			40.0	28000	2.4
2013	Ulloa et al. [98]	C_2			0.42	2.6	50		20	19	2330	2590	6.1	1.2	34.6	29.1		41.6		
		C_2			0.51	2.3	100		20	19	2330		6.1		34.6			31.4		
		C_2			0.52	2.6	50		20	19	2330	2590	6.1	1.2	34.6	29.1		35.5		
		C_2			0.61	2.3	100		20	19	2330		6.1		34.6			26.0		
		C_2			0.44	2.6	50		20	19	2320	2590	5.8	1.2	32.2	29.1		44.6		
		C_2			0.51	2.3	100		20	19	2320		5.8		32.2			36.7		
		C_2			0.62	2.3	100		20	19	2320		5.8		32.2			29.5		
		C_2			0.41	2.8	20		20	19	2360	2590	3.9	1.2	30.8	29.1		46.1		
		C_2			0.42	2.6	50		20	20	2360	2590	3.9	1.2	30.8	29.1		45.1		
		C_2			0.45	2.3	100		20	20	2360		3.9		30.8			42.9		
		C_2			0.50	2.8	20		20	20	2360	2590	3.9	1.2	30.8	29.1		39.3		
		C_2			0.52	2.6	50		20	20	2360	2590	3.9	1.2	30.8	29.1		39.5		
		C_2			0.54	2.3	100		20	20	2360		3.9		30.8			37.7		
		C_2			0.42	2.8	20		20	20	2350	2590	4.5	1.2	28.5	29.1		48.1		
		C_2			0.43	2.6	50		20	20	2350	2590	4.5	1.2	28.5	29.1		41.0		
		C_2			0.40	2.3	100		20	20	2350		4.5		28.5			38.7		
		C_2			0.51	2.8	20		20	20	2350	2590	4.5	1.2	28.5	29.1		42.7		
		C_2			0.52	2.6	50		20	20	2350	2590	4.5	1.2	28.5	29.1		35.4		
		C_2			0.50	2.3	100		20	20	2350		4.5		28.5			31.4		
		C_2			0.42	2.8	20		20	20	2350	2590	4.7	1.2	30.1	29.1		48.5		
		C_2			0.42	2.6	50		20	20	2350	2590	4.7	1.2	30.1	29.1		45.4		
		C_2			0.43	2.3	100		20	20	2350		4.7		30.1			37.0		
		C_2			0.52	2.8	20		20	20	2350	2590	4.7	1.2	30.1	29.1		41.3		
		C_2			0.52	2.6	50		20	20	2350	2590	4.7	1.2	30.1	29.1		36.8		
		C_2			0.56	2.3	100		20	20	2350		4.7		30.1			31.2		
2013	Xiao et al. [99]	S_2	C_1		0.41	2.6	0		32	20		2820		0.4				47.2	33100	
		S_2	C_1		0.38	2.6	33		32	20	2578	2820	9.3	0.4				42.4	30940	
		S_2	C_1		0.36	2.6	53		32	20	2578	2820	9.3	0.4				45.7	31910	
		S_2	C_1		0.34	2.6	72		32	20	2578	2820	9.3	0.4				36.7*	29090*	
		S_2	C_1		0.31	2.6	100		32	20	2578		9.3					38.9*	26510	
2013	Younis and Pilakoutas [9]	S_1			0.47	3.8	0		20	25		2610		1.0				53.1		
		S_1			0.47	3.7	20		20	25	2336	2610	3.6	1.0				50.0		
		S_1			0.47	3.6	50		20	25	2315	2610	3.6	1.0				45.3		

		S_1				0.47	3.6	75		20	25	2295	2610	3.6	1.0					44.0*			
		S_1				0.47	3.5	100		20	25	2273		3.6						41.6			
2014	Andreu and Miren [100]	S_2	C_1	B_1	C_1	0.29	2.9	0		10	10		2680		2.1		24.8	2510		102.1	50410	6.5	5.1
		S_2	C_1	B_1	C_1	0.29	2.8	20	100.0	10	10	2470	2680	3.7	2.1	24	24.8	2500		108.0*	48540	7.4*	5.7
		S_2	C_1	B_1	C_1	0.29	2.8	50	100.0	10	10	2470	2680	3.7	2.1	24	24.8	2480		104.8*	47930	7.7*	5.6*
		S_2	C_1	B_1	C_1	0.29	2.7	100	100.0	10	10	2470		3.7		24		2430		108.5*	46100	6.8*	5.1*
		S_2	C_1	B_1	C_1	0.29	2.8	20	60.0	10	10	2390	2680	4.9	2.1	25.2	24.8	2440		102.5	47790	8.0*	6.3*
		S_2	C_1	B_1	C_1	0.29	2.7	50	60.0	10	10	2390	2680	4.9	2.1	25.2	24.8	2400		103.1*	44280	6.8	5.1
		S_2	C_1	B_1	C_1	0.29	2.6	100	60.0	10	10	2390		4.9		25.2		2340		100.8*	40090	6.3	5.9*
		S_2	C_1	B_1	C_1	0.29	2.8	20	40.0	10	10	2300	2680	5.9	2.1	24.3	24.8	2470		104.3	48290	6.7	5.3
		S_2	C_1	B_1	C_1	0.29	2.7	50	40.0	10	10	2300	2680	5.9	2.1	24.3	24.8	2430		96.8*	43040	6.8	6.2*
		S_2	C_1	B_1	C_1	0.29	2.5	100	40.0	10	10	2300		5.9		24.3		2390		91.2*	37150	6.5	4.2
2014	Beltrán et al. [101]	C_2		B_1	C_2	0.65	4.6	0		20	30		2680		1.53		20			18.0*		2.4*	2.1
		C_2		B_1	C_2	0.65	4.7	25		20	30	2380	2680	6.94	1.53	29	20			14.7*		2.1*	1.8
		C_2		B_1	C_2	0.65	4.8	50		20	30	2380	2680	6.94	1.53	29	20			14.6*		1.9*	2.0
		C_2		B_1	C_2	0.65	4.8	75		20	30	2380	2680	6.94	1.53	29	20			14.2*		1.9*	1.7*
		C_2		B_1	C_2	0.72	5.8	0		20	20		2680		1.53		20			30.8		2.3*	2.3
		C_2		B_1	C_2	0.72	5.9	20		20	20	2380	2680	6.94	1.53	29	20			26.8		2.7	2.5
		C_2		B_1	C_2	0.72	6.0	40		20	20	2380	2680	6.94	1.53	29	20			26.6		2.0*	2.1
		C_2		B_1	C_2	0.45	1.9	0		16	20		2680		1.53		20			66.9		3.8	4.3
		C_2		B_1	C_2	0.45	2.3	20		16	20	2380	2680	6.94	1.53	29	20			49.3		2.8*	3.3
		C_2		B_1	C_2	0.45	2.5	40		16	20	2380	2680	6.94	1.53	29	20			40.9		2.7*	2.8
2014	Beltrán et al. [102]	C_2	C_2	B_2		0.60	3.5	0		16	20		2680		1.9			2167	2390	42.0	27300	4.7	
		C_2	C_2	B_2		0.60	3.4	20		16	20	2380	2680	6.9	1.9			2098	2330	42.9	26200	4.7	
		C_2	C_2	B_2		0.60	3.4	50		16	20	2380	2680	6.9	1.9			2060	2290	42.5	25900	4.7	
		C_2	C_2	B_2		0.60	3.2	100		16	20	2380		6.9				1989	2240	40.9	25100	4.8	
		C_2	C_2	B_2		0.50	2.7	0		16	20		2680		1.9			2188	2370	50.2	30000	5.1	
		C_2	C_2	B_2		0.50	2.6	20		16	20	2380	2680	6.9	1.9			2136	2330	51.6	29900	5.1	
		C_2	C_2	B_2		0.50	2.5	50		16	20	2380	2680	6.9	1.9			2112	2320	51.6	27200	5.1	
		C_2	C_2	B_2		0.50	2.4	100		16	20	2380		6.9				1998	2240	50.3	26400	5.3	
2014	Çakır and Sofyanlı [103]	C_2			C_1	0.50	3.4	0		22	22		2670							46.7			3.3
		C_2			C_1	0.50	3.4	50		12	22	2380	2670							46.9			3.8

		C_2			C_1	0.50	3.4	50		22	22	2380	2670						46.4			3.7
		C_2			C_1	0.50	3.4	100		22	22	2380							48.6			3.4
2014	Carneiro et al. [104]	C_1	C_1	B_2	C_1	0.52	2.2	0		19	10		2810		0.4				29.9	31100	3.6	3.2
		C_1	C_1	B_2	C_1	0.49	2.1	25		19	10	2500	2810	6.6	0.4				32.6	32100	3.3*	3.2
2014	Dilbas et al. [3]	C_2	C_2		C_2	0.50	3.5	50		8	20	2330	2750	3.8	0.8	41.4	24.3	2478	33.0	23437		2.2
		C_2	C_2		C_2	0.50	3.2	50		8	20	2280		4.1				2038	29.1	22896		1.6*
2014	Duan and Poon [105]	S_1	C_1		C_1	0.68	3.8	0		20	20		2600		0.9				34.5	25100		2.6
		S_1	C_1		C_1	0.68	3.6	100		20	20	2450		3.1					35.0	20850		2.5
		S_1	C_1		C_1	0.68	3.4	100		20	20	2370		7.1					29.2	21900		2.4
		S_1	C_1		C_1	0.68	3.4	100		20	20	2360		7.8					27.7	20490		1.9
		S_1	C_1		C_1	0.51	3.3	0		20	20		2600		0.9				48.3	30680		3.2
		S_1	C_1		C_1	0.51	3.1	100		20	20	2450		3.1					47.6	28860		3.4
		S_1	C_1		C_1	0.51	3.0	100		20	20	2370		7.1					42.0	24460		2.6
		S_1	C_1		C_1	0.51	3.0	100		20	20	2360		7.8					42.9	26550		2.6
		S_1	C_1		C_1	0.44	2.5	0		20	20		2600		0.9				61.6	32360		3.8
		S_1	C_1		C_1	0.44	2.4	100		20	20	2450		3.1					60.0	29420		3.9
		S_1	C_1		C_1	0.44	2.3	100		20	20	2370		7.1					53.7	24610		3.7
		S_1	C_1		C_1	0.44	2.3	100		20	20	2360		7.8					53.2	28500		3.4
		S_1	C_1		C_1	0.34	2.2	0		20	20		2600		0.9				80.8	35430		4.3
		S_1	C_1		C_1	0.34	2.1	100		20	20	2450		3.1					78.2	34760		4.7
		S_1	C_1		C_1	0.34	2.0	100		20	20	2370		7.1					71.2	29520		4.1
		S_1	C_1		C_1	0.34	2.0	100		20	20	2360		7.8					65.4	30620		4.2
2014	Folino and Xargay [106]	C_1	C_1		C_1	0.50	3.1	0		19	19		2730		0.3			2420	36.5	31667		4.0
		C_1	C_1		C_1	0.50	3.0	30		19	19	2570	2730	2.7	0.3			2385	33.6	28617		3.9
		C_1	C_1		C_1	0.50	3.0	60		19	19	2570	2730	2.7	0.3			2382	30.4	24533		3.9
		C_1	C_1		C_1	0.50	2.8	100		19	19	2570		2.7				2346	29.1	20750		3.3
2014	Gayarre et al. [107]	C_2				0.65	3.1	0		20	19		2500		1.7		32.0	2370	40.5			
		C_2				0.65	3.2	20		20	19	2300	2500	5.2	1.7	40.2	32.0	2340	39.5			
		C_2				0.65	3.2	50		20	19	2300	2500	5.2	1.7	40.2		2330	40.8			
		C_2				0.65	3.2	100		20	19	2300		5.2		40.2	32.0	2320	43.7*			
		C_2				0.65	3.1	0		20	19		2500		1.7		32.0	2370	40.5			
		C_2				0.65	3.1	20		20	19	2300	2500	5.5	1.7	28.6	32.0	2360	41.0			

		C_2				0.65	3.1	50		20	19	2300	2500	5.5	1.7	28.6	32.0		2350	38.8			
		C_2				0.65	3.2	100		20	19	2300		5.5		28.6			2350	39.9*			
2014	Kang et al. [108]	C_1	C_1	B_2	C_1	0.42	2.7	0		25	25		2570		1.1					38.6	29200	10.2*	3.3
		C_1	C_1	B_2	C_1	0.40	2.7	16		25	25	2200	2570	5.4	1.1					32.7*	29200	9.7*	3.0
		C_1	C_1	B_2	C_1	0.39	2.2	37		25	25	2200	2570	5.4	1.1					31.7*	26500	9.0*	2.7
		C_1	C_1	B_2	C_1	0.36	2.7	52		25	20	2200	2570	5.4	1.1					29.0*	25300	8.9*	2.7
2014	Pedro et al. [109]	S_1	C_2		C_2	0.86	4.6	0		22	20		2537		1.3					23.9	33300*		2.8
		S_1	C_2		C_2	0.65	3.4	0		22	20		2537		1.3					38.7	36700		3.2
		S_1	C_2		C_2	0.41	2.9	0		22	20		2537		1.3					71.1	46900		5.2
		S_1	C_2		C_2	0.87	4.6	100		22	20	2451		7.8						19.7	25200		2.0
		S_1	C_2		C_2	0.66	3.4	100		22	20	2387		6.9						35.7	29500		2.9
		S_1	C_2		C_2	0.42	2.8	100		22	20	2362		4.2						66.8	40300*		4.6*
		S_1	C_2		C_2	0.86	4.6	100		22	20	2456		7.5						21.8	26500		2.0
		S_1	C_2		C_2	0.65	3.5	100		22	20	2455		6.4						36.1	30000		2.9
		S_1	C_2		C_2	0.42	2.9	100		22	20	2496		4.2						68.5	40300*		4.8*
		S_1	C_2		C_2	0.81	4.9	0		22	20		2665		1.0					27.5	34700*		2.9
		S_1	C_2		C_2	0.63	3.6	0		22	20		2665		1.0					42.4	38300		3.3
		S_1	C_2		C_2	0.40	3.0	0		22	20		2665		1.0					72.3	47600		5.5*
		S_1	C_2		C_2	0.84	4.5	100		22	20	2401		7.6						21.0	25900		2.1
		S_1	C_2		C_2	0.63	3.5	100		22	20	2484		5.4						41.1	31200		3.0
		S_1	C_2		C_2	0.40	2.8	100		22	20	2363		3.6						70.2	40400*		4.9*
		S_1	C_2		C_2	0.82	4.7	100		22	20	2447		6.9						23.6	27800*		2.2
		S_1	C_2		C_2	0.64	3.4	100		22	22	2458		5.8						39.7	31500*		3.0
		S_1	C_2		C_2	0.42	2.9	100		22	22	2464		3.9						66.5	40200*		5.0*
2014	Pepe et al. [110]	C_1	C_1		C_1	0.64	3.0	0		19	20		2634		1.3					33.0	24770		3.9
		C_1	C_1		C_1	0.77	3.1	100		19	20	2268		4.9						27.5	24860		3.4*
		C_1	C_1		C_1	0.70	3.4	100		19	20	1946		11.9						29.9	24400		3.7*
2014	Thomas et al. [111]	C_1	C_1		C_1	0.60	3.6	0		19	19		2730		0.5		23.0		2410	47.8	34200		4.0
		C_1	C_1		C_1	0.59	3.3	20		19	19	2320	2730	5.3	0.5	37	23.0		2400	49.3	32300		4.1
		C_1	C_1		C_1	0.57	3.3	50		19	19	2320	2730	5.3	0.5	37	23.0		2380	47.5	30500		4.7*
		C_1	C_1		C_1	0.54	3.0	100		19	19	2320		5.3		37			2380	53.7*	30100		4.9*
		C_1	C_1		C_1	0.46	2.6	0		19	19		2730		0.5		23.0		2480	62.0	37400		4.6
		C_1	C_1		C_1	0.45	2.5	20		19	19	2320	2730	5.3	0.5	37	23.0		2450	64.8	36100		4.7
		C_1	C_1		C_1	0.44	2.5	50		19	19	2320	2730	5.3	0.5	37	23.0		2450	63.5*	34000		4.8*

		C_1	C_1		C_1	0.42	2.3	100		19	19	2320		5.3		37			2430	65.1*	31400		5.0*
		C_1	C_1		C_1	0.67	3.6	0		19	19		2730		0.5		23.0		2380	62.0*	34900		2.7
		C_1	C_1		C_1	0.68	3.4	20		19	19	2320	2730	5.3	0.5	37	23.0		2350	64.8*	32200		2.5
		C_1	C_1		C_1	0.67	3.0	50		19	19	2320	2730	5.3	0.5	37	23.0		2340	63.5*	30100		2.4
		C_1	C_1		C_1	0.70	2.3	100		19	19	2320		5.3		37			2300	65.1*	26800		2.3
		C_1	C_1		C_1	0.53	2.7	0		19	19		2730		0.5		23.0		2430	57.3	34900		3.7
		C_1	C_1		C_1	0.53	2.5	20		19	19	2320	2730	5.3	0.5	37	23.0		2410	54.9	33800		3.2
		C_1	C_1		C_1	0.53	2.2	50		19	19	2320	2730	5.3	0.5	37	23.0		2400	51.5*	32700		2.7
		C_1	C_1		C_1	0.52	1.8	100		19	19	2320		5.3		37			2370	50.3	30200		2.4
		C_1	C_1		C_1	0.51	3.1	0		19	19		2730		0.5		23.0		2430	60.1	36300		3.3
		C_1	C_1		C_1	0.52	3.2	20		19	19	2320	2730	5.3	0.5	37	23.0		2420	56.5	35500		2.9
		C_1	C_1		C_1	0.54	3.0	50		19	19	2320	2730	5.3	0.5	37	23.0		2400	48.9	33400		2.6
		C_1	C_1		C_1	0.58	2.8	100		19	19	2320		5.3		37			2340	43.1	31500		2.4
		C_1	C_1		C_1	0.42	2.7	0		19	19		2730		0.5		23.0		2490	72.9	38700		4.1
		C_1	C_1		C_1	0.42	2.9	20		19	19	2320	2730	5.3	0.5	37	23.0		2460	67.4	35900		3.5
		C_1	C_1		C_1	0.44	2.7	50		19	19	2320	2730	5.3	0.5	37	23.0		2400	61.2	32900		2.9
		C_1	C_1		C_1	0.49	2.5	100		19	19	2320		5.3		37			2390	53.7	28400		2.5
2014	Wardeh et al. [28]	S_1	C_1	B_1	C_1	0.50	2.9	0		20	20			6.5						37.0	39500	4.9	3.5
		S_1	C_1	B_1	C_1	0.50	2.5	30		20	20	2240		6.5						33.0	36000	4.7	3.2
		S_1	C_1	B_1	C_1	0.50	1.4	65		20	20	2240		6.5						39.5*	33500*	4.4*	3.2*
		S_1	C_1	B_1	C_1	0.50	1.2	100		20	20	2240								39.0	30500	4.0	3.0
2014	Capitanio et al. [112]	C_1	C_1	B_1	C_2	0.55	2.8	0		12	12		2710		2.0				2347	40.9	29300	5.1	3.2
		C_1	C_1	B_1	C_2	0.53	2.6	25		12	12	2220	2710	6.1	2.0				2289	41.0	29000	4.7	2.6
		C_1	C_1	B_1	C_2	0.51	2.5	50		12	12	2220	2710	6.1	2.0				2236	40.5	28200	4.6	2.6
		C_1	C_1	B_1	C_2	0.47	2.1	100		12	12	2220		6.1					2199	40.3	27200	3.7	2.4
		C_1	C_1	B_1	C_2	0.47	2.1	100		7	7	2220			2.0				2138	38.0	26700	3.4	2.3
		C_1	C_1	B_1	C_2	0.53	2.7	0		7	7		2570	4.1	2.0				2287	40.1	28100	5.3	3.3
		C_1	C_1	B_1	C_2	0.49	2.4	50		7	7	2150	2570	4.1	2.0				2174	41.2	27900	5.0	3.0
		C_1	C_1	B_1	C_2	0.45	2.1	100		7	7	2150	2570	4.1	2.0				2147	40.8	25700	3.9	2.5
		C_1	C_1	B_1	C_2	0.45	2.1	100		7	7	2150		4.1					2115	39.2	25100	3.6	2.4

*Datasets that deviated significantly from the global trend-lines of the database (i.e. ± 50%)

C_1 = 100 × 200 mm cylinders; C_2 = 150 × 300 mm cylinders; S_1 = 100 mm cubes; S_2 = 150 mm cubes; B_1 = 100 × 100 × 500 mm beam specimens; B_2 = 150 × 150 × 750 mm beam specimens.

Appendix 2. Supporting information of GO study

This section includes materials and testing figures, enlarged SEM images, and TGA results.

Graphene materials, AFM analysis, and Raman spectra

Figures A1(a)-(c) show the graphite powder, final GO solution, and AFM analysis results on GO solution, respectively. Figure A1(d) shows a typical Raman spectrum of GO with its characteristic D and G bands at 1350 and 1590 cm^{-1}, respectively, due to its amorphous state. As can be seen in Fig. A1(d), graphite is highly crystalline which is supported by its small defect D band, sharp graphitic G band, and the appearance of the typical 2D band at 2720 cm^{-1}, showing the complete transformation of GO from the exfoliated graphite.

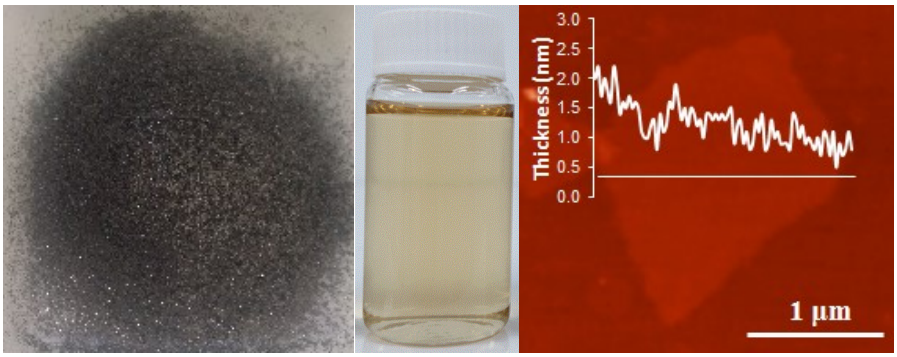

(a) (b) (c)

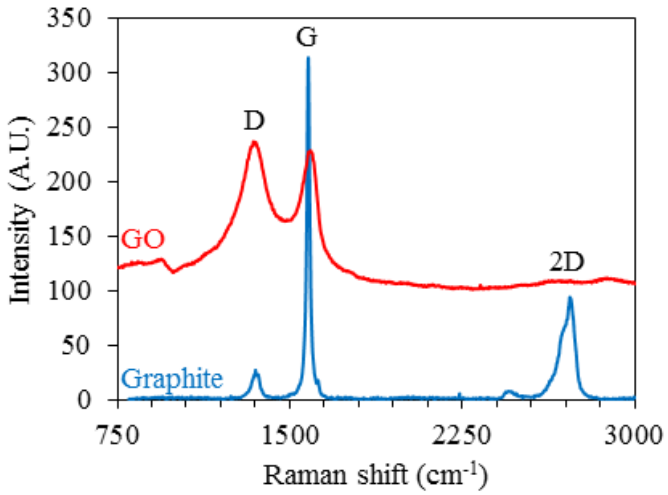

(d)

Figure A1. Illustration of (a) graphite powder, (b) GO solution (1 mg/ml), (c) AFM image of a GO sheet with the height profile superimposed onto the image, (d) Raman spectra of graphite and GO

Sand and cement properties, mix proportions, properties of superplasticizer. and flowability test results

Tables A1 and A2 show the particle size distribution of the sand and chemical composition of the Portland cement used in this study, respectively. The mix proportions of different mixes are shown in Table A3. Table A4 shows the properties of the superplasticizer. Table A5 presents the flowability tests results of the GO-cement mortar composites.

Table A1. Particle size distribution of sand

Mesh size (mm)	2	1.6	1	0.5	0.16	0.08
Remaining on the sieve (%)	0	7 ± 5	33 ± 5	67 ± 5	87 ± 5	99 ± 1

Table A2. Chemical composition of Portland cement (%)

SiO_2	Al_2O_3	Fe_2O_3	CaO	MgO	Na_2O	K_2O	SO_3	P_2O_5
19.95	4.79	3.14	63.28	2.03	0.29	0.4	2.69	0.04

Table A3. Mix proportions of the GO–cement mortar samples

GO (%)	*w/c*	Cement (kg/m^3)	Water (kg/m^3)	GO (kg/m^3)	Sand (kg/m^3)	Superplasticizer (kg/m^3)
0	0.485	527	256	0.0	1448	1.4
0.01	0.485	527	256	0.1	1448	1.4
0.03	0.485	527	256	0.2	1448	1.4
0.05	0.485	527	256	0.3	1448	1.4
0.07	0.485	527	256	0.4	1448	1.4
0.1	0.485	527	256	0.5	1448	1.4
0.3	0.485	527	256	1.6	1447	1.4
0.5	0.485	527	256	2.6	1446	1.4

Table A4. Properties of polycarboxylic ether polymer-based superplasticizer

Density (20°C) (kg/dm^3)	pH	Boiling temperature (°C)	Flash point (°C)	Vapour pressure (20°C) (hPa)	Solid content (mass, %)
1.06	6.4	≥ 100	> 100	23	30.7

Table A5. Flowability tests results of GO-cement mortar composites

GO (%)	0	0.01	0.03	0.05	0.07	0.1	0.3	0.5
Flow (%)	140	140	139	138	138	138	135	131

Tension and compression tests

Figure A2 shows samples used in direct tension and compression tests. Figure A3 shows the universal and material testing machines for tension and compression tests.

Figure A2. GO–cement mortar composite samples

(a)

(b)

Figure A3. (a) Universal testing machine for tension test; (b) Material testing machine for compression test

Enlarged SEM images

Figures A4 and A5 show the enlarged SEM images of cracking pattern and GO dispersion of GO–cement mortar composites, respectively.

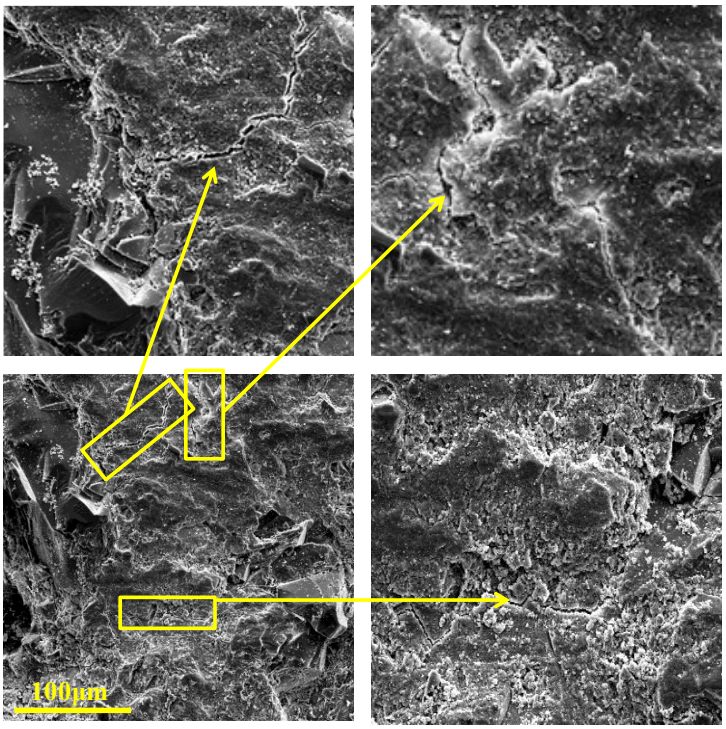

(a)

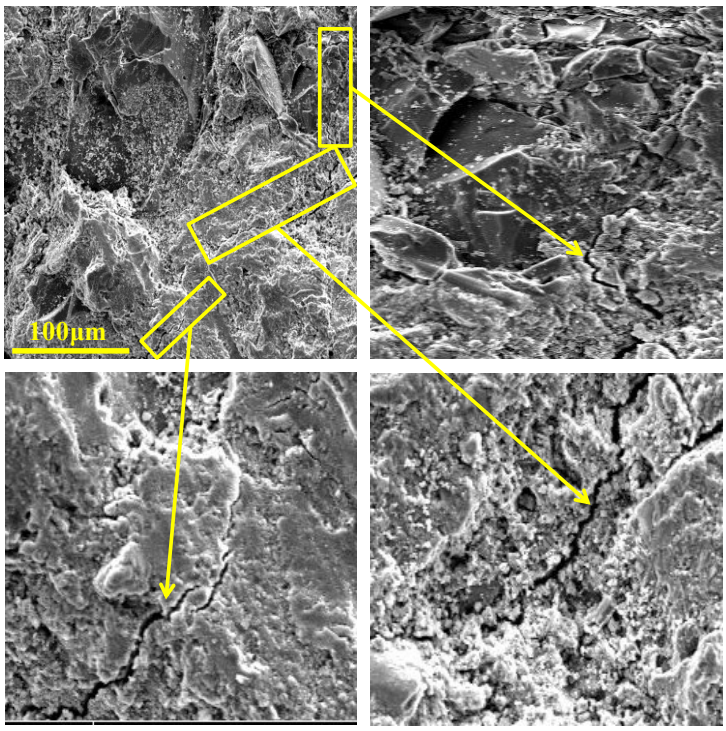

(b)

Figure A4. Enlarged SEM images of cracking patterns of cement mortar composite with: (a) GO=0%; (b) GO=0.5%

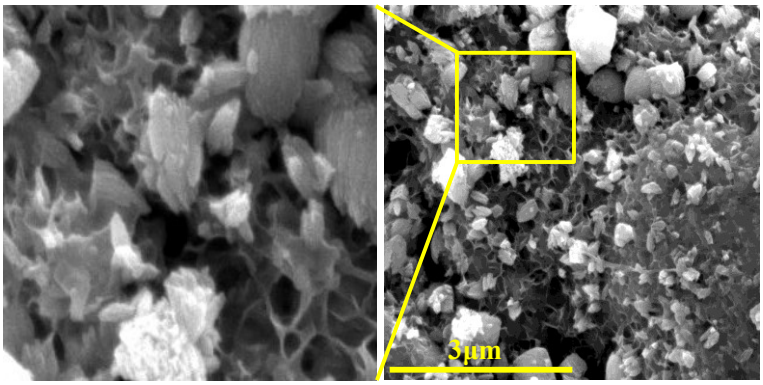

(a)

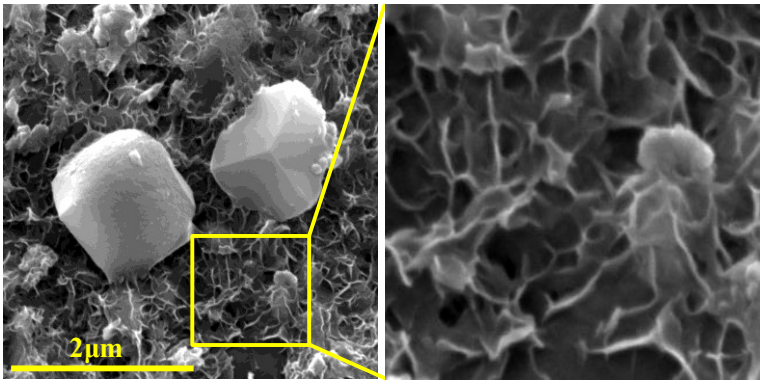

(b)

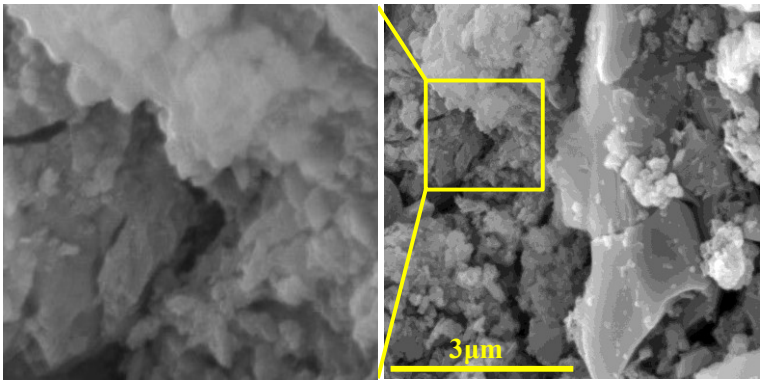

(c)

Figure A5. Enlarged SEM images of: (a) dispersed GO sheets between cement mortar particles in composite with GO=0.03%; (b) dispersed cement particles between GO sheets in composite with GO=0.1%; (c) poor dispersed cement particles between GO platelets in composite with GO=0.5%

TGA results

Figures A6 shows the TGA test results on cement mortar composites.

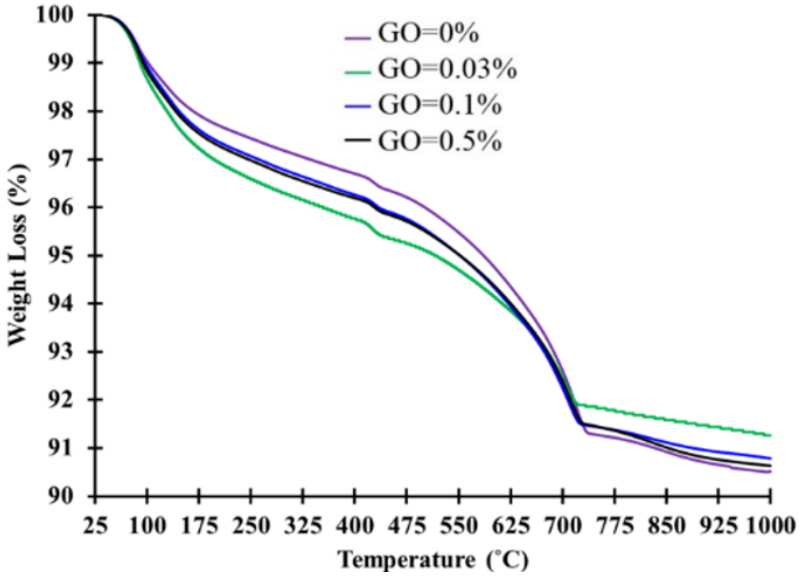

(a)

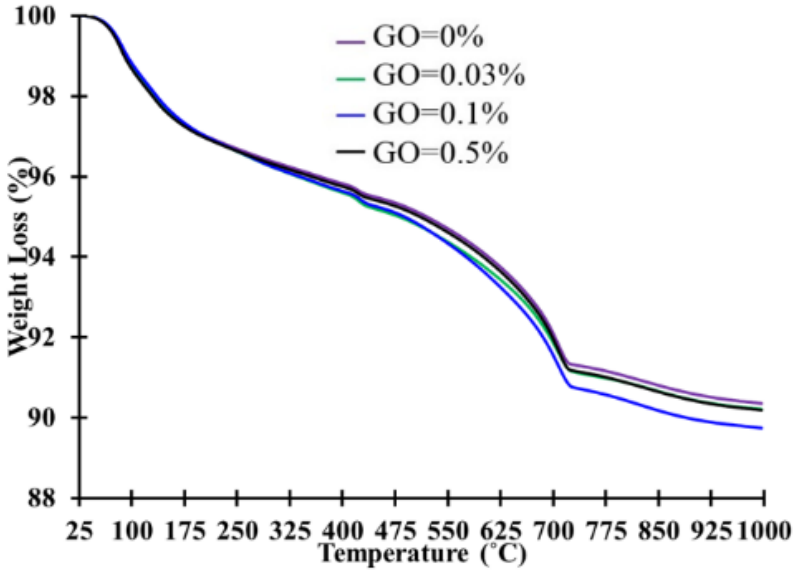

(b)

Figure A6. TGA curves of GO–cement composite with different GO contents as a function of temperature after: (a) 7 days; (b) 28 days curing

Comparative FTIR spectra

Figure A7 shows the FTIR results of GO, cement, sand, and Go-cement mortar composites.

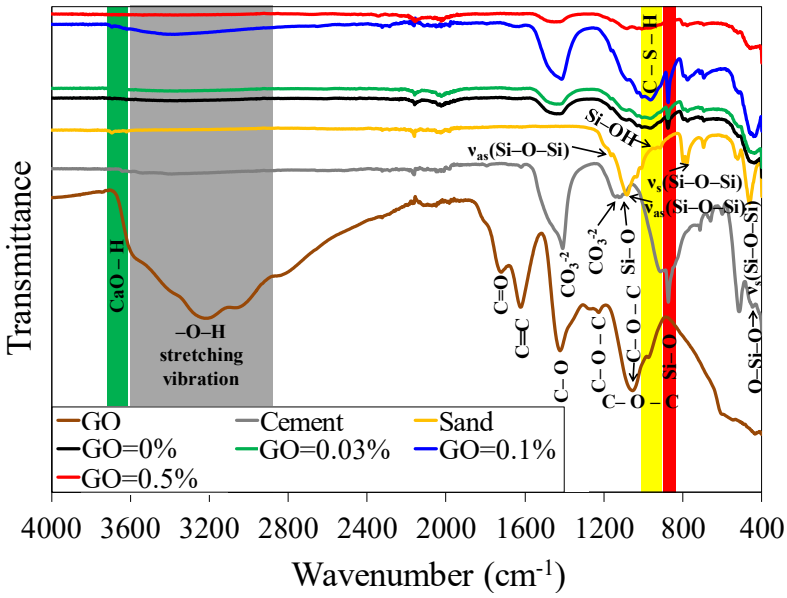

Figure A7. Comparative FTIR spectra of GO (control), Cement (control), Sand (control), and GO–cement mortar with 0%, 0.03%, 0.1%, and 0.5% GO

Appendix 3. Supporting information of rGO study

This section includes materials, testing figures, contact angle curves of GO/rGO, TGA analysis, and tension and compression test results.

Hydrazine amount for GO oxygen reduction

Table A6 presents the hydrazine amounts (volume, weight percentage of GO, and concentration) used in this study for reduction of oxygen functionalities of GO.

Table A6. Amount of hydrazine used in GO

No.	Volume (ml)	Weight percentage of GO (%)	Concentration (mg/ml)
1	0.6	0.1	12.2
2	0.9	0.15	18.4
3	1.2	0.2	24.5
4	1.8	0.3	36.7
5	2.4	0.4	49.0

Cement and sand materials and mix proportions of the composite

Tables A7 and A8 show the particle size distribution of sand and chemical composition of cement, respectively. Table A9 shows the mix proportions of different mixes.

Table A7. Particle size distribution of sand

Mesh size (mm)	2	1.6	1	0.5	0.16	0.08
Remaining on the sieve (%)	0	7 ± 5	33 ± 5	67 ± 5	87 ± 5	99 ± 1

Table A8. Chemical composition of Portland cement (%)

SiO_2	Al_2O_3	Fe_2O_3	CaO	MgO	Na_2O	K_2O	SO_3	P_2O_5	LOI
19.95	4.79	3.14	63.28	2.03	0.29	0.4	2.69	0.04	3.39

Table A9. Mix proportions of the cement mortar composites

Mix	*w/c*	Cement (kg/m^3)	Water (kg/m^3)	Sand (kg/m^3)	Hydrazine (%)	Oxygen reduction time (min)	GO or rGO (kg/m^3)	Superplasticizer (kg/m^3)
Plain	0.485	527	256	1448	0	0	0	1.4
GO	0.485	527	256	1448	0	0	0.4	1.4
RG1.2T5	0.485	527	256	1448	0.2	5	0.4	1.4
RG1.2T10	0.485	527	256	1448	0.2	10	0.4	1.4
RG1.2T15	0.485	527	256	1448	0.2	15	0.4	1.4
RG1.2T30	0.485	527	256	1448	0.2	30	0.4	1.4
RG1.2T60	0.485	527	256	1448	0.2	60	0.4	1.4
RG0.6T15	0.485	527	256	1448	0.1	15	0.4	1.4
RG0.9T15	0.485	527	256	1448	0.15	15	0.4	1.4
RG1.8T15	0.485	527	256	1448	0.3	15	0.4	1.4
RG2.4T15	0.485	527	256	1448	0.4	15	0.4	1.4

Tension and compression testing

Figure A8 shows the universal and material testing machines for tension and compression tests.

(a) (b)

Figure A8. (a) Universal testing machine for tension test; (b) Material testing machine for compression test

Characterization of GO

Figure A9 shows the characterization results of GO material used in this study by TEM, XRD, TGA, and AFM analysis.

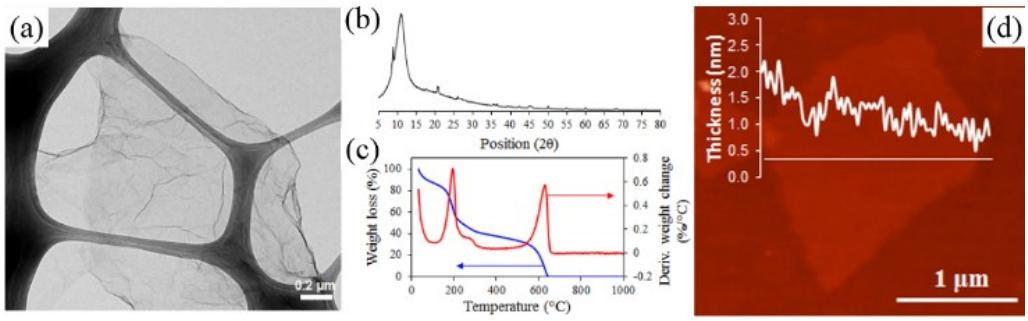

Figure A9. (a) TEM image, (b) XRD analysis, (c) TGA analysis, and (d) AFM image of a GO sheet with the height profile superimposed onto the image

Contact angle curves of GO and rGO

Figure A10 shows the optical microscopy images of the static water bubble on the GO/rGO films.

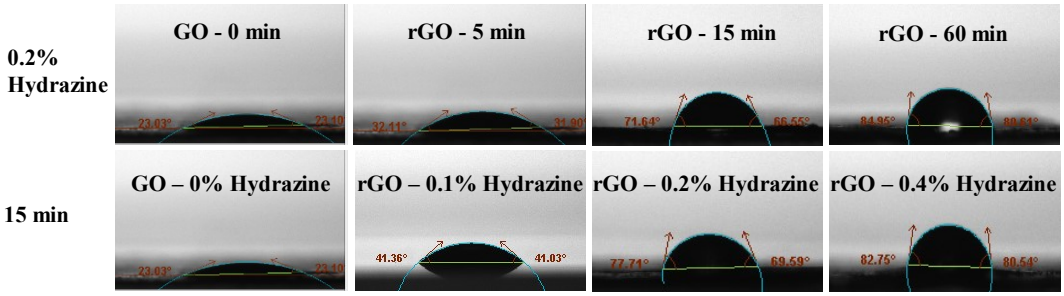

Figure A10. The optical microscopy images of the static water bubble on the GO/rGO films together with contact angle measurement for different reduction conditions: (top row) fixed hydrazine percentage (0.2%), different reduction times (5, 15, and 60 min), (bottom row) fixed reduction time (15 min), different hydrazine weight percentages (0.1, 0.2, and 0.4%)

TGA curves

The TGA analysis results from the samples were plotted in Fig. A11.

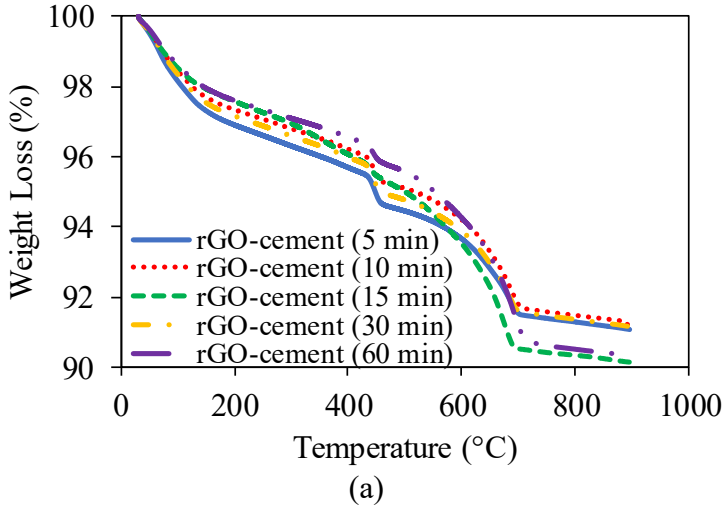

(a)

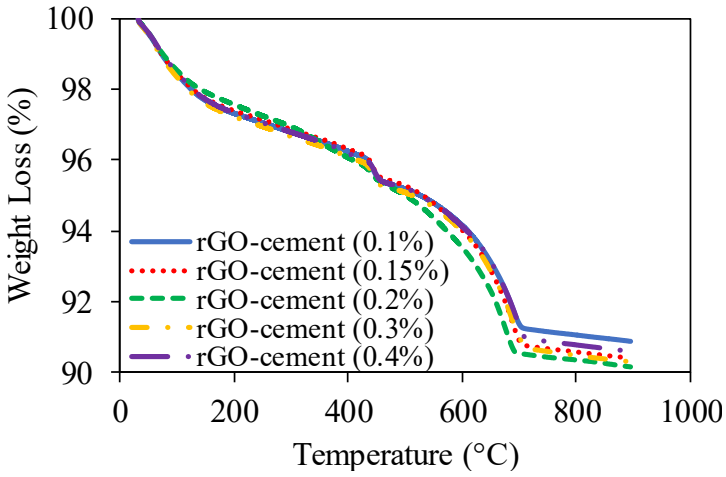

(b)

Figure A11. TGA curves of the rGO–cement paste composite at 28 days: a) fixed hydrazine concentration (0.2%), different reduction times (5, 10, 15, 30, and 60 min); b) fixed reduction time (15 min), different hydrazine concentrations (0.1, 0.15, 0.2, 0.3, and 0.4%)

Tensile and compressive strength test results

Table A10 shows the tensile and compressive strength test results and strength enhancements compared to the control plain mortar.

Table A10. Tensile and compressive strength test results of the cement mortar composites

Mix	Tensile strength (MPa)		Enhancement compared to Plain mix (%)		Compressive strength (MPa)		Enhancement compared to Plain mix (%)	
	7-day	28-day	7-day	28-day	7-day	28-day	7-day	28-day
Plain	3.6	4.0 (11.1)*	–	–	25.2	30.0 (19.0)	–	–
GO	5.2	5.5 (5.8)	44.4	37.5	36.8	53.3 (44.8)	46.0	77.7
RG0.2T5	4.7	5.1 (8.5)	30.6	27.5	33.3	49.1 (47.4)	32.1	63.7
RG0.2T10	5.2	5.6 (7.7)	44.4	40.0	37.5	53.4 (42.4)	48.8	78.0
RG0.2T15	5.3	5.8 (9.4)	47.2	45.0	38.2	55.1 (44.2)	51.6	83.7
RG0.2T30	4.9	5.3 (8.2)	36.1	32.5	35.4	52.3 (47.7)	40.5	74.3
RG0.2T60	4.5	4.8 (6.7)	25.0	20.0	29.2	45.2 (54.8)	15.9	50.7
RG0.1T15	5.2	5.6 (7.7)	44.4	40.0	37.1	53.2 (43.4)	47.2	77.3
RG0.15T15	5.3	5.7 (7.5)	47.2	42.5	37.9	54.2 (43.0)	50.4	80.7
RG0.3T15	5.1	5.6 (9.8)	41.7	40.0	37.4	53.4 (42.8)	48.4	78.0
RG0.4T15	5.0	5.4 (8.0)	38.9	35.0	35.1	50.6 (44.2)	39.3	68.7

* Values in parenthesis is the increase in the strength from 7-day to 28-day in percentage.

Appendix 4. Supplemantary file of SFRC study

The script code used for the concrete material behaviour based on the developed damage-plasticity model is presented as a supplementary file.

```
##########################
# UNITS are in SI (mm) #
# Length = millimetre  #
# Force  = Newton      #
# Time   = Second      #
# Mass   = Tonne       #
##########################
CompressionForm = 'damageplasticity'
concreteMats        = {'Concrete': 131.6}
volumefraction      = {'vf': 0.015}
aspectratio         = {'ar': 67}
Density              = 2.5E-9 #Tonne/mm3
Meu                  = 0.18
DilationAngle        = 35
Eccentricity         = 0.1
ViscosityParam       = 0
TensionRecovery   = 0
CompresRecovery = 1
#############################################################################
from part import *
from material import *
from section import *
from assembly import *
from step import *
from interaction import *
from load import *
from mesh import *
from optimization import *
from job import *
```

```
from sketch import *
from visualization import *
from connectorBehavior import *
##########################################################################
session.journalOptions.setValues(replayGeometry=COORDINATE,
recoverGeometry=COORDINATE)
##########################################################################
def roundList(list,V):
    for x in range(len(list)):
        list[x]=round(list[x],V)
    return(list)
f_cc = f_c + 5.2*(1 + 0.065*vf)*(f_c**0.91)*(0 / f_c)**(f_c**(-0.06))
def Concrete(f_cc):
    elim  =  1- exp(-f_c/80.)
    if elim>0.4: elim= 0.4
    fb0_fc0  =  1.57*(f_c**(-.09))
    K  =  0.71*(f_c**(-.025))
    Ec  =  4400.*f_c**0.5 *((Density / (2.4E-9))**1.4)
    e_c0  =  elim*f_c / Ec
    f_cres  =  1.6*f_cc*(0 / f_c**0.32)
    n  =  f_c/17. + 0.8
    e_c  =  f_c/Ec * n/(n-1)
    e_ci  =  (2.8*e_c*(f_cres / f_cc)*(f_c**(-.12))+10*e_c*(1-(f_cres /
  f_cc))*(f_c**(-.47)))*((Density /  (2.4E-9))**.4)
    r  =  (Ec) / (Ec-(f_cc / e_c))
    Sf  =  f_c / 10.
    e_ct  =  Sf / Ec
    ecut  =  10*e_ct
    frac  =  5.
    strainc  =  [x*(e_c-e_c0)/frac for x in range(70)]
    if   CompressionForm =='damageplasticity':
        stressc = [f_cc*r*((strainc[x]+e_c0)/e_c)/(r-1+((strainc[x]+e_c0)/e_c)**r) if
       e_c0 <= strainc[x]+e_c0 else f_cc-((f_cc-f_cres)/(1+((strainc[x]+e_c0-
       e_c)/(e_ci-e_c)))**(-2)) for x in range(70)]
```

```
        dc  =  [1-stressc[x]/f_c if (strainc[x]+e_c0)> e_c else 0.0 for x in range(70)]
        straint = [x*e_ct for x in range(5)]
        stresst = [Sf*(e_ct/(straint[x]+e_ct))**0.85 for x in range(5)]
        dt  =  [1-stresst[x]/Sf if (straint[x])> 0.0 else 0.0  for x in range(5)]
        e_c = (e_l / (3*(1+(e_l/3*e_c0)**n)^0.33)) +
        0.04*(e_l**0.7)*(1+0.23*vf*ar**(-     0.5))*(1+21*(0/f_c)**0.8)
        DilationAngle = -1.5*((e_c/e_l) + 2) / ((e_c/e_l) - 1)
        CompreB = zip(roundList(stressc,5),roundList(strainc,5))
        CompreD = zip(roundList(dc,5),roundList(strainc,5))
        TensioB = zip(roundList(stresst,5),roundList(straint,5))
        TensioD = zip(roundList(dt,5),roundList(straint,5))
        A  =  [stresst[x]/Sf for x in range(len(stresst))]
        TenStif = zip(roundList(A,5),roundList(straint,5))
        return (CompreB,CompreD,TensioB,TensioD,TenStif,round(Ec,5))
######################################################################
for x in concreteMats.keys():
    CompreB,CompreD,TensioB,TensioD,TenStif,Ec = Concrete(concreteMats[x])
    mdb.models['Model-1'].Material(name=x+'CDP')
    mdb.models['Model-1'].materials[x+'CDP'].Density(table=((Density, ), ))
    mdb.models['Model-1'].materials[x+'CDP'].Elastic(table=((Ec,Meu), ))
    mdb.models['Model-
     1'].materials[x+'CDP'].ConcreteDamagedPlasticity(table=((DilationAngle,
     Eccentricity,fb0_fc0,K,ViscosityParam), ))
    mdb.models['Model-1'].materials[x+'CDP'].concreteDamagedPlasticity.
     ConcreteCompressionHardening(rate=OFF,table=CompreB)
    mdb.models['Model-1'].materials[x+'CDP'].concreteDamagedPlasticity.
     ConcreteCompressionDamage(tensionRecovery=TensionRecovery,table=Comp
     reD)
    mdb.models['Model-1'].materials[x+'CDP'].concreteDamagedPlasticity.
     ConcreteTensionStiffening(rate=OFF,table=TensioB)
    mdb.models['Model-1'].materials[x+'CDP'].concreteDamagedPlasticity.
     ConcreteTensionDamage(compressionRecovery=CompresRecovery,table=Tens
     ioD)
```

Appendix 5. Concrete damage-plasticity model

This section presents the details of the concrete damage-plasticity method. The failure surface of the concrete damage-plasticity method is presented by Eq. A1 [36].

$$F = \frac{1}{1-\alpha}\left(\bar{q} - 3\alpha\bar{p} + \beta\left(\bar{\varepsilon}_p\right)\langle-\bar{\sigma}_{min}\rangle - \gamma\langle\bar{\sigma}_{min}\rangle\right) - \bar{\sigma}_c\left(\bar{\varepsilon}_{c,p}\right) \leq 0 \quad \text{(A1)}$$

where $\overline{\sigma}_{min}$ is the minimum principal effective stress and the parameters $\bar{p}$, $\bar{q}$, α, $\beta(\overline{\varepsilon}_p)$, and γ are defined in Eqs. A2 to A6, respectively.

$$\bar{p} = \frac{-\bar{I}_1}{3} \quad \text{(A2)}$$

$$\bar{q} = \sqrt{3\bar{J}_2} \quad \text{(A3)}$$

$$\alpha = \frac{f'_{bo} - f'_{co}}{2f'_{bo} - f'_{co}} \quad \text{(A4)}$$

$$\beta\left(\bar{\varepsilon}_p\right) = \frac{\overline{\sigma}_c\left(\bar{\varepsilon}_{c,p}\right)}{\overline{\sigma}_t\left(\bar{\varepsilon}_{t,p}\right)}(1-\alpha) - (1+\alpha) \quad \text{(A5)}$$

$$\gamma = \frac{3(1-K_c)}{2K_c - 1} \quad \text{where} \quad K_c = \frac{q_{tm}}{q_{cm}} \quad \text{(A6)}$$

where $\bar{p}$ is the equivalent effective stress, $\bar{q}$ is the cylindrical coordinates of equivalent pressure, $\bar{I}_1$ and $\bar{J}_2$ are the first invariant of effective stress and second invariant of the effective stress deviator, f'_{bo} and f'_{co} are the biaxial and uniaxial compressive strengths, $\overline{\sigma}_c$ and $\overline{\sigma}_t$ are the effective compressive and tensile cohesion stresses, $\overline{\varepsilon}_{c,p}$ and $\overline{\varepsilon}_{t,p}$ are the equivalent compressive and tensile plastic strains, and q_{tm} and q_{cm} are the second stress invariants on the tensile and compression meridians, respectively. As was shown in Refs. [31,34] of Paper No. 12, f'_{bo}/f'_{co} and tensile-to-compression meridian stress ratio (K_c) are defined as $1.57{f'_{co}}^{-0.09}$ and $0.71{f'_{co}}^{-0.025}$, respectively, which were obtained based on a large experimental database of confined plain concrete.

Parameter of α in Eq. A5 is defined by the following expression for addressing the exact and curve shape compression and tensile meridians while satisfying the original form of f'_{bo}/f'_{co} ratio.

$$\alpha = \frac{k_b - 1}{2 + k_b}\left(\frac{\gamma}{3} + 1\right) - \frac{\gamma}{3} \tag{A7}$$

in which k_b is the enhancement ratio of f^*_{cc} under uniform confining pressure (f^*_l) and it is obtained from the following expression:

$$k_b = \frac{f^*_{cc} - f'_{co}}{f^*_l} \tag{A8}$$

Eq. 12.8 is used to establish a relationship between f^*_{cc} and f^*_l in Eq. A8.

The non-associated potential flow rule with the plastic potential function (G) and the plastic strain vector ($d\varepsilon_p$) are defined by Eqs. A9 and A10 in concrete damage-plasticity theory, respectively.

$$G = \sqrt{(\epsilon f'_t \tan\psi)^2 + \bar{q}^2} - \bar{p}\tan\psi \tag{A9}$$

$$d\varepsilon_p = \lambda \frac{\partial G}{\partial \sigma} \tag{A10}$$

in which ψ is the plastic dilation angle measured in the $\bar{p}$–$\bar{q}$ plane at high confining pressure, f'_t is the uniaxial tensile strength, and ϵ is the eccentricity parameter that defines the rate at which the G function tends to a straight line as the eccentricity tends to zero. The relationship between ψ and plastic strains is defined by Eq. A11 [29].

$$\tan\psi = -\frac{3\left(d\varepsilon_{c,p} + 2d\varepsilon_{l,p}\right)}{2\left(d\varepsilon_{c,p} - d\varepsilon_{l,p}\right)} \tag{A11}$$

For calculating ψ, Eq. 12.3 is used to define the relationship between the axial strain (ε_c) and lateral strain (ε_l) of FRP-confined SFRCs. In Eq. 12.3, f_l is a variable parameter for the FRP-confined SFRC that gradually increases with an increase in ε_l until $\varepsilon_{h,rup}$ (determined using Eq. 12.1) is reached and the resulting $f_{lu,a}$ is developed.